

Engineering Optimization: Methods and Applications

V. K. Mathew

Tapano Kumar Hotta

Hafiz Muhammad Ali

Senthilarasu Sundaram *Editors*

# Energy Storage Systems

Optimization and Applications



Springer

# **Engineering Optimization: Methods and Applications**

## **Series Editors**

Anand J. Kulkarni, Department of Mechanical Engineering, Symbiosis Institute of Technology, Pune, Maharashtra, India

Amir H. Gandomi, Engineering & Information Technology, University of Technology Sydney, Sydney, NSW, Australia

Seyedali Mirjalili, Brisbane, QLD, Australia

Nikos D. Lagaros, National Technical University of Athens, Athens, Greece

Warren Liao, LSU, Construction Management Department, Baton Rouge, LA, USA

Optimization carries great significance in both human affairs and the laws of nature. It refers to a positive and intrinsically human concept of minimization or maximization to achieve the best or most favorable outcome from a given situation. Besides, as the resources are becoming scarce there is a need to develop methods and techniques which will make the systems extract maximum from minimum use of these resources, i.e. maximum utilization of available resources with minimum investment or cost of any kind. The resources could be any, such as land, materials, machines, personnel, skills, time, etc. The disciplines such as mechanical, civil, electrical, chemical, computer engineering as well as the interdisciplinary streams such as automobile, structural, biomedical, industrial, environmental engineering, etc. involve in applying scientific approaches and techniques in designing and developing efficient systems to get the optimum and desired output. The multifaceted processes involved are designing, manufacturing, operations, inspection and testing, forecasting, scheduling, costing, networking, reliability enhancement, etc. There are several deterministic and approximation-based optimization methods that have been developed by the researchers, such as branch-and-bound techniques, simplex methods, approximation and Artificial Intelligence-based methods such as evolutionary methods, Swarm-based methods, physics-based methods, socio-inspired methods, etc. The associated examples are Genetic Algorithms, Differential Evolution, Ant Colony Optimization, Particle Swarm Optimization, Artificial Bee Colony, Grey Wolf Optimizer, Political Optimizer, Cohort Intelligence, League Championship Algorithm, etc. These techniques have certain advantages and limitations and their performance significantly varies when dealing with a certain class of problems including continuous, discrete, and combinatorial domains, hard and soft constrained problems, problems with static and dynamic in nature, optimal control, and different types of linear and nonlinear problems, etc. There are several problem-specific heuristic methods are also existing in the literature.

This series aims to provide a platform for a broad discussion on the development of novel optimization methods, modifications over the existing methods including hybridization of the existing methods as well as applying existing optimization methods for solving a variety of problems from engineering streams. This series publishes authored and edited books, monographs, and textbooks. The series will serve as an authoritative source for a broad audience of individuals involved in research and product development and will be of value to researchers and advanced undergraduate and graduate students in engineering optimization methods and associated applications.

V. K. Mathew · Tapano Kumar Hotta ·  
Hafiz Muhammad Ali · Senthilarasu Sundaram  
Editors

# Energy Storage Systems

Optimization and Applications

 Springer



*Editors*

V. K. Mathew  
Department of Mechanical Engineering,  
MIT School of Engineering  
MIT-ADT University  
Pune, Maharashtra, India

Hafiz Muhammad Ali  
Department of Mechanical Engineering  
Interdisciplinary Research Center for  
Renewable Energy and Power Systems  
(IRC-REPS)  
King Fahd University of Petroleum  
and Minerals  
Dhahran, Saudi Arabia

Tapano Kumar Hotta  
School of Mechanical Engineering  
Vellore Institute of Technology  
Vellore, India

Senthilarasu Sundaram  
School of Engineering and the Built  
Environment  
Edinburgh Napier University  
Edinburgh, UK

ISSN 2731-4049

ISSN 2731-4057 (electronic)

Engineering Optimization: Methods and Applications

ISBN 978-981-19-4501-4

ISBN 978-981-19-4502-1 (eBook)

<https://doi.org/10.1007/978-981-19-4502-1>

© The Editor(s) (if applicable) and The Author(s), under exclusive license to Springer Nature Singapore Pte Ltd. 2023

This work is subject to copyright. All rights are solely and exclusively licensed by the Publisher, whether the whole or part of the material is concerned, specifically the rights of translation, reprinting, reuse of illustrations, recitation, broadcasting, reproduction on microfilms or in any other physical way, and transmission or information storage and retrieval, electronic adaptation, computer software, or by similar or dissimilar methodology now known or hereafter developed.

The use of general descriptive names, registered names, trademarks, service marks, etc. in this publication does not imply, even in the absence of a specific statement, that such names are exempt from the relevant protective laws and regulations and therefore free for general use.

The publisher, the authors, and the editors are safe to assume that the advice and information in this book are believed to be true and accurate at the date of publication. Neither the publisher nor the authors or the editors give a warranty, expressed or implied, with respect to the material contained herein or for any errors or omissions that may have been made. The publisher remains neutral with regard to jurisdictional claims in published maps and institutional affiliations.

This Springer imprint is published by the registered company Springer Nature Singapore Pte Ltd. The registered company address is: 152 Beach Road, #21-01/04 Gateway East, Singapore 189721, Singapore

---

The original version of this book was inadvertently published without the “Acknowledgements” section in the front matter. This section have been included in the book.

# **Acknowledgements**

Hafiz Muhammad Ali thankfully acknowledges the support of King Fahd University of Petroleum and Minerals, Dhahran, 31261, Saudi Arabia.

# Contents

<b>1</b>	<b>Artificial Intelligence Based Integrated Renewable Energy Management in Smart City</b> .....	<b>1</b>
	Avinash Kaldate, Amarsingh Kanase-Patil, and Shashikant Lokhande	
<b>2</b>	<b>The Role of Lower Thermal Conductive Refractory Material in Energy Management Application of Heat Treatment Furnace</b> .....	<b>21</b>
	Akshay Deshmukh, Virendra Talele, and Archana Chandak	
<b>3</b>	<b>Thermal Energy Storage Methods and Materials</b> .....	<b>39</b>
	Santosh Chavan	
<b>4</b>	<b>Heat Flow Management in Portable Electronic Devices</b> .....	<b>63</b>
	Sagar Mane Deshmukh and Virendra Bhojwani	
<b>5</b>	<b>A Review on Phase Change Material–metal Foam Combinations for Li-Ion Battery Thermal Management Systems</b> .....	<b>115</b>
	S. Babu Sanker and Rajesh Baby	
<b>6</b>	<b>Performance Enhancement of Thermal Energy Storage Systems Using Nanofluid</b> .....	<b>135</b>
	Vednath P. Kalbande, Pramod V. Walke, Kishor Rambhad, Man Mohan, and Abhishek Sharma	
<b>7</b>	<b>Inoculum Ratio Optimization in Anaerobic Digestion of Food Waste for Methane Gas Production</b> .....	<b>151</b>
	Parag K. Talukdar, Varsha Karnani, and Palash Saikia	
<b>8</b>	<b>Nano-Mixed Phase Change Material for Solar Cooker Application</b> .....	<b>165</b>
	C. V. Papade and A. B. Kanase-Patil	

<b>9</b>	<b>Technical Review on Battery Thermal Management System for Electric Vehicle Application</b> .....	177
	Virendra Talele, Pranav Thorat, Yashodhan Pramod Gokhale, and Hemalatha Desai	
<b>10</b>	<b>Battery Thermal Management System for EVs: A Review</b> .....	227
	Amit Jomde, Prashant Patane, Anand Nadgire, Chetan Patil, Kshitij Kolas, and Virendra Bhojwani	
<b>11</b>	<b>Design and Development of a Water-Cooled Proton Exchange Membrane Fuel Cell Stack for Domestic Applications</b> .....	249
	Justin Jose, Rincemon Reji, and Rajesh Baby	
<b>12</b>	<b>Analysis of Combustion and Performance Characteristics of a Producer Gas-Biodiesel Operated Dual Fuel Engine</b> .....	267
	Pradipta Kumar Dash, Shakti Prakash Jena, and Harish Chandra Das	
<b>13</b>	<b>Influence of Biogas Up-Gradation on Exhaust Emissions of a Dual-Fuel Engine with Thermal Barrier Coating</b> .....	279
	Sanjaya Kumar Mishra, Pradipta Kumar Dash, Shakti Prakash Jena, and Premananda Pradhan	
<b>14</b>	<b>Predicting the Performance Enhancement of Proton Exchange Membrane Fuel Cell at Various Operating Conditions by Artificial Neural Network</b> .....	293
	Tino Joe Tenson and Rajesh Baby	
<b>15</b>	<b>Role of Phase Change Material Thermal Conductivity on Predicting Battery Thermal Effectiveness for Electric Vehicle Application</b> .....	303
	Virendra Talele, Pranav Thorat, Yashodhan Pramod Gokhale, Archana Chandak, and V. K. Mathew	
<b>16</b>	<b>Thermal Design and Numerical Investigation of Cold Plate for Active Water Cooling for High-Energy Density Lithium-Ion Battery Module</b> .....	343
	Virendra Talele, Rushikesh Kore, Hemalatha Desai, Archana Chandak, Hemant Sangwan, Gaurav Bhale, Amit Bhirud, Saurabh Pathrikar, Anurag Nema, and Naveen G. Patil	
<b>17</b>	<b>An Effective Reduction of Exhaust Emissions from Combustive Gases by Providing a Magnetic Field Through the Fuel Supply Line: SI Engine, CI Engine, and LPG Gas Stove</b> .....	365
	Rakesh Kumar Sidheshware, S. Ganesan, and Virendra Bhojwani	

<b>18 Thermo-Hydraulic Performance of High Heat Flux Electronic Chip Cooling Through Microchannel Heat Sinks with Fins on Base Plate</b> .....	385
Vasujeet Singh, Pruthiviraj Nimalipuri, Harish Chandra Das, Vivek Vitankar, Malay Kumar Pradhan, Asita Kumar Rath, and Swaroop Jena	
<b>19 Review on Characteristic Features of Jet Impingement that Favours Its Application in Solar Air Heaters</b> .....	415
M. Harikrishnan, R. Ajith Kumar, and Rajesh Baby	
<b>20 Thermal Management of Electronics Systems—Current Trends and Future Applications</b> .....	435
Ganesan Dhanushkodi	
<b>21 Carbon Dioxide Storage and Its Energy Transformation Applications</b> .....	449
Manoj S. Choudhari, Vinod Kumar Sharma, Mukesh Thakur, Sanjay Gupta, and Shajiullah Naveed Syed	

# Editors and Contributors

## About the Editors

**V. K. Mathew** completed his Ph.D. in Mechanical Engineering at Vellore Institute of Technology, Vellore, India. He has published several articles in Scopus and SCI-listed Journals. His areas of research interest are thermal management systems, computational fluid dynamics, heat transfer and numerical methods, battery cooling systems, hybrid electric, vehicle, nonconventional energy, artificial intelligence, and machine learning.

**Tapano Kumar Hotta** is currently working as Associate Professor in the School of Mechanical Engineering, VIT Vellore. He has pursued his Ph.D. in Mechanical Engineering from IIT Madras in the area of Electronic Cooling. He has around 15 years of academic and research experience in different institutes of repute. His areas of research are in a broad sense include active and passive cooling of electronic devices, heat transfer enhancement, optimization of thermal systems, etc. He has around 40 publications to his credit in journals and conferences of international repute. He has guided more than 30 UG students and a dozen PG students in their project work. Two students have obtained their degrees leading to a Ph.D. under his guidance in the field of heat transfer enhancement. He has filed a patent on “Innovative Design of PCM Based Cascade Heat Sinks Integrated with Heat Pipes for the Thermal Management of Electronics”. He is a member of the editorial board and a reviewer for various international journals and conferences related to the field of heat transfer.

**Hafiz Muhammad Ali** is currently working as an Associate Professor of Mechanical Engineering at King Fahd University of Petroleum and Minerals, Saudi Arabia. He received his doctoral degree in mechanical engineering from the School of Engineering and Materials Science, Queen Mary, University of London, United Kingdom, in 2011. He was a postdoc at the Water and Energy Laboratory of the University of California at Merced, the USA in 2015–16. He is a noted faculty member having

thermal sciences, heat transfer, and solar energy as his major areas of interest. Over several years, he supervised numerous undergraduate and postgraduate students, and his work produced more than 260 papers featured in various reputed international journals with citations over 11,000 and H-Index of 56. He is the recipient of highly cited research (HCR) award 2021 by Clarivate Analytics. He also represented his institution and country at several international and national conferences as an invited and keynote speaker. His other research interests include electronics cooling, condensation, nanofluids, heat transfer devices, and thermal management.

**Senthilarasu Sundaram** is currently working as Senior Lecturer in the Department of Renewable Energy at the Environmental and Sustainability Institute (ESI), University of Exeter, United Kingdom. He has a total of 18 years' research experience in solar energy, material, and system. His research focus is on third-generation photovoltaics involving different technologies, as well as on the applications of nanostructured oxide materials and developing flexible solar cells on metal and polymer foils. In addition, he is concentrating on fundamental scientific studies of new materials, thin films, and low-cost device concepts. He is also a member of the renewable energy department in the College of Engineering, Mathematics, and Physical Sciences. He has over 127 journal article publications.

## Contributors

**Ajith Kumar R.** Department of Mechanical Engineering, Amrita Vishwa Vidyapeetham, Amritapuri, India

**Babu Sanker S.** Department of Mechanical Engineering, St. Joseph's College of Engineering and Technology, Palai, Kerala, India

**Baby Rajesh** Department of Mechanical Engineering, St. Joseph's College of Engineering and Technology, Palai, Kottayam, Kerala, India

**Bhale Gaurav** Department of Mechanical Engineering, MIT School of Engineering, MIT ADT University, Pune, Maharashtra, India

**Bhirud Amit** Department of Mechanical Engineering, MIT School of Engineering, MIT ADT University, Pune, Maharashtra, India

**Bhojwani Virendra** Department of Mechanical Engineering, MIT ADT University, Loni, Pune, India;

Department of Mechanical Engineering, MIT School of Engineering, MIT-ADT University, Pune, Maharashtra, India

**Chandak Archana** Department of Mechanical Engineering, MIT School of Engineering, MIT ADT University, Pune, Maharashtra, India



**Chavan Santosh** Department of Mechanical Engineering, Bule Hora University, Bule Hora, Ethiopia

**Choudhari Manoj S.** Department of Mechanical Engineering, RCET, Bhilai, Chhattisgarh, India

**Das Harish Chandra** Department of Mechanical Engineering, NIT Meghalaya, Shillong, India

**Dash Pradipta Kumar** Department of Mechanical Engineering, SOA Deemed to be University, Bhubaneswar, India

**Desai Hemalatha** Mechanical and Aerospace Engineering Department, University of California, Los Angeles, CA, USA

**Deshmukh Akshay** School of Physics, Engineering, and Computer Science, University of Hertfordshire, Hatfield, UK

**Deshmukh Sagar Mane** Department of Mechanical Engineering, Tolani Maritime Institute, Induri, Pune, India

**Dhanushkodi Ganesan** Centre for Electromagnetics, SAMEER, Chennai, India

**Ganesan S.** Mechanical Engineering Department, Sathyabama Institute of Science and Technology, Chennai, Tamil Nadu, India

**Gokhale Yashodhan Pramod** Institute for Mechanical Process Engineering, Otto-Von-Guericke University Magdeburg, Magdeburg, Germany

**Gupta Sanjay** School of Mechanical Engineering, Vellore Institute of Technology, Vellore, Tamil Nadu, India

**Harikrishnan M.** Department of Mechanical Engineering, Amrita Vishwa Vidyapeetham, Amritapuri, India

**Jena Shakti Prakash** Department of Mechanical Engineering, SOA Deemed to be University, Bhubaneswar, India

**Jena Swaroop** Directorate of Factories and Boilers, Government of Odisha, Bhubaneswar, India

**Jomde Amit** Dr. Vishwanath Karad, MIT World Peace University, Pune, India

**Jose Justin** Department of Mechanical Engineering, St. Joseph's College of Engineering and Technology, Palai, Kottayam, Kerala, India

**Kalbande Vednath P.** Department of Mechanical Engineering, G H Raisoni College of Engineering, Nagpur, India

**Kaldate Avinash** Department of Mechanical Engineering, Sinhgad College of Engineering, Savitribai Phule Pune University, Pune, India

**Kanase-Patil A. B.** Department of Mechanical Engineering, Sinhgad College of Engineering, Savitribai Phule Pune University, Pune, Maharashtra, India

**Kanase-Patil Amarsingh** Department of Mechanical Engineering, Sinhgad College of Engineering, Savitribai Phule Pune University, Pune, India

**Karnani Varsha** Department of Mechanical Engineering, Jorhat Engineering College, Jorhat, Assam, India

**Kolas Kshitij** Fraunhofer ENAS, Chemnitz, Germany

**Kore Rushikesh** Department of Mechanical Engineering, MIT School of Engineering, MIT ADT University, Pune, Maharashtra, India

**Lokhande Shashikant** Department of Electronics and Telecommunication Engineering, Sinhgad College of Engineering, Savitribai Phule Pune University, Pune, India

**Mathew V. K.** Department of Mechanical Engineering, MIT School of Engineering, MIT ADT University, Pune, Maharashtra, India

**Mishra Sanjaya Kumar** Department of Mechanical Engineering, SOA Deemed to be University, Bhubaneswar, India

**Mohan Man** Department of Mechanical Engineering, Rungta College of Engineering and Technology, Bhilai, India

**Nadgire Anand** Dr. Vishwanath Karad, MIT World Peace University, Pune, India

**Nema Anurag** Department of Mechanical Engineering, MIT School of Engineering, MIT ADT University, Pune, Maharashtra, India

**Nemalipuri Pruthiviraj** Department of Mechanical Engineering, NIT Meghalaya, Shillong, India

**Papade C. V.** Department of Mechanical Engineering, N. K. Orchid. College of Engineering and Technology, Dr. DBATU University, Solapur, Maharashtra, India; Department of Mechanical Engineering, Sinhgad College of Engineering, Savitribai Phule Pune University, Pune, Maharashtra, India

**Patane Prashant** Dr. Vishwanath Karad, MIT World Peace University, Pune, India

**Pathrikar Saurabh** Department of Mechanical Engineering, MIT School of Engineering, MIT ADT University, Pune, Maharashtra, India

**Patil Chetan** Dr. Vishwanath Karad, MIT World Peace University, Pune, India

**Patil Naveen G.** School of Engineering, Ajeenkya DY Patil University, Lohegaon, Pune, India

**Pradhan Malay Kumar** Government of Odisha, OSDMA, Bhubaneswar, India

**Pradhan Premananda** Department of Mechanical Engineering, SOA Deemed to be University, Bhubaneswar, India

**Rambhad Kishor** Department of Mechanical Engineering, St. John College of Engineering and Management, Palghar, India

**Rath Asita Kumar** Department of Mechanical Engineering, Raajdhani Engineering College, Bhubaneswar, Odisha, India

**Reji Rincemon** Department of Mechanical Engineering, St. Joseph's College of Engineering and Technology, Palai, Kottayam, Kerala, India

**Saikia Palash** Department of Mechanical Engineering, Jorhat Engineering College, Jorhat, Assam, India

**Sangwan Hemant** Department of Mechanical Engineering, MIT School of Engineering, MIT ADT University, Pune, Maharashtra, India

**Sharma Abhishek** Department of Mechanical Engineering, Manipal University Jaipur, Jaipur, India

**Sharma Vinod Kumar** Mechanical Engineering Department, National Institute of Technology Calicut, Kerala, India

**Sidheshware Rakesh Kumar** Sathyabama Institute of Science and Technology, Chennai, Tamil Nadu, India

**Singh Vasujeet** Department of Mechanical Engineering, NIT Meghalaya, Shillong, India

**Syed Shajiullah Naveed** School of Mechanical Engineering, Vellore Institute of Technology, Vellore, Tamil Nadu, India

**Talele Virendra** Department of Mechanical Engineering, MIT School of Engineering, MIT ADT University, Pune, Maharashtra, India

**Talukdar Parag K.** Department of Mechanical Engineering, Jorhat Engineering College, Jorhat, Assam, India

**Tenson Tino Joe** Department of Mechanical Engineering, Providence College of Engineering, Chengannur, Kerala, India

**Thakur Mukesh** NMDC DAV Polytechnic Dantewada, Shri Atal Bihari Vajpayee Education City Jawanga, Dantewada, Chhattisgarh, India

**Thorat Pranav** Department of Mechanical Engineering, MIT School of Engineering, MIT ADT University, Pune, Maharashtra, India

**Vitankar Vivek** NIT Meghalaya, Shillong, India;  
FluiDimensions, Pune, India

**Walke Pramod V.** Department of Mechanical Engineering, G H Raison College of Engineering, Nagpur, India

# Chapter 1

## Artificial Intelligence Based Integrated Renewable Energy Management in Smart City



Avinash Kaldate, Amarsingh Kanase-Patil, and Shashikant Lokhande

### 1.1 Introduction

Problems related to the integration of AI technology into smart energy systems need to provide a multifaceted understanding of economic and social issues using software. This type of socio-technological integration requires a clear definition of the domain of energy management in which the problem exists. (Kanase-Patil et al. 2011a). As the energy sector becomes more complex in various sectors, effective mechanisms are needed to successfully manage the available systems and make the right decisions at the right time. Artificial Neural Networks (ANN), Genetic Algorithms (GA), Ant Colony Algorithm, Hill Climbing Algorithm, and Particle Swarm Algorithm have been used in AI technology to solve problems of classification, optimization, forecasting, and control strategy (Javed et al. 2012). Many Integrated Renewable Energy Sources (IRES) system operations are executed at a fundamental level of automation due to lack of information on automated control resources (Kanase-Patil et al. 2011b). It would be beneficial to use AI in the system to give a new direction to the IRES design and power grid control. Optimization of controllable loads through AI techniques reduces the effect in the form of cost. The AI algorithm should be systematically used for the management of IRES to optimize to satisfy controllable loads. AI approaches give numerous effective and strong solutions to address the constraints of traditional optimization and control methods by utilizing existing data (Vinay and Mathews 2014).

---

A. Kaldate · A. Kanase-Patil (✉)

Department of Mechanical Engineering, Sinhgad College of Engineering, Savitribai Phule Pune University, Pune 411041, India

S. Lokhande

Department of Electronics and Telecommunication Engineering, Sinhgad College of Engineering, Savitribai Phule Pune University, Pune 411041, India

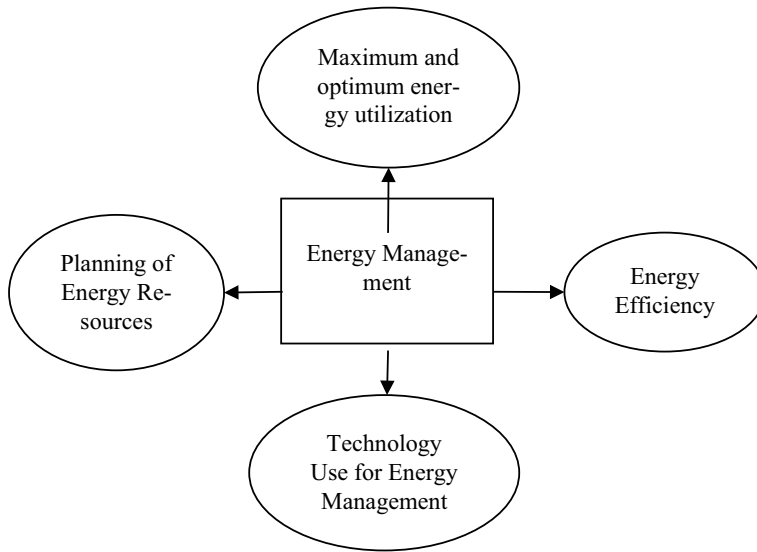
e-mail: [sdlokhande.scoe@sinhgad.edu](mailto:sdlokhande.scoe@sinhgad.edu)

This chapter reviews current advances and challenges for the use of IRES in smart cities, explaining the role of the use of AI in future energy generation in smart city energy management. The use of AI-managed solutions will transform the energy sector in the future. Electrical grids in the smart city are also controlled by the use of AI, which allows them to use energy and interact bilaterally between the customer and the energy supplier. The use of smart grids with AI responds well to rapid energy demand changes in emergencies (Qamar and Khosravi 2015). The management of smart meters and sensors is important in this; AI collects, analyzes, and optimizes the information obtained from them. In order to manage energy through AI in cities, it is necessary to first get acquainted with the essential concepts and principles of energy management, as well as study how to integrate them in the context of smart cities. Energy management depends on various levels such as directing, systematic supply of energy, controlling energy consumption, increasing productivity, and reducing energy costs through efficient use of energy (Ibrahim et al. 2011).

Energy management in the city is about energy saving, monitoring, controlling, and conserving energy. These include optimized energy consumption, proper management of energy resources, and increased active energy efficiency. As urban areas expand rapidly, the challenge is to make the most of the energy available in the city. The rapid development of existing cities and their transformation into smart cities has made energy management an integral part of urban transformation. Proper adaptation of the resources available in the smart city will give a high quality of life to the residents. Smart use of IRES will make cities more autonomous but it is expected to be managed more effectively using AI algorithms. Smart energy management is an integral part of smart city development that will be used to optimize energy conservation (Rozali et al. 2015). Smart City Energy Management integrates multiple domains through a combination of technology with information and communication technology and ensures the sustainability of its solution (Shum and Watanabe 2009). This chapter examines the basic structure of the AI algorithms. Moreover, each algorithm case study is studied which will be useful for understanding the use of AI in IRES field. Figure 1.1 shows dimensions of energy management. The mainstream of the city's energy management mainly includes proper planning of energy systems, energy awareness, proper training in energy use and measures to be taken for energy conservation.

## 1.2 Smart City

Creating a smart city means integrating existing buildings and infrastructure with smart technology. In certain cities, for example, if the Internet of Things (IoT)-based infrastructure and public services are created and managed, it is able to become a smart city (Zekic-Susac et al. 2020). It will have the same facilities as before and will have only smart technology. Another example is that the city is made smart by using a variety of electronic sensors to collect urban area data and by connecting it to the Internet or software, then this collected data is used for energy fulfillment



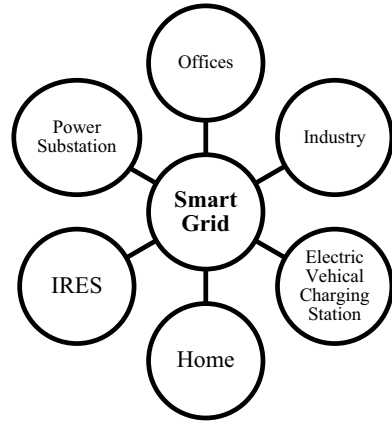
**Fig. 1.1** Dimensions of energy management

of a city. Smart technology is used to solve various challenges in the city. Data collected in smart cities is used to control a variety of things, including traffic flow, waste collection, smart energy use, and distribution automation. Many authors and organizations have contributed to the development of the smart city concept (Menon 2017).

The problems of energy management and waste management in the smart city are rapidly increasing due to the growing population. These problems are mitigated by systematic planning and optimization, which requires the use of smart technology. Energy planning is usually based on smart grids and other relevant energy factors such as the design of the IRES system need to be considered in order to use energy. The energy needs of modern cities are abundant, so modern cities need to improve existing energy systems and better implement new solutions by harmonizing all these energy solutions. The growing internal demands for renewable resources as well as the growing need for energy in the electric transport system need to be considered in energy planning without being seen separately in the city's energy planning. These examples represent the challenges facing the energy sector. To better comprehend urban dynamics and assess the impact of various energy-policy alternatives, simulation tools are utilized (Brenna et al. 2012).

This includes using AI to develop a complete smart city model that encompasses all energy-related activities in order to satisfy the expanding energy demands of present and future cities while also addressing their complexity. When looking at the entire world, it is clear that more than half of the population now lives in cities, and urbanization does not seem to be decreasing; By 2030, 60% of the population will live in cities (Riffat et al. 2016). Therefore, as cities grow, it is imperative to find

**Fig. 1.2** Smart city energy management using smart grid

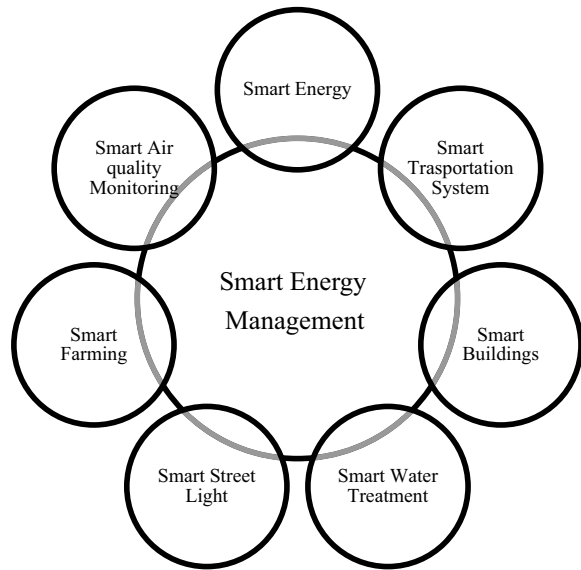


better ways to manage this population and meet their energy needs and the services they need. Due to this increasing urbanization, urban people consume two-thirds of the world's total energy and therefore global carbon emissions are increasing at an extremely high rate. Therefore, it is necessary to find more renewable energy sources than before and use existing renewable energy more efficiently. Proper energy management requires smart city data collection and digital connectivity of the city and the use of AI technology to properly analyze the information received. For this, it is necessary to consider the concept of smart energy in the city (Qamar and Khosravi 2015). Figure 1.2 shows how it is possible to connect various establishments in the city using smart grids to solve energy-related problems.

### 1.3 Energy Management

Energy management in a smart city is the process of saving in building energy usage and optimizing the energy system with the information of energy consumption obtained and knowing the energy cost from it. One of the few steps for energy management is to continuously collect information and analyze the information obtained. AI algorithms are often used to calculate the return on investment in IRES. Energy optimization solutions based on AI have been implemented in many places. Proper energy management regulates the energy consumption of a building and seeks to reduce the cost of resources involved in energy generation. Using IRES helps reduce carbon emissions in the city. Excessive energy consumption increases energy consumption which leads to energy scarcity. Therefore, this risk is reduced by managing energy and controlling it through proper energy planning. The AI system is used for energy management to reduce energy generation costs and make optimal use of energy. IRES is used in the size of AI to make energy-efficient, economical, and efficient (Nge et al. 2019). Energy management involves the following things.

**Fig. 1.3** Smart energy management



- Strategy and commitment is energy management.
- Proper planning of energy use
- Proper monitoring of energy use
- Planning for energy conservation
- Monitoring energy use
- Establishing the effectiveness of energy conservation measures.

In energy management, short-term, medium, and long-term energy supply plans need to be implemented to ensure minimum costs and minimum pollution. Using AI, it is possible to select and optimize the optimal energy for each type of energy consumption in order to reduce energy costs and improve productivity, quality of life, and the environment. It balances energy supply and demand for personal and national interests. Energy management is the key to saving energy in the city (Wang et al. 2015). This will reduce the damage to the entire earth. The use of IRES reduces our dependence on fossil fuels, which needs to happen because its supply is limited to a growing population. Figure 1.3 reviews the systems required in smart energy management.

## 1.4 Integrated Renewable Energy System

Integrated renewable energy systems provide a number of advantages over traditional energy systems, including decentralized energy generation and improved energy security. In many regions of the world, renewable energy sources are extensively

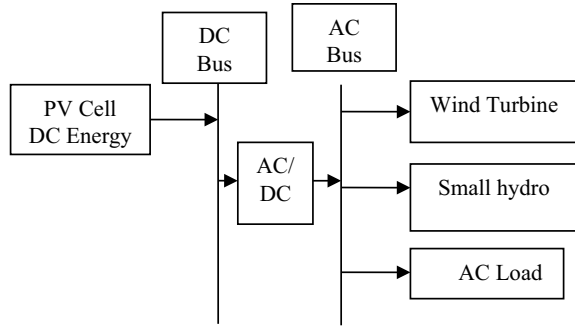


available. Other forms of renewable energy sources are not as widely available as solar radiation (Kanase-Patil et al. 2010). Certain types of renewable energy, such as geothermal and marine thermal energy, are only available in certain places (Kanase-Patil et al. 2010). Solar, wind, hydropower, biomass, geothermal, and ocean energy are all examples of renewable energy systems. These renewable resources are converted into usable products using a variety of energy conversion technologies. For example, using PV cells, solar energy is converted into thermal or electrical energy. Solar thermal systems are used to run many industrial processes that require moderate to high temperatures. An integrated photovoltaic system is achieving great solar-to-electrical efficiency. Wind energy is also widely available. The available kinetic energy is converted into other useful forms, for which turbines are rotated using wind speed. Hydropower is available in many different forms, including energy from dams, kinetic energy from rivers, and ocean waves (Bansal et al. 2012).

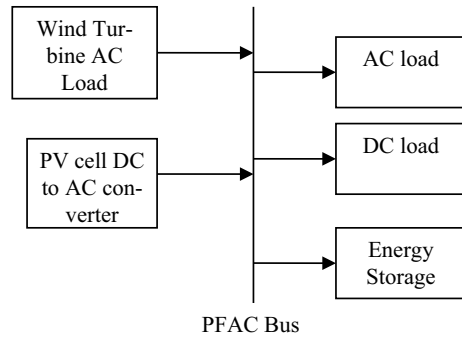
Because all renewable energy sources have their own unique features, integrated systems are utilized to combine all (Kanase-Patil et al. 2020). To integrate available renewable energy sources, various alternative configurations are made, including DC-connected configurations, AC-connected configurations, and hybrid-connected configurations (Kaldate et al. 2020). In the DC configuration, there is only one DC bus to which renewable energy sources are connected via an appropriate electrical interfacing circuit (Ahmed et al. 2011). The DC bus is directly connected to DC power sources. It entails loading DC from the DC bus via a DC/DC converter in order to maintain the DC voltage level. It also uses a configuration inverter to supply power to the AC load. It appears that when the inverter fails, the entire system will be unable to supply energy for AC loading. The DC-connected configuration of the hydro-wind-solar-based integrated system is shown in Fig. 1.4. The power frequency AC and high-frequency AC connections are separated in the AC coupled configuration integration configuration. The scheme diagram of power frequency AC (PFAC) bus shown in Fig. 1.5 considers wind-solar-based integrated system. Electrical circuits also connect power sources to the energy-frequency AC bus. At the same time, a converter connects the storage system to the bus. The DC-AC paired configuration hybrid scheme in the hybrid system has both DC and PFAC buses. PFAC power sources are connected directly without any interfacing circuits shown in Fig. 1.5. This eliminates the use of converters. The usage of converters is no longer necessary. As a result, when compared to DC coupled and AC linked schemes, the hybrid DC-AC coupled design has a lesser price and higher energy efficiency (Chauhan and Saini 2014). Because the hybrid approach requires complicated control and energy management, AI techniques appear to be required for optimization.

Distributed production, energy storage, thermal active technology integration, and demand response in transmission systems are all areas where renewable energy integration is focused. AI algorithms are being utilized to overcome technological, financial, regulatory, and organizational constraints to renewable and distributed energy systems. Planning, grid operations, and demand-side management are all integrated with the AI algorithm. IRES assist in the reduction of carbon emissions through the use of renewable energy and other environmentally friendly distributed energy sources. It utilizes the available energy to meet peak loads by combining distributed

**Fig. 1.4** AC/DC hydro-wind-solar based integrated system



**Fig. 1.5** Scheme diagram of PFAC’s planned wind-solar-based integrated system



systems and customer loads. Reliability, security, and flexibility are enhanced by microgrid applications. Smart integrated renewable energy systems have the potential to overcome challenging obstacles. This helps to improve durability as well as improve efficiency and adequacy in their energy and consumption sectors. Proper analysis of the market value chain is done by appropriate technology and appropriate decisions are made regarding the structure of the market and the processing of flexible provisions.

Financial viability is also improved by providing “demand response” information (Bhoyar and Bharatkar 2013). Long-term planning decisions that include demand-side flexibility resources serve as the foundation for developing new design standards for off-grid renewable energy systems. Advanced information and communication technology presents opportunities in addition to promoting smart integrated renewable energy systems as an active community resource for active customers to support grid services. Smart integrated renewable energy systems are a viable solution to energy issues (Kaygusuz et al. 2013).

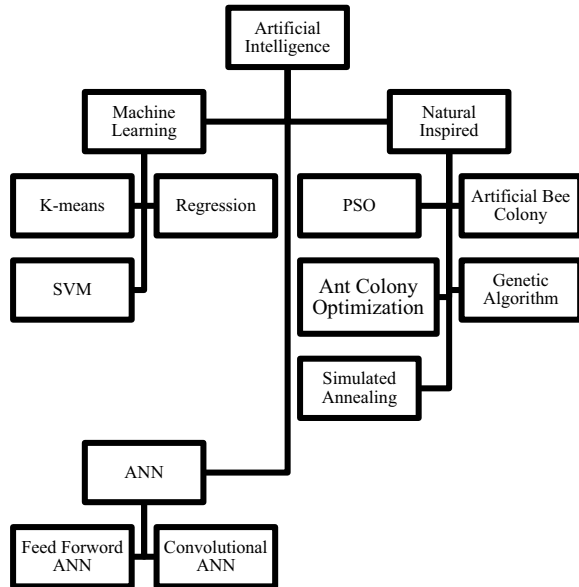
## 1.5 Artificial Intelligence (AI)

New advances are being made in the areas of computer vision, machine learning, and deep learning, now the AI utility has added a new dimension to it. The functionality of AI is huge. AI is equally efficient in retrieving and analyzing data from data sources. AI analyzes the information obtained and identifies various sets of samples and makes appropriate recommendations and estimates based on the analyzed data (Saraiva et al. 2015). AI provides insight into the machine and therefore helps to fix it accurately, independently, and well for applications without human intervention. More strategies are being developed for the use of AI, as well as the importance of IRES in global energy use. In this, AI provides a good opportunity for proper energy management and meeting demand and supply in the design of IRES. In this global utility sector, the system based on efficient power generation AI is able to meet the high demand for electricity from the customers (Qamar and Khosravi 2015).

AI capabilities are used by energy companies and grid operators to increase renewable energy use and increase energy efficiency. IoT Connected AI technology helps to improve the management of the grid for renewable energy generation to balance demand and supply. It helps manage energy in AI malls, hotels, and many other sector services to improve the production and supply of renewable energy (Varshney et al. 2008). AI is opening up a new opportunity to connect different decentralized energy sources and make them the right size. AI capabilities are being used to optimize IRES usage. When using energy systems, AI capabilities with a combination of machine learning and deep learning algorithms easily bring insights into the operation of energy operations. The AI algorithm analyzes the data and suggests a proactive approach to IRES energy management while helping to save on unnecessary energy consumption costs.

The AI algorithm offers a customized solution that works with the synchronization of the IRES system. AI is also applied in energy production or storage. It is possible to analyze the data obtained from there together and help IRES to run efficiently. This includes helping to manage energy purchases at a lower cost by optimizing AI. Using AI supports managing power demand and balancing the grid. For hybrid energy system optimization, AI has algorithms such as Genetic Algorithm (GA), Particle Swarm Optimization (PSO), Simulated Annealing (SA), Artificial Neural Network (ANN), Genetic Algorithms (GA), Simulated Annealing (SA), and Particle Swarm Optimization (PSO) related to various optimization techniques (Qamar and Khosravi 2015). In addition, algorithms are used to help researchers for cost-effective solutions of IRES. AI algorithms have been studied in IRES considering various case studies. Figure 1.6 shows that classification of AI algorithms.

**Fig. 1.6** Classification of AI algorithm



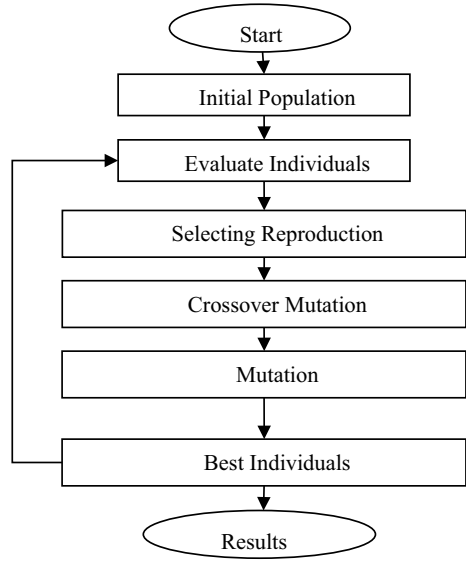
### 1.5.1 Genetic Algorithm (GA)

GA is driven by evolution’s ability to adapt to the challenges of living in difficult conditions. The method helps population evolution by identifying the most suitable individuals for reproduction. GA relies on the natural selection process and the concept of the existence of fitness. It operates with a fixed size population of possible solutions to the problem. There are three stages in GA: selection, crossover, and mutation (Strasser et al. 2015). The idea of a genetic algorithm is based on Darwin’s theory. In which strong individuals in the population are more likely to produce offspring. Genetic Algorithms are used to perform optimization processes that contain the principles of natural heredity and natural selection. This is done to change the chosen solution and help the next generation choose the most suitable offspring to carry on. The GA algorithm considers multiple problems at once and provides fast circulation for the best possible solution to the problem. Genetic Algorithms are also used in conjunction with other technologies, including neural networks, expert systems, and case-based reasoning. The solution is reached through a multipurpose optimization method to achieve optimal solution in IRES. Figure 1.7 explains flow chart of Genetic Algorithm.

#### Case Study Based on Genetic Algorithm for Charge Regulation in IRES

IRES combines renewable energy sources and lead batteries using genetic algorithms to reduce Net Present Cost (NPC). Mathematical equations should be considered to combine PV, wind, and hydro systems (Homer software mathematical model 2021).

**Fig. 1.7** Genetic algorithm flow chart



PV power

$$P_{pv} = \eta_{pv} \times N_{pvp} \times N_{pvs} \times V_{pv} \times I_{pv} \quad (1.1)$$

where,  $P_{pv}$  solar energy output on an hourly basis of PV array  $\eta_{pv}$  PV module conversion efficiency,  $N_{pvp}$  and  $N_{pvs}$  s the number of solar cells coupled in parallel and series,  $V_{pv}$  operating voltage,  $I_{pv}$  operating current.

Wind Power

$$P_w = 0.5 \times \eta_w \times \eta_g \times \rho_a \times C_p \times A \times V_r^3 \quad (1.2)$$

where  $\rho_a$  air density,  $A$  the area of the windmill which is perpendicular to the wind,  $V$  wind speed,  $C_p$  Power Coefficient,  $\eta_w$  and  $\eta_g$  transmission efficiency and generator efficiency.

Hydro Power System

$$P_h = \eta_h \times \rho_{water} \times g \times H_{net} \times Q \quad (1.3)$$

where  $\eta_h$ ,  $\rho_{water}$ ,  $g$ ,  $H_{net}$ ,  $Q$  represents efficiency, density of water, gravity, flow rate, and head, respectively.

IRES power output

$$P(t) = \sum_{h=1}^{n_h} P_h + \sum_{w=1}^{n_w} P_w + \sum_{s=1}^{n_s} P_s \quad (1.4)$$

### Battery Charging

$$P_b(t) = P_b(t-1) \times (1 - \sigma) - [P_{bh}(t)/\eta_{bi} - P_{bl}(t)] \quad (1.5)$$

where  $P_b(t-1)$ ,  $P_b(t)$  the energy stored in the battery at the start and end of the interval  $t$ ,  $P_{bl}(t)$  at time  $t$ , the load demand,  $P_{bh}(t)$  PV array total energy generated,  $\sigma$  the self-discharge factor,  $\eta_{bi}$  the battery efficiency.

Net present cost (NPC) for each component is derived using

$$C_{NPC} = \frac{C_{ann,tot}}{CRF} \quad (1.6)$$

where  $C_{ann,tot}$  total annualized cost,  $C_{NPC}$  net present cost, CRF capital recovery factor

$$CRF = \frac{i \times (1 + i)^N}{(1 + i)^N - 1} \quad (1.7)$$

where  $N$  is the number of years and  $i$  is the annual real discount rate.

Step to be used by genetic algorithm to calculate NPC using genetic algorithm.

- Adjusting the number of individuals in the population, number of generations, crossing rate, and mutation rate for genetic algorithm.
- The genetic algorithm of reproduction, crossing, and mutation is used to make the right choice for the next generation. In this the roulette-wheel method is used, the crossing is done using a crossing point method, and the elements of some individuals are mutated by randomly changing.
- The genetic algorithm generates randomly component size vectors for PV, wind, hydro turbines, and batteries. A genetic algorithm is used for this selection.
- Calculate for each selected component meet load demand is found. Find the random generation of operation strategy vectors. It calculates operating cost for each strategy.
- Battery charging or discharging will be decided on the additional energy available. It calculates the lowest operating cost and NPC for the size of the IRES. Finally, the solution with the lowest NPC is considered.

### 1.5.2 Particle Swarm Optimization (PSO)

There have been several studies related to the social behavior of animal groups in the PSO. This shows that some of the animals, birds, and fish in the group share information in their group and thus have a great benefit in the survival of the animals. This is used in PSO nonlinear optimization and the solution to the problem is found. To solve the complex problem, the behavior of the herd of animals has been studied

to create a PSO optimization algorithm. Finding the point at which the whole flock should land is a complex issue, as it depends on many factors. The goal of birds is to maximize food availability and minimize the risk of predation.

In the PSO algorithm, the same mechanism is applied. PSO is a frequently used swarm intelligence optimization technique in which the answer to a question is determined by the speed of the particles. PSO does not require any overlap and mutation calculations, simple calculations, and fast search speeds. PSO is a population-based search process that uses particles to change the position of particles in a problem area. In PSO, the search location is multidimensional, with each particle's position being changed based on the experience of nearby particles (Jadhav et al. 2011).

Algorithm of particle swarm optimization.

- Step 1: Entering system parameters.
- Step 2: Initialize the PSO settings.
- Step 3: The iteration is set at the beginning and then the particle population is started rapidly at random positions and dimensions.
- Step 4: For each particle, the objective function is calculated and compared with the individual best value. Based on this, the first best value is modified with a higher value and the current state of the particles is reported.
- Step 5: The particles corresponding to the individual best particles in all particles are selected and the values are set as the global best.
- Step 6: The speed and position of each particle is updated.
- Step 7: If the number of iterations reaches the maximum limit. Go to Step 8; otherwise, set the next iteration and go to Step 4.
- Step 8: The best particle denoted by global best provides the optimal solution/or the problem.

Energy Management System using Particle Swarm Optimization.

The power management system requires production to control the flow of electricity during grid-connected operation and to match the load in the microgrid. The PSO algorithm has been used to reduce the cost of energy extracted from the grid, generated in the grid, and used by loads. The mathematical models of generator functions, solar generation function, and construct functions are given below (Gaing 2003).

Functions of Generators

$$F_j(P_j) = \alpha_j + \beta_j P_j + \gamma_j P_j^2 \quad (1.8)$$

where  $j$  = generating source;  $P$  = a source's power output  $j$ ;  $F$  = source's operating costs  $j$ ,  $\alpha$ ,  $\beta$ ,  $\gamma$  are the cost coefficients.

Function of solar generation

$$F(P_s) = a P_s + G^e P_s \quad (1.9)$$

where,  $P_s$  solar generation,  $a$  annuitization coefficient,  $G^e$  Operation and Maintenance (O & M) costs per unit generated energy,

### Functions of Constraints

$$P_{\text{generated}} \neq P_{\text{Load}} \quad (1.10)$$

$$P_{\text{grid}} = P_{\text{generated}} - P_{\text{Load}} \quad (1.11)$$

$$P_j^{\min} \leq P_j \leq P_j^{\max} \quad (1.12)$$

Step to be used by Particle Swarm Optimization for energy management.

- In this case it is necessary to first provide the necessary data for the required algorithm. In this case, the forecasted load, solar power generation and wind power generation should be provided.
- The algorithm selects the initial parameters, including the population size.
- The algorithm will start to find the fitness evaluation of each parameter.
- The diesel generator is turned on using a microgrid. But this involves applying the PSO algorithm to find the optimal way to send all available diesel generators to meet the load demand while reducing operating costs.
- The termination condition is checked and if it is satisfied, the system will output a power reference signal for each diesel generator at intervals each time. If the termination condition is not satisfied, the system will go back again.

### 1.5.3 Ant Colony Optimization (ACO)

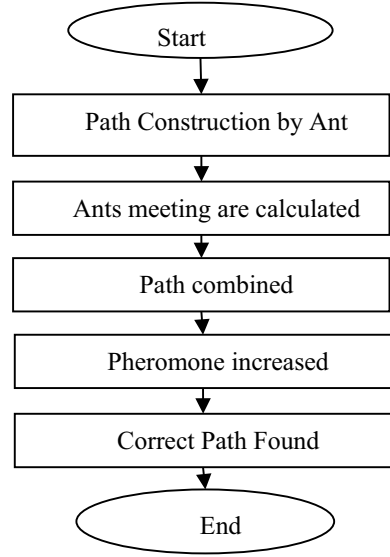
ACO is an algorithm in the class of biologically induced heuristics. The basic idea of ACO in this algorithm is that it works in the same way that it is collaborated in ant colonies. Dorigo first used ACO in 1992 to solve the problems of oxidation. The ants go out to find food and return to their nests. During this journey, ants release a chemical pathway called pheromones to the ground. Pheromones guide other ants to food. When facing an obstacle, the ant has an equal chance to choose the left or right path. So this pheromone is used to choose the right path. Each ant creates a complete solution to the food search problem according to the potential state transition rules. The whole purpose of the scheduling problem using ACO in IRES is to reduce the electricity bill by making optimal use of electricity from the grid. Figure 1.8 shows working flow chart of Ant Colony Algorithm (Qamar and Khosravi 2015).

#### Energy Management System Using Ant Colony Optimization

It uses ACO to reduce electricity bills as well as grid and waiting time by making optimal use of schedule issues. The cost of electricity must be reduced in each time slot, while the waiting time for shiftable equipment must be reduced. The main concern in this work is to increase the level of convenience of end-users by reducing the cost of electricity. The cost of electricity must be reduced in each time slot, while the waiting time for shiftable equipment must be reduced. This work has increased



**Fig. 1.8** Ant colony algorithm flow chart



the level of convenience of end-users by reducing the cost of electricity (Rahim et al. 2015).

Model of energy consumption

$$E^a(t) = \{E_{t_1}^a + E_{t_2}^a + E_{t_3}^a + \dots + E_{t_{24}}^a\} \quad (1.13)$$

where,  $E_{t_1}^a, E_{t_2}^a, E_{t_3}^a \dots E_{t_{24}}^a$  each appliance's energy consumption needs at the appropriate time slot

$$E_T = \sum_{t=1}^{24} \left( \sum_{a=1}^A E_{(i,t)} \right) \quad (1.14)$$

where,  $E_T$  the overall energy consumption requirement for all appliances on a daily basis.

Model for calculating energy prices

$$E(t) = \sum_{t=1}^{24} (v(t) + \Delta(t) + \kappa(t)) \quad (1.15)$$

where,  $E(t)$  the total amount of energy used by all appliances

$$C(t) = \begin{cases} C_1(t) & 0 \leq E(t) \leq E_{th}^1(t) \\ C_2(t) & E_{th}^1(t) \leq E(t) \leq E_{th}^2(t) \\ C_3(t) & E_{th}^2(t) < E(t) \end{cases} \quad (1.16)$$

where  $E_{th}^1$  and  $E_{th}^2$  thresholds for power consumption,  $C_1$ ,  $C_2$  and  $C_3$ , costs in these specific circumstances.

Objective function and its solution via ACO

$$\min \sum_{t=1}^{24} \left( a_1 \cdot \sum_{a=1}^A (E_a(t) \times C_a(t)) \right) + a_2 (\varphi_a(t)) \quad (1.17)$$

where,  $C_a$  the cost of electricity in each time slot must be kept to a minimum,  $a_1$  and  $a_2$  weights of two parts of objective.

Step to be used by Ant Colony Optimization for energy management.

1. The algorithm initializes all parameters as well as includes data related to equipment and time slots.
2. The algorithm randomly generates a population of ants.
3. Each individual ant update evaluates pheromones and the objective function of each individual ant.
4. Calculates electricity bill using algorithm.
5. Each ant local pheromone is updated and then the best solution is selected.

### 1.5.4 Hill Climbing Optimization

Hill climbing is an approximate algorithm used for optimization problems in the field of AI. This algorithm performs the right input and a good genetic function, giving the algorithm the best possible solution to the problem in a short period of time. This given satisfaction may not be the absolute best given every time but it is good enough considering the time it takes to get the satisfaction. This algorithm lists all possible options in the search algorithm based on the information available (Bhandari et al. 2015). It helps the algorithm to choose the shortest path possible. The average increase in energy gain using MPPT using the Hill Climbing Algorithm has been found to be 16–43%. To calculate the power in this algorithm, one immediately measures the voltage (V) and the current (I) and then compares it with the last calculated power. If the operating point difference is positive, the algorithm continuously overlaps the system, otherwise, if the operating point difference is positive, the direction of the object is changed. Hill Climbing (HC) is a mathematical method for optimizing a problem that belongs to the domain of local search methods (Mhusa and Nyakoe 2015). The HC technique begins with the creation of the initial state, i.e., the initial solution. The following steps depict the optimization process using the hill climbing algorithm. This algorithm is used to size IRES by minimizing the Levelized cost of energy in IRES.

The algorithm is as follows:

- Step 1: Find a possible solution.
- Step 2: Verify that each solution is correct.

Step 3: If each solution is correct then move on to the next step.

Step 4: Choose the most suitable solution for each of these solutions.

### Hill Climbing Algorithm for MPPT

When MPPT is performed, it uses Boost Converter as a duty cycle feedback parameter. The main disadvantage of this technique is that the system shuts down during the period of continuous radiation. A very small value of the difference in the duty cycle is required for the period of stable radiation;  $\Delta D$  reduces the energy gained by the PV thus reducing the strong oscillation of the force about the peak power point. At the same time, rapidly changing radiation requires a higher charge cycle value to increase the pursuit of peak power. This is done by measuring the values of PV voltage and current. Also, the generated power is calculated and the result of the comparison is seen to be complementary or unchanged compared to its value in the previous iteration and the PWM output duty cycle is changed accordingly (Sher et al. 2015).

The PV module's current output is

$$I_{\text{mpp}} = K_i I_o \left[ \exp\left(\frac{V_{\text{oc}}}{n N_{\text{sc}} V_T}\right) - 1 \right] \quad (1.18)$$

where  $I_o$  current in an open circuit,  $K_i$  the current proportionality constant,  $V_{\text{oc}}$  open-circuit voltage,  $N_{\text{sc}}$  series cells,

The PV module's voltage output is

$$V_{\text{mpp}} = \frac{V_T \left[ \exp\left(\frac{V_{\text{oc}}}{V_T}\right) - 1 \right]}{\left(1 - 1/K_i\right) \exp\left(\frac{V_{\text{oc}}}{V_T}\right) - 1} \quad (1.19)$$

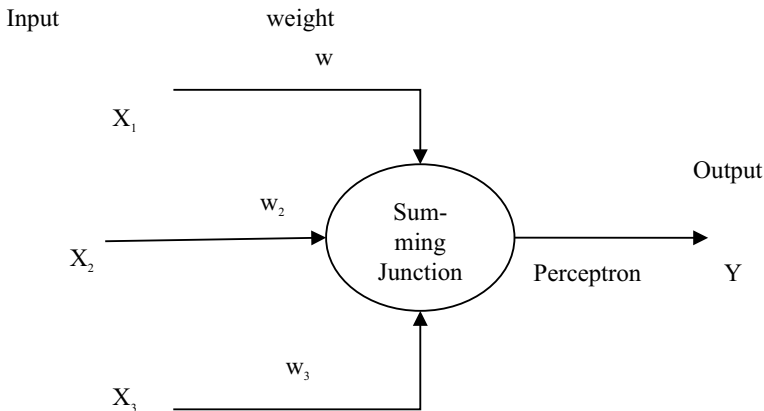
where  $V_T$  is the maximum power point voltage.

### Step to Be Used by Hill Climbing Optimization Algorithm MPPT of PV

- It collects data of voltage and current from PV.
- Calculate power from the from voltage and current
- The algorithm compares its value to the previously calculated power value.
- The previous value is determined more or less and the power is added or decreased accordingly.

### 1.5.5 Neural Network Algorithm

Advances in biological research have made it possible to understand the process of natural decision-making. The brain is a sophisticated parallel computer that has the power to make decisions faster than any advanced computer. It has the ability to learn, remember and generalize new things. The ANN algorithm was developed in



**Fig. 1.9** Basic neuron diagram for ANN

1943 to study this ability of the brain. Mathematical models of biological neurons are presented in the ANN algorithm (Ranganayaki et al. 2016). The model has the ability to calculate any logical expression. The standard weight also performs a similar function, as do the different synaptic forces of biological neurons in ANN.

For the synaptic weight of the synaptic strength of biological neurons, some inputs are more important than others. Therefore ensures that more significant factors have a greater impact on the process function principle when they produce nerve responses. ANNs have adjustable coefficients of weight in the network and determine the strength of the input signal as indicated by the artificial neuron. Weight determines the connection strength of the input and it is possible to train on the basis of different training sets with respect to the specific architecture of the network or its learning rules. The individual inputs in the perceptron are multiplied by its corresponding connection weight. Figure 1.9 shows basic neuron diagram for ANN (Ata 2015).

### 1.5.6 Artificial Neural Network Approach in IRES

Power management is done on a distributor hybrid grid using ANN. The problem is that the voltage drop and power quality can be reduced, thus the power stability is managed using ANN. In real-time monitoring, ANN algorithms are used to perform power management based on the quality and stability of the power system. The IRES have solar, wind or hydro time series nonlinear and static data, using ANN algorithms to learn from data patterns and predict future behavior of weather events is possible (Rahman et al. 2021).

Step to be used by ANN to predict renewable resource output.

- Data is collected from energy sources and the environment
- The original data is normalized and pre-processed

- The ANN model is trained, the accuracy of the training samples is evaluated, and the pre-trained model is certified by the verification samples.
- The designed ANN model is used to estimate the power output by the test dataset.
- The weather information available in it is matched with the information in the history and it determines how much energy will be obtained from IRES.

## 1.6 Concluding Remarks

This chapter explores the use of AI algorithms in the architecture of public sector energy management systems to increase energy efficiency, estimate energy consumption, and be used as part of a smart city. It explains how the AI algorithm is used to optimum sizing of parts of the IRES system. This chapter provides information on Genetic Algorithms, Particle Swarm Optimization, Anti-Colony Algorithms, Hill Climbing Algorithms, and Artificial Neural Networks. It turns out that many things can be simplified in IRES using AI algorithms. This chapter explains the basic design of AI algorithms and the various IRES problems solved by AI algorithms.

## References

- Ahmed NA, Al-Othman AK, Alrashidi MR (2011) Development of an efficient utility interactive combined wind/photovoltaic/fuel cell power system with MPPT and DC bus voltage regulation. *Electr Power Syst Res* 81:1096–1106. <https://doi.org/10.1016/j.epsr.2010.12.015>
- Ata R (2015) Artificial neural networks applications in wind energy systems: a review. *Renew Sustain Energy Rev* 49:534–562. <https://doi.org/10.1016/j.rser.2015.04.166>
- Bansal M, Saini RP, Khatod DK (2012) An off-grid hybrid system scheduling for a remote area. In: 2012 IEEE students' conference electr electronics and computer science innovation for humanity SCEECS 2012 9–12. <https://doi.org/10.1109/SCEECS.2012.6184799>
- Bhandari B, Lee K, Lee G, et al (2015) Optimization of hybrid renewable energy power systems : a review. 2:99–112
- Bhoyar RR, Bharatkar SS (2013) Renewable energy integration in to microgrid: powering rural Maharashtra State of India. In: 2013 Annual IEEE India conference INDICON 2013. <https://doi.org/10.1109/INDCON.2013.6725877>
- Brenna M, Falvo MC, Foiadelli F, et al (2012) Challenges in energy systems for the smart-cities of the future. 755–762
- Chauhan A, Saini RP (2014) A review on integrated renewable energy system based power generation for stand-alone applications: configurations, storage options, sizing methodologies and control. *Renew Sustain Energy Rev* 38:99–120. <https://doi.org/10.1016/j.rser.2014.05.079>
- Gaing Z (2003) Particle swarm optimization to solving the economic dispatch considering the generator constraints. 18:1187–1195
- Homer software mathematical model. <https://www.homerenergy.com/>. Accessed 4 Oct 2021
- Ibrahim M, Khair A, Ansari S (2011) A review of hybrid renewable/alternative energy systems for electric power generation : *IEEE Trans Sustain Energy* 2:392–403. <https://doi.org/10.1109/TSTE.2011.2157540>
- Jadhav HT, Patel J, Sharma U, Roy R (2011) An elitist artificial bee colony algorithm for combined economic emission dispatch incorporating wind power. In: 2011 2nd International conference on

- computer and commun technology ICCCT-2011, pp 640–645. <https://doi.org/10.1109/ICCCT.2011.6075213>
- Javed F, Arshad N, Wallin F et al (2012) Forecasting for demand response in smart grids: an analysis on use of anthropologic and structural data and short term multiple loads forecasting. *Appl Energy* 96:150–160. <https://doi.org/10.1016/j.apenergy.2012.02.027>
- Kaldate AP, Kanase-Patil AB, Lokhande SD (2020) Optimization and techno-economic analysis of PV-wind power systems for rural location in India. *E38 Web Conf* 15:170. <https://doi.org/10.1051/c3sconf/3/202017001015>
- Kanase-Patil AB, Saini RP, Sharma MP (2010) Integrated renewable energy systems for off grid rural electrification of remote area. *Renew Energy* 35:1342–1349. <https://doi.org/10.1016/j.renene.2009.10.005>
- Kanase-Patil AB, Saini RP, Sharma MP (2011a) Development of IREOM model based on seasonally varying load profile for hilly remote areas of Uttarakhand state in India. *Energy* 36:5690–5702. <https://doi.org/10.1016/j.energy.2011.06.057>
- Kanase-Patil AB, Saini RP, Sharma MP (2011b) Sizing of integrated renewable energy system based on load profiles and reliability index for the state of Uttarakhand in India. *Renew Energy* 36:2809–2821. <https://doi.org/10.1016/j.renene.2011.04.022>
- Kanase-Patil AB, Kaldate AP, Lokhande SD et al (2020) A review of artificial intelligence-based optimization techniques for the sizing of integrated renewable energy systems in smart cities. *Environ Technol Rev* 9:111–136. <https://doi.org/10.1080/21622515.2020.1836035>
- Kaygusuz A, Keles C, Alagoz BB, Karabiber A (2013) Renewable energy integration for smart sites. *Energy Build* 64:456–462. <https://doi.org/10.1016/j.enbuild.2013.05.031>
- Menon A (2017) Smart cities, livable cities. *GfK Mark Intell Rev* 9:48–52. <https://doi.org/10.1515/gfkmir-2017-0008>
- Mhusa NJ, Nyakoe GN (2015) Power management in photovoltaic-wind hybrid system based on artificial intelligence. 2:
- Nge CL, Ranaweera IU, Midtgård OM, Norum L (2019) A real-time energy management system for smart grid integrated photovoltaic generation with battery storage. *Renew Energy* 130:774–785. <https://doi.org/10.1016/j.renene.2018.06.073>
- Qamar M, Khosravi A (2015) A review on artificial intelligence based load demand forecasting techniques for smart grid and buildings. *Renew Sustain Energy Rev* 50:1352–1372. <https://doi.org/10.1016/j.rser.2015.04.065>
- Rahim S, Khan SA, Javaid N, et al (2015) Towards multiple knapsack problem approach for home energy management in smart grid. In: *Proceedings—2015 18th International conference on network-based information system NBiS 2015*, pp 48–52. <https://doi.org/10.1109/NBiS.2015.11>
- Rahman MM, Shakeri M, Tiong SK et al (2021) Prospective methodologies in hybrid renewable energy systems for energy prediction using artificial neural networks. *Sustain* 13:1–28. <https://doi.org/10.3390/su13042393>
- Ranganayaki V, Deepa SN, Ranganayaki V, Deepa SN (2016) An intelligent ensemble neural network model for wind speed prediction in renewable energy systems. *Sci World J* 2016:1–14. <https://doi.org/10.1155/2016/9293529>
- Riffat S, Powell R, Aydin D (2016) Future cities and environmental sustainability. *Futur Cities Environ* 2:1. <https://doi.org/10.1186/s40984-016-0014-2>
- Rozali NEM, Wan Alwi SR, Manan ZA, et al (2015) A process integration approach for design of hybrid power systems with energy storage. *Clean Technol Environ Policy* 1–18. <https://doi.org/10.1007/s10098-015-0934-9>
- de Saraiva FO, Bernardes WMS, Asada EN (2015) A framework for classification of non-linear loads in smart grids using artificial neural networks and multi-agent systems. *Neurocomputing* 170:328–338. <https://doi.org/10.1016/j.neucom.2015.02.090>
- Sher HA, Murtaza AF, Noman A et al (2015) A new sensorless hybrid MPPT algorithm based on fractional short-circuit current measurement and P&O MPPT. *IEEE Trans Sustain Energy* 6:1426–1434. <https://doi.org/10.1109/TSTE.2015.2438781>

- Shum KL, Watanabe C (2009) An innovation management approach for renewable energy deployment-the case of solar photovoltaic (PV) technology. *Energy Policy* 37:3535–3544. <https://doi.org/10.1016/j.enpol.2009.04.007>
- Strasser T, Andren F, Kathan J, et al (2015) A review of architectures and concepts for intelligence in future electric energy systems. *Ind Electron* 62:2424–2438. 10.1109/TIE.2014.2361486
- Varshney N, Sharma MP, Khatod DK (2008) International journal of emerging technology and advanced engineering sizing of hybrid energy system using HOMER. *Certif J* 9001:436
- Vinay P, Mathews MA (2014) Modelling and analysis of artificial intelligence based MPPT techniques for PV applications. 56–65
- Wang X, Palazoglu A, El-Farra NH, Dash P (2015) Operational optimization and demand response of hybrid renewable energy systems. *Appl Energy* 143:324–335. <https://doi.org/10.1016/j.apenergy.2015.01.004>
- Zekic-Susac M, Mitrovic S, Has A (2020) Machine learning based system for managing energy efficiency of public sector as an approach towards smart cities. *Int J Inf Manage* 102074. <https://doi.org/10.1016/j.ijinfomgt.2020.102074>

# Chapter 2

## The Role of Lower Thermal Conductive Refractory Material in Energy Management Application of Heat Treatment Furnace



Akshay Deshmukh, Virendra Talele, and Archana Chandak

### 2.1 Introduction

In a modern scenario of translation of technology causes more production of versatile products which needs to go from the heat treatment process to increase its working effectiveness. In this translation of the production sector where demand had sustainably increased, the use of energy to run this heat treatment furnace is also increased. The extensive use of power to fulfil the functional requirement of the furnace is a typical result of an increasing number of reactive chemicals such as CO and HC, which cause growing greenhouse gases in the atmosphere (Lisienko et al. 2016). The cause of global warming by industrial applications is an intensive problem, on which several national-level government bodies are working to curb the level of emissions under control despite the strict policy no significant growth for emission reduction is observed if companies on primary ground start to work on energy management solution this problem can be effectively solved in upcoming years (Källén 2012). The heat treatment of any product is an intensive process that consumes a large amount of fuel to fulfil temperature requirement in the furnace, the typical working temperature in heat treatment range from 900 C to 1200 °C depending on the application and intensity of work the requirements of temperature corresponding to the fuel is burned which causes an emission of harmful gases (Stål och värmebehandling – En handbok 2010). Most of these greenhouse gases expelled from the furnace contribute towards pollution and lowers efficiency. Methane, the other GHG, is secondary resource energy (SER) and is used in metallurgical units

---

A. Deshmukh (✉)

School of Physics, Engineering, and Computer Science, University of Hertfordshire,  
Hatfield AL109AB, UK  
e-mail: [ad18abx@herts.ac.uk](mailto:ad18abx@herts.ac.uk)

V. Talele · A. Chandak

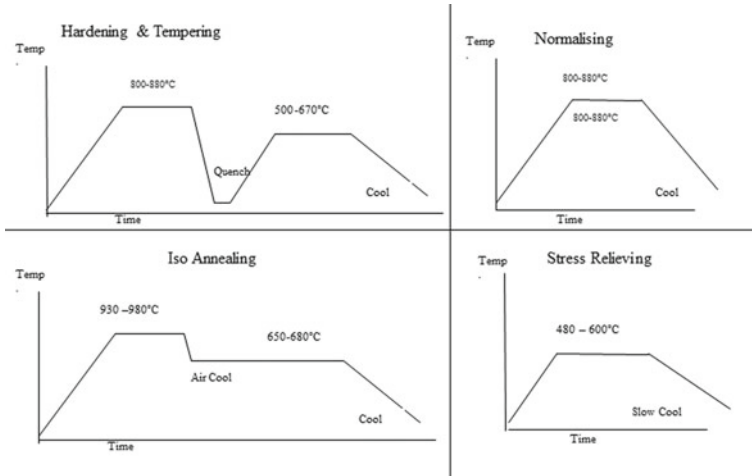
Department of Mechanical Engineering, MIT School of Engineering, MIT ADT University,  
Pune 412201, India



for burning carbon dioxide. Hyl-3 processes are used in iron and steel manufacturing processes, such as Corex, Romelt, and Midrex. Iron or sponge iron is loaded into steel arc furnaces (EAF) with added scrap iron (Cvinolobov and Brovkin 2004; Yusfin and Pashkov 2007; Romenets, et al. 2005; Voskoboynikov et al. 1998). In metallurgical furnaces, the main source of heat is natural gas combustion. Energy costs are an integral part of manufacturing, covering costs, and energy savings in high-temperature processes are extremely important. The chamber furnaces are part of a group of regular furnaces commonly used to forge and warm heavy components. For chamber furnaces, the time change in the chamber temperature should be held in line with technical requirements. Therefore, it is very important to save energy by reducing the heat transfer rate by isolating the furnace walls (Rusinowski and Szega 2001). The energy loss in the furnace can be calculated by correlation with energy balance for the burning in which the furnace's thermal condition varies over time, and the performance of energy consumption depends heavily on the length of the specific process step. The energy input must equate with energy production to ensure the oven's continuous function and a relatively straightforward calculation of heat loss from the walls (Chen et al. 2005). In periodic chamber furnaces, the measure of heat loss is further complicated by the deposition of energy in the furnace walls. The loss of energy is primarily dependent upon the temperature of the insulation, thickness of isolation, the temperature of the furnace chamber, and the mode of operation of a furnace (Han et al. 2011). In the event of transient heat piping, calculating the heat loss from the furnace wall entails the time change in furnace walls. Heat loss occurs during discharge or refreshment in the furnace as thermal treatment is carried out from the interior wall surface. Obtaining exact heat loss value in fined tuned accurate CFD simulation which was proposed by Yang et al. (2007) where they performed time variation transient CFD simulation of product to predict the thermal performance, in which the model consists of turbulent flow with intensive calibration of the system. From the various literatures (Dubey and Srinivasan 2014; Kim et al. 2000; Kim and Huh 2000; Mayr et al. 2017, 2015; Jaklič et al. 2007; Quested et al. 2009), it is observed that there is a scant amount of research performed on energy conservation system of furnace influence by lining material, so the current study is an attempt to perform practical validation of furnace influence by lower thermal conductive in lining refractories material. The achieved data are correlated by using advanced neural network technique to find a correlation between input data with conventional refractories and the target set of pyro block refractories.

### ***2.1.1 Heat Treatment in Furnaces***

The heating is carried out in the different furnaces using different heating mediums. A large amount of energy is required to heat the components. In the total manufacturing cost of forgings, a major share is consumed by the energy cost. Typically, the heating furnace is used to carry out a thermophysical operation such as.



**Fig. 2.1** Heat treatment operations

1. Hardening tempering
2. Normalizing
3. Iso annealing
4. Stress revealing.

Maximum consumption of heat is required in the operation of hardening and tempering, normalizing, and iso annealing. The typical heat contribution is achieved by burning fuel. The below chart shows the temperature range for the operation (Fig. 2.1).

The furnace efficiency is determined by the ratio of thermal input from the furnace to the material. All the heat applied to the furnace can be used for heating the material or components of industrial heating furnaces. The part is heated by continuously incorporating specific quantities of thermal energy into the product placed in the chamber. Figure 2.2 shows a schematic of various energy losses in furnaces.

### 2.1.2 Refractory Material

Refractory isolation is used to decrease the heat loss rate across furnace walls. This is due to a high level of porosity and the desired pore configuration of tiny, uniform pores that are spaced uniformly throughout the entire refractory brick to reduce thermal conductivity. Refractory material selection is conducted based on its application where the need for material to be chemically and physically stable in the high-temperature application. In the present investigation, typical refractory material as fire brick used in bogie hearth furnace will be replaced with lower thermal conductive pyro block material on which a detailed comparative energy conservation analysis

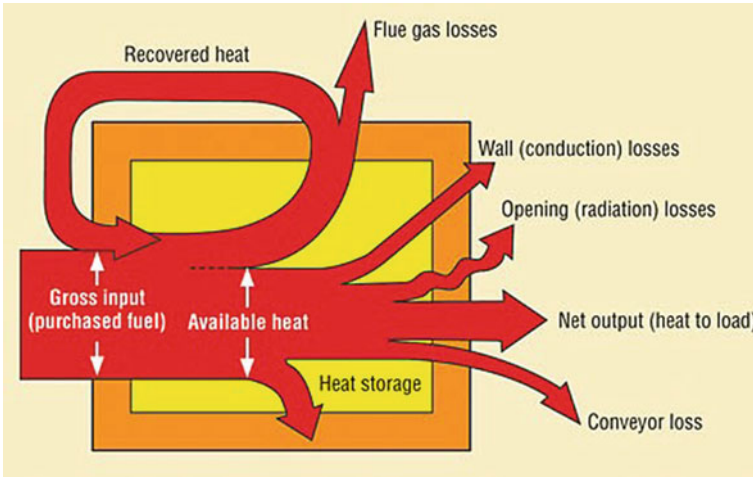


Fig. 2.2 Furnace energy losses

is presented. The output data are verified and validated using the advanced data analytics ANN technique based on the generic optimization process.

## 2.2 Methodology

The present investigation is performed to study the importance of refractory material and its impact on the energy conservation system of heat treatment furnaces. The practical validation is proposed in the study based on a comparative analysis based on refractories with wall brick material, further replaced with the ceramic fibre wall material. The flowing outline shows the performed detail of the investigation (Fig. 2.3).

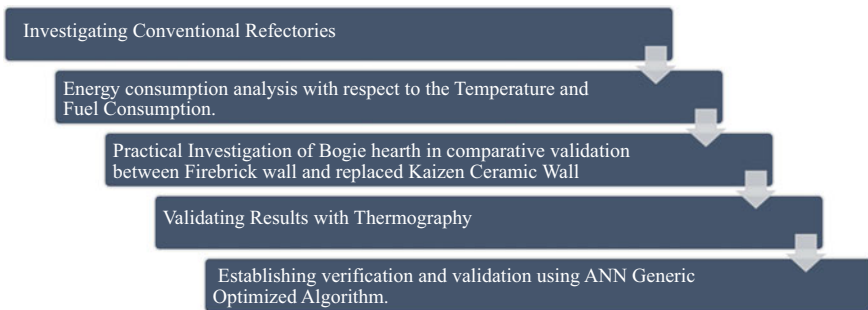
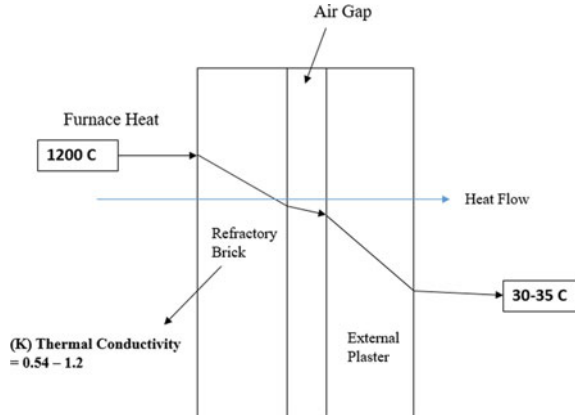


Fig. 2.3 Methodology flow chart

**Fig. 2.4** Conventional fire brick



### 2.2.1 Investigating Conventional Refractories

In Bogie Hearth furnaces, the conventional material used for the lining is made up of firebricks, whose temperature rating of about 1649 C in preliminary life condition. This material requires to make thermal insulation for the heat treatment furnace by isolating generated heat inside the furnace. The typical advantage of thermal fire brick offers effective working across wide temperature use; it has a lower level of impurities and a lower level of shrinkage value. The disadvantage of this material offer is that it has too many pores in structure, making it weaker with an increment of the application life cycle. It does not provide soundproof coating; it is having lower thermal resistance to the thermal properties. In the present investigation, the Boogie Hearth furnace was initially loaded with conventional refractory brick, further replaced with lower conductive ceramic brick classified as a pyro block. The below table shows the comparative properties between conventional fire brick and replaced pyro block. The mathematical modelling of thermally insulated refractories is shown in Figs. 2.4 and 2.5.

Table 2.1 represents the properties of both fire brick and ceramic fibre (pyro block)

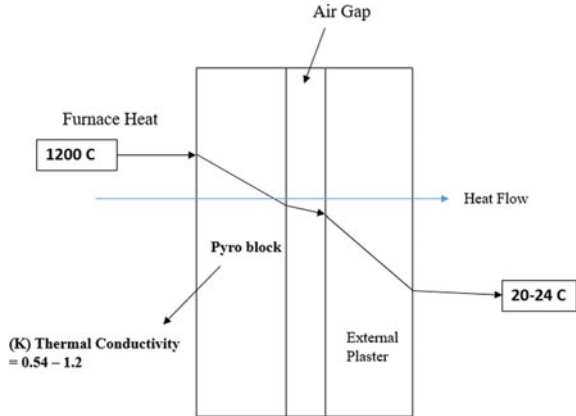
### 2.2.2 Development Scope for Existing Boogie Furnace

In the designing operation of furnaces, it is particularly beneficial to utilize the heating value of fuel as economically as practicable in the design and operation of furnaces. Inevitably, though, some of this heat is lost to the environment because of

1. Incomplete combustion of fuel
2. Flue gas sensible heat
3. Convection and radiation from the furnace wall.

Below is the key furnace classified resulting in heat loss.

**Fig. 2.5** Ceramic fibre (pyro block)



**Table 2.1** Refractory properties

Parameter	Firebrick	Pyro block
Density	< 2300	160–240
Chemical composition	Up to 1648 °C	1260 °C
Al <sub>2</sub> O <sub>3</sub>	<44%	44–50%
SiO <sub>2</sub>	<78%	50–56%
Thermal conductivity	1.2	< 0.340

**2.2.2.1 Burner**

The burner should burn its fuel efficiency by maintaining an adequate fuel-air ratio in circulation mode. If this condition is not getting satisfied, there is a creation of instability in the burner’s flame. Multiple burners are used to sustain flame and achieve heat inside the furnace to keep the stability of flame creation.

**2.2.2.2 Furnace**

In several applications, firebricks have been phased out and replaced by cast plastic refractories. Utilize the optimal insulation width. Reduce air and flue gas leakage by improved furnace design. Increase the vertical depth of the furnace to allow for increased heat transfer by radiation. Consider the likelihood of creating a temperature profile by separating the furnace into zones to reduce the amount of fuel required, the option of using a serial device, which often results in a reduction of energy requirements.

The present investigation aims to increase the thermal stability of the furnace by increasing production efficiency in lower proportionate consumption of fuel. The replacement of conventional firebricks is done with the lower thermal conductive pyro block material, which works as thermal insulation to store generated heat within

the furnace only. The validation of the presented study was generated by using thermographic plots near the furnace's outer door compared to the furnace wall insulated with fire bricks vs the furnace wall insulated with lower thermal conductive pyro block material. The following achieved results multi-objective study presented using advanced data predictive artificial neural network study.

The artificial neural network (ANN) is the most recently developed and commonly used technique for predicting parameters for various input and output values. In the current analysis, the association data points are used as feedback to the ANN. In ANN, the Levenberg Med algorithm is used to consider feed-forward backpropagation. 70% of the data were used for preparation, 15% for research, and 15% for validation. The number of neurons between the input and output layers varies, as is the degree of neuron independence. The network with the lowest MSE error value and the highest regression coefficient is considered. In the present study, the regressive multi-optimization study generated between the input fuel value required to achieve the desired output as a production quantity in a furnace in correlation with the exact amount of energy needed.

Table 2.2 illustrates the possible areas where improvisation needs to be done along with its priority (Table 2.3).

### 2.3 Implementation of Proposed Ceramic Fibre

The present investigation is carried over Boogie Hearth furnace investigated over two types of refractory material: furnace with fire brick thermal refractory and pyro block refractory. The practical validation is generated using thermographic plots placed on the furnace's door to account for the variable of heat lost in the environment between both materials. In this investigation, replacing conventional material with pyro block, a detailed energy account is implemented with the audit of kaizen implementation as part of quality check and continuous improvement policy of energy conservation approach. The below section shows the account for the implementation of kaizen technology on the furnace refractories. Pyro block modules are ceramic fibre lining devices explicitly developed for use in high-temperature furnaces. The module is made from a high-purity mix of raw materials used to make standard and zirconia type ceramic fibres. The monolithic fibre is easily sliced to match through holes and modified in the field. Additionally, these modules are compact, have a low-heat storage capacity, and have a long-lasting operation (Fig. 2.6).

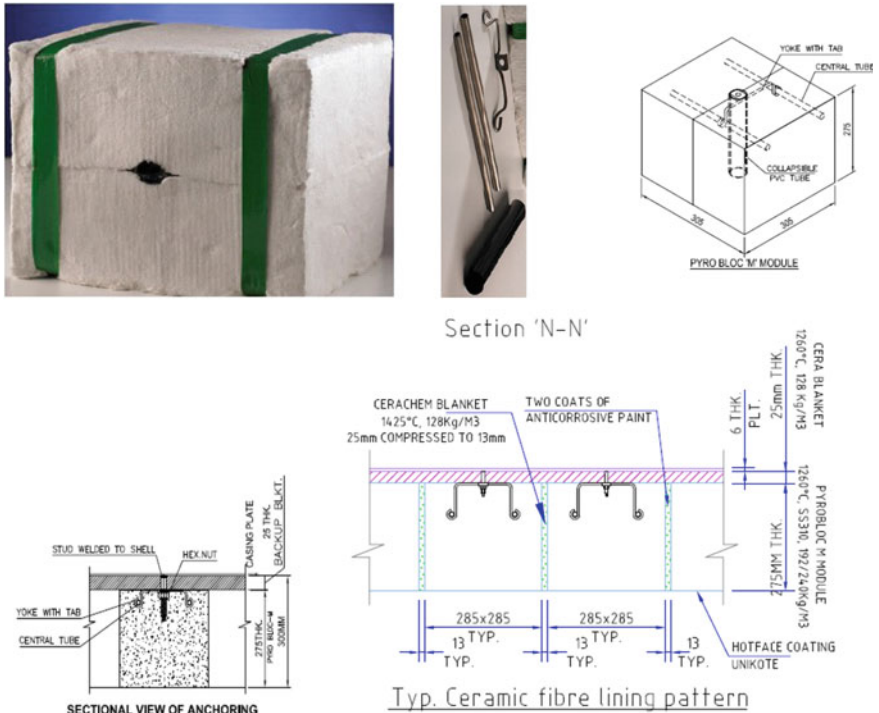
The heat loss calculation is shown in Table 2.4. The prosed improvement of pyro block offers versatile amounts of benefits to the working of the furnace by keeping generated latent heat inside the furnace only, ensuring sustainability for the production of the products. Due to the phenomenon of a pyro block, which offers lower thermal conductivity on working furnace temperature, suggest that the storage required in batches of output for the case of existing bricks lining gives around 2,448,236 kcal. In comparison, when the pyro block is implemented, the total heat needed for a storage unit for batch-wise production is about 1,221,506 kcal. The

**Table 2.2** Improvement kaizen SPN chart

Principles	Questions to be asked for the process	Process No.	Solution	Effective	The benefit to cost ratio	Adaptability	SPN
Modification	Can we modify the furnace design for energy conservation	Heating	Furnace lining bricks replaced by ceramic fibre	5	3	3	45
		Combustion	Used biofuel instead of SKO-2	3	5	5	75
Automation	Can we automate the process partially or fully with or without a close loop system?	Combustion	Oxygen sensor for to control the excess air	3	3	3	27
Utilities	Can we identify the individual elements of energy consumption by looking at the tree structure of utility						
Ideal running	Can we record the cycle in terms of energy parameters and reduce the idle running time?	Utility	Provision of VFD motor for combustion blower	3	3	3	27
Benchmarking	Can we do a benchmark against the most efficient process within	Heating	To improve furnace efficiency up to 20 from 13%	2	2	2	8

**Table 2.3** Solution priority criteria chart index

	Effective	Cost benefit	Adaptability
<i>Solution priority number (SPN) criteria</i>			
Low	1	1	1
Medium	3	3	3
High	5	5	5



**Fig. 2.6** Pyro block annealing to the wall section pre-processing

gross difference in value is about 52% which suggests the correct implementation of the kaizen strategy (Fig. 2.7 and 2.8).

### 2.4 Validation of Results

The validation of results is generated by using thermographs to plot the thermal visuals around the furnace door. The thermographic plot suggests how the furnace's thermal loss was encountered before implementing kaizen strategic pyro block where



**Table 2.4** Furnace datasheet

Description	Unit	Existing	Proposed	Remarks
Furnace length	M	5.40	5.40	
Furnace width	M	3.77	3.77	
Furnace height	M	2.55	2.30	
Wall thickness	M	0.45	0.4	
Top thickness	M	0.55	0.50	
Bottom thickness	M	0.75	0.55	
Material		Fire bricks	Ceramic bricks	
Furnace working temp.	°C	880	880	
Ambient temp.	°C	28	28	
Furnace heat losses	kCal/Hr	34,231	17,831	16,400
	Kwh/Hr	40	21	19
Furnace heat storages	Kcal	4,950,000	1,530,000	3,420,000
	Kwh	5776	1785	3991
Considering bricks 50% heat transfer	Kwh/batch	2888	1785	1103



**Fig. 2.7** Furnace before kaizen



**Fig. 2.8** Furnace after installation of pyro block



inner refractories lines are equipped with fire bricks vs inner refractories lined with pyro block (Tables 2.5 and 2.6).

### 2.4.1 Thermographs

From the above validation for comparative cases, it can be validated that when Boogie Hearth furnace was implemented on conventional lining wall brick material, it fails to store the maximum amount of generated heat inside the system thus, local hot spot creation can be observed over the thermographs of furnace door in case 1, comparatively when the kaizen implementation allocated in strategic product development to save the cost of burning fuel and increase the sustainability, thermograph visual shows at the same furnace door, there is less creation of local hot spot; thus, the generated heat tends to be stored inside the furnace only. Furnace effectiveness concerning the energy consumption to the product can be seen in Figs. 2.9 and 2.10

In heat treatment of any product, the primary intention is to generate heat and store it inside the confined space so maximum heat can be used to treat the product. Heat can produce by burning fuel inside the burner, so it is essential to monitor fuel spend to achieve heat versus heat spend. In the present study, the initial furnace was loaded with conventional fire brick refractories. The burning fuel LPG was net around 10,059 M<sup>3</sup>, compared to when the furnace loaded with strategic Kaizen implemented pyro block specific reduction fuel consumption has achieved for around same production rate. The total energy conservation saving achieved around 50%. The saving of fuel

**Table 2.5** Result validation

Energy conservation			
Heat losses are reduced by insulation, energy saving by using high-velocity burners and furnace	Implementation (target)	Investment cost: 2.40 RML	
Before Kaizen	After Kaizen		
			
Consumption (basic calculation): (A)	Consumption (basic calculation): (B)		
Before implementation, energy consumption	After implementation, tempering furnace LPG consumption is 7.30 M <sup>3</sup> /MT		
F or hardening furnace LPG consumption was 13.34 M <sup>3</sup> /MT			
Reduction: (A)–(B) LPG 6.0 M <sup>3</sup> /MT, i.e. 35% energy saving and ROI is 12% PM	CO <sub>2</sub> reduction: 190. MT/ Year/F C		
Heat treatment team		LPG M <sup>3</sup> /MT	Remarks
	Before	13,34	Energy saving
	After	6.94	45%
	Saving	6.40	
F or CO <sub>2</sub> calculation: 1 kg LPG–2.83 kgs CO <sub>2</sub> emits			

**Table 2.6** Energy consumption report

	LPG consumption in M <sup>3</sup>	Production in MT	M <sup>3</sup> /MT
Before	3.023	271	11.15
	3.494	215	16.25
	3.542	268	13.22
	10.059	754	13.34
	After	1.031	146
	1.204	169	7.14
	1.299	198	6.56
	1.593	251	6.35
	5.127	763	6.72
Energy saving	M <sup>3</sup> /MT		6.62
	Percentage		50%

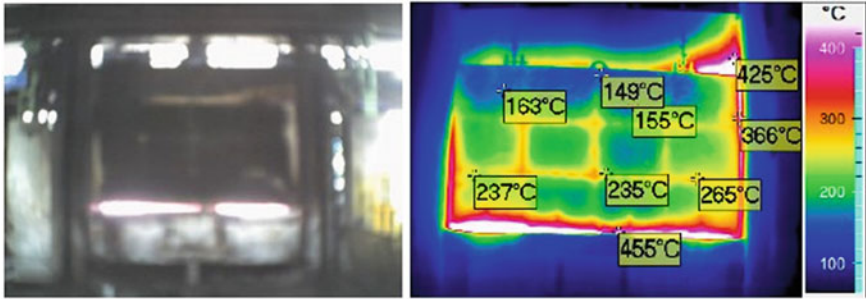


Fig. 2.9 Before Kaizen

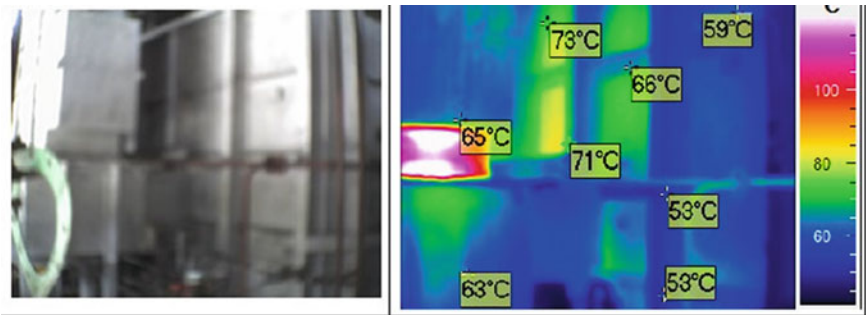


Fig. 2.10 After Kaizen

leads to saving working costs and amount of CO<sub>2</sub> emission in the environment. The increased sustainability of the furnace is presented in Table 2.7. The expected CO<sub>2</sub> emission for a standard 1 kg LPG tends to be a 1.5 kg/kg production value. In this, 1 M<sup>3</sup>/MT = 1000 kg of production ([https://people.exeter.ac.uk/TWDavies/energy\\_conversion/Calculation%20of%20CO2%20emissions%20from%20fuels.htm](https://people.exeter.ac.uk/TWDavies/energy_conversion/Calculation%20of%20CO2%20emissions%20from%20fuels.htm)).

**Table 2.7** Effective utilization of comparative fire brick wall vs pyro block

S. No.	Fire brick wall	Pyro block
LPG	13.34 M <sup>3</sup> /MT	6.72 M <sup>3</sup> /MT
CO <sub>2</sub> estimation	13,340 kg LPG × 1.5 kg/Kg CO <sub>2</sub>	6720 kg LPG × 1.5 kg/Kg CO <sub>2</sub>
Total CO <sub>2</sub> (tonne/MT)	20.01 tonne/MT	10.01 tonne/MT
Effectiveness	By pyro block = 45% less CO <sub>2</sub> emission	

## 2.5 Artificial Neural Network

The artificial neural network (ANN) is the most recently developed and commonly used technique for predicting parameters for a range of input and output values. In the current analysis, the association data points are used as feedback to the ANN. In ANN, the Levenberg Marquadt algorithm is used to consider feed-forward backpropagation. 80% of the data were used for preparation, 10% for a test, and 10% for validation (Talele et al. 2021; Talele et al. 2021; Talele et al. 2021). The number of neurons between the input and output layers is varied. Analysis of neuron independence is also conducted, with the network with the lowest MSE error value and the highest regression coefficient being regarded. The present study uses a network of ten layers, and it is found that the contribution of the ANN is specific and reliable in predicting the working effectiveness of the furnace. The topmost close fitting of a curve can be observed value near the one shown in Fig. 2.11.

This is the form of multi-objective analysis where the predictive correlation is built between both cases to determine a correlative difference in the working effectiveness of the furnace. The data visualization is performed by Python code where the object is set to be the production value against which fuel must burn in the specific case. The mathematical array developed in both the comparative cases, as shown in Fig. 2.12.

Figure 2.12 represents formulated data visualization with an available mathematical array. A comparative plot can be seen as in Fig. 2.12, where the burning value of instantaneous fuel is compared with the total effectiveness of the system. A furnace equipped with a conventional lining of fire bricks consumes more fuel, with the strategic kaizen implementation to change material of furnace wall with pyro block lining results conversion of energy within system and consume less amount of burning fuel.

## 2.6 Conclusion

Furnaces are one of the essential tools in the steel, forging, and metallurgy industries. As evolution occurs and the world moves towards net-zero emission, it is essential to maximize energy utilization. Replacing existing refractories, using clean fuel, and ensuring complete burning are the primary stages. The study performed illustrates that ceramics play a prominent role and often are efficient solutions for energy storage-related problems. We can conclude that ceramic fibres (pyro block) can be used as efficient furnace linings to fulfil both cost-saving and energy saving aspects during this performed experiment. As a result of low-thermal conductivity, the amount of heat that was dissipated through the furnace walls was drastically reduced. This helped keep the internal combustion chamber heated for a longer time and equal temperature distributions.

As discussed, the thermal conductivity of conventional refractories is 1.2 W/Mk, and that of ceramic is as low as 0.34. This lower thermal conductivity has reduced

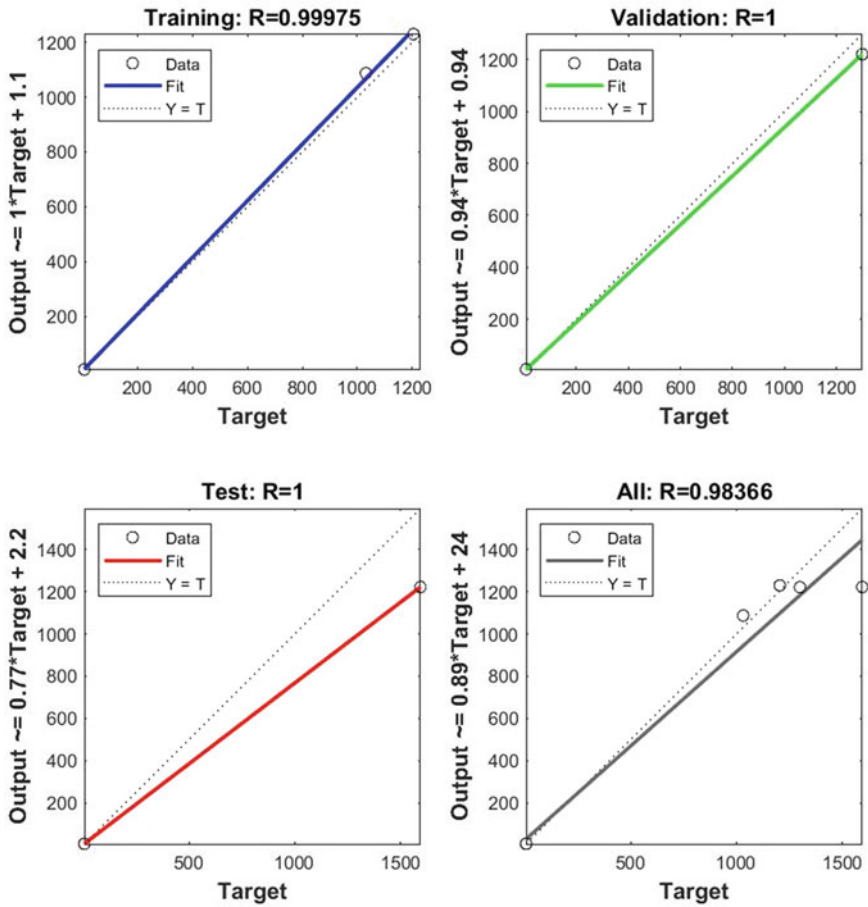


Fig. 2.11 Coefficient of regression obtained from ANN

the conduction through walls. This results in maximum heat acquisition and reduced burner operating time. The development of smart burner technology makes it possible to control heating and concentration on areas with low temperatures. This has drastically reduced the fuel consumption required per batch. Alongside all these industrial benefits, these low-thermal conductivity ceramic fibres contribute significantly to the environment. These new furnace linings have reduced fuel consumption gives clean burning without leaving any residues. It has also reduced CO<sub>2</sub> emissions. Furnaces are also equipped with oxygen sensor which prohibits fresh/non-polluted air to escape through chimneys. This air is reheated using recuperators and reused for better combustion. A multi-objective analysis is conducted based on neurons study for practically validated data of the furnace. It can be seen that the plot of the neurons is near to the value of 1 for the 3 cases, which predict the quality of results.

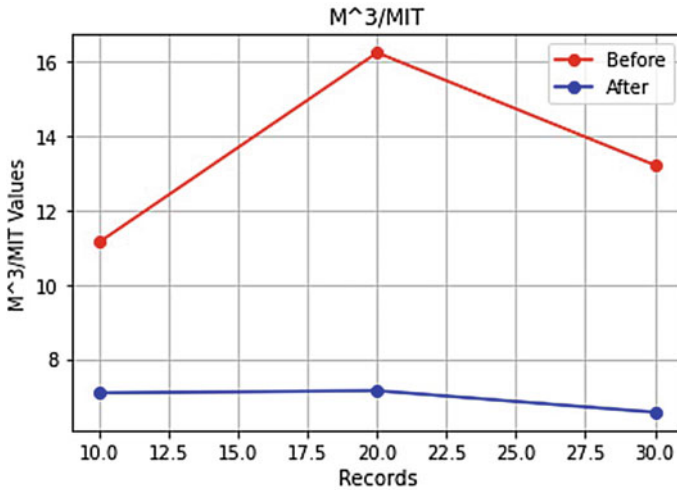


Fig. 2.12 Before and after case for burned fuel versus effective ratio

## References

- Chen WH, Chung YC, Liu JL (2005) Analysis on energy consumption and performance of reheating furnaces in a hot strip mill. *Int Commun Heat Mass Transfer* 32:695–706
- Cvinolobov NP, Brovkin VL (2004) *Furnaces of ferrous metallurgy: Learner's guide for universities*. Porogi, Dnepropetrovsk, p 154
- Dubey SK, Srinivasan P (2014) Development of three-dimensional transient numerical heat conduction model with the growth of oxide scale for steel billet reheat simulation. *Int J Thermal Sci* 84:214–227.Z
- Han SH, Chang D, Huh C (2011) Efficiency analysis of radiative slab heating in a walking-beam-type reheating furnace. *Energy* 36:1265–1272
- [https://people.exeter.ac.uk/TWDavies/energy\\_conversion/Calculation%20of%20CO2%20emissions%20from%20fuels.htm](https://people.exeter.ac.uk/TWDavies/energy_conversion/Calculation%20of%20CO2%20emissions%20from%20fuels.htm)
- Jaklič A, Vode F, Kolenko T (2007) Online simulation model of the slab-reheating process in a pusher-type furnace. *Appl Therm Eng* 27(5–6):1105–1114
- Källén M (2012) Energy efficiency opportunities within the heat treatment industry. Division of Heat and Power Technology, Chalmers University of Technology Göteborg, Sweden
- Kim JG, Huh KY (2000) Prediction of transient slab temperature distribution in the reheating furnace of a walking-beam type for rolling of steel slabs. *ISIJ Int* 40(11)
- Kim JG, Huh KY, Kim IT (2000) Three-dimensional analysis of the walking-beam-type slab reheating furnace in hot strip mills. *Nume Heat Transfer: Part A: Appl* 38(6):589–609
- Lisienko VG, et al (2016) *IOP Conf Ser: Mater Sci Eng* 150:012023
- Mayr B, et al CFD and experimental analysis of a 115 kW natural gas-fired lab-scale furnace under oxy-fuel and air-fuel conditions. *Fuel* 159:864–875
- Mayr B, et al (2017) CFD analysis of a pusher type reheating furnace and the billet heating characteristic. *Appl Thermal Eng* 115:986–994
- Quested PN et al (2009) Measurement and estimation of thermophysical properties of nickel-based superalloys. *Mater Sci Technol* 25(2):154–162
- Romenets VA, et al (2005) *Romelt process*. M.: MISiS, Publishing House “Ore and Metals”, p 400

- Rusinowski H, Szega M (2001) The influence of the operational parameters of chamber furnaces on the consumption of the chemical energy of fuels. *Energy* 26:1121–1133
- Stål och värmebehandling – En handbook (2010) Swerea IVF
- Talele V, Mathew VK, Sonawane N, Sanap S, Chandak A, Nema A (2021) CFD and ANN approach to predict the flow pattern around the square and rectangular bluff body for high Reynolds number. *Mater Today: Proc* 1(47):3177–3185
- Talele V, Thorat P, Gokhale YP, Mathew VK (2021) Phase change material based passive battery thermal management system to predict delay effect. *J Energy Storage* 15(44):103482
- Talele V, Karambali N, Savekar A, Khatod S, Pawar S (2021) External aerodynamic investigation over Ahmed body for optimal topology selection between upper and under bodywork using ANN approach. *Int J Mod Phys C* 23:2250047
- Voskoboynikov VG, Kudrin VA, Yakishev AM (1998). *General metallurgy*. M.: Metallurgiya, p 768
- Yang Y, De Jong RA, Reuter MA (2007) CFD prediction for the performance of a heat treatment furnace. *Progr Comput Fluid Dyn Int J* 7(2–4):209–218
- Yusfin YuS, Pashkov NF (2007) *Metallurgy of iron: textbook for universities*. M.: IKTs “Akademkniga”, p 464



# Chapter 3

## Thermal Energy Storage Methods and Materials



Santosh Chavan

### Abbreviations and Nomenclature

CTESM	Composite thermal energy storage materials
HTF	Heat transfer fluids
LTES	Latent heat energy storage
PCM	Phase change material
STES	Sensible heat storage
TCS	Thermochemical storage
TES	Thermal energy storage
TESM	Thermal energy storage material
VAR	Vapor absorption refrigeration
$K$	Thermal conductivity
TSD	Thermal storage density
CNTs	Carbon nanotubes
EG	Expanded graphite
GA	Graphene aerogel
GNFs	Graphite nanofibers
GnPs	Graphene nanoplatelets
GNPs	Graphite nanoparticles
$\text{LiNaCO}_3$	Lithium carbonates and Sodium carbonates
L-MWCNTs	Long Multi-walled carbon nanotubes
NG	Nano-graphite
OA	Octadecanoic acid
PA	Palmitic Acid

---

S. Chavan (✉)

Department of Mechanical Engineering, Bule Hora University, Bule Hora, Ethiopia

e-mail: [santosh.chavan083@gmail.com](mailto:santosh.chavan083@gmail.com)

### 3.1 Thermal Energy Storage Methods

#### 3.1.1 Introduction

Thermal energy storage (TES) is an extensive technology adopted for energy conservation and reutilization due to its excellent practical importance. This technology is most suitable for especially for heating cooling applications. This can be used for wide range of applications, such as ice storage, heat storage, building, and agriproduct preservation applications. The TES technology showing a great impact on modern technology due to its wide range of adaptability. In this field, a significantly strengthening actions are required in domestic and commercial sectors to utilize the stored thermal energy up to its maximum potential. TES can considerably reduce or completely minimize the gap between the supply and energy demand. TES can also reduce non-renewable energy dependence from the society by fulfilling their energy requirements, alongside it is environment friendly. TES is a prominent part of thermal systems and desirable thermal systems should possess minimum energy loss with time so that stored thermal energy can be retained for longer-term use (Sharma et al. 2009). There are different modes of thermal energy storage which are shown in Fig. 3.1 with some examples and applications.

For each storage, mode offers different possibilities depending on the available temperature range and required application. TES through sensible heat storage mode is generally preferred for short-term storage because as the storage material has some surface temperature and tends to lose heat to the surrounding. One of the examples of liquid medium sensible heat storage is domestic solar water heater and example of solid medium sensible heat storage is spreading of pebbles in swimming pools, which will absorb heat during day time and slowly releases the heat when water temperature starts decreasing. Sensible heat storage capacity is relatively lower than the latent heat storage mode.

<b>Thermal Energy Storage Methods</b>	Sensible Heat Storage	Heat Storage in Liquid Medium	Ex: Heat Stored in Water, Oil or any other Fluids
		Heat Storage in Solid Medium	Ex: Heat Stored in Rocks, Soil and Stones
	Latent Heat Storage	Solid-Solid	
		Solid-liquid	
		Liquid-gas	
	Chemical Heat Storage	Exothermic	Heat Absorption Process for Cooling
		Endothermic	Heat Rejection for Heating

Fig. 3.1 Different modes of thermal energy storage with some examples (Chavan et al. 2018a)

Latent heat storage mode is preferably used due to its large storage capacity even at lower temperature ranges. As in latent heat, storage takes place through phase change process and storage material surface temperature is almost constant the heat loss is assumed to be very low. Most common example of latent heat storage is the conversion of water to ice.

Chemical heat storage mode is not widely used due to its limited energy storage capacity (limited heat absorption and heat rejection). It is preferred only for some specific applications, when the heat is to be removed from surrounding space an endothermic chemical reaction is triggered at specific temperature so the endothermic chemical reaction absorbs the heat and reduces the surrounding temperature. Similarly, when the heat supply is required exothermic reaction is triggered at specific temperature to release the heat from the chemical reaction (Muthukumar 2005).

### ***3.1.2 Available Thermal Energy and Its Utilization***

Most of the industries involve thermal processes within it, and small part of this thermal energy is either reused for secondary applications or it is simply left to the sink. Several industries with heat treatment processes of different stages can utilize it up to certain level but still, it is not been utilized up to maximum extent. For example, a textile industry uses hot water to separate the threads and process it for interweaving these individual threads, at later stage, these interweaved threads are sent to the dyeing where color pigment is slightly heated. In this complete process, the priorly heated water can be used for secondary heating application in the dyeing section. Another industry makes use of heat to convert it into gases, liquids, solids, evaporation of vapors, and generate heat from chemical reactions. Among others, scientists, engineers, technologists, researchers, and others must understand the heat transfer phenomenon and its practical application.

Solar energy is the largest source of thermal energy available the daytime available solar thermal energy can be stored and same can be utilized for night use. For example, a vapor absorption refrigerator (VAR) can be operated after sunset with stored solar thermal energy. Solar thermal energy storage can reduce the non-renewable energy dependency, especially in the rural places where availability of electricity is uncertain. A large-scale solar thermal energy storage-based VAR can be built for a particular public area so that they can store their agriproducts commonly without depending on the electricity with low cost. Figure 3.2 shows thermal energy utilization for different applications.

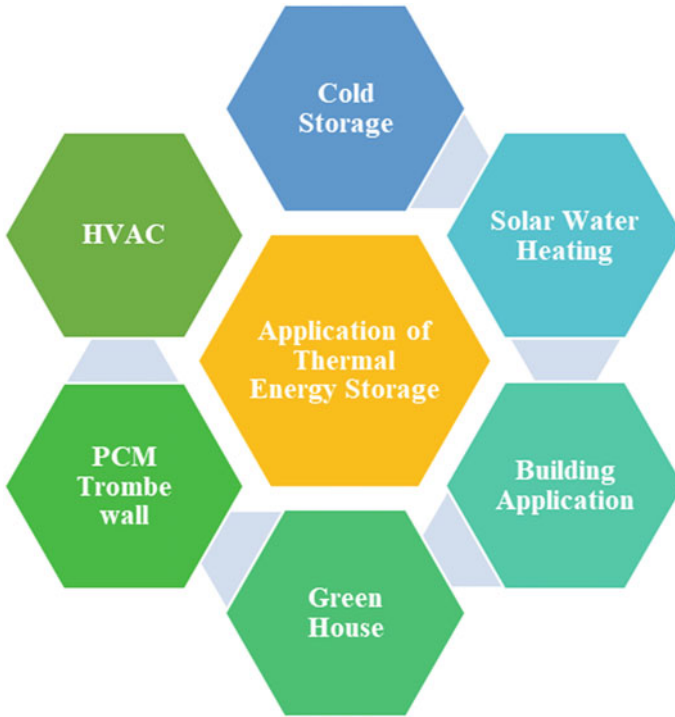
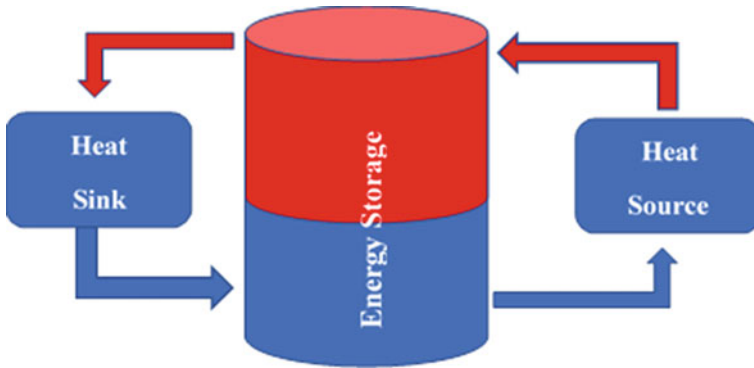


Fig. 3.2 Thermal energy utilization for various applications

### 3.1.3 Thermal Energy Storage

TES technology is recently most trending domain with its significant impact on modern technology. TES is more essential, especially during the energy intermittency like solar thermal energy. In winter, when solar energy is much less accessible and therefore less useful, the TES application is more important. It is important for society to create energy sources that are more environmentally friendly, as well as more efficient, which can then be used for heating and cooling buildings, providing power for aerospace, and for utility services as well. Most people favor TES technology for its superior characteristics such as lower energy costs, reduced energy consumption, enhanced indoor air quality, reduced initial and maintenance costs, and enhanced flexibility. Along with these TES exhibits some more advantages like condensed equipment size, supplementary efficient and active utilization of equipment, preservation of fossil fuels, and reduction of pollutant emissions (Mohamed et al. 2017). TES frameworks have a gigantic potential to build the viability of energy-conversion equipment use and for encouraging enormous scope in fuel replacements on the world's economy. TES is unpredictable and can't be assessed as expected without a nitty gritty comprehension of energy supplies and end-use contemplations.



**Fig. 3.3** Thermal energy storage tank connected with heat source and sink

By and large, a planned arrangement of activities is required in a few areas of the energy framework for the greatest potential benefits of TES to be figured it out. TES execution models can help in deciding if forthcoming progressed frameworks have execution qualities that make them valuable and alluring and, subsequently, worth seeking after through the high-level turn of events and showing stages.

The benefits of potential TES frameworks should be estimated, in any case, as far as the conditions that are relied upon to exist after innovative work is finished. Care ought to be taken not to apply too restricted a scope of estimates to those conditions. Care additionally ought to be taken to assess specific capacity framework ideas in wording that represents their maximum capacity sway. The adaptability of some TES innovations in various application zones ought to be represented in such appraisals (Kant et al. 2017). Figure 3.3 shows thermal energy storage tank connected with heat source and sink. TES utilization can be understood by observing figure as shown below.

A generous and reliable supply of energy is essential for the present industrial revolution. In general, this is done through heat liberation for the conversion of raw energy into energy that can be regulated. An illustration is heat energy is obtained through wood and coal combustion and then transferred to water to produce steam so it can be used in industrial processes. It is becoming increasingly popular to use electrical energy but to this electricity is derived from burning fossil fuels. When the mismatch between the demand and supply is wider an alternative energy-conversion system should be adopted so that this can convert available energy into the desired form of energy.

In addition to industrial and utility applications, TES has some interesting possibilities. Storage space may be necessary in structures that consume a lot of energy, such as residential and commercial buildings, in order to reduce the peak demand for air conditioning imposed by past electric systems. It would be possible to use TES for replacing these peak loads and similar way many applications can be buffered (Sivasamy et al. 2018). Increasing fuel costs, increasing difficulties in raising capital for expansions of natural gas and nuclear power plants, as well as the emergence

of the latest TES technologies, have led to a recent resurgence of interest in these TES methods. Depending on the production cost as well as market demand, energy is a product your power provider values. Energy is valued based on its role in the creation of goods and services, as well as for the convenience and comfort of its consumers. There is no doubt that there will be discussions on the merits of alternative power in the foreseeable future, but for now, energy decisions will be made based on pricing data for various alternative means. The choice between using TES methods or not will appear to be based on prospective cost reductions in either production or consumption unless legislative or regulatory requirements are in place. The prospect of economic viability is among the major considerations that need to be considered for TES systems to become commercially viable (Chavan et al. 2020a).

### **3.1.3.1 Techniques of Thermal Energy Storage**

A high rate of heat transfer makes active heat storage more effective since it is a forced convection heat storage system. Heat transfer into the storage material from a forced convection system identifies an active storage system. During continuous circulation, the medium we store is heated. It is important to note that active energy storage refers to the storage of energy during the day and its use on cloudy days, but passive energy storage uses more light throughout the building to charge and discharge a solid medium. There are two types of active thermal storage: a single tank and a double tank. Heat transfer fluid (HTF) is used for charging and discharging passive storage systems. There is no circulation in the storage medium. Systems with passive storage (also known as regenerators) typically use two mediums. Concrete and castable materials are the main components of passive storage systems.

### **3.1.4 Energy Demand**

Every day, weekly, and at ground level, energy consumption varies in commercial, public, and domestic sectors. Different energy-conversion systems should work together to meet these needs. Peak hour energy generation would be the most costly and hard to supply. Gas turbines and diesel generators are often used to meet peak energy demands, but they are dependent on high-priced and abundant fossil fuels. TES offers an energy solution, one, which is certainly an alternative to peak energy demands. Systems for managing temperature and humidity can improve operation of cogeneration, solar, wind, and hydropower facilities, too. TES can be applied to the following projects:

- **Utility:** TES systems can be charged during the daytime and can be reutilized in night or off-peak on a regular basis. This will reduce dependence on old-fashioned gas and oil peaking generators during peak periods as the stored energy will be used during these times.

- **Industry:** Industrial processes can generate high-temperature waste heat that can be utilized to pre-heat as well as to reheat the required components.
- **Cogeneration:** With a cogeneration system, heat and electricity are closely grouped, and since neither is always needed exactly, extra electricity or heat is stored.
- **Solar energy systems:** Through TES, rising capacities can be achieved with solar technology methods since TES can store excess energy on sunny days and use it on cloudy or dark days.

### ***3.1.5 Energy Storage Future aspects***

Several automotive applications require lighter than current battery packs, which researchers are devoted to making lighter and smaller. For controlling the vehicle temperature TES can be employed over the roof or coating the phase change materials (PCM) all over the vehicle body can minimize battery dependency. Actual heat is used to store energy sources in these working methods. The latent heat of melting salts and paraffins could also be used as a source of thermal energy. Latent storages decrease the amount for the storage space unit by a greater extent but after a few decades of analysis nearly all their problems that are practical still have not been fixed (Singh and Ramadesigan 2017).

The study of TES technology has many encouraging aspects. It is evident that a sustained effort to develop TES is within reach considering the cost gap and, consequently, the potential benefits of TES. There is a possibility that advanced-level TES systems will not be required for several decades with solar energy applications. Solar power usage is likely to grow as more affordable TES options become available in the near future. Some research this is certainly existing development areas into the field of TES tend to be as follows: higher-level TES and transformation systems with phase transformation, chemical, and electrochemical responses; There are several concepts in a TES to generate and to absorb the thermal energy such as thermochemical reactions. Thermochemical reactions are those where two or more chemicals start reacting with heat liberation (Exothermic reaction) or heat absorption (Endothermic reaction).

### ***3.1.6 Energy Storage Methods***

The storage element is an essential component of most energy technologies. Among the many examples of fuel that we can use as examples of energy storage, oil stands out as a particularly good one. Fuel, gasoline oil, and petrochemicals are dependable and economically available because of massive quantities of petroleum saved around the world. The Thermal energy storage systems hold transferred heat in a thermodynamically useful form before it is used in other ways. The most common

application is the example of storage of domestic and industrial hot water. This may make heating water or steam more convenient, but it is probably not often considered for periods longer than a day. New innovations in storage can sometimes be made possible by advancements in storage and are often an integral part of other new technologies. The most notable benefit of improved storage is solar power. A number of techniques tend to be under development.

A substance's energy can be maintained by increasing or decreasing its temperature by changing its phase (latent energy), or by combining the short-term storage and long-term storage methods. Power technologies tend to create new TES applications of both types. For later use, large- or low-temperature materials may be temporarily stored for later use. Solar power can be stored for nighttime home heat, summertime temperatures for winter use, winter ice for summer cooling, and electrical heat or cool from off-peak hours can be stored for use during peak times in the evening. Like fossil fuels, solar energy is not always available. The cooling loads are also often present after sunset when solar radiation is less where thermal energy supply and demand mismatch can be remedied by TES. TES can take into account the quality of the energy being used as a function of the temperature of the goods that enter, leave, and are stored. A greater range of jobs may be completed using a greater heat method following discharge of the stored thermal energy. Daily, irregular, and seasonal energy demands for manufacturing, commercial, and residential purposes vary widely. Different TES systems must operate synergistically in such diverse sectors, matching carefully to each application that is specifically selected for TES based on their application areas (Chavan et al. 2020b).

In order to understand the optimum potential benefits of thermal energy and other forms of TES, there needs to be a coordinated group of people in many sectors of the energy system.

There are three main types of thermal storage:

1. Sensible thermal energy storage (STES)
2. Latent heat thermal energy storage (LTES)
3. Thermochemical energy storage (TCS).

The most precisely established and familiar mode of storage is sensible thermal storage, followed by latent heat thermal storage which is still under development and demonstration stage and then thermochemical energy storage. Table 3.1 shows the different modes of thermal storage with capacity and efficiency data.

The energy needs of industries, commercial establishments, and the utility sector can differ daily, weekly, or seasonally. TES methods that function synergistically can help match these demands. Applications of TES include air conditioning, room heating, and cooling. With commercial fields becoming increasingly effected by electricity in the last four or five decades, TES practice has evolved into a variety of practices. Such TES systems have actually an enormous potential to help make the using thermal power equipment far better as well as assisting large-scale power substitutions from a perspective that is financial. Generally speaking, a group this is certainly coordinated of in a number of sectors regarding the energy system will



**Table 3.1** Different modes of thermal storage with capacity and efficiency data

Type of storage	Development filed	Storage capacity (kWh/ton)	Efficiency (%)
Sensible heat storage	Commercial	10–50	50–90
Latent heat storage	R&D/Demonstration/Commercial	50–150	75–90
Thermochemical storage	R&D only	120–250	75–100

<http://energystoragehub.org/technologies/thermal/thermal-storage/>

become necessary if the prospective benefits of thermal storage is to be totally realized.

This crucial energy preservation is certainly enabled by numerous types of energy storage. It is possible to save premium fuel costs with energy storage in many industrial processes that produce waste energy that can be recovered. There are different ways in which energy can be stored, but the most feasible means is to transfer it and create it as heat energy, the basis for thermal energy storage systems. This refers to the process of storing energy when it is cooled, heated, melted, solidified, or vaporized; the vital component is the heat released when the method is reversed. Its effectiveness depends on the specific heat capacity (the heat that can be stored in a material when it rises or falls in temperature). A form of TES called latent heat storage occurs when a solid or liquid transitions to a fluid or vapor without noticing any noticeably higher temperature. The main material used in sensible storage techniques is rock, surface, or liquid as the storage medium, and in addition, the heat generated by the storage material is used as a means to store energy. PCMs are used as latent heat storage systems, which allow energy to be stored or released. Generally, PCMs are packaged in tubes, shallow panels, synthetic bags, etc. or are enclosed in wall paneling, ceilings, or other components of conventional buildings (Prasad et al. 2019).

In addition to solar photovoltaic applications, TES also closely works with solar heating systems. There are a number of battery packs on the market today, chilled water storage, hot water storage, and ice storage that fulfill a number of the functions associated with it. Energy storage space applications typically receive direct bonuses from utilities, while high time-of-day prices and needs indirectly encourage consumers to consider these options. Short-term thermal energy storage is generally required for TES since it requires storing large- or low-temperature energy. For instance, TES can store solar power during the day and use it at night, heat during the summer for cold temperatures during the winter, ice during the summer for room cooling, heat created electrically during low-peak hours, and used at peak times (Fredri et al. 2020).

It is impossible to obtain solar energy on a regular basis, unlike fossil fuels. Solar power radiation reaches its peak after sunset, which often coincides with soothing loads. Therefore, solar energy produces heat that seldom escapes into the atmosphere for as long as it takes to heat the item. Because of this, solar energy rarely releases heat directly into the surrounding environment for an extended period of time. Due to this,

warm air is rarely released into the surrounding environment until a long time after solar energy has been used. TES will compensate for this mismatch between need and availability. Commercial prosperity and technological competition rely heavily on energy. In order to meet the future's power requirements, it would be helpful to possess a varied range of technologies that can be readily accessed. This is a result of forecasts which are improving and are often imprecise. In addition, the technologies developed should be ones that are environmentally responsible, efficient, and high in quality (Sarbu and Sebarchievici 2018).

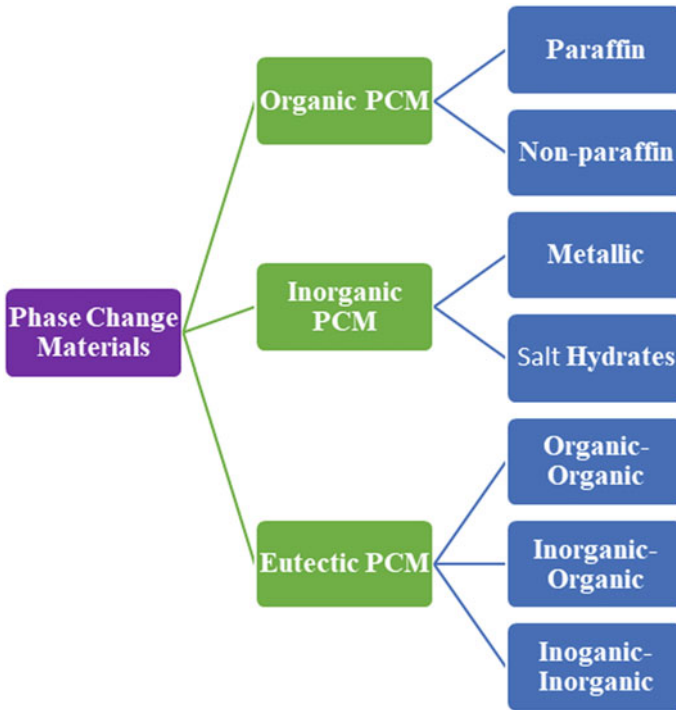
As TES is used to reduce complete energy consumption, it conserves petroleum and reduces oil import prices. It is being marketed as an efficient way to reduce the energy needs of the world. After proven performance solves the technical and economic challenges, TES is predicted to become a mainstream option that affects both the manufacturing and commercial sectors potentially resulting in enhanced power efficiency and environmental benefits, among other benefits. We identify TES as a potential method of reducing future peak-power shortages by substantially lowering peak-power demands. A significantly significant portion of our rapidly increasing needs for heating and cooling, particularly for production facilities and commercial entities, can be met by the use of waste heat and climatic power. There are numerous ecological advantages to waste-energy sources as well. There are numerous ecological advantages to waste-energy sources as well. Waste-energy sources have a number of ecological advantages as well. TES technologies have been incorporated into several different kinds and applications. TES are often used in refrigeration and/or for space heating and cooling applications and can be either sensible (oils, molten salts) or latent (ice, phase change materials). Many laboratories are conducting research on TES for its commercial, domestic, and industrial applications around the world (Zhang et al. 2016).

## 3.2 Thermal Energy Storage Materials

### 3.2.1 Introduction

In recent year's significant attempts have been put forward for efficient harnessing of different types of energies. Constant escalation in the level of greenhouse gas emissions and hike in fuel costs is the driving force for looking toward thermal energy storage (Kenisarin and Mahkamov 2007). To recover the waste heat energy available new methods and technology have to be developed (Ahmed et al. 2017). Figure 3.4 shows classification of phase change materials.

Reutilization of low-grade available energy from lower temperature range isn't positive due to several technical constraints of grabbing exergy and energy from low-grade heat. Large amount of heat energy is available between 35 and 55 °C from numerous process industries. Various types of thermal energy are stored by changing the energy they contain such as sensible heat, latent heat, and thermochemical storage.



**Fig. 3.4** Classification of phase change materials

A thermal storage device's primary component is its material. Materials decide the amount of energy to be stored at given temperature range (Bhatt et al. 2010). These thermal energy storage materials (TESM) are of different characteristics and thermophysical properties which may be suitable for specific kinds of applications. The TESH is divided into various categories based on the mode of heat storage like sensible heat storage materials, latent heat storage materials, and thermochemical storage materials.

These TESMs are further divided into sub-categories based on the medium and mode of heat transfer, like sensible heat can be stored using solid and liquid materials, whereas latent heat-storing materials are phase-changing materials also known as phase change materials. These materials may change their phase after absorbing or rejecting certain amount of heat energy. Also, TESH of low temperature can be divided into different categories depending on the melting point, which makes them suitable for a number of applications such as domestic liquid home heating, direct home heating or heat pump assisted room heating, greenhouse heating, solar cooling, among others. Medium temperature thermal storage (100–180 °C) used for several manufacturing processes, e.g., meals, reports, substance companies, etc. High-temperature storage materials (working temperature range above 900 °C) used for power-plant and metallurgical applications (Akeiber et al. 2016).

The PCMs come to be significant because of its excessive power storage ability, it lowers the fluctuation of temperature through the day period and stabilizes conditions within the range that is required. The limitations of TESM can be eliminated blending with any suitable additive (such as nanoparticles), materials to form composite thermal energy storage materials (CTESM), which allows the material to increase the storage capacity by enhancing their thermophysical properties.

### ***3.2.2 Types of Thermal Energy Storage Materials (TESM)***

Depending on the mode of thermal energy storage TESMs are divided into different categories different materials are chosen such as.

1. Sensible heat-storing materials
2. Thermochemical heat-storing materials
3. Latent heat storage materials.

**Sensible Heat-Storing Materials** These materials don't undergo phase change process only its surface temperature will change with energy absorption. These are probably solids or liquid materials and gaseous materials are not feasible due to their lower storage capacity. Solid materials used for sensible heat storage including metals, metal alloys, concrete, rocks, sand and bricks. These materials are specially used for both high and low-temperature energy storage because they will not boil or freeze. Rocks piles and pebbles are majorly used due to their lower cost and abundantly availability. Rocks are usually made of slackly packed materials and act as porous media which is very efficient for heat transfer. Heating process involves circulation of hot air through the gaps between the rocks, and while cooling process, cold air is circulated. Heat transfer process is more efficient due to availability of larger surface area through which the air interacts with rocks, Concrete and rocks approximately store 36 kJ/kg of energy, at a temperature difference of 50 °C. Liquid sensible heat storage materials also used the best example is domestic solar water heater. Likewise, numerous oils or fluids are used in various industries for storing and reutilizing the waste heat energy available from various processes (Wang et al. 2020).

### ***3.2.3 Thermochemical Heat Storage***

Thermochemical heat energy is stored in the form of chemical bonds due to their chemical structure. As per the required applications, whether heating or cooling is required, we can initiate the exothermal or endothermal chemical reaction using some specific chemicals, to break the bonds in their chemical structure which releases large amount of heat energy. Various oxides compounds are used in solar chemical

**Table 3.2** Thermal energy storage materials and their working temperature range (Prasad et al. 2019)

S. No.	Materials	Temperature range (°C)
1	Hydroxides	500
2	Iron carbonates	180
3	Metal hydrates	200–300
4	Metal oxides (Ze and Fe)	2000–2500
5	Methane/water	500–1000
6	Methanolation	NA
7	Demethanolation	200–250

reactors, including  $\text{Fe}_3\text{O}_4/\text{FeO}$ ,  $\text{MgO}/\text{Mg}$ ,  $\text{ZnO}/\text{Zn}$ , etc. However, potentiality of thermochemical energy storage is extensively encouraged the researchers to put forward their exertions, but this method is not succeeded due to its inherent limitations, such as chemical stability, durability, long-term reaction reversibility, etc. Table 3.2 shows list of thermochemical energy storage materials with temperature range and change of enthalpy.

### 3.2.4 Latent Heat Storage Materials/Phase Change Materials (PCMs)

Latent heat storage is the most efficient method of storing heat even at lower temperature ranges. Latent heat storage involves absorption and rejection of heat during phase conversion process, the phase conversion may be solid–solid, solid–liquid, or liquid–gas. Solid–gas phase change materials are impractical for the storage mechanism. Solid–solid phase change involves only internal lattice changes and less efficient to store. Solid–liquid phase change materials are mostly preferable one due to their larger storage capacity. Liquid–gas phase change materials are not preferred due to their larger volume requirements and lower storage capacity (Chavan et al. 2018b).

### 3.2.5 Classification of Phase Change Materials

In phase change materials, a substance melts and solidifies at certain temperatures. The phase change temperature identifies the temperature at which the change occurs. The selection of suitable PCM for particular range of temperature is important, for different temperature ranges and modes of applications an appropriate material should be selected for achieving superior results.

PCMs are used for both short-term (daily) and long-term (seasonal) energy storage, using different methods and materials. Some of the applications are as follows:

1. Enhancement of thermal energy storage capacity by implementing in gypsum board, plaster, concrete, etc. of the building structure, which can be utilized in peak-load shifting at working temperature range of 22–25 °C.
2. Cold storage applications in cooling plants, especially where the operating temperature range is 7–15 °C.
3. Heat storage in heating systems with working at temperature range of 40–50 °C.
4. Heat storage in solar-based heating and cooling systems working at temperature range of 80–90 °C (Gao et al. 2015).

PCMs are widely classified depending on their thermophysical transformation during heat absorption and rejection capabilities. There are several types of paraffins, most of which have straight hydrocarbon chains as well as small amounts of branching near the end. These are alkanes ( $C_nH_{2n+2}$ ). The inorganic PCMs are not much preferred due to the effect of supercooling, corrosivity as well as other harmful properties. However, use of paraffin can be complicated because of their leakage and that is undesirable in molten conditions. To reach better storability with safety, 2 or 3 materials are blended to form binary or eutectics which can be ternary also with tailored storage properties. As an example, sodium hydrate (eutectic blend) has more storage density and higher thermal conductivity than paraffin, and it melts and solidifies without accumulation or segregation of component materials.

### ***3.2.6 Characteristics of Phase Change Materials***

The PCMs selected for particular applications should possess the abilities as follows.

1. Sustain the operating temperature with correct period transition
2. Possess high latent heat capacity that reduces the size of the storage space
3. High thermal conductivity to make system charge quicker
4. Possess high density that provides better stability in melting and solidification processes
5. The volume requirement should be less and it should not undergo supercooling
6. PCMs should be chemically stable.

### ***3.2.7 Thermal Energy Storage Materials and their Properties***

Since TES materials have different inherent properties, they each have different advantages and disadvantages. Some properties with their desirableness are listed in Table 3.3.

**Table 3.3** Classification of TESM with their desirable and undesirable properties

Material	Type	Desirable properties	Undesirable properties	
Organic materials	Paraffins	Non-corrosive	Lower thermal conductivity	
		Chemically steady up to 500 °C	Not suitable with plastic container	
		Less expensive	Moderately flammable	
		Reliable		
		Safe and predictable		
	Non paraffins	High heat of fusion	Inflammability	
		No supercooling	Low thermal conductivity	
		Fatty acids are preferred for low-temperature heat storage applications	Low flashpoints Variability at higher temperatures	
	Inorganic materials	Salt Hydrate	Specific heat capacity is high	Contaminated
			Higher thermal conductivity	Needs supercooling
Phase change volume is small				
Anti-corrosive				
Companionable with plastics				
Metallic		Higher thermal conductivity	Specific heat capacity is less	
		Lower specific heat capacity	Vapor pressure is low	

### 3.2.8 Composite Thermal Energy Storage Materials

The provision of thermal energy storage using composite thermal energy storage materials is among the best methods of enhancing the thermophysical properties of PCMs. These materials are able to deliver excellent and appealing results with various compositions of different base materials and additives. A wide range of thermal storage applications benefits from materials with high storage capacity. Researchers continuously finding new ways to enhance the storage capacity increase the efficiency of the TES systems. One of the ways is to prepare tailored materials for specific applications with desired characteristics, by enhancing the desired characteristics and reducing undesired properties. For example, advancement of specific properties such as low thermal conductivity, supercooling and incongruent melting, will significantly influence the TES system performance.

### ***3.2.9 Effect of Nano-additives on Thermal-Physical Properties Enhancement***

Composite materials are the next hope for the future energy storage technology. Achieve better thermal storage performance with any single material is a very difficult and hence any suitable materials can be blended with different combinations of materials. Some of the composite materials with different additive materials are listed below to understand how these different additives affect the base material properties. Table 3.4 shows effect of nano-additives on thermophysical properties of TESMs with different combinations.

#### **3.2.9.1 Conclusions and Future Trends**

Sensible heat storage is appropriate to domestic water heating systems, district heating, and industrial requirements. A well-known commercial heat storage medium is considered to be water, due to its thermophysical properties and availability, with large number of domestic and industrial applications. In large-scale applications, underground storage of sensible heat is preferable, which utilizes both liquids and solids; however, the long-term storage of sensible heat imposes limitations on the method and is limited. Moreover, sensible heat storage systems necessitate proper design and fabrication. Phase change materials overcome the limitations of sensible heat storage and offer a higher storage capacity with the latent heat storage mode.

Phase change materials also allow to focus on a particular discharge temperature which is generally phase change temperature of the specific material. The most important properties of phase change materials are melting temperature, latent heat of fusion, and thermophysical properties which greatly influence the storage capacity. Most of the literature is attentive on repetitive and marketed materials such as paraffin. It is suggested to focused on composite materials with a wide working temperature range such as paraffins as base materials and carbon-based nanomaterials are most suitable combination for various applications. Since composite materials also suffer with some limitations like lower thermal reliability, phase-segregation, and subcooling issues which need to be studied intensely.

In future greenhouses, thermal energy storage systems can be combined with heating/cooling or humidification/dehumidification processes and also can be attached to poly-generation systems. Further research can be conducted on finding the possible candidate materials for different modes of storage that can be extensively implemented in a more cost-effective method.



**Table 3.4** TESM's with different combinations of nano-additives

Refs.	TESMs combination		Constraints analyzed	Result
	Base materials	Blends		
Tang et al. (2016)	Lithium and Sodium carbonates (43%) and (57%), respectively	MgO and CNTs*	Thermal conductivity ( $K$ ) and thermal storage density (TSD)	$K = 4.3$ (W/m K), TSD = 530 kJ/kg
Bailey (2010)	Na <sub>2</sub> CO <sub>3</sub> /MgO	MWCNTs*	TES, and constancy	Enhanced*
André et al. (2016)	Polyurethane	Graphene*	Thermal and chemical stability	Enhanced*
Zhou et al. (2014)	GA (30%) and MA (70%)	Graphite and silver iodide (0.5 wt%)	Heat of fusion	Enhanced up to 34%
Ye et al. (2014)	PEG	Acrylic polymers*	$K$ and TSD	Enhanced*
Pielichowska et al. (2016)	PEG	Cellulose and GNPs (5.3 wt%)	$K$ , and enthalpy	$K$ enhanced by 463%
Paul et al. (2015)	MA	PA and SL*	Thermal stability	Enhanced*
Torkkeli (2003)	Sodium and potassium nitrate (60:40)	Alumina nanoparticle (0.78%)	Specific heat	Improved up to 30.6%
Yang et al. (2016a)	Paraffin wax	CNTs (S-MWCNTs), L-MWCNTs, CNFs, and GNPs (5wt%.)	$K$	$K$ enhanced 164%
Fan et al. (2013)	PDMS	PDMS-G-NF *	Enthalpy	65.72% Enhanced
Wang et al. (2016)	SA	EG*	$K$	$K$ enhanced by four folds
Şahan and Paksoy (2017)	PA-SA	GnPs and EG*	$K$	$K$ enhanced 2.7 folds
Zheng (1995)	OA	GA*	$K$	$K$ enhanced 14 folds
Audichon et al. (2017)	n-Tricosane	GNFs*	Phase change	Solidification time reduced by 61%
Yuan et al. (2016)	Paraffin wax	NG*	$K$	$K$ enhanced 70%
Sanusi et al. (2011)	Epoxy	Graphene oxide and graphene*	Thermo-mechanical properties	Enhanced*
Arthur and Karim (2016)	Aluminate cement paste	Nano-MgO (NM) and Polycarboxylate*	$K$	$K$ enhanced 40.8%

(continued)

**Table 3.4** (continued)

Refs.	TESMs combination		Constraints analyzed	Result
	Base materials	Blends		
Yuan et al. (2014)	Paraffin	Cu nanoparticles (1 wt%)	Phase change characteristics	Melting time abridged by 13.1%
Liu et al. (2017a)	Clathrate hydrates	Water*	Thermal characteristic	Enhanced*
Ferrão (2017)	Paraffin	Water*	Heat transfer mechanism	Heat release rate (HRR) enhanced 25%
Wang et al. (2017)	Water	Octadecane*	TSD	$C_p$ condensed
Liu et al. (2017b)	Water	Copper nanoparticles*	Phase change characteristics	Shorten the melting time*
Pina et al. (2017)	Fatty acid	EG*		
Xu et al. (2016)	Paraffin	Alumina nanoparticles (3–8%)		
Wu et al. (2012)	Ba (OH) <sub>2</sub> ·8H <sub>2</sub> O	Cu nanoparticles*	Heat transfer rate	Enhanced*
Delgado et al. (2012)	NaNO <sub>3</sub>	Porous copper matrix*	Heat transfer characteristics	$K$ and HRR improved*
Rao et al. (2012)	Water	CuO nano particles*	Phase change characteristics	Melting period reduced*
Khodadadi and Hosseinizadeh (2007)	CaCl <sub>2</sub> –6H <sub>2</sub> O	Cu, Al <sub>2</sub> O <sub>3</sub> and CuO nanoparticles*	Energy capacity	Energy consumption condensed 43%
Lu et al. (2014)	NaNO <sub>3</sub> /KNO <sub>3</sub>	Metallic foam and sponge*	$K$	Enhanced*
Lv et al. 2016a)	Erythritol	EG *	Thermal properties	Melting time condensed 16.7% $K$ and HRR Improved*
Parsazadeh and Duan (2017)	Water	Copper nanoparticles*		
Yang et al. (2018)	Paraffin wax	xGnP-1 and xGnP-15*		
Alkan (2006)	Docosane And Hexacosane	Sulfuric Acid*		

(continued)

**Table 3.4** (continued)

Refs.	TESMs combination		Constraints analyzed	Result
	Base materials	Blends		
Jegadheeswaran et al. (2012)	Hydrated salt	Micro-copper particles*		
Karaipekli et al. (2017)	Eicosane (C20)	CNTs (1 wt%)	<i>K</i>	<i>K</i> enhanced 113.3%
Wang et al. (2014)	OP10E (30%)/water (70%)	Graphite nanoparticles (5 wt%)	<i>K</i>	<i>K</i> improved*
Li et al. (2017)	Paraffin ( <i>RT</i> 42)	EG Powder (20 wt%)	<i>K</i> and TSD	<i>K</i> enhanced 7.5 folds
Lee et al. (2016)	Epoxy	Graphene*	Thermal characteristics	Enhanced*
Yang et al. (2016b)	Paraffin	Copper foam*		Abridges melting time*
Lv et al. (2016b)	Paraffin	Kaolin*	<i>K</i>	TSD and HRR enhanced*
Lv et al. (2016c)	Polyethylene glycol	EG*	Thermal characteristics	Enhanced TSD 46.52%,
Luo et al. (2015)	Paraffin			Condense melting time*

## References

- Ahmed SF, Khalid M, Rashmi W, Chan A, Shahbaz K (2017) Recent progress in solar thermal energy storage using nanomaterials. *Renew Sustain Energy Rev* 67:450–460. <https://doi.org/10.1016/j.rser.2016.09.034>
- Akeiber H, Nejat P, Majid MZA, Wahid MA, Jomehzadeh F, Zeynali Famileh I, Calautit JK, Hughes BR, Zaki SA (2016) A review on phase change material (PCM) for sustainable passive cooling in building envelopes. *Renew Sustain Energy Rev* 60:1470–1497. <https://doi.org/10.1016/j.rser.2016.03.036>
- Alkan C (2006) Enthalpy of melting and solidification of sulfonated paraffins as phase change materials for thermal energy storage. *Thermochim Acta* 451:126–130. <https://doi.org/10.1016/j.tca.2006.09.010>
- André L, Abanades S, Flamant G (2016) Screening of thermochemical systems based on solid-gas reversible reactions for high temperature solar thermal energy storage. *Renew Sustain Energy Rev* 64:703–715. <https://doi.org/10.1016/j.rser.2016.06.043>
- Arthur O, Karim MA (2016) An investigation into the thermophysical and rheological properties of nanofluids for solar thermal applications. *Renew Sustain Energy Rev* 55:739–755. <https://doi.org/10.1016/j.rser.2015.10.065>
- Audichon T, Guenot B, Baranton S, Cretin M, Lamy C, Coutanceau C (2017) Preparation and characterization of supported RuxIr(1-x)O<sub>2</sub> nano-oxides using a modified polyol synthesis assisted by microwave activation for energy storage applications. *Appl Catal B Environ* 200:493–502. <https://doi.org/10.1016/j.apcatb.2016.07.048>
- Bailey J (2010) Modelling phase change material thermal storage systems. Open access dissertations theses. <http://digitalcommons.mcmaster.ca/opendissertations/4419/>

- Bhatt VD, Gohi K, Mishra A (2010) Thermal energy storage capacity of some phase changing materials and ionic liquids. *Int J ChemTech Res* 2:1771–1779
- Chavan S, Gumtapure V, Perumal DA (2018a) A Review on thermal energy storage using composite phase change materials. 1–13. <https://doi.org/10.2174/2212797611666181009153110>
- Chavan S, Arumuga Perumal D, Gumtapure V (2018b) Numerical studies for charging and discharging characteristics of composite phase change material in a deep and shallow rectangular enclosure. *IOP Conf Ser Mater Sci Eng* 376:012059. <https://doi.org/10.1088/1757-899X/376/1/012059>
- Chavan S, Gumtapure V, Perumal DA (2020a) Performance assessment of composite phase change materials for thermal energy storage-characterization and simulation studies 1–11. <https://doi.org/10.2174/2212797613999200708140952>
- Chavan S, Gumtapure VAPD (2020b) Numerical and experimental analysis on thermal energy storage of polyethylene/functionalized graphene composite phase change materials. *J Energy Storage*. 27:101045. <https://doi.org/10.1016/j.est.2019.101045>
- Delgado M, Lázaro A, Mazo J, Marín JM, Zalba B (2012) Experimental analysis of a microencapsulated PCM slurry as thermal storage system and as heat transfer fluid in laminar flow. *Appl Therm Eng* 36:370–377. <https://doi.org/10.1016/j.applthermaleng.2011.10.050>
- Fan LW, Fang X, Wang X, Zeng Y, Xiao YQ, Yu ZT, Xu X, Hu YC, Cen KF (2013) Effects of various carbon nanofillers on the thermal conductivity and energy storage properties of paraffin-based nanocomposite phase change materials. *Appl Energy* 110:163–172. <https://doi.org/10.1016/j.apenergy.2013.04.043>
- Ferrão P (2017) ScienceDirect ScienceDirect ScienceDirect and performance of composite building materials with phase change material for assessing the feasibility of using the heat demand-outdoor thermal temperature forecast a, b, function for a, b district a, c heat. *Energy Procedia* 143:125–130. <https://doi.org/10.1016/j.egypro.2017.12.659>
- Fredi G, Dorigato A, Fambri L, Pegoretti A (2020) Multifunctional structural composites for thermal energy storage. *Multifunct Mater* 3. <https://doi.org/10.1088/2399-7532/abc60c>
- Gao L, Zhao J, Tang Z (2015) A review on borehole seasonal solar thermal energy storage. *Energy Procedia*. 70:209–218. <https://doi.org/10.1016/j.egypro.2015.02.117>
- Jegadheeswaran S, Pohekar SD, Kousksou T, Investigations on thermal storage systems containing micron-sized conducting particles dispersed in a phase change material. *Mater Renew Sustain Energy* 1. <https://doi.org/10.1007/s40243-012-0005-7>
- Kant K, Shukla A, Sharma A (2017) Advancement in phase change materials for thermal energy storage applications. *Sol Energy Mater Sol Cells* 172:82–92. <https://doi.org/10.1016/j.solmat.2017.07.023>
- Karaipekli A, Biçer A, Sari A, Tyagi VV (2017) Thermal characteristics of expanded perlite/paraffin composite phase change material with enhanced thermal conductivity using carbon nanotubes. *Energy Convers Manag* 134:373–381. <https://doi.org/10.1016/j.enconman.2016.12.053>
- Kenisarin M, Mahkamov K (2007) Solar energy storage using phase change materials. *Renew Sustain Energy Rev* 11:1913–1965. <https://doi.org/10.1016/j.rser.2006.05.005>
- J.M. Khodadadi, S.F. Hosseinzadeh, Nanoparticle-enhanced phase change materials (NEPCM) with great potential for improved thermal energy storage ☆. 34:534–543. <https://doi.org/10.1016/j.j.cheatmasstransfer.2007.02.005>
- Lee M, Wang T, Tsai J (2016) Characterizing the interfacial shear strength of graphite/epoxy composites containing functionalized graphene. *Compos Part B* 98:308–313. <https://doi.org/10.1016/j.compositesb.2016.05.001>
- Li Q-F, Wang C, Lan X-Z (2017) Solid-solid phase transition of  $(1-C_{14}H_{29}NH_3)_2ZnCl_4$  in nanopores of silica gel for thermal energy storage. *Chinese Chem Lett* 28:49–54. <https://doi.org/10.1016/j.ccllet.2016.05.024>
- Liu Z, Hu D, Lv H, Zhang Y, Wu F, Shen D, Fu P (2017b) Mixed mill-heating fabrication and thermal energy storage of diatomite / paraffin phase change composite incorporated gypsum-based materials. *Appl Therm Eng* 118:703–713. <https://doi.org/10.1016/j.applthermaleng.2017.02.057>

- Liu Z, Wu B, Fu X, Yan P, Yuan Y, Zhou C, Lei J (2017a) Solar energy materials and solar cells two components based polyethylene glycol/thermosetting solid-solid phase change material composites as novel form stable phase change materials for flexible thermal energy storage application. 170:197–204. <https://doi.org/10.1016/j.solmat.2017.04.012>
- Lu J, Yu T, Ding J, Yuan Y (2014) Thermal analysis of molten salt thermocline thermal storage system with packed phase change bed. Energy Procedia 61:2038–2041. <https://doi.org/10.1016/j.egypro.2014.12.070>
- Luo J-F, Yin H-W, Li W-Y, Xu Z-J, Shao Z-Z, Xu X-J, Chang S-L (2015) Numerical and experimental study on the heat transfer properties of the composite paraffin/expanded graphite phase change material. Int J Heat Mass Transf 84:237–244. <https://doi.org/10.1016/j.jheatmasstransfer.2015.01.019>
- Lv Y, Zhou W, Yang Z, Jin W (2016a) Characterization and numerical simulation on heat transfer performance of inorganic phase change thermal storage devices. Appl Therm Eng 93:788–796. <https://doi.org/10.1016/j.applthermaleng.2015.10.058>
- Lv P, Liu C, Rao Z (2016b) Experiment study on the thermal properties of paraffin/kaolin thermal energy storage form-stable phase change materials. Appl Energy 182:475–487. <https://doi.org/10.1016/j.apenergy.2016.08.147>
- Lv Y, Zhou W, Jin W (2016c) Experimental and numerical study on thermal energy storage of polyethylene glycol/expanded graphite composite phase change material. Energy Build 111:242–252. <https://doi.org/10.1016/j.enbuild.2015.11.042>
- Mohamed SA, Al-Sulaiman FA, Ibrahim NI, Zahir MH, Al-Ahmed A, Saidur R, Yılbaş BS, Sahin AZ (2017) A review on current status and challenges of inorganic phase change materials for thermal energy storage systems. Renew Sustain Energy Rev 70:1072–1089. <https://doi.org/10.1016/j.rser.2016.12.012>
- Muthukumar P (2005) Thermal energy storage : methods and materials. Mech Eng
- Parsazadeh M, Duan X (2017) Numerical and statistical study on melting of nanoparticle enhanced phase change material in a shell-and-tube thermal energy storage system. Appl Therm Eng 111:950–960. <https://doi.org/10.1016/j.applthermaleng.2016.09.133>
- Paul A, Shi L, Bielawski CW (2015) A eutectic mixture of galactitol and mannitol as a phase change material for latent heat storage. Energy Convers Manag 103:139–146. <https://doi.org/10.1016/j.enconman.2015.06.013>
- Pielichowska K, Nowak M, Szatkowski P, Macherzyńska B (2016) The influence of chain extender on properties of polyurethane-based phase change materials modified with graphene. Appl Energy 162:1024–1033. <https://doi.org/10.1016/j.apenergy.2015.10.174>
- Pina A, Ferrão P, Fournier J, Lacarrière B, Le Corre O (2017) ScienceDirect ScienceDirect preparation of microencapsulated phase change materials (MEPCM) assessing the feasibility of Kokogiannakis using the heat temperature function for a long-term district heat demand forecast. Energy Procedia 121:95–101. <https://doi.org/10.1016/j.egypro.2017.07.485>
- Prasad DMR, Senthilkumar R, Lakshmanarao G, Krishnan S, Naveen Prasad BS (2019) A critical review on thermal energy storage materials and systems for solar applications. AIMS Energy 7:507–526. <https://doi.org/10.3934/energy.2019.4.507>
- Rao Z, Wang S, Wu M, Zhang Y, Li F (2012) Molecular dynamics simulations of melting behavior of alkane as phase change materials slurry. Energy Convers Manag 64:152–156. <https://doi.org/10.1016/j.enconman.2012.05.013>
- Şahan N, Paksoy H (2017) Investigating thermal properties of using nano-tubular ZnO powder in paraffin as phase change material composite for thermal energy storage. Compos Part B Eng 126:88–93. <https://doi.org/10.1016/j.compositesb.2017.06.006>

- Sanusi O, Warzoha R, Fleischer AS (2011) Energy storage and solidification of paraffin phase change material embedded with graphite nanofibers. *Int J Heat Mass Transf* 54:4429–4436. <https://doi.org/10.1016/j.ijheatmasstransfer.2011.04.046>
- Sarbu I, Sebarchievici C (2018) A comprehensive review of thermal energy storage *Sustain* 10. <https://doi.org/10.3390/su10010191>
- Sharma A, Tyagi VV, Chen CR, Buddhi D (2009) Review on thermal energy storage with phase change materials and applications. *Renew Sustain Energy Rev* 13:318–345. <https://doi.org/10.1016/j.rser.2007.10.005>
- Singh S, Ramadesigan V (2017) Advances in energy research
- Sivasamy P, Devaraju A, Harikrishnan S (2018) ScienceDirect review on heat transfer enhancement of phase change materials (PCMs). *Mater Today Proc* 5:14423–14431. <https://doi.org/10.1016/j.matpr.2018.03.028>
- Tang Y, Alva G, Huang X, Su D, Liu L, Fang G (2016) Thermal properties and morphologies of MA-SA eutectics/CNTs as composite PCMs in thermal energy storage. *Energy Build.* 127:603–610. <https://doi.org/10.1016/j.enbuild.2016.06.031>
- Torkkeli A (2003) Droplet microfluidics on a planar surface. *VTT Publ.* 52:3–194. <https://doi.org/10.1002/aic>
- Wang XJ, Li XF, Xu YH, Zhu DS (2014) Thermal energy storage characteristics of Cu-H<sub>2</sub>O nanofluids. *Energy* 78:212–217. <https://doi.org/10.1016/j.energy.2014.10.005>
- Wang C, Lin T, Li N, Zheng H (2016) Heat transfer enhancement of phase change composite material: copper foam/paraffin. *Renew Energy* 96:960–965. <https://doi.org/10.1016/j.renene.2016.04.039>
- Wang Y, Liang D, Liu F, Zhang W, Di X, Wang C (2017) A polyethylene glycol/hydroxyapatite composite phase change material for thermal energy storage. *Appl Therm Eng* 113:1475–1482. <https://doi.org/10.1016/j.applthermaleng.2016.11.159>
- Wang W, Cao H, Liu J, Jia S, Ma L, Guo X, Sun W (2020) A thermal energy storage composite by incorporating microencapsulated phase change material into wood. *RSC Adv* 10:8097–8103. <https://doi.org/10.1039/c9ra09549g>
- Wu S, Wang H, Xiao S, Zhu D (2012) Numerical simulation on thermal energy storage behavior of Cu/paraffin nanofluids PCMs. *Procedia Eng* 31:240–244. <https://doi.org/10.1016/j.proeng.2012.01.1018>
- Xu T, Chen Q, Huang G, Zhang Z, Gao X, Lu S (2016) Preparation and thermal energy storage properties of d-mannitol/expanded graphite composite phase change material. *Sol Energy Mater Sol Cells* 155:141–146. <https://doi.org/10.1016/j.solmat.2016.06.003>
- Yang J, Zhang E, Li X, Zhang Y, Qu J, Yu ZZ (2016a) Cellulose/graphene aerogel supported phase change composites with high thermal conductivity and good shape stability for thermal energy storage. *Carbon NY* 98:50–57. <https://doi.org/10.1016/j.carbon.2015.10.082>
- Yang J, Yang L, Xu C, Du X (2016b) Experimental study on enhancement of thermal energy storage with phase-change material. *Appl Energy* 169:164–176. <https://doi.org/10.1016/j.apenergy.2016.02.028>
- Yang X, Bai Q, Zhang Q, Hu W, Jin L, Yan J (2018) Thermal and economic analysis of charging and discharging characteristics of composite phase change materials for cold storage. *Appl Energy* 225:585–599. <https://doi.org/10.1016/j.apenergy.2018.05.063>
- Ye F, Ge Z, Ding Y, Yang J (2014) Multi-walled carbon nanotubes added to Na<sub>2</sub>CO<sub>3</sub>/MgO composites for thermal energy storage. *Particuology* 15:56–60. <https://doi.org/10.1016/j.partic.2013.05.001>
- Yuan H, Shi Y, Xu Z, Lu C, Ni Y, Lan X (2014) Effect of nano-MgO on thermal and mechanical properties of aluminate cement composite thermal energy storage materials. *Ceram Int* 40:4811–4817. <https://doi.org/10.1016/j.ceramint.2013.09.030>
- Yuan Y, Zhang N, Li T, Cao X, Long W (2016) Thermal performance enhancement of palmitic-stearic acid by adding graphene nanoplatelets and expanded graphite for thermal energy storage: a comparative study. *Energy* 97:488–497. <https://doi.org/10.1016/j.energy.2015.12.115>

- Zhang P, Ma F, Xiao X (2016) Thermal energy storage and retrieval characteristics of a molten-salt latent heat thermal energy storage system. *Appl Energy* 173:255–271. <https://doi.org/10.1016/j.apenergy.2016.04.012>
- Zheng JP (1995) Hydrous ruthenium oxide as an electrode material for electrochemical capacitors. *J Electrochem Soc* 142:2699. <https://doi.org/10.1149/1.2050077>
- Zhou M, Bi H, Lin T, Lü X, Wan D, Huang F, Lin J (2014) Heat transport enhancement of thermal energy storage material using graphene/ceramic composites. *Carbon NY* 75:314–321. <https://doi.org/10.1016/j.carbon.2014.04.009>

# Chapter 4

## Heat Flow Management in Portable Electronic Devices



Sagar Mane Deshmukh and Virendra Bhojwani

### 4.1 Introduction

The recent developments in the technologies help to reduce the size of the electronic devices. The electronic devices are very compact, which are prepared from assembly of more number of small components (dense arrangement). The devices mentioned come into the category of the portable electronics devices/components. The applications of which are mentioned as follows: (a) cassette players, (b) audio devices, (c) radios, (d) telephones, (e) mobile phones, (f) laptop computers, (g) pagers, (h) wrist watches with remind capabilities, (i) small toys, (j) switches and (k) resonators, etc. The power back up to the systems is generally provided by the batteries (Yeatman 2007) and or fuel cells (Ali et al. 2014). The power supplied to the different locations must be conditioned. The small components consuming the power in the electronic devices generate heat. Because of the space constraint dissipation of the heat from the devices becomes very difficult and hence heat flow management is key concern in the small electronic devices.

The maximum allowable temperature on the electronic component would be between 80 and 120 °C (Mjallal 2017). The hand-held devices should be maintained with temperature in the range of 42–45 °C. The conventional cooling techniques cannot be used at small scale because of different issues related to transfer of the heat, e.g. heat transferring media (air) has poor thermal conductivity, no space available for the movement of the heat-carrying media, placement-related issues, etc.

In case if the heat is not removed from the system, it may lead to following shortcomings (Mjallal 2017), (a) decreased life of the electronic components, (b) low voltage problems, (c) power conversion issues, power leakage issues and degradation

---

S. M. Deshmukh (✉)

Department of Mechanical Engineering, Tolani Maritime Institute, Induri, Pune, India  
e-mail: [manedeshmukhsagar5@gmail.com](mailto:manedeshmukhsagar5@gmail.com)

V. Bhojwani

Department of Mechanical Engineering, MIT ADT University, Loni, Pune, India



of the chip life, (d) poor overall efficiency of the device, etc. It is very essential to maintain proper heat balance in the portable electronic devices.

In order to achieve a proper heat balance and/or to avoid the locally observed hotspots, diffusion of the heat should be done at fast rate and in large amounts. Heat flow management in the micro-electronic systems is based on cooling techniques used to remove the heat. This chapter explains the different cooling techniques used in the electronics cooling.

## **4.2 Recent Techniques Used to Get the Heat Flow Management in Electronics Systems (Cooling Technologies)**

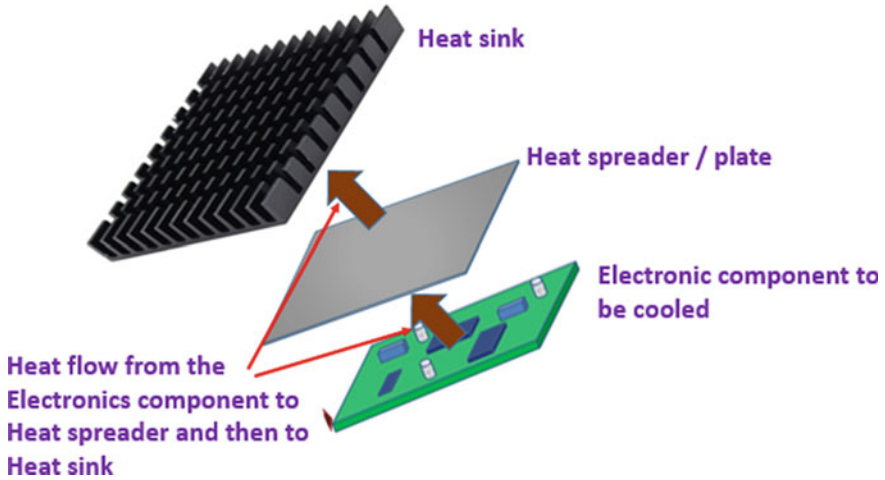
Following are the technologies used for heat flow management in the electronic systems,

- Heat Sinks
- Cold plates for the electronics cooling
- The natural air cooling
- Forced air cooling
- Use of the heat pipes
- Use of the Peltier effect for cooling
- Use of the synthetic jets for cooling
- Electrostatic fluid acceleration cooling
- Immersion cooling
- Use of the phase change materials.

All the above cooling technologies used to cool the micro-electronics systems are discussed in detail below.

### **4.2.1 Heat Sink Designs**

Heat sink is a device often called as heat exchanger which is made up of metallic surfaces like copper or aluminium, etc. The simple heat sink with rectangular fins is shown in Fig. 4.1. It collects heat from the electronic device (location or platform where heat is generated) and transfers it to the transferring media (generally fluids like air, water, etc.). The main purpose of using the heat sinks in the electronic devices is to increase the area of surface for heat sharing. Sometimes the surface on which the heat sink is to be placed is not similar to the surface of the heat sink and heat spreaders are used. Heat spreaders are the connections between the heat sinks and the electronic device from which heat is to be removed.



**Fig. 4.1** Heat Sink with rectangular fins

Three types of heat transfers are generally involved in the process (as shown in Fig. 4.1) viz. (a) Conduction of the heat from electronic device to heat spreader and (b) conduction of the heat from heat spreader to surface of the heat sink and (c) convection and radiation from heat sink to cooling media.

**4.2.1.1 Heat Conduction**

The heat conduction is a phenomenon that occurs because of the energy sharing between the molecules with higher energy levels and lower energy levels. The energy transfer occurs from the higher energy level to lower energy level. Following equation can be used to calculate the heat by conduction:

$$q = -KA \frac{dT}{dX}$$

where,

- $q$  Heat transfer from electronic chip to the heat sink through heat spreader in ‘Watt’.
- $K$  Thermal conductivity of the heat spreader and heat sink (it varies from metal to metal), ‘W/mK’.
- $A$  Surface area used for heat transfer, ‘m<sup>2</sup>’.
- $\frac{dT}{dX}$  The temperature gradient existing along ‘X’ direction, ‘K/m’.

The general equation for heat conduction in all the three directions can be written as:

$$q = -KA \nabla T,$$

where,

$$\nabla T = i \frac{\delta}{\delta x} + j \frac{\delta}{\delta y} + k \frac{\delta}{\delta z}$$

where,

$i$ ,  $j$  and  $k$  are the unit vectors along  $x$ ,  $y$  and  $z$  directions.

#### 4.2.1.2 Convection

The convection of heat occurs generally between solid surfaces (e.g. heat sink surface) to the fluids (e.g. air) which are in the motion. The equation used is as follows:

$$q = hA(T_{\text{surface}} - T_{\text{fluid}})$$

where,

- $h$  Heat transfer coefficient for convection,  $\text{W/m}^2\text{K}$ ,
- $T_{\text{surface}}$  Temperature of the surface (e.g. Surface of heat sink),  $\text{K}$
- $T_{\text{fluid}}$  Temperature of the fluid in motion (e.g. Temperature of air),  $\text{K}$ ,

#### 4.2.1.3 Radiation

The energy transferred through the electromagnetic waves is called as radiation heat transfer.

$$q = \sigma \epsilon A (T_{\text{surface}}^4 - T_{\text{fluid}}^4)$$

where,

- $\sigma$  Stefan Boltzmann constant,
- $\epsilon$  Emissivity.

### 4.2.2 Cold Plates for Portable Electronic Cooling

The method allows use of the metal plate (cold plate) between electronic component (source of the heat) and the working fluid which collects the heat from metal plate. The method is used to cool the micro-electronic circuits require higher thermal conductivity and higher heat flux carrying capacity. The liquids have a higher capacity to carry heat compared to the air. The method which facilitates to use liquids in cooling of the electronic systems is use of cold plates. The simple sketch of the cold plates used in the cooling applications is shown in Fig. 4.2. The cold plates are very simple

in construction which includes cold plate surface/s (either on one side or both side), which are mounted on the hot zones created by the system (e.g. Electronic components generating heat) from which heat is to be removed. The heat collected by the surface of the cold plate is supplied to the working fluid flowing through the passages by convection mainly. Depending on the nature of the working fluid, the temperature is increasing or it is converted into the vapour phase. Figure 4.2 shows following locations, entry for the cold working fluid, front side and back side surfaces for collecting heat from system and outlet for the hot working fluid. The collected heat by working fluid can then be rejected at a required place. The working fluids used in the cold plates are single-phase or two-phase substances. The single-phase working fluids are oil-based fluids. The two-phase working fluids are mainly dielectric fluids and different refrigerant series.

The different arrangements of the cold plates are shown in Figs. 4.3, 4.4, 4.5 and 4.6. Figure 4.4 shows the arrangement of batteries combined together without addition of the cold plates in between them.

Figure 4.5 gives the clear picture of how cold plates are arranged between the batteries. It also shows the holding supports required in the arrangement.

This arrangement includes the use of cold plates between the batteries and fans placed on both the sides of the module. The performance of this system is better than the first module because it includes the heat collection from the hot battery surfaces by working fluid in the cold plate and the air circulation by the fan. The air used in

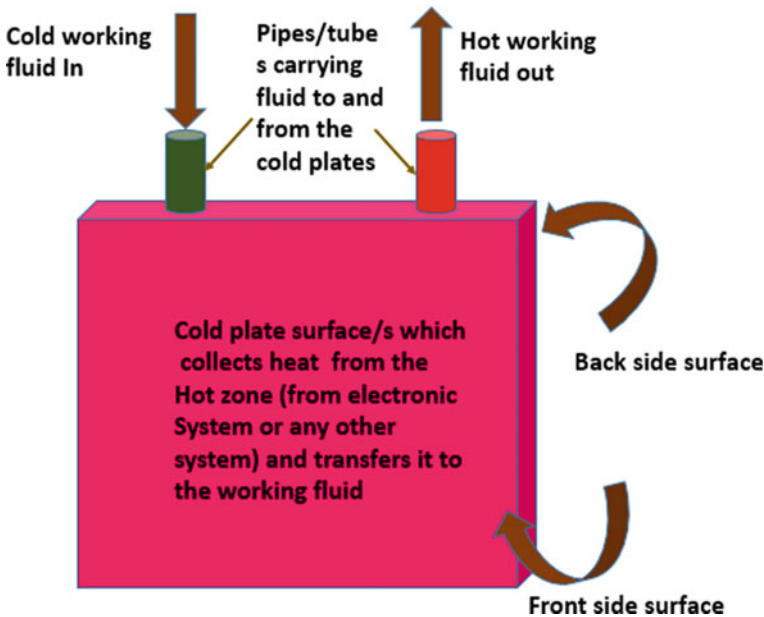
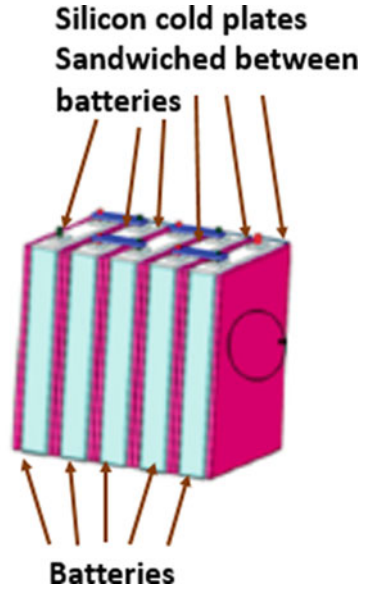
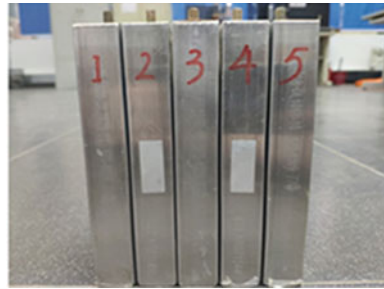


Fig. 4.2 Simple cold plates used in the cooling applications

**Fig. 4.3** Silicon cold plates sandwiched between the batteries (Li et al. 2019)



**Fig. 4.4** Normal module (without cold plates) (Li et al. 2019)



**Fig. 4.5** Cold plates of silicon material are placed in between batteries (Li et al. 2019)



**Fig. 4.6** Cold plates of silicon material and air flow circulation over it by fans (Li et al. 2019)



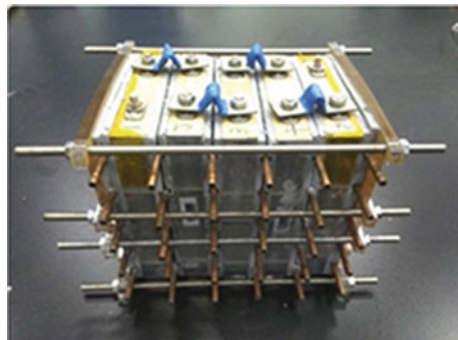
the system has a low thermal conductivity and hence the heat dissipation rates can be decreased.

Figure 4.7 shows the module in which the cold plates made from silicon are connected to the copper tubes. The performance of the system is improved because of the higher heat dissipation by copper tubes. Table 4.1 presents the data related to different types of the cold plate designs and related data.

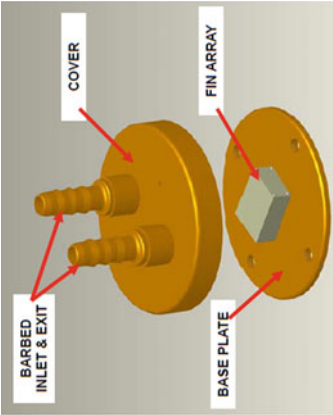
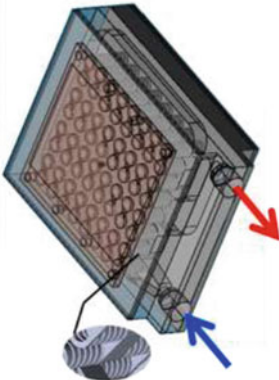
The working fluids used in the cold plates should have following properties:

- (a) Higher thermal conductivity (required to carry maximum possible heat from the hot zones)
- (b) Higher specific heat (required to raise the temperature of the working fluid at the fast rate and to ensure the collection of the heat is performed at faster possible rates.
- (c) Lower viscosity (This property is important for the faster fluid movement and to allow the lowest possible size of the tubes used for cold plates)
- (d) Freezing point should be as low as possible (to avoid its freezing on the inner surface of the pipes)
- (e) Higher flash point (to avoid explosions in the system)
- (f) Low toxicity
- (g) Low corrosion

**Fig. 4.7** Cold plates of silicon material connected to the copper tubes (Li et al. 2019)

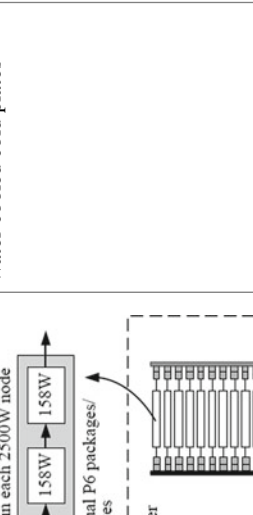
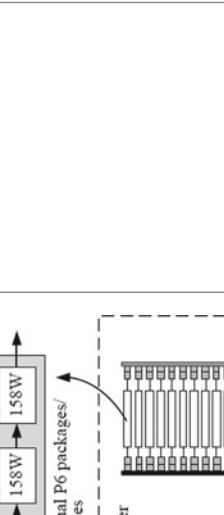


**Table 4.1** The different cold plate designs

Sr. No.	Authors	Design of the cold plate	Material used	Applications
1	Sukhvinder Kang et al. (2007)		Copper disc-shaped and water-based fluid	CPU cooling and GPU cooling
2	Sukhvinder S. Kang (2012)		Vortex liquid plate design and water glycol coolant	IGBT cooling

(continued)

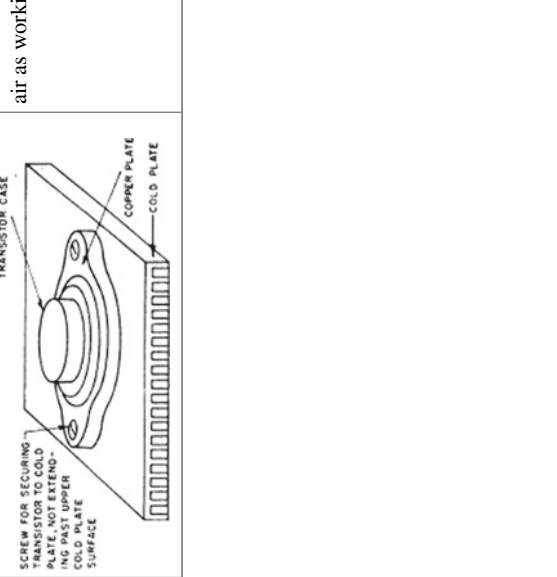
Table 4.1 (continued)

Sr. No.	Authors	Design of the cold plate	Material used	Applications
3	Levi Campbell (2012)	 <p>1 of 4 parallel circuits in each 2500W node              158W → 158W → 158W → 158W              Individual P6 packages/              coldplates              0.95 liters/min              T<sub>fw,i</sub> T<sub>fw,o</sub> RD H-Xer CDU Rack Facility H<sub>2</sub>O              T<sub>w,i</sub> 14 Nodes Rack H<sub>2</sub>O</p>	Water-cooled cold plates	CPU cooling for IBM p575 supercomputer
4	Li et al. (2019)		Silicon cold plates with water flowing through the tubes	Used for thermal management of the batteries

(continued)



**Table 4.1** (continued)

Sr. No.	Authors	Design of the cold plate	Material used	Applications
5	Mark (1958)		Aluminium cold plates used air as working fluid	Transistor cooling

- (h) Higher thermal stability (to maintain the required properties in the fluid)
- (i) Higher chemical stability
- (j) Low cost
- (k) Easily available.

The commonly used working fluids in the cold plates are as follows:

- (a) Water
- (b) Deionized water
- (c) Inhibited Glycol and water solutions
- (d) Dielectric fluid.

Some of the commonly used working fluids in cold plates along with their properties have mentioned in Table 4.2.

### **Advantages**

- (a) Simple in construction
- (b) This method does not require the additional power to cool the system
- (c) The additional surface area needed to enhance the heat transfer is not required (e.g. in case of heat sinks it is required)
- (d) It can be directly connected to the electronic components
- (e) Localized cooling of the electronic components is possible
- (f) The heat transfer capacity is higher compared to the air cooling system
- (g) Because of number of cold plate materials available in the market, weight of the system can be reduced by proper selection of the material
- (h) Less space is required for its installation
- (i) Can be operated in any orientation by setting the required flow direction
- (j) No moving parts and hence less maintenance is required
- (k) No noise and vibrations are generated in the system.

### **Disadvantages**

- (a) Because of more number of connected parts, chances of failure increases
- (b) It needs working fluid to carry away heat from the electronic system (water cannot be used all the time)
- (c) This system needs the micro channels for the flow of liquid which are to be fabricated by precise techniques and hence cost increases
- (d) Pressure drop in the micro channels is main trouble (maintaining required flow rate is problematic).

### **Applications**

- (a) Cooling of the computer CPU
- (b) Cooling of the micro-electronics (IGBT)
- (c) Cooling of transistor

**Table 4.2** Common working fluids suitable to use in cold plates and their properties (Rowe 1995, Thermal systems manual)

Working fluid in cold plate	Freezing point in °C	Flash point in °C	Viscosity in kg/ms	Thermal conductivity In W/m K	Specific heat, J/kg K	Density, kg/cu. m
Aromatic (DEB)	< -80	57	0.001	0.14	1700	880
Silicate ester (Coolanol 25 R)	< -50	>175	0.009	0.132	1750	900
Aliphatic (PAO)	< -50	>175	0.009	0.137	2150	770
Silicon	< -110	46	0.0014	0.11	1600	850
Fluorocarbon	< -100	None	0.0011	0.06	1100	1800
EG/Water (50% EG by volume and 50% water by volume)	-37.8	None	0.0038	0.37	3285	1087
PG/Water (50% EG by volume and 50% water by volume)	-35	None	0.0064	0.36	3400	1062
Methanol/water (40% methanol by wt. and 60% water by wt.)	-40	29	0.002	0.4	3560	935
Ethanol/water (44% by wt. Ethanol and 56% by wt. water)	-32	27	0.003	0.38	3500	927
Potassium format/water (Potassium 40% by wt. and Water 60% by wt.)	-35	None	0.0022	0.53	3200	1250
Ga-In-Sn	-10	None	0.0022	39	365	6363

- (d) Cooling of the battery
- (e) Cooling of higher power lasers
- (f) Cooling of fuel cells
- (g) Cooling of medical equipments
- (h) Cooling of motor drives.

### 4.2.3 Convective Air Cooling

This is the old and simple method used to cool the electronic systems. In this method, the naturally available air is used to cool the electronic systems. This method utilizes the concept of density difference to carry away heat from the systems. The cold air (with more density) is supplied to the system (to be cooled), it absorbs heat and becomes hot (with less density). The buoyancy effect pushes the less dense air upward and the fresh air can again be supplied at the bottom or the side of the system. This process of supplying the air at the bottom and its removal at the top or side of the system will be continued constantly to remove heat. Looking at the requirement of the system vents are provided at the top or the side of the electronic systems (for outgoing air) and at the bottom or side (for incoming fresh air). The heat flux carried in this method depends on the amount air supplied and the space which is available to carry the heat flux from the system. The distribution of temperatures on IC chips was analyzed using the ANSYS FLUENT in mixed convection mode (Mathew et. al. 2018).

The Newton's law of cooling can be used to find out how much heat flux is carried by air. The following is the equation to find out the heat flux (Incropera 2007 Edition)

$$Q = hA(T_s - T_a)^b$$

where,

- $Q$  Heat carried away by the air, W
- $h$  Heat transfer coefficient,  $W/m^2K$
- $A$  Cross-sectional area of the surface,  $m^2$
- $T_s$  Temperature of the source of heat or electronic surface, K
- $T_a$  Temperature of the air, K
- $b$  scaling exponent

#### Advantages

- (a) Easy air availability and
- (b) No power required to run this cooling system.

#### Disadvantages

1. The heat-carrying capacity depends on the natural air movement
2. It cannot be used when large amount of heat is to be carried
3. It cannot be used in micro-electronic systems because of space constraints.

#### Applications

- (a) Electronic board cooling (comparatively large size)
- (b) Condenser cooling in absence of the forced air draught.

#### **4.2.4 Forced Air Cooling**

This method includes creation of the forced draught of the air through external agency (e.g. Fans or blowers). This is very common method used to cool the electronic systems. The air is used as media to remove the heat from the electronic components.

##### **Advantages**

- (a) The heat flux carrying capacity is more compared to natural type air cooling
- (b) The size of the system can be reduced for the same heat flux carrying capacity
- (c) The air supply and removal vents location can be changed based on orientation and space availability
- (d) Easy air availability.

##### **Disadvantages**

- (a) It needs power to drive the fans or blowers, etc.
- (b) Cost increases because of the additional accessories
- (c) The amount of heat carried is less compared to other recently developed cooling techniques which use the liquid coolants.

##### **Applications**

- (a) Computer CPU cooling
- (b) Laptop battery cooling
- (c) Cooling of an electronic chip
- (d) Cooling of the LEDs
- (e) Cooling of the Inverters.

#### **4.2.5 Heat Pipes**

Heat pipes have found to be the best method for portable electronic cooling devices. The heat pipe technology is used because of its simple structure, high efficiency, cost-effective and flexibility. The heat pipe uses the working fluids whose phase change can be used to collect the heat from one location and to transfer it to the another location. It is effectively used in the portable electronic devices for cooling purposes because of its capacity to handle the heat is more than the generally used heat sinks of higher thermal conductivity (e.g. Copper or Aluminium). The heat pipe facilitates large amount of heat transfer with minimum temperature drop.

### 4.2.5.1 Principle of Operation of the Heat Pipe

The operation of the heat pipes depends on collection of the heat at the evaporator’s location (Working fluid collects the heat from the electronic device which is heated) and discharging the heat at the condenser’s location (working fluid rejects the heat in the cooling media or to the environment). The simple construction of the heat pipe is shown in Fig. 4.8. In the construction of the heat pipe following components play a significant role (a) Evaporator—The heat transfer takes place from the electronic device (hot spot) to the heat pipe and then it’s given to the working fluid which helps in the evaporation of the fluid (Heat collection process).

(b) The working fluid in the vapor form is transferred from the evaporator to the condenser by pressure drop in the fluid.

(c) Condenser—The working fluid reaching in the vapour form is converted into liquid form (Heat rejection process).

(d) Wick –The working fluid in the liquid form returns from condenser to the evaporator through wick by the influence of the capillary action and pressure drop.

The main condition to get the movement of the working fluid in the heat pipes is

$$\Delta P_{\text{capillary}} > \Delta P_{\text{liquid}} + \Delta P_{\text{vapour}} + \Delta P_{\text{gravity}}$$

where,

- $\Delta P_{\text{capillary}}$  The maximum capillary force inside the wick or structure
- $\Delta P_{\text{liquid}}$  Pressure drop required to transfer the fluid from condenser to evaporator
- $\Delta P_{\text{vapour}}$  Pressure drop required to transfer the fluid from evaporator to condenser

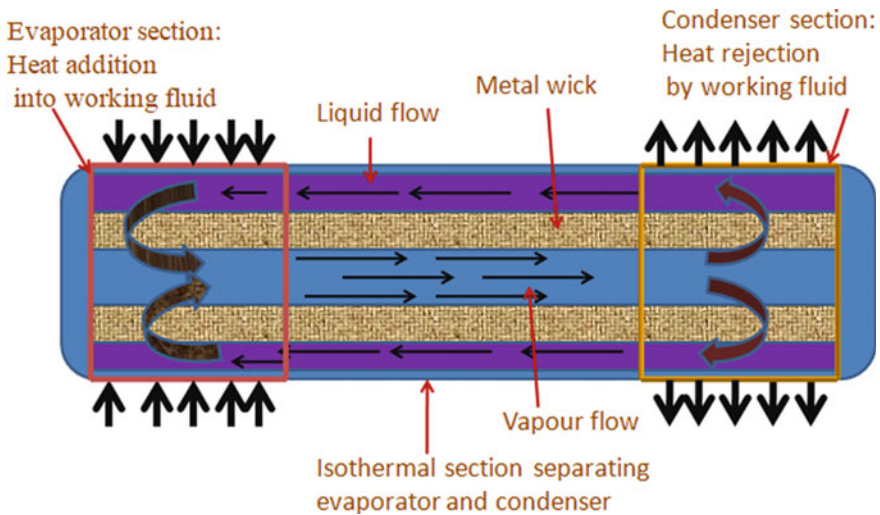


Fig. 4.8 Principle of operation of the heat pipe

$\Delta P_{\text{gravity}}$  Pressure drop because of the gravity force (it depends on the orientation of the heat pipe)

$$\Delta P_{\text{liquid}} = \frac{\mu_{\text{liquid}} L Q}{\rho_{\text{liquid}} K A_w h_{fg}}$$

where,

$\mu_{\text{liquid}}$  Viscosity of the working fluid in the liquid form  
 $L$  Effective length used for the transfer of the fluid in heat pipe,  
 $Q$  Fluid flow rate  
 $\rho_{\text{liquid}}$  Density of the working fluid  
 $K$  Permeability of the wick structure  
 $A_w$  Wick cross-sectional area  
 $h_{fg}$  Latent heat of vaporization of the liquid.

The vapour pressure drop can be calculated from the following formulae

$$\Delta P_{\text{vapour}} = \frac{16\mu_{\text{vapour}} L_{\text{effective}} Q}{2 \frac{D_{\text{vapour}}^2}{4} A_{\text{vapour}} \rho_{\text{vapour}} h_{fg}}$$

where,

$\mu_{\text{vapour}}$  Viscosity of the vapour phase of the working fluid  
 $L_{\text{effective}}$  Effective length  
 $A_{\text{vapour}}$  Cross-sectional area of the vapour chamber  
 $\rho_{\text{vapour}}$  Density of the vapour  
 $h_{fg}$  Latent heat  
 $Q$  Fluid flow rate  
 $D_{\text{vapour}}$  Distance of the vapour chamber

The maximum pressure drop in capillary is calculated as follows

$$\Delta P_{\text{capillary}} = \frac{2\sigma_{\text{liquid}}}{r_{\text{effective}}}$$

where,

$\Delta P_{\text{capillary}}$  Maximum pressure drop in the capillary  
 $\sigma_{\text{liquid}}$  Surface tension  
 $r_{\text{effective}}$  Effective radius of the wick pores

The maximum allowable heat transfer is

$$Q_{\text{max}} = \left( \frac{\rho_{\text{liquid}} \sigma_{\text{liquid}} h_{fg}}{\mu_{\text{liquid}}} \right) \left( \frac{A_w K}{L_{\text{effective}}} \right) \left( \frac{2}{r_{\text{effective}}} - \frac{\rho_{\text{liquid}} g L_{\text{effective}} \sin \theta}{\sigma_{\text{liquid}}} \right)$$

where,

$\emptyset$  The angle between heat pipe axis and horizontal (This is considered to be positive when the evaporator is installed above the condenser and it is negative for opposite case)

If,  $\emptyset = 0$ ,

Then the equation is modified as follows,

$$Q_{\max} = \left( \frac{\rho_{\text{liquid}} \sigma_{\text{liquid}} h_{fg}}{\mu_{\text{liquid}}} \right) \left( \frac{A_w K}{L_{\text{effective}}} \right) \left( \frac{2}{r_{\text{effective}}} \right)$$

#### 4.2.5.2 Heat Pipe Structural Details

The structure of the heat pipe includes three parts which are, (a) The container used in the pipe, (b) wick structure used and (c) working fluid used for handling the heat (may be heat collection or heat rejection).

##### The Container Used in the Heat Pipe

The container of the heat pipe is a metallic body that allows flow of heat through its structure from and to working fluid. Generally, it is selected based on following parameters,

- (a) High thermal conductivity
- (b) Good wettability
- (c) Good machinability
- (d) Ability to get welded easily
- (e) High strength to weight ratio
- (f) Good compatibility with the surrounding
- (g) Good compatibility with the working fluid
- (h) Less porous
- (i) Ability to maintain minimum temperature difference between wick structure and the heat source.

##### Wick Structure Used

This is very important part of the heat pipe which helps to transfer the fluid from condenser to the evaporator by capillary action in any required orientation/position of the heat pipe.





**Fig. 4.9** Wick with sintered structure (Elnaggar 2016)

The wick structures are observed in following types.

- (a) Wick with sintered structure
- (b) Wick with grooves
- (c) Wick with screen mesh.

All these wicks are discussed in detail below,

**(a) Wick with sintered structure**

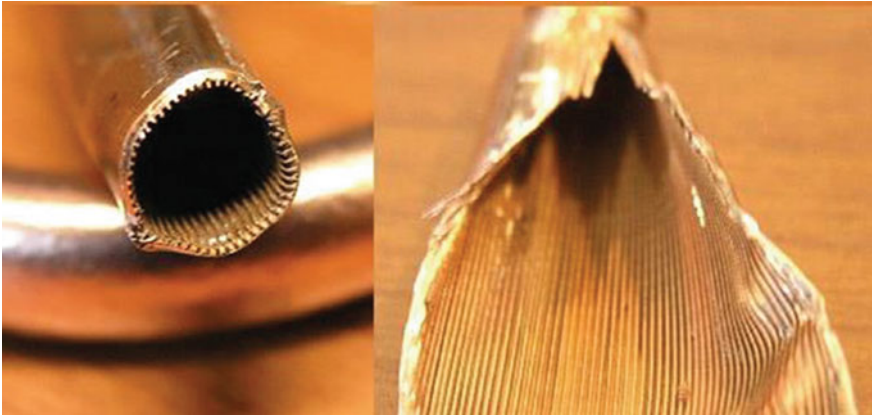
Figure 4.9 shows wick with sintered structure. In this type of wick, very small pore size increases capillarity force generated in the process, which is essential during the antigravity applications. The permeability is low. This type of wick helps to maintain the very small temperature differences between condenser and the evaporator. The lower thermal resistance in the arrangement leads to improve the thermal conductivity of the heat pipe. The cylindrical wicks are shown in Fig. 4.9 The Permeability values of the rectangular heat pipes were similar to the cylindrical ones. The copper powder can be sintered at a temperature of 800–1000 °C.

**(b) Wick with grooves**

Figure 4.10 shows the wick picture with grooves fabricated on the internal surface of the channel carrying the working fluids. This can be used in any orientation but with low capillary force used to drive the fluids. It's used for the small-capacity power applications. The different parameters which are important while designing this type of wick is size of the grooves and its material.

**(c) Screen mesh wick**

The screen mesh wick is shown in Fig. 4.11. This wick shows very good characteristics when more power is to be handled at any random orientation. In this type of



**Fig. 4.10** Wick with grooves (Elnaggar 2016)



**Fig. 4.11** Screen mesh wick (Elnaggar 2016)

the wick structure major role is played by the wick thickness, number of layers of fiber, material of the fiber used and type of the fluid used.

Characteristics of the working fluids used in the heat pipes.

The working fluid which is circulated in the flow channels plays a very important role in heat pipes. It has to carry heat from one location and drop it to the other location. The working fluid must have following characteristics.

1. It must not react with the wick structure and materials of the walls
2. Lower viscosities
3. It should have higher thermal conductivity
4. It should have higher latent heat

**Table 4.3** Properties of the working fluids used in the heat pipe (Elnagar 2016)

Working fluid	Boiling points (°C)	Melting points (°C)	Useful working range (°C)
Helium	-261	-271	-271 to -269
Nitrogen	-196	-210	-203 to -160
Ammonia	-33	-78	-60 to 100
Acetone	57	-95	0-120
Methanol	64	-98	10-130
Flutec PP2	76	-50	10-160
Ethanol	78	-112	0-130
Water	100	0	30-200
Toluene	110	-95	50-200
Mercury	361	-39	250-650

5. It should possess good wet ability with the wick structure and material of the wall
6. It should be thermally stable
7. It should have good surface tension.

The properties of the working fluids used in the heat pipes are presented in Table 4.3. The distilled water is used as a working fluid normally but many scientists have conducted trials by adding the nano-particles in the water to check the performance. Other fluids listed in the table have been also used for electronic cooling.

#### 4.2.5.3 Types of the Heat Pipes

##### Cylindrical Heat Pipe

In this type of the heat pipe, the arrangement to circulate the working fluid is provided in the structure (through wicks). This is one of the old types of the heat pipe and it is simple in construction.

Figure 4.12 shows the cylindrical heat pipe which involves three sections mainly (a) evaporator section, (b) middle section (adiabatic zone) and (c) condenser section.

The studies conducted earlier show that design of the cylindrical heat pipe with very less heat loss at the middle section is possible. The cylindrical copper heat pipe with working fluid water was tested. The two layers of the wicks were used with 150 meshes. The temperature drops of less than 5 K were observed in their studies. The steady-state value of the temperature of the vapour was found to be increasing with either increasing the heat input or decreasing the water flow rate.

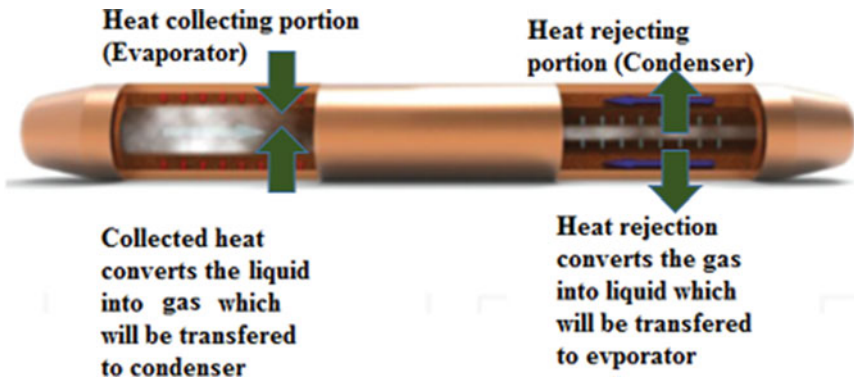


Fig. 4.12 Cylindrical heat pipe (Elnaggar 2016)

### Flat Heat Pipe

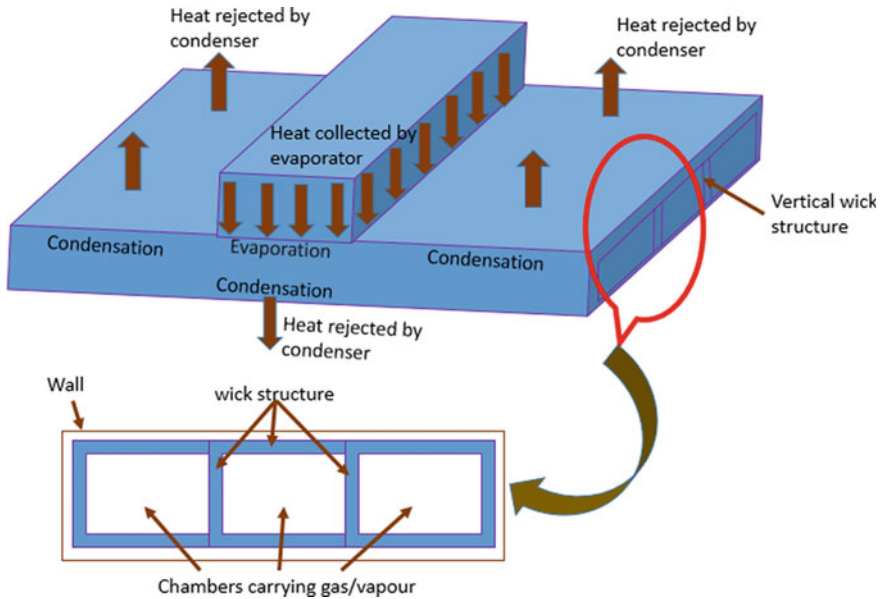
The flat heat pipe consists of the evaporator section and the condenser section which is rectangular in shape. One section of the evaporator can be maintained at the middle of the device and remaining three sections of condenser placed surrounding the evaporator section. Figure 4.13 shows the flat type of the heat pipe. The model in the figure was prepared by the Wang and Vafai (2000). Temperature difference was found to be uniform on the surfaces. The coefficient of the heat transfer was calculated and it was  $12.4 \text{ W/m}^2 \text{ }^\circ\text{C}$  and the fluxes was varying between  $425$  and  $1780 \text{ W/m}^2$ .

### Micro Heat Pipe

Figure 4.14 shows the micro heat pipes. Micro heat pipes have fabricated as wick with groove of sharp edges. The sharp edges provided improve the capillary pressure to force the liquid. Figure shows the different shapes of the micro heat pipe which were fabricated and tested by (Hung and Seng 2011). Micro heat pipes with different designs were fabricated square star (4 corners), hexagonal star (6 corners), octagonal star (8 corners) grooves and corners with width 'w' were tested. The configuration included apex angles which were varied between  $20^\circ$  and  $60^\circ$ . The following important parameters play very important role in the design of the micro heat pipe, which were total length, area of the cross-section, shape of the cross-section, number of corners and acuteness in the angles at corners.

### Oscillating/Pulsating Heat Pipe

The schematic diagram of the oscillating heat pipe is shown in Fig. 4.15. The construction of this type of the heat pipe does not include the wick structure to

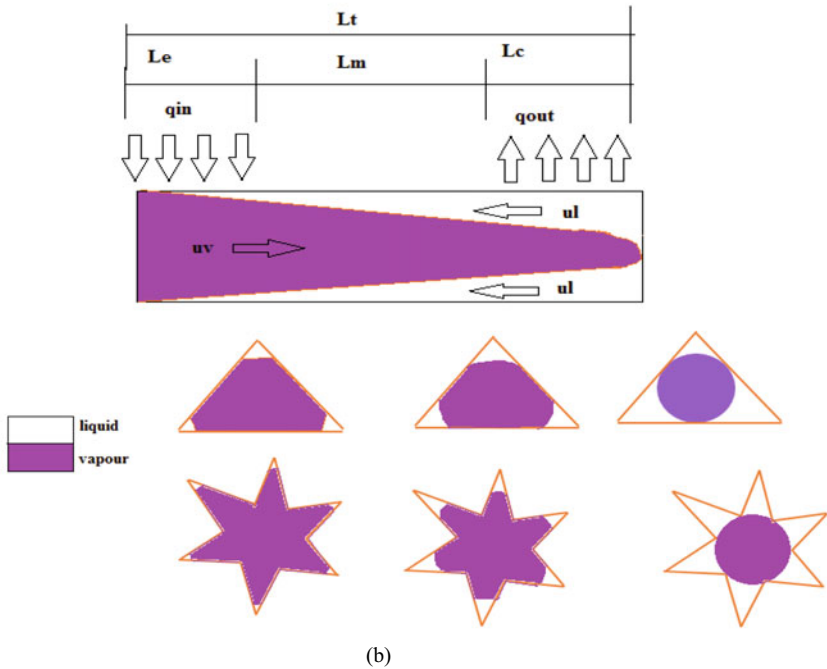
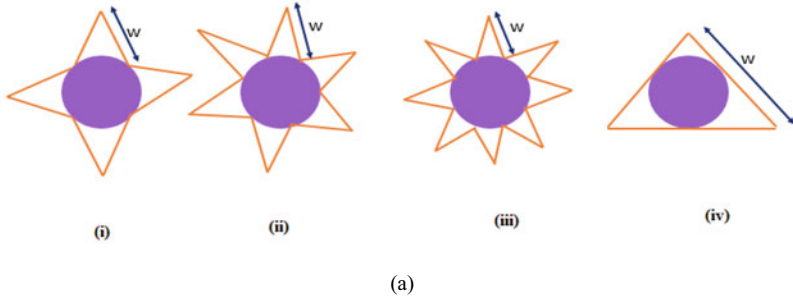


**Fig. 4.13** Flat heat pipe (Elnaggar 2016)

transport the condensate back to heating section and hence there is no scope for counter-current movement of liquid and vapour in pipeline. The fluctuation of the pressure waves drives the self-exciting oscillation inside the channels/passages, the oscillation creator accelerates the heat transfer from end to end. The heat transfer is enhanced with the oscillating mechanism in this type of the heat pipe. The changes in the pressure results into the increasing the volume and the contraction during the change of phase from vapour to liquid results into thermally excited oscillating motion of the liquid plugs and vapour bubbles between evaporator section and condenser section. This was a result of the flow of both liquid and vapour in the same direction. The important parameters which control the performance of this type of the heat pipe are diameter of the tube, number of turns provided, filling ratio, nano fluids, etc.

#### 4.2.5.4 General Design Consideration for Heat Pipes

The analytical and numerical methods can be used for designing the heat pipes. The measurement of the pressure and the velocity inside the heat pipe is not possible because of its smaller size. The calculations by analytical approach give an idea about these parameters. The numerical approach is very useful in understanding the thermal resistances and the heat flow conditions in the heat pipes by knowing the temperature profiles generated at various locations. The successful running of the cooling systems used in the electronic devices depends on the characteristics of the flowing fluid in the system.



**Fig. 4.14** micro heat pipes (Elnaggar 2016). (a) Different cross-sectional areas of the heat pipes (i) square star grooves, (ii) hexagonal star groove, (iii) Octagonal star groove, (iv) equilateral triangle. (b) Optimally charged equilateral triangle and star groove micro heat pipes ( $L_t$ -total length,  $L_e$ -Evaporator length,  $L_c$ -Condenser section length,  $L_m$ -length of the middle section,  $q_{in}$ -heat in the system,  $q_{out}$ -heat out from the system,  $u_l$ -liquid velocity,  $u_v$ -vapour velocity)

**Considerations While Designing the Heat Pipe Systems**

- (a) The fluid used in the system is incompressible, it is at steady state, 2D analysis is accurate and flow is laminar.
- (b) The working fluid is ideal gas
- (c) Phase change does not lead to heat generation

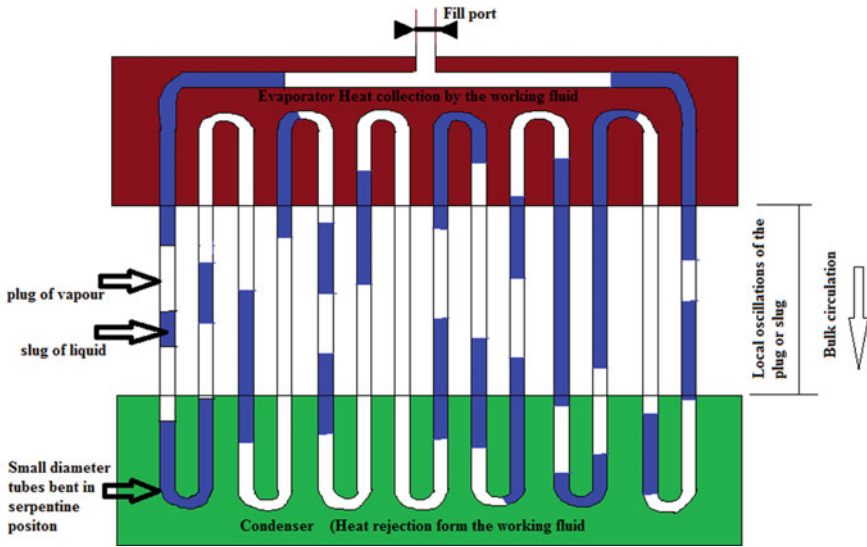


Fig. 4.15 Oscillating heat pipe (Elnaggar 2016)

- (d) No chemical reaction
- (e) Physical properties are supposed to be constant
- (f) Proper coupling between liquid–vapour, liquid–surface and vapour surface interfaces.

### Advantages

- (a) Ability to transfer large amount of heat at very small temperature difference between the condenser and evaporator section, because of very high thermal conductivity (cycle operated on two-phase cycle)
- (b) No moving components and hence its maintenance-free, noise-free, vibrations free and more life
- (c) Size of the heat pipe can be very small and easily installed in the portable electronic devices
- (d) The device can be operated at any orientation and hence can be used in portable electronic devices.
- (e) It can be fitted at a location where conventional fans can't be placed
- (f) The sizes of the condenser and evaporator could be different with controlled evaporation and condensation rates. It helps to accommodate the heat pipes in available space.



### Disadvantages

- (a) Less suitable for the applications with less space availability
- (b) The configurations of the heat pipes with multiple pipe design need more space and it is costlier
- (c) Not suitable for high-power micro-electronic systems
- (d) Less flexibility compared to the vapour chambers (cannot be placed in the systems which have uneven platforms).

### Applications

The heat pipes have been used in the following applications mainly:

- (a) Refrigerator systems for cooling purposes
- (b) Air conditioning systems for cooling purposes
- (c) Heat exchanger systems for heat collection and rejection
- (d) Capacitor cooling
- (e) Transistor cooling
- (f) Desktop cooling
- (g) Laptop cooling.

#### 4.2.5.5 Heat Pipes for Computer Applications

The biggest benefit of higher thermal conductivity of the heat pipes leads to increases its applications in electronic cooling systems. In heat pipes, heat transfer rate is very fast. The scientists have suggested a perfect match of heat pipes in electronic cooling systems, notebooks, personal computers, etc. The systems which include integration of the fins and the heat pipes to cool the high power and high-temperature systems were developed by Ligierski and Wiecek (2001). The heat pipe system used to cool the desktop PC is shown in Fig. 4.16.

The simple cooling systems with due modifications (heat pipes with cooling fins) were compared with the basic systems by Kim et al (2003). The system showed reduced noise levels and increased cooling effect.

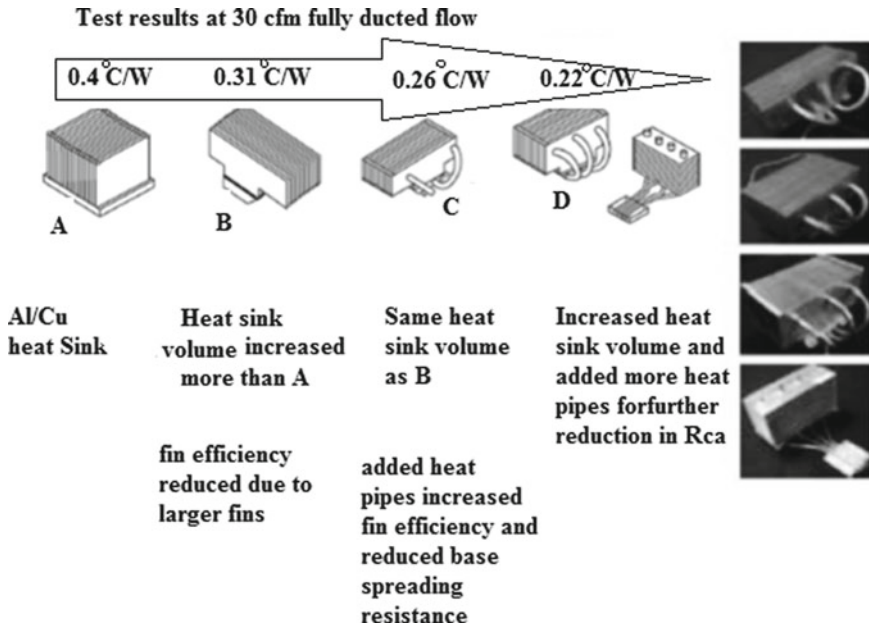
The systems proposed by the Yu and Harvey (2000) designed heat pipe for the Pentium II machine and found that the performance of the machine in terms of the mechanical and thermal management systems was improved.

The system of heat pipes with heat sink was fabricated to reduce the noise level in cooling system of the PC CPU which includes heat sink with fan.

The design (as shown in Fig. 4.17) which includes the close-end oscillating heat pipes which were used for cooling of the CPU of the of PC, fabricated by Wang et al. (2007).

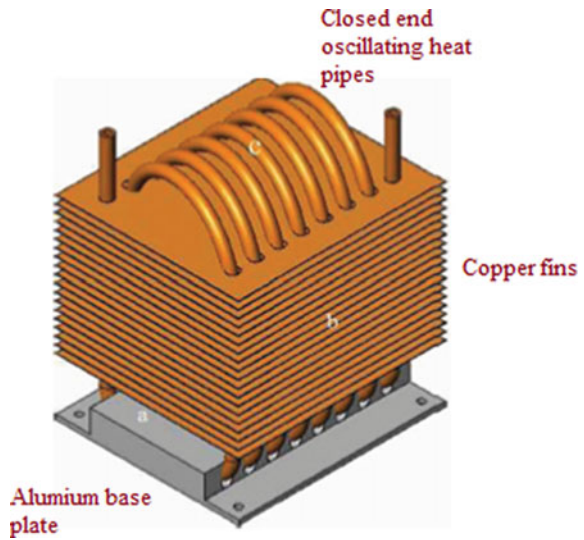
The diagram included the evaporator Sect. (0.05 m) and the condenser Sects. (0.16 m) with vertical orientation. The working fluid used was R134a. The model was developed to take a load of 70 W. The system performance was improved

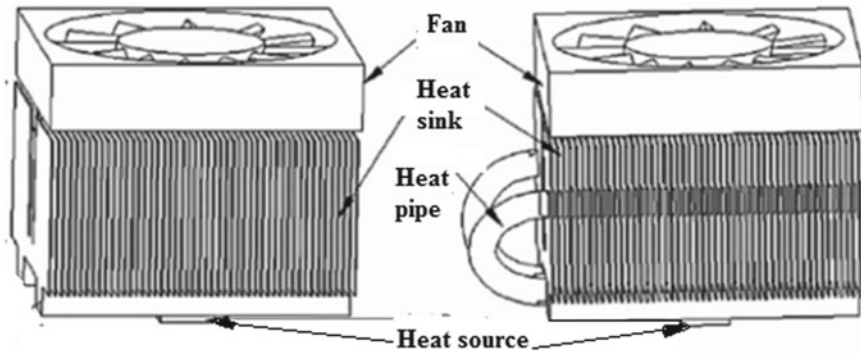




**Fig. 4.16** Cooling systems (heat sinks with heat pipes) used to cool the desktop PCs (Elnaggar 2016)

**Fig. 4.17** Cooling system to take load on PC CPU (Elnaggar 2016)

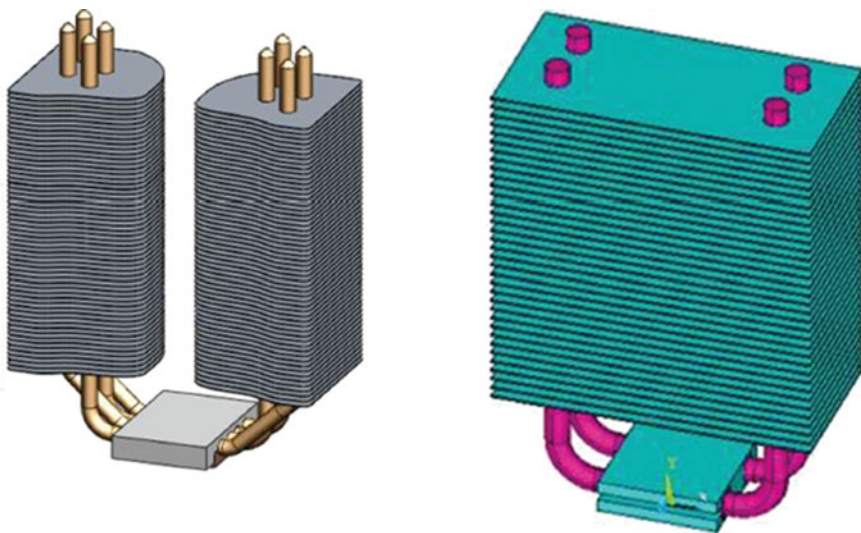




**Fig. 4.18** Heat sink with and without heat pipe integration (Elnaggar 2016)

compared to the conventional heat sink system. The design of heat sink with and without heat pipe integration is shown in Fig. 4.18.

The heat pipe with U shape fitted in the fins (as shown in Fig. 4.19) was developed to cool the high-frequency processors (Intel core 2 duo, Intel core 2 Quad, AMD Athlon 64 series, AMD phenomenon series). This system included the phenomenon of transfer of the heat from the CPU to the flat base plate and then to the heat sinks and heat pipes. The calculation of the thermal resistance was the main target in the study conducted by Wang (2008). The lowest thermal resistance value of 0.27 °C/W was observed during their studies.



**Fig. 4.19** U-shaped heat pipes used in cooling system of desktop **a** Multiple heat pipes and, **b** Twin heat pipes (Elnaggar 2016)

**Table 4.4** Different heat pipe designs (Elnaggar 2016)

Sr. No	Type of the heat pipe	Number of heat pipes used in the system	Arrangement of the heat pipe	The total thermal resistance obtained	Authors
01	L-type	3	Horizontal	0.475 °C/W	Kim et al. (2003)
02	U-type	2	Horizontal	0.27 °C/W	Wang et al. (2007)
03	U-type	2 and 4	Horizontal	0.24 °C/W	Wang (2008)
04	U-type	1	Horizontal	0.5 °C/W	Liang and Hung, (2010)
05	L-type	6	Vertical	0.22 °C/W	Wang (2011)
06	U-type	4	Vertical	0.181 °C/W	Elnaggar et al (2011a, b)
07	U-type	2	Vertical	0.2 °C/W	Elnaggar et al (2011a, b)

The velocity and heat input played a significant role in controlling the thermal resistance in the cooling systems designed above. The cooling system performance of the vertical arrangement was found to be superior to the horizontal arrangement. The lowest value of the thermal resistance was observed to be 0.181 °C/W for heat load equal to 24 W and velocity of coolant equal to 3 m/s. The second cooling system was designed to increase the effective thermal conductivity to improve the performance of the system. The data related to the different types of the heat pipes is presented in Table 4.4.

### Important Points

- (a) The heat sinks with heat pipes are more efficient systems compared to conventional systems.
- (b) The orientation of the system plays a significant role in deciding the performance of the cooling system.
- (c) Vertical orientation is superior in performance compared to the horizontal one
- (d) Multi-heat pipe's performance is better than the single heat pipes.

The system which uses heat pipes to cool the laptop system is shown in Fig. 4.20. Elnaggar et al. (2013) developed system which was implemented to cool the processor (size 10 mm X 10 mm) of the laptop. In the system, the heat pipe was fixed on the processor surface where heat is picked up by the evaporator section and transferred to the condenser section where it is rejected by conventional methods.

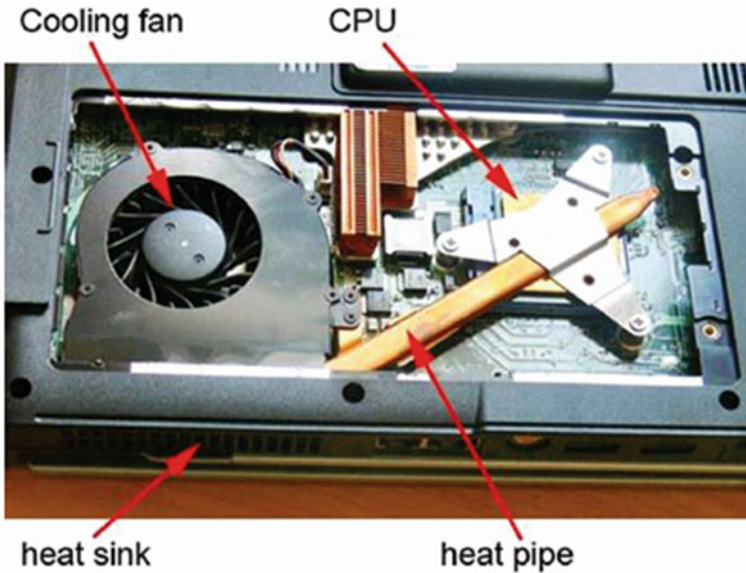
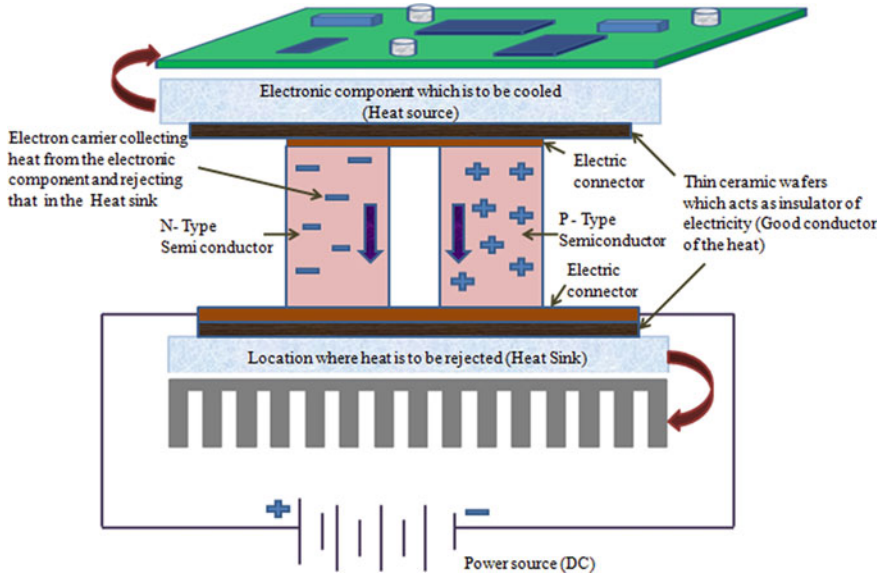


Fig. 4.20 Laptop cooling through the heat pipe system (Elnaggar 2016)

### 4.2.6 Peltier Cooling Devices

The Peltier cooling devices work on the principle of the Peltier effect. The Peltier effect was first introduced in the market in 1834. As per this effect when two dissimilar metals are connected together to form the junctions and if DC current is applied at these junctions, this causes a temperature difference across these junctions. The Peltier effect is also called as thermoelectric effect. The device which produces the Peltier effect is shown in Fig. 4.21. In this device the P- and N-type semiconductor material is sandwiched between these ceramic wafers. The ceramic material acts as a good electric insulator and increases the strength and rigidity of the system. The N-type semiconductor material has excess of the electrons and the P-type semiconductor material has deficit of it. The couple formed by N- and P-type semiconductors is shown in Fig. 4.21. The thermoelectric system used in cooling applications may have several hundreds of the couples working to generate cooling effect. The electrons from the P-type semiconductor material move to the N-type semiconductor material through the electric wires/connectors and the electrons attain the high energy absorbing state which is used to collect the heat from heat source (e.g. Electronic component). The electrons will continue its flow through the lattice structure and move from the N-type semiconductor material to the P-type semiconductor material and lower the energy level by dropping the heat at heat sink (location where heat is to be rejected).

The performance of the Peltier cooling device depends mainly on the temperature of the heat source (electronic component to be cooled), temperature of the heat sink



**Fig. 4.21** Basic working principle of the Peltier cooling device

(location of the heat rejection) and amount of heat that is to be transferred/handled by the cooling system. The temperature and heat of the location (heat sink) where heat is to be rejected is calculated by using following mathematical Eqs. (4.1) and (4.2)

$$T_{hot,side} = T_{ambient} + R_{thermal} Q_{hot,side} \tag{4.1}$$

$$Q_{hot,side} = Q_{cold,side} + P_{input} \tag{4.2}$$

The temperature difference across the Peltier cooling module is calculated by the following Eq. (3).

$$\Delta T_{Peltier\ device} = T_{hot,side} - T_{cold,side} \tag{4.3}$$

where,

- $T_{hot,side}$  The temperature of the hot side or sink side, K
- $T_{cold,side}$  The temperature of the cold side or electronic component side, K
- $T_{ambient}$  The temperature of the surrounding, K
- $R_{thermal}$  The thermal resistance offered by the heat exchanger, K/W.
- $Q_{hot,side}$  The amount of the heat rejected by thermoelectric device at its hot side or sink side, W

**Table 4.5** Allowable temperature rise above surrounding

Sr. No	Modes of heat transfer	Allowable temperature rise at heat sink °C
1	Natural convection	20–40
2	Forced convection	10–15
3	Cooling by liquids	2–5 (this rise is considered above the coolant temperature)

$Q_{\text{cold,side}}$  The amount of the heat collected by thermoelectric device at its cold side or electronic component side, W

$P_{\text{input}}$  The input electrical power supplied to the Peltier cooling device, W

$\Delta T_{\text{Peltier device}}$  The temperature difference across the Peltier cooling device, K

The heat sink temperature close to ambient temperature helps in retaining the performance of the Peltier cooling device and in maintaining the required temperature on the cold side of the cooling device. If the thermal resistance of the heat sink is increasing because of any reason in that case, following are the allowable rise in the temperatures of heat sink above surrounding for different modes of heat transfer. The data of the Allowable temperature rise above surrounding for different modes is presented in Table 4.5.

The total heat load on the device includes following

- (a) Heat load from the electronic components, because of its power consumption
- (b) Heat load generated because of chemical reaction at various locations
- (c) Heat load because of two close electronic or other components with temperature difference because of radiation
- (d) Heat load because of convection
- (e) Heat load because of the insulation losses
- (f) Heat load because of the conduction losses through the metallic components (accessories used for connecting the parts screws, nuts, bolts, etc.)
- (g) Heat load because of the transient response of the system (accumulated load).

### Advantages

- (a) No moving parts involved in the cooling system
- (b) Two-fold use (Can be used as heater or cooler)
- (c) No noise
- (d) No vibrations
- (e) No cooling fluids used in the circuits
- (f) Less maintenance
- (g) More life
- (h) Leak proof
- (i) Can be produced easily with small size
- (j) Very much flexible.

**Table 4.6** The materials used for preparing the Peltier device (Chanyoung et al. 2015)

Sr. No	Material of the Peltier device	Working temperature range, K
1	Bismuth telluride	Near to 300
2	Lead telluride	600–900
3	Silicon germanium	Up to 1300
4	Bismuth-antimony alloys	Near to 300

### Disadvantage

- (a) Costly for the same cooling capacities
- (b) Lower cooling efficiency
- (c) Needs power supply.

### Applications of the Peltier Cooling Device

These devices are generally used for following purposes (a) heating, (b) cooling and (c) maintaining temperature.

- (a) Cameras (Charge coupling devices also called as CCDs)
- (b) The micro-processors used in electronic circuits
- (c) The laser diodes
- (d) The blood analyzing device
- (e) The portable coolers used during picnics, etc.

The different materials used for fabricating the Peltier device and their working temperature ranges are mentioned in Table 4.6.

## 4.2.7 Synthetic Jet Air Cooling

The synthetic jet technology is well-proven technology in which flow of the air is generated with the help of the diaphragm (or actuator) movement in the cavity. The movement of the diaphragm is periodic and it is confined to one of the walls of the cavity. The simple sketch of the synthetic jet formation is shown in Fig. 4.22.

The different devices used for actuation are mentioned below,

### Mechanical Drivers

Mainly pistons are widely used as an actuator under this category. This type of actuator can be used for producing the round synthetic jets. Important features of the mechanical drivers are as follows:

- (a) These actuators are rigid and sturdy
- (b) It cannot be used in small systems (limitation on size)
- (c) Noise and vibrations is a big problem under fast running of the system
- (d) Response time is more compared to other systems.



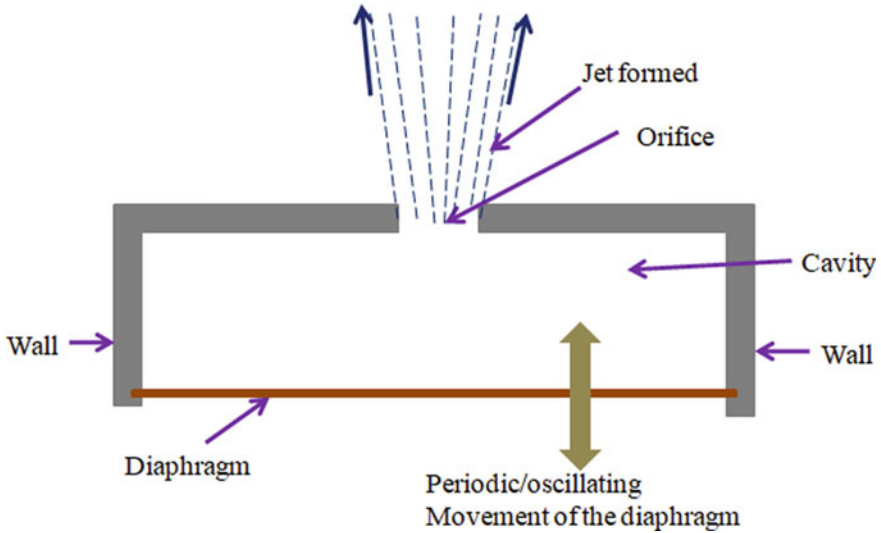


Fig. 4.22 Simple sketch of the synthetic jet actuator

### Electromagnetic

The electromagnetic type of actuators is mainly solenoid actuators. Important features of electromagnetic type of actuators are as follows:

- (a) Quick in response time
- (b) Less vibrations and noise
- (c) Flow control is easy
- (d) Actuator movement control is precise
- (e) More reliable.

### Piezoelectric Actuator

The Bimorphs, thunder actuators, plasma actuators are the piezoelectric actuators used to generate the synthetic jets. The important features of the actuator are as follows:

- (a) Quick response,
- (b) Suitable for micro systems,
- (c) Light in weight,
- (d) Capability to get a very small displacement in given response time,
- (e) Minimum energy consumption for the required output.

### Acoustic Actuator

The best example of the acoustic actuator is the loudspeaker. This was used for underwater vehicle propulsion. Following are the important features of the acoustic actuator.



- (a) Can be used in small systems
- (b) The displacement of the actuator can be controlled easily
- (c) Light in weight.

The most widely used diaphragms in this system are piezoelectric (preferred because of its less weight and power consumption abilities) and electromagnetic (preferred because of its reliability and low noise characteristics). The following main two strokes are performed to supply the required cooling air in this technique.

**Compression Stroke**

The upward movement of the diaphragm creates the compression stroke because of which the air collected in the cavity will be forced through the orifice present at the top of the system and vortices are generated in the downstream direction because of the boundary separation (Didden 1979). The vortices generated in the zones near to the orifice will be smaller in dimensions compared to the vortices in the zones away from the orifice. During this stroke, the vortices will vanish after some particular length in the downstream direction and continuous jet will be formed. The compression stroke working is shown in Fig. 4.23.

**Suction Stroke**

Figure 4.24 shows the suction stroke performed by the diaphragm. The downward movement of the diaphragm creates the suction of the air from ambient (zone near to the orifice) in the cavity. During this movement of the air the previously formed vortices during the compression stroke are pushed away from the orifice. If system is not running as per the design conditions, the vortex formed during the compression stroke is carried back to the orifice and required jet characteristics will not be obtained (Rampungoon 2001).

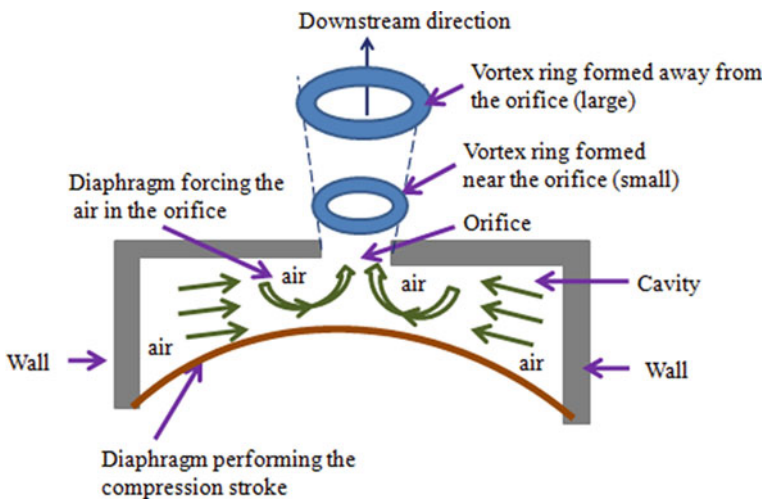
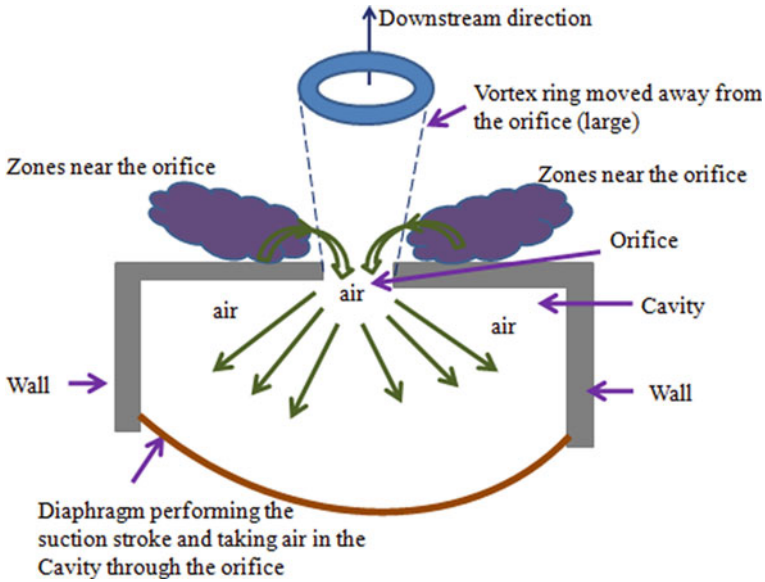


Fig. 4.23 Diaphragm performing the compression stroke



**Fig. 4.24** Diaphragm performing the suction stroke

### Advantages

- (a) It has capacity to carry the higher heat flux from the electronics components even with the lower air flow rates
- (b) The noise produced in this system is comparatively less
- (c) High reliability of the system (Mahalingam et al. 2007)
- (d) It can be connected to the electronic systems without the aid of any complicated fixtures (can be designed as per the requirement of the space)
- (e) Construction costs are less
- (f) Operated with less noise
- (g) The size of the system is less compared to conventional cooling systems where natural convection is used
- (h) More number of options available for the actuators
- (i) It can be operated in any orientation (Cheung et al. 2009)
- (j) Preparation of multiple orifices is easy to increase the flow rates.

### Disadvantages

- (a) The most of the actuators operated with electric power
- (b) The cost increases when the synthetic jet cooling system is to be produced precisely in the small size as per the shape of the electronic system
- (c) The cooling system with mechanical type of the actuators has less response
- (d) The control of the flow rate increases the complexity of the design.

## Applications

- (a) Cooling of the electronic systems, e.g. Laptop, handheld PCs, controllers, etc.
- (b) The transfer of the thermal energy (Gil and Wilk 2020; Arshad et al. 2020)
- (c) Flow control (Gil 2019)
- (d) For mixing of the fluids, e.g. automobile, medical, chemical, plastic industries (Le Van 2019).

### 4.2.8 Electrostatic Fluid Acceleration

The method involves the use of device called as electrostatic fluid accelerator to get the movement of the targeted fluid (e.g. air) in the required direction. This technique uses the Coulomb force to accelerate the electrically charged molecules of the fluid (e.g. air). There are mainly three steps that are important in order to get the movement of the fluid in this technique and these are mentioned below:

- (a) Ionization of the working fluid particle
- (b) Movement of the ionized and non-ionized working fluid particles in the downstream direction (through ion-ion or ion-neutral particle collisions)
- (c) Deionization of the working fluid particle.

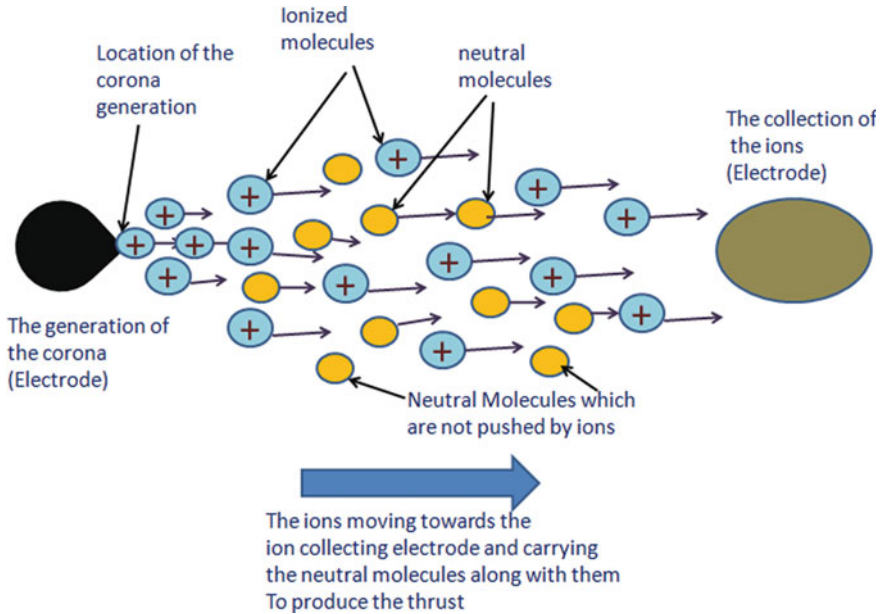
The air available is abundant and most of the times the working fluid used in the micro-electronic systems are air. Let us discuss the working principle with the help of air as a working fluid. The principle of the working of the electrostatic fluid accelerator is shown in Fig. 4.25.

#### (a) Ionization of the working fluid particle

In this step the air is ionized (also called as process of charging the air). The ions produced in these processes possess the effective/net electrical charge. The process used to ionize the air molecules is called as corona discharge. This process of corona discharge is very simple which does not require extreme conditions (e.g., high temperatures, low pressures, etc.).

#### (b) The movement of the ionized particles in downstream direction

The ionized particles will have a net charge because of which they will be repelled by the same charge electrode and attracted by the opposite electrode. The driving force is mainly created by creating the electric field across the electrodes. Out of all air molecules, some may not get ionized. So, when ionized particles are moving towards the oppositely charged electrodes, they travel to carry non-ionized particles with them. This process generates a thrust. The propelling of the ions from the electrode will bump these ions on neutral molecules and accelerate them. It is possible because of the electric field applied. The ions during this process supply the potent energy and generate kinetic energy in the molecules of the air (that is a process of accelerating the air molecules). Part of the energy is wasted to increase the air temperature or driving force is not created in the required direction.



**Fig. 4.25** The working principle of the electrostatic fluid accelerator

(c) **Losing the charge to electrode**

Once the ions reach to the electrode of opposite charge they will lose their charge by receiving the electrons from electrode. During this process, those ions which are not colliding with the electrode will be moving back upstream in towards the attracting electrode. In such situation addition electric field needs to be created to minimize this effect.

**Advantages**

- (a) The generation of the near laminar profiles of the air with required control over flow velocity (Michael 2006)
- (b) Flexibility in designing the system (very simple electrode geometry in solid-state)
- (c) Manufacture is easy
- (d) The amount of power consumption is low (Michael 2006)
- (e) Benefit of carrying large amount of heat compared to conventional system and
- (f) The ability to decrease the boundary layer formed between the solid-liquid interface within the closed structure (Michael 2006)
- (g) No rotary parts and hence no vibrations and noise in the system
- (h) The temperature of the working fluid (air) will be maintained.

## Disadvantages

- (a) Electric power consumption for ionization
- (b) Limitations on the air flow rate because of the restriction on size of the device
- (c) This system has the problem of the reverse air flow
- (d) The chances of the sparking in the device are more if the electronic components (layers) are placed very near to each other
- (e) The voltage supplied needs to be carefully controlled in order to get required corona strength.

## Applications

- (a) Cooling of the micro-electronics (e.g. micro-processor cooling **by thorn technologies**)
- (b) Development of fluid flow pattern
- (c) To filter the air (Michael 2006)
- (d) To add the moisture content in the air (humidification) (Michael 2006)
- (e) Audio speakers
- (f) Propulsion of the small vehicles (Michael 2006).

## 4.2.9 Immersion Cooling Technology

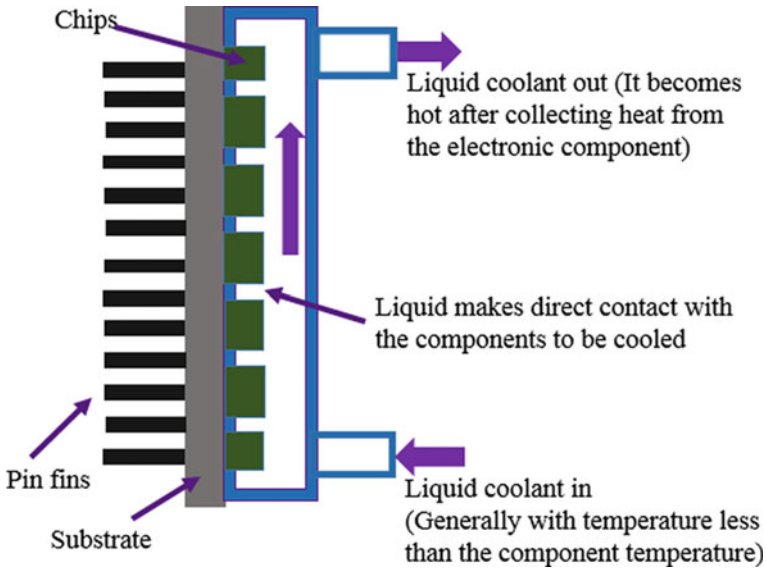
The emersion cooling technology involves the use of liquids to collect the heat from the source (location where heat is generated). This technique is useful to remove more heat flux compared to the conventional method of removing heat with the help of heat sinks.

There are mainly two types available in this category; (a) Direct cooling and (b) Indirect cooling.

### 4.2.9.1 Direct Cooling

In this method, the liquid coolant supplied in the channels makes direct contact with the electronic component. The direct cooling arrangement is shown in Fig. 4.26. In this arrangement the cooling liquid is supplied at the bottom (right side) and it comes into contact with the heat-generating sources (e.g. chips, substrates, etc.) during its path in the upward direction (as shown Fig. 4.26) and the hot liquid exits at the top on the right side. Because of the direct contact of the liquid coolant and the heat sources, the thermal resistance offered in the direct contact type method is removed and the heat flux carrying capacity of this method increases. The liquid coolants used in this type should not be conductive type (e.g. Mineral oils should be used).

This method offers the temperature of the electronic component maintained always below the liquid coolant temperature because of the high heat transfer coefficient. The amount of heat collected by the liquid coolant depends upon the coolant



**Fig. 4.26** Immersion cooling through direct contact of liquid coolant with the component to be cooled

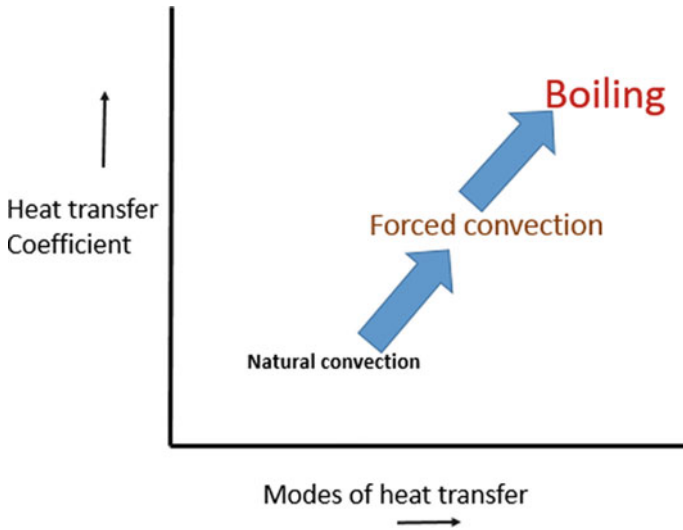
type and the type of the heat transfer mode. The modes of the heat transfer are mainly forced convection, natural convection and boiling. The boiling mode always carries the highest heat through the liquid coolants because of its higher heat transfer coefficients. Figure 4.27 shows the comparison of the different modes of the heat transfer and their heat transfer coefficients.

The heat-carrying capacity of this method is more than the air cooling methods. The water cannot be used as liquid coolant in this method, because of its incompatibility with the hardware used in micro-electronic systems. The most widely used liquid coolants in direct type of the immersion cooling are the (a) FC-72, (b) FC-77 and (c) FC-86.

Important thermo-physical properties comparison for different liquid coolants is presented in Table 4.7. From Table 4.7 it is very much clear that the thermo-physical properties (mainly boiling point, specific heat, thermal conductivity and heat of vaporization) of water is superior compared to FC-72, FC-77 and FC-86. Because of their compatibility with the electronic components, these are used in the direct immersion cooling technology.

#### 4.2.9.2 Indirect Cooling

This method involves the cooling of the electronic components with the indirect contact between liquid coolant and the electronic components. The principle of the working of indirect method of cooling of the electronic components is shown in Fig. 4.28. The liquid coolant is supplied through the channel at its one end (Fig. 4.28



**Fig. 4.27** Comparison of the different modes of the heat transfer and their heat transfer coefficients

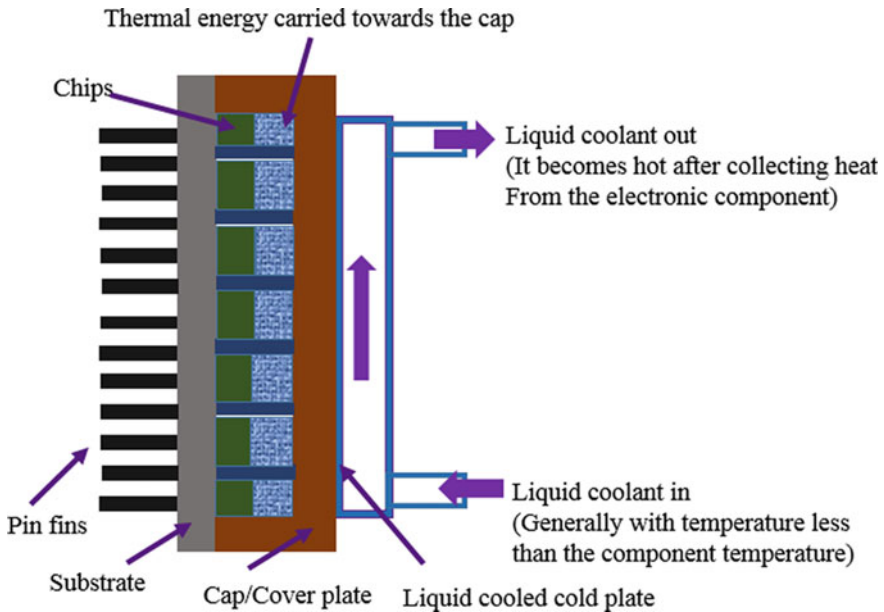
**Table 4.7** Thermo- physical properties of the liquid coolant (Danielson et al. 1987)

Thermo-physical property	H <sub>2</sub> O	FC-77	FC-72	FC-87
Boling point in °C (at 1.013 bar)	100	97	56	30
Density (kg/m <sup>3</sup> )	1000	1780	1680	1633
Specific Heat KJ/kg K)	4.179	1.172	1.088	1.088
Thermal Conductivity (w/m K)	0.613	0.057	0.0545	0.0551
Heat of vaporization × 10 <sup>-4</sup> (w s/kg)	243.8	8.37	8.79	8.79

at the bottom right side) and it moves through the channel to collect the heat from the cap/cover plate and exits from its other end of the channel (Fig. 4.28 at the top right side). The cap is receiving the heat from the various electronic components (e.g. chips, substrates, etc.). Because of the indirect contact between liquid coolant and the electronic components the thermal resistance increases and the heat-carrying capacity of this type is less than the direct type. Water can be used very easily as a liquid coolant because of its good thermo-physical properties.

#### 4.2.9.3 Single-Phase Immersion Cooling

In this type of cooling the working fluid does not change its phase while collecting the heat from the electronic components/system and hence it is called single-phase immersion cooling. The simple working principle of the single-phase immersion



**Fig. 4.28** Immersion cooling through the indirect contact of the liquid with the electronic components to be cooled

cooling system is shown in Fig. 4.29. The system used to cool the IT equipment is shown in Fig. 4.30. The most widely used phase of the working fluid is liquid, because of its high heat-carrying capacity. The amount of heat carried in this type of method is more than the air type of cooling. Because of no phase conversion (liquid to gas), chances of explosion are avoided.

#### 4.2.9.4 Two-Phase Immersion Cooling

In this method, the working fluid used in the circuit changes its phase from liquid to gas after collecting the heat from the electronic components and hence it is called as two-phase immersion cooling system. The heat-carrying capacity of this type is more than the single-phase type, which helps to increase the power density up to 10 times as that of the power density of single-phase systems. It has simple construction and less cost. Figure 4.31 shows the two-phase immersion cooling system.

#### Advantages

- More heat-carrying capacity compared to the air cooling methods
- Water can be used as coolant which is easily available
- Cost is less with water-cooled systems
- Can be used in different-sized electronic systems
- Two-phase immersion cooling system allows to increase the power density



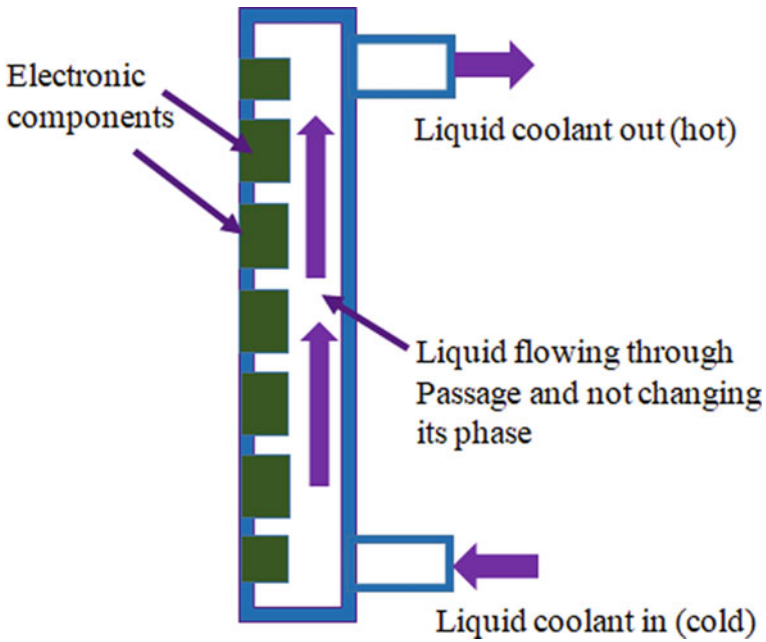


Fig. 4.29 Single-phase immersion cooling system

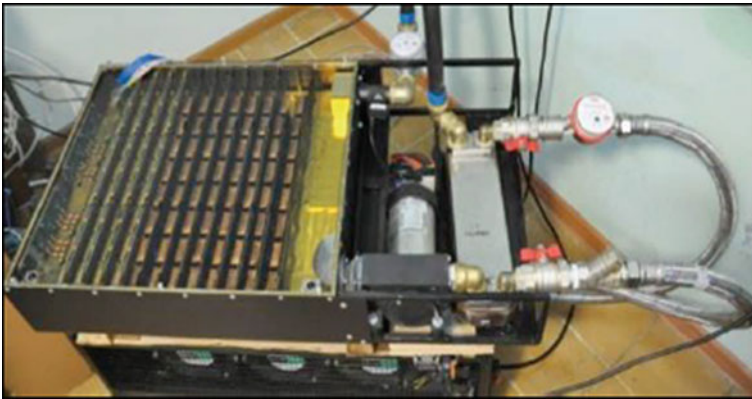
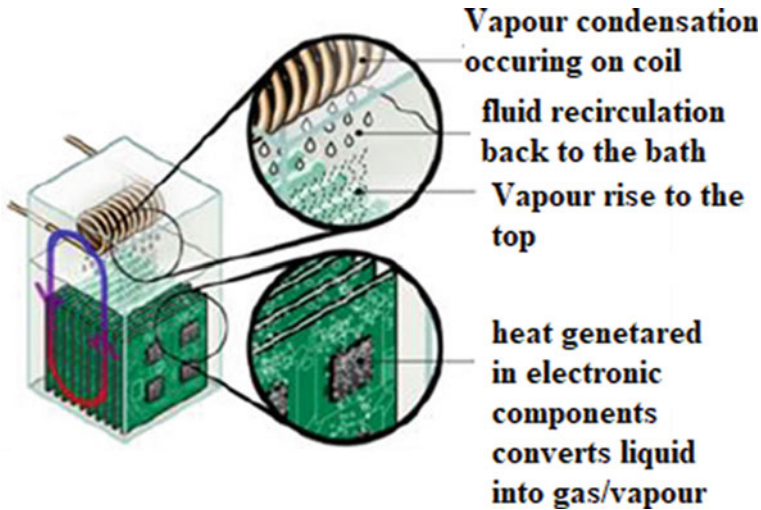


Fig. 4.30 Single-phase immersion cooling system used to cool IT equipment (Levin 2016)

### Disadvantage

- (a) The basic structure of the electronics needs to be modified as per the cooling system
- (b) The cost of the system increases with coolants other than water
- (c) The space required is more



**Fig. 4.31** Two-phase immersion cooling system (Kuncoro et al. 2019)

- (d) The chances of leakage cannot be tolerated after some usage
- (e) The weight of the system may increase.

### **Applications**

- (a) Cooling of the super computers
- (b) Cooling of the commodity server (Kuncoro 2019)
- (c) Cooling of the server clusters
- (d) Cooling of the data centres (this is targeted application recently)
- (e) Cooling of the solar cell through single-phase method (Sun et al. 2014)
- (f) Cooling of the transformer through single-phase method (Testi 2018)
- (g) Cooling of the IT equipment through single-phase method (Shah et al. 2016; Levin 2016)
- (h) Cooling of the server through two-phase method (Lamaison et al. 2017)

#### **4.2.10 Use of the Phase Change Material**

The use of the phase change materials in the heat flow management of the micro-electronics cooling is increased because of its easy availability and flexibility in design. This cooling method includes two important steps,

- (a) Collection of the heat from the electronics components and
- (b) Rejection of the collected heat.

**(a) Collection of the heat from the electronics components**

This process involves absorption of the sensible heat and latent heat. Initially, phase change material absorbs the sensible heat from the electronic components (source of the heat) and its temperature increases without changing its phase (its state is solid). The process involves storing of heat in the phase change material. When the temperature reaches to the melting point of the phase change material it starts absorbing latent heat from the electronic components and it starts melting. The large amount of latent heat is absorbed by the phase change material at constant temperature and the procedure is continued till the complete melting of the phase change material occurs. Hence before selecting the phase change material, one should have idea about amount of heat that is to be removed from the electronic components. The latent heat absorbed is generally higher than the regular materials (which cannot be reinstated by addition and removal of the heat).

**(b) Rejection of the collected heat**

During this process, the heat is rejected by the phase change material when the temperature of the surrounding drops. The heat rejection process converts the phase change of material from liquid into solid state and it is ready for the next cycle of the heat collection.

This type of cooling method is called as passive way of heat flow management in the electronic system. The phase change materials which include gas phases (e.g. liquid to gas or solid to gas) increase the volume of the cooling systems and hence these are not preferred in the micro-electronic cooling systems. The phase change materials can be used for continuous heat storage and intermittent heat storage. The details of the different phase change materials and their benefits and drawbacks for different applications are mentioned in Table 4.8.

**Advantages**

- (a) These systems can be fabricated with low cost
- (b) Systems are flexible in design because of different materials availability
- (c) It gives more reliability in the cooling process
- (d) This system can be used for both the intermittent and continuous cooling operations
- (e) These systems can be fabricated in the smaller size (well below the size of electronic device)
- (f) The capacity to absorb the heat (latent heat mainly) is more than other materials and hence effective way of cooling the systems
- (g) These materials are readily available in the market
- (h) These materials are chemically and thermally stable and hence can be connected directly in the electronic systems
- (i) No electrical energy is required to operate the cooling system.

**Table 4.8** Summary of phase change materials

Sr. No	PCM	Design	Benefits	Drawback	Reference
1	paraffin wax	The aluminium enclosure with 128 mm X 10 mm dimensions and internal cavity	The good transient response with intermittent operation reduced the weight and size of the system	The design of the phase change material with heat sinks was also tried and no significant change was observed	Kandasamy et al. (2008)
2	n-eicosane	The heat storage systems with cavity (filled with n-eicosane)	It was possible to stabilize the temperature and extend the duration of the operation of the system		Tan and Tso (2004)
3	n-eicosane	The heat sinks filled with the PCM (n-eicosane) The heat sinks with fins (21 mm height) and without fins	Decreases the rate of increase of the temperature	only applicable for the intermittent operations, e.g. Mobiles	Tan and Tso (2004)
4	Thermal energy storage	PCM with filled Thermal energy storage devices (size -101 mm X 62 mm X 12 mm)	Was able to control the temperature of the electronic components		Alawadhi and Amon (2003)
5	Paraffin	PCM for intermittent and continuous operation	Increase in the critical time by 320% The critical time is the time required to reach 77 °C		Gharbi et al. (2017)
6	Heat Pipe with tricosane	The heat pipes charged with both (a) tricosane and (b) water	PCM can lower the temperature of heater significantly (almost by 17 °C)		Weng et al. (2011)

(continued)

**Table 4.8** (continued)

Sr. No	PCM	Design	Benefits	Drawback	Reference
7	(PMCD-32SP) paraffin) in polyethylene in a composite sheet form	The MPCM/polyethylene PCM used in tablets with sheet of 1.6 mm in thickness	It is possible to reduce the temperature and only polyethylene is sufficient to get delay in temperature rise by 50 °C in the study		Tomizawa et al. (2016)
8	PCM TES	PCM with TES with sheet thickness less than 2 mm	The delay in temperature observed for electronic system and its cover by 34% compared to the case of without PCM The PCMs with the melting temperature below 39 °C is suitable for the heat flow management in the electronic systems		Sponagle et al. (2017)
9	PCM TES	Use of the PCM for the tablets and tested for different heat inputs (3 W, 4 W, 6 W and 8 W)	PCMs can be used for continuous operations up to 60 min and temperatures were reduced substantially compared to case of without PCM		Ahmed et al. (2018)

### Disadvantages

- (a) The materials are corrosive in nature (Inorganic phase change materials)
- (b) Problem of the instability of the material
- (c) The complete conversion of the liquid to solid is not achieved in all the materials and all the time

- (d) Some materials show a tendency of the super cool (Inorganic phase change materials)
- (e) Phase change materials with conversion of solid to gas or liquid to gas cannot be used because of the restrictions on the volume in the micro-electronics cooling systems
- (f) Less experience with long-term operation of the phase change material and cycles of operation.

### **Applications**

- (a) The thermal energy storage and its release based on systems requirements in micro-electronics cooling
- (b) The use of the phase change material is in the storing the solar energy and using it as per requirement during cooking of food
- (c) Cooling of the batteries
- (d) Cooling of the electrical and the heat engines
- (e) Food storage by maintain the cold space temperature (heat removal from the space)
- (f) Cooling of the human body under heavily worn clothes
- (g) Heat balance in the micro-electronic systems (computer cooling, laptop cooling, other portable electronics cooling).

### **4.3 Summary**

This chapter emphasizes mainly on the heat flow management required in the micro-electronic systems. The old and recently developed cooling techniques are discussed in detail. The working principle of all the recently developed cooling techniques along with advantages, disadvantages and the specific applications of particular techniques are presented under every single cooling technique. The different electronics cooling techniques such as heat sinks, cold plates, natural air cooling, forced air cooling, use of the heat pipes, Peltier effect for cooling, synthetic jets cooling, electrostatic fluid acceleration cooling, immersion cooling, phase change materials are compared and presented below in tabular form to understand their significance, dependence on parameters and use for specific application.

Heat sinks	Cold plates	Natural air cooling	Forced air cooling	Heat pipes	Peltier effect cooling	Synthetic jet cooling	Electrostatic fluid acceleration cooling	Immersion cooling	Phase change materials
<p>Used to cool the electronics components which are smaller to medium size and cooling occurs by transferring the heat from electronics components to heat spreader through and then to fins through conduction, the heat from fins is convected and radiated in the cooling media. This is old method of cooling the electronic components.</p> <p>Performance depends on material of the heat sink, method used to supply air the heat sink</p>	<p>This method uses the metal plate (cold plate) between electronic component (source of the heat) and the working fluid which collects the heat from metal plate. The method is used to cool the micro-electronic circuits require higher thermal conductivity and higher heat flux carrying capacity. This is recent method and performance depends on fluid used for cooling, velocity of flow and material of the cold plate</p>	<p>This is the old and simple method used to cool the electronic systems. In this method, the naturally available air is used to cool the electronic systems. This method utilizes the concept of density difference to carry away heat from the systems. The performance depends on the amount of air available near the components, space available for the movement of the air, direction of the air movement</p>	<p>This method includes creation of the forced draught of the air through external agency (e.g. Fans or blowers). This is very common method used to cool the electronic systems. The air is used as media to remove the heat from the electronic components. The performance depends on material of semiconductor used, temperatures of hot side and cold side, amount of heat transferred, losses in the system</p>	<p>Heat pipes have found to be the best method for portable electronic cooling devices. The heat pipe technology is used because of its simple structure, high efficiency, cost-effective and flexibility. The heat pipe uses the working fluids whose phase change can be used to collect the heat from one location and to transfer it to the another location. The performance depends on heat pipe material, fluid used in system, wick structure used, orientation of the pipe, etc.</p>	<p>The Peltier cooling devices works on the principle of the Peltier effect. As per this effect when two dissimilar metals are connected together to form the junctions and if DC current is applied at these junctions, this causes a temperature difference across these junctions. The performance depends on material of semiconductor used, temperatures of hot side and cold side, amount of heat transferred, losses in the system</p>	<p>The synthetic jet technology is well-proven technology in which flow of the air is generated with the help of the diaphragm (or actuator) movement in the cavity. The movement of the diaphragm is periodic and it is confined to one of the wall of the cavity. The performance depends on type of the actuator, cavity size, movement of the diaphragm, etc.</p>	<p>The method involves the use of electrostatic fluid accelerator to get the movement of the targeted fluid (e.g. air) in the required direction. This technique uses the Coulomb force to accelerate the electrically charged molecules of the fluid (e.g. air). There are mainly three steps which are important in order to get the movement of the fluid in this technique and these are mentioned below, (a) Ionization of the working fluid particle, (b) ionized and non-ionized working fluid particles in the downstream direction (through ion-ion or ion-neutral particle collisions), (c) Deionization of the working fluid particle. The performance depends on ionization and deionization of the working particles and movement of the particle, etc.</p>	<p>The immersion cooling technology involves the use of liquids to collect the heat from the source (location where heat is generated). This technique is useful to remove more heat flux compared to the conventional method of removing heat with the help of heat sinks. The performance depends on method of cooling (direct or indirect), working fluid used, heat transfer mode, etc.</p>	<p>The use of the phase change materials in the heat flow management of the micro-electronics cooling is increased because of its easy availability and flexibility in design. This cooling method includes two important steps, (a) Collection of the heat from the electronics components and (b) Rejection of the collected heat. The performance depends on material, type of cooling operation, surrounding temperature, etc.</p>

(continued)

(continued)

Heat sinks	Cold plates	Natural air cooling	Forced air cooling	Heat pipes	Peltier effect cooling	Synthetic jet cooling	Electrostatic fluid acceleration cooling	Immersion cooling	Phase change materials
Applications: cooling of CPU, laptop, engine, etc.	Applications: cooling of CPU, IGBT, transistor, battery, fuel cells, medical equipments, etc.	Applications: cooling of electronic board and condenser, etc.	Applications: cooling of the CPU, laptop battery, LEDs, inverters, etc.	Applications: cooling of capacitor, transistor, desktop laptop, etc. and can work as a refrigeration and air condition systems	Applications: cooling of Camera's (CCD), micro-processors, laser diodes, blood analyzing devices, etc.	Applications: cooling of Laptop, handheld PCs, controllers, etc.	Applications: Micro-processor cooling, development of flow patterns etc.	Applications: Cooling of super computers, commodity server, server clusters, data centres, solar cell, transformer, IT equipment, etc.	Applications: Storing the solar energy and cooling of the batteries, electrical and the heat engines, computer, laptop, etc.



Comparison of the cooling techniques:

#### 4.4 Future Scope/Recommendations

There is lot of scope to work in the following fields,

- (a) Development of the Peltier materials
- (b) Development of the cold plate designs which can be very easily connected to the micro-electronic systems
- (c) Development of the heat pipes or vapours chambers in micro-electronic components (e.g. mobiles, laptops, etc.)
- (d) Developments in the synthetic jet techniques
- (e) Scope to check the compatibility of different working coolants used in the different cooling techniques
- (f) Scope to minimize the losses in the connectivity of micro-electronic structures
- (g) Scope to minimize the pressure losses and improve flow characteristics in the micro channels.

#### References

- Ahmed T, Bhourri M, Groulx D, White MA (2018) Passive thermal management of tablet PCs using phase change materials: continuous operation. *Int J Thermal Sci* 134:101–115
- Alawadhi EM, Amon CH (2003) PCM thermal control unit for portable electronic devices: experimental and numerical studies. *IEEE Trans Compon Packag Technol* 26:116–125
- Ali MS, Kamarudin SK, Masdar MS, Mohamed A (2014) An overview of power electronics applications in fuel cell systems: DC and AC converters. *Sci World J* 2014(103709)
- Arshad A, Jabbar M, Yan Y (2020) Synthetic jet actuators for heat transfer enhancement—a critical review. *Int J Heat Mass Transfer* 146:118815
- Chanyoung K, Hongchao W, Je-Hyeong B, Hoon K, Woochul K (2015) Thermoelectric materials and devices. *Hierarchical Nanostruct Energy Devices* 35
- Cheung C, Noska B, Van der Heide K (2009) Comparison of passive and active cooling effectiveness. *LED Prof Rev Mag*
- Danielson RD, Tousignant L, Bar-Cohen A (1987) Saturated pool boiling characteristics of commercially available perfluorinated liquids. In: *Proceedings of ASME/JSME thermal engineering joint conference*
- Didden N (1979) On the Formation of Vortex Rings: Rolling-up and Production of Circulation. *J Appl Math Phys (ZAMP)* 30:101–116
- Elnaggar MH, Abdullah MZ, Abdul Mujeeb M (2011a) Experimental analysis and FEM simulation of finned U-shaped multi heat pipe for desktop PC cooling. *Energy Convers Manag* 52(8–9):2937–2944
- Elnaggar MHA, Abdullah MZ, Mujeeb M (2011b) Experimental investigation and optimization of heat input and coolant velocity of finned twin U-shaped heat pipe for CPU cooling. *Exp Tech*
- Elnaggar MH, Abdullah MZ, Munusamy SR (2013) Experimental and numerical studies of finned L-shape heat pipe for notebook-PC cooling. *IEEE Trans Compon Packag Manuf Technol* 3(6): 978–988

- Ennaggar MH, Edwan E (2016) Heat pipes for computer cooling applications. *Electron Cooling*
- Gharbi S, Harmand S, Jabrallah SB (2017) Experimental study of the cooling performance of phase change material with discrete heat sources—continuous and intermittent regimes. *Appl Therm Eng* 111:103–111
- Gil P (2019) Bluff body drag control using synthetic jet. *J Appl Fluid Mech* 12:293–302
- Gil P, Wilk J (2020) Heat transfer coefficients during the impingement cooling with the use of synthetic jet. *Int J Therm Sci* 147:106132  
<http://www.nordichardware.com/news-archive/112-archive/18645.html>
- Hung YM, Seng QB (2011) Effects of the geometric design on the thermal performance of star groove micro heat pipes. *Int J Heat Mass Transf* 54(5–6):1198–1209
- Incropera, DeWitt, Bergam, Lavine (2007) Introduction to heat transfer, 5th edn., p 6. ISBN 978-0-471-45727-5
- Kandasamy R, Wang XQ, Mujumdar AS (2008) Transient cooling of electronics using phase change material (PCM)-based heat sinks. *Appl Therm Eng* 28(8–9):1047–1057
- Kim KS, Won MH, Kim JW, Back BJ (2003) Heat pipe cooling technology for desktop PC CPU. *Appl Therm Eng* 23(9):11371144
- Kuncoro IW, Pambudi NA, Biddinika MK, Widiastuti I, Hijriawan M, Wibowo KM (2019) Immersion cooling as a next technology for data center cooling: a review. *J Phys Conf Ser* 1402:044057
- Lamaion N, Ong CL, Marcinichen JB, Thome JR (2017) Two-phase mini-thermosyphon electronics cooling: dynamic modeling, experimental validation and application to 2U servers. *Appl Therm Eng* 110:481–494
- Legierski J, Wiecek B (2001) Steady state analysis of cooling electronic circuits using heat pipes. *IEEE Trans Compon Packag Technol* 24(4):549–553
- Levi C, Phillip T (2012) Numerical prediction of the junction-to-fluid thermal resistance of a 2-phase immersion-cooled IBM dual core POWER6 processor. In: 28th IEEE SEMI-THERM symposium
- Levin III, Dordopulo AII, Doronchenko YII, Raskladkin MKK, Fedorov AMM, Kalyaev ZVV (2016) Immersion liquid cooling FPGA-based reconfigurable computer system. *IFAC-Papers On Line* vol 49 (Elsevier B.V.), pp 366–71
- Levine MA (1989) Solid state cooling with thermoelectric. *Electron Packag Prod*
- Li Y, Zhou W, He J, Yan Y, Li B, Zeng Z (2019) Thermal performance of ultra-thin flattened heat pipes with composite wick structure. *Appl Therm Eng* 102:487–499
- Liang TS, Hung YM (2010) Experimental investigations on the thermal performance and optimization of the heat sink with U-shape heat pipes. *Energy Convers Manage* 51(11):2109–2116
- Mahalingam R, Huffington S, Jones L, Williams R (2007) Synthetic jets for the forced air cooling of electronics. *Electron Cooling*
- Mark M (1958) Cold plate design for airborne electronic equipment. *IRE Trans Aeronaut Navigational Electron*
- Mathew VK, Hotta TK (2018) Numerical investigation on optimal arrangement of IC chips mounted on a SMPS board cooled under mixed convection. *Therm Sci Eng Progress*
- Melcor Corporation (1995) *Thermoelectric Handbook*
- Michael JF (2006) Design and testing of micro-fabricated electrostatic fluid accelerator. *ELECTRONICS-NNIN REU 2006, Research Accomplishments*
- Mjallal I, Farhat H, Hammoud M, Ali S, Shaer AA, Assi A (2017) Cooling performance of heat sinks used in electronic devices. ISBN 978-1-5090-5173-1 © 2017 IEEE
- Mohammad E, Ezzaldeen E (2016) Heat pipes for the computer cooling applications
- Rampungoon P (2001) Interaction of a synthetic jet with a flat-plate boundary layer, PhD thesis, Department of Mechanical Engineering, University of Florida, Gainesville
- Rowe DM (1995) *CRC handbook of thermoelectrics*. CRC Press, Inc.
- Shah JM, Eiland R, Siddarth A, Agonafer D (2016) Effects of mineral oil immersion cooling on IT equipment reliability and reliability enhancements to data center operations. In: *Proceedings of the 15th InterSociety conference on thermal and thermomechanical phenomena in electronic systems, ITherm*, pp 316–325

- Smythe R (1995) Thermoelectric coolers take the heat out of today's hotchips. *Electronic Products*
- Sponagle B, Maranda S, Groulx D (2017) investigation of the thermal behaviour of thin phase change material packages as a solution to temperature control in electronics. In: *Proceedings of the ASME 2017 summer heat transfer conference*, Bellevue, WA, USA, 9–14 July 2017
- Sukhvinder K, David M, John C (2007) Closed loop liquid cooling for high performance computer systems. *ASME InterPACK '07*, July 8–12, Vancouver, British Columbia, CANADA
- Sukhvinder SK (2012) Advanced cooling for power electronics. Presented by invitation at international conference on integrated power electronics systems CIPS 2012, March 6–8, Nuremberg, Germany
- Sun Y, Wang Y, Zhu L, Yin B, Xiang H, Huang Q (2014) Direct liquid-immersion cooling of concentrator silicon solar cells in a linear concentrating photovoltaic receiver. *Energy* 65:264–271
- Tan F, Tso CP (2004) Cooling of mobile electronic devices using phase change materials. *Appl Therm Eng* 24:159–169
- Testi D (2018) Heat transfer enhancement by an impinging ionic jet in a viscous transformer coolant. *Int Commun Heat Mass Transf* 91:256–261
- Thermal management system for portable electronic devices, US Patent.
- Tomizawa Y, Sasaki K, Kuroda A, Takeda R, Kaito Y (2016) Experimental and numerical study on phase change material (PCM) for thermal management of mobile devices. *Appl Therm Eng* 98:320–329
- Tousif A, Maha B, Dominic G, Mary AW (2019) Passive thermal management of tablet PCs using phase change materials: intermittent operation. *Appl Sci* 9:902. <https://doi.org/10.3390/app9050902>
- Van Le L, Nhu CN, Tai TN, Dinh TX, Tran C, Bao LD, Bui TT, Dau VT, Duc TC (2019) Liquid pumping and mixing by PZT synthetic jet. In: *20th international conference on solid-state sensors, actuators microsystems, transducers EUROSENSORS XXXIII*. IEEE, Berlin, pp 198–201
- Wang JC (2008) Novel thermal resistance network analysis of heat sink with embedded heat pipes. *Jordan J Mech Indust Eng* 2(1):23–30
- Wang JC (2011) L-type heat pipes application in electronic cooling systems. *Int J Thermal Sci* 50(1):97–105
- Wang Y, Vafai K (2000) An experimental investigation of the thermal performance of an asymmetrical flat plate heat pipe. *Int J Heat Mass Transf* 43(15):2657–2668
- Wang JC, Huang HS, Chen SL (2007) Experimental investigations of thermal resistance of a heat sink with horizontal embedded heat pipes. *Int Commun Heat Mass Transfer* 34(8):958–970
- Weng YC, Cho HP, Chang CC, Chen SL (2011) Heat pipe with PCM for electronic cooling. *Appl Energy* 88:1825–1833
- Xinxi L, Dequan Z, Guoqing Z, Cong W, Ruheng L, Zhaoda Z (2019) Experimental investigation of the thermal performance of silicon cold plate for battery thermal management system. *Appl Therm Eng* 155:331–340
- Yeatman EM (2007) Applications of MEMS in power sources and circuits. *J Micro-Mech Micro-Eng* 17:184–188
- Yu ZZ, Harvey T (2000) The precision engineered heat pipe for cooling Pentium II in Compact PCI design. *Thermal and Thermo-Mechanical Phenomena in Electronic Systems, ITherm 2000 The Seventh Intersociety Conference*, vol 102, pp 102–105

# Chapter 5

## A Review on Phase Change Material–metal Foam Combinations for Li-Ion Battery Thermal Management Systems



S. Babu Sanker and Rajesh Baby

### *Abbreviations*

BTMS	Battery thermal management system
EVs	Electric vehicles
GcN	Graphene-coated nickel foam
$k_{\text{PCM}}$	Thermal conductivity of phase change materials
$k_{\text{CPCM}}$	Thermal conductivity of composite phase change materials
Li-ion	Lithium-ion
HEVs	Hybrid electric vehicles
PHEV	Plugin hybrid electric vehicles
PCMs	Phase change materials
PPI	Pores per inch.
TCE	Thermal conductivity enhancers

### *List of symbols*

$\rho$	Density ( $\text{kg/m}^3$ )
$k$	Thermal conductivity ( $\text{W/m-K}$ )
$T_m$	Melting temperature ( $^{\circ}\text{C}$ )

---

S. Babu Sanker · R. Baby (✉)  
Department of Mechanical Engineering, St. Joseph's College of Engineering and Technology,  
Palai, Choondacherry P.O., Kerala 686579, India  
e-mail: [rajeshbaby@sjcetpalai.ac.in](mailto:rajeshbaby@sjcetpalai.ac.in)

## 5.1 Introduction

The increasing pollution of the environment and the issues of global warming triggered the policy makers, environmentalists and researchers to find a clean and appropriate alternative to fossil fuels. About 80% global energy consumption is fuelled by fossil fuels (Vidadili et al. 2017). The transportation industry, such as road, railway, marine, and aviation sectors are one of the largest consumers of fossil fuels. Energy shortage and serious environmental pollutions issues are booming all over the world, by replacing of fossil-fuelled vehicles, to those types using renewable energy, it is possible to reduce greenhouse emissions. Recently by the introduction of various types EVs such as HEVs, PHEV and fuel cell vehicles, greatly helps in reducing pollution, greenhouse gases as well as noise levels to a great extent. Anderson et al. (2009) reported that the use of EVs might result in a measurable reduction in emission of greenhouse gases by 40%. Hence, they are more fuel-efficient and environmentally clean than conventional internal combustion engines. The battery is the main component of the EVs and is used to store renewable energy.

Though various types of batteries are commercially available in the market, Li-ion batteries have emerged as the potential source of energy storage for electric vehicles by virtue of their superior features such as high specific power, long-cycle life, low auto discharge rate, no memory effect, high nominal voltage (Zou et al. 2019; Panchal et al. 2016) and so on. However, the main deficiency of these batteries is the excessive heat generation, especially whilst they work at high discharge rate. Heat generated inside the battery will cause increase in temperature and can adversely affect the reliability and durability of these systems. The sudden temperature rise may lead to battery overheating, resulting in safety concerns, performance degradation and thermal runoff (Wang et al. 2018). In order to circumvent these issues, numerous research designs have been proposed for effective ways to develop a high performance BTMS.

### 5.1.1 Battery Thermal Management System (BTMS)

One of the major challenges in the battery pack design is to the management of heat accumulation inside the battery, during charging and discharging as well. When the temperature of the battery is too high, there will be an undesirable, non-uniform temperature distribution within the cell. Function of BTMS is to maintain a working temperature range and consistent distribution throughout the cell, module and the battery pack at various discharging rates.

Permissible operating temperature range of a Li-ion battery is in the range of  $-20$ – $60$  °C (Väyrynen and Salminen 2012). Furthermore, to get maximum output of the battery, it is recommended to be operated between  $15$  °C and  $35$  °C. It is also reported that the expected temperature difference between cell to cell and module to module should not exceed  $5$  °C (Pesaran and Nrel 2013; Siddique et al. 2018). If

the temperature falls below 15 °C, there will be a reduction in capacity and performance. Also, when the temperature exceeds 35 °C, irreversible reactions can lead to deterioration in the battery lifetime.

The degradation of battery performance at elevated temperature is due to reversible and irreversible reactions taking place inside the battery. The heat produced in the reversible reactions (entropy heat) comes from reversible entropy change that occurs during chemical reaction in the cells. There are mainly four irreversible reactions generating heat during charging and discharging cycle (Ma et al. 2018).

1. Ohmic heating
2. heating due to mixing
3. Enthalpy change
4. Activation polarization.

According to Bernardi et al., and Gu et al. (1985; 2000) the following simplified equations can be used to compute the heat generation of the entire cell

$$q = I(U - V) - I\left(T \frac{dU}{dT}\right) \quad (5.1)$$

$q$  is the heat generation,  $I$  indicate the charge/discharge current passing through the cell, where  $U$  is the open circuit voltage and  $V$  represents the cell voltage. The expression  $I(U - V)$  indicates the irreversible heat caused by the resistance in the cell. The term  $(U - V)$  is overpotential of the cell caused by charge transfer reactions at the electrodes and electrolyte interfaces, the diffusion and migration of Li-ion through electrodes and electrolyte and the ohmic losses. The reversible entropy heat during the electrochemical reactions is denoted by the second expression  $I\left(T \frac{dU}{dT}\right)$ . The term  $\frac{dU}{dT}$  is the entropy coefficient and the term  $T$  is the instantaneous temperature.

Various active and passive cooling strategies are used in practise to mitigate the thermal management issues. Active BTMS require an external energy source to boost the heat transfer rate. These systems include air-cooling (Ling et al. 2015; Lazrak et al. 2018; Jiaqiang et al. 2018a), liquid-cooling (Rao et al. 2017; Jiaqiang et al. 2018b; Cao et al. 2020) and thermoelectric-cooling (Jiang et al. 2019) and so on. In active cooling systems, the use of cooling fluids, need for various components like pumps, pipes and valves are in use which will increase the weight, noise levels, thereby higher energy requirements.

A passive system is any mechanism that does not require additional heating or cooling. Heat–pipe-based methods (Wang et al. 2014; Wu et al. 2017), cooling with fins and PCM incorporated cooling are examples of these systems. Compared with active cooling systems, passive cooling systems are popular because of their simplicity, lightweight, high efficiency and less maintenance requirements. PCMs, on the other hand, are a promising concept that is still in the early stages of research amongst the passive systems described.

The application of phase change material to battery thermal management system can result a very reliable and efficient solution for the thermal management of power

batteries and related systems. In recent years, researchers have investigated the performance enhancement using metal foam composite PCMs. A good combination of phase change material in tandem with metal foam is an attractive option to maintain the batteries within a predefined temperature.

### 5.1.2 Battery C-rating

An important characteristic of the battery is C-rate. The C-rate can be defined as the rate at which the battery discharged or charged relative to its capacity. 1C, means that a fully charged battery with a capacity of 1Ah can provide 1A for 1 h.

- 1 C rate—Discharge or charge in 1 h.
- 2 C rate—Discharge or charge in 1/2 h.
- 5 C rate—Discharge or charge in 1/5 h.
- 0.1 C rate—Discharge or charge in 10 h.

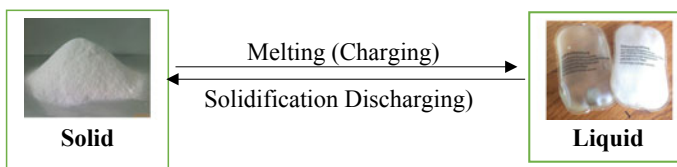
#### 5.1.2.1 Phase Change Materials

In sensible heat storage, the addition or removal of heat result in rise of temperature, whereas the storage medium undergoes a change in phase at constant temperature in latent heat storage systems. The latent heat capacity of the PCMs are utilized for thermal management purposes.

Phase change materials are substances, which stores and retrieves sufficient thermal energy at phase transition in order to provide useful heating and cooling the phase transition process of phase change materials is shown in Fig. 5.1.

As the temperature increases, the chemical bonds break up which leads to the phase transformation. Phase transformation having wide applications are mainly solid to liquid form.

Over the last two decades, numerous researchers have been intensively investigated PCM-based thermal management systems because of their desired thermal, physical, chemical, kinetic and economical properties. These desirable properties for various application of PCM are summarized in Table 5.1. Recently, it received greater attention in the areas of battery thermal management systems for electric vehicles.



**Fig. 5.1** Phase transition in phase change process

**Table 5.1** Desirable properties for various application of PCM (Chen et al. 2013; Ibrahim et al. 2017)

Physical	Chemical	Kinetics	Economical	Thermal
Small volume change on phase change Low vapour pressure High energy density	Chemically stable Non toxic Non flammable Non explosive	No-sub cooling during freezing Sufficient crystallisation rate	Availability in large quantities In expensive in nature	Large latent heat of fusion High thermal cyclic stability High specific heat High thermal conductivity

**Table 5.2** Pros and cons of PCM

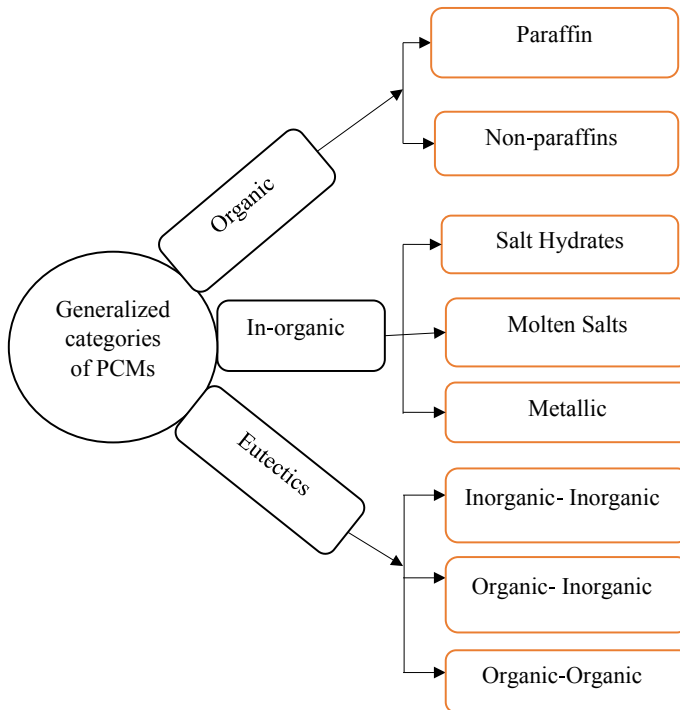
Pros	Cons
1.Higher storage density than sensible heating	1. High cost
2.Small volume change during the phase change	2. Corrosiveness
3.Smaller temperature change during storing and releasing energy	3. Density changes
4.Congruent melting	4. Low thermal conductivity
	5. Phase segregation
	6. Super cooling

Major applications of PCMs are (a) thermal storage units (b) heating (c) spacecraft (d) building (e) textiles and (f) BTMS. Pros and cons associated with the use of PCMs are given in Table. 5.2. PCM thermal management depends on latent heat storage. Though, theoretically no temperature change associated with phase change, there may be small temperature change in practise. This fact is mentioned as smaller temperature change during storing and releasing energy in Table 5.2.

**5.1.2.2 Classification of PCMs**

PCMs are categorised as organic, inorganic and eutectic materials. A schematic diagram on the different categories of PCMs are shown in Fig. 5.2.





**Fig. 5.2** Various categories of PCMs

### 5.1.2.3 Organic PCM

Organic PCMs having mainly paraffins, fatty acids and polyethylene glycol (PEG). Broadly it can be categorized as paraffin and non-paraffin. Examples are wax, hydroquinone, salicylic acid, alpha glucose, acetamide and so on. Compounds with chemical formula of  $C_nH_{2n+2}$  are categorized as paraffins. Paraffin wax is mainly composed of straight chain n-alkanes containing 8 to 40 carbon atoms with the common formula  $CH_3-(CH_2)_n-CH_3$  (Voronin et al. 2020). Heat of fusion and melting point increases with increasing carbon atom count. For example,  $C_2$  is with lesser heat of fusion and melting point than  $C_4$  (Sharma and Sagara 2005).

### 5.1.2.4 Inorganic PCM

Inorganic PCM consists of salt hydrates, nitrates and metallics. They are having a high heat of fusion and is used for higher temperature applications. Metallic inorganic types include low melting point metals and eutectic metals. Most of these metals have high thermal conductivity. These are rarely used in PCM applications due to weight penalties. Molten salts are extensively used for solar power plants, which rely on

energy to produce steam or electricity. In solar power plant, the molten salt is used as heat transfer medium.  $\text{NaNO}_3$ ,  $\text{NaCl}$  and  $\text{KNO}_3$  are examples of inorganic PCM.

### 5.1.2.5 Eutectic

A Eutectic PCMs are mixtures of two or more components at a certain composition. It is a minimum melting composition of these components. Details of various eutectic combinations are given in Fig. 5.2. Eutectics melt and freeze congruently. The merits and demerits of various PCMs discussed are shown in Table 5.3.

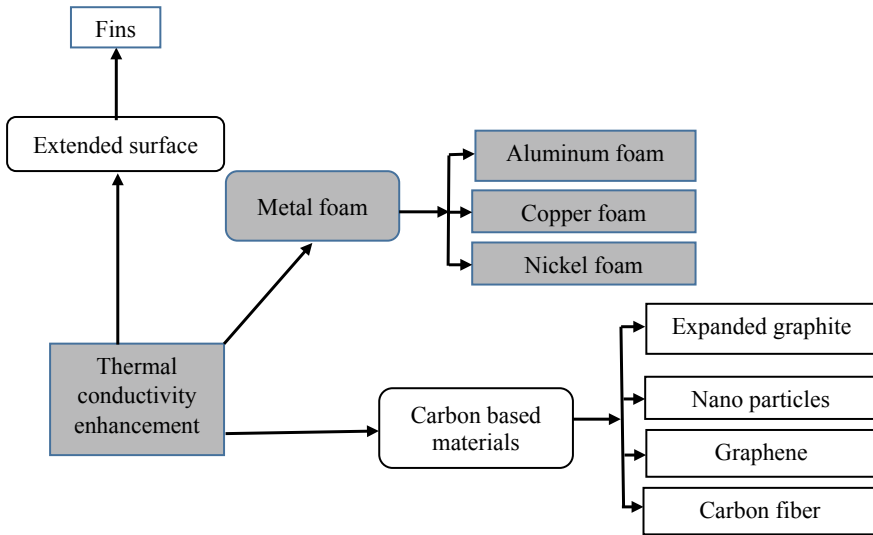
Though, PCMs are having a number of merits associated as described earlier, low thermal conductivity of the PCM is certainly a demerit to be used in thermal management applications. However, using PCM in conjunction with thermal conductivity enhancers can change this situation. Various thermal enhancement techniques are detailed in the following section.

### 5.1.3 Thermal Conductivity Enhancement Techniques

Thermal Conductivity Enhancers (TCE) such as fin, expanded graphite, carbon-based nanoparticles and metal foams (Copper, aluminium and nickel foams) are widely used in a number of applications. Details of various TCEs are given in Fig. 5.3.

**Table 5.3** Merits and demerits of organic and inorganic, and eutectic Phase change materials (Ghani et al. 2020)

Types	Merits	Demerits
Organic	Chemically stable High latent heat of fusion No tendency of super cooling	Low thermal conductivity Mildly corrosive in nature Material cost is too high
Inorganic	Thermal conductivity high High latent heat of fusion Lower volume change Sharp melting point Low cost and easily available	Material degradation Corrosive Low specific heat Less cyclic stability Segregation
Eutectic	Wide range of phase change temperature Good thermal and chemical stability Large heat capacity Little supercooling	Leakage during the phase transition Less thermal conductivity



**Fig. 5.3** Various thermal conductivity enhancement techniques in PCMs

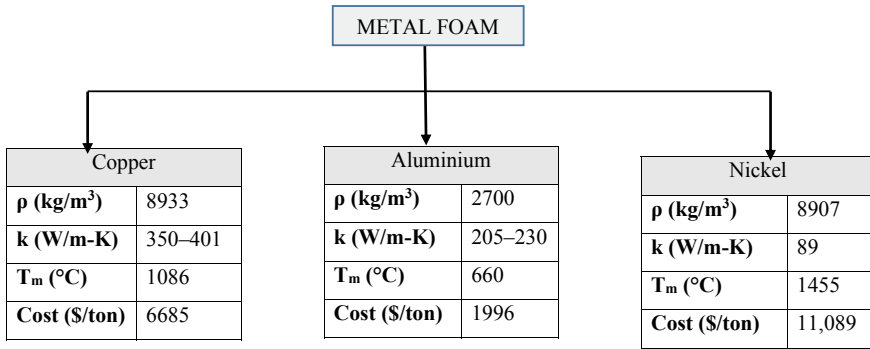
High thermal conductivity, porosity, surface area to volume ratio, complicated three-dimensional network, good thermos-physical properties and mechanical strength made the use of metal foam popular, especially in the BTMS. Various types of these metal foams are essential to enhance the effective thermal conductivity of PCMs thereby maintaining the uniformity of the temperature distribution within the battery.

Adequate thermal management system is essential for proper heat dissipation from batteries during discharge. In recent years, researchers have investigated heat transfer characteristics of various metal foams in conjunction with PCMs.

## 5.2 Metal Foams: Research Progress, Prospects and Challenges

Metal foam is a cellular structure made up of a solid metal, with cells generated by ligaments that are randomly oriented and distributed. It also consists of a solid metal, large volume fraction of gas or fluid filled open and closed pores. In general, metal foams can be categorized into (1) open cell metal foam (2) Closed cell metal foam (pore can be sealed).

These pores can either be sealed (closed cell foam) or an interconnected network is not closed (open cell foam) each other and gas or fluid can easily flow through one cell to another the cells. PPI and relative density are the key parameters to classify the open—cell foam. PPI is the number of pores that can be counted in a linear inch. Higher PPI shows a high number of pores, meaning the average diameter of the pore



**Fig. 5.5** Properties of different metal foam materials (adapted from Rehman et al. (2019))

is smaller. The relative density is the ratio between the density of the foam and the density of the material, which the foam is made of.

Porosity is another parameter of interest in porous medium. It is the ratio of the volume of free space to the total volume of the porous media. Copper, aluminium and nickel are some of the metal forms used. Large contact area to volume ratio, high thermal conductivity, low apparent density, lightweight and high structural strength are the merits of metal foams for various applications. Porous materials offer gap for PCM and the high thermal conductivity of porous materials support more effective heat transfer in metal form PCM combinations.

Metal foam are widely used for PCM-based BTMS can be used for the following types (1) Copper metal foam, (2) Aluminium metal form, (3) Nickel metal foam. A block diagram of various metal foams and their properties are shown in Fig. 5.5.

Following sections details the research progress, prospects and challenges associated with various metal forms namely copper, aluminium, nickel and combination of metal foams and other thermal conductivity enhancers.

### 5.2.1 Review on Copper Foam–PCM Combinations

Details of some of the recent papers on experimental, numerical and Combined experimental and numerical techniques of PCM with copper foam is detailed in the following section.

#### 5.2.1.1 Experimental: metal foam–PCM combinations

Many experimental works are available on copper metal foam–PCM combinations employed in Li-ion battery thermal management. Li et al. (2014) experimentally evaluated PCM-based thermal management system of Li-ion battery using composite

PCM with copper foam and tested at 0.5 C, 1 C and 3 C discharge rate, respectively. The result showed that the temperature of the battery was reduced by 3 to 10 °C compared to the pure PCM, in accordance with foam porosity and discharge rates. Rao et al. (2015) conducted an experimental study on a cylindrical 42,110-size (42 mm in diameter and 110 mm in height) LiFePO<sub>4</sub> battery, using paraffin /copper foam that was installed into an electric vehicle and worked on the lane. The experiment was carried out at 3C and 5C discharge rates. When the battery at a high discharge rate, the temperature difference of the module and the individual cell were 45 °C and 5 °C, respectively. When the battery module is at constant discharge (5C), the maximum local temperature of battery module was 40.89 and 42.33 °C corresponding to the ambient temperatures of 29 °C and 33 °C, respectively.

Zhang and Li (2017) experimentally analysed the thermal performance of LiFePO<sub>4</sub> battery for PCM-based BTMS using copper metal foam saturated with PCM at discharge rates of 2C, 3C and 5C. It was observed that at high discharge of 5 C, the maximum temperature of the battery managed by PCM composite and copper foam was is much lower than that of pure PCM. Wang et al. (2017) investigated the performance study of copper foam/phase change material combined thermal management system for three different types of batteries like square (105 mm × 28 mm × 71 mm) 26,650 (26 mm diameter 650 mm height) and 42,110 (42 mm diameter and 110 mm height) were examined experimentally under different discharge rates of 1C, 3C and 5 C, respectively. It was observed that at 1C, 3C and 5C discharge rate the battery surface temperature of 26,650 has been enhanced by 34.7 °C, 41.68 °C and 62.77 °C, respectively. And also observed that the at the discharge rate of 5C, maximum temperature of the three different batteries of 26,650, 42,110 and square batteries with a Copper foam/ composite PCM integrated battery management system was controlled to below 44.37 °C, 51.45 °C and 50.69 °C, respectively.

He et al. (2019) investigated the thermal performance of Li-ion battery using a novel composite PCM with expanded graphite and copper foam at 1C, 3C and 5C, respectively. Bending, tensile, impact and compressive strength of the composite PCM was analysed after adding EG and copper foam to the composite PCM. It is found that with the addition of EG and copper foam, the temperature of the battery has been lowered by 8.37% as compared to pure PCM. Kermani et al. (2019) designed a novel thermal management system for pouch Li-ion battery using integrated copper foam-based PCM and forced air-cooling. The thermal performance of combined battery thermal management system has been compared with that of active air-based battery thermal management system and passive PCM-based battery thermal management system. The maximum temperature of the battery was decreased by 18.6%, 22.3% and 40.3%, respectively, as compared to natural convection using passive, active and integrate BTMS.

### 5.2.1.2 Numerical: Metal Foam–PCM Combinations

Qu et al. (2014) numerically investigated on 2-D transient model for a PCM-based battery thermal management system using copper foam saturated PCM at 1C and

3C discharge rates. The battery efficiency of composite PCM-based BTMS was compared to natural convection. It was observed that, at discharge rate of 1C and 3C, the temperature of the battery was decreased by 33% and 35%, respectively.

### 5.2.1.3 Combined Experimental and Numerical Investigations

Wang et al. (2018) performed combined experimental and numerical studies on lithium-ion titanate battery with cell dimensions of 6.1 mm × 203 mm × 127 mm using copper foam and composite PCM at the discharge rate of 3C and 4C, respectively. The findings suggested that at 4C discharge rate the BTMS was able to maintain the battery temperature at 42 °C. Kiani et al. (2020) conducted experimental and numerical investigation on BTMS of a Li-ion battery using paraffin, copper metal foam (porosity of 0.9 and 20 PPI) combined with active cooling system with nano fluid (Table 5.4).

## 5.2.2 Review on Aluminium Foam–PCM Combinations

Details of investigations on aluminium foam–PCM combinations are discussed in this section. Khateeb et al. (2005) designed BTMS of 18,650 Li-ion batteries used in electric scooters using aluminium foam paraffin composite to handle the temperature of the Li-ion battery. It was observed that the temperature of the battery surface was further reduced by 4 °C in comparison to that of the pure PCM. Wang et al. (2015) conducted experiments at a heat flux of 7000 and 12,000 W/m<sup>2</sup>. According to the experimental results with heat fluxes of 7000 and 12,000 W/m<sup>2</sup>, the addition of aluminium foam decreases the time of phase transition by 26.4% and 25.6%, respectively.

The numerical investigations on the Li-ion battery thermal management system made from pure octadecane, gallium and octadecane-aluminium foam composite materials were carried out by Alipanah and Li (2016). When aluminium foam of 0.88 porosity is used in tandem with octadecane led to 7.3 times longer discharge time in comparison with pure octadecane. Saw et al. (2017) used CFD model (ANSYS-CFX) to investigate the thermal response of LiFePO<sub>4</sub> pouch cell battery pack using Al foam with different types. Pore size (10, 20, 40 PPI) and porosity of (0.918, 0.794, 0.682, 0.924, 0.774, 0.679 and 0.93), respectively. According to the numerical results, it was observed that Al foam (10 PPI, 0.918 porosity) offered decreasing flow resistance and also provides largest thermal performance under the discharge rate of 3C. Summary of various investigations using aluminium metal foam–PCM combinations is given in Table 5.5.

**Table 5.4** Summary of the various investigation using copper metal foam-PCM combination

PCM Melting Point (T in °C)	Thermal Conductivity W/m-K		Porosity	Pores per inch	Battery layout/Dimensions (mm)	Nature of work/Battery load	Authors/Year of publication
	k PCM	kPCPCM					
Paraffin (RT 44HC 42.76-49.24	0.2	11.0.33	0.90	20	Li-ion battery pack L × W × T = 140 × 65 × 15 mm 10 Ah, 3.8 V	Experimental 0.5 C, 1 C and 3 C	Li et al. (2014)
		6.35	0.95	20			
		0.80	0.97	20			
		0.80	0.97	10			
		0.80	0.97	40			
Paraffin 42.76-49.24	0.3(s) 0.1(l)	-	0.90	20	Square Li-ion battery L × W × T = 14 × 14 × 14 mm 10 Ah, 3.8 V	Numerical 1C and 3C	Qu et al. (2014)
Paraffin 37	0.2	-	-	20	LiFePO <sub>4</sub> 42,110 cylindrical 24 cells module 20Ah, 3.8 V 12S × 2P	Experimental 3 C and 5C	Rao et al. (2015)
Paraffin 35-40	0.21	-	0.9	50	LiFe P04 Battery pack 70 × 100 × 27 mm 13.5 Ah 3.65 V	Experimental 2C, 3C, 4C and 5C	Zhang and Li (2017)

(continued)

**Table 5.4** (continued)

PCM Melting Point (T in °C)	Thermal Conductivity W/m–K		Porosity	Pores per inch	Battery layout/Dimensions (mm)	Nature of work/Battery load	Authors/Year of publication
	k PCM	kCPCM					
Paraffin 45–47	–	–	–	–	26,650,3000mAh,3.2 V 42,110,10000mAh,3.2 V and square (105 m × 28 mm × 71 mm 10,000 mAh,3.2 V	Experimental 1C,3C and 5C	Wang et al. (2017)
n-eicosane 36.5	0.274	5.28	0.95	–	lithium–ion titanate 6.1 mm × 203 mm × 127 10Ah 2.3 V	Experimental/ numerical 2C, 3C and 4C	Wang et al. (2018)
Pure paraffin 48 °C	0.23	2.9	0.8	10	LiCoO2 batteries (GRPA875175-3.7 V) 16 Ah	Experimental 1C,3C and 5C	He et al. (2019)
Paraffin 37.80–44.23	0.205(l) 0.317(s)	–	0.9	20	Li-ion pouch cell	Experimental 2.5 W,4.5 W,5 W and 10 W	Mehrabi-Kermani et al. (2019)
Paraffin 42–45	0.2	–	0.9	20	Pouch Li-ion battery	Experimental/Numerical 41 W, 65 W	Kiani et al. (2020)



**Table 5.5** Summary of the various investigations using aluminium metal foam–PCM combinations

PCM melting point (T in °C)	Thermal conductivity (k) (W/m–K)		Porosity	Pores per inch	Battery layout/dimensions (mm)	Nature of work/battery load	Authors/year of publications
	$k_{PCM}$	$k_{CPCM}$					
Paraffin 41–44	0.29	43.80	0.80	40	18,650 cylindrical Li-ion battery	Experimental	Khateeb et al. (2005)
paraffin	0.21(l) 0.29(s)	46.06	0.70 0.90		Rectangular LiFeP04 Li-ion battery (L) × W × H = 119 × 70 × 27 16.5 Ah	Experimental 1C,2C	Wang et al. (2015)
Octadecane	0.358	6.56	0.97		Rectangular Li-ion battery thickness (L) of 12.5 and height (H) of 200 mm	Numerical	Alipanah and Li (2016)
		15.86	0.92.5				
		25.15	0.88				
			0.918 0.794 0.682 0.924 0.774 0.79 0.923	10 10 10 20 20 20 40	LiFePo4 pouch cell battery module 160 × 227 × 8 19.5Ah.,3.3 V	Numerical 3C	Saw et al. (2017)

### 5.2.3 Review on Nickel Foam–PCM Combinations

As the melting point of nickel is high (1455 °C), it is also used in conjunction with PCMs for BTMS. The thermal conductivity of nickel is only 89 W/ m–K, much lower than that of copper and aluminium. Hussain et al. (2016) experimentally investigated on passive thermal management system of 18,650 Li-ion batteries using composite PCM with nickel foam. The experiment was carried out and compared with natural convection mode and cooling mode with pure paraffin at various discharge rates of 0.5C, 1.5C and 2C, respectively. It was found that at discharge rate of 2C, the surface temperate of the battery managed by PCM composite and nickel foam was reduced by 31 and 24% as compared to natural convection and pure paraffin. Hussain et al. (2018) experimentally investigated thermal performance of Li-ion battery using graphene—coated nickel foam (GcN) saturated with PCM. The result showed that, the thermal conductivity of pure paraffin wax is increased by 23 times when using GcN foam, whereas with nickel foam, it has been raised only six times.

### 5.2.4 *Combination of Metal Foam and Other Thermal Conductivity Enhancers*

Deng et al. (2016) studied experimentally the thermal characteristics of cylindrical 18,650 (18 mm in diameter, 65 mm in length) lithium-ion battery using phase change materials combined with metallic foams and fins, at different power levels of 6.6, 8.8 and 13.2 W, respectively, corresponding to high discharge rates of 8 to 11C and the heating time for each corresponding power was controlled so that the housing temperature reached the peak temperature of 53.8 °C. Paraffin was used as a phase change materials with a melting temperature range between 47 and 53.8 °C. The experiment has been designed and tested different cases with pure PCM, PCM combined with metallic foam, and PCM combined with fins and metallic foams. The results showed that the addition of metal foam improves the heat conduction and reduces the battery temperature when the temperature of the housing was reached at 53.8 °C, the battery temperature was 65.9 °C which dropped by 3.4 °C compared to pure paraffin at heat input of 6.6 W. the similarly decreased battery temperature with the addition of copper foam can be found at an increased heating power of 8.8 and 13.2 W, respectively. The temperature of the battery at the moment when the fully fused PCM is 3.4–6.6 °C lower than that of the pure PCM at a heating power of 6.66 to 13.2 W. Mallow et al. (2018) experimentally studied the thermal performance of Li-ion battery using aluminium foam with different pore size of 10, 20 and 40 PPI saturated with PCM. The result finding showed that using 40 PPI metal foam give the temperature decreased was 85%, compared with 10 PPI. Moreover, they compared aluminium foam with compressed natural expanded graphite foam (CENG) and it was observed that CENG gave better performance than aluminium foam because of their low density, small pore size and high thermal conductivity.

Barnes and Li (2020) carried out a combined experimental and numerical study of passive thermal management system of LiFe PO<sub>4</sub> using different types of coolant such as water, air, PCM, PCM /Aluminium foam with pore size of (5 PPI and 40 PPI) and PCM /carbon foam with pore size of (45 PPI), at discharge rates of 1C, 3C and 5C, respectively. It was observed that at 3C discharge rate, the average battery surface temperature was enhanced at a level of 25 °C. Heyhat et al. (2020) numerically investigated the thermal performance of phase change materials (PCM) based battery thermal management system (BTMS) of the 18,650 (18 mm in diameter and 65 mm in length) Li-ion battery. They also studied the effect of various fin count 1, 2 and 5 numbers and found that having more fins were no longer beneficial. The result show that the maximum temperature of the battery was reduced from 2 °C and 4 °C at discharge rate of 4.6 W and 9.2 W, respectively. To improve the thermal performance of battery systems, nanoparticles, fins and metal foam are used with PCM combinations to enhance thermal management performance and their effects on system performance. It was observed that the metal foam was more effective than fins, but the fins were more efficient than the nanoparticles.

For a single battery application, Ghalambaz and Zhang (2020) numerically and experimentally investigated the conjugate flow of phase change materials embedded

in nickel foam with a pore size of 10 PPI and porosity of 0.975 and also saturated with paraffin wax in the annular space of the heatsink. The inner surface of annuli is subjected to a pulse heat load, whilst the outside surface is cooled by convection. During the pulse load, heat sink with PCM results in four times the cooling power in comparison with pure external convection. Veismoradi et al. (2020) numerically investigated the heat transfer and thermal characteristics of a Li-ion battery cell filled with paraffin wax embedded in copper metal foam for various heat loads. They found that efficiency is proportional to the heat pulse given. Ranjbaran et al. (2020) investigated numerically, nine passive Li-ion BTMS based on paraffin wax as pure PCM, and copper foam as conductive additive. Copper is added from 1 to 9 vol% in steps of 1%. It is found that adding 6% copper foam to the cell has the optimal cooling effect and keeps the cell within the specified temperature range.

### 5.3 Conclusions

From the preceding discussions, it can be seen that several works are available on the thermal management of PCM-based metal foam combinations.

- Majority of the experimental investigations on the BTMS is employed using copper and aluminium foams. Use of nickel foam / paraffin composite as a passive thermal management system for Li-ion batteries have rarely explored. Furthermore, nickel foam is cheaper than that of copper and aluminium foams and also shows a better thermal stability since it is more resistant to corrosion than copper and aluminium foams, thus providing another attractive PCM–metal foam combination for battery thermal management solutions.
- The foam with large pore density is suitable for the BTMS applications due to increased surface area at the same porosity. In order to have greater conduction heat transfer, low porosity foam is better, but low porosity of foam is retarding convection heat transfer.
- The effective thermal conductivities of the composite PCMs are drastically enhanced with the use of metal foams, compared to that of pure paraffin in all cases.
- To increase the heat transfer rate, the foam with low porosity is preferred, similarly foam with high porosity is suitable for increasing the heat storage capacity. Small pore size and thicker ligament leads to higher diffusivity. Larger pore size and thinner ligament leads to larger heat storage unit.
- Though many studies are available for the BTMS with the use of metal foam–PCM combinations, investigations pertaining to the optimization of the amount of PCM used, power level, quantity of metal foam required for maintaining the optimum temperature limits are still scarce in the literature.

## References

- Alipanah M, Li X (2016) Numerical studies of lithium-ion battery thermal management systems using phase change materials and metal foams. *Int J Heat Mass Transf* 102:1159–1168. <https://doi.org/10.1016/j.ijheatmasstransfer.2016.07.01>
- Andersen PH, Mathews JA, Rask M (2009) Integrating private transport into renewable energy policy: the strategy of creating intelligent recharging grids for electric vehicles. 37:2481–2486. <https://doi.org/10.1016/j.enpol.2009.03.032>
- Barnes D, Li X (2020) Battery thermal management using phase change material-metal foam composite materials at various environmental temperatures. *J Electrochem Energy Convers Storage* 17(2):1–7. <https://doi.org/10.1115/1.4045326>
- Bernardi D, Pawlikowski E, Newman J (1985) A general energy balance for battery systems. *J Electrochem Soc* 132(1):5–12
- Cao J, Luo M, Fang X, Ling Z, Zhang Z (2020) Liquid cooling with phase change materials for cylindrical Li-ion batteries: an experimental and numerical study. *Energy*, 191(xxxx):116565. <https://doi.org/10.1016/j.energy.2019.116565>
- Chen YJ, Nguyen DD, Shen MY, Yip MC, Tai NH (2013) Thermal characterizations of the graphite nanosheets reinforced paraffin phase-change composites. *Compos A Appl Sci Manuf* 44(1):40–46. <https://doi.org/10.1016/j.compositesa.2012.08.010>
- Deng YC, Zhang HY, Xia X (2016) Experimental investigation of thermal characteristics of lithium ion battery using phase change materials combined with metallic foams and fins. *IOP Conf Series: Earth Environ Sci* 40(1). <https://doi.org/10.1088/1755-1315/40/1/012045>
- Ghalambaz M, Zhang J (2020) Conjugate solid-liquid phase change heat transfer in heatsink filled with phase change material-metal foam. *Int J Heat Mass Transf* 146:118832. <https://doi.org/10.1016/j.ijheatmasstransfer.2019.118832>
- Ghani SAA, Jamari SS, Abidin SZ (2020) Waste materials as the potential phase change material substitute in thermal energy storage system: a review. *Chem Eng Commun* 1–21. <https://doi.org/10.1080/00986445.2020.1715960>
- Gu WB, Wang CY (2000) Thermal-electrochemical modeling of battery systems. *J Electrochem Soc* 147(8):2910. <https://doi.org/10.1149/1.1393625>
- He J, Yang X, Zhang G (2019) A phase change material with enhanced thermal conductivity and secondary heat dissipation capability by introducing a binary thermal conductive skeleton for battery thermal management. *Appl Therm Eng* 148(September 2018):984–991. <https://doi.org/10.1016/j.applthermaleng.2018.11.100>
- Heyhat MM, Mousavi S, Siavashi M (2020) Battery thermal management with thermal energy storage composites of PCM, metal foam, fin and nanoparticle. *J Energy Storage* 28(September 2019):101235. <https://doi.org/10.1016/j.est.2020.101235>
- Hussain A, Tso CY, Chao CYH (2016) Experimental investigation of a passive thermal management system for high-powered lithium ion batteries using nickel foam-paraffin composite. *Energy* 115:209–218. <https://doi.org/10.1016/j.energy.2016.09.008>
- Hussain A, Abidi IH, Tso CY, Chan KC, Luo Z, Chao CYH (2018) Thermal management of lithium ion batteries using graphene coated nickel foam saturated with phase change materials. *Int J Therm Sci* 124(September 2017):23–35. <https://doi.org/10.1016/j.ijthermalsci.2017.09.019>
- Ibrahim NI, Al-Sulaiman FA, Rahman S, Yilbas BS, Sahin AZ (2017) Heat transfer enhancement of phase change materials for thermal energy storage applications: a critical review. *Renew Sustain Energy Rev* 74(October 2015):26–50. <https://doi.org/10.1016/j.rser.2017.01.169>
- Jiang L, Zhang H, Li J, Xia P (2019) Thermal performance of a cylindrical battery module impregnated with PCM composite based on thermoelectric cooling. *Energy* 188:116048. <https://doi.org/10.1016/j.energy.2019.116048>
- Jiaqiang E, Yue M, Chen J, Zhu H, Deng Y, Zhu Y, Zhang F, Wen M, Zhang B, Kang S (2018a) Effects of the different air cooling strategies on cooling performance of a lithium-ion battery module with baffle. *Appl Therm Eng* 144:231–241. <https://doi.org/10.1016/j.applthermaleng.2018.08.064>

- Jiaqiang E, Han D, Qiu A, Zhu H, Deng Y, Chen J, Zhao X, Zuo W, Wang H, Chen J, Peng Q (2018b) Orthogonal experimental design of liquid-cooling structure on the cooling effect of a liquid-cooled battery thermal management system. *Appl Therm Eng* 132:508–520. <https://doi.org/10.1016/j.applthermaleng.2017.12.115>
- Khateeb SA, Amiruddin S, Farid M, Selman JR, Al-Hallaj S (2005) Thermal management of Li-ion battery with phase change material for electric scooters: experimental validation. *J Power Sources* 142(1–2):345–353. <https://doi.org/10.1016/j.jpowsour.2004.09.033>
- Kiani M, Ansari M, Arshadi AA, Houshfar E, Ashjaee M (2020) Hybrid thermal management of lithium-ion batteries using nanofluid, metal foam, and phase change material: an integrated numerical–experimental approach. *J Therm Anal Calorim* 141(5):1703–1715. <https://doi.org/10.1007/s10973-020-09403-6>
- Lazrak A, Fourmigué JF, Robin JF (2018) An innovative practical battery thermal management system based on phase change materials: Numerical and experimental investigations. *Appl Therm Eng* 128:20–32. <https://doi.org/10.1016/j.applthermaleng.2017.08.172>
- Li WQ, Qu ZG, He YL, Tao YB (2014) Experimental study of a passive thermal management system for high-powered lithium ion batteries using porous metal foam saturated with phase change materials. *J Power Sources* 255:9–15. <https://doi.org/10.1016/j.jpowsour.2014.01.006>
- Ling Z, Wang F, Fang X, Gao X, Zhang Z (2015) A hybrid thermal management system for lithium ion batteries combining phase change materials with forced-air cooling. *Appl Energy* 148:403–409. <https://doi.org/10.1016/j.apenergy.2015.03.080>
- Ma S, Jiang M, Tao P, Song C, Wu J, Wang J, Deng T, Shang W (2018) Temperature effect and thermal impact in lithium-ion batteries: a review. *Prog Nat Sci: Mater Int* 28(6):653–666. <https://doi.org/10.1016/j.pnsc.2018.11.002>
- Mallow A, Abdelaziz O, Graham S (2018) Thermal charging performance of enhanced phase change material composites for thermal battery design. *Int J Therm Sci* 127(December 2017):19–28. <https://doi.org/10.1016/j.ijthermalsci.2017.12.027>
- Mehrabi-Kermani M, Houshfar E, Ashjaee M (2019) A novel hybrid thermal management for Li-ion batteries using phase change materials embedded in copper foams combined with forced-air convection. *Int J Therm Sci* 141(February):47–61. <https://doi.org/10.1016/j.ijthermalsci.2019.03.026>
- Panchal S, Dincer I, Agelin-Chaab M, Fraser R, Fowler M (2016) Experimental and theoretical investigations of heat generation rates for a water cooled LiFePO<sub>4</sub> battery. *Int J Heat Mass Transf* 101:1093–1102. <https://doi.org/10.1016/j.ijheatmasstransfer.2016.05.126>
- Pesaran A, Nrel GK (2013) Addressing the impact of temperature extremes on large format Li-Ion batteries for vehicle applications (Presentation), NREL (National Renewable Energy Laboratory). 30Th International Battery Seminar
- Qu ZG, Li WQ, Tao WQ (2014) ScienceDirect Numerical model of the passive thermal management system for high-power lithium ion battery by using porous metal foam saturated with phase change material 9. <https://doi.org/10.1016/j.ijhydene.2013.12.136>
- Ranjbaran YS, Haghparast SJ, Shojaeefard MH, Molaeimanesh GR (2020) Numerical evaluation of a thermal management system consisting PCM and porous metal foam for Li-ion batteries. *J Therm Anal Calorim* 141(5):1717–1739. <https://doi.org/10.1007/s10973-019-08989-w>
- Rao Z, Huo Y, Liu X, Zhang G (2015) Experimental investigation of battery thermal management system for electric vehicle based on paraffin/copper foam. *J Energy Inst* 88(3):241–246. <https://doi.org/10.1016/j.joei.2014.09.006>
- Rao Z, Qian Z, Kuang Y, Li Y (2017) Thermal performance of liquid cooling based thermal management system for cylindrical lithium-ion battery module with variable contact surface. *Appl Therm Eng* 123:1514–1522. <https://doi.org/10.1016/j.applthermaleng.2017.06.059>
- Rehman T. ur, Ali HM, Janjua MM, Sajjad U, Yan WM (2019) A critical review on heat transfer augmentation of phase change materials embedded with porous materials/foams. *Int J Heat Mass Transf* 135(May 2020):649–673. <https://doi.org/10.1016/j.ijheatmasstransfer.2019.02.001>

- Saw LH, Ye Y, Yew MC, Chong WT, Yew MK, Ng TC (2017) Computational fluid dynamics simulation on open cell aluminium foams for Li-ion battery cooling system. *Appl Energy* 204:1489–1499. <https://doi.org/10.1016/j.apenergy.2017.04.022>
- Sharma SD, Sagara K (2005) Latent Heat Storage Materials and Systems: A Review. *Int J Green Energy* 2(1):1–56. <https://doi.org/10.1081/ge-200051299>
- Siddique ARM, Mahmud S, Heyst BV (2018) A comprehensive review on a passive (phase change materials) and an active (thermoelectric cooler) battery thermal management system and their limitations. *J Power Sources* 401(August):224–237. <https://doi.org/10.1016/j.jpowsour.2018.08.094>
- Väyrynen A, Salminen J (2012) Lithium ion battery production. *J Chem Thermodyn* 46:80–85. <https://doi.org/10.1016/j.jct.2011.09.005>
- Veismoradi A, Modir A, Ghalambaz M, Chamkha A (2020) A phase change/metal foam heatsink for thermal management of battery packs. *Int J Therm Sci* 157(January):106514. <https://doi.org/10.1016/j.ijthermalsci.2020.106514>
- Vidadi N, Suleymanov E, Bulut C, Mahmudlu C (2017) Transition to renewable energy and sustainable energy development in. *Renew Sustain Energy Rev* 80(April):1153–1161. <https://doi.org/10.1016/j.rser.2017.05.168>
- Voronin DV, Ivanov E, Gushchin P, Fakhruллин R, Vinokurov V (2020) Clay composites for thermal energy storage: A review. *Molecules* 25(7):1–26. <https://doi.org/10.3390/molecules25071504>
- Wang Q, Jiang B, Xue QF, Sun HL, Li B, Zou HM, Yan YY (2014) Experimental investigation on EV battery cooling and heating by heat pipes. *Appl Therm Eng* 88:54–60. <https://doi.org/10.1016/j.applthermaleng.2014.09.083>
- Wang Z, Zhang Z, Jia L, Yang L (2015) Paraffin and paraffin/aluminum foam composite phase change material heat storage experimental study based on thermal management of Li-ion battery. *Appl Therm Eng* 78:428–436. <https://doi.org/10.1016/j.applthermaleng.2015.01.009>
- Wang Z, Li X, Zhang G, Lv Y, He J, Luo J, Yang C, Yang C (2017) Experimental study of a passive thermal management system for three types of battery using copper foam saturated with phase change materials. *RSC Adv* 7(44):27441–27448. <https://doi.org/10.1039/c7ra03963h>
- Wang X, Xie Y, Day R, Wu H, Hu Z, Zhu J, Wen D (2018) Performance analysis of a novel thermal management system with composite phase change material for a lithium-ion battery pack. *Energy* 156:154–168. <https://doi.org/10.1016/j.energy.2018.05.104>
- Wu W, Yang X, Zhang G, Chen K, Wang S (2017) Experimental investigation on the thermal performance of heat pipe-assisted phase change material based battery thermal management system. *Energy Convers Manage* 138(April):486–492. <https://doi.org/10.1016/j.enconman.2017.02.022>
- Zhang Z, Li Y (2017) Experimental study of a passive thermal management system using copper foam-paraffin composite for lithium ion batteries. *Energy Procedia* 142:2403–2408. <https://doi.org/10.1016/j.egypro.2017.12.174>
- Zou D, Liu X, He R, Zhu SX, Bao J, Guo J, Hu Z, Wang B (2019) Preparation of a novel composite phase change material (PCM) and its locally enhanced heat transfer for power battery module. *Energy Convers Manage* 180(November 2018):1196–1202. <https://doi.org/10.1016/j.enconman.2018.11.064>

# Chapter 6

## Performance Enhancement of Thermal Energy Storage Systems Using Nanofluid



Vednath P. Kalbande, Pramod V. Walke, Kishor Rambhad, Man Mohan,  
and Abhishek Sharma

### 6.1 Introduction

Due to upsurge in the energy demand the usage of fossil fuel has increased dramatically. Search of alternative and pollution free energy sources are the prime task of the scientist and researchers. One of the potential substitutes is to store the available energy by thermal energy storage (TES) systems with the help of phase change materials (PCM). There are different forms of energy such as solar, industrial waste heat, heat energy available in IC engine exhaust, etc. are available, and particularly solar which can be stored and used for different applications. Nature has provided sun energy freely and that can be kept with the help of TES systems. In the growth of interest in wind energy, TES system would be a promising technique storing wind energy due to its intermittent nature (Yamaki et al. 2020). Thermal energy storage using PCM to store energy is the essential requirement of the current scenario. The important properties such as thermal conductivity, melting point, heat of fusion etc. are considered for selection of PCM. Phase change material such as Paraffin wax, Erythritol, and Nitrate salt can be used to store thermal energy. So, it is required to explore the performance of TES systems using different types of PCM through the literature in details. The fusion during change of phase from solid to liquid absorbs

---

V. P. Kalbande · P. V. Walke

Department of Mechanical Engineering, G H Raison College of Engineering, Nagpur, India

K. Rambhad

Department of Mechanical Engineering, St. John College of Engineering and Management, Palghar, India

M. Mohan (✉)

Department of Mechanical Engineering, Rungta College of Engineering and Technology, Bhilai, India

e-mail: [man.mohan.soni@rungta.ac.in](mailto:man.mohan.soni@rungta.ac.in)

A. Sharma

Department of Mechanical Engineering, Manipal University Jaipur, Jaipur, India



energy when it solidified. The sensible heat of materials is nearly same about 110 °C temperature so the (PCM) is important for the potential of heat storage. Generally, stearic acid, tin, nitrate salt mixture etc. are promising latent heat storage material. A single material cannot fulfil all the requirement of latent heat storage system. Hence, optimization of the latent heat storage system such as operational range of melting temperature, preferred thermal performance, and cost analysis has been done in recent past (Rathod and Banerjee 2013; Mussard 2013).

Renewable energy in various forms such as solar, wind, energy from biomass, ocean is available generously but few challenges such as efficient conversion technology, its intermittent in nature need to be tackled in appropriate way. In this regard, TES system can be considered one of the possible solutions to store the available energy and use it when required. Best many research investigations have been carried out to enhance the performance of TES system using nanofluid (A solution in which nano-sized particles are dispersed in base fluid) (Jouhara et al. 2020; Ahmed et al. 2017). Thermal conductivity depends upon size and shape of the nanomaterial, base fluid, operating temperature range, and volume fraction etc. (Shima et al. 2009). Different models have also been developed to find the effect of size and surface adsorption of nanomaterial on the thermal conductivity (Wang et al. 2003).

The problem related while using different types of PCM in the latent heat storage system and methods of PCM insertion in the storage was studied and discussed in this chapter. The shell and tube, pipe, and cylinder model for filling PCM, comparison between various PCM and charging and discharging methods of TES systems have also been covered in this chapter. The heat transfer solutions related to PCMs and numerical methods were elaborated in further section (Agyenim et al. 2010). The commonly used PCM can be categorized as solid–liquid, liquid–gas, solid–gas, and solid–solid and is depicted in Fig. 6.1.

Properties enhancement of the Paraffin wax has been carried out with the help of nano-additives for the applications of thermal storage system. The nano-additives are the iron, copper, zinc, and aluminum at the concentrations of 0.5, 1.0, and 1.5 wt.% of each nano-additives. The thermal conductivity of nanocomposite enhanced up to 20.6% and 61.5% by using copper and zinc nano-additives respectively in the Paraffin wax. This nanocomposite was tested for charging and discharging in thermal storage using flat plate solar collector. It was noticed that the capacity of the thermal energy storage has been improved (Owolabi et al. 2016).

A latent heat TES of vertical shell and tube type heat exchanger was used to determine the melting and solidification of the Erythritol as PCM. The heat transfer fluid as air was taken in the system. During the charging increase in mass flow rate and inlet temperature, enhanced the charging of PCM-based thermal storage (Wang et al. 2016). The charging of thermal storage with Erythritol as PCM using parabolic through solar collector was investigated. The  $\text{Al}_2\text{O}_3$ /soybean oil nanofluid was used as heat transfer fluid (Kalbande et al. 2019). To enhance the heat capacity of nitrate salt (mixture of  $\text{KNO}_3$  and  $\text{NaNO}_3$  with 40:60 ratio), the nanoparticles such as  $\text{Al}_2\text{O}_3$  and  $\text{SiO}_2$  with 1.0 wt.% were dispersed at higher temperature i.e. 300 °C in PCM. Specific heat of this type of PCM was enhanced by 52.1% at solid state and 18.6% at liquid state (Chieruzzi et al. 2017).



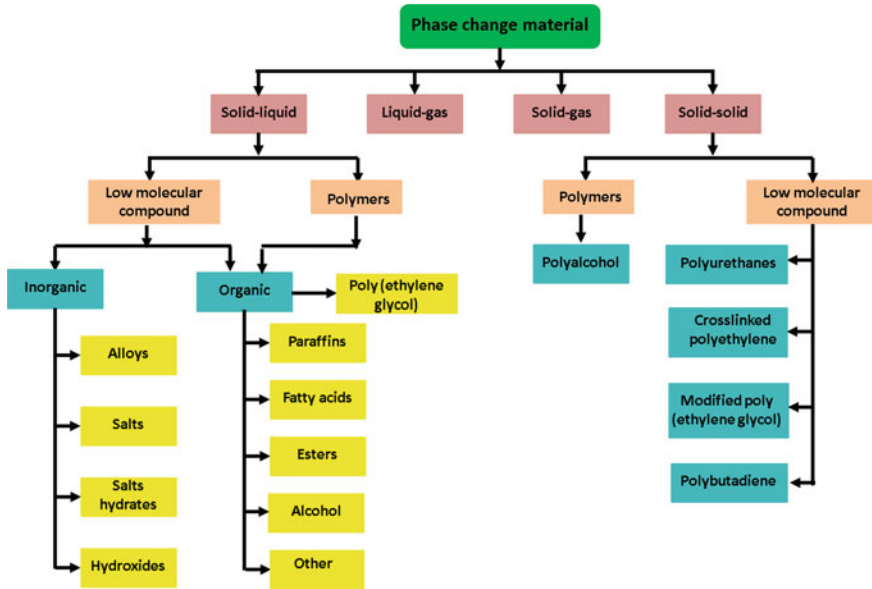


Fig. 6.1 Classification of phase change materials (Pielichowska and Pielichowski 2014; Kancane et al. 2016)

## 6.2 Thermal Energy Storage

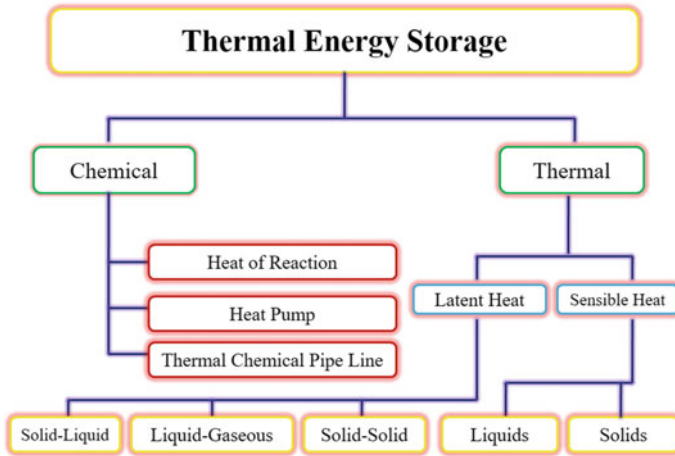
The general types of solar TES are shown in Fig. 6.2. The chemical type of energy storages is heat pump, thermal chemical and due to heat of reaction. The chemical energy depends on the dissociation of the reaction, source of energy, and various thermo-physical properties of the energy storage system. Nowadays the PCM-based thermal storage is used to collect solar energy. Basically, the solar energy thermal storage is divided into following two groups.

1. Sensible heat storage
2. Latent heat storage.

Both the heat storage has its own importance and identification. Latent and sensible heat storage are more dominant energy storage as compared to reaction-based energy storage for storing the solar energy.

### 6.2.1 Sensible Heat Storage

Sensible heat storage depends on to the decreasing or increasing temperature limit of the storage materials. The variables such as volume and pressure do not change during the change in temperature. The sensible heat principle of storing thermal energy is



**Fig. 6.2** Types of different solar energy thermal storage (Frank 1979; Sharma et al. 2009)

very simple and widely used. Charging and discharging of storage is occurred due to change in temperature of the storage materials. Heat capacity of the system also depends on charging and discharging of storage. The operations of charging and discharging are reversible for the number of cycles (Garg and Mullick 1985).

The capacity of heat storage by material due to change in temperature is given by formula:

$$Q = \int_{T_1}^{T_2} m C_p dT \quad (6.1)$$

where,  $Q$  is total capacity of heat storage (J);  $m$  is mass of storage materials (kg);  $C_p$  is specific heat of heat storage material, and  $dT$  is the temperature difference between temperature  $T_1$  and  $T_2$  (K).

## 6.2.2 Latent Heat Storage

Latent heat is the isothermal process system in which the storage gained or released its thermal energy during the process of phase transition. The phase transition of material from solid to liquid (melting) or the liquid to solid (freezing) is the important process for the thermal energy storage system (Lane 1983; Kalaiselvam and Parameshwaran 2014).

The capacity of heat storage by material at given melting point for a range of temperature is given by formula:

$$Q = \int_{T_1}^{T_m} m C_p dT + mh + \int_{T_m}^{T_2} m C_p dT \quad (6.2)$$

where,  $Q$  is total capacity of heat storage (J);  $m$  is mass of storage materials (kg);  $C_p$  is specific heat of heat storage material dependent on temperature, and  $dT$  is the temperature difference between temperature  $T_1$  to  $T_m$  and  $T_m$  to  $T_2$  (K).

The mixture of nitrate salt i.e.  $\text{NaNO}_3$  and  $\text{KNO}_3$  with the molar ratio of 60:40 was studied by mussard (Mussard 2013; Mussard and Nydal 2013a, 2013b) at NTNU for oil-based and aluminum-based thermal storage system.

### 6.3 Nanofluid

The term nanofluid was used by Choi (Choi and Eastman 1995; Lee et al. 1999) who has used nanoparticles to enhance thermal conductivity of base fluid. The nanofluid is basically the nanoparticle suspension in base fluid. The summary of the thermo-physical properties of the word done in past on the use of different nanoparticles with base fluid thermo-physical properties are given in Table 6.1.

A comparative study on the enhancement in thermal performance of TES, with and without addition of nanoparticles in the PCM is presented in Table 6.2.

#### 6.3.1 Preparation of Nanofluid

The nanometers size tiny particles known as nanoparticles uniformly suspended in the fluid, called as nanofluid. One basic fluid is for suspension of nanoparticles is known as base fluid. Nanoparticles or nanotubes are added into base fluid with some proportion (Kasaeian et al. 2015). Nanoparticles are suspended in base fluid for example water, oil, glycol etc. by using magnetic stirring or ultrasonic stirring. Generally, nanoparticles are metallic or non-metallic in nature. The nanoparticles have high value of thermal conductivity which enhances the heat transfer rate through convection when added with base fluid. The applications of nanofluid in heating, cooling systems are due to the enhanced properties of nanofluid (Kasaeian et al. 2015; Lomascolo et al. 2015). The preparation method of nanofluid is described in Fig. 6.3.

#### 6.3.2 Hybrid Nanofluid

The nanofluid is prepared using single nanoparticles and multiple nanoparticles. Single nanoparticles-based nanofluid is termed as mono nanofluid and multiple

**Table 6.1** Thermo-physical properties such as density, thermal conductivity, and specific heat of some base fluid and nanoparticles (Kamyar et al. 2012; Namburu et al. 2007; Collins and Avouris 2000; Kumar et al. 2018; Yuan et al. 2016; Pop et al. 2012; Faizal et al. 2013; Turkyilmazoglu 2015; Jamshed and Aziz 2018; Cárdenas Contreras et al. 2019)

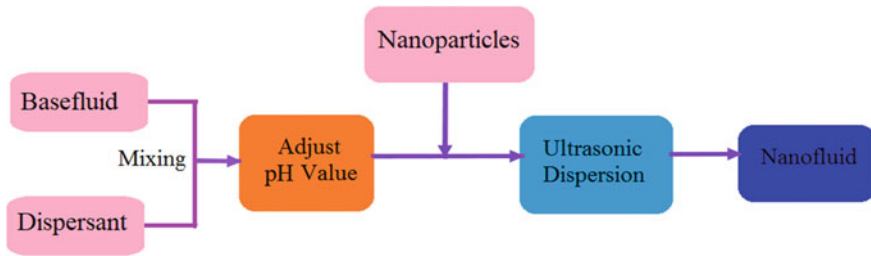
Name of nanoparticles and base fluid/formula	Density (kg/m <sup>3</sup> )	Thermal conductivity (W/m-K)	Specific heat in (kJ/kg K)
Copper Oxide/CuO (Kamyar et al. 2012; Faizal et al. 2013)	5999	34	0.554
Titanium di Oxide/TiO <sub>2</sub>	4229	8.400	0.689
Ferro/Fe <sub>3</sub> O <sub>4</sub> (Jamshed and Aziz 2018)	5181	9.700	0.672
Silver/Ag (Kamyar et al. 2012; Turkyilmazoglu 2015)	10,486	429	0.236
Carbon nanotubes (Collins and Avouris 2000; Yuan et al. 2016)	1351	2999	0.739
Alumina/Al <sub>2</sub> O <sub>3</sub> (Kamyar et al. 2012; Faizal et al. 2013; Kalbande et al. 2021a)	3959	39	0.775
Graphene (Cárdenas Contreras et al. 2019)	2099	4999	0.710
Graphite (Kamyar et al. 2012; Yuan et al. 2016)	2158	122	0.704
Silicon di Oxide/SiO <sub>2</sub> (Namburu et al. 2007; Faizal et al. 2013)	3967	38	0.767
Ethylene Glycol/EG (Jamshed and Aziz 2018)	1113	0.254	2.414
Water (H <sub>2</sub> O) base fluid (Faizal et al. 2013; Turkyilmazoglu 2015)	998	0.602	4.183
Methanol/methyl (Jamshed and Aziz 2018)	795	0.206	2.544

nanoparticles-based nanofluids are termed as hybrid nanofluid. In recent years, it was noticed that hybrid nanofluid enhances the performance of TES system (Kalbande et al. 2021b).

Sidik et al. (2016) a review was discussed for heat transfer applications by using hybrid nanofluid. The hybrid nanofluid was suitable for the higher temperature range of working fluid. The review mainly discussed about the preparation on hybrid nanofluid and, experimental and numerical results by using hybrid nanofluid. It was concluded that the hybrid nanofluid can be a new generation of working fluid but there was requirement to find thermo-physical characteristics such as viscosity, density,

**Table 6.2** Comparative study on the enhancement in thermal performance of TES, with and without addition of nanoparticles in the PCM

Author	PCM	Nanoparticles	Remarks for without nanoparticles	Remarks for with nanoparticles
Owolabi et al. (2016)	Paraffin wax	Al, Cu, Zn, Fe	The energy absorbed factor rate was 0.5908 and efficiency of the system was reported 53.5%	The energy absorbed factor rate was 0.5892 and efficiency of the system was reported 58.5%
Al-Kayiem et al. (2014)	Paraffin wax	Cu	The overall efficiency of the system was 51.1%. Thermal conductivity of PCM was 0.172 W/m °C	The overall efficiency of the system was 52.0%. Thermal conductivity of PCM was 0.226 W/m °C
Prado et al. (2020)	Stearate PCM	MgO and GnPs	The thermal diffusivity was found less as compared to nanocomposite PCM	Results indicated that, when GnPs and MgO were distributed in the PCM, the thermal diffusivity was increased
Avid et al. (2020)	Paraffin wax	MWCNT	Thermal conductivity was less than nano-PCM	The thermal conductivity of the nano-PCM improved by about 30% when the MWCNTs content was increased to its maximum
Elarem et al. (2021)	Pure paraffin wax	Cu	Heat transfer fluid temperature recorded less than to nanocomposite PCM	Optimal heat transfer fluid temperature obtained at 1% mass concentration of nanoparticles
Prabhu et al. (2020)	Paraffin wax	TiO <sub>2</sub> -Ag	Before Thermal cycling process the latent heat storage capacity at melting stage was 124.7 J/g	Before Thermal cycling process the latent heat storage capacity at melting stage was 139.9 J/g



**Fig. 6.3** Preparation of nanofluid (Yang and Du 2017; Kalbande et al. 2020)

thermal conductivity etc. and the physical parameter such as concentration range of hybrid nanoparticles, shape, and size. Zahan et al. (2019) numerically studied the flow of hybrid nanofluid in sinusoidal triangular enclosure with combined convective lid-driven. A wavy bottom surface of sinusoidal is used in triangular enclosure to investigate performance of hybrid nanofluid of Cu and  $\text{Al}_2\text{O}_3$  with water as base fluid. It was noticed that heat transfer enhancement was obtained by using combinations of two or more nanoparticles for nanofluid preparations. The enhancement was achieved in Nusselt number for the hybrid nanofluid as compared to conventional nanofluid.

Dinarvand et al. (2019) have investigated the effect of hybrid nanofluid of  $\text{CuO-TiO}_2/\text{water}$  flow over the static or moving wedge/corner. The thermal performance of the hybrid nanofluid was higher than the base fluid and mono-nanofluid. The cylinder, sphere, and brick shape of nanoparticles were less effective for enhancement in local Nusselt number as compared to platelet shape of  $\text{TiO}_2$  and  $\text{CuO}$  nanoparticles. Dalkilic et al. (2019) studied experimentally the performance of various quad-channel twisted tape inserts in horizontal tube to predict heat transfer analysis of graphite- $\text{SiO}_2/\text{water}$  hybrid nanofluid. As the volume concentration and mass flow rate increased, the Nusselt number also increased. The Re number was in the range of 3400–11,000. The longer tape inserts were preferred for the increasing Reynolds number and pressure drop with higher concentrations.

Shah et al. (2020) studied the various properties of hybrid nanofluid effect on the performance of thermal and heat transfer system. The rheological and thermo-physical characteristics were studied. Those characteristics were nanoparticle concentration, nanoparticle size, base fluid, sonication period, surfactant, pH value, temperature, clustering, and nanoparticles Brownian motion were studied. Author concluded that the higher concentration of nanoparticle results into the higher thermal conductivity of the hybrid nanofluid and hydraulic diameter increases due to the clustering of nanoparticles. Babu et al. (2017) summarized the study on thermo-physical properties, synthesis, heat transfer characteristics, fluid flow characteristics, and hydrodynamic behavior of the hybrid nanofluid which was carried by several researchers. Due to synergistic effect the hybrid nanofluid possesses better rheological properties and thermo-physical properties. Nanoclusters in base fluid result into the increasing relative viscosity of hybrid nanofluid.

From the above discussion it can be understood that hybrid nanofluid can be prepared similar to mono nanofluid. Also, it is seen that hybrid nanofluid enhanced the heat transfer in the thermal system. The research work done in past revealed that hybrid nanofluid is efficient way to boost the performance of TES system. From above literature of hybrid nanofluid says that it is future heat transfer fluid for the heat transfer and thermal systems.

## 6.4 Phase Change Materials

In this section, the research study on Paraffin wax, Erythritol, and Nitrate salt has been studied in detail with properties and their melting point.

### 6.4.1 Paraffin Wax

Paraffin wax as a PCM material is one of the good options for the TES system. Paraffin wax is readily available at lowest cost so it is very useful in the thermal storage system to store energy. The paraffin wax was used in the solar-based TES system to store solar energy. The Paraffin wax was filled in the tube of triple concentric horizontal heat exchanger which is heated from the solar energy through solar collector (Ravi and Rajasekaran 2018). The thermo-physical properties of Paraffin wax are given in Table 6.3. The properties of Paraffin wax can be used for thermal storage.

### 6.4.2 Erythritol ( $C_4H_{10}O_4$ )

Erythritol ( $C_4H_{10}O_4$ ) as a PCM in thermal storage system is another option. Many authors used Erythritol as PCM in solar-based thermal storage. The thermo-physical properties of Erythritol are given in Table 6.3. Charging and discharging of thermal storage using Erythritol as PCM is carried out, thermal storage was based on solar energy (Sharma et al. 2005).

Energy release has been carried out through heat exchanger with direct contact to PCM (Erythritol). A vertical cylinder was used for the heat storage system to energy in PCM. The PCM-based heat storage unit was heated with the help of heat transfer oil through the heater. The effectiveness of 0.83 was achieved at high temperature and at height of cylinder 0.2 m. As the flow rate of heat transfer oil increases, the average volume heat transfer coefficient also increases with decreasing the PCM height (Nomura et al. 2013).

**Table 6.3** Thermo-physical properties of the Paraffin wax, Erythritol (C<sub>4</sub>H<sub>10</sub>O<sub>4</sub>), and Nitrate Salt

S. No.	Properties	paraffin wax	Erythritol (C <sub>4</sub> H <sub>10</sub> O <sub>4</sub> )	Nitrate Salts (KNO <sub>3</sub> and NaNO <sub>3</sub> )
1	Melting point	58–60 °C (Ravi and Rajasekaran 2018)	118 °C (Sharma et al. 2005; Honguntikar and Pawar 2019)	220 °C (Mussard and Nydal 2013a, 2013b; Foong et al. 2011; Okello et al. 2014; Mussard et al. 2013)
2	Heat of fusion	214 kJ/kg (Ravi and Rajasekaran 2018)	339 kJ/kg (Sharma et al. 2005; Honguntikar and Pawar 2019)	108.67 kJ/kg (Foong et al. 2011; Okello et al. 2014)
3	Density	845–925 kg/m <sup>3</sup> (Al-Waeli et al. 2019)	1480 kg/m <sup>3</sup> @ 20 °C and 1300 kg/m <sup>3</sup> @ 140 °C (Sharma et al. 2005; Honguntikar and Pawar 2019)	1800 kg/m <sup>3</sup> @ T ≤ 220 °C and 1700 kg/m <sup>3</sup> @ T ≥ 220 °C (Mussard 2013; Foong et al. 2011; Okello et al. 2014)
4	Heat conductivity	0.24 W/m–K (Ravi and Rajasekaran 2018)	2.64 W/m K @ 20 °C and 1.17 W/m K @ 140 °C (Sharma et al. 2005; Honguntikar and Pawar 2019)	0.8 W/m–K (Foong et al. 2011; Okello et al. 2014)
5	Specific heat	1.85 kJ/kgK (Ravi and Rajasekaran 2018)	1.38 kJ/kg °C @ 20 °C and 2.76 kJ/kg °C @ 140 °C (Sharma et al. 2005; Honguntikar and Pawar 2019)	0.75 kJ/kgK if T < 105 °C 4.1 kJ/kgK if 105 °C ≤ T ≤ 115 °C 1.4 kJ/kgK if 115 °C < T < 215 °C 12 kJ/kgK if 215 °C ≤ T ≤ 225 °C 1.6 kJ/kgK if T > 225 °C (Mussard and Nydal 2013a, 2013b; Foong et al. 2011; Mussard et al. 2013)
6	Viscosity	0.003 Pa-s (Ravi and Rajasekaran 2018)	2.9 × 10 <sup>-2</sup> Pa-s @ 120 °C and 1.6 × 10 <sup>-2</sup> Pa-s @ 140 °C (Nomura et al. 2013)	2.59 × 10 <sup>-3</sup> Pa-s (Tiari and Qiu 2015)



### 6.4.3 Nitrate Salts ( $KNO_3$ and $NaNO_3$ )

The thermal storage system is working at higher temperature than Nitrate Salt as PCM is the best option to store energy. The nitrate salt has melting point in the range of 210–220 °C. So, it can be useful for the higher temperature ranges and to store energy at elevated temperature. The thermo-physical properties of the Nitrate Salt are given in Table 6.3 (Foong et al. 2011; Okello et al. 2014).

Solar energy-based thermal storage using Nitrate Salt of  $KNO_3$  and  $NaNO_3$  mixture in molar ratio of 40:60 as a phase change material has been studied and charging and discharging of thermal storage was carried out. The parabolic trough solar collector was used to transfer solar energy to thermal storage. The PCM cavity was used to fill nitrate salt in thermal storage. The heat transfer fluid was high temperature oil such as Duratherm etc. Two types of thermal storages were used in that study one was Aluminum-based thermal storage and second was oil-based thermal storage. The PCM melting in storage was achieved at higher temperature using solar collector (Mussard and Nydal 2013a, 2013b).

Kamimoto et al. (1980) investigated the use of nitrate salts as phase change materials, among heat storage options latent heat storage is most suitable for applications which require temperature stability as due to high energy storage density it can offer reliable buffer during off peak hours. Another characteristic is constant temperature during charging and discharging which makes latent heat storage better option for both small and large application. But it is not easy to apply it as it has various factors involved. Most important being temperature of phase change. The use of sodium hydroxide, potassium hydroxide, and mixed salts was evaluated in that work. The experimental results indicated that  $NaNO_3$  and other nitrates showed temperature history similar for charging and discharging thus it is suitable to be used in thermal storage.

Zhang et al. (2016) studied numerically and experimentally molten salt in the latent heat storage system for retrieval characteristics analysis. Oil as a heat transfer fluid was chosen to investigate retrieval characteristics of thermal storage. A composite foam of nickel and PCM was developed. The detailed study of solidification/melting was carried out for the behavior of PCM. The pure molten salt was less effective in performance than the pure molten salt as the flow rate of heat transfer fluid increases.

## 6.5 Conclusion

The use of nanoparticle for enhancement of performance of TES systems is one of the promising techniques. In recent past, variety of nanoparticles materials have been used for thermal storage applications. The nanomaterials such as  $Al_2O_3$ , CuO,  $SiO_2$ ,  $TiO_2$ , Fe, Au, Ag, Cu, Graphene, Graphite, CNT, and MWCNT have been used frequently with different base fluid. Also, the use of hybrid nanofluid is one of options for the performance improvement of the TES systems. The previous work done by

researchers suggested that the hybrid nanofluid improves the heat transfer rate which improves the performance of TES systems. The past research work revealed that the Paraffin wax, Erythritol, and Nitrate salt, have the properties which can be used in lower temperature range TES systems. The Erythritol and Nitrate salt is a suitable PCM for the higher temperature ranges thermal storage applications. But Erythritol can be used for only temperature range around 150 °C. For the temperature range of 200–230 °C a Nitrate salt as PCM in thermal storage is better option. So Erythritol and Nitrate salt can be used for the higher heat gain medium.

## References

- Agyenim F, Hewitt N, Eames P, Smyth M (2010) A review of materials, heat transfer and phase change problem formulation for latent heat thermal energy storage systems (LHTESS). *Renew Sustain Energy Rev* 14:615–628. <https://doi.org/10.1016/j.rser.2009.10.015>
- Ahmed SF, Khalid M, Rashmi W, Chan A, Shahbaz K (2017) Recent progress in solar thermal energy storage using nanomaterials. *Renew Sustain Energy Rev* 67:450–460. <https://doi.org/10.1016/j.rser.2016.09.034>
- Al-Kayiem HH, Lin SC (2014) Performance evaluation of a solar water heater integrated with a PCM nanocomposite TES at various inclinations. *Sol Energy* 109:82–92. <https://doi.org/10.1016/j.solener.2014.08.021>
- Al-Waeli AHA, Chaichan MT, Sopian K, Kazem HA, Mahood HB, Khadom AA (2019) Modeling and experimental validation of a PVT system using nanofluid coolant and nano-PCM. *Sol Energy* 177:178–191. <https://doi.org/10.1016/j.solener.2018.11.016>
- Avid A, Jafari SH, Khonakdar HA, Ghaffari M, Krause B, Pötschke P (2020) Surface modification of MWCNT and its influence on properties of paraffin/MWCNT nanocomposites as phase change material. *J Appl Polym Sci* 137:1–10. <https://doi.org/10.1002/app.48428>
- Cárdenas Contreras EM, Oliveira GA, Bandarra Filho EP (2019) Experimental analysis of the thermohydraulic performance of graphene and silver nanofluids in automotive cooling systems. *Int J Heat Mass Transf* 132:375–387. <https://doi.org/10.1016/j.ijheatmasstransfer.2018.12.014>
- Chieruzzi M, Cerritelli GF, Miliozzi A, Kenny JM, Torre L (2017) Heat capacity of nanofluids for solar energy storage produced by dispersing oxide nanoparticles in nitrate salt mixture directly at high temperature. *Sol Energy Mater Sol Cells* 167:60–69. <https://doi.org/10.1016/j.solmat.2017.04.011>
- Choi SUS, Eastman JA (1995) Enhancing thermal conductivity of fluids with nanoparticles. Argonne National Lab., IL (United States)
- Collins PG, Avouris P (2000) Nanotubes for electronics. *Sci Am* 283:62–69
- Dalkılıç AS, Türk OA, Mercan H, Nakkaew S, Wongwises S (2019) An experimental investigation on heat transfer characteristics of graphite-SiO<sub>2</sub>/water hybrid nanofluid flow in horizontal tube with various quad-channel twisted tape inserts. *Int Commun Heat Mass Transf* 107:1–13. <https://doi.org/10.1016/j.icheatmasstransfer.2019.05.013>
- Dinarvand S, Rostami MN, Pop I (2019) A novel hybridity model for TiO<sub>2</sub>-CuO/water hybrid nanofluid flow over a static/moving wedge or corner. *Sci Rep* 9:1–11. <https://doi.org/10.1038/s41598-019-52720-6>
- Elarem R, Alqahtani T, Mellouli S, Aich W, Ben Khedher N, Kolsi L, Jemni A (2021) Numerical study of an evacuated tube solar collector incorporating a Nano-PCM as a latent heat storage system. *Case Stud Therm Eng* 24:100859. <https://doi.org/10.1016/j.csite.2021.100859>
- Faizal M, Saidur R, Mekhilef S, Alim MA (2013) Energy, economic and environmental analysis of metal oxides nanofluid for flat-plate solar collector. *Energy Convers Manag* 76:162–168. <https://doi.org/10.1016/j.enconman.2013.07.038>

- Foong CW, Nydal OJ, Løvseth J (2011) Investigation of a small scale double-reflector solar concentrating system with high temperature heat storage. *Appl Therm Eng* 31:1807–1815. <https://doi.org/10.1016/j.applthermaleng.2011.02.026>
- Frank B (1979) Low temperature thermal energy storage: a state of the art survey. Rep. no. SERI/RR/-54–164. Golden, Color. USA Sol Energy Res Inst
- Garg HP, Mullick SC (1985) B.A.K.: sensible heat storage. In: *Solar thermal energy storage*. In: Springer, Dordrecht, Dordrecht, Holland, pp 82–153
- Honguntikar, P., Pawar, U.: Characterization of Erythritol as a Phase Change Material. In: *International Journal for Science and Advance Research in Technology*, pp. 329–332 (2019).
- Jamshed W, Aziz A (2018) A comparative entropy based analysis of Cu and Fe<sub>3</sub>O<sub>4</sub>/methanol Powell-Eyring nanofluid in solar thermal collectors subjected to thermal radiation, variable thermal conductivity and impact of different nanoparticles shape. *Results Phys*. 9:195–205. <https://doi.org/10.1016/j.rinp.2018.01.063>
- Jouhara H, Żabnieńska-Góra A, Khordehghah N, Ahmad D, Lipinski T (2020) Latent thermal energy storage technologies and applications: A review. *Int J Thermofluids*. 5:100039
- Kalaiselvam S, Parameshwaran R (2014) Thermal energy storage systems design. In: *Thermal energy storage technologies for sustainability*, pp 237–245. <https://doi.org/10.1016/b978-0-12-417291-3.00010-4>
- Kalbande VP, Walke PV, Shelke R (2019) Aluminum-based thermal storage system with solar collector using nanofluid. *Energy Storage*. 1:1–7. <https://doi.org/10.1002/est2.99>
- Kalbande VP, Walke PV, Kriplani CVM (2020) Advancements in thermal energy storage system by applications of nanofluid based solar collector: a review. *Environ Clim Technol* 24:310–340. <https://doi.org/10.2478/rtuect-2020-0018>
- Kalbande VP, Walke PV, Rambhad K (2021) Performance of oil-based thermal storage system with parabolic trough solar collector using Al<sub>2</sub>O<sub>3</sub> and soybean oil nanofluid. *Int J Energy Res* 45:15338–15359. <https://doi.org/10.1002/er.6808>
- Kalbande VP, Walke PV, Rambhad K, Nandanwar Y, Mohan M (2021b) Performance evaluation of energy storage system coupled with flat plate solar collector using hybrid nanofluid of CuO+Al<sub>2</sub>O<sub>3</sub>/water. *J Phys Conf Ser* 1913:12067. <https://doi.org/10.1088/1742-6596/1913/1/012067>
- Kamimoto M, Tanaka T, Tani T, Horigome T (1980) Investigation of nitrate salts for solar latent heat storage. *Sol Energy* 24:581–587. [https://doi.org/10.1016/0038-092X\(80\)90357-6](https://doi.org/10.1016/0038-092X(80)90357-6)
- Kamyar A, Saidur R, Hasanuzzaman M (2012) Application of computational fluid dynamics (CFD) for nanofluids. *Int J Heat Mass Transf* 55:4104–4115. <https://doi.org/10.1016/j.ijheatmasstransfer.2012.03.052>
- Kancane L, Vanaga R, Blumberga A (2016) Modeling of building envelope's thermal properties by applying phase change materials. *Energy Procedia*. 95:175–180. <https://doi.org/10.1016/j.egypro.2016.09.041>
- Kasaiean A, Eshghi AT, Sameti M (2015) A review on the applications of nanofluids in solar energy systems. *Renew Sustain Energy Rev* 43:584–598. <https://doi.org/10.1016/j.rser.2014.11.020>
- Kumar HGP, Xavior MA, Ashwath P (2018) Ultrasonication and microwave processing of aluminum alloy-Graphene-Al<sub>2</sub>O<sub>3</sub> nanocomposite. *Mater Manuf Process* 33:13–18
- Lane GA (1983) *Solar heat storage: background and scientific principles*. CRC Press
- Lee S, Choi SU-S, Li S, Eastman JA (1999) Measuring thermal conductivity of fluids containing oxide nanoparticles. *J Heat Transfer* 121:280. <https://doi.org/10.1115/1.2825978>
- Lomascolo M, Colangelo G, Milanese M, De Risi A (2015) Review of heat transfer in nanofluids: conductive, convective and radiative experimental results. *Renew Sustain Energy Rev* 43:1182–1198. <https://doi.org/10.1016/j.rser.2014.11.086>
- Mussard M, Nydal OJ (2013a) Comparison of oil and aluminum-based heat storage charged with a small-scale solar parabolic trough. *Appl Therm Eng* 58:146–154. <https://doi.org/10.1016/j.applthermaleng.2013.03.059>

- Mussard M, Nydal OJ (2013b) Charging of a heat storage coupled with a low-cost small-scale solar parabolic trough for cooking purposes. *Sol Energy* 95:144–154. <https://doi.org/10.1016/j.solener.2013.06.013>
- Mussard M, Gueno A, Nydal OJ (2013) Experimental study of solar cooking using heat storage in comparison with direct heating. *Sol Energy* 98:375–383. <https://doi.org/10.1016/j.solener.2013.09.015>
- Mussard M (2013) A solar concentrator with heat storage and self-circulating liquid, <http://ntnu.diva-portal.org/smash/record.jsf?pid=diva2:646128&dsid=5423>
- Namburu PK, Kulkarni DP, Dandekar A, Das DK (2007) Experimental investigation of viscosity and specific heat of silicon dioxide nanofluids. *Micro Nano Lett.* 2:67–71
- Nomura T, Tsubota M, Oya T, Okinaka N, Akiyama T (2013) Heat release performance of direct-contact heat exchanger with erythritol as phase change material. *Appl Therm Eng* 61:28–35. <https://doi.org/10.1016/j.applthermaleng.2013.07.024>
- Okello D, Foong CW, Nydal OJ, Banda EJK (2014) An experimental investigation on the combined use of phase change material and rock particles for high temperature (~350 C) heat storage. *Energy Convers Manag* 79:1–8. <https://doi.org/10.1016/j.enconman.2013.11.039>
- Owolabi AL, Al-Kayiem HH, Baheta AT (2016) Nanoadditives induced enhancement of the thermal properties of paraffin-based nanocomposites for thermal energy storage. *Sol Energy* 135:644–653. <https://doi.org/10.1016/j.solener.2016.06.008>
- Pielichowska K, Pielichowski K (2014) Phase change materials for thermal energy storage. *Prog Mater Sci* 65:67–123. <https://doi.org/10.1016/j.pmatsci.2014.03.005>
- Pop E, Varshney V, Roy AK (2012) Thermal properties of graphene: fundamentals and applications. *MRS Bull* 37:1273–1281
- Prabhu B, ValanArasu A (2020) Stability analysis of TiO<sub>2</sub>-Ag nanocomposite particles dispersed paraffin wax as energy storage material for solar thermal systems. *Renew Energy* 152:358–367. <https://doi.org/10.1016/j.renene.2020.01.043>
- Prado JI, Lugo L (2020) Enhancing the thermal performance of a stearate phase change material with graphene nanoplatelets and MgO nanoparticles. *ACS Appl Mater Interfaces* 12:39108–39117. <https://doi.org/10.1021/acsami.0c09643>
- Ranga Babu JA, Kumar KK, Srinivasa Rao S (2017) State-of-art review on hybrid nanofluids. *Renew Sustain Energy Rev* 77:551–565. <https://doi.org/10.1016/j.rser.2017.04.040>
- Rathod MK, Banerjee J (2013) Thermal stability of phase change materials used in latent heat energy storage systems: a review. *Renew Sustain Energy Rev* 18:246–258. <https://doi.org/10.1016/j.rser.2012.10.022>
- Ravi R, Rajasekaran K (2018) Experimental study of solidification of paraffin wax in solar based triple concentric tube thermal energy storage system. *Therm Sci* 22:973–978. <https://doi.org/10.2298/TSCI160311021R>
- Shah TR, Koten H, Ali HM (2020) Chapter 5—performance effecting parameters of hybrid nanofluids. Presented at the. <https://doi.org/10.1016/B978-0-12-819280-1.00005-7>
- Sharma SD, Iwata T, Kitano H, Sagara K (2005) Thermal performance of a solar cooker based on an evacuated tube solar collector with a PCM storage unit. *Sol Energy* 78:416–426. <https://doi.org/10.1016/j.solener.2004.08.001>
- Sharma A, Tyagi VV, Chen CR, Buddhi D (2009) Review on thermal energy storage with phase change materials and applications. *Renew Sustain Energy Rev* 13:318–345. <https://doi.org/10.1016/j.rser.2007.10.005>
- Shima PD, Philip J, Raj B (2009) Role of microconvection induced by Brownian motion of nanoparticles in the enhanced thermal conductivity of stable nanofluids. *Appl Phys Lett* 94:223101
- Sidik NAC, Adamu IM, Jamil MM, Kefayati GHR, Mamat R, Najafi G (2016) Recent progress on hybrid nanofluids in heat transfer applications: a comprehensive review. *Int Commun Heat Mass Transf* 78:68–79. <https://doi.org/10.1016/j.icheatmasstransfer.2016.08.019>
- Tiari S, Qiu S (2015) Three-dimensional simulation of high temperature latent heat thermal energy storage system assisted by finned heat pipes. *Energy Convers Manag* 105:260–271. <https://doi.org/10.1016/j.enconman.2015.08.004>

- Turkyilmazoglu M (2015) Anomalous heat transfer enhancement by slip due to nanofluids in circular concentric pipes. *Int J Heat Mass Transf* 85:609–614. <https://doi.org/10.1016/j.ijheatmasstransfer.2015.02.015>
- Wang B-X, Zhou L-P, Peng X-F (2003) A fractal model for predicting the effective thermal conductivity of liquid with suspension of nanoparticles. *Int J Heat Mass Transf* 46:2665–2672
- Wang Y, Wang L, Xie N, Lin X, Chen H (2016) Experimental study on the melting and solidification behavior of erythritol in a vertical shell-and-tube latent heat thermal storage unit. *Int J Heat Mass Transf* 99:770–781. <https://doi.org/10.1016/j.ijheatmasstransfer.2016.03.125>
- Yamaki A, Kanematsu Y, Kikuchi Y (2020) Lifecycle greenhouse gas emissions of thermal energy storage implemented in a paper mill for wind energy utilization. *Energy* 205:118056
- Yang L, Du K (2017) A comprehensive review on heat transfer characteristics of TiO<sub>2</sub> nanofluids. *Int J Heat Mass Transf* 108:11–31. <https://doi.org/10.1016/j.ijheatmasstransfer.2016.11.086>
- Yuan W, Zhang Y, Cheng L, Wu H, Zheng L, Zhao D (2016) The applications of carbon nanotubes and graphene in advanced rechargeable lithium batteries. *J Mater Chem A* 4:8932–8951
- Zahan I, Nasrin R, Alim MA (2019) Hybrid nanofluid flow in combined convective lid-driven sinusoidal triangular enclosure. *AIP Conf Proc* 2121:1–9. <https://doi.org/10.1063/1.5115908>
- Zhang P, Ma F, Xiao X (2016) Thermal energy storage and retrieval characteristics of a molten-salt latent heat thermal energy storage system. *Appl Energy* 173:255–271. <https://doi.org/10.1016/j.apenergy.2016.04.012>

# Chapter 7

## Inoculum Ratio Optimization in Anaerobic Digestion of Food Waste for Methane Gas Production



Parag K. Talukdar, Varsha Karnani, and Palash Saikia

### *Nomenclatures*

<i>AC</i>	Ash Content
<i>AD</i>	Anaerobic Digestion
<i>BMP</i>	Biochemical Methane Potential
<i>CD</i>	Cow Dung
<i>CV</i>	Calorific Value
<i>F/M</i>	Food to Microorganisms ratio
<i>FW</i>	Food Waste
<i>MC</i>	Moisture Content
<i>TS</i>	Total Solid
<i>VFA</i>	Volatile Fatty Acid
<i>VS</i>	Volatile Solid

### 7.1 Introduction

According to the Food and Agricultural Organization (FAO) of United Nations, the food waste (FW) is any healthy or edible substance, such as fresh vegetables, fruit, fish, meat, bakery and dairy products, etc., which is wasted, lost, or degraded at every stage of the food supply chain (Yang et al. 2018; Pecar et al. 2020; Chen et al. 2017). Out of the total food produced in the world, around one-third (amounting to 1.3 billion tonnes) gets wasted every year. This accounts for nearly US\$ 680 billion in industrialized countries and US\$ 310 billion in developing countries (Barua et al.

---

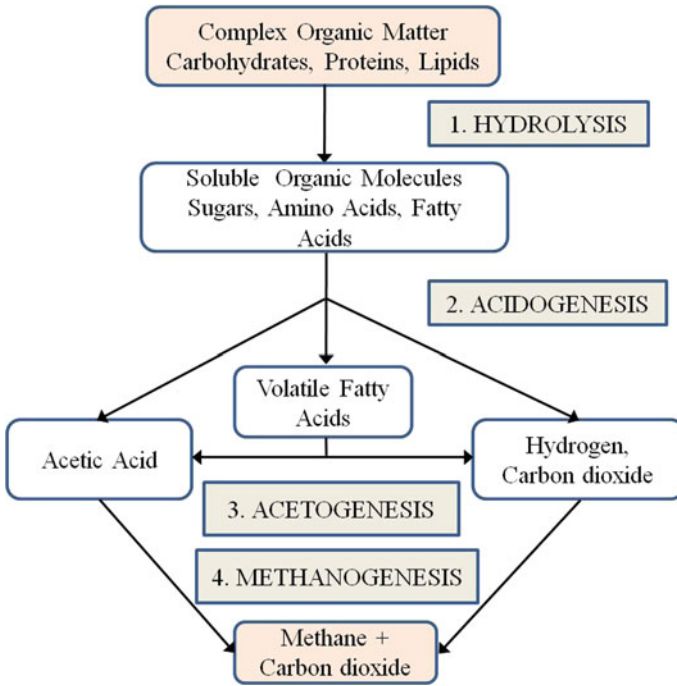
P. K. Talukdar (✉) · V. Karnani · P. Saikia  
Department of Mechanical Engineering, Jorhat Engineering College, Jorhat, Assam 785007, India  
e-mail: [t.parag@alumni.iitg.ac.in](mailto:t.parag@alumni.iitg.ac.in)

2018; FAO 2011). Most of the generated is either directly dumped in landfills or used as feedstock in animal husbandries; but these practices have created serious environmental and health issues (Mir et al. 2016).

The physiochemical characteristics of FW are affected by its composition. For instance, the FW comprising of rice, pasta and vegetables is enriched with carbohydrates, while the FW consisting of meat, fish and eggs has abundant amount of proteins (Pecar et al. 2020). But in general, FW can be considered to have moisture content (MC) of around 74–90%, volatile solids (VS) of around  $85 \pm 5\%$ , and mean pH of around  $5.1 \pm 0.7$  (Pecar et al. 2020; Fisgativa et al. 2016; Zhang et al. 2007). The high MC and perishable nature of FW makes the treatment by traditional methods (incineration, pyrolysis and composting) to be less effective (Li et al. 2018; Zhao et al. 2019). However, AD involves multiphase and multistage chains of complex biological process and produces biogas from organic waste (Zhao et al. 2019; Ren et al. 2018; Xu et al. 2018). It has emerged as a promising technique where FW can be used to produce large amount of energy.

Of late, India has emerged as world's second largest LPG importer after China and the demand for LPG is projected to rise 34% from 2014 to 2025. LPG is used by 59% of Indian houses for their cooking needs (Apte et al. 2013). However, the importance of non-conventional energy resources is slowly increasing because of sharp rise in energy demand and depletion of conventional resources of the country at a large scale. Further, replacing even 20% of LPG by biogas produced from FW as feedstock can result in significant saving of foreign exchange, thereby upgrading the economy of the nation (Desai and Jadhav 2016). Biogas is a clean renewable energy resource that can be obtained through biological degradation of organic waste during AD process (Mir et al. 2016; Appels et al. 2011). The biogas obtained through this process mostly contains 60–75% of methane and 20–40% of carbon dioxide as well as traces of other gases. Further, the several operating parameters such as solid concentration, temperature, pH, and retention period influence the typical gas yield during AD.

The AD is a biological process that produces biogas by degrading and stabilizing complex organic matter in an anaerobic environment with the help of a consortium of microbes (Akyol 2020). According to various studies, AD proceeds through four steps: hydrolysis, acidogenesis, acetogenesis and methanogenesis as shown in Fig. 7.1 (Senthilkumar et al. 2016; Deepanraj et al. 2015; Achinas and Euverink 2019). During hydrolysis, conversion of complex organic molecules (proteins, polysaccharides and fat) into simpler ones (peptides, saccharides and fatty acids) occurs with the help of exoenzymes (cellulose, protease, lipase) produced by hydrolytic and fermentative bacteria. In acidogenesis, the products of hydrolysis are broken down into smaller molecules of low molecular weight (organic acid alcohols, carbon dioxide, hydrogen and ammonium), which are then converted into acetic acid, hydrogen and carbon dioxide by acetate bacteria. The products of the acetogenesis are converted into methane gas in the final step by two groups of microbes—acetoclastic methanogens. It converts the acetate into carbon dioxide, methane and hydrogen-utilizing methanogens, which reduces the hydrogen and carbon dioxide into methane (Mir et al. 2016).



**Fig. 7.1** Anaerobic degradation process (Bouallagui et al. 2005; Madigan et al. 1997; Ray et al. 2013)

It is critical to have prior understanding of the methane potential of the feedstock for any digestion facility to work properly in the long run (Deepanraj et al. 2015; Koch and Drewes 2014; Koch et al. 2017). The Biochemical Methane Potential (BMP) test was developed by Owen et al. (Owen et al. 1979), and is an important tool for the study of potential of methane generation from different wastes as this test determines the maximum quantity of methane that can be produced from a substrate (Elbeshbishy et al. 2012; Owens and Chynoweth 1993; Wang and Barlaz 2016; Krause et al. 2018). Castellón-Zelaya et al. (Castellón-Zelaya and González-Martínez 2021) studied the effects of solids concentration and substrate to inoculum ratio on production of methane from organic municipal solid waste. The methane production from fermented organic fraction of municipal solid waste was found to be increased by 32% when compared to fresh organic fraction of municipal solid waste. Furthermore, the substrate to inoculum ratio for optimum production of methane from the fermented organic part of municipal solid waste was reported to be 1.0.



**Fig. 7.2** Unmanaged landfill site at Garmur, Jorhat, Assam, India (26.7498° N, 94.2353° E)



### **7.1.1 Motivation**

Figure 7.2 shows the scenario of the unmanaged landfill site at Garmur, Jorhat, Assam, India. The waste generated in the town is dumped directly into this landfill and burnt, situated alongside Tocklai rivulet which falls in the Bhogdoi river, Assam without any treatment process, like incineration or composting. The condition is deplorable with stray animals, foul odors, and flies, thereby raising serious concerns among the residents. Also, there is a municipality water supplier plant nearby. As a result, these wastes have the potential to damage all of the living environment's essential components: air, land and water. The Jorhat Municipal Board (JMB) operates and handles waste from 19 wards in the town, which spreads across 9.25 km<sup>2</sup>. The total waste generated per day in the town is around 60 tonnes, which is picked up every day from 121 collection points located across the town. FW makes up a large component of the municipal solid waste organic fraction, which can be easily separated at the source (residences, restaurants, school canteens, etc.) and treated anaerobically to produce energy-rich biogas. This will not only help in managing food waste efficiently, but will also provide an alternative source of energy to meet the increasing energy requirements coupled with rapidly depleting coal and petroleum resources.

### **7.1.2 Present Objective**

Considering the energy deficit and waste management problem in Jorhat, Assam, an attempt has been made to determine the potential of kitchen waste to produce biogas through AD. The present study aims to optimize the F/M ratio in order to obtain maximum methane gas, during AD of FW using cow dung as inoculum. This kind of investigation is unique because no such study has been reported for Jorhat,

Assam, India. For this, initial characterization of the kitchen waste and inoculum (cow dung) has been done to evaluate the MC, volatile matter content, ash content, fixed carbon content and calorific value. Further, BMP test is conducted on different Food to Microorganisms ratios (F/M) viz. 1:1, 1.5:1, 2:1 and 2.5:1 to identify the optimum F/M ratio for maximum production of methane using cow dung (CD) as inoculum.

## 7.2 Materials and Methods

### 7.2.1 Initial Characterization of Substrate and Inoculum

In the present study, FW is used as the substrate and fresh cow dung is used as the inoculum. Cow dung is found to be the best inoculum, as reported by Dhamodharan et al. (2015). The FW was collected from hostels of Jorhat Engineering College, Jorhat, Assam, India as shown in Fig. 7.3, while fresh cow dung is sourced from a nearby goshala in Jorhat, Assam, India. The FW used mainly consists of cooked rice, vegetables, chapattis and uncooked vegetable peels. The waste is mixed thoroughly and grinded in a mixer grinder. The homogenously mixed samples of substrate and inoculum is then evaluated for determination of basic characteristics, viz. Moisture content (MC), Total solids (TS), Volatile solid (VS), Ash content (AC), Fixed carbon content (FC) and pH. The hot air oven and furnace for initial characterization are shown in Fig. 7.4. APHA (APHA 2005) standards were used to measure MC, TS and VS. AC is measured using standard procedure as per ASTM D 2974–87 (ASTM D 2974–87 1993). The pH meter is used to determine the pH of the samples.



(a) FW before grinding;



(b) Homogenously mixed FW after grinding

**Fig. 7.3** Food waste (FW)



(a) Hot air oven (for moisture determination) (b) Furnace (for VS and AC determination)

**Fig. 7.4** Hot air oven and furnace for initial characterization

## 7.2.2 Data Measurement

### 7.2.2.1 Moisture Content (MC) and Total Solid (TS)

At first a known weight of the sample was dried in hot air oven at  $105 \pm 5^\circ\text{C}$  for 24 h. The weight of the oven dried sample is measured.

$$\%TS = \frac{\text{weight of the sample after drying at } 105 \pm 5^\circ\text{C}}{\text{weight of the sample taken}} \times 100 \quad (7.1)$$

$$\%MC = \frac{\text{loss in weight of the sample}}{\text{weight of the sample taken}} \times 100 \quad (7.2)$$

### 7.2.2.2 Volatile Solid (VS)

The oven dried sample was then covered with a lid and heated in a furnace at  $550 \pm 10^\circ\text{C}$  for around 2 h.

$$\%VS = \frac{\text{loss in weight of the oven dried sample at } 550 \pm 10^\circ\text{C}}{\text{weight of the oven dried sample}} \times 100 \quad (7.3)$$

### 7.2.2.3 Ash Content (AC)

Oven dried sample is uncovered and heated in a furnace at  $440 \pm 10^\circ\text{C}$  until the specimen is completely ashed.

$$\%AC = \frac{\text{weight of the residue left in the crucible}}{\text{weight of the oven dried sample}} \times 100 \quad (7.4)$$

#### 7.2.2.4 Fixed Carbon (FC)

$$\%FC = 100 - (\% \text{Moisture} + \% \text{Volatile Content} + \% \text{Ash}) \quad (7.5)$$

### 7.2.3 BMP Test Setup

The methodology employed for carrying out the BMP test is followed as described by Owen et al. (Owen et al. 1979). The overall testing has been conducted for 35 days, using four different F/M ratios (VS basis), namely 1:1, 1.5:1, 2:1, 2.5:1 and a control (cow dung only). On the basis of VS content, the different quantities of FW and cow dung to be mixed to get the required F/M ratios is as shown in Table 7.1. The accurately weighed samples were put in 1000 mL reagent bottles. The level of all the batch reactors was maintained  $600 \pm 10$  mL by adding distilled water. To maintain the anaerobic state, nitrogen gas was purged into the reactor bottles. The bottles were made air-tight using rubber corks, and then connected to aspirator bottles as shown in Fig. 7.5. To measure the amount of biogas production water displacement method has been used. In place of water, the aspirator bottles are filled with 1.5 N NaOH solution, so that the  $\text{CO}_2$  produced reacts with NaOH to form sodium carbonate ( $\text{Na}_2\text{CO}_3$ ), and thus can be separated from methane gas (Saha et al. 2018; Walker et al. 2009). Thus, the amount of solution displaced in the aspirator bottles indicates the volume of methane gas produced. At different stages of anaerobic digestion, the pH value varies because of change in concentrations of volatile fatty acids (VFA), bicarbonates, alkalinity and  $\text{CO}_2$  (Mir et al. 2016). With increase in the amount of VFA produced, the pH drops and below a  $\text{pH} = 6.0$ , the methane production is significantly inhibited. During this study,  $\text{NaHCO}_3$  has been added to keep the pH value in the range of 6.5–7.5 (Owen et al. 1979; Saha et al. 2018; Singh et al. 2017).

**Table 7.1** Various amount of FW and CD to be used for different F/M ratio based on VS

F/M ratio	FW (g)	CD (g)
Control	–	50
1.0	53.09	50
1.5	79.63	50
2.0	106.17	50
2.5	132.72	50

**Fig. 7.5** BMP test setup

### ***7.2.4 Analysis of Different Parameters***

The volume of methane production has been measured on daily basis using water displacement method. In place of water, 1.5 N NaOH was used to separate CO<sub>2</sub> from methane. When the biogas generated passed from the reagent bottles into the aspirator bottles containing NaOH, the CO<sub>2</sub> reacted with NaOH, and the pressure of the methane gas displaced the NaOH solution out of the aspirator bottles. The volume of NaOH displaced has been measured by using a measuring cylinder and this indicated the amount of methane gas produced (Saha et al. 2018). The MC, TS, VS are examined weekly according to the method described in APHA (APHA 2005) standards. At first, a known weight of the sample is dried in hot air oven at 105 ± 5 °C for 24 h. The weight of the oven dried sample expressed as a percentage of the original weight is the TS. The loss in weight due to drying in hot air oven is expressed as a percentage of the original weight is the MC. The oven dried sample is then covered with a lid and heated in a furnace at 550 ± 10 °C for around 2 h. The loss in weight is expressed as a percentage of the weight of the oven dried sample indicated the VS. The room temperature is measured on daily basis using a thermometer.

## **7.3 Results and Discussion**

### ***7.3.1 Characterization of Food Waste and Inoculum (Cow Dung)***

The characterization of FW and inoculum (cow dung) is enumerated in Table 7.1 and 7.2, respectively and the results obtained in the present study are compared with the results reported by Zhang et al. (Zhang et al. 2007) (for FW) and Saha et al. (Saha

**Table 7.2** Characterization of FW

Parameter	Unit	Present study	Results obtained by Zhang et al. (2007)
MC	% (w.b.)	71.1	69.1
TS	% (w.b.)	29.9	30.9
VS	% (w.b.)	20.65	26.4
VS/TS ratio	%	69.1	85.3
AC	% (w.b.)	6.91	–
FC	% (w.b.)	1.34	–
pH	–	6.02	–

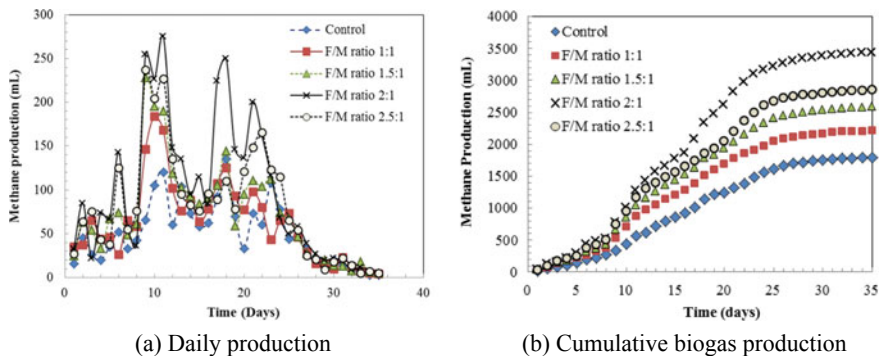
**Table 7.3** Characterization of CD

Parameter	Unit	Present study	Results obtained by Saha et al. (2018)
MC	% (w.b.)	78.74%	80 ± 2.0
TS	% (w.b.)	21.26%	18.98 ± 0.2
VS	% (w.b.)	15.90	82 ± 0.4
	% (d.b.)	75.86	
VS / TS	%	74.8	–
AC	% (w.b.)	3.24%	–
FC	% (w.b.)	2.12%	–
pH	–	7.11	7.13

et al. 2018) (for cow dung). The MC, TS, VS, AC, FC, VS/TS ratio, and pH of the FW and inoculum (cow dung) are listed in the Table 7.2 and 7.3, respectively. The MC of FW is found to be high (around 71.1%) which makes it a potential feedstock for AD. The VS/TS percentage of both FW and cow dung is high, indicating that their consumable organic fraction is high, thereby producing more energy (Dhamodharan et al. 2015). The pH value of the FW is obtained to be slightly acidic (pH = 6.02) while the pH value of cow dung is 7.11.

### 7.3.2 Biogas / Methane Production

In AD, the most vital parameter to be optimized is the quantity of methane gas production, which depends on various factors like inoculum source and quantity, TS, VS, VFA and temperature etc. (Dhamodharan et al. 2015). In the present study, the BMP test of different F/M ratios (g VS FW/g VS CD), namely 1:1, 1.5:1, 2:1, 2.5:1 and a control (only CD) is done, to determine the optimum F/M ratio, corresponding to the maximum production of methane gas. The daily methane production and the cumulative methane production from each of the ratios have been plotted in Fig. 7.6. The experimental observation showed that for AD of FW with cow dung



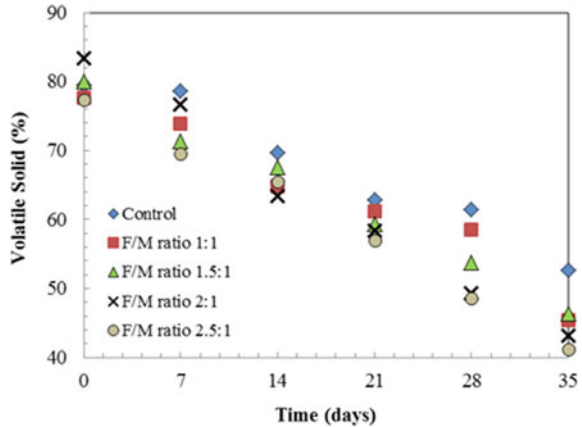
**Fig. 7.6** Biogas production

as inoculum, the F/M ratio of 2:1 yielded the maximum amount of methane, with ratios 2.5:1 and 1.5:1 following it. At F/M = 2:1, the total methane yield is 3428 mL for a period of 35 days, while for F/M = 2.5:1 and 1.5:1, the methane yields are 2850 mL and 2582 mL, respectively. Further, F/M = 1:1, the cumulative methane yield is 2210.5 mL and in the control, it was around 1789 mL. From the methane production trend, it can be observed that as the F/M is increased from 1 to 2, the methane production also increased. After F/M = 2:1, the methane production started decreasing. Thus, the optimum order of F/M ratios with respect to methane gas production from AD of FW is 2:1 > 2.5:1 > 1.5:1 > 1:1.

### 7.3.3 Volatile Solids

From Fig. 7.7, it can be observed that for all F/M ratios, VS follows a decreasing pattern over time. These decreasing trends of VS indicate the decreasing mass, which can be correlated to biogas production. The inoculum activity and its adaptability toward the substrate influence the VS reduction. Therefore, in order to improve the microbial activity, it is necessary to maintain a balanced combination between inoculum and substrate (Dhamodharan et al. 2015). In the present BMP test, at F/M ratio of 2:1, a maximum of 40% VS reduction is observed. At F/M ratios of 2.5 and 1.5, the VS reduction of 36.15% and 33.36% respectively is observed. Further, the F/M = 1:1 is having a VS reduction of 32.32%, followed by control having 26.81%. This order of VS reduction (2:1 > 2.5:1 > 1.5:1 > 1:1) is found to be in order with the cumulative methane production.

**Fig. 7.7** Volatile solids (%) at different F/M ratio



### 7.3.4 Variation of Room Temperature Outside the Digester

The operating temperature has a vital role for sustaining the microorganisms of AD. The microorganisms that are taking part in AD process can be classified into three categories (Singh et al. 2017):

- Cryophiles (Psychrophiles), occupying the area of cryophilic digestive regime (operating temperature range 12–24 °C).
- Mesophiles, occupying the area of mesophilic digestive regime (operating temperature range 22–40 °C).
- Thermophiles, occupying the area of thermophilic digestive regime (operating temperature range 50–60 °C).

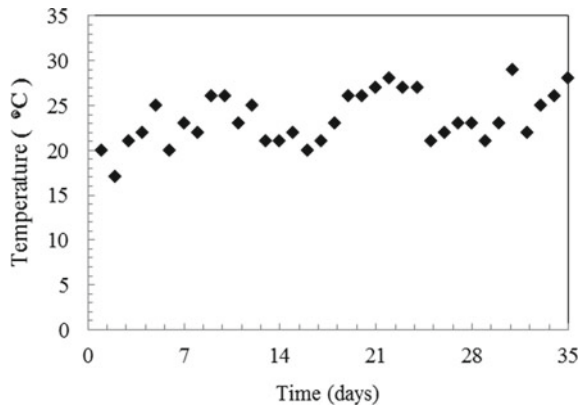
Figure 7.8 depicts the variation of room temperature outside the digesters during the test period of 35 days. As the BMP test is performed during the month of March, the operating temperature was on a lower side. The temperature fluctuated in between 17 °C and 29 °C, which lies in between cryophilic and mesophilic conditions. As the thermophilic condition has high conversion rate and biogas productivity, so higher methane yield can be expected during summer when temperature is higher.

## 7.4 Conclusions

Pollution is caused by wastes, and the form and extent of pollution is determined by the nature of the wastes. It also aids in the selection of the required management application, engineering design, and technology. Furthermore, the composition of waste is influenced by community's socioeconomic status, living style, composition pattern and cultural behavior. Here, an effort has been made to tackle the increasing problem of waste management in Jorhat, Assam, India. The production of biogas



**Fig. 7.8** Variation of daily ambient temperature



from AD of FW has been investigated using cow dung as inoculum. To check the potential of FW to be used as substrate for AD process, initial characterization of FW has been done. Along with this, characterization of inoculum (CD) is also performed. The moisture content and volatile solid content of FW is found to be high and thus suitable for biological degradation. On the basis of VS of the substrate and inoculum, four F/M ratios varying from 1.0 to 2.5 are chosen, and BMP test have been carried out for these ratios for five weeks. The daily methane production, cumulative methane production, and weekly VS degradation are discussed.

From the experiments, the F/M ratio of 2:1 has been found to be most suitable for AD of FW with cow dung. At this F/M ratio a volume of 3428 mL methane gas has been produced at duration of 35 days. Thus, with around 60 tonnes/day of waste material, the Jorhat town has a good potential of biogas generation. It can be used in cooking, biogas-based small-scale electricity generation system. For F/M ratios lower and higher than 2:1, the methane yield is observed to be decreased. As the temperature during the study was fluctuating in between 17 °C and 29 °C (in between cryophilic and mesophilic conditions), therefore, the biogas yield was found to be slightly low. Future studies can be performed taking F/M ratio of 2:1 as optimum, by maintaining high temperature bath, so as to observe the enhanced methane production at high temperature. In addition, the effect of pre-treatment of the FW on biogas production can be analyzed. Based on the composition of the biogas produced, future study may be pursued on purification of the FW so as to remove the impurities and increase the methane percentage and thus, obtain higher calorific value of the gas. The co-digestion of the FW with other potential feed stocks can also be studied.

**Acknowledgements** The authors wish to thank CSIR-North East Institute of Science and Technology for providing some technical support.

## References

- Achinas S, Euverink GJW (2019) Effect of combined inoculation on biogas production from hardly degradable material. *Energies* 12(217):1–13
- Akyol C (2020) In search of the optimal inoculum to substrate ratio during anaerobic co-digestion of spent coffee grounds and cow manure. *Waste Manage Res* 00:1–6
- APHA (2005) Methods for the examination of water and wastewater, twentieth ed., American Public Health Association, American Water Works Association, and Water Environment Federation, Washington DC, USA
- Appels L, Assche AV, Willems K, Degreve J, Impe JZ, Dewil R (2011) Peracetic acid oxidation as an alternative pre-treatment for the anaerobic digestion of waste activated sludge. *Biores Technol* 102:4124–4130
- Apte A, Cheernam V, Kamat M, Kamat S, Kashikar P and Jeswani H (2013) Potential of using kitchen waste in a biogas plant. *Int J Environ Sci Develop* 4(4)
- ASTM D 2974–87 (1993) Standard test methods for moisture, ash, and organic matter of peat and other organic soils. *Am Soc Test Mater* 31–33.
- Barua VS, Rathore V, Kalamdhad AS (2018) Comparative evaluation of anaerobic co-digestion of water hyacinth and cooked food waste with and without pre-treatment. *Bioresource Technol Rep* 4:202–208
- Bouallagui H, Touhami Y, Cheikh RB, Hamdi M (2005) Bioreactor performance in anaerobic digestion of fruit and vegetable wastes. *Process Biochem* 40:989–995
- Castellón-Zelaya MF, González-Martínez S (2021) Effects of solids concentration and substrate to inoculum ratio on methane production from fermented organic municipal solid waste. *Multi J Waste Resour Residues* 15:3–12
- Chen H, Jiang W, Yang Y, Man X (2017) State of the art on food waste research: a bibliometrics study from 1997 to 2014. *J Clean Prod* 140:840–846
- Deepanraj B, Sivasubramanian V, Jayaraj S (2015) Experimental and kinetic study on anaerobic digestion of food waste: The effect of total solids and pH. *J Renew Sustain Energy* 7:063104
- Desai SS, Jadhav VN (2016) Design of small scale anaerobic digester using kitchen waste in rural development countries. *Res J Chem Environ Life Sci* 4(4S):129–133
- Dhamodharan K, Kumar V, Kalamdhad AS (2015) Effect of different livestock dungs as inoculum on food waste anaerobic digestion and its kinetics. *Biores Technol* 180:237–241
- Elbeshbishy E, Nakhla G, Hafez H (2012) Biochemical methane potential (BMP) of food waste and primary sludge: influence of inoculum pre-incubation and inoculum source. *Biores Technol* 110:18–25
- FAO (2011) Swedish Institute for Food and Biotechnology, Global Food Losses and Food Waste Study Conducted for the International Congress
- Fisgativa H, Tremier A, Dabert P (2016) Characterizing the variability of food waste quality: a need for efficient valorization through anaerobic digestion. *Waste Manage* 50:264–274
- Koch K, Drewes JE (2014) Alternative approach to estimate the hydrolysis rate constant of particulate material from batch data. *Appl Energy* 120:11–15
- Koch K, Lippert T, Drewes JE (2017) The role of inoculum's origin on the methane yield of different substrates in biochemical methane potential (BMP) tests. *Biores Technol* 243:457–463
- Krause MJ, Chickering GW, Townsend TG, Pullammanappallil P (2018) Effects of temperature and particle size on the biochemical methane potential of municipal solid waste components. *Waste Manage* 71:25–30
- Li L, Peng X, Wang X, Wu D (2018) Anaerobic digestion of food waste: a review focusing on process stability. *Biores Technol* 248:20–28
- Madigan M, Martin KJ, Porter J (1997) Brock biology of microorganisms Upper Saddle River, 1st edn. Pearson Prentice Hall publisher, NJ
- Mir MA, Hussain A, Verma C (2016) Design considerations and operational performance of anaerobic digester: a review. *Cogent Eng* 3:1181696

- Owen WF, Stuckey DC, Healy JB, Young LY, McCarty PL (1979) Bioassay for monitoring biochemical methane potential and anaerobic toxicity. *Water Res* 13:485–492
- Owens J, Chynoweth DP (1993) Biochemical methane potential of municipal solid waste (MSW) components. *Water Sci Technol* 27:1–14
- Pecar D, Smerkolj J, Pohleven F, Gorsek A (2020) Anaerobic digestion of chicken manure with sawdust and barley straw pre-treated by fungi. *Biomass Convers Biorefinery*. <https://doi.org/10.1007/s13399-019-00583-2>
- Ray NHS, Mohanty MK and Mohanty RC (2013) Anaerobic digestion of kitchen waste: Biogas production and pre-treatment waste, a review. *Int J Sci Res Publ* 3(11)
- Ren Y, Yu M, Wu C, Wang Q, Gao M, Huang Q, Liu Y (2018) A comprehensive review on food waste anaerobic digestion: research updates and tendencies. *Biores Technol* 247:1069–1076
- Saha B, Sathyan A, Mazumder P, Choudhury SP, Kalamdhad AS, Khwairakpam M, Mishra U (2018) Biochemical Methane Potential Test for *Ageratum conyzoides* to optimize ideal F/M ratio. *J Environ Chem Eng* 6(4):5135–5140
- Senthilkumar N, Deepanraj B, Vasantharaj K, Sivasubramanian V (2016) Optimization and performance analysis of process parameters during anaerobic digestion of food waste using hybrid GRA-PCA technique. *J Renew Sustain Energy* 8:1–11
- Singh G, Jain VK, Singh A (2017) Effect of temperature and other factors on anaerobic digestion process, responsible for bio gas production. *Int J Theor Appl Mech* 12(3):637–657
- Walker M, Zhang Y, Heaven S, Banks CM (2009) Potential errors in the quantitative evaluation of biogas production in anaerobic digestion processes. *Biores Technol* 100:6339–6346
- Wang X, Barlaz MA (2016) Decomposition and carbon storage of hardwood and softwood branches in laboratory-scale landfills. *Sci Total Environ* 557:355–362
- Xu F, Li Y, Ge X, Yang L, Li Y (2018) Anaerobic digestion of food waste—challenges and opportunities. *Biores Technol* 247:1047–1058
- Yang Y, Bao W, Xie GH (2018) Estimate of restaurant food waste and its biogas production potential in China. *J Clean Prod* 211:309–320
- Zhang R, El-Mashad HM, Hartman K, Wang F, Liu G, Choate C, Gamble P (2007) Characterization of food waste as feedstock for anaerobic digestion. *Biores Technol* 98:929–935
- Zhao X, Li L, Wu D, Xiao T, Ma Y, Peng X (2019) Modified Anaerobic digestion model no. 1 for modelling methane production from food waste in batch and semi- continuous anaerobic digestions. *Biores Technol* 271:109–117

# Chapter 8

## Nano-Mixed Phase Change Material for Solar Cooker Application



C. V. Papade and A. B. Kanase-Patil

### 8.1 Introduction

The solar energy is stowed in the various forms like sensible heat and latent heat stowage etc. Well-organized and consistent heat storage systems are essential for solar based applications to overcome their present irregular wildlife and unexpected variation in climate conditions. Thermal stowage units that operate PCM as latent based heat stowage material have received better kindness in current years (Buddhi et al. 2000; Sharma et al. 2009a, 2005, 2009b; Patel and Krunal 2015; Joudi and Ahmed 2012; Pankaj et al. 2014; Saxena et al. 2013; Chaudhary et al. 2013; Tian and Zhao 2013; Muthusivagami et al. 2010; Hussein et al. 2008; Bauer et al. 2010; Miqdam et al. 2015; Purohit 2010; Chen et al. 2009; Yuan et al. 2018; Li et al. 2017a; Kabir et al. 2018; Dheep and Sreekumar 2018). It has more heat stowage capacity with large cycle time and isothermal wildlife during accusing and discharging process. The stowage of heat energy is achieved by revampment of the core energy of a quantifiable by way of sensible heat, dormant heat, and thermo-chemical hotness, or mixture of these. Workable heat stowage structure uses the specific heat bulk of the ingredient and the temperature of a quantifiable. PCM review article is available for many applications but the review related to solar cookers are mission therefore in this chapter, an attempt has been made to recap the examination of the solar cooking technology incorporating nano-mixed PCMs. This chapter helps to find the design and development of suitable nano-mixed PCM storage unit for solar based cooking applications. Temperature of the element upsurges through charging and decreases through discharging. Latent heat storage (LHS) is based on captivation or

---

C. V. Papade

Department of Mechanical Engineering, N. K. Orchid. College of Engineering and Technology,  
Dr. DBATU University, Solapur, Maharashtra, India

C. V. Papade · A. B. Kanase-Patil (✉)

Department of Mechanical Engineering, Sinhgad College of Engineering, Savitribai Phule Pune  
University, Pune, Maharashtra, India

proclamation of heat when a stowing material suffers a phase change. Again, there are nearly disadvantages of the PCM used for the stowage of the sun energy such as the less thermal conductivity with large melting point and less specific heat etc. The improvement of thermal chattels such as latent heat and thermal conductivity of PCMs is discussed (Karunamurthy et al. 2012; Obaid et al. 2013; Ahmad and Sharma 2012; Polvongsri and Tanongkit 2011; Hajare et al. 2014; Saw et al. 2013; Li et al. 2017b). Because of this, there is a need of mixing nano particles in to the base PCM to progress the chattels of PCM. Nano elements play an important role in this situation because of their unique chattels at the nano level. By combination of the PCM and nanoparticles the properties of PCM can be refurbished by mixing the nano elements in exact proportion. Hence the effective, efficient and user-friendly energy storage option need to be investigated or developed done.

## 8.2 Phase Change Materials

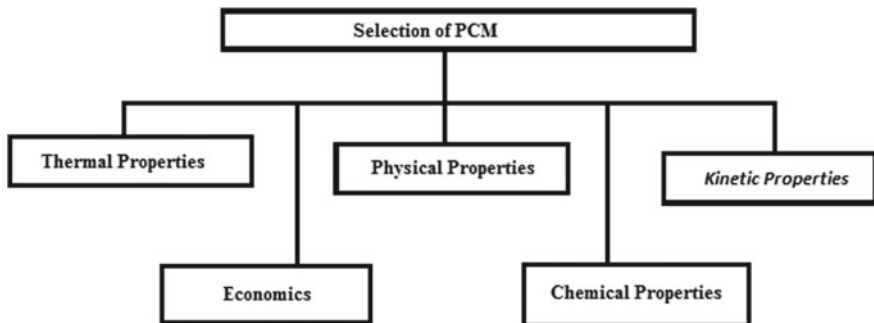
There are huge number of different types of PCMs (organic, inorganic and eutectic) existing in somewhat required temperature series. Here are a huge number of organic and inorganic natural materials, which can be recognized as PCM from the opinion of assessment melting temperature and dormant heat of mixture. Though, but for the melting argument in the working range, common of PCMs does not content the criteria mandatory for a satisfactory storage media as conversed earlier. As no sole material can have wholly the required chattels for perfect thermal-storage media, one has to use the obtainable materials and effort to kind up for the unfortunate physical stuff by a satisfactory arrangement design. The PCM to be used in the thermal stowage arrangements should permit wanted thermo physical, kinetics and chemical chattels which are as follows (Obaid et al. 2013). There are an enormous number of inorganic and organic chemical materials, PCM known from point of view various thermal properties such as melting temperature and latent heat of fusion. Various types of PCMs along with thermal properties such as heat of fusion, melting temperature, density and thermal conductivity have mentions in Table 8.1. During solar based cooking applications there is used PCM for energy stowage, so cooking is done after sunset and selection is based on different properties of PCM with respective types of solar cookers or any solar based systems.

## 8.3 Selection of PCM

The choice of the PCM to stay used is a vital idea which depends on a specific application and its effective temperature (Kumar and Shukla 2015; Harmim et al. 2010). The PCM to be selected in a particular thermal energy stowage system need to study passes of desirable properties such as kinetics, thermal, physical, kinetics organic which are shown in Fig. 8.1.

**Table 8.1** Different types of PCM (Saxena et al. 2011; Nandwani et al. 1997; Li et al. 2017b)

Compound/types of PCM	Heat of fusion (kJ/kg)	Melting temp. (°C)	Density (kg/m <sup>3</sup> )	Thermal conductivity (W/m K)
i.MgCl <sub>2</sub> & 6H <sub>2</sub> O	168.6	117	1450 (liquid, 120 °C)	0.570 (liquid, 120 °C)
			1569 (solid, 20 °C)	0.694 (solid, 90 °C)
ii.NaNO <sub>3</sub>	107.67 (KJ/Kg)	308	2257 (solid,18 °C)	0.514 (solid,316 °C)
iii. KNO <sub>3</sub>	108.67 (KJ/Kg)	330	2109 (solis,16 °C)	0.411 (solid,339 °C)
Paraffin wax	173.6	64	790 (liquid, 65 °C)	0.167(liquid, 63.5 °C)
			916 (solid, 24 °C)	0.346 (solid, 33.6 °C)
Polyglycol E600	127.2	22	1126 (liquid, 25 °C)	0.189 (liquid, 38.6 °C)
			1232 (solid, 4 °C)	–
Palmitic acid	185.4	64	850 (liquid, 65 °C)	0.162 (liquid, 68.4 °C)
			989 (solid, 24 °C)	–
Capric acid	152.7	32	878 (liquid, 45 °C)	0.153 (liquid, 38.5 °C)
			1004 (solid, 24 °C)	–
Caprylic acid	148.5	16	901 (liquid, 30 °C)	0.149 (liquid, 38.6 °C)
			981(solid, 13 °C)	–
Naphthalene	147.7	80	976 (liquid, 84 °C)	0.132 (liquid, 83.8 °C)
			1145(solid, 20 °C)	0.341 (solid, 49.9 °C)



**Fig. 8.1** Selection of PCM

### **8.3.1 Thermal Properties**

Choosing PCM for demanding bid depends upon the working temperature of the heating or cooling must be synchronized to the change temperature of the PCM. The latent heat must be as high as probable, particularly on a volumetric basis, to lessen the substantial scope of the store. Thermal conductivity advanced would help the energy storage during accusing and squaring (Sharma et al. 2009b).

### **8.3.2 Physical Properties**

These properties during phase immovability and throughout chilly melting would assist near setting heat stowage and high density is popular to allow a lesser size of storage pot. Minor volume changes on phase change and minor vapor pressure at working temperatures to decrease the repression problem (Sharma et al. 2009b). Table 8.1 presents data of the investigational thermo physical chattels of both the liquid and solid states for several PCMs as stated by Lane (Amer 2003) and Farid et al. (Saxena et al. 2011).

### **8.3.3 Kinetic Properties**

Kinetic properties of PCM are very important. Great freezing has been a difficult feature of PCM growth, mostly for salt hydrates. Super cooling of additional than only some degrees are hamper with correct heat removal from the accumulate, and 5–10 8 °C great cooling stop it completely (Sharma et al. 2009b).

### **8.3.4 Chemical Properties**

PCM hurt from squalor by damage of water of hydration, chemical decomposition or mismatch with materials of creation. PCMs must be non-toxic, non-flammable and non-explosive for security (Sharma et al. 2009b).

### **8.3.5 Economics**

Very low price and large-scale accessibility of the PCMs is also extremely significant.

## 8.4 Nano-Mixed Phase Change Material

Latent heat stowage is found on incorporation or discharge of heat when a storage material undertakes a stage modify. There are a few drawbacks of the phase change material used for the storage of the solar energy such as the less thermal conductivity, high melting point, less specific heat etc. (Karunamurthy et al. 2012; Obaid et al. 2013; Ahmad and Sharma 2012; Polvongsri and Tanongkit 2011; Hajare et al. 2014; Saw et al. 2013). Because of this, there is a need to mix nano particles in to the base PCM to develop its properties. Nano particles play a vital role in this condition because of their unique properties at the nano stage. The properties of PCM can be revamped by mixing the nanoparticles in accurate proportion. Hence thermal energy storage investigation nano-mixed PCM is required.

PCMs are used for various applications, limited investigations have been done regarding the use of their materials for sun energy applications. Therefore, in this chapter, an endeavor has been made to abridge the study of the solar cooking gadgets incorporating nano-mixed PCMs. This review helps summarizing the procedure for design and development of proper nano-mixed PCM stowage unit for solar based cooker gadgets.

## 8.5 Selection of Nanoparticles

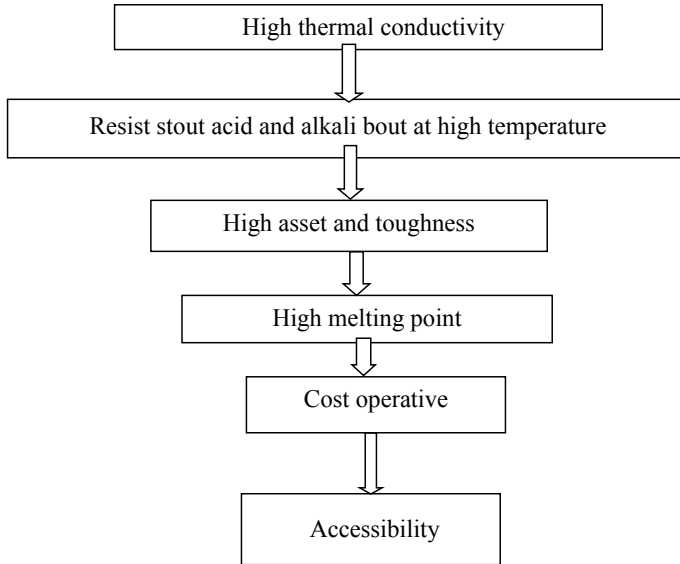
Choice of nanoparticles is built on several constraints such as cost, element size, thermal conductivity, size part and kind of base material etc. Part size is a significant constraint because reduction particles down to nano scale rises the outward area virtual to size and provides well spreading into the base PCM. While selecting the nanoparticle, consider the above flow diagram of Fig. 8.2. The application of nanofluids in solar based application such as collectors and water heaters are studied for the effectiveness, monetary and environmental features. Some studies showed on thermal conductivity and visual properties of nanofluids are also temporarily studied, because these constraints can limit the ability of nanofluids to improve the concert of solar based systems. Collectors and solar based water heaters, Solar based stills, Solar PV panels, Solar cells, Thermal energy stowage, Photovoltaic/Thermal based systems, Solar based thermoelectric cells etc., (Nandwani et al. 1997).

Reliant upon all these principle nano elements are nominated for the diffusion in the base PCM. Table 8.2 displays the dissimilar types of nano elements with chattels.

## 8.6 Types of Solar Cookers

Many researchers developed different types of solar based cookers such as box type and focused type which are capable to make cooking operations. Normally in solar





**Fig. 8.2** Selection of nanoparticles

**Table 8.2** Different types of nano particles (Nandwani et al. 1997)

Sr. No.	Name of nano particles	Color	Nanoparticles approximate crystalline size in (nm)	Thermal conductivity in w/m k	Density in kg/m <sup>3</sup>	Specific heat in kJ/kg. k
1	SiO <sub>2</sub>	White	20–30	1.38	2200	0.740
2	TiO <sub>2</sub>	White	30	8.95	4250	0.686
3	Al <sub>2</sub> O <sub>3</sub>	White	20	35	3890	0.880
4	ZnO	White	30	29	5600	0.710
5	CuO	Black	50	33	6400	0.540
6	Graphene Oxide	Black	4–20	3000	3600	0.765

cookers are used PCM for thermal energy storing for performing cooking operation. Many researchers have tried to explore a moderately simple technique for scheming parabolic dish collector incorporated through PCM.

### **8.6.1 Box Type Solar Cooker Systems**

Solar operated cooking was started with box cookers (Buddhi et al. 2000) especially in the twentieth period, box type of solar based cooker gadget demonstrated a substantial progress in surroundings of design and concert limits. A large amount expansion and change has been ended in various types of solar operated cookers except naturally, expansion has been made in the box type cookers due to its immediate ease and users approachable. Particularly the works done on box type solar cooker is inadequate to only for research determination. A very few projects have been able to resolve the setback with objective i.e., use solar energy for cooking operation.

Buddhi et al. (2000) developed that the box type solar based cooker with PCM and melting temperature of PCM would be between 105 and 110 °C for cooking for cloudy atmosphere and after sunset. There was to find after sunset cooking need a stowage material through proper melting idea and quality for cooking in the evening. Performance of box type solar cooker was calculated with PCM and three reflectors were used. The commercial grade acetanilides PCM with melting point  $-118$  °C, fusion heat of latent  $-222$  kJ/kg are used for thermal energy storage. The cooker performance was experimentally tested under different loading conditions. Sharma et al. (2009a) discussed the research of PCM integrated solar cooking technology. This chapter is an anthology of ample of useful information on limited selected PCMs used in a box type solar based cooker and concentrated solar based cooker. Telkes (1959) observed on box type solar based cooker are shown to heat awake, but effort finds even wherever there are diffuse rays, convective heat beating is caused by squall, irregular cloud wrap and short ambient temperature. Harmim et al. (2010) inspected a box-type solar based cooker using finned surface absorber dish. Tests were conducted in Saharan situation of Algeria at Adrar on the trial stand of the solar energies examine unit. The outcomes indicated that by using fins with box type solar cooker was 7% additionally capable than the usual cookers. By using finned absorber plate heating water was reduced 12%.

### **8.6.2 Parabolic Concentrator Solar Cooker Systems**

The initial solar functioned parabolic type cooker was settled by Ghai in 1950. After that few researchers (Lof and Fester 1961) designed a variety of geometries and swelling shapes of solar powered parabolic cookers. Parabolic types of solar based cookers paying attention to people without delay all over the world due to their wonderful performance. The solar operated parabolic cookers attain high temperatures with less time and not like solar operated box cookers; they prepare, not require a unique cooking pot. The system performance assessment procedure was developing by Purohit (2010). Studies show the rustic and metropolitan people depend primarily, on non-commercial energies to gather their energy requirements. Solar based cooking is one potential result but its approval has been restricted somewhat

due to some difficulties. Solar cooker cannot cook the food after sunset and cloudy atmosphere. That difficulty is solved by thermal energy storage material. So that food cooks at late evening (Chen et al. 2009; Abhay and Yogesh 2013; Saman 1997; Gary et al. 1994). Presented results of cooking through the sun have become a hypothetically practical replacement for fuel-wood in food homework in much of the emergent world. Vigor necessities for catering account for 36% of entire primary energy utilization in India. Mohammed (2013) developed a parabolic type dish solar cooker for native cooking has been offered, jointly with the predicted and actual recital of the system. The calculated different design factors related to the collector for cooking purpose, even though no detailed thermal recital study is accessible, the cooking experiment outcomes illustrate that the cooker is all the time capable of cooking food correspondent of 3 kg of dry rice at a time, within the predictable length of time and solar energy levels.

Soud et al. (2010) designed a parabolic type solar based cooker with involuntary with trailing system. The trial outcomes presented that the water temperature privileged the cooker's tube reached 90 °C when the extreme indicated ambient temperature remained at 36 °C. Arenas (2007) developed a moveable solar based kitchen with parabolic type solar reflector that pleated up addicted to a little size. The investigational study designated that power effectiveness of 26.6% with power output 175 W. This control scale provides sufficient power to cook a meek meal for two persons in a normal time of 2 h. Lecuonaa et al. (2013) discussed inventive layout of moveable solar operated concentrating parabolic cooker with TES. The utmost use of solar rays was achieved by using an inventive type of a solar collector that is concentrated parabolic collector. The situation has verified ability to boil and cook fast also which is robust one. This idea infers a bulky heating power and a top cooking temperature for boiling, frying and burning in sunny time. Suple and Thombre (2013) studied solar power for cooking applications. Aim is to create the solar operated cooking as at ease as feasible and it is related to conservative cooking system. In solar operated box cooker by using flat collectors only boiling and steaming was achievable. However, use of solar operated concentrating collector permits every one operation like boiling, steaming, roasting and frying with comparative capacity. Ibrahim (2013) designed and developed solar operated thermal cooker with parabolic dish having aperture diameter 1.8 m. The cooker remained intended to cook food comparable of 12 kg of dehydrated rice per day, for a relatively average size domestic. The cooker was able of cooking 3.0 kg of rice in 90–100 min, and this muscularly agreed with the expected period of 91 min.

## 8.7 Conclusion

In spite of the existing one, there is requirement of solar energy which should be able to accumulate the sun thermal energy in satisfactory amount effectively and efficiently with the help of PCM for solar cooker applications. Again, there are almost some disadvantages of PCM such as high melting point, less thermal conductivity. Such chattels of energy stowage materials have to be refurbished with the help of the nano materials. So that immense amount of solar energy stored in the energy stowing materials and the solar based cooker applications work properly and efficiently. By revampment of properties of PCM with the aid of nanoparticles energy storing capacity increased and also other thermal properties improved.

## References

- Abhay B, Yogesh R (2013) Review on phase change material as thermal energy storage medium: materials, application. *Int J Eng Res Appl* 3(4):916–921
- Ahmad N, Sharma S (2012) Green synthesis of silver nanoparticles using extracts of ananascomosus. *Green Sustain Chem* 2:141–147
- Amer EH (2003) Theoretical and experimental assessment of a double exposure solar cooker. *Energy Convers Manage* 44:2651–2663
- Arenas JM (2007) Design, development and testing of a portable parabolic solar kitchen. *Renew Energy* 32:257–266
- Bauer T, Laing D, Tamme R (2010) Overview of PCMs for concentrated solar power in the temperature range 200 to 350 °C. *Adv Sci Technol* 2010(74):272–277
- Buddhi D, Sharma SD, Sawhney RL, Sharma A (2000) Design, development and performance evaluation of a latent heat storage unit for evening cooking in a solar cooker. *Energy Convers Manage* 41(14):1497–1508
- Chaudhary A, Kumar A, Yadav A (2013) Experimental investigation of a solar cooker based on parabolic dish collector with phase change thermal storage unit in Indian climatic conditions. *J Renew Sustain Energy* 3:1144–1152
- Chen CR, Sharma A, Murty VV, Shukla A (2009) Solar cooker with latent heat storage systems: a review. *Renew Sustain Energy Rev* 13(6):1599–1605
- Dheep RG, Sreekumar A (2018) Investigation on thermal reliability and corrosion characteristics of glutaric acid as an organic phase change material for solar thermal energy storage applications. *Appl Therm Eng* 129:1189–1196
- Gary J, Tom W, Tim W (1994) Advanced reflector materials for solar concentrators. *Natl Renew Energy Lab* 3:1–11
- Hajare V, Narode AR, Gawali BS, Bamane SR (2014) Experimental investigation of enhancement in heat transfer using nano—mixed PCM. *Int J Eng Res Technol (IJERT)* 3(11):843–848
- Harmim A, Belhamel M, Boukar M, Amar M (2010) Experimental investigation of a box type solar cooker with a finned absorber plate. *Energy* 35:3799–3802
- Hussein HMS, El-Ghetany HH, Nada SA (2008) Experimental investigation of novel indirect solar cooker with indoor PCM thermal storage and cooking unit. *Energy Convers Mgmt* 49:2237–2246
- Ibrahim LM (2013) Design and development of a parabolic dish solar thermal cooker. *Int J Eng Res Appl* 3(4):1179–1186
- Joudi K, Ahmed K (2012) Simulation of heat storage and heat regeneration in phase change material. *J Eng* 18:2210–2217

- Kabir E, Pawan K, Sandeep K, Adelodun AA, Kim KH (2018) Solar energy: potential and future prospects. *Renew Sustain Energy Rev* 82:894–900
- Karunamurthy K, Murugumohan K, Suresh S (2012) Use of CuO nano-material for the improvement of thermal conductivity and performance of low temperature energy storage system of solar pond. *Digest J Nonmater Biostruct* 7:1833–1841
- Kumar A, Shukla SK (2015) A Review on thermal energy storage unit for solar thermal power plant application. *Int Conf Technol Mater Renew Energy Environ Sustain* 74:462–469
- Lecuonaa A, Nogueira JI, Ventas R, Rodrigues MC, Legrand M (2013) Solar cooker of the portable parabolic type incorporating heat storage based on PCM. *Appl Energy* 11:1136–1146
- Li X, Yuan Z, Hongen N, Xinxing Z, Ouyang D, Ren X, Jinbo Z, Chunxi H, Yue S (2017a) Advanced nanocomposite phase change material based on calcium chloride hexahydrate with aluminium oxide nanoparticles for thermal energy storage. *Energy Fuels* 31:6560–6567
- Li M, Qiangang G, Steven N (2017b) Carbon nanotube/paraffin/montmorillonite composite phase change material for thermal energy storage. *Sol Energy* 146:1–7
- Lof G, Fester D (1961) Design and performance of folding umbrella-type solar cooker. *Proc UN Conf New Sources Energy* 5:347–352
- Miqdam T, Chaichan, Shaimaa H, Abdul-Mohsen N, Al-Ajeely (2015) Thermal conductivity enhancement by using nano-material in phase change material for latent heat thermal energy storage systems. *Saussurea* 5(6):48–55
- Mohammed IL (2013) Design and development of a parabolic dish solar thermal cooker. *Int J Eng Res Appl (IJERA)* 3(4):1179–1186
- Muthusivagami RM, Velraj R, Sethumadhavan R (2010) Solar cookers with and without thermal storage—a review. *Renew Sustain Energy Rev* 14(2):691–701
- Nandwani SS, Steinhart J, Henning HM, Rommel M, Wittwer V (1997) Experimental study of multipurpose solar hot box at Freiburg Germany. *Renew Energy* 12(1):1–20
- Obaid HN, Majeed AH, Farhan LR, Ahmed H (2013) Thermal energy storage by nanofluids. *J Energy Technol Policy* 3(5):2224–2232
- Pankaj S, Vrind S, Charanjit S (2014) Performance evaluation of thermal storage unit based on parabolic dish collector for indoor cooking application. *J Acad Indus Res (JAIR)* 3(7):304–310
- Patel D, Krunal K (2015) Performance analysis of latent heat storage unit with packed bed system—an experimental approach for discharging process. *Sol Energy* 3(4):105–111
- Polvongsri S, Tanongkit K (2011) Enhancement of flat-plate solar collector thermal performance with silver nano-fluid. *Second TSME Int Conf Mech Eng* 2:30–37
- Purohit I (2010) Testing of solar cookers and evaluation of instrumentation error. *Renew Energy* 35(9):2053–2064
- Saman W, Wakilaltojjar S (1997) Evaluation of a thermal storage system employing multiple phase-change materials. *Proc Solar 97—Australian New Zealand Solar Energy Soc Paper* 102:29–35
- Saw C, Al-Kayiem CH, Owolabi A (2013) Experimental investigation on the effect of PCM and nano-enhanced PCM of integrated solar collector performance. *WIT Trans Ecol Environ* 179:899–909
- Saxena A, Varun PSP, Srivastav G (2011) A thermodynamic review on solar box type cookers. *Renew Sustain Energy Rev* 15:3301–3318
- Saxena A, Shalini L, Vineet T (2013) Solar cooking by (using PCM as thermal heat storage. *Int J Mech Eng* 3(2):766–772
- Sharma SD, Iwata T, Hiroaki K, Sagara K (2005) Thermal performance of a solar cooker based on an evacuated tube solar collector with a PCM storage unit. *Sol Energy* 78(3):416–426
- Sharma A, Chen C, Murty VVS, Anant S (2009a) Solar cooker with latent heat storage systems: a review. *Renew Sustain Energy Rev* 13:1599–1605
- Sharma A, Tyagi V, Chen CR, Buddhi D (2009b) Review on thermal energy storage with phase change materials and applications. *Renew Sustain Energy Rev* 13:318–345
- Soud MS, Abdallah E, Akayleh A, Abdallah S, Hrayshat ES (2010) A parabolic solar cooker with automatic two axes sun tracking system. *Appl Energy* 8:463–470

- Suple YR, Thombre SB (2013) Performance evaluation of parabolic solar disc for indoor cooking. *J Mech Civil Eng* 4(6):42–47
- Telkes M (1959) Solar cooking ovens. *Sol Energy* 3(1):1–10
- Tian Y, Zhao CY (2013) Review of solar collectors and thermal energy storage in solar thermal applications. *Appl Energy* 104:538–553
- Yuan K, Yan Z, Wanchun S, Xiaoming F, Zhengguo Z (2018) A polymer-coated calcium chloride hexahydrate/expanded graphite composite phase change material with enhanced thermal reliability and good applicability. *Compos Sci Technol* 156:78–86

# Chapter 9

## Technical Review on Battery Thermal Management System for Electric Vehicle Application



Virendra Talele, Pranav Thorat, Yashodhan Pramod Gokhale,  
and Hemalatha Desai

### *Nomenclature*

Degree Celsius	Temperature ( $^{\circ}\text{C}$ )
volts	Voltage (V)
seconds	Time (s)
Joule/second	Angular momentum (J/s)
1/h	Current 1/h

### *Abbreviation*

EV	Electric Vehicle
PHEV	Plug-in hybrid electric vehicles
BEV	Battery electric vehicle
Li-ion	Lithium-ion
Nicad	Nickel-cadmium
NiMH	Nickel-metal hydride
Li-MnO <sub>2</sub>	Lithium manganese dioxide

---

V. Talele (✉) · P. Thorat  
Department of Mechanical Engineering, MIT School of Engineering, MIT ADT University, Pune,  
Maharashtra, India  
e-mail: [virendratalele1@gmail.com](mailto:virendratalele1@gmail.com)

Y. P. Gokhale  
Institute for Mechanical Process Engineering, Otto-Von-Guericke University Magdeburg,  
Universitätsplatz 2, 39106 Magdeburg, Germany

H. Desai  
Mechanical and Aerospace Engineering Department, University of California, Los Angeles,  
CA 90095, USA

Li-(CF) <sub>x</sub>	Lithium carbon monofluoride
Li-SOCl <sub>2</sub>	Lithium tetra chloroaluminate
Li-SO <sub>2</sub> Cl <sub>2</sub>	Lithium tetra chloroaluminate in sulfuryl chloride
Li-FePO <sub>4</sub>	Lithium iron phosphate
LiNiMnCoO <sub>2</sub>	Lithium-Nickel-Manganese-Cobalt-Oxide
PEMFC	Proton Exchange Membrane Fuel Cell
PCM	Phase change material
CAE	Computer-aided engineering
TIM	Thermal Interference Material
TR	Thermal runaway
LIB	Lithium-ion battery
BTMS	Battery thermal management system
GRK	Greenhouse gases
TEC	Thermoelectric coolers

## 9.1 Introduction

The primary challenges to the deployment of large fleets of cars equipped with lithium-ion batteries on public roads are safety, costs associated with cycle and calendar life, and performance. These difficulties are compounded by thermal phenomena in the battery, such as capacity/power fading, thermal runaway, electrical imbalance between several cells in a battery pack, and low-temperature performance. Most batteries should ideally function at an optimal average temperature with a relatively limited differential range. When constructing a battery cell, pack, or system, the rate of heat dissipation must be quick enough to prevent the battery from reaching thermal runaway temperature.

Interest in electric vehicles (EV), which HEVs (hybrid electric vehicles), PHEVs (plug-in hybrid electric cars), and BEVs (battery electric vehicles) are examples of hybrid electric vehicles (BEV), has increased significantly in recent years as environmental regulations regulate greenhouse gases. (GRK) emissions become more severe. Since the turn of the twentieth century, environmental degradation and energy scarcity have become a global problem, with the transportation industry playing an important role. The government has made great efforts to promote electric cars (EVs) for environmental and energy-saving benefits (Johnson et al. 1997), including a number of preferential regulations. The increasing electric vehicle industry requires high specific power and high specific energy density batteries to suit the operational needs of electric cars (Khateeb et al. 2004). Lead-acid, zinc/halogen, metal/air, sodium beta, nickel-metal hydride (NiMH), and lithium-ion batteries are all available for electric cars and HEVs (Li-ion). For FCEV, a proton exchange membrane fuel cell (PEMFC) is also an option. On the one hand, because the battery controls the performance of electric cars, battery safety is an important issue for electric vehicle applications. On the other hand, price is a significant obstacle to the continuity of electric cars for



**Table 9.1** Types of cells

Battery type	Nominal voltage V	Specific energy Wh/kg	Energy density Wh/lit	Overview
Lead acid	2.0	30–40	60–75	May et al. 2018)
Nickel–Cadmium	1.2	40–60	15–150	Valøen and Shoesmith 2007)
Nickel-metal Hydride	1.2	30–80	140–300	<a href="https://www.pow erstream.com, NiMH.htm">https://www.pow erstream.com, NiMH.htm</a>
<i>Lithium-ion—Classified based on chemistry</i>				
Li-MnO <sub>2</sub> (Lithium manganese dioxide)	3	280	580	Johnson et al. 1997)
Li-(CF) <sub>x</sub> (Lithium carbon monofluoride)	3	360–500	1000	Greatbatch et al. 1996 )
Li-SOCl <sub>2</sub> (Lithium tetra chloroaluminate)	3.5	500–700	1200	Morrison and Marincic 1993)
Li-SO <sub>2</sub> Cl <sub>2</sub> (Lithium tetra chloroaluminate in sulfuryl chloride)	3.7	330	720	Hall and Koch 1982)
Li-FePO <sub>4</sub> (Lithium iron phosphate)	3–3.2	90–160	325	Safoutin et al. 2015)
LiNiMnCoO <sub>2</sub> (Lithium-Nickel-Manganese-Cobalt-Oxide)	3.6–3.7	150–220	300	Liu et al. 2020)

both producers and consumers. Therefore, it is very important to optimize battery power and cycle time. In battery-electric cars, lithium-ion batteries are commonly used because of their high specific energy, specific power, energy density (Etacheri et al. 2011; Cosley and Garcia 2004; Huber and Kuhn 2015; George and Bower xxxx; Kim et al. 2019) (Table 9.1).

Because of its better energy density, higher specific power, and lower weight, rechargeable lithium-ion (Li-ion) batteries have been universally acknowledged as the best energy storage solution for electric vehicles (EVs) since the early 2000s. Other rechargeable batteries, such as lead-acid, nickel–cadmium (NiCad), and nickel-metal hydride (NiMH) batteries, have lower rates, lower self-discharge rates, faster recycling, and longer cycle life (Keyser et al. 1999; Bukhari et al. 2015; Li et al. 2014). To improve cycle life, energy storage capacity, and overall performance, it is critical to keep the battery temperature within an acceptable range. This is because lithium-ion batteries are very susceptible to thermal runaway when exposed to high temperatures. This type of lithium-ion battery is very sensitive to temperature, which affects its performance, life, and safety (Scrosati 2011; Zia et al. 2019; Lyu et al. 2019; Liang et al. 2017). In part, this is due to the large variety of electrode materials and electrolyte mixtures used in commercial batteries, making it difficult to establish a consistent and comprehensive process that causes lithium-ion battery performance and safety

to deteriorate. On the other hand, it is undeniable that the performance and due to the fact that batteries are influenced by external conditions and emit heat as the result of a series of chemical processes that occur during charging and discharging, temperature changes are almost always unavoidable. As a result, an effective battery thermal management system (BTMS) is needed to maintain the appropriate temperature range of these batteries and to reduce the temperature gradient of these batteries in order to avoid detrimental consequences from temperature fluctuations (Selman et al. 2001; Lin et al. 1995; Saito 2005; Katoch et al. 2020). Elevated temperatures have the potential to ignite very flammable electrolytes, resulting in explosions, fires, capacity loss, and short circuits in lithium batteries. As a result, one of the most essential elements of lithium-ion batteries is the battery thermal management system (BTMS). Battery thermal management may be accomplished via the use of a variety of cooling techniques, including natural or forced air cooling, liquid cooling, and PCM cooling. In electric cars, liquid cooling is often used, while air cooling is more cost-effective in two-wheeler segments, the detailed classification of cooling strategy is given in two types as such (Holzman 2005; Zhao et al. 2015; Liaw et al. 2003)—(a) active cooling strategy and (b) passive cooling strategy. In thermal management systems degradation of cells with increasing temperature can be numerically correlated based on Arrhenius correlation which suggests temperature-dependent physical chemistry profile as the exact relation of electrochemistry with the temperature-dependent design of battery (Qin et al. 2014; Pearce 2015; Lewerenz et al. 2017; Wang et al. 2011; Zhao et al. 2020).

- (A) Active cooling strategy—In an active thermal management system to shed out heat from the source an external aid of power is required. Forced convection (Fan cooling), Cold plate cooling, Direct immersion cooling are examples of active thermal management systems. The first active thermal management system was developed in the late 19's which was based on force convection cooling using fans for an electronic application. Over the years with the development of verification and CAE tools active thermal management has become more efficient by using strategic product development such as customized cold plates for avionics application, direct contact dielectric immersion cooling. The active thermal management system has capabilities for a variety of customization to increase conjugate heat transfer characteristics for heat sources (Patil and Hotta 2018; Hotta and Patil 2018; Panchal et al. 2016; Panchal et al. 2016; Panchal et al. 2016; Kurhade et al. 2021; Sun et al. 2019)
- (B) Passive cooling strategy—In the passive cooling strategy there is external power required to cool down electronic elements, this system involves utilizing the availability of latent heat from the heat source to cool down the element with ambient temperature. This cooling strategy involves for variety of applications ranging from electronic cooling up to the battery and engine cooling. Extended surface fins cooling, PCM cooling, two two-phasing heat pipes, etc. are some of the examples of the passive thermal management system. Passive systems can be easily customized according to the availability of design space and requirement to pull out the generated amount of heat by making thermal equilibrium. Passive

thermal strategy is a very cost-effective approach for economically constrained design since it doesn't require any aid of external power requirement to cool down heat source (Safdari et al. 2020; Chen et al. 2019; Ranjbaran et al. 2020; Ramadass et al. 2002; Liu et al. 2019; Mathew and Hotta 2019; Mathew and Hotta 2020; Mathew and Hotta 2021; Kurhade et al. 2021; Talele et al. 2021).

It should be noted that there are no thorough studies on battery temperature control in the literature. This article discusses the evolution of power battery, including the implications for clean cars and power battery, as well as mathematical models of battery thermal behavior. In the present paper the details of different thermal management techniques are reviewed and contrasted, particularly the PCMs battery thermal management system and the thermal conductivity of materials. This study is anticipated to be beneficial to electric car manufacturers, researchers, and aspirants in the scientific community.

## 9.2 Battery Thermal Management Systems

### 9.2.1 Temperature Effect on Battery Performance

The battery cell after 800 cycles at 50 °C, the battery cell loses more than 60% of its original power and 70% at 55 °C after 500 cycles. Lithium-ion batteries have a cycle life of 3323 cycles at 45 °C but drop to 1037 cycles at 60 °C (Hu et al. 2016 Jan 1; Ran et al. 2020; Das et al. 2018). This shows that temperature has a significant effect on battery cycle time and energy capacity. The impact of temperature on the battery life cycle is shown in Fig. 9.1. Automotive batteries are classified into three categories: cells, modules, and packs. Thousands of lithium-ion batteries are connected in various configurations such as series, parallel, or a combination of both to create large-capacity, large-scale battery packs (Wang et al. 2020; Wen et al. 2018; Kim et al. 2012). During the charging and discharging of the battery, a series of chemical processes occur and a large amount of heat is generated, resulting in an unavoidable change in battery temperature (Liang, et al. 2017; Ke et al. 2015; Nagpure et al. 2010). The majority of temperature impacts are caused by chemical processes inside the batteries and also by the materials utilized within the batteries. In the case of chemical processes, the connection between rate and reaction temperature follows the Arrhenius equation, and temperature fluctuation may result in a change in the rate of electrochemical reactions in batteries. Apart from chemical processes, temperature influences the ionic conductivities of electrodes and electrolytes. For example, at low temperatures, the ionic conductivity of lithium salt-based electrolytes diminishes (Jow et al. 2018; Bandhauer et al. 2011; Lisbona and Snee 2011; Finegan 2017). With these impacts in mind, the LIBs used in EVs and HEVs are unlikely to fulfill the United States Advanced Battery Consortium's (USABC) 10-year life expectation. The next sections will address the impacts of low temperature on LIBs as well as the effects of high temperature on LIBs. At elevated temperatures, the consequences are

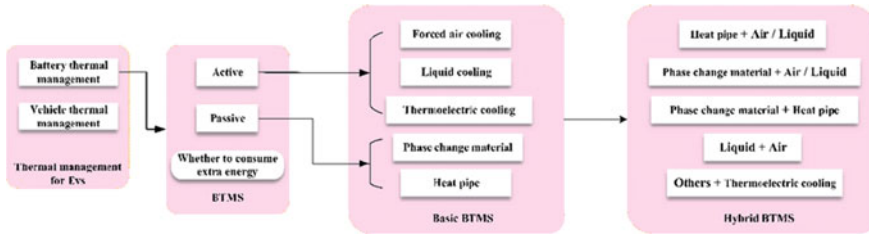
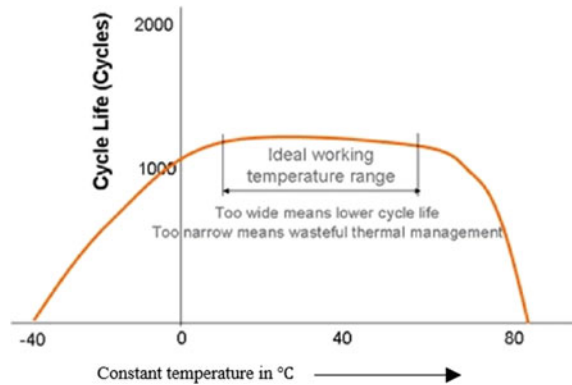


Fig. 9.1 Battery thermal management system classification (Patil and Hotta 2021)

Fig. 9.2 Effect of temperature on battery life



much more complicated than at low temperatures. Heat is produced within the LIBs during operation and knowing how this heat is generated is important for reducing the high temperature impacts in LIBs (Fig. 9.2).

### 9.2.2 Thermal Runaway Propagation in Lithium-Ion Batteries

Thermal runaway in lithium-ion (Li-ion) battery occurs when a cell, or a region inside a cell, reaches dangerously high temperatures as a result of thermal breakdown, mechanical failure, internal/external short-circuiting, or electrochemical abuse, among other causes. Exothermic breakdown of the cell components starts when the temperature is raised over a certain point. At some point, the cell's self-heating rate exceeds the rate at which heat can be dispersed to its surroundings, causing the temperature of the cell to increase exponentially and the cell to lose its capacity to maintain its stability. As a consequence of the loss of stability, all of the remaining thermal and electrochemical energy is released into the surrounding environment. Thermal runaway events may be triggered by a variety of factors. It is possible for a thermal runaway to be triggered by mechanical or thermal problems. Thermal

runaway may also be triggered by electro-chemical abuse, such as overcharging or over-discharging battery cells. Additionally, there is the potential of an internal short circuit occurring inside the cell, which may result in thermal runaway (Blomgren 2017; Kim et al. 2007; Liu et al. 2020). The occurrence of any of these events may result in increased temperatures that are high enough to cause the rapid exothermic breakdown of the cell's constituent components. To understand why we observe such fast heating rates, we must first get a better understanding of the breakdown processes that are taking on. A Li-ion cell, or a tiny area inside a Li-ion cell, reaches a specific critical temperature range, at which point the components contained within the cell begin to break down and break down. In nature, these breakdown processes are exothermic, which is why we see self-heating behavior as a result of them. The decomposition rates, which are directly related to the exothermic self-heating rates, also follow the Arrhenius form, which implies that the decomposition rate, therefore, the self-heating rate increases exponentially as the temperature increases. Simply said, when the temperature rises, the rate of decomposition accelerates, and the rate of self-heating accelerates in the same way. The consequence is a rise in the self-feeding heating rate inside the cell, which continues to grow until the cell loses stability and ruptures, releasing all the remaining thermal and electrochemical energy into the surrounding environment (Feng et al. 2018). Although over the past years research importance for thermal runaway was not given so much over the recent application of lithium battery for energy storage increases for heavy-duty applications such as Buses, Heavy trucks, Cranes, etc. which demand a higher amount of power to propel the application which causes certain infield failure in the system as if one of the cells goes in thermal runaways, it causes interaction of the whole module which causes serial breakdown of desired application hence due to safety concern in strategy product design thermal runaway must give importance. In recent years several academic, as well as industrial research initiates, were taken to account the behavior of thermal runaway condition which is summarized in Table 9.2.

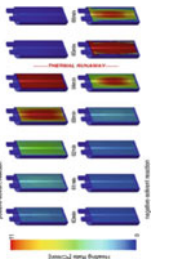
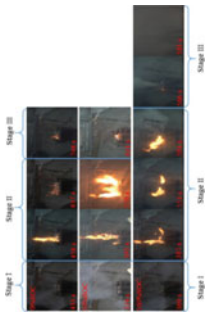
Over the years the problem of thermal runaway causes severe breakdown in working operation of automotive, Table 9.3 shows some examples of recent accidents caused by thermal runaway of automotive.

The abuse condition in Lithium-ion battery can be unpredictable from the Table 9.3, it is reviewed that causing field failure of the a lithium-ion battery can be any which leady cell causing thermal runaway for example vehicle leading to the crash causes mechanical abuse which leads to the thermal runaway, overcharge of battery also causes local thermal runaway of the cell which spreads wide over the pack, internal short circuit also leads to thermal runaway conditions. The categorization of thermal runaway can be classified as below.

### 9.2.2.1 Mechanical Abuse

Mechanical abuse is characterized by destructive deformation and displacement produced by an applied force. Mechanical damage often occurs as a result of a vehicle accident, crushing or penetrating the battery pack (Xia et al. 2014b). During a vehicle

**Table 9.2** Thermal runaway mitigation

Thermal runaway	Image	Highlights	References
Thermal abuse based on overheating		<p>The model findings indicate that smaller cells reject heat more rapidly than bigger cells, which may save them from thermal runaway under similar abuse circumstances</p> <p>If local hot spots are simulated within a large cylindrical cell, the three-dimensional model predicts that the reactions initially propagate in azimuthal and longitudinal directions and form a hollow cylindrical reaction zone</p>	Wang et al. (2021)
Overheating causes thermal runaway and fire behavior in lithium iron phosphate batteries		<p>A large prismatic Lithium-ion battery are studied</p> <p>A heating plate is placed in the battery which heats them evenly as TIM</p> <p>In thermal runaway propagation cell has shown steady-state combustion rather than instants</p> <p>No jet fire at 0% Soc</p> <p>The jet fire occurred in 50% to 100% Soc</p> <p>A blow of gas observed after jet fire</p>	Two-way nonlinear mechanical-electrochemical-thermal coupled analysis method to predict thermal runaway of lithium-ion battery cells caused by quasi-static indentation (2020)

(continued)

**Table 9.2** (continued)

Thermal runaway	Image	Highlights	References
<p>Internal short circuit causing Thermal Runaway time sequence map for Lithium-ion batteries</p>	<p>(A) Graph showing Temperature (°C) vs Time (h) for a Lithium-ion battery. The temperature starts at 25°C and rises to 100°C (T<sub>1</sub>) at 1.5h, then to 150°C (T<sub>2</sub>) at 2.5h, and finally to 200°C (T<sub>3</sub>) at 3.5h. The graph is divided into three regions: (1) Normal operation, (2) Pre-ignition, and (3) Ignition of TR. Key events include: (1) Normal operation, (2) Pre-ignition, (3) Ignition of TR, (4) Onset of heat generation, and (5) Onset of heat generation. The graph also shows the maximum temperature of TR (T<sub>max</sub>) and the time to reach T<sub>max</sub> (t<sub>TR</sub>).</p> <p>(B) Photograph of a battery cell during thermal runaway, showing a bright orange flame and smoke.</p> <p>(C) Photograph of a battery cell during thermal runaway, showing a bright orange flame and smoke.</p>	<p>The TSM (thermal runaway) mechanism of lithium-ion batteries is proposed in this article. The graphical approach depicts the major physical/chemical processes during battery TR. The TSM depicts the fundamental mechanics of battery TR by sequencing important physical/chemical processes. Two battery samples' TR findings validate the TSM</p> <p>The internal short circuit (ISC) is critical to trigger the oxidation–reduction reaction but is not the major heat source that heats the cell to 800°C or more. The TSM also depicts the battery TR research horizons</p> <p>It recommends future battery TR research should concentrate on: (1) the connection between ISC and TR; (2) the mechanism of the oxidation–reduction process between the cathode and anode; and (3) precise reaction mechanisms for a particular thermodynamic system inside the cell</p>	<p>Bu10m Porsche up in flames as battery charging goes wrong, (2018)</p>

(continued)

**Table 9.2** (continued)

Thermal runaway due to over charging	Image	Highlights	References
		<p>In this study, four 40 Ah Li-ion batteries with varying cathode materials were overcharged. The overcharge process has five phases followed by the NCM111 Li-ion cell. In NCM Li-ion cells, the duration between TR reduces as the cathode nickel ratio rises. For cathode materials, the TR risk is LFP &gt; NCM811 &gt; NCM622 &gt; NCM111, while the overcharge tolerance is LFP &gt; NCM811 &gt; NCM622 &gt; NCM111. NCM811 &gt; NCM622 &gt; NCM111 &gt; LFP. Overcharge tolerance (or low TR risk) of NCM Li-ion cells is superior to LFP Li-ion cells (or less TR hazards). The thermal stability of cathode materials decreases with an increasing nickel content in NCM Li-ion cells, increasing TR risks.</p>	<p>CGTN (2019)</p>

(continued)



**Table 9.2** (continued)





Thermal runaway	Image	Highlights	References
Thermal abuse modeling based on the mechanical indication		<p>An internal short circuit produced by quasi-static indentation may be analyzed using a two-way nonlinear mechanical–electrical–thermal coupled analytical model</p> <p>The material nonlinearity of the LIB components was utilized to determine the mechanical deformation and internal short-circuit induced by cathode–anode contact</p> <p>The thermal model computed temperature using a heat conduction equation based on the electrochemical model’s Joule, reversible, and irreversible heat sources</p> <p>A study of mechanical–electrochemical–thermal coupled estimated the internal short-circuit, heat, and temperature increase in each timestep. To test the linked analytical model, 3.2 Ah pouch cells were indented with spherical punches of three sizes</p> <p>An internal short-circuit was predicted by the three indentation tests by 3.3%, and the response force by 5.3%</p> <p>Moreover, the peak temperature owing to thermal runaway reduced with increasing indenter diameter, according to the findings</p>	Sun et al.

(continued)

**Table 9.2** (continued)

Thermal runaway	Image	Highlights	References
<p>18,650 lithium-ion battery thermal runaway cell venting and gas-phase reactions</p>		<p>We examined the flow and thermal behavior of the existing numerical framework and categorized venting occurrences into two stages: cell breach (internal gas pressure exceeds venting pressure) and thermal runaway</p> <p>We found that the initial stage had little impact on propagation propensity</p> <p>The bulk of reactive gas production happens during the second stage of thermal runaway</p> <p>The quantity and concentration of reactive gas (<math>H_2</math>, <math>CO_2</math>, <math>CH_4</math>, etc.) tend to rise with state-of-charge (SOC)</p> <p>Furthermore, during thermal runaway, the pressure inside the cell casing rises (up to 4.25 bar at 100% SOC) and may trigger a pressure-induced side-wall rupture</p> <p>Also, with larger SOC, heat from gas-phase reactions may dominate overall heat production, implying that gas-phase reactions cannot be disregarded for safe battery design</p> <p>The numerical framework developed here will be used to compare different cell choices and packaging architectures for next-generation battery modules, taking into account not only thermal runaway propagation due to heat conduction but also thermal runaway propagation due to heat convection and reactive flow</p>	<p>Blanco (2013)</p>

**Table 9.3** Thermal runaway propagation through accident

Location	Picture	Accident cause	Reference
Chogging China		Spontaneous ignition causing a fire	Lambert (2017)
Thailand		Fire peak due to overcharge	Zhang et al. (2015)
Seattle, USA		A Model S Tesla caught fire after a road collision. Mechanical abuse thermal runaway	Xia et al. (2014a)
Austria		Tesla Model S crashed into a semi trailer causing a fire. Mechanical abuse post-crash thermal runaway	Maleki and Howard (2009)

accident, it is very likely that the battery pack may be deformed. The arrangement of the battery pack onboard the electric vehicle has an impact on the battery pack's collision reaction. The deformation of the battery pack may have the following potentially hazardous consequences: It is possible that: (1) the battery separator may be ripped, resulting in an internal short circuit (ISC); (2) the flammable electrolyte will spill, with the potential for the battery to catch fire. Studying the crush behavior of a battery pack at several scales, from the material level to the cell level and finally to the pack level, is required. To verify the design under durability conditions several CAE investigations perform on battery packs such as frequency responses, NVH, deformation, etc. (文浩, 谢达明, 罗斌, 梁活开. 动力锂电池安全国家标准 GB, T 31485 与 IEC 62660-3 的比较. 收藏. 2018;11; 杨桃, 邹海曙, 吉盛, 黄伟东 2019; Menale et al. 2021).

Penetration is another frequent occurrence that may occur after a vehicle accident and is difficult to predict. When compared to the crush circumstances, severe ISC may be initiated very instantly after penetration begins to take place. Penetration is controlled in certain mandatory lithium-ion battery test standards, such as GB/T 31,485–2015, SAE J2464-2009, and others, in order to mimic the ISC in the abuse test, for example. Mechanical destruction and electrical shorting take place at the same time, and the abused state of penetration is more severe than the abuse condition of simple mechanical or electric abuse alone. On the nail penetration test of lithium-ion batteries for electric vehicles, difficult issues are being presented. Previously, the nail penetration test method was considered to be a replacement for the ISC's other test approaches. The reproducibility of the nail penetration test, on the other hand, is being called into question by battery makers. Some think that the lithium-ion battery with greater energy density would never pass the nail penetration test in standards, and as a result, a revolution is taking place in the battery industry. The issue of whether to improve the repeatability of the penetration test or to look for a replacement test method remains an open and difficult one in the field of lithium-ion battery safety research (Roth and Doughty 2004; Bugryniec et al. 2018; Leising et al. 2001; An et al. 2019; Zhao et al. 2016).

### 9.2.2.2 Electrical Abuse

In lithium-ion batteries thermal runaway propagation due to electrical abuse can be classified in 3 main types such as—(a) External short circuit, (b) Internal short circuit (ISC), (c) Overcharge and (d) Over discharge.

- (a) External short circuit—an external short circuit can occur if two electrodes with a voltage difference are connected to each other through conductors. Deformation after a vehicle accident, immersion in water, contamination with conductors, or an electrical shock during maintenance are examples of external shorts that can occur with battery packs. The heat generated in the circuit of an external short circuit does not usually heat the cell in the same way compared to penetration. For the most part, external shorting behaves more like a rapid discharge process,

with the peak current limited by the material transport rate of the lithium ions. The use of electrical protection devices can minimize the risk of an external short circuit. The main function of protection devices is to disconnect the circuit in the event of a short circuit with high current. When it comes to preventing external short circuits, fuses are the most effective option. However, devices with a positive thermal coefficient (PTC) can also shut down the circuit if the temperature rises excessively. According to the manufacturer, magnetic switches and bimetallic thermostats are other options to avoid the risk of an external short (Lee et al. 2015; Ren et al. 2021; Huang et al. 2021; Zhang et al. 2017).

- (b) Internal short circuit—The ISC is the most frequently seen element of TR. There are CSIs associated with almost all abusive conditions. In general, ISC occurs when the cathode and anode come into direct contact with each other due to the failure of the battery separator. When ISC is activated, the electrochemical energy contained in materials is released spontaneously, creating heat. ISC can be classified into three types based on the failure mechanism of the separator. These are: (1) Mechanical abuse, such as deformation and breakage of the spacer caused by penetration or crushing of the nails; (2) electrical abuse, such as dendrites that pierce the separator, whose growth can be induced by overload/over discharge; (3) Thermal abuse, such as the shrinkage and collapse of the separator with massive ISC caused by extremely high temperatures; (4) Thermal abuse, such as the shrinkage and collapse of the separator with massive ISC caused by extremely high temperatures. Massive ISC, which is often produced by mechanical and thermal abuse, will immediately cause TR to occur. As an alternative, moderate ISC produces minimal heat and does not result in TR being triggered. As the degree of the separator fracture increases, so does the amount of time between the ISC and TR required for energy release. As a result, the likelihood of ISC resulting from misuse is very minimal since all cell products must pass the appropriate testing requirements before they can be sold. However, there is still one kind of ISC, known as spontaneous ISC or self-induced ISC, that cannot be adequately controlled by existing test criteria since it occurs spontaneously. It is thought that the spontaneous ISC is caused by contamination or flaws during the production process. The ISC, which is the most frequent characteristic of TR, deserves more investigation. The following research are encouraged: (1) investigation of the processes behind the progressive growth of the spontaneous ISC; (2) development of a more reliable replacement ISC test; and (3) development of an easy-to-use ISC simulation model. Furthermore, the connection between the ISC and the TR has to be explained and defined. Section 9.4 will examine the function of the International Standards Committee (ISC) in the TR process (Zhu et al. 2020; Chen et al. 2020; Ren et al. 2017; Huang et al. 2019; Mendoza-Hernandez et al. 2015).
- (c) Overcharge—Overcharge is one of the root causes of the battery pack going under thermal runaway conditions (Finegan et al. 2016). Overcharge can be one of the most disastrous reasons for the failure of cells which is typically form due to the failure of the battery management system to withhold the required amount of energy in the battery pack. Overcharging is characterized by the production

of heat and gas, which are two qualities that are frequent. The ohmic heat and side reactions that generate the heat are responsible for heat production. First, the lithium dendrite develops at the surface of the anode because of excessive lithium intercalation on the surface of the anode. The stoichiometric ratio of the cathode and anode may influence the onset of lithium dendrite development. Lithium dendrite growth is a slow process. Second, excessive de-intercalation of lithium results in the collapse of the cathode structure, which results in heat production and the release of oxygen into the atmosphere. Increased oxygen availability expedites electrolyte degradation, which results in the emission of large amounts of gas. Because of the rise in internal pressure, the cell may begin to vent. The interaction between the active elements inside the cell and the surrounding air may result in increased heat production after the cell has been vented. The result of an overcharge experiment is dependent on the test circumstances. The cell burst when exposed to high current, while it merely swelled when exposed to low current (Wang et al. 2020a; Wang et al. 2020b; Lopez et al. 2015; Feng et al. 2018).

- (d) **Over discharge**—Over-discharge is another potential electrical abuse issue to be aware of. It is inevitable, in most cases, for the voltage discrepancy between the cells in a battery pack to exist. Consequently, if the battery management system (BMS) fails to monitor the voltage of a single cell, the cell with the lowest voltage will be over-discharged as a result. The process of over-discharge abuse differs from that of other types of misuse, and the potential danger may be overestimated as a result. During an over-discharge, the cells linked in series with the lowest voltage in the battery pack may cause the cell with the lowest voltage in the battery pack to be forcefully discharged. While under forceful discharge, the pole of the cell reverses, and the voltage of the cell drops to a negative value, causing anomalous heat production at the overloaded cell. The over-discharge of the cell has the potential to cause the cell's capacity to degrade. During the process of over-discharge, the excessive delithiation of the anode results in the breakdown of SEI, which results in the production of gases such as CO or CO<sub>2</sub>, which causes the cell to expand. The discharging is less likely to result in cell fires or explosions, and it is thus less dangerous than overcharging. The little amount of current research on over-discharging is mainly concerned with the effects of shallow over-discharge on the number of battery cycles that may be used (Wang et al. 2019; Yuan et al. 2019).

### 9.2.2.3 Thermal Abuse

Thermal abuse is the direct cause of thermal runaway in the battery pack. The cause of local heating in a battery pack with a cell spreads out over the pack with localized heating of contact cell. In battery pack overheat of localized cell in thermal abuse condition has not only happened by mechanical/electrical abuse but also by loss contacts with connectors, this may typically cause due to manufacturing defects. With the loss of contact when the pack gets in operational work on road condition,

it causes localized heating over the cell which spread in module causing thermal runaway condition (Abada et al. 2018). Thermal abuse can also actuate in hot ambient working conditions for the battery as such when the requirement on delivery power for the vehicle is more, battery pack gets heated at the same time if thermal stability over the cooling system is not sufficient it causes coupling of hot ambient temperature with a thermal load of battery pack, hence cell faces the problem of TR for high C-rate requirement (Kong et al. 2021; Zhang et al. 2020; Lai et al. 2020; Tian et al. 2020).

### ***9.2.3 Thermal Runaway Preventive Strategy***

The safety issues associated with lithium-ion batteries (LIBs) have been the most significant barriers to their widespread use in portable electronic gadgets, electric cars, and energy storage systems, among other uses. This kind of issue is caused by flammable solvent-containing liquid electrolytes that may be readily oxidized when exposed to high temperatures, resulting in additional heat buildup and, ultimately, thermal runaway (Yang et al. 2020; Wilke et al. 2017). In concern with the issue of thermal runaway, recently there are several research that has been developed to prevent thermal runaway in highly flammable LIBs which is shown in Table 9.4.

From the literature it is seen that thermal runaway is very stagnant process which can initiate in number of different scenarios, recently several research is developed on electrochemistry, mechanical and thermal mode to prevent cell from going into thermal runaway condition (Jindal et al. 2021; Yukse et al.; Yang et al. 2016; Al-Zareer et al. 2017).

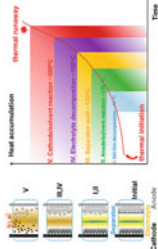
## **9.3 Active and Passive Cooling Strategy**

In BTMS, the primary goal is to maintain stated temperature of cell below 50 °C for efficient working and utilized every cent of available energy from it. In concern with thermal abuse and overheat cell condition, it is essential to design stable thermal management system which increases the thermal stability of cell by preventing it undergoing in overshoot temperature and post-gas dynamic condition in which gas out of the burn cell gets entrap in the enclosure. In the present section, a detailed breakdown of recent research and methodology developed by BTMS is reviewed.

### ***9.3.1 Need of Battery Thermal Management***

Electrochemical operation and joule heating due to the passage of electrons within a battery cell are the two main sources of heat creation in a battery cell. The temperature

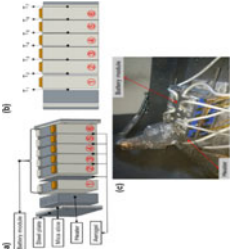
**Table 9.4** Thermal runaway preventive strategy

Prevention strategy	Image	Highlight	References
Safe electrolyte for preventing thermal runaway		<p>The design methods for a safe electrolyte may be used to regulate the flammability and volatility of the liquid electrolyte, to avoid thermal runaway, and to finally guarantee the risk-free and fire-free operation of LIBs. A safe electrolyte for LIBs is reviewed here, including the inclusion of flame retardant chemicals, overcharge additives, and stable lithium salts, as well as the use of solid-state electrolytes, ionic liquid electrolytes, and thermosensitive electrolytes. These methods' benefits and disadvantages are contrasted and explored, and a safer electrolyte for future LIBs is suggested</p>	Tian et al. (2020)

(continued)

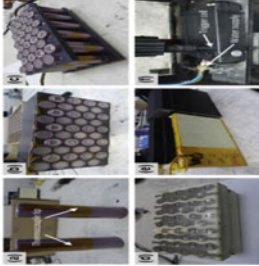


**Table 9.4** (continued)

Prevention strategy	Image	Highlight	References
<p>Preventing Thermal Runaway Propagation in Lithium-Ion Battery Module Using Aerogel and Liquid cooling plate together</p>		<p>Preventing thermal runaway is important to improving electric car fire safety. The impacts of aerogel, liquid cooling plate, and their combination on the preventive mechanism of thermal runaway propagation are studied. Temperature, voltage, mass loss, and venting parameters during thermal runaway propagation are compared and evaluated. However, adding the liquid cooling plate alone does not seem to stop the thermal runaway propagation, but rather accelerates it. Using aerogel and a liquid cooling plate together may stop the thermal runaway propagation. The research tells us that to successfully avoid thermal runaway propagation, battery thermal management system safety design should include all heat transfer routes</p>	<p>Yang et al. (2020)</p>

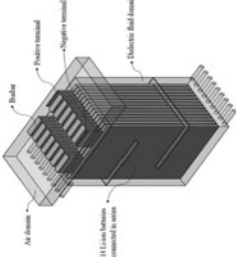
(continued)

**Table 9.4** (continued)

Prevention strategy	Image	Highlight	References
Preventing thermal runaway propagation in lithium-ion battery packs using a phase change composite material		<p>Phase change composite materials (PCCTM) provide passive protection at low weight and cost while reducing system complexity. In this study, we compare the efficacy of PCC thermal control in avoiding propagation of thermal runaway in a Li-ion battery pack for small electric cars. A penetration cell causes complete propagation of packs without PCC whereas PCC does not propagate. Packs without PCC may propagate without external short circuits, but not consistently. In all test circumstances, PCC reduces the highest temperature by 60°C or more. On the basis of postmortem data, we deduce the propagation sequence and features of pack failure</p>	<p>Wilke et al. (2017)</p>

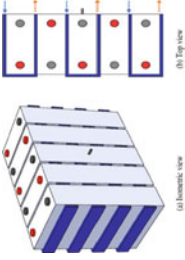
(continued)

**Table 9.4** (continued)

Prevention strategy	Image	Highlight	References
dielectric fluid immersion cooling technology to prevent thermal runaway		<p>The MSMD method was used to construct the electrochemical-thermal model of a Li-ion pouch cell with flowing dielectric fluid and tab cooling. The findings of the numerical research and the experimental data agreed within 5%. The maximum temperature of the 50 V battery pack was kept below 40°C for 5°C discharge at 81.7 W. The suggested DFIC aided with tab cooling technique reduced the maximum battery pack temperature by 9.3% compared to the traditional cooling approach. The battery pack reached 341.7 °C when subjected to thermal abuse with an internal short circuit, however the battery pack did not overheat except for the afflicted cell. An effective thermal management technique for high-density and high-capacity Li-ion batteries in electric cars was shown in this research</p>	<p>Patil et al. (2021)</p>

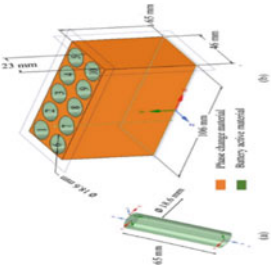
(continued)

**Table 9.4** (continued)

Prevention strategy	Image	Highlight	References
Preventing thermal runaway of battery through mini channel cooling	 <p>(a) Isometric view</p> <p>(b) Top view</p>	<p>This paper presents a minichannel cooling system for battery modules and tests its effectiveness in preventing thermal runaway. Internal short circuits may be triggered by car accidents or manufacturing flaws. The conjugate heat transport and reaction kinetics models were used to investigate thermal runaway. The impacts of flow rate, thermal abuse responses, nail penetration depth, and nail diameter were studied using numerical models. Minichannel cooling at the cell level cannot stop thermal runaway in a single cell, but it can stop thermal runaway propagation across cells</p>	<p>Xu et al. (2017)</p>

(continued)

**Table 9.4** (continued)

Prevention strategy	Image	Highlight	References
<p>Preventing heat propagation and thermal runaway in electric vehicle battery modules using integrated PCM and micro-channel plate cooling system</p>		<p>This technique prevents heat propagation and thermal runaway in a battery module comprised of 18,650 cells damaged by nail penetration of up to three cells. Using the Newman 2D pseudo electrochemical model, short-circuit model, and thermal abuse model, we achieved intense heat production of the order of 106 J/s under thermal abuse conditions. They examined scenarios of 3 cell nail penetration. Heat transmission between three thermally abused cells was avoided by applying 3.9 L min<sup>-1</sup> water flow and a counter-current flow to two micro-channel plates. The temperature of the cells next to the thermally abused cell was kept below 363 K, avoiding thermal runaway in the battery module. Integrated cooling kept coolant temperature below boiling point at the utilized coolant volumetric flow rate, preventing unwanted circumstances of coolant boiling</p>	<p>Kshetrimayum et al. (2019)</p>

(continued)

**Table 9.4** (continued)

Prevention strategy	Image	Highlight	References
Use of polymer—substrate to prevent battery thermal runaway		<p>Protecting electrical components from internal short circuits may help avoid thermal runaway in lithium-ion batteries. A metal-coated polymer current collector is tried in 18,650 batteries to disconnect internal short circuits by drawing from the heating zone. Cells with metal coated polymer current collectors have a decreased danger of thermal runaway during nail penetration. With the use of high-speed synchrotron X-ray radiography and X-ray computed tomography, we can learn more about how 18,650 cells work. It compares to 18,650 batteries with commercial aluminum and copper current collectors. During nail penetration, cells with aluminum-coated polymer current collectors maintained a cell voltage &gt; 4.00 V, whereas conventional cells suffered thermal runaway</p>	<p>Pham et al. (2021)</p>

range of 25–40 °C is excellent for Li-ion batteries, whereas temperatures beyond 50 °C are hazardous to the batteries' lifespan. The immaturity of even a single cell is a deterrent, can significantly affect the overall performance and efficiency of the battery pack, the major goal of the BTMS is to regulate the temperature of the battery's cells and hence extend the battery's lifespan. Active systems and passive systems are the two primary forms of BTMS. The active system is mostly reliant on the forced circulation of a specific coolant, such as air or water. A passive system is one that does not require any action on the part of the user. A passive system, which uses methods such as heat pipes, hydrogels, and phase change materials to have zero power consumption, enhances the vehicle's net efficiency. In this publication, a full evaluation of BTMS is presented based on accessible literature, with research for future advancement highlighted.

### ***9.3.2 Active Cooling Strategy***

Active cooling refers to a cooling technology that relies on external equipment to improve heat transfer. Active cooling strategy increases the fluid flow rate in the convection process, thereby significantly increasing the heat dissipation rate. The active cooling solution includes forced air supply by fans or blowers, forced liquid, and thermoelectric coolers (TEC), which can be used to optimize thermal management at all levels when natural convection is not enough to dissipate heat use of a fan is recommended (Table 9.5).

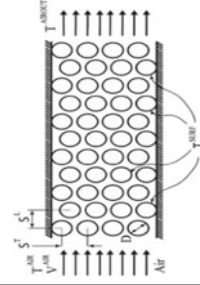
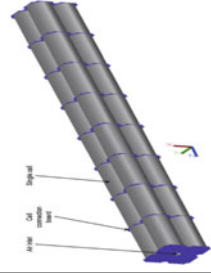
### ***9.3.3 Passive Cooling Strategy***

Passive cooling maximizes radiation and convection heat transfer modes by using a radiator or heat sink, thereby achieving a high level of natural convection and heat dissipation. By keeping the electronic products below the maximum allowable operating temperature, can provide adequate cooling and thermal comfort for the electronic products in the home or office building. This growth trend can be observed in Battery Technology commonly referred to as passive Cooling in the industry (Table 9.6).

### ***9.3.4 Hybrid Thermal Management Approach***

Over the recent years as the demand for energy storage to fulfill power requirement is increased for which the present form of thermal management system cannot fulfill the exact cooling requirement hence hybrid thermal management system approach is widely adaptable for the desired application. In the hybrid approach basic two or more

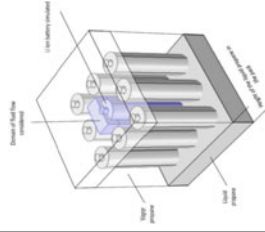
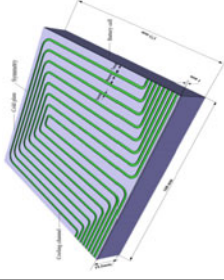
**Table 9.5** Active cooling strategy for BTMS

Research paper title	Image	Highlight	References
<p>Battery thermal management for PHEV over the variety of ambient condition for LFP cell</p>	 <p>The diagram shows a cross-section of a battery pack with multiple layers of cells. Arrows indicate air flow from the bottom and top. Labels include <math>T_{AMB}</math> for ambient temperature, <math>T_{TOP}</math> and <math>T_{BOT}</math> for top and bottom temperatures, and <math>T_{CELL}</math> for cell temperature. A velocity vector <math>V_{AIR}</math> is also shown.</p>	<p>In this paper, they modeled electric vehicle with an air-cooled battery pack made of cylindrical Lithium iron phosphate cells and simulated the effects of thermal management, driving conditions, regional climate, and vehicle system design on battery life. Developed a simulation model of battery and automatic operation, heat generation, heat transfer, battery degradation during vehicle operation, charging, and idle to estimate the degradation of the PHEV battery under various conditions</p>	<p>Shen et al. (2020)</p>
<p>Investigation of thermal performance of battery pack using air cooling</p>	 <p>The image shows a 3D perspective of a battery pack with air flow arrows indicating cooling from the top and bottom. Labels include 'Air flow', 'Cell', and 'Terminal'.</p>	<p>The thermal performance of axial air cooling for lithium-ion battery packs was investigated with 32 individual cells and solved numerically by coupling the liquid transport equations. To calculate the heat generation rate of the battery pseudo-2D model is used. Numerical simulations are used to study the thermal performance of the air cooling system</p>	<p>Xia et al. (2019)</p>

(continued)


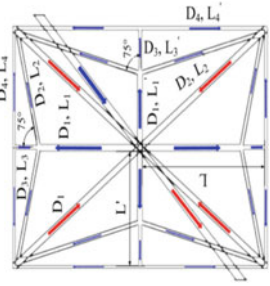


**Table 9.5** (continued)

Research paper title	Image	Highlight	References
<p>A novel study to enhance the thermal performance of the battery pack</p>		<p>This article proposes a new BTMS (Battery Thermal Management System), a PCM for battery packs in hybrid electric vehicles, and a 3D electrochemical thermal model. Liquid propane is used to dissipate a numerical thermo-electrochemical model that studies the performance of the cooling system</p>	<p>Deng et al. (2019)</p>
<p>Thermal Management of prismatic Lithium-Ion cells using liquid cooling</p>		<p>The intention of this investigates a powerful cooling technique of prismatic Li-ion batteries for an electric-powered vehicle, a layout of BTMS, the usage of minichannel bloodless plates is established. The overall performance of the BTMS is parametrically studied with the aid of using the usage of exceptional configurations, glide rates, and inlet coolant temperatures. To remedy the thermal control trouble of a fifty-five Ah Li-ion battery, a minichannel bloodless plate—primarily based totally liquid cooling designed with the aid of using the usage of numerical simulation technique</p>	<p>Wiriyasart et al. (2020)</p>

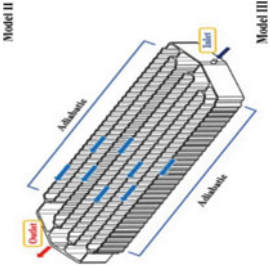
(continued)

**Table 9.5** (continued)

Research paper title	Image	Highlight	References
Use of liquid cooling for improving the thermal performance of cells in electric vehicle		<p>In this study, a liquid-cooled layout is proposed from the percent stage to enhance the thermal overall performance of cells % primarily based totally on the warmth dissipation strategy, standard thermal control subject turned into deliberate as a reference fashion for the battery %. The 3-d temporary thermal version turned into used</p>	<p>Kalhaus et al. (2018)</p>
Splitting mini-channels cooling plate for prismatic Li-ion battery design optimization		<p>The work carried out in this article is to optimize the dissipation of cold plates embedded with leaf-shaped mesh according to the structural theory. A distributed network layer has been created, but together with a collection network layer, it has been designed to reduce the inherent disadvantages of standard single-channel gradients. In this article, a leaf-shaped network structure applied as a cold plate for a lithium-ion battery is analytically optimized</p>	<p>Park (2013)</p>

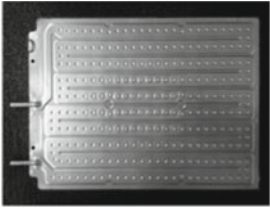
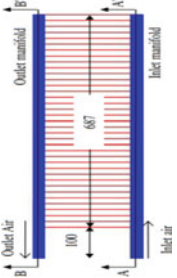
(continued)

**Table 9.5** (continued)

Research paper title	Image	Highlight	References
Nanofluid cooling of battery packs		<p>The temperature distribution and pressure drop employing nanofluids flowing within the corrugated mini-channel of the EV coil cooling module are described in this paper using a computational analytical approach. There are 444 cylindrical lithium-ion cells in the EV battery module (18,650 type). The refrigerant flow direction, mass flow rate, and refrigerant type were determined to have the greatest impact on the temperature distribution. The suggested module's (model II) most effective cooling performance was achieved with nanofluid as the refrigerant, resulting in a 28.65% lower temperature than the standard cooling module (model I)</p>	<p>Effat et al. (2016)</p>

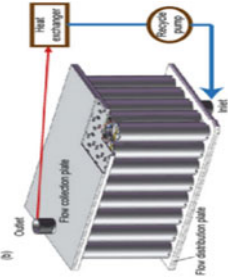
(continued)

**Table 9.5** (continued)

Research paper title	Image	Highlight	References
Use of cooling plates in electric vehicles		<p>In this study, the effects of inactive components, such as cooling plates and protective shells of modules, on the deformation and failure of individual cells are taken into account. They carried out experiments in the hole of the EV battery module with and without these components. 3 different scenarios were recorded during this study:</p> <ul style="list-style-type: none"> <li>(i) stacks of cells</li> <li>(ii) stacks of cells with cooling plates inserted in each second cell</li> <li>(iii) stacks of cells with cold plates and with the plastic plate</li> </ul>	Choi and Kang (2014)
A design for cooling li-ion batteries in hev using an airflow configuration		<p>In this article, a selected type of cooling coil system is examined on paper to meet the desired thermal specifications battery. In a hybrid electric vehicle, the battery is made up of cells connected in series and parallel configuration, so cooling performance based on the distribution of fluid channels is indisputable that even if the current battery system layout/design is not dynamic, the desired cooling performance can be achieved using the conical elbow and pressure relief vent</p>	Saw et al. (2016)

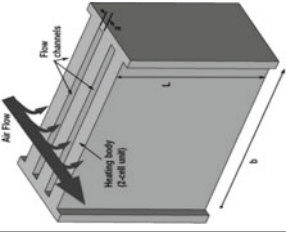
(continued)

**Table 9.5** (continued)

Research paper title	Image	Highlight	References
<p>A review of modeling efforts in the major areas of heat control and lithium-ion battery cell safety</p>		<p>The objective of this study is to provide an informative summary of the thermal management and safety of LIBs in a very fast but inexpensive way. In this regard, the article discusses the modeling efforts carried out in four main topic areas, namely</p> <ul style="list-style-type: none"> <li>(1) chemical science models,</li> <li>(2) coupled electrochemical-thermal models,</li> <li>(3) Lithium-ion battery cooling</li> <li>(4) LIB abuse and thermal escape</li> </ul> <p>We have a tendency to specialize in modeling due to development and technology style of lithium batteries</p>	<p>Giuliano et al. (2012)</p>

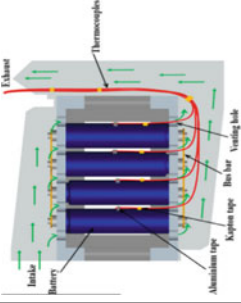
(continued)

**Table 9.5** (continued)

Research paper title	Image	Highlight	References
Air cooling of the battery pack to examine the thermodynamic behavior		<p>In this research work, an acceptable thermal management system is designed, modeling methodology is proposed that describes the thermal behavior of an air-cooled lithium-ion battery system from the point of view of a vehicle component designer</p> <p>A proposed mathematical model is constructed to support the electrical and mechanical properties of the battery. Validation test results for lithium-ion battery systems are presented</p> <p>The results show that current model can provide a good estimate for simulating convection heat transfer cooling</p>	<p>Jiaqiang et al. (2018)</p>

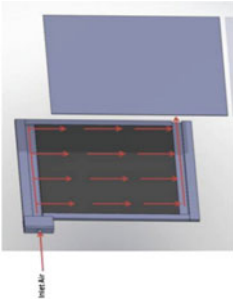
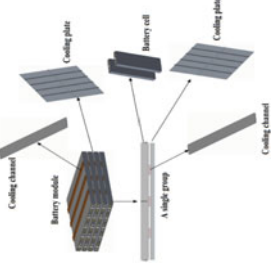
(continued)

**Table 9.5** (continued)

Research paper title	Image	Highlight	References
Li-ion battery pack with air cooling: CFD and thermal analysis		<p>The study deals with CFD to analyze the air conditioning system for a 38,120-cell. The pack contains 24 38,120 cells, copper bus bars, intake and exhaust plenums, and support plates with ventilation holes. Accelerated rate calorimeter is used to calculate the heat generation rate during the charging state. The thermal performance of the battery pack was analyzed with various cooling air mass flow rates using steady-state simulation. The simulation results show an increase in cooling airflow which will effect in a rise in the heat transfer coefficient and a decrease in pressure</p>	<p>Sun and Dixon (2014)</p>

(continued)

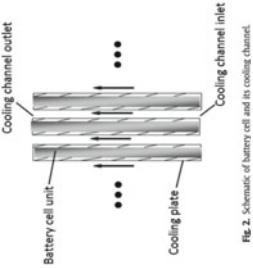
**Table 9.5** (continued)

Research paper title	Image	Highlight	References
<p>Experimental investigation of an air-cooled system for lithium-ion cells</p>		<p>As part of this study, the implementation of an air-cooled system was examined. The authors describe the procedure for the design and testing of an air-cooled thermal management system under laboratory conditions and draw conclusions about its effectiveness. The experimental results provided an idea of the influence of the SOC of the cell on the internal resistance and, therefore, on the general thermal behavior. Designed and manufactured an air that uses metal foam-based insole panels for heat dissipation capacity. Experiments were performed on Allair nano 50 Ah battery on a variety of charge-discharge cycle streams at two airflow speeds</p>	<p>Saad and Oudiah January (2022)</p>
<p>An Orthogonal experimental design of cooling battery packs</p>		<p>In order to examine the influence of parameters on the cooling effect of the liquid-based cooling strategy model, an orthogonal array L16 (4<sup>4</sup>) was chosen to model sixteen models to perform and measure parametric to identify primary and secondary factors, then a combined model was found. The results show that the pipe number has the effect on the temperature of the cold plate in four constraints, and the coolant flow rate is the second, the pipe height has the least effect</p>	<p>Buonomo et al. (2018)</p>

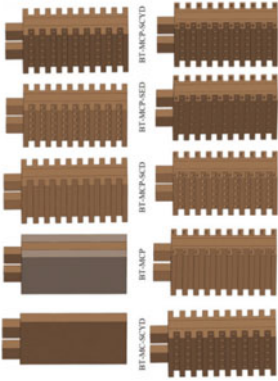
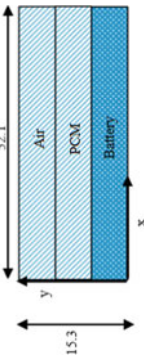
(continued)



**Table 9.5** (continued)

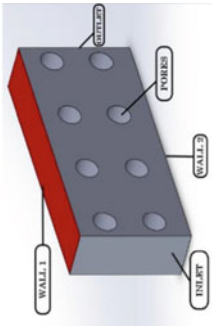
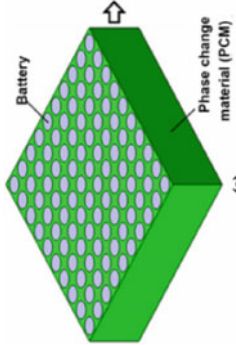
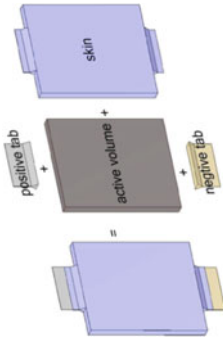
Research paper title	Image	Highlight	References
Use of air cooling method for battery application	 <p>Fig. 2. Schematic of battery cell and its cooling channel.</p>	<p>This article shares a study of the cooling strategy development methodology for cold lithium-ion bag cells used in hybrid electric vehicles (HEV). The 3D transient thermal model of the battery pack was developed by incorporating the three-dimensional flow sub-model of the battery pack, the one-dimensional network sub-model of the battery pack, and the thermal cell/battery module sub-model across the battery cell heat generator attributable to charge transfer rates at the interface of the battery cell solution, and the potential gradient expressed between the types of User Delineated Functions (UDFs)</p>	<p>Harish et al. (2021)</p>

**Table 9.6** Passive cooling strategy for BTMS

Research paper title	Image	Highlight	Reference
Using fins and perforations for increasing performance of the battery		<p>In this research work, the fins consists of circular perforations which are used to reduce the battery temperature, fins with circular perforations can be used to reduce the temperature significantly</p>	<p>Song (2018)</p>
Metal foam containing phase transition materials has been used to cool lithium-ion batteries	 <p>Fig.1 Physical Domain</p>	<p>The research work was based on a 2-D domain, in which PCM was used for the delay in critical temperature of the battery pack. The metal foam was used for uniform heat distribution</p>	<p>Chen et al. (2016)</p>

(continued)

**Table 9.6** (continued)

Research paper title	Image	Highlight	Reference
<p>Study of thermal behavior of Aluminum foams in batteries of electric vehicles</p>		<p>In this research paper numerical simulation of battery, the model was done with metal foam for high thermal performance. The study determined a 45% reduction in temperature</p>	<p>Fathabadi (2014 Jun)</p>
<p>Influence of phase change material for enhancing thermal performance of lithium ion battery</p>		<p>In this paper, phase change material was filled in the gaps between cells. The study showed that by increasing the spacing between the cells the delay effect can be increased</p>	<p>Javani et al. (2014)</p>
<p>Cooling using phase change material</p>		<p>Researched methods for using phase change materials for cooling and found that they can provide several benefits in limiting peak temperatures. Some researchers have used porous foam or carbon fiber</p>	<p>Bamdezh and Molaeimanesh (2020)</p>

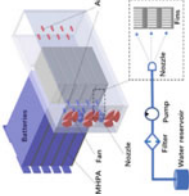
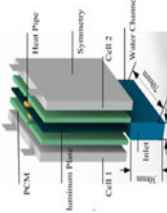
BTMS is combined to generate the maximum amount of heat transfer coefficient to wipe out the desired temperature from the source. To overcome the obstacles and maximize the effectiveness of BTMS, several researchers have suggested a combination of BTMS. This kind of BTMS combines active and passive BTMS, or two passive BTMS, which is referred to as hybrid BTMS. PCMs with air circulation, PCMs with liquid circulation, and PCMs with heat pipes are all often utilized in the modern-day. The below table shows recent research developed in combination strategy for hybrid BTMS (An et al. 2017; Zhao et al. 2020; Bamdezh et al. 2020; Patel and Rathod 2020; Al-Zareer et al. 2017; Hekmat and Molaeimanesh 2020; Jin et al. 2021; Yue et al. 2021; Zhang et al. 2021; Qin et al. 2019) (Table 9.7).

## 9.4 Conclusion and Future Recommendation

Power cells having big capacity, high energy density, and quick charging are becoming more popular in electric cars, resulting in a broad range of temperature distribution. As a result of the rise in the rate of heat production, batteries have safety issues such as life span ageing, degradation acceleration, and loss of stability. This article examines the thermal model of a battery pack and categorizes the battery thermal management system for battery pack cooling. The need and scope of having a battery thermal management system is also covered in a manuscript. The general classification of BTMS is divided in three segments as shown in Fig. 9.1 Hierarchy. The selection of battery thermal management system is totally dependable on various customization and end-user need, from regressive literature it is found that selection criteria for BTMS depend on associated factors such as cost (if its lower budget application generally passive BTMS is proven as best selection), feasibility to increase HTC, robustness as preventing it undergoing thermal runaway condition which covers in safety functional aspect. Furthermore, regressive literature is developed on the cause of thermal runaway and preventive strategies which can save battery packs from going in a thermal runaway condition. Recent development in BTMS in terms of a hybrid approach to come up with the limitation of the passive thermal management system is also reviewed.

Concluding remark future recommendations are suggested in terms of techno-commercial aspect as of the BTMS which primarily takes into account the relationship between beneficial work production by BTMS and its electric consumptions, may improve the overall economic efficiency of the system predicting the driving environment using the vehicle to everything (V2X) technology that can accurately forecast the output power of the LIB, which has a major impact on temperature increase. To manage the multi-physical BTMS, which includes the preheating system and cooling system, an intelligent control strategy that is self-adaptive and takes economic considerations into account should be developed. Several emerging cooling techniques, such as thermoelectric cooling, hydrogel-based cooling, thermoacoustic cooling, and magnetic cooling, are emerging today and have the potential to provide many advantages over air cooling or liquid cooling methods, including

**Table 9.7** Hybrid cooling strategy for BTMS

Research paper title	Image	Highlight	Reference
<p>Under dynamic working conditions, a hybrid battery thermal management system for electric vehicles</p>		<p>In this study, hybrid cooling is suggested for electric vehicles. The performance using the cooling strategy was increased to 62% which reduced the energy consumption</p>	<p>Behi et al. (2020)</p>
<p>Hybrid technique for Battery Thermal Management System based on PCM, HP, and LP created for surrogate model</p>		<p>The authors suggest a hybrid thermal management system consisting of PCM, HP, and liquid cooling. Based on the Adaptive-Kriging-HDMR technique, a surrogate model is created. Global sensitivity analysis is used to identify four sensitive variables. The improved system is tested under cycling and thermal runaway conditions</p>	<p>Mathew and Hotta (2018)</p>

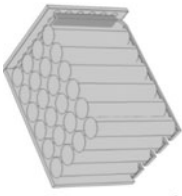
(continued)

**Table 9.7** (continued)

Research paper title	Image	Highlight	Reference
Use of PCM and air cooling for novel hybrid technique		<p>This article proposes a new hybrid BTMS that blends air-forced convection and PCM. The proposed BTMS's efficacy was then shown using dynamic cycling at 1 C, 2 C, 3 C, and 4 Crates. Both the maximum temperature and the maximum temperature differential are kept within the specified limits. Meanwhile, thermal performance was evaluated between active and passive cooling. TMax and TMax have both been substantially lowered since the advent of active cooling. Experiments demonstrate that the passive approach is incapable of maintaining the maximum temperature within the optimal range at a pace of 3 C. Additionally, the experimental findings verify the numerical model, which consists of a three-dimensional heat transport model linked with an electrochemical model. The spacing between batteries is further adjusted based on the simulation, and the suggested gap for application is 5 mm</p>	<p>Mathew and Hotta (2021 )</p>

(continued)

**Table 9.7** (continued)

Research paper title	Image	Highlight	Reference
<p>For electric vehicles cooling battery using air conditioning and heat, pipe</p>		<p>This article proposes a hybrid thermal management system &amp; # 40; TMS' for electric cars using air cooling and heat piping (EV). The thermal behavior of a battery module with 24 cylindrical cells is mathematically and thermally predictable. The difference between natural and forced air cooling TMS is explored. Optimizations include changing cell spacing, air velocity, ambient temperature, and inserting copper foil heat pipes (HPCS). COMSOL Multiphysics® programmed in commercial CFD solves mathematical models. According to the modeling and experimental results, the suggested cooling technique holds for optimizing TMS with HPCS, providing recommendations for future optimization of similar system designs. The maximum temperature of the modules for forced-air cooling, heat pipes, and HPCS are 42.4 °C, 37.5 °C, and 37.1 °C, i.e., 34.5, 42.1, and 42.7% lower than natural air cooling. The battery module temperature uniformity increased by 39.2, 66.52, and 73.42%</p>	<p>Mathew and Hotta (2019)</p>

significant energy and potential savings cost, as well as high potential for scalability and scalability. Then, sensors are used to monitor the operating status of the battery pack, such as its temperature, current, and voltage, which can be used to interact with the temperature prediction model to correct errors in the model. Furthermore, we recommend using data predictive modeling based on multi objective analysis in which the upper bound limit must need to set as per the desired output constraint from end customer to turn a research concept in an actual feasible product that can be easily implemented from a paper to application.

## References

- Abada S, Petit M, Lecocq A, Marlair G, Sauvart-Moynot V, Huet F (2018) Combined experimental and modeling approaches of the thermal runaway of fresh and aged lithium-ion batteries. *J Power Sources* 30(399):264–273
- Al- M, Dincer I, Rosen MA (2017) Novel thermal management system using boiling cooling for high-powered lithium-ion battery packs for hybrid electric vehicles. *J Power Sources* 30(363):291–303
- Al- M, Dincer I, Rosen MA (2017) Novel thermal management system using boiling cooling for high-powered lithium-ion battery packs for hybrid electric vehicles. *J Power Sources* 363:291–303. <https://doi.org/10.1016/j.jpowsour.2017.07.06>
- An Z, Jia L, Ding Y, Dang C, Li X (2017) A review on lithium-ion power battery thermal management technologies and thermal safety. *J Therm Sci* 26(5):391–412
- An Z, Shah K, Jia L, Ma Y (2019) Modelling and analysis of thermal runaway in Li-ion cell. *Appl Therm Eng* 1(160):113960
- Bamdezh MA, Molaeimanesh GR (2020 May) Impact of system structure on the performance of a hybrid thermal management system for a Li-ion battery module. *J Power Sources* 1(457):227993
- Bamdezh MA, Molaeimanesh GR, Zanganeh S (2020) Role of foam anisotropy used in the phase-change composite material for the hybrid thermal management system of lithium-ion battery. *J Energy Storage* 1(32):101778
- Bandhauer TM, Garimella S, Fuller TF (2011) A critical review of thermal issues in lithium-ion batteries. *J Electrochem Soc* 158:R1
- Behi H, Karimi D, Behi M, Ghanbarpour M, Jaguemont J, Sokkeh MA, Gandoman FH, Berecibar M, Van Mierlo J (2020) A new concept of thermal management system in Li-ion battery using air cooling and heat pipe for electric vehicles. *Appl Therm Eng* 25(174):115280
- Blanco S (2013) Tesla Model S catches fire near Seattle, no injuries reported. *Autoblog*. <https://www.autoblog.com/2013/10/02/tesla-model-s-fire>
- Blomgren GE (2017) The development and future of lithium ion batteries. *J Electrochem Soc* 164:A5019–A5025
- Bt10m Porsche up in flames as battery charging goes wrong (2018) *The Nation*, 16 Mar 2018. <https://www.nationthailand.com/news/30341102>
- Bugryniec PJ, Davidson JN, Brown SF (2018) Assessment of thermal runaway in commercial lithium iron phosphate cells due to overheating in an oven test. *Energy Procedia* 1(151):74–78
- Bukhari SM, Maqsood J, Baig MQ, Ashraf S, Khan TA (2015) Comparison of characteristics--lead acid, nickel based, lead crystal and lithium based batteries. In: 2015 17th UKSim-AMSS international conference on modelling and simulation (UKSim), IEEE, pp. 444–450
- Buonomo B, Ercole D, Manca O, Menale F (2018) Thermal cooling behaviors of lithium-ion batteries by metal foam with phase change materials. *Energy Procedia* 148:1175–1182. <https://doi.org/10.1016/j.egypro.2018.08.0>



- CGTN (2019) Tesla car catches fire in China, investigation underway. <https://news.cgtn.com/news/3d3d514d7a416a4d34457a6333566d54/index.html>
- Chen D, Jiang J, Kim G-H, Yang C, Pesaran A (2016) Comparison of different cooling methods for lithium-ion battery cells. *Appl Therm Eng* 94:846–854
- Chen J, Kang S, Jiaqiang E, Huang Z, Wei K, Zhang B, Zhu H, Deng Y, Zhang F, Liao G (2019) Effects of different phase change material thermal management strategies on the cooling performance of the power lithium ion batteries: a review. *J Power Sources* 1(442):227228
- Chen M, Lin S, Song W, Lv J, Feng Z (2020) Electrical and thermal interplay in lithium-ion battery internal short circuit and safety protection. *Int J Energy Res* 44(8):6745–6757
- Choi YS, Kang DM (2014) Prediction of thermal behaviors of an air-cooled lithium-ion battery system for hybrid electric vehicles. *J Power Sources* 270:273–280. <https://doi.org/10.1016/j.jpowsour.2014.07.12>
- Cosley MR, Garcia MP (2004) Battery thermal management system. Telecommunications Energy Conference, 2004. INTELEC 2004. 26th Annual International, IEEE
- Das A, Li D, Williams DK (2018) Joining technologies for automotive battery systems manufacturing. *World Electr Veh J* 9:22
- Deng T, Ran Y, Zhang G, Chen X, Tong Y (2019) Design optimization of bifurcating mini-channels cooling plate for rectangular Li-ion battery. *Int J Heat Mass Transf* 139:963–973. <https://doi.org/10.1016/j.ijheatmasstransfer>
- Effat MB, Wu C, Ciucci F (2016) Modeling efforts in the key areas of thermal management and safety of lithium ion battery cells: a mini review. *Asia-Pac J Chem Eng* 11(3):399–406. <https://doi.org/10.1002/apj.1999>
- Esho I, Shah K, Jain A (2018) Measurements and modeling to determine the critical temperature for preventing thermal runaway in Li-ion cells. *Appl Therm Eng* 25(145):287–294
- Etacheri V, Marom R, Elazari R, Salitra G, Aurbach D (2011) Challenges in the development of advanced Li-ion batteries: a review. *Energy Environ Sci* 4:3243–3262
- Fathabadi H (2014) High thermal performance lithium-ion battery pack including hybrid active-passive thermal management system for using in hybrid/electric vehicles. *Energy* 1(70):529–538
- Feng X, Zheng S, He X, Wang L, Wang Y, Ren D, Ouyang M (2018) Time sequence map for interpreting the thermal runaway mechanism of lithium-ion batteries with LiNi<sub>x</sub>CoyMnzO<sub>2</sub> cathode. *Front. Energy Res.* 6:126. <https://doi.org/10.3389/fenrg.2018.00126>
- Feng X, Ouyang M, Liu X, Lu L, Xia Y, He X (2018) Thermal runaway mechanism of lithium ion battery for electric vehicles: a review. *Energy Storage Mater* 1(10):246–267
- Finegan DP, Scheel M, Robinson JB, Tjaden B, Di Michiel M, Hinds G, Brett DJ, Shearing PR (2016) Investigating lithium-ion battery materials during overcharge-induced thermal runaway: an operando and multi-scale X-ray CT study. *Phys Chem Chem Phys* 18(45):30912–30919
- Finegan DP et al (2017) Identifying the cause of rupture of Li-ion batteries during thermal runaway. *AdvSci* 1700369. <https://doi.org/10.1002/advs.201700369>
- George S (2018) Keith Ritter Bower, <http://www.hybridcars.com/bmw-and-lg-chem-trump-tesla-in-battery-thermal-management> [Accessed 27 Feb 2018]. Google Scholar
- Giuliano MR, Prasad AK, Advani SG (2012) Experimental study of an air-cooled thermal management system for high capacity lithium–titanate batteries. *J Power Sources* 216:345–352. <https://doi.org/10.1016/j.jpowsour.2012.05.07>
- Greatbatch W, Holmes CF, Takeuchi ES, Ebel SJ (1996 Nov) Lithium/carbon monofluoride (Li/CFx): a new pacemaker battery. *Pacing Clin Electrophysiol* 19(11):1836–1840
- Hall JC, Koch M (1982) Studies Leading to the Development of High-Rate Lithium Sulfuryl Chloride Battery Technology. Gould research center rolling meadows IL materials Lab
- Harish S, Jeyanthi S, Abinash M, Suresh Kumar R, Agarwal S, Venkatachalam G (2021) Study of thermal behavior of Aluminium foams in batteries of electric vehicles. *IOP Conf Series: Mater Sci Eng* 1128(1):012042. <https://doi.org/10.1088/1757-899x/1128/1/012042>
- Hekmat S, Molaeimanesh GR (2020) Hybrid thermal management of a Li-ion battery module with phase change material and cooling water pipes: an experimental investigation. *Appl Therm Eng* 5(166):114759

- Holzman DC (2005) Driving up the cost of clean air *Environ. Health Perspect* 113:A246–A249
- Hotta T, Patil N (2018 Apr) A review on cooling of discrete heated modules using liquid jet impingement. *Frontiers Heat Mass Transfer (FHMT)* 21:11  
<https://www.powerstream.com/NiMH.htm>
- Hu M, Wang J, Fu C, Qin D, Xie S (2016 Jan 1) Study on cycle-life prediction model of lithium-ion battery for electric vehicles. *Int J Electrochem Sci* 11(1):577–589
- Huang KD, Tzeng SC, Chang WC (2005) Energy-saving hybrid vehicle using a pneumatic-power system. *Appl Energy* 81(1):1–8
- Huang L, Zhang Z, Wang Z, Zhang L, Zhu X, Dorrell DD (2019) Thermal runaway behavior during overcharge for large-format Lithium-ion batteries with different packaging patterns. *J Energy Storage* 1(25):100811
- Huang L, Liu L, Lu L, Feng X, Han X, Li W, Zhang M, Li D, Liu X, Sauer DU, Ouyang M (2021) A review of the internal short circuit mechanism in lithium-ion batteries: inducement, detection and prevention. *Int J Energy Res* 45(11):15797–15831
- Huber C, Kuhn R (2015) Thermal management of batteries for electric vehicles. *Adv Battery Technol Electric Vehicles* 327–358
- Javani N, Dincer I, Naterer GF, Yilbas BS (2014) Exergy analysis and optimization of a thermal management system with phase change material for hybrid electric vehicles. *Appl Therm Eng* 64(1–2):471–482
- Jiaqiang E, Han D, Qiu A, Zhu H, Deng Y, Chen J, Peng Q et al (2018) Orthogonal experimental design of liquid-cooling structure on the cooling effect of a liquid-cooled battery thermal management system. *Appl Therm Eng* 132:508–520. <https://doi.org/10.1016/j.applthermaleng.2017>
- Jin L, Tian J, Gao S, Xie P, Akbarzadeh M, Kalogiannis T, Berecibar M, Lan Y, Hu D, Ding Y, Qiao G (2021) A novel hybrid thermal management approach towards high-voltage battery pack for electric vehicles. *Energy Convers Manage* 1(247):114676
- Jindal P, Bhattacharya J (2019) Understanding the thermal runaway behavior of Li-Ion batteries through experimental techniques. *J Electrochem Soc* 166(10):A2165
- Jindal P, Kumar BS, Bhattacharya J (2021) Coupled electrochemical-abuse-heat-transfer model to predict thermal runaway propagation and mitigation strategy for an EV battery module. *J Energy Storage* 1(39):102619
- Johnson CS, Dees DW, Mansuetto MF, Thackeray MM, Vissers DR, Argyriou D, Loong CK, Christensen L (1997) Structural and electrochemical studies of  $\alpha$ -manganese dioxide ( $\alpha$ -MnO<sub>2</sub>). *J Power Sources* 68(2):570–577
- Jow TR, Delp SA, Allen JL, Jones JP, Smart MC (2018) Actors limiting Li+ charge transfer kinetics in li-ion batteries. *J Electrochem Soc* 165:A361–A367
- Kalnaus S, Wang H, Watkins TR, Kumar A, Simunovic S, Turner JA, Gorney P (2018) Effect of packaging and cooling plates on mechanical response and failure characteristics of automotive Li-ion battery modules. *J Power Sources* 403:20–26. <https://doi.org/10.1016/j.jpowsour.2018.09.07>
- Katoch SS, Eswaramoorthy M (2020) *IOP Conf Ser: Mater Sci Eng* 912:042005
- Ke L, Wang Y, Hu Y (2015) Safety design of power bank based on standard. *Autom Inf Eng* 36:45–48
- Keyser M, Pesaran AA, Oweis S, Chagnon G, Ashtiani C (1999) Thermal evaluation and performance of highpower lithium-ion cells. In: *Proceedings of the 16th international electric vehicle symposium, Beijing, China*
- Khateeb SA, Farid MM, Selman JR, Al- S (2004) Design and simulation of a lithium-ion battery with a phase change material thermal management system for an electric scooter. *J Power Sources* 128(2):292–307
- Kim GH, Pesaran A, Spotnitz R (2007 Jul 10) A three-dimensional thermal abuse model for lithium-ion cells. *J Power Sources* 170(2):476–489
- Kim J, Shin J, Chun C (2012) Stable configuration of a Li-ion series battery pack based on a screening process for improved voly-age /SOC balancing. *IEEE Trans Power Electron* 27:411–424

- Kim J, Oh J, Lee H (2019) Review on battery thermal management system for electric vehicles. *Appl Therm Eng* 25(149):192–212
- Kong D, Wang G, Ping P, Wen J (2021) Numerical investigation of thermal runaway behavior of lithium-ion batteries with different battery materials and heating conditions. *Appl Therm Eng* 5(189):116661
- Kshetrimayum KS, Yoon YG, Gye HR, Lee CJ (2019) Preventing heat propagation and thermal runaway in electric vehicle battery modules using integrated PCM and micro-channel plate cooling system. *Appl Therm Eng* 1(159):113797
- Kurhade A, Talele V, Rao TV, Chandak A, Mathew VK (2021) Computational study of PCM cooling for electronic circuit of smart-phone. *Mater Today: Proc* 1(47):3171–3176
- Kurhade A, Talele V, Rao TV, Chandak A, Mathew VK (2021) Computational study of PCM cooling for electronic circuit of smart-phone. *Mater Today: Proc*
- Lai X, Jin C, Yi W, Han X, Feng X, Zheng Y, Ouyang M (2020) Mechanism, modeling, detection, and prevention of the internal short circuit in lithium-ion batteries: recent advances and perspectives. *Energy Storage Mater*
- Lambert F (2017) Tesla Model S fire vs 35 firefighters—watch impressive operation after a high-speed crash. *Electrek*, 18 October 2017. <https://electrek.co/2017/10/18/tesla-model-s-fire-high-speed-crash-video-impressive-operation/>
- Lee CH, Bae SJ, Jang M (2015) A study on the effect of lithium-ion battery design variables upon features of thermal-runaway using mathematical model and simulation. *J Power Sources* 20(293):498–510
- Leising RA, Palazzo MJ, Takeuchi ES, Takeuchi KJ (2001) Abuse testing of lithium-ion batteries: characterization of the overcharge reaction of LiCoO<sub>2</sub>/graphite cells. *J Electrochem Soc* 148(8):A838–A844
- Lewerenz M, Käbitz S, Knips M, Münnix J, Schmalstieg J, Warnecke A, Sauer DU (2017) New method evaluating currents keeping the voltage constant for fast and highly resolved measurement of Arrhenius relation and capacity fade. *J Power Sources* 15(353):144–151
- Li WQ, Qu ZG, He YL, Tao YB (2014) Experimental study of a passive thermal management system for high-powered lithium ion batteries using porous metal foam saturated with phase change materials. *J Power Sources* 255:9–15
- Li R, Zhang H, Li W, Zhao X, Zhou Y (2020) Toward group applications: a critical review of the classification strategies of lithium-ion batteries. *World Electric Vehicle J* 11:58. <https://doi.org/10.3390/wevj11030058>
- Liang J et al (2017) Investigation on the thermal performance of a battery thermal management system using heat pipe under different ambient temperatures. *Energy Convers Manage*
- Liang J et al (2017) Investigation on the thermal performance of a battery thermal management system using heat pipe under different ambient temperatures. *Energy Convers Manage*
- Liaw BY, Roth EP, Jungst RG, Nagasubramanian G, Case HL, Doughty DH (2003) Correlation of Arrhenius behaviors in power and capacity fades with cell impedance and heat generation in cylindrical lithium-ion cells. *J Power Sources* 1(119):874–886
- Lin Q, Yixiong T, Ruizhen Q, Zuomin Z, Youliang D, Jigiang W (1995) General safety considerations for high power Li/SOCl<sub>2</sub> batteries. *J Power Sources* 54(1):127–133
- Lisbona D, Snee T (2011) A review of hazards associated with primary lithium and lithium-ion batteries. *Process Saf Environ Protect* 89:434–442
- Liu W, Jia Z, Luo Y, Xie W, Deng T (2019 Nov) Experimental investigation on thermal management of cylindrical Li-ion battery pack based on vapor chamber combined with fin structure. *Appl Therm Eng* 5(162):114272
- Liu P, Liu C, Yang K, Zhang M, Gao F, Mao B, Li H, Duan Q, Wang Q (2020) Thermal runaway and fire behaviours of lithium iron phosphate battery induced by overheating. *J Energy Storage* 31. <https://doi.org/10.1016/j.est.2020.101714>
- Liu Y, Liao YG, Lai MC (2020) Lithium-ion battery cell modeling with experiments for battery pack design. *SAE Technical Paper*

- Lopez CF, Jeevarajan JA, Mukherjee PP (2015) Experimental analysis of thermal runaway and propagation in lithium-ion battery modules. *J Electrochem Soc* 162(9):A1905
- Lyu Y et al (2019) Electric vehicle battery thermal management system with thermoelectric cooling. *Energy Rep*
- Maleki H, Howard JN (2009) Internal short circuit in Li-ion cells. *J Power Sources* 191(2):568–574
- Mathew VK, Hotta TK (2018) Numerical investigation on optimal arrangement of IC chips mounted on a SMPS board cooled under mixed convection. *Therm Sci Eng Progress* 1(7):221–229
- Mathew VK, Hotta TK (2019 Dec) Role of PCM based mini-channels for the cooling of multiple protruding IC chips on the SMPS board-A numerical study. *J Energy Storage* 1(26):100917
- Mathew VK, Hotta TK (2020) Experiment and numerical investigation on optimal distribution of discrete ICs for different orientation of substrate board. *Int J Ambient Energy* 15:1–8
- Mathew VK, Hotta TK (2021) Experimental investigation of substrate board orientation effect on the optimal distribution of IC chips under forced convection. *Experiment Heat Transf* 34(6):564–585
- Mathew VK, Hotta TK (2021) Performance enhancement of high heat generating IC chips using paraffin wax based mini-channels-a combined experimental and numerical approach. *Int J Therm Sci* 1(164):106865
- May GJ, Davidson A, Monahov B (2018) Lead batteries for utility energy storage: a review. *J Energy Storage* 15:145–157. <https://doi.org/10.1016/j.est.2017.11.008>
- Menale C, Constà S, D'Annibale F, Scotini A, Sglavo V (2021) Experimental investigation of the overcharge effects on commercial li-ion batteries with two different anode materials. *Chem Eng Trans* 15(86):457–462
- Mendoza-Hernandez OS, Ishikawa H, Nishikawa Y, Maruyama Y, Umeda M (2015) Cathode material comparison of thermal runaway behavior of Li-ion cells at different state of charges including over charge. *J Power Sources* 15(280):499–504
- Morrison MM, Marincic N (1993) Studies in lithium oxyhalide cells for downhole instrumentation use of lithium tetrachlorogallate electrolyte in Li/SOCl<sub>2</sub> cells. *J Power Sources* 45(3):343–352
- Nagpure SC, Dinwiddie R, Babu S, Rizzoni G, Bhushan B, Frech T (2010) Thermal diffusivity study of aged Li-ion batteries using flash method. *J Power Sources* 195:872–876
- Panchal S, Dincer I, Agelin-Chaab M, Fraser R, Fowler M (2016) Thermal modeling and validation of temperature distributions in a prismatic lithium-ion battery at different discharge rates and varying boundary conditions. *Appl Therm Eng* 5(96):190–199
- Panchal S, Dincer I, Agelin-Chaab M, Fraser R, Fowler M (2016) Experimental and theoretical investigation of temperature distributions in a prismatic lithium-ion battery. *Int J Therm Sci* 1(99):204–212
- Panchal S, Dincer I, Agelin-Chaab M, Fraser R, Fowler M (2016) Experimental and theoretical investigations of heat generation rates for a water cooled LiFePO<sub>4</sub> battery. *Int J Heat Mass Transf* 1(101):1093–1102
- Park H (2013) A design of air flow configuration for cooling lithium ion battery in hybrid electric vehicles. *J Power Sources* 239:30–36. <https://doi.org/10.1016/j.jpowsour.2013.03.10>
- Patel JR, Rathod MK (2020) Recent developments in the passive and hybrid thermal management techniques of lithium-ion batteries. *J Power Sources* 31(480):228820
- Patil NG, Hotta TK (2018 Nov) Role of working fluids on the cooling of discrete heated modules: a numerical approach. *Sādhanā* 43(11):1–9
- Patil NG, Hotta TK (2021 Feb 1) Heat transfer characteristics of high heat generating integrated circuit chips cooled using liquid cold plate—a combined numerical and experimental study. *J Therm Sci Eng Appl* 13(1):011019
- Patil MS, Seo JH, Lee MY (2021) A novel dielectric fluid immersion cooling technology for Li-ion battery thermal management. *Energy Convers Manage* 1(229):113715
- Pearce JA (2015) Improving accuracy in arrhenius models of cell death: adding a temperature-dependent time delay. *J Biomech Eng* 137(12):121006
- Pham MTM, Darst JJ, Walker WQ, Heenan TMM, Patel D, Iacoviello F, Rack A, Olbinado MP, Hinds G, Brett DJL, Darcy E, Finegan DP, Shearing PR (2021) Prevention of lithium-ion battery

- thermal runaway using polymer-substrate current collector. *Cell Rep Phys Sci* 2:100360. <https://doi.org/10.1016/j.xcrp.2021.100360>
- Qin Z, Balasubramanian SK, Wolkers WF, Pearce JA, Bischof JC (2014) Correlated parameter fit of Arrhenius model for thermal denaturation of proteins and cells. *Ann Biomed Eng* 42(12):2392–2404
- Qin P, Liao M, Zhang D, Liu Y, Sun J, Wang Q (2019) Experimental and numerical study on a novel hybrid battery thermal management system integrated forced-air convection and phase change material. *Energy Convers Manage* 1(195):1371–1381
- Ramadass PH, Haran B, White R, Popov BN (2002) Capacity fade of Sony 18650 cells cycled at elevated temperatures: part i cycling performance. *J Power Sources* 112(2):606–613
- Ranjbaran YS, Haghparast SJ, Shojaeefard MH, Molaeimanesh GR (2020) Numerical evaluation of a thermal management system consisting PCM and porous metal foam for Li-ion batteries. *J Therm Anal Calorim* 141(5):1717–1739
- Ren D, Feng X, Lu L, Ouyang M, Zheng S, Li J, He X (2017) An electrochemical-thermal coupled overcharge-to-thermal-runaway model for lithium ion battery. *J Power Sources* 1(364):328–340
- Ren D, Feng X, Liu L, Hsu H, Lu L, Wang L, He X, Ouyang M (2021) Investigating the relationship between internal short circuit and thermal runaway of lithium-ion batteries under thermal abuse condition. *Energy Storage Mater* 1(34):563–573
- Sun P, Bisschop R, Niu H, Huang X A review of battery fires in electric vehicles
- Roth EP, Doughty DH (2004) Thermal abuse performance of high-power 18650 Li-ion cells. *J Power Sources* 128(2):308–318
- Saad KE, Oudah K (2022) Thermal management analysis of li-ion battery-based on cooling system using dimples with air fins and perforated fins. *Int J Therm Sci* 171:107200
- Safdari M, Ahmadi R, Sadeghzadeh S (2020 Feb) Numerical investigation on PCM encapsulation shape used in the passive-active battery thermal management. *Energy* 15(193):116840
- Safoutin M, Cherry J, McDonald J, Lee S (2015) Effect of current and SOC on round-trip energy efficiency of a lithium-iron phosphate (LiFePO<sub>4</sub>) battery pack. SAE Technical Paper
- Saito Y (2005) Thermal behaviours of lithium-ion batteries during high-rate pulse cycling. *J Power Sources* 146(1–2):770–774
- Saw LH, Ye Y, Tay AAO, Chong WT, Kuan SH, Yew MC (2016) Computational fluid dynamic and thermal analysis of Lithium-ion battery pack with air cooling. *Appl Energy* 177:783–792. <https://doi.org/10.1016/j.apenergy.2016.05.12>
- Scrosati B (2011) History of lithium batteries. *J Solid State Electrochem*
- Selman JR, Al S, Uchida I, Hirano Y (2001) Cooperative research on safety fundamentals of lithium batteries. *J Power Sources* 1(97):726–732
- Shen J, Wang Y, Yu G, Li H (2020) Thermal management of prismatic lithium-ion battery with minichannel cold plate. *J Energy Eng* 146(1):04019033. [https://doi.org/10.1061/\(asce\)ey.1943-7897.0000621](https://doi.org/10.1061/(asce)ey.1943-7897.0000621)
- Shunping JI, Hongqin PE, Shuang LI, Zhang X (2009) Review of transportation and energy consumption related research. *J Transp Syst Eng Inf Technol* 9(3):6–16.
- Song L (2018) Thermal performance analysis of the battery thermal management using phase change material *Open Access Libr*. J 5:1–13
- van der Steen M, Van Schelven RM, Kotter R, Van Twist MJ, Peter van Deventer MP (2015) EV policy compared: an international comparison of governments' policy strategy towards E-mobility. In: *E-mobility in Europe 2015*. Springer, Cham, pp 27–53
- Sun H, Dixon R (2014) Development of cooling strategy for an air cooled lithium-ion battery pack. *J Power Sources* 272:404–414. <https://doi.org/10.1016/j.jpowsour.2014.08.10>
- Sun Z, Fan R, Yan F, Zhou T, Zheng N (2019 Dec) Thermal management of the lithium-ion battery by the composite PCM-Fin structures. *Int J Heat Mass Transf* 1(145):118739
- Talele V, Thorat P, Gokhale YP, Mathew VK (2021) Phase change material based passive battery thermal management system to predict delay effect. *J Energy Storage* 44(Part B):103482, ISSN 2352–152X

- Tian X, Yi Y, Fang B, Yang P, Wang T, Liu P, Qu L, Li M, Zhang S (2020) Design strategies of safe electrolytes for preventing thermal runaway in lithium ion batteries. *Chem Mater* 32(23):9821–9848
- Two-way nonlinear mechanical-electrochemical-thermal coupled analysis method to predict thermal runaway of lithium-ion battery cells caused by quasi-static indentation (2020). *J Power Sources* 475:228678
- Valøen LO, Shoesmith MI (2007) The effect of PHEV and HEV duty cycles on battery and battery pack performance (PDF). 2007 Plug-in Highway Electric Vehicle Conference: Proceedings. Retrieved 11 June 2010
- Wang J, Liu P, Hicks-Garner J, Sherman E, Soukiazian S, Verbrugge M, Tataria H, Musser J, Finamore P (2011) Cycle-life model for graphite-LiFePO<sub>4</sub> cells. *J Power Sources* 196(8):3942–3948
- Wang Z, Yang H, Li Y, Wang G, Wang J (2019) Thermal runaway and fire behaviors of large-scale lithium ion batteries with different heating methods. *J Hazard Mater* 5(379):120730
- Wang D, Zheng L, Li X, Du G, Zhang Z, Feng Y, Jia L, Dai Z (2020) Effects of overdischarge rate on thermal runaway of NCM811 Li-Ion batteries. *Energies* 13(15):3885. <https://doi.org/10.3390/en13153885>
- Wang CJ, Zhu YL, Gao F, Qi C, Zhao PL, Meng QF, Wang JY, Wu QB (2020) Thermal runaway behavior and features of LiFePO<sub>4</sub>/graphite aged batteries under overcharge. *Int J Energy Res* 44(7):5477–5487
- Wang Z, Yuan J, Zhu X, Wang H, Huang L, Wang Y, Shiqi X (2021) Overcharge-to-thermal-runaway behavior and safety assessment of commercial lithium-ion cells with different cathode materials: a comparison study. *J Energy Chem* 55:484–498. <https://doi.org/10.1016/j.jechem.2020.07.028>
- Wang S, Yin Z, Zheng Z, Wang Y, Zou H, Yan Y (2020) A sorting method for retired battery modules based on voltage curves. In: Proceedings of the CSEE, Barcelona, Spain
- Wen C-G, Wang Y-Y, Feng W-F, Ma W-T (2018) Study of separation process of Li-battery based on multivariable data fitting. *Chin J Power Sources* 42:1480–1482
- Wilde S, Schweitzer B, Khateeb S, Al-S (2017) Preventing thermal runaway propagation in lithium ion battery packs using a phase change composite material: an experimental study. *J Power Sources* 1(340):51–59
- Wiriyasart S, Hommalee C, Sirikasemsuk S, Prurapark R, Naphon P (2020) Thermal management system with nanofluids for electric vehicle battery cooling modules. *Case Stud Therm Eng* 100583. <https://doi.org/10.1016/j.csite.2020.100583>
- Xia Y, Wierzbicki T, Sahraei E, Zhang X (2014a) Damage of cells and battery packs due to ground impact. *J Power Sources* 267:78–97
- Xia Y, Li T, Ren F, Gao Y, Wang H (2014b) Failure analysis of pinch–torsion tests as a thermal runaway risk evaluation method of Li-ion cells. *J Power Sources* 265:356–362
- Xia L, Huang Y, Lai Z, Wang et al (2019) Thermal analysis and improvements of the power battery pack with liquid cooling for electric vehicles. *Energies* 12(16):3045. <https://doi.org/10.3390/en12163045>
- Xu J, Lan C, Qiao Y, Ma Y (2017) Prevent thermal runaway of lithium-ion batteries with minichannel cooling. *Appl Therm Eng* 5(110):883–890
- Yang X, Duan Y, Feng X, Chen T, Xu C, Rui X, Ouyang M, Lu L, Han X, Ren D, Zhang Z (2020) An Experimental study on preventing thermal runaway propagation in lithium-ion battery module using aerogel and liquid cooling plate together. *Fire Technol* 56:2579–2602
- Yang T, Yang N, Zhang X, Li G (2016) Investigation of the thermal performance of axial-flow air cooling for the lithium-ion battery pack. *Int J Therm Sci*
- Yuan C, Wang Q, Wang Y, Zhao Y (2019) Inhibition effect of different interstitial materials on thermal runaway propagation in the cylindrical lithium-ion battery module. *Appl Therm Eng* 5(153):39–50
- Yue QL, He CX, Jiang HR, Wu MC, Zhao TS (2021 Jan) A hybrid battery thermal management system for electric vehicles under dynamic working conditions. *Int J Heat Mass Transf* 1(164):120528



- Yuksel T, Litster S, Viswanathan V, Michalek JJ Plug-in hybrid electric vehicle LiFePO<sub>4</sub> battery life implications of thermal management, driving conditions, and regional climate
- Zhang C, Santhanagopalan S, Sprague MA, Pesaran AA (2015) A representativesandwich model for simultaneously coupled mechanical-electric-thermal simulation of a lithium-ion cell under quasi-static indentation tests. *J Power Sources* 298:309–321
- Zhang M, Du J, Liu L, Stefanopoulou A, Siegel J, Lu L, He X, Xie X, Ouyang M (2017) Internal short circuit trigger method for lithium-ion battery based on shape memory alloy. *J Electrochem Soc* 164(13):A3038
- Zhang J, Zhang L, Sun F, Wang Z (2018) An overview on thermal safety issues of lithium-ion batteries for electric vehicle application. *Ieee Access*. 3(6):23848–23863
- Zhang L, Zhao P, Xu M, Wang X (2020) Computational identification of the safety regime of Li-ion battery thermal runaway. *Appl Energy* 1(261):114440
- Zhang W, Liang Z, Wu W, Ling G, Ma R (2021) Design and optimization of a hybrid battery thermal management system for electric vehicle based on surrogate model. *Int J Heat Mass Transf* 1(174):121318
- Zhao R, Zhang S, Liu J, Gu J (2015) A review of thermal performance improving methods of lithiumion battery electrode modification and TMS. *J Power Sources* 299:557–577
- Zhao R, Liu J, Gu J (2016) Simulation and experimental study on lithium-ion battery short circuit. *Appl Energy* 1(173):29–39
- Zhao C, Zhang B, Zheng Y, Huang S, Yan T, Liu X (2020) Hybrid battery thermal management system in electrical vehicles: a review. *Energies* 13(23):6257
- Zhao C, Zhang B, Zheng Y, Huang S, Yan T, Liu X (2020) Hybrid battery thermal management system in electrical vehicles: a review. *Energies* 13:6257. <https://doi.org/10.3390/en13236257>
- Zhu X, Wang H, Wang X, Gao Y, Allu S, Cakmak E, Wang Z (2020) Internal short circuit and failure mechanisms of lithium-ion pouch cells under mechanical indentation abuse conditions: an experimental study. *J Power Sources* 15(455):227939
- Zia MF et al (2019) Optimal operational planning of scalable DC microgrid with demand response, islanding, and battery degradation cost considerations. *Appl Energy*
- 文浩, 谢达明, 罗斌, 梁活开. 动力锂电池安全国家标准 GB/T 31485 与 IEC 62660-3 的比较. 收藏. 2018;11
- 杨桃, 邹海曙, 吉盛, 黄伟东. 富锂锰基锂正极材料和动力电池的性能研究. 电池工业. 2019;1:31–5

# Chapter 10

## Battery Thermal Management System for EVs: A Review



Amit Jomde, Prashant Patane, Anand Nadgire, Chetan Patil, Kshitij Kolas, and Virendra Bhojwani

### 10.1 Introduction

With the rapid reduction in fossil fuels, increasing crude oil prices, and environmental pollution, the demand for electric vehicles (EVs) and hybrid electric vehicles (HEVs), has been increasing significantly. Nowadays many countries are setting up policies and assist financially to support the development of EVs to overcome the demand and environmental pollution regulations on greenhouse gas (GHG) emissions [1–6] Keiner et al. (2019); Nazari et al. (2019); Chen et al. (2019a); Sun et al. (2020); Kim et al. (2019a). These policies show strong support for the healthy growth of EVs over this decade. According to Global EV Outlook 2021, with Sustainable Development Scenario, predicts that, the global EVs can reach up to 230 million vehicles excluding two and three wheelers by the end of this decade with a stock share of 12%. However, one of the critical challenges in developing EVs is a high-density energy storage system that could support fast charging, high mileage, and high-performance driving with lighter weight. Compared among all energy storage currently used, lithium-ion batteries are being widely used owing to their high energy density, high power capacity, low self-discharge rate, and long service life Smas et al. (2015); Lowe et al. (2010). The Li-ion batteries include Li-Co, Li-Fe, Li-Mn, and Li-NiCoMn batteries Vazquez-Arenas et al. (2014). These Li-ion batteries also do not have the memory effect. The memory effects are commonly found in nickel–metal hydride and nickel–cadmium batteries. The memory effect in the batteries occurs if the batteries are recharged continuously if it gets discharged partially which slowly

---

A. Jomde (✉) · P. Patane · A. Nadgire · C. Patil  
Dr. Vishwanath Karad, MIT World Peace University, Pune, India  
e-mail: [amit.jomde@mitwpu.edu.in](mailto:amit.jomde@mitwpu.edu.in)

K. Kolas  
Fraunhofer ENAS, Chemnitz, Germany

V. Bhojwani  
MIT Art, Design and Technology University, Pune, India



decreases the usable capacity of battery leading to reduced working voltage. These batteries suppressed the energy density of all earlier competing batteries, due to which these batteries are extensively used for automobiles.

However, thermal management and safety are still significant challenges in the development of lithium-ion batteries. The thermal management of the battery is more challenging with fast charging and high-performance driving as there is rapid heat generation. These Li-ion batteries' capacity, service life, performance, and safety are susceptible to temperature Bandhauer et al. (2011). The temperature change in any battery is inevitable as heat is released during charging and discharging due to chemical reactions, which highly depend on the rate of these processes Smith and Wang (2006). In addition to this, resistive heating also affects the thermal behavior of the batteries. The operating and even storage temperature can harm the performance and lifespan of batteries. The lower temperature will significantly reduce the battery capacity; however, the high temperature negatively impacts battery life and capacity. It is essential to study the characteristics of the specific battery to optimize its performance.

Generally, the operational temperature for EV batteries ranges from  $-40$  to  $60$  °C Ma et al. (2018). However, to obtain the EV's optimal performance and prolonged lifespan, the battery is to be operated in the range of  $15$  to  $35$  °C, and the temperature gradient within the battery pack needs to be maintained below  $5$  °C Kitoh and Nemoto (1999); Ramadass et al. (2002); Rugh et al. (2011). The operating temperature outside this range harms the performance of the battery. The lifespan of Li-ion batteries drops by two months for each temperature degree rise Zhao et al. (2015). In a hot climate without battery cooling, aggressive driving may decrease battery life by  $2/3$  Yuksel et al. (2017).

If a Li-ion battery is operated at a lower ambient temperature for a long term may also result in a considerable decrease in battery life due to dendrites formed on the battery's anode Friesen et al. (2016). Safety is the main concern in the large-scale Li-ion batteries, but the formation of lithium dendrites hampers the safe working of Li-ion batteries with graphite anodes Wang et al. (2017). The electrolytes react with lithium dendrites violently at higher temperature to generate gases which increase the internal pressure of the battery continuously leading to problems like electrolyte leakage and battery explosion. The growth of lithium dendrites destroys the thermal stability of solid electrolyte interphase (SEI) film. In addition, the reaction between electrolytes and lithium dendrites increases the decomposition of SEI films, reducing the thermal run away temperature of the battery Yamaki et al. (1998). The performance of Li-ion batteries is seriously affected if operated below subzero temperatures as their internal resistance increases drastically below  $-20$  °C, which ultimately leads to a reduction in their lifespan and performance Hu et al. (2020).

Another significant aspect of the battery safety is a thermal runaway, caused mainly by local overheating. Thermal runaway is a severe safety issue, which refers to an uncontrolled chain reaction in the battery that is very difficult to stop once started and may result in smoke, fire, and even explosion. The total heat released from the batteries of about  $12\%$  is sufficient to trigger thermal runaway in adjacent

batteries Feng et al. (2015). The local overheating due to mechanical, electrical, or thermal abuse can trigger the thermal runaway Feng et al. (2018).

Therefore, the battery thermal management system (BTMS) is essential for maintaining the appropriate temperature range, reducing the temperature gradient within the battery pack, and preventing thermal runaway. There are two main parameters to be considered to evaluate the performance of BTMS: the maximum temperature rise and temperature gradient within the battery pack. Numerous methods for BTMS have been proposed by researchers, which can be classified as shown in Fig. 10.1.

The pre-heating BTMSs are used to pre-heat the battery pack, which is used in cold operating conditions. In cold climates the performance of Li-ion batteries decreases leading to decrease in battery capacity, sudden increase in battery resistance, difficulty in charging and discharging and severe degradation leading to decrease in life cycle. Thus there is need of battery heating equipments to keep Li-ion batteries working satisfactorily under low temperature environment. There are three ways of battery heating: self-internal heating, convective heating, and mutual phase heating Khan et al. (2017). Self-internal heating is most simple and efficient and it gains the heat during battery charging and discharging. In convective heating method, the battery can be heated both internally and externally. In this methodology, the fan and resist heaters are used and heat generated by resist heaters is passed convectively using fan. The mutual phase heating method is rarely used and in this methodology the battery output power is used for heating itself Ji et al. (2013). Cooling BTMSs

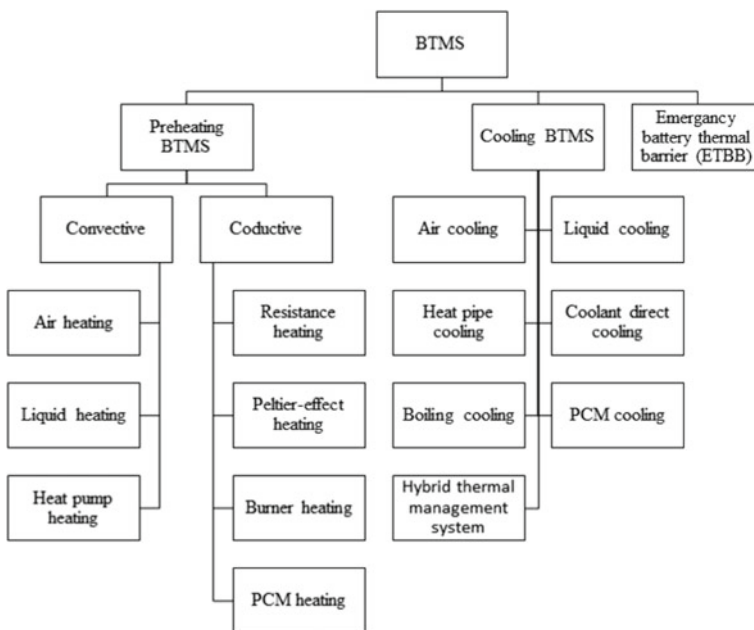


Fig. 10.1 Classification of BTMS

are used for effective cooling of the battery, operating at higher ambient temperature, whereas the ETBT are designed to suppress the potential hazard of the thermal runaway. This chapter presents the heat generation phenomenon, different and significant BTM systems available with pros and cons. In this chapter, the approach is to have qualitative analysis only; and the quantitative analysis can be a future scope.

## 10.2 Heat Generation in Batteries

Heat generation in batteries is a significant con of battery systems. Two types of heat generation occur in batteries: 1. Irreversible  $Q_{\text{irr}}$  (through resistance offered to flow of electrons), 2. Reversible  $Q_{\text{rev}}$  [through chemical reactions while charging/discharging] Arora et al. (2017). This phenomenon can be presented in equation format as

$$Q = Q_{\text{irr}} + Q_{\text{rev}}$$

where,

$$Q_{\text{irr}} = I^2 R_{\text{int}}; Q_{\text{rev}} = -IT * \frac{dE_{\text{ov}}}{dT}$$

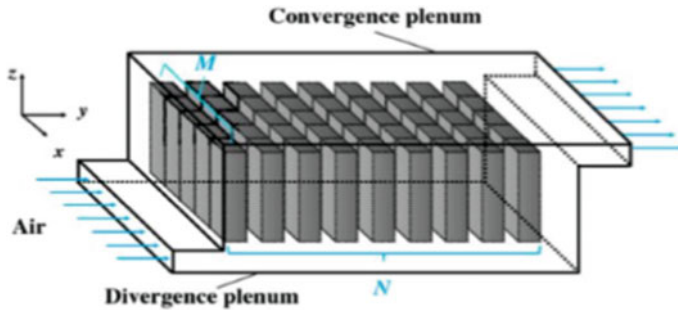
In these equations,  $I$  is current,  $R_{\text{int}}$  is internal resistance,  $T$  is temperature. The  $R_{\text{int}}$  is a function of SoC (state of charge) and temperature. Through many numerical and experimental analyses, it has been found that the heat generation in the batteries depends on multiple factors, out of which the significant factors are Current, Temperature, SoC, SoH (state of health), and Electrochemistry. One can find an ample amount of literature discussing the methods to reduce heat generation and strategies to increase the dissipation of heat generated from the batteries. While designing lithium-ion batteries, two significant parameters need to be considered, i.e., heat capacity and thermal conductivity Buidin and Mariasiu (2021); Kim et al. (2019b). The coming sections will discuss the methods to increase the dissipation of heat generated from batteries.

## 10.3 Air Cooling

Air-cooled BTM systems use air as a working fluid to cool the batteries. Many configurations of air-cooled BTMS are proposed till date depending upon the criteria mentioned in Table 10.1. Each configuration has its pros and cons, so one must select the best suitable configuration for a defined application. Battery conditioning, i.e., maintaining battery temperature, can be done by cooling or heating the battery and

**Table 10.1** Classification of the air-cooling system

SN.	Criteria for classification		Classification	
1	Air driving mechanism	Natural cooling	Forced cooling	
2	Source of air supplied	Active cooling	Passive cooling	
3	Cooling structure	Parallel cooling	Serial cooling	Mixed cooling
4	Contact type	Direct cooling	Indirect cooling	
5	Thermal cycle	BTMS with VCC	BTMS without VCC	



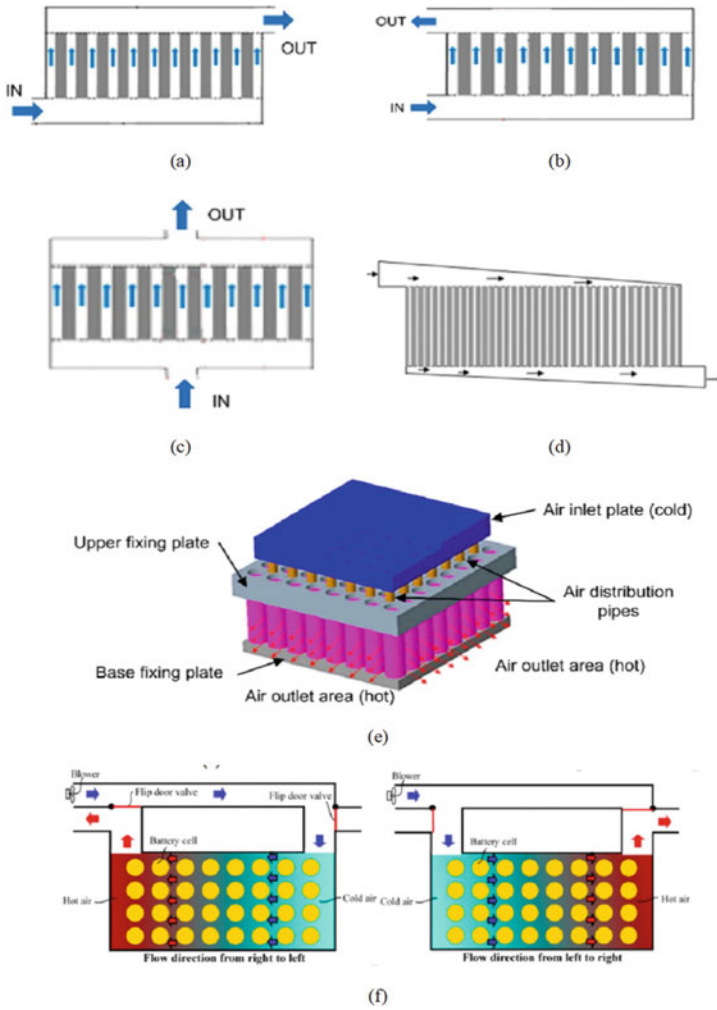
**Fig. 10.2** Typical air-cooled BTM system.

providing ventilation through the system Kim et al. (2019b); Lin et al. (2021a). The BTM systems using air as working fluid have the advantage that the same air maintains the ventilation. The typical air-cooled BTM system is shown in Fig. 10.2.

Various researchers presented many other air-cooled BTM systems [refer to Fig. 10.1] along with this typical system. The air-cooled BTM systems are simple in construction and are low-cost systems. Air’s heat carrying capacity is much less than most conventional liquids used for liquid-cooled BTM systems; hence liquid-cooled BTM systems have higher efficiency Lin et al. (2021a). The liquid BTM systems are discussed in the next section in detail (Fig. 10.3).

### 10.4 Liquid Cooling

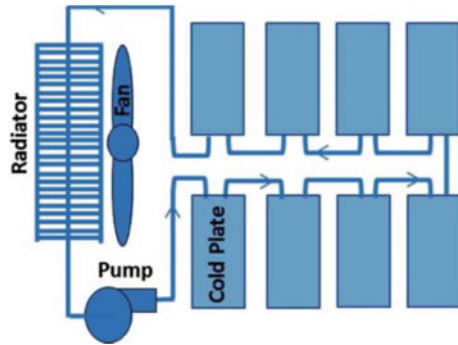
As discussed in the previous section, liquids have higher heat carrying capacity, and hence liquid-cooled systems perform better than air-cooled systems. These systems compact, achieve, maintain a low temperature, and are uniformly distributed. Because of all these advantageous characteristics, it has been accepted widely in electrical vehicle EV applications. With these pros, the liquid-cooled systems also have cons like; more weight, complex structure, leakage, and additional power for liquid circulation. Prismatic battery systems adopted liquid-cooled systems due to their simple construction compared to cylindrical battery systems. The most commonly used



**Fig. 10.3** Different air-cooled BTM systems; **a** Z type, **b** U type, **c** symmetrically modified type, **e** distribution pipe type, **f** reciprocating airflow type

working fluids are water and ethylene glycol. The indirect contact type liquid-cooled systems are preferred over direct contact type systems due to their more practical approach Lin et al. (2021a). The typical liquid-cooled BTM system is shown in Fig. 10.4.

**Fig. 10.4** Typical liquid-cooled BTM system  
Lin et al. (2021a)



## 10.5 Phase Change Material Cooling

The load on batteries goes on increasing day by day; thus, the BTMS is using multi-channel liquid cooling loops as a powerful cooling technique. However, this technique is complex and consumes more power. So to overcome these difficulties, cooling using phase change material (PCM) is one of the good options Sharma et al. (2009). The PCM is a promising alternative to conventional air and liquid cooling due to its easy coupling with passive cooling Buidin and Mariasiu (2021). The phase change material (PCM) technique is used in many industries to absorb or dissipate the heat through the phase change technique without energy consumption Elefsiniotis et al. (2014), Kuznik et al. (2011), Jaguemont et al. (2018). Sharma et al. (2015) have extensively investigated and classified phase change materials. There is a lot of different material available which can be used as PCM for the BTMS application. It includes organic materials such as organic acid, paraffin wax, and alkane, and some inorganic materials such as salt hydrate, aqueous solution, and eutectic Chen et al. (2019b). The different PCM materials with the properties required for thermal management system are given in Table 10.2. The critical parameter that needs to be considered for PCM application to BTMS is selecting appropriate phase change material. The PCM chosen should have large heat carrying capacity, latent heat, thermal conductivity, and temperature range during phase change within the battery's operating temperature range. Also, the PCM must be non-toxic, stable chemically, and has a shallow sub-cooling effect during the process of freezing Jaguemont et al. (2018).

PCM stores or releases heat as its phase changes from one state to another at a particular temperature. The PCM schematic is used for battery cooling, as shown in Fig. 10.5 by Kim et al. (2019b). As shown in Fig. 10.1, the cells are in direct contact with the phase change material (PCM), and these are solid material blocks either modeled or machined such that the cells can be inserted easily. Four plates surround the PCM, one on the top and bottom side each and one on the right and left side each, which is used to release the heat gained by the PCM. A tremendous amount of heat generation occurs during the battery charging or discharging process. The heat generated is passed to phase change material, as they are in direct contact

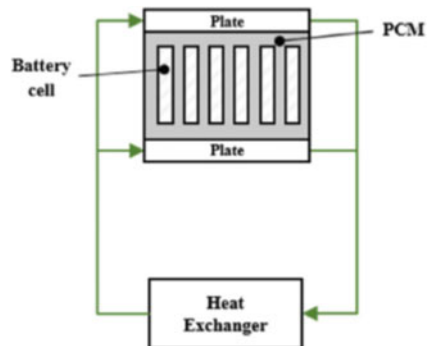
**Table 10.2** Different PCM materials with its characteristics

Property or characteristics	Paraffin wax	Non-paraffin organics	Metallics	Hydrated salts	Sugar alcohol	Polyethylene glycol
Heat of fusion	High	High	Medium	High	High	High
Thermal conductivity	Very Low	Low	Very high	High	High	High
Melt temperature (°C)	-20 to 100+	5 to 100+	150 to 800 +	0 to 100+	70 to 180	-50 to 62.5
Latent heat (kJ/kg)	200-280	90-250	25-100	60-300	290-350	105-183
Corrosive	Non corrosive	Mildly corrosive	Varies	Corrosive	Non-corrosive	Corrosive
Cost	Moderate cost	High cost	Costly	Low cost	Low cost	Low
Thermal cycling	Stable	At higher temperature, decomposition can take place	Stable	Unstable over repeated cycles	Stable	Stable
Weight	Medium	Medium	Heavy	Light	Medium	Medium

with the battery cells via conduction mode of heat transfer depending upon the temperature difference. The phase change material initially absorbs the heat as latent heat. As the phase change process starts, it absorbs a considerable amount of latent heat at a constant temperature and will absorb the heat until it reaches the melting point temperature. Thus, PCM can work under sudden battery temperature variation without sudden temperature rising and temperature unevenness Wilke et al. (2017).

Numerous research works have been carried out to enhance the low thermal conductivity of PCM Azizi et al. Azizi and Sadrameli (2016) developed a BTMS using wire mesh plates of aluminium and PCM to increase thermal efficiency conductivity. The wire mesh plates with higher voltage values are considered over the

**Fig. 10.5** Phase change material (PCM) cooling technique Kim et al. (2019b)



aluminium foams to quickly fill pores during PCM phase change. Yan et al. Yan et al. (2016) have designed and developed a sandwich model of PCM for the battery pack cooling. The PCM board has an excellent ability during normal and abusing conditions over normal air or cooling board. Yan et al. have also summarized that as the heat capacity of PCM increases, it also increases the rate of heat dissipation of the battery pack. Zhao et al. (2017b, 2018) used a compact structure of PCM cores into the cylindrical batteries, resulting in high heat transfer efficiency. It has been observed from the experimental result that such construction consumes less PCM and achieves a smaller rise in the temperature of the battery and higher temperature uniformity compared to external BTMS. A research carried out by Al-Hallaj et al. Kizilel et al. (2008) summarized that if a battery pack is working at 45 °C atmospheric temperature and 2C discharge rate, 90% PCM pack capacity can be utilized; however, 50% utilization can take place without PCM before the temperature of battery increased above safety limits. Paraffin wax as PCM is the most appropriate material. Still, it has the limitation of lower thermal conductivity as other phase change material Wang et al. (2015), i.e., it responds slowly during high-demand applications. Several studies are going on to enhance the thermal conductivity of PCM without disturbing their good properties. There are three ways to enhance PCM's thermal conductivity: first by using metal fins, second by using thermally conductive materials such as nano-powdered carbon, and third by using porous materials such as an expanded graphite matrix (EGM) Kim et al. (2019b). Though many efforts are taken to improve PCM's thermal conductivity, it is still challenging to use for automobile BTMS due to a few limitations like poor mechanical properties, leakage, and a very low heat transfer rate between PCM and the surroundings.

The use of BTMS shows a significant enhancement in the overall performance of BTMS. Due to its fluidity, the PCM technique improves thermal uniformity, like observed in the direct liquid cooling technique. In addition, the unique benefit of the PCM technique is that the energy utilization efficiency is higher due to the latent heat of PCM. The PCM is extensively used to pre-heat EVs for energy-saving Zhao et al. (2020). PCM technique is more flexible as the melting point of PCMs can be varied with various components. Thus, the BTMS can work well in different conditions by varying its melting point. The latent of PCM will help BTMS work in extreme cases for a more extended period. Thus, PCM is a practical approach over forced air cooling, and it simplifies the BTMS structure Kizilel et al. (2009). However, one of the difficulties of using only PCM for BTMS is that the PCM cannot be operated continuously because it may melt entirely due to hot environmental conditions or continuous charging and discharging of batteries Ling et al. (2015). Hence, an extra cooling system that can transfer the PCM heat to the surrounding is essential. Also, adding PCM mass increases the phase change completion time, improving the overall weight, and hampers EV performance. Therefore, the mass of PCM should be determined appropriately. Thus, the PCM technique is generally combined with active cooling methods to overcome these difficulties, gaining PCM's thermal energy storage capacity.



The conventional cooling systems like air-cooling BTMS require extra power and liquid-cooling BTMS requires complicated equipments to assure the effect. Therefore, PCM-based BTMS is nowadays becoming more popular. PCM-based cooling can absorb the heat and the battery pack temperature can be kept under normal working temperature range for longer duration without any external power supply. The PCM-based cooling system has simple structure and operation, no need of additional equipment, excellent temperature control performance without any energy consumption and low cost. PCM-based cooling can enhance the heat dissipation efficiency by using in combination with fillers like expanded graphite (EG) and metal foams for their higher thermal conductivity. In last few years, the trend on new energy development and environment protection has rapidly developed PCMs. The unique feature of PCM of keeping temperature constant during the phase change process, allows it be used for building and solar energy storage, thermal equipment management Alimohammadi et al. (2017), Dyer et al. (2002), Krishna et al. (2017), Alshaer et al. (2015), Salimpour et al. (2016) and other related fields. The large amount of phase change latent heat allows PCM to absorb and loose heat to work within the normal working temperature for longer duration. The use of PCM also reduces the temperature difference between each battery more efficiently. The rapid development in PCM since last few years the different composite PCMs has application in power battery packs and showed an effective solution to overheating of batteries and can maintain the temperature within 45° during discharging of battery.

In addition, the PCM shows very good performance of providing quick response to temperature and efficient control of temperature but still there are few difficulties that cannot be neglected such as low thermal conductivity, leaking problem, and lower strength. Many researchers used various techniques such as addition of fillers of higher thermal conductivity into the PCM or using PCM matrix impregnated with EG Mills and Al-Hallaj (2005) to overcome these difficulties. But still there are few difficulties to be overcome in the future like super cooling and is the major difficulty which will affect the thermal performance and PCMs stability and it is important to be improved and investigated further. Further the unbalanced requirement and availability of PCM, higher average cost of PCM and therefore how to manufacture PCM at lower cost is the major problem that needs to be addressed.

## 10.6 Hybrid Thermal Management System

The combined use of two or more basic BTMSs is considered a hybrid BTMS technique. The various basic BTMS has their benefits and limitations, respectively. The hybrid BTMS can use the help of basic BTMS and improve thermal performance Zhao et al. (2020). However, the hybrid BTMS has a few drawbacks with its energy consumption, volume, and weight Zhao et al. (2020). The hybrid BTMS is classified into different types and is listed in Table 10.3 and is discussed.

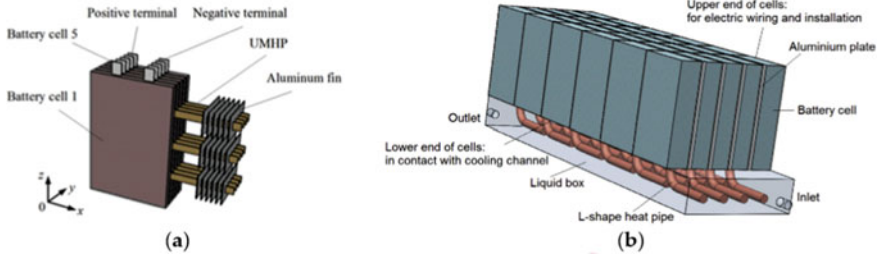
A hybrid BTMS is always shown higher thermal performance using higher power consumption but possesses a complex structure. In such systems, HP is always

**Table 10.3** The primary classification of hybrid BTMS

Sr. No.	Type	Hybrid BTMS
1	HP combined with either liquid or air cooling	HP + liquid
		HP + air PCM + HP
2	PCM combined with HP	CM + HP + Air PCM + HP + liquid
3	PCM combined with Liquid or air active cooling	PCM + liquid
		PCM + air
4	TEC combined with other BTMS	TEC + liquid + Air
		PCM + TEC
5	Liquid combined with air	Liquid + air

provided with forced-air cooling as shown in Fig. 10.6a and liquid cooling as shown in Fig. 10.6b. The HP coupled with forced-air cooling BTMS uses an ultra-thin micro heat pipe (UMHP) connected to a fan. In this the individual cell of the pack is numbered from cell 1 to 5 in y-direction. All the UMPH of sintered copper–water is fixed between the cell cavity and it forms a sandwiched like structure. There are total 3 groups of pipes with spacing in between in z-direction and all the groups have 4 pipes arranged parallel with spacing in y-direction. The heat generated by cells is conducted more efficiently; the evaporator of all the pipes is attached to the cell surface by using silicone. The cooling system is provided with air convection on each side of condenser pipe and aluminium fins with spacing in-between in x-direction and are attached to condenser pipe with silicone. It has been observed that the use of UMHP decreases the maximum temperature by 7.10 C from the starting of discharging at a 2C rate over without HP system. Also, the maximum temperature can be maintained below 400 C with 4 m/s speed Liu et al. (2016). As observed in Fig. 10.2b, the heat pipes are inserted into the cavity of each battery cell and condenser and evaporator of it is attached to aluminium plate for temperature flattening. Below the battery pack the liquid channel acts as a heat exchanger to supply and remove the heat from battery as per requirement. This will result in bi-directional advantage by the heat pipe so that system will provide either heating or cooling without moving parts.

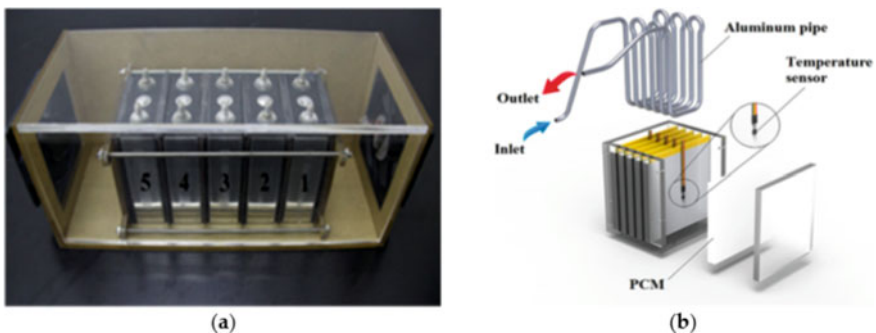
The BTMS using only PCM or composite PCM (CPCM) cannot maintain the battery pack temperature in a required range due to accumulation of heat caused due to poor natural air-cooling technique. Thus, active cooling methods are required to recover the thermal energy storage capacity of PCMs. Figure 10.7a shows a BTMS system that uses CPCM (expanded graphite/enhanced paraffin and copper mesh) and copper fins exposed from the CPCM to improve heat transfer rate Wu et al. (2016). The battery pack composed of 5 batteries and 6 CM-PCMP is arranged in a compact sandwich structure. All the batteries were arranged in series connection and a fan was used to such that the air flows into the channel from one side of pack. The two battery packs of same configurations with and without PCMP were assembled for comparison purpose. The experimental result shows that the CP-PCMP shows improved



**Fig. 10.6** Hybrid BTMS combined with **a** ultra-thin micro heat pipe and **b** liquid cooling Liu et al. (2016)

performance for dissipation of heat and temperature uniformity over PCMP and traditional ANC technology under harsh working environment. However, the BTMS shown in Fig. 10.3b uses PCM and cooling water pipes Hekmat and Molaeimanesh (2020). The experimental setup operates in three modes of active, passive, and hybrid with small modifications. The battery module consists of 5 prismatic Li-ion cells of  $148 \times 129 \times 4 \text{ mm}^3$  and 3.8 V normal voltage and of 5000 mA h nominal capacity. All the cells are held vertically in a glass box with 14 mm distance in-between them. Each cell surface is provided with sensor for temperature measurement. The cells are fixed in the module and are sealed and separate six zones are created for employing aluminium cooling pipes. Meanwhile, the zones can be filled with silicone oil or PCM or can be left with free air. It has been observed that, the use of silicone oil or PCM in-between cells decreases the maximum temperature to 450 C and 320 C respectively; however maximum temperature difference decreases to 5.10 C and 1.20 C respectively compared to atmospheric air. However, the BTMS shown in Fig. 10.7b uses PCM and cooling water pipes Hekmat and Molaeimanesh (2020).

Ling et al. have compared the battery’s performance with the PCM technique and PCM combined with forced air convection cooling Ling et al. (2015). The experimental setup has 20 Li-ion cells of cylindrical geometry with five and four cells in

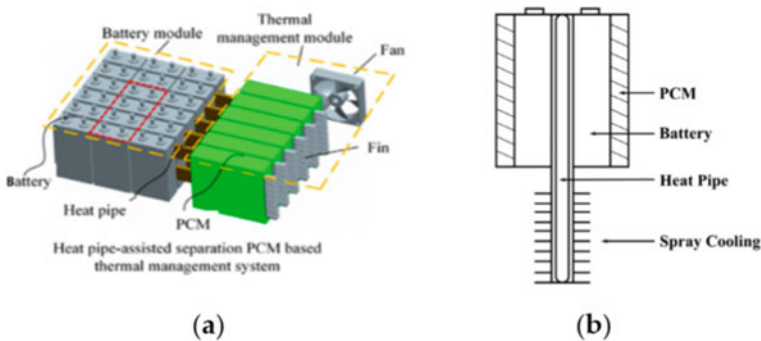


**Fig. 10.7** Hybrid BTMS using PCM with **a** air Wu et al. (2016) **b** liquid Hekmat and Molaeimanesh (2020)

series and parallels, respectively. They used RT44HC/expanded graphite (EG) with appropriate melting point temperature and high specific phase change enthalpy. It has been observed that the maximum temperature of the battery pack using PCM only increases above 60 °C in two cycles. However, PCM coupled with forced air convection cooling controlled the maximum temperature below 50 °C in all processes. Further, Wu et al. have studied the cooling performance of battery modules using para- fin/E.G. composites with pyrolytic graphite sheet (PGS) and without PGS by varying the convective heat transfer coefficient Wu et al. (2017). It has been observed that PCM with PGS module shows better temperature uniformity and heat dissipation performance for last charge/discharge cycles.

The PCM is easy to combine with hybrid BTMS, and PCM can enhance thermal uniformity Zhao et al. (2020). In a similar way of coupling the PCM with active cooling like air and liquid, HP can also be associated with the PCM because of its quick response and improved efficiency. The PCM can be filled between HP and HTF or battery cells, as shown in Fig. 10.8a Zhang et al. (2020). In this experimentation prismatic LiFePO4 batteries having capacity of 2.7 Ah are used. The battery pack has total 18 cells, 3 cells are arranged in parallel and 6 cells in series. The system is provided with a protection board to avoid overcharge or over discharge. Total 10 heat pipes are used in the system. The evaporation sections of heat pipes are placed in between every two batteries however the condenser is extended outside the battery pack and compactly placed with metal foams. In order to reduce the thermal contact resistance, the contact surface is coated with the layer of thermally conductive adhesives. It has been observed that, the maximum temperature of battery pack without auxiliary fan with 1C, 3C, and 4C discharge rates are under 45 °C. Also at higher discharge rate of 5 °C, the maximum temperature difference can be controlled within 5 °C.

Lei et al. (2020) coupled PCM, spray cooling, and HP to control the battery pack’s temperature, as shown in Fig. 10.8b. In this hydrated salt is for battery thermal management and is filled in and around the batteries. The hydrated salt is used due to its high specific latent heat, appropriate melting point, and large density. It has been

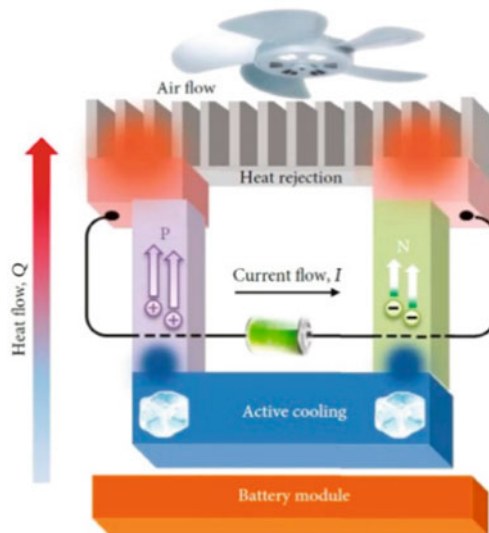


**Fig. 10.8** Hybrid BTMS **a** HP provided with PCM as BTMS. Zhang et al. (2020), **b** HP provided with PCM associated with spray cooling Lei et al. (2020)

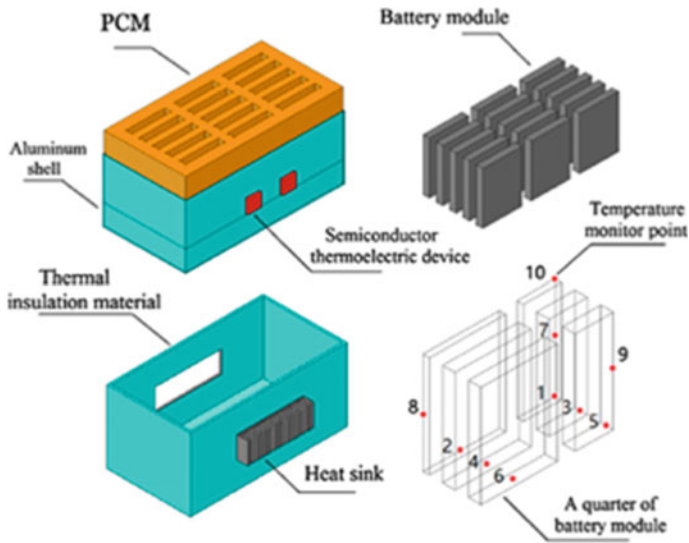
observed that, this technique holds the battery surface temperature rise below  $8\text{ }^{\circ}\text{C}$ , at a discharge current of  $24\text{ A}$  and a high atmospheric temperature ( $40\text{ }^{\circ}\text{C}$ ).

Zhao et al. (2017a) tested the PCM and heat pipe (HP) coupled BTM module experimentally. It has been observed that PCM and HP as a BTMS can maintain the maximum temperature below  $50\text{ }^{\circ}\text{C}$  for a more extended period compared to air and PCM-based BTMS techniques. Hemery et al. Hémerly et al. (2014) designed and developed a PCM and active liquid coupled hybrid BTMS to cool the melted PCM. They used the two water-cooled plates above and below the PCM in the experimentation's aluminum cans. The electric heaters are used instead of cells. It has been observed that PCM was completely solidified when the battery charging was done at a  $2\text{C}$  rate after discharge three driving cycles where the temperature of the water was maintained constant at  $22\text{ }^{\circ}\text{C}$ .

Thermoelectric cooling (TEC) is not generally considered for BTM of EV because of its poor efficiency. But it is mainly used in electronics cooling applications due to its compact construction Zhao et al. (2020). Few of the researchers have coupled TEC with hybrid BTMS for improving the rate of heat transfer. Figure 10.9 shows the typical layout of TEC coupled with hybrid BTMS Li et al. (2019). Lyu et al. Lyu et al. (2019) have coupled the TEC with active cooling techniques. The condenser side heat is transferred using TEC, and the forced air helps the TEC pass the heat to the outer side. It has been observed that the battery surface temperature reduces by  $12\text{ }^{\circ}\text{C}$  from  $55\text{ }^{\circ}\text{C}$ . Song et al. Song et al. (2018) designed and developed a BTMS for standby batteries with thermoelectric semiconductor device coupled with PCM, as shown in Fig. 10.10. The experimental setup was tested to study the heat preservation time (4.15 days), cooling time (14 h) circularly under atmospheric temperature ( $323\text{ K}$ ).



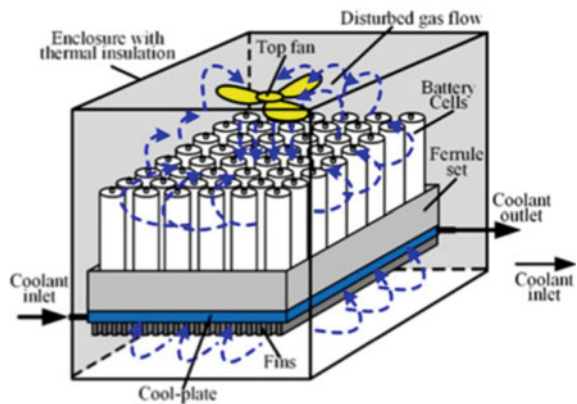
**Fig. 10.9** The schematic layout of TEC in hybrid BTMS Li et al. (2019)



**Fig. 10.10** The hybrid BTMS of PCM coupled with TEC Lyu et al. (2019)

Some of the researchers used forced-air and liquid cooling technique simultaneously. Wang et al. designed a BTMS, as shown in Fig. 10.11, by combining an LCP and the gas circle Wang et al. (2017). They studied the effect of various structures, the intensity of the liquid and gas cycles on the thermal performance of BTMS. It has been observed that the system with a fan under LCP could make a fully developed flow field. Compared to cooling with LCP only in the vacuum-packed battery, the maximum temperature and temperature difference are lowered by 3.88 and 3.45 K under the condition of total heat generation of 576 W.

**Fig. 10.11** The schematic of liquid coupled with air BTMS Wang et al. (2017)

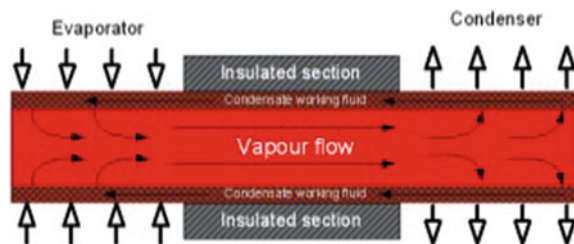


## 10.7 Heat Pipe Cooling

Temperature is the most critical parameter which directly affects battery efficiency. The BTM system is a system which ensures the overall performance of the battery along with its life, reliability and prevents economic loss. This is the best system to control the temperature of battery thermal management systems and has lightweight, portable size, flexible geometry, and low cost. This is a passive system because it does not consume power. The heat pipe is a heat conduction device that usually works by keeping the partial vacuum in the casing and transporting the maximum heat even at minimal temperature differences. An aluminum fin to the heat pipe section efficiently enhanced the heat dissipation rate. The utilization of heat pipe has migrated into various applications because of its wide range of working temperature. It is expanded in various sectors to invent a more structured system that improves thermal efficiency. The enhancement in the efficiency of heat pipes containing the Nanofluids can be increased because of having a high heat transfer rate compared to conventional fluids. In this case, efficiency is depending on the type of nanoparticles and their concentrations. But for a certain application, it may create complexities for high-temperature applications. Thermal conductivity is the most important parameter to enhance the heat transfer performance of a fluid. The flat, micro heat pipe reduces weight, high heat flow density, space and improves the heat transfer rate when subjected to forced convection and better temperature uniformity. Figure 10.12 shows the working of a heat pipe.

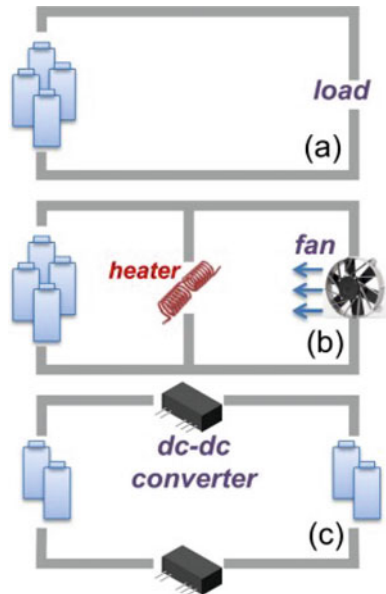
The different phase change materials are used in lithium-ion battery along with a heat pipe such as paraffin copper foam, paraffin, EG composite, meliorate paraffin with composite paraffin with nanoparticles, carbon fiber, Cu mesh, refrigerant R404a, paraffin expanded graphite, and hydrated salt is the coupled cooling methods, i.e., heat pipe cooling method Lin et al. (2021a). Because of the higher thermal conductivity, the heat transfer rate of the heat pipes is more efficient than the phase change material. It works on the pooled effect of phase change and thermal conductivity. They generate heat transferred to the heat pipe through the battery's modules and then absorbed by the phase change material. In the system, the heat source is coupled to the evaporator section. The operating fluid moved to the condenser by absorbing heat from the heating side. The working fluid condenses in the condenser with the help of an external heat exchanger, i.e., it can be air or liquid and finally comes to the evaporator section. This system doesn't require an external power source as it's an utterly natural

**Fig. 10.12** Heat pipe working cycle Jouhara et al. (2017)





**Fig. 10.13** Heating strategies using battery power **a** self-internal heating, **b** convective heating, **c** mutual pulse heating Ji and Wang (2013)



circulation method. Still, this method's disadvantage is that it cannot be adequately cooled during the discharge of the cycle.

In some cases, forced convection cooling should be applied to have better cooling performance. Heat pipe cooling methods have excellent heat transfer efficiency work on the principle of evaporation. For better thermal performance, the BTM module uses air to control the temperature by changing air velocity. The coolant flow rate also enhances the performance of the heat pipe. In recent years pulsating pipe or oscillating heat pipe gives the high thermal performance. It is combined with a multi-physical system to control the temperature and its optimum range, i.e., from 20 to 45 °C, ensuring low battery temperature for long-time cycling Zhao et al. (2020).

The comparison between the basic and hybrid battery thermal management techniques is given in Tables 10.4 and 10.5 respectively.

## 10.8 Battery Heating Strategies

The temperature variation inside the battery is the critical parameter in the battery's overall performance, life, and reliability. Lithium ion batteries play a crucial role as a power source in the electric vehicle field due to their high-power density. At low temperatures, its performance is drastically degraded because of low diffusivity and poor conductivity, and finally, it tends to damage the battery life. There are various strategies of battery heating methods shown in Fig. 10.1. These strategies are essential for the functioning of an effective battery management system. In the



**Table 10.4** Comparison between basic BTMSs

System characteristics		Air	Liquid (direct)	Liquid (indirect)	PCM	CPCM	Heat pipe
Cooling capacity		Very small	High	Medium	Very small	Small	Medium
Energy consumption		Low	High	Medium	None	None	None
Temperature distribution		Uneven	Uneven	Uneven	Even	Even	Uneven
Size		Large	Medium	Compact	Large	Large	Compact
Weight		Light	Heavy	Medium	Heavy	Heavy	Light
Complexity		Simple	Medium	Complex	Medium	Medium	Simple
Cost		Low	Medium	Medium	Low	Medium	High
Reliability		High	Medium	Medium	Very low	Low	High
Adaptability	Cylindrical	Easy	Moderate	Difficult	Easy	Easy	Difficult
	Prismatic	Moderate	Difficult	Easy	Easy	Easy	Easy
	Pouch	Moderate	Difficult	Easy	Moderate	Moderate	Easy

**Table 10.5** Comparison between hybrid BTMSs

System characteristics		PCM + Air	PCM + Liquid	HP + air	HP + liquid	PCM + HP + air
Cooling capacity		Medium	High	High	Very high	High
Energy consumption		Low	Medium	Low	Medium	Low
Temperature distribution		Even	Even	Uneven	Uneven	Even
Size		Large	Very large	Large	Medium	Very large
Weight		Heavy	Very heavy	Light	Medium	Heavy
Complexity		Medium	Complex	Medium	Complex	Very complex
Cost		Medium	High	High	Very high	High
Reliability		Low	Very low	High	Medium	Low
Adaptability	Cylindrical	Easy	Easy	Difficult	Difficult	Easy
	Prismatic	Easy	Easy	Easy	Moderate	Easy
	Pouch	Moderate	Moderate	Easy	Moderate	Moderate

convective heating strategy method, battery heat both internally and externally. The power source, i.e., fan, produces a convective flow, and this heating process occurs. It requires the battery, cell, fan, and other components in a closed-loop system Ji et al. (2013). The air or liquid can be used for convective heat transfer. Heat creation occurs in the self-internal heating process while the charging and discharging process heats the cell through internal resistance. Heating performance can be improved by adjusting the frequency and amplitude through pulse charging and discharging.

In some cases, heat generation devices are used in batteries such as nickel foil for heating purposes. The heating performance can be increased from  $-20$  to  $0$  °C in 12.5 s without consuming more battery energy. These can be achieved by using suitable electrolytes and modified anode material to restore the thermal performance of the battery. There are four criteria for heating strategy evaluations: electric energy consumption or driving range, heating time, the durability of the battery, and overall system cost. So different heating strategies can be compared with the above four criteria. The convective heating process takes minimum time for heating, and mutual pulse heating requires the least battery capacity.

Battery degradation, cost, enhancement of thermal performance, and durability are the most critical factors in the electric battery. The main objective of the battery is to work efficiently for the stated period for different operating ambient temperatures. The experimental implementation and verification of all strategies will be a challenging task in the future.

## 10.9 Conclusions

The objective of the chapter is to discuss different BTM systems and their pros and cons; the following qualitative conclusions can be drawn based on the literature available.

1. Air-cooled BTM systems are simple in construction and cheap too, but those are low efficient.
2. The liquid-cooled BTM systems are also more efficient and compact, but these are heavy and have leakage issues.
3. The PCM cooling technique is a good choice for BTMS as it can absorb battery heat at a constant temperature with a minimal amount of energy consumption. However, the significant hurdles of PCM are its low thermal conductivity, leakage, and battery heat load management after complete phase change of PCM. The composite PCM can overcome these hurdles and requires further investigations.
4. Hybrid BTMS is an emerging trend in developing BTM systems, and it has shown great potential and feasibility, specifically for extreme working environments. Hybrid BTMS are more flexible and efficient and can overcome the hurdles of basic BTMS.

## References

- Alimohammadi M, Aghli Y, Alavi E, Sardarabadi M, Passandideh-Fard M (2017) Experimental investigation of the effects of using nano/phase change materials (NPCM) as coolant of electronic chipsets, under free and forced convection. *Appl Therm Eng* 111:271–279
- Alshaer W, Nada S, Rady M, Le Bot C, Del Barrio E (2015) Numerical investigations of using carbon foam/PCM/Nano carbon tubes composites in thermal management of electronic equipment. *Energy Convers Manag* 89:873–884
- Arora S, Shen W, Kapoor A (2017) Critical analysis of open circuit voltage and its effect on estimation of irreversible heat for Li-ion pouch cells. *J Power Sources* 350:117
- Azizi Y, Sadrameli SM (2016) Thermal management of a LiFePO<sub>4</sub> battery pack at high-temperature environment using a composite of phase change materials and aluminum wire mesh plates. *Energy Convers Manag* 128:294–302
- Bandhauer TM, Garimella S, Fuller TF (2011) A critical review of thermal issues in lithium-ion batteries. *Electrochem Soc* 158:1–25
- Buidin TIC, Mariasiu F (2021a) <https://doi.org/10.3390/en14164879>
- Chen J, E J, Kang S, Zhao X, Zhu H, Deng Y, Peng Q, Zhang Z (2019a) Modeling and characterization of the mass transfer and thermal mechanics of the power lithium manganate battery under charging process. *Energy* 187:115924–115924
- Chen J, Kang S, Jiaqiang E, Huang Z, Wei K, Zhang F, Zhang B, Zhu H, Deng Y, Liao G (2019b) Effects of different phase change material thermal management strategies on the cooling performance of the power lithium-ion batteries: a review. *J Power Sources* 442:227,228–227,228
- Dyer C (2002) Fuel cells for portable applications. *J Power Sources* 106:31–34
- Elefsiniotis A, Becker T, Schmid U (2014) Thermoelectric energy harvesting using phase change materials (PCMs) in high temperature environments in aircraft. *Electron Mater* 43:1809–1814
- Feng X, Ouyang M, Liu X, Lu L, Xia Y, He X (2018) Thermal runaway mechanism of lithium ion battery for electric vehicles: a review. *Energy Storage Mater* 10:246–267
- Feng X, Sun J, Ouyang M, Wang F, He X, Lu L, Peng H (2015) Characterization of penetration induced thermal runaway propagation process within a large format lithium ion battery module. *J Power Sources* 275
- Friesen A, Horsthemke F, Mönninghoff X, Brunklus G, Krafft R, Börner M, Risthaus T (2016) F.M. Impact of cycling at low temperatures on the safety behavior of 18650-type lithium ion cells: combined study of mechanical and thermal abuse testing accompanied by post-mortem analysis. *J Power Sources* 334:1–1
- Hekmat S, Molaieimaneh GR (2020) Hybrid thermal management of a Li-ion battery module with phase change material and cooling water pipes: an experimental investigation. *Appl Therm Eng* 166:114759–114759
- Hémery CV, Pra F, Robin JF, Marty P (2014) Experimental performances of a battery thermal management system using a phase change material. *Power Sources* 270:349–358
- Hu X, Zheng Y, Howey DA, Perez H, Foley A, Pecht M (2020) Battery warm-up methodologies at subzero temperatures for automotive applications: recent advances and perspectives. *Prog Energy Combust Sci* 77–77
- Jaguemont J, Omar N, Bossche PVD, Mierlo JV (2018) Phase-change materials (PCM) for automotive applications: a review *Appl Therm Eng* 132:308–320
- Ji Y, Chao Y, Wang (2013) Heating strategies for Li-ion batteries operated from subzero temperatures. *Electrochimica Acta* 107:664–674
- Jouhara H, Chauhan A, Nannou T, Almahmoud S, Delpech B, Wrobel LC (2017) Heat pipe-based systems —advances and applications, vol 128. *Energy* Katoch SS, Eswaramoorthy M (2020) IOP ConfSer: Mater Sci Eng 912:42005–42005
- Keiner D, Ram M, Barbosa LDSNS, Bogdanov D, Breyer C (2019) Cost optimal self-consumption of PV prosumers with stationary batteries, heat pumps, thermal energy storage and electric vehicles across the world up to 2050. *Sol Energy* 185:406–423
- Khan M, Swierczynski M, Kaer S (2017) Batteries 3:9

- Kim J, Oh J, Lee H (2019a) Review on battery thermal management system for electric vehicles. *Appl Therm Eng* 149:192–212
- Kim J, Oh J, Lee H (2019b) Review on battery thermal management system for electric vehicles. *Appl Therm Eng* 149:192–212
- Kitoh K, Nemoto H (1999) 100 Wh large size Li-ion batteries and safety tests. *J Power Sources* 887–890
- Kizilel R, Lateef A, Sabbah R, Farid MM, Selman JR, Al-Hallaj S (2008) *J Power Sources* 183:370–370
- Kizilel R, Sabbah R, Selman JR, Al-Hallaj S (2009) An alternative cooling system to enhance the safety of Li-ion battery packs. *J Power Sources* 194:1105–1112
- Krishna J, Kishore P, Solomon A (2017) *Exp Therm Fluid Sci.* 81:84–92
- Kuznik F, David D, Johannes K, Roux JJ (2011) A review on phase change materials integrated in building walls. *Renew Sustain Energy Rev* 15:379–391
- Lei S, Shi Y, Chen G (2020) A lithium-ion battery-thermal-management design based on phase-change-material thermal storage and spray cooling. *Appl Therm Eng* 168:114792–114792
- Li X, Zhong Z, Luo J, Wang Z, Yuan W, Zhang G, Yang C, Yang C (2019) Experimental investigation on a thermoelectric cooler for thermal management of a lithium-ion battery module. *Int J Photoenergy* 1–10
- Lin J, Liu X, Li S, Zhang C, Yang S (2021a) A review on recent progress, challenges and perspective of battery thermal management system. *Int J Heat Mass Transf* 167
- Ling Z, Wang F, Fang X, Gao X, Zhang Z (2015) A hybrid thermal management system for lithium-ion batteries combining phase change materials with forced-air cooling. *Appl Energy* 148:403–409
- Liu F, Lan F, Chen J (2016) Dynamic thermal characteristics of heat pipe via segmented thermal resistance model for electric vehicle battery cooling. *J Power Sources* 321:57–70
- Lowe M, Tokuoka S, Trigg T, Gereffi G (2010) Lithium-ion batteries for electric vehicles. Governance and Competitiveness: the U.S. Value Chain
- Lyu Y, Siddique ARM, Majid SH, Biglarbegian M, Gadsden SA, Mahmud S (2019) Electric vehicle battery thermal management system with thermo-electric cooling. *Energy Rep* 5:822–827
- Ma S, Jiang M, Tao P, Song C, Wu J, Wang J, Deng T, Shang W (2018) Temperature effect and thermal impact in lithium-ion batteries: a review. *Prog Nat Sci Mater Int* 28:653–666
- Mills A, Al-Hallaj S (2005) Simulation of passive thermal management system for lithium-ion battery packs. *J Power Sources* 141:307–315
- Nazari F, Rahimi E, Mohammadian A (2019) Simultaneous estimation of battery electric vehicle adoption with endogenous willingness to pay. *ETransportation* 1:100088
- Ramadass P, Haran B, White R, Popov BN (2002) Capacity fade of Sony 18650 cells cycled at elevated temperatures: Part I. Cycling performance. *J Power Sources* 112:606–613
- Rugh JP, Pesaran A, Smith K (2011) Electric vehicle battery thermal issues and thermal management techniques (presentation); NREL. Golden, CO, USA
- Salimpour M, Kalbasi R, Lorenzini G (2016) Constructal multi-scale structure of PCM-based heat sinks. *Contin Mech Therm* 29:477–491
- Sharma A, Tyagi VV, Chen CR, Buddhi D (2009) Review on thermal energy storage with phase change materials and applications. *Renew Sustain Energy Rev* 13:318–345
- Sharma RK, Ganesan P, Tyagi MHSCV, Sandaran SC (2015) Developments in organic solid-liquid phase change materials and their applications in thermal energy storage. *Energy Convers Manag* 95:193–228
- Smas, Bukhari J, Maqsood MQ, Baig S, Ashraf TA, Khan (2015) Comparison of characteristics-lead acid, nickel based, lead crystal and lithium based batteries. In: 17th UKSIM-AMSS International Conference on Modelling and Simulation IEEE Model Simul
- Smith K, Wang CY (2006) Power and thermal characterization of a lithium-ion battery pack for hybrid-electric vehicles. *Power Sources* 160:662–673

- Song W, Bai F, Chen M, Lin S, Feng Z, Li Y (2018) Thermal management of standby battery for outdoor base station based on the semiconductor thermoelectric device and phase change materials. *Appl Therm Eng* 137:203–217
- Sun P, Bisschop R, Niu H, Huang X, Pan YW, Hua Y, Zhou S, He R, Zhang Y, Yang S, Liu X, Lian Y, Yan X, Wu B (2020) A computational multi-node electro-thermal model for large prismatic lithium-ion batteries. *J Power Sources* 459:228070–228070
- Vazquez-Arenas J, Gimenez LE, Fowler M, Han T, Chen SK (2014) A rapid estimation and sensitivity analysis of parameters describing the behavior of commercial Li-ion batteries including thermal analysis. *Energy Convers Manage* 87:472–472
- Wang Z, Zhang Z, Jia L, Yang L (2015) Paraffin and paraffin/aluminum foam composite phase change material heat storage experimental study based on thermal management of Li-ion battery. *Appl Therm Eng* 78:428–436
- Wang S, Li Y, Li Y, Mao Y, Zhang Y, Guo W, Zhong M (2017) A forced gas cooling circle packaging with liquid cooling plate for the thermal management of Li-ion batteries under space environment. *Appl Therm Eng* 123:929–939
- Wilke S, Schweitzer B, Khateeb S, Al-Hallaj S (2017) Preventing thermal runaway propagation in lithium ion battery packs using a phase change composite material: An experimental study. *Power Sources* 340:51–59
- Wu W, Wu W, Wang S (2017) Thermal optimization of composite PCM based large format lithium-ion battery modules under extreme operating conditions. *Energy Convers Manage* 153:22–33
- Wu W, Yang X, Zhang G, Ke X, Wang Z, Situ W, Li X, Zhang J (2016) An experimental study of thermal management system using copper mesh-enhanced composite phase change materials for power battery pack, vol 113. *Energy*
- Yamaki J, Tobishima S, Hayashi K, Saito K, Nemoto Y, Arakawa M (1998) *J Power Sources* 74(2):219–227
- Yan J, Wang Q, Li K, Sun J (2016) Numerical study on the thermal performance of a composite board in battery thermal management system. *Appl Therm Eng* 106:131–131
- Yuksel T, Litster S, Viswanathan V, Michalek J (2017) Plug-in hybrid electric vehicle LiFePO<sub>4</sub> battery life implications of thermal management, driving conditions, and regional climate. *J Power Sources* 338:49–49
- Zhang W, Qiu J, Yin X, Wang D (2020) A novel heat pipe assisted separation type battery thermal management system based on phase change material. *Appl Therm Eng* 165:114571–114571
- Zhao R, Gu J, Liu J (2015) An experimental study of heat pipe thermal management system with wet cooling method for lithium ion batteries. *J Power Sources* 273:1089–1097
- Zhao J, Lv P, Rao Z (2017a) Experimental study on the thermal management performance of phase change material coupled with heat pipe for a cylindrical power battery pack. *Exp Therm Fluid Sci* 82:182–188
- Zhao R, Gu J, Liu J (2018) Performance assessment of a passive core cooling design for cylindrical lithium-ion batteries. *Int J Energ Res* 42:2728–2728
- Zhao R, Gu J, Liu J (2017b) Optimization of a phase change material based internal cooling system for cylindrical Li-ion battery pack and a hybrid cooling design. *Energy* 811
- Zhao C, Zhang B, Zheng Y, Huang S, Yan T, Liu X (2020) Hybrid battery thermal management system in electrical vehicles: a review. *Energies* 2020, 13:6257

# Chapter 11

## Design and Development of a Water-Cooled Proton Exchange Membrane Fuel Cell Stack for Domestic Applications



Justin Jose, Rincemon Reji, and Rajesh Baby

### 11.1 Introduction

Energy production, storage and conversion are the buzz words today in the global energy scenario and will be the focus in the coming years also. The ever-decreasing fossil fuel reserves is the main triggering factor in the development of renewable energy technologies. Energy technologies, that are replenishable on use are generally termed as renewable energy source. These energy sources like wind, solar are highly reliable if they are distributed over a large geographical location. Moreover, these technologies are highly helpful in stabilizing energy prices at the global level. Many of the renewable technologies with few or no moving parts makes operation cost at lower levels. Clamor for reducing the carbon footprint globally is also a motivating factor for the countries to switch to new and renewable energy sources and technologies.

In the recent past, due to advances in the hydrogen storage and handling, fuel cell technology is very popular and widely used. It can be used in both stationary and portable power applications as well as transportation sector. Fuel cells work similar to batteries without consuming the electrode and these cells are capable of producing electricity as long as the fuel (hydrogen or a source of hydrogen) and oxidizer (air or oxygen) is available. Efficient, quiet and no harmful emissions (only heat and water), in comparison with internal combustion engines are the reasons for the wide acceptance of fuel cells globally. Often times, a single fuel is incapable of producing the required power output and this necessitates the use of fuel cell stacks.

Many researchers worked extensively on fuel cell stacks and in this chapter, focus is given on Proton Exchange Membrane Fuel Cell (PEMFC) stacks. Luo et al. (2019) experimentally studied on PEM fuel cell stack employed air cooling. They found that distribution of temperature in the cells is greatly affected by the cooling air flow

---

J. Jose · R. Reji · R. Baby (✉)

Department of Mechanical Engineering, St. Joseph's College of Engineering and Technology,  
Palai, Kottayam, Choondacherry P.O., Kerala 686579, India

e-mail: [rajeshbaby@sjcetpalai.ac.in](mailto:rajeshbaby@sjcetpalai.ac.in)

and uneven water distribution. Syampurwadi et al. (2017) studied the influence of number of cells and stack on the fuel cell performance. In this study, experiment was conducted in two steps. In the first step, the gas flow rate is varied and the number of cells was kept constant at one. Subsequently, number of cells was varied. When the number of cells is on increase, current density also increased, thereby causing an increase in fuel cell temperature. Due to the increase in temperature, the performance of the cell was increased but the risk of failure was also on increase. Chen et al. (2016) developed a 2 kW, 4 cell high power air cooled PEMFC stack. Youssef et al. (2018) developed and analyzed performance of PEMFC stack based on different bipolar plate designs. The maximum power output is 70 W from 11 cell stack. Karthikeyan et al. (2014) conducted experiments on PEMFC based on various flow channel design for an active area of 25 cm<sup>2</sup> and 70 cm<sup>2</sup>, for single and two cell stacks. The flow channel with Landing:Channel (L:C) ratio of 1:1 gives maximum output for all cases compared to all other flow channels. Wan et al. (2014) measured the temperature on each cell of a 5 k W PEMFC stack by using situ temperature measurement technique using 36 T-type thermocouples. Due to temperature difference across each cell of the stack, it is found that the overall performance was decreased. Neto et al. (2013) developed and described the thermal and experimental characterization of 1 k W PEMFC stack which contains 24 cells.

Zhang et al. (2010) developed a 100 W PEM fuel cell and tested at elevated temperature under various humidity. It was found that adequate anode humidification is indispensable for elevated temperature of PEMFC. Wen et al. (2009) studied and compared the effects of clamping on the performance of a single cell and a ten-cell PEMFC stack. From the experiment, they found that power density is proportional to the bolt number, when the clamping torque is same. The mix of 6-bolt with 16 Nm clamping torque gave maximum power output. Kim and Hong (2008) discussed the effect of humidity and temperature on 10 stack PEM fuel cell. Compared to change in temperature, change in humidity is seriously affected by the performance of fuel cell. Chen and Zhou (2008) explained the steady and dynamic behavior of commercial 10 stack PEM fuel cell. The pressure drop signal is used to predict the power. Yim et al. (2008) operated 40 W PEM fuel cell under low humidifying condition. Husar et al (2007) explained failure of 7 stack PEM fuel cell due to gasket degradation. Leakage of reactants causes the degradation and other issues in the gaskets and as a result a dip in performance of fuel cells is found. Yan et al. (2007) studied on unsteady characteristics of PEM FC during dynamic loading. In dynamic loading, air stoichiometry, humidity, loading rates are significantly influencing the temperature inside the fuel cell.

Santarelli et al. (2007) studied the variations in the electrical performance of a PEMFC stack under the influence of different cathode flow rates. Water flooding is the major issue in PEM fuel cell when air stoichiometry value decreases. The current density increases with increase in air stoichiometry value due to the higher rate of electrochemical reaction. Higher rate of electrochemical reaction will increase the cell temperature and this in turn will reduce the flooding effect. Park and Li (2006) analyzed the performance of PEMFC stack under different flow rates and operating temperatures. From their results it is very clear that the effect of temperature is more

significant than the flow rate. Rodatz et al. (2004) developed 6 kW, 100 cell PEM stack and studied the operational aspects of stack under practical conditions. The major issues in large fuel cell are uneven flow distributions of the reactant gases and non-uniform temperature distribution due to the leakage of membrane. The membrane leaks due to hot spots, as well as large pressure difference. Scholta et al (2004) developed and tested 10 kW PEMFC stack. In order to achieve cost reduction, a stack concept using graphite composite bipolar plates was developed. Johnson et al (2001) assembled a 3-kW cell and tested under different loading conditions as well as carried out a thermodynamic analysis. Murphy et al. (1998) analyzed a light weight PEM fuel cell stack. For manufacturing of fuel cell parts, they used a metal conductive element together with nonconductive elements fabricated from thermoplastics through an inexpensive mass production technique. The maximum power output from the cell was 520 W.

Siddiqui and Dincer (2019) developed a direct ammonia fuel cell stack. Authors improved energy and exergy efficiencies of fuel cells at higher humidifier temperatures. Zhang and Kandlikar (2012) presented a review on various cooling techniques in PEMFC stacks. They reviewed the pros and cons of heat spreaders, liquid and air cooling. Details of phase change cooling were also presented. In comparison with air cooling, water cooling is very much effective to counter the variation in temperature across different cells in the stack.

From the proceeding review, it is clear that many investigators were studied in detail, about fuel cell stacks employing air and water cooling. As water cooling is very efficient in comparison with the air-cooling strategies, the present chapter, details of the design, fabrication and testing of a water-cooled PEMFC stack employing 10 cells each having an active area of 50 cm<sup>2</sup>. Usually, detailed description of the design and fabrication is missing in most of the literature, but in this chapter the relevant details of the components used, including the design and fabrication of the water plate, details of mono polar and bipolar plates, gaskets, current collector, flow channels, arrangement of major components used and so on are described for the benefit of researchers in this area.

## 11.2 Design and Fabrication Details of PEMFC Stack

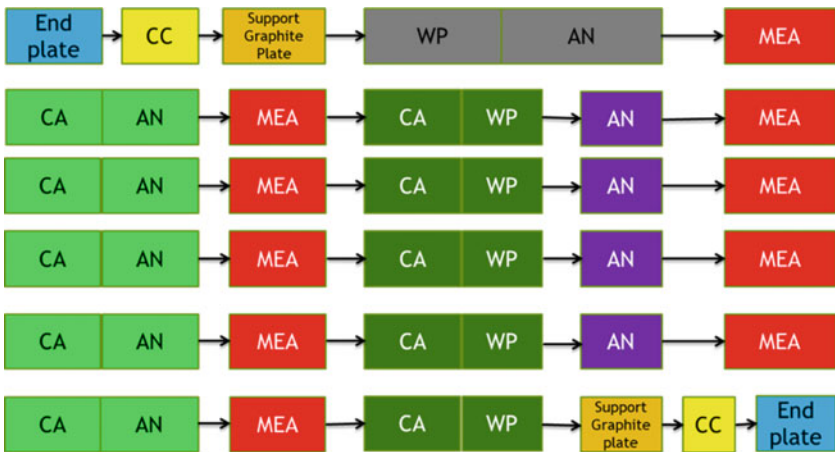
The details regarding the design of various components in the fuel cell stack and the fabrication details are given in this section. Table 11.1 gives the details of the major components used in the development of the PEMFC stack in the present study. Schematic arrangement of the major components used in the PEMFC stack is shown in Fig. 11.1.

Details of the design and fabrication of some of the major components are explained in the following section.



**Table 11.1** Details of the major components used in the PEMFC stack

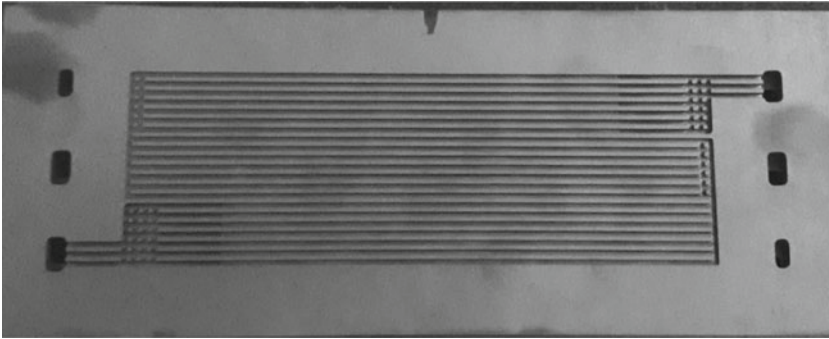
Sl. No	Name of the component	Represented in Fig. 11.1	Quantity (nos.)
1	Membrane electrode assembly	MEA	10
2	End plate	Endplate	2
3	Current collector	CC	2
4	Cathode with water plate	CA-WP	5
5	Bipolar plates	CA-AN	5
6	Water plate with anode	WP-AN	1
7	Monopolar (anode)	AN	4
8	Support graphite plate	Support graphite plate	2



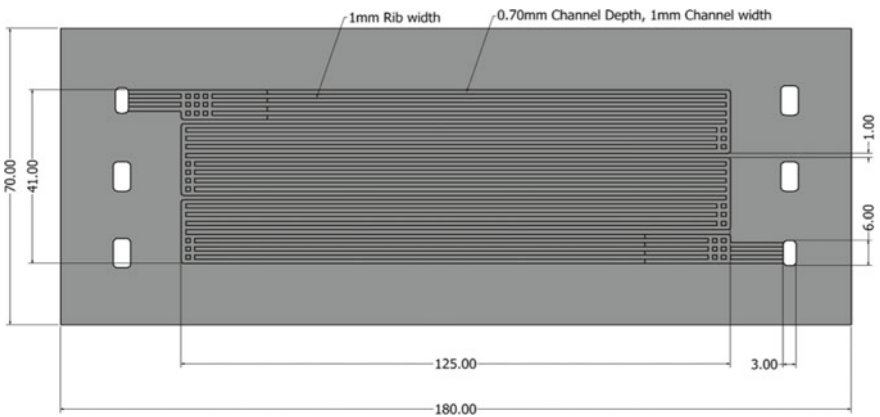
**Fig. 11.1** Schematic arrangement of major components used in the development of the PEMFC stack

### 11.2.1 Design and Fabrication of Cathode Flow Channel

Figure 11.2 shows a photograph of the cathode 3 pass serpentine flow channel. The channel to landing ratio for this flow channel is 1:1. The channels are made on the graphite plate by Computer Numerical Control (CNC) machining. Generally, the graphite material is used for the manufacturing of flow channels due to the high



**Fig. 11.2** A photograph of cathode 3 pass serpentine flow channel



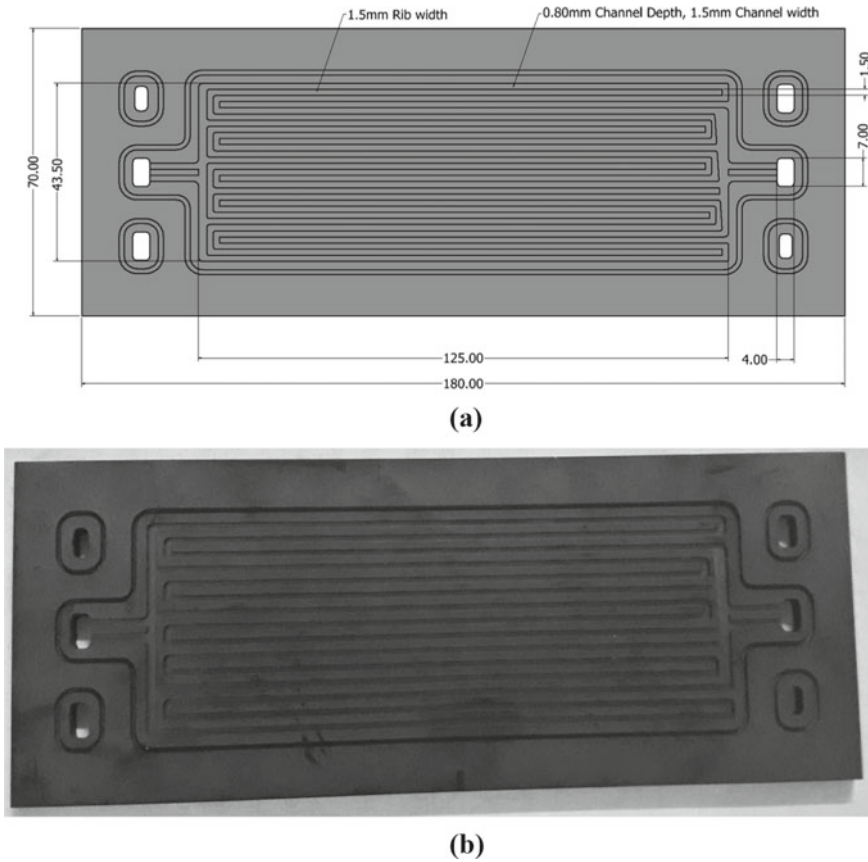
**Fig. 11.3** Design of anode 5 pass flow channel

machinability and less corrosiveness. On the other side of the cathode plate contain water channel.

Figure 11.3 shows details of anode 5 pass flow channel. The plate is having an overall dimensions of 180 mm × 70 mm. The flow field is with dimensions of 125 mm x 41 mm. The channel to landing ratio is kept at 1:1. The channel depth is 0.70 mm. These are also made of graphite plate by CNC machining process.

### 11.2.2 Design and Fabrication of Water Plate

Figure 11.4a shows the detailed design of the water plated used in fuel cell. Water plates will be useful for the effective flow of cooling water. Due to the reactions occurring in the fuel cell, temperature build up is present and it can deteriorate the performance of the fuel cell. Also, for the working of the fuel cell initially, hot water



**Fig. 11.4** a Design of water plate used in the present study. b A photograph of water plate used in the present study

is supplied through the water channel. The channel to landing (rib width) ratio used for this flow channel is 1:1. The channel width is 1.5 mm and the rib width is 1.5 mm. The channel depth is 0.80 mm. A photograph of the water plate used in the present study is shown in Fig. 11.4b.

### 11.2.3 Nafion Membrane Preparation

Commercially available Nafion 115 membrane is treated before the use in PEMFC. The pre-treatment is done using a standard procedure:

- (1) The membrane is boiled in 5 wt%  $\text{H}_2\text{O}_2$  solution at 80 °C for 1 h
- (2) Rinsed with de-ionized (DI) water at 80 °C for 1 h

- (3) Boiling membrane in 0.5 M H<sub>2</sub>SO<sub>4</sub> at 80 °C for 1 h
- (4) Rinsing with DI water at 80 °C for 1 h.

### ***11.2.4 Catalyst Layer Fabrication***

Catalyst fabrication is done using colloidal procedure based on the modification of the Photoetch methods. The procedure of modified Photoetch method is as described below:

- (1) Sulfite complexes of Pt are decomposed by hydrogen peroxide at 80–90 °C to form aqueous colloidal solution of Pt.
- (2) The colloidal Pt particles are absorbed on carbon black to form the catalyst.
- (3) Any amorphous oxide formed is reduced in Hydrogen steam.

### ***11.2.5 Membrane Electrode Assembly (MEA)***

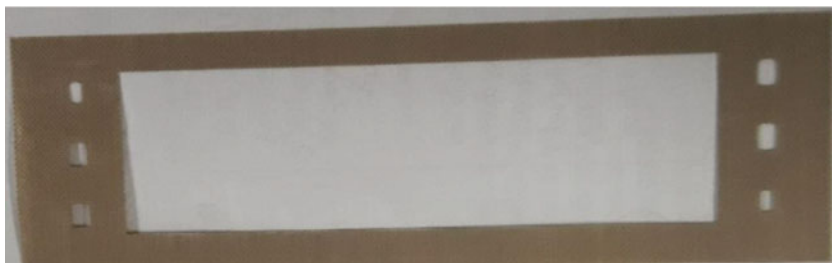
Commercially available MEA are five layered which consists of: Anode gas diffusion layer, anode catalyst layer, Nafion 115, cathode catalyst layer and cathode gas diffusion layer. For manufacturing MEA the gas diffusion layer (GDL), catalyst layer and the polymer electrolyte membrane is done at 135 °C and 4 MPa under a hydraulic hot press for 2 min.

### ***11.2.6 Gaskets***

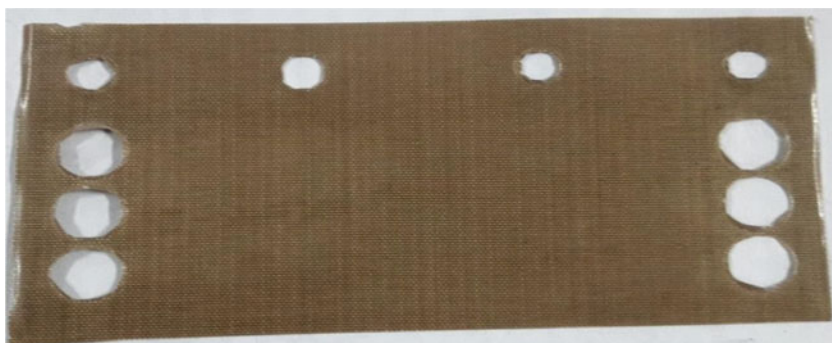
Gaskets are the important part in fuel cell. It acts as an insulator and leakage protector. In the development of the present fuel cell stack, two different gaskets with different thickness, 0.2 mm and 0.1 mm are made with the same material. Normally gaskets are used in 3 places, between the anode flow channel and MEA, cathode flow channel and MEA and between current collector and flow channels. Here, 0.2 mm thickness gasket is used between the anode flow channel and MEA as shown in Fig. 11.5 and between the current collector and flow channel as shown in Fig. 11.6. The gasket has thickness of 0.1 mm is used in between the cathode flow channel and MEA as shown in Fig. 11.7.

### ***11.2.7 Current Collector***

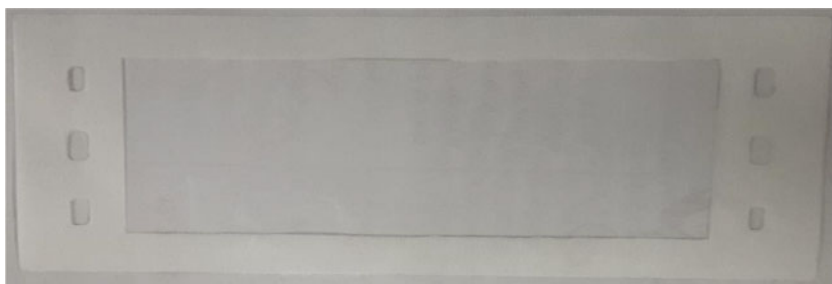
Current collector plate is used to collect the electrons that are produced in the fuel cell.



**Fig. 11.5** Gasket used between anode flow channel and MEA



**Fig. 11.6** Gasket used between current collector and flow channel



**Fig. 11.7** Gasket with thickness 0.1 mm

Normally, it is made up of copper material. The electrons move to the external circuit from current collector. Here one side of the current collector is coated with carbon for increasing the number of electrons. Figure 11.8 is a photograph of the current collector without carbon coating and Fig. 11.9 is the current collector with carbon coating.



**Fig. 11.8** A photograph of the current collector without carbon coating



**Fig. 11.9** A photograph of the current collector with carbon coating

### ***11.2.8 Fuel Cell Assembly: Ten Stack Fuel Cell***

One cell consists of a membrane electrolyte assembly sandwiched between two graphite plates machined with 1:1 serpentine flow field. Here, similar ten cells are used to make the stack. The assembly was clamped by two aluminium fixtures using M5 screws, with a torque of 4 Nm by using torque wrench. A photograph of the fuel cell stack used in the present study is shown in Fig. 11.10.

### ***11.2.9 Monopolar Plates***

In the monopole cell pack, the monopolar plate has only one flow channel on each side to supply of fuel or oxidant.

A computer aided design (CAD) model of the monopolar stack configuration is shown in Fig. 11.11. Monopole design is mainly applied to low power and high voltage devices.



Fig. 11.10 A photograph of the PEMFC stack used in the present study

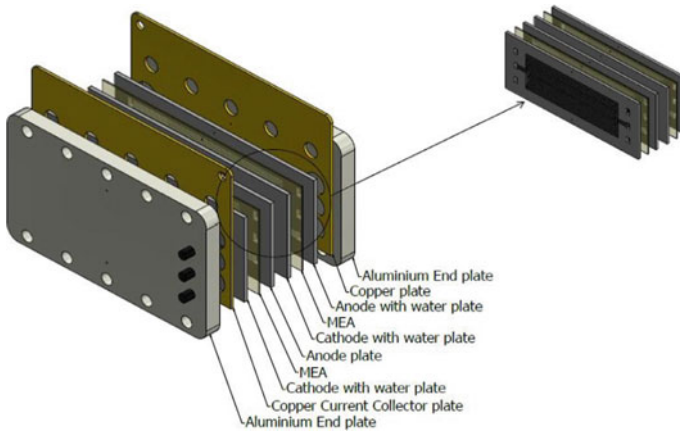
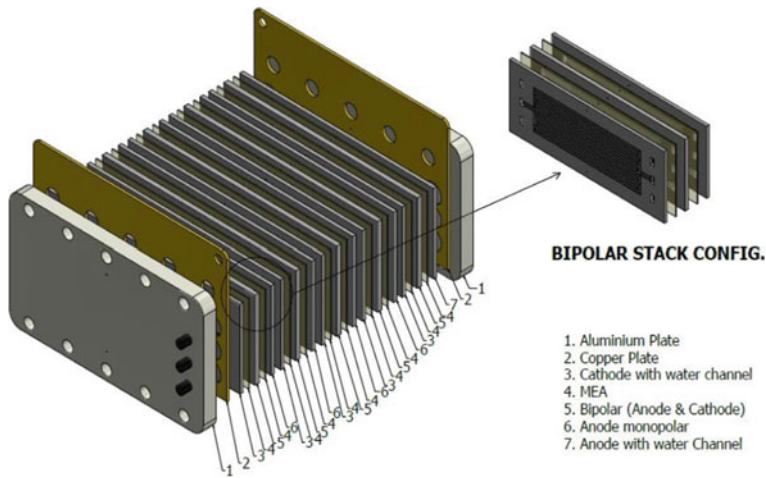


Fig. 11.11 CAD model of the monopolar plates stack configuration

### 11.2.10 Bipolar Plates

A CAD model of the stack configuration using bipolar plates is shown Fig. 11.12. In order to supply the fuel and the oxidant, flow channels are made on both sides of the graphite plate, so the plate becomes a bipolar plate. Though many shapes are used to make the flow channel, a serpentine design is used in the present case. For



**Fig. 11.12** CAD model of the bipolar plates stack configuration

the present experimental investigations, both monopolar and bipolar plates are used to develop the 10 stack PEMFC.

### 11.2.11 Test Rig

The test station consists of electronic load box and control system. Electronic load box is used to measure voltage produced corresponding to the given input. Electronic load box is connected with the monitoring system for the performance analysis of the fuel cell. Anode side of the cell is connected to the negative side of the load box and cathode side with positive side. In inside the loading box change in resistance gives the corresponding loads. In the present work, BK PRECISION loading box, model no: 8518, made in India is used for the loading purpose. Figure 11.13 shows the loading box.

The controlling system consists of temperature control, humidity control, reactant flow rate control, cooling water flow control and temperature controls. Cooling water is supplied to the cell by using peristaltic pump as shown in Fig. 11.14. The peristaltic pump is by M/s Ravel Hitechs Pvt. Ltd with model no: RH120S, made in India.

For the best performance and avoiding the damage to the membrane electrode assembly, the humidity control is essential. In the present study, 80% relative humidity is given for both hydrogen and oxygen. For hydrogen and oxygen, two separate humidity controller systems are used. A photograph of the humidity controller arrangement is shown in Fig. 11.15.





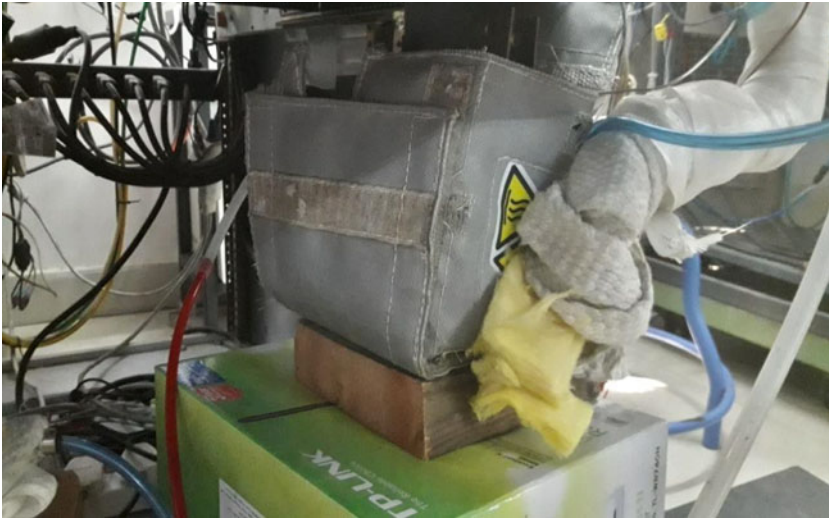
Fig. 11.13 Electronic load box



Fig. 11.14 Peristaltic pump used in the present study

### 11.3 Experimental Investigations

Results of the experimental investigations carried out on single cell, two cell stack and the 10-cell stack are detailed in the following section. Experiments are carried out to assess the performance of the PEMFC under various conditions by changing different parameters such as operating temperatures and oxygen flow rates. All the experiments are done at atmospheric pressure. These experiments helped to study the behavior of the fuel cell and understand how the performance of the fuel cell varies with changes in different operating conditions. It is observed that the results obtained through the experiments are in good agreement with the behavior of fuel cells in the literature.



**Fig. 11.15** Humidity controller

### ***11.3.1 Single Cell Fuel Cell***

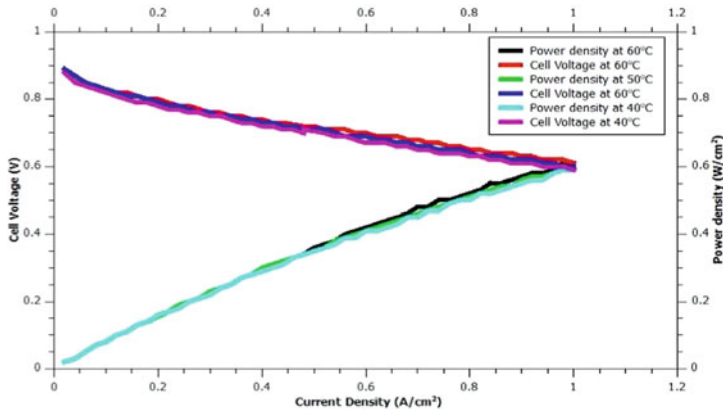
Experiments are conducted on single cell. Power density of single cell at various temperatures are measured. A photograph of the single cell on test station is shown in the Fig. 11.16. The maximum open circuit voltage produced on the cell is 0.9 V. The maximum power output from the cell is 30.5 W (50 A, 0.61 V) at a hydrogen flow rate at 720 ccm and Oxygen flow rate at 500 ccm.

#### **11.3.1.1 Effect of Operating Temperature**

The performance of PEMFC at various temperatures 40 °C, 50 °C and 60 °C is shown in Fig. 11.17. PEMFC showed an increasing performance (increase in power

**Fig. 11.16** Single cell fuel cell on test station





**Fig. 11.17** Effect of operating temperature on the performance of a single fuel cell

density) as the operating temperature is increased. This is because of the fact that the increase in the temperature contributed to the improvement of chemical kinetics of reactions. Hence the performance was increased due to the increase in electron productivity. When the temperature is increased beyond 60 °C, it is found that the membrane is getting damaged, so the temperature is controlled such that it should not rise more than 60 °C.

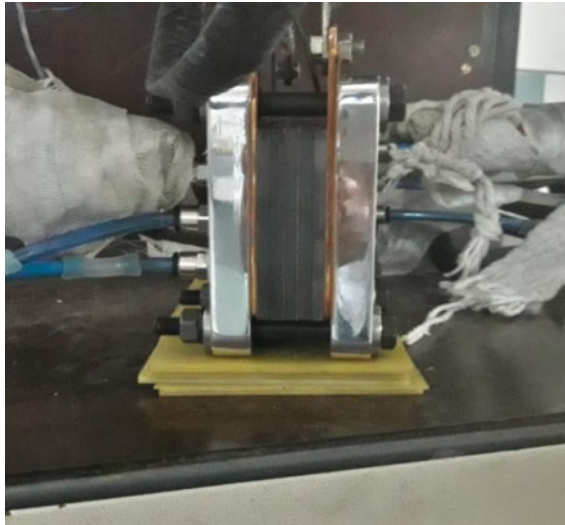
### 11.3.2 Two Stack PEM Fuel Cell

Power density of the fuel cell with two stacks is also reported. The open cell voltage is 1.89. Two stack PEMFC on test station is shown in the Fig. 11.18. The maximum power output from the cell is 66.5 W at a temperature of 60 °C (50 A, 1.33 V) when the hydrogen flow rate at 1700 ccm and oxygen flow rate at 1400 ccm. A comparison of the power density at 40, 50 and 60 °C is shown in Fig. 11.19. Power density is found to be better at 60 °C in comparison with the other operating temperatures.

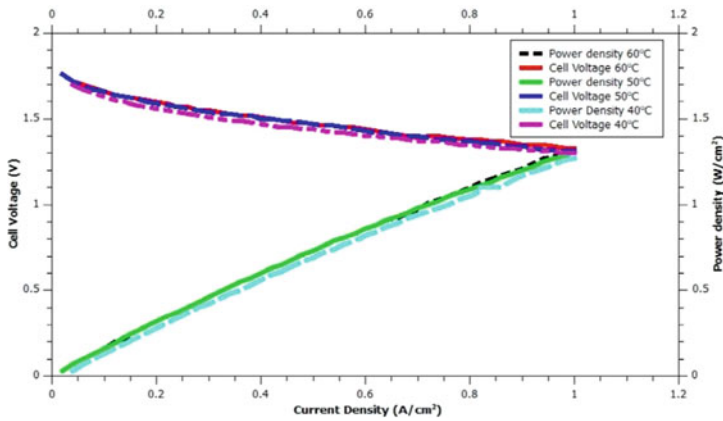
### 11.3.3 Ten Stack Proton Exchange Membrane Fuel Cell

Power density of ten stacks fuel cell at various temperature and flow rate is measured. Ten stack PEMFC on test station is shown in the Fig. 11.20. The open circuit voltage is 9.6 V. The maximum power output from the cell is 303 W (50 A, 6.06 V) when the hydrogen flow rate at 5000 ccm and Oxygen flow rate at 2700 ccm.

The performance of PEMFC at various temperatures 40 °C, 50 °C and 60 °C for the 10 stack fuel cell is given in Table 11.2. The cell showed an increasing performance



**Fig. 11.18** Two stack PEM fuel cell



**Fig. 11.19** Performance of two stack PEMFC

trend as the operating temperature is increased. The ten stack PEMFC showed a maximum power of 303 W at an operating temperature of 60 °C.

**11.3.3.1 Influence of Flow Rate**

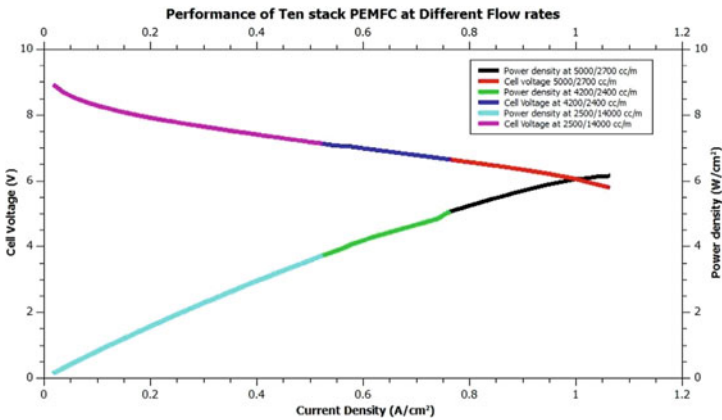
Figure 11.21 shows the variation of cell voltage and power density with different flow rate of oxygen and hydrogen (2500/1400 cc/m, 4200/2400 cc/m and 5000/2700 cc/m) at 60 °C. The flow rate is increased as the current density is increased.



**Fig. 11.20** Ten stack PEMFC on test station

**Table 11.2** Performance of ten stack PEMFC at various temperatures

Sl. No	Temperature (°C)	Current density (A/cm <sup>2</sup> )	Voltage (V)	Power (W)
1	40	0.96	5.88	282.5
2	50	1	5.94	297
3	60	1	6.06	303



**Fig. 11.21** Performance of PEMFC at various flow rates

## 11.4 Conclusions

A ten-stack water-cooled PEMFC stack is designed, fabricated and tested. Each cell is having an active area of 50 cm<sup>2</sup>. Salient features of this work can be summarized as follows:

- The stack performed better at 60 °C, in order to deliver maximum power output. When the temperature is increased from 40 to 60 °C, the output power increased by 20.5 W.
- The maximum power output from the single cell is 30.5 W (50 A and 0.61 V) at a hydrogen flow rate at 720 ccm and Oxygen flow rate at 500 ccm.
- The maximum power output from the two-cell stack is 66.5 W at a temperature of 60 °C (50A and 1.33 V) when the hydrogen flow rate at 1700 ccm and Oxygen flow rate at 1400 ccm.
- The maximum power output from the 10 stack PEM fuel cell is 303 W (50 A and 6.06 V) when the hydrogen flow rate at 5000 ccm and Oxygen flow rate at 2700 ccm.

**Acknowledgements** This work was financially supported by Agency for Non- Conventional Energy and Rural Technology (ANERT), Department of Power, Government of Kerala, India (ANERT-TECH/346/2018-S(NEP)) and St. Joseph's college of Engineering and Technology, Palai. This work was also technically supported by M/s Sainergy Fuel Cell India Private Limited, Chennai, India.

## References

- Chen C-Y, Huang K-P, Yan W-M, Lai M-P (2016) Development and performance diagnosis of a high power air-cooled PEMFC stack. *Int J Hydrogen Energy* 11784–11793
- Chen J, Zhou B (2008) Diagnosis of PEM fuel cell stack dynamic behaviors. *J Power Sources* 177:83–95
- Husar A, Serra M, Kunusch C (2007) Description of gasket failure in a 7 cell PEMFC stack. *J Power Sources* 169:85–91
- Johnson R, Morgan C, Witmer D, Johnson T (2001) Performance of a proton exchange membrane fuel cell stack. *Int J Hydrogen Energy* 26:879–887
- Karthikeyan P, Velmurugan P, George AJ, Kumar RR, Vasanth RJ (2014) Experimental investigation on scaling and stacking up of proton exchange membrane fuel cells. *Int J Hydrogen Energy* 39:11186–11195
- Kim S, Hong I (2008) Effect of humidity and temperature on a proton exchange membrane fuel cell (PEMFC) stack. *J Ind Eng Chem* 14:357–364
- Luo L, Jian Q, Huang B, Huang Z, Zhao J, Cao S (2019) Experimental study on temperature characteristics of an air-cooled proton exchange membrane fuel cell stack. *Renew Energy* 143:1067–1078
- Murphy OJ, Cisar A, Clarke E (1998) Low-cost light weight high power density PEM fuel cell stack. *Electrochim Acta* 43(24):3829–3840
- Neto RC, Teixeira JC, Azevedo JLT (2013) Thermal and electrical experimental characterization of a 1 KW PEM fuel cell stack. *Int J Hydrogen Energy* 38:5348–5356

- Park J, Li X (2006) Effect of flow and temperature distribution on the performance of a PEM fuel cell stack. *J Power Sources* 162:444–459
- Rodatz P, Buchi F, Onder C, Guzzella L (2004) Operational aspects of a large PEMFC stack under practical conditions. *J Power Sources* 128:208–217
- Santarelli MG, Torchio MF, Cali M, Giaretto V (2007) Experimental analysis of cathode flow stoichiometry on the electrical performance of a PEMFC stack. *Int J Hydrogen Energy* 32:710–716
- Scholta J, Berg N, Wilde P, Jorissen L, Garche J (2004) Development and performance of a 10 kW PEMFC stack. *J Power Sources* 127:206–212
- Siddiqui O, Dincer I (2019) Development and performance evaluation of a direct ammonia fuel cell stack. *Chem Eng Sci* 200:285–293
- Syampurwadi A, Onggo H, Indriyati, Yudianti R (2017) Performance of PEM fuel cell stack as affected by number of cell and gas flow-rate. In: *IOP conference series: earth and environmental science* 60. ISSN 1755–1315 (Online)
- Wan Z, Shen J, Zhang H, Tu Z, Liu W (2014) In situ temperature measurement in a 5 kW-class proton exchange membrane fuel cell stack with pure oxygen as the oxidant. *Int J Heat Mass Transf* 75:231–234
- Wen C-Y, Lin Y-S, Lu C-H (2009) Experimental study of clamping effects on the performances of a single proton exchange membrane fuel cell and a 10-Cell stack. *J Power Sources* 192:475–485
- Yan X, Hou M, Sun L, Cheng H, Hong Y, Liang D, Shen Q, Ming P, Yi B (2007) The study on transient characteristic of proton exchange membrane fuel cell stack during dynamic loading. *J Power Sources* 163:966–970
- Yim S-D, Sohn Y-J, Yoon Y-G, Um S, Kim C-S, Lee W-Y (2008) Operating characteristics of 40 W-class PEMFC stack using reformed gas under low humidifying conditions. *J Power Sources* 178:711–715
- Youssef MES, Amin RS, El-Khatib KM (2018) Development and performance analysis of PEMFC stack based on bipolar plates fabricated employing different designs. *Arab J Chem* 609–614
- Zhang G, Kandlikar SG (2012) A critical review of cooling techniques in proton exchange membrane fuel cell stacks. *Int J Hydrogen Energy* 37:2412–2429
- Zhang H, Yang D, Tao K, Zheng X, Ma J (2010) Investigation of PEMFC stack operating at elevated temperature. *World Electr Veh J* 4:481–486

# Chapter 12

## Analysis of Combustion and Performance Characteristics of a Producer Gas-Biodiesel Operated Dual Fuel Engine



Pradipta Kumar Dash, Shakti Prakash Jena, and Harish Chandra Das

### Nomenclature

aTDC	After top dead centre
B10	10% Volume blend of biodiesel with diesel
B20	20% Volume blend of biodiesel with diesel
BMEP	Brake mean effective pressure
BSEC	Brake specific energy consumption
BTE	Brake thermal efficiency
CA	Crank angle
CIE	Compression ignition engine
CP	Cylinder pressure
CO	Carbon monoxide
CO <sub>2</sub>	Carbon dioxide
CR	Compression ratio
CV	Calorific value
DAS	Data acquiring system
DF	Dual fuel
HC	Hydrocarbon
KOH	Potassium hydroxide
KOME	Karanja oil methyl ester
MCT	Mean combustion temperature
NHRR	Net heat release rate

---

P. K. Dash · S. P. Jena (✉)

Department of Mechanical Engineering, SOA Deemed to Be University, Bhubaneswar 751030, India

e-mail: [shaktiprakash.mech@gmail.com](mailto:shaktiprakash.mech@gmail.com)

H. C. Das

Department of Mechanical Engineering, NIT Meghalaya, Shillong 793003, India



NO <sub>x</sub>	Oxides of nitrogen
PG	Producer gas

## 12.1 Introduction

Air pollution is a cause of some major respiratory diseases like asthma and several health complications. Oxides of nitrogen (NO<sub>x</sub>) emissions cause pneumonia, irritation of lungs and bronchitis. Again, prediction suggests that 8.6 billion metric tons of carbon dioxide (CO<sub>2</sub>) will be emitted during 2020 to 2035 that will further increase the green house emission (Sahoo et al. 2021). Keeping in view the worldwide energy emergency, reliance on petroleum fuels and its effect on environment and human, the attention is calling towards finding out the feasible alternative fuels (Dewangan et al. 2020; Jena and Acharya 2019). Developing countries like India require a very large amount of energy to maintain their growth. Considering the rising oil consumption those countries rely more on the imports for fulfilling the demand of petroleum. To combat with the present crisis of energy the researchers must take some innovative steps. One of the important prospects could possibly be the adoption of suitable technology for utilization of non-traditional renewable energy resources to gratify energy requirement. As a source of renewable gaseous fuel, many researchers experimented with hydrogen, compressed natural gas, producer gas and biogas. Producer gas (PG) can be considered as a suitable combustible gaseous fuel synthesized by flowing controlled air stream through the bed of coal or hot coke, with the purpose of completely gasifying the feed material in the gasifier. Diesel engines with very minute modifications can run on gaseous fuels. The gaseous fuel mix with air outside the cylinder in an intake manifold prior to entering through the inlet valve. The dual fuel (DF) engines can be a revolutionary way out as they reduce the dependency on the conventional petroleum fuels thus eliminating the problems arising due to its use. PG operates more efficiently with diesel engines in DF mode due to its high compression ratio. It also plays a very crucial role in reducing NO<sub>x</sub> emissions, smoke and particulate matter. Researchers have used PG as inducted fuel in DF engine with various alternative pilot fuels. Nayak and Mishra (2019) experimented to accomplish higher thermal efficiency and lower engine exhausts in a DF engine. They found that biodiesel-PG showed proficient result for overall engine performance, emission. It showed lower brake thermal efficiency and minimal exhaust emission of hydrocarbon (HC), NO<sub>x</sub> and smoke opacity. Caliguirri and Renzi (2017) examined the combustion modelling of a diesel engine using PG as inducted fuel. Based on the observation, they concluded that it can be very helpful in determining the in-cylinder pressure and mechanical power for different substitutions of diesel. Chunkaew et al. (2016) observed the influence of compression ratio (CR) on brake power. They used a petrol engine running on PG for this experiment. They found that CR 9.3:1 gave a maximum brake power of 1443.6 W at 3800 rpm and CR 7.5:1 gave 1101.7 W at 2900 rpm. The maximum speed of 4500 rpm was achieved at 75% with unload

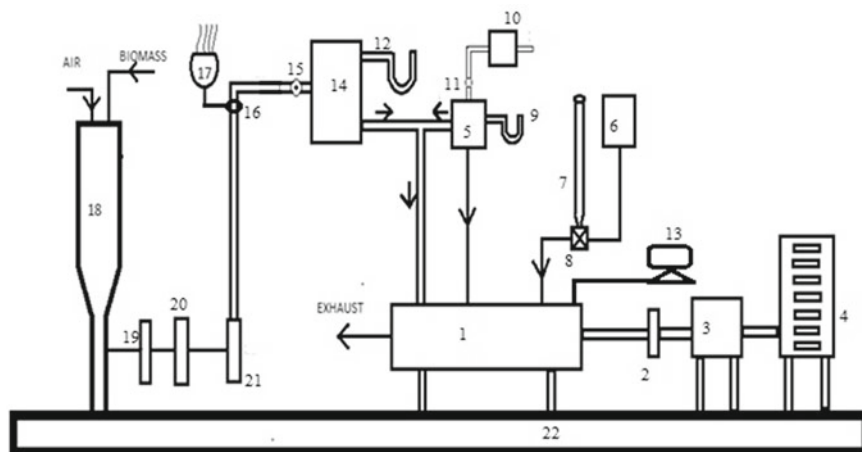
opened air inlet valve and 3100 rpm at 30% without load. Bates and Dolle (2018) experimented on a DF engine using PG derived from woodchips. They found that approximately 75% of the diesel fuel can be saved by using PG to operate a genset. Akkoli et al. (2021) experimented the influence of variation in injector nozzle diameter, number of nozzle holes on brake thermal efficiency (BTE) of the CIE running in DF mode. They concluded that, 0.25 mm nozzle diameter along with 6 number of nozzle holes gave 5.8% enhancement in BTE. Yaliwal and Banapurmath (2021) performed experiment using biodiesel-PG in DF mode with and without hydrogen enrichment. They found that, hydrogen enrichment has improved the net heat release and combustion pressure with reduction in exhaust emissions during biodiesel-PG operation. Suryawanshi and Yarasu (2021) studied the effect of different angle of Y-shape carburetors on PG-air mixing. They found that, 90° angle of mixing gave best reduction in engine emissions with PG induction.

Very few works were found in the literature exploring combustion trends of DF engine operated with PG. In the current work we tried to analyze the combustion and performance attributes of twin cylinder engine running with standard diesel, and its blends with Karanja oil biodiesel as pilot fuel along with PG induction.

## 12.2 Experimental Method

Figure 12.1 shows the schematic diagram of the DF engine, chosen for experimentation. A downdraft gasifier was utilized to deliver PG from woodchip of eucalyptus with moisture percentage 10.21% was chopped into desired size is utilized as feed-stock in the gasifier. The constituents in PG sample were tested through a Gas Chromatograph (model GC2010 Chromatography and Instrument Co, India). The gas constituents of PG is presented in Table 12.1.

The specifications of the selected engine are 14hp, 4-stroke, twin cylinder, 50.27 J deg<sup>-1</sup> observed CIE with rated speed of 1500 rpm and 16.5:1 compression ratio. A 3-phase, 415 V AC alternator was used to apply and vary the engine load. A water manometer, orifice meter, and flow control valve are attached to the gas surge tank to regulate and measure the substitution rate of PG. An injector was fitted into the inlet pipeline to inject the PG with the intake air. A data acquiring system (DAS) is fitted to collect, record, and investigate the observed results. Before allowing the PG to gas surge tank its flammability test was performed at the burner, where a bluish flame was observed. The CV of the PG used was found to be 5.64 MJ Nm<sup>-3</sup>. Software package “Engine Soft LV” of version 9 was used for online performance analysis. The crude Karanja oil was first obtained from the crusher mill and was treated with phosphoric acid at a concentration of 1% volume ratio during this process. The Karanja oil is degummed before being processed for biodiesel synthesis using the transesterification method. The esterification of crude oil was performed, in which degummed Karanja oil was blended properly with 22% volume of methanol and 1% volume ratio of sulphuric acid. Then it is heated for one hour at 65 °C in a constant temperature bath with continuous stirring. Then in transesterification, methanol of



**Fig. 12.1** Block diagram of the engine setup. 1. Engine, 2. Coupling, 3. Alternator, 4. Loading unit, 5. Air box, 6. Fuel tank, 7. Burette, 8. Valve, 9. Manometer, 10. Air filter, 11. Orifice meter, 12. Manometer, 13. DAS, 14. Gas surge tank, 15. Orifice meter, 16. Gas control valve, 17. Burner, 18. Gasifier, 19. Cooling unit, 20. Passive filter, 21. Fine filter, 22. Bed

**Table 12.1** Constituents and CV of PG

Gas composition	H <sub>2</sub>	CO <sub>2</sub>	CO	CH <sub>4</sub>	N <sub>2</sub>
PG, %volume	19.22	10.5	20.03	2.75	46.49

volume ratio 22% and potassium hydroxide (KOH) base catalyst (0.5% volume ratio) were used to make a reagent combination. The combined charge was then swirled at a speed of 80 rpm for about 2 h at 60 °C. The churning and heating were then turned off, and the mixture was left to settle for around 24 h. Then the collected Karanja oil methyl ester (KOME) was water washed and heated at 70 °C for 30 min to evaporate unreacted methanol and moisture present in it. The studies were carried out using two volume fractions (10 and 20%) of KOME with diesel were prepared to run the CIE in DF mode at full loading condition with gradual hike in PG substitution. At maximum load run when PG flow rate increased beyond 21.49 kg h<sup>-1</sup>, huge engine vibration with high noise was observed. Hence the PG flow rate was fixed at 21.49 kg h<sup>-1</sup> to record the further dual fuel observations. The physical properties of all the selected pilot fuels were represented in Table 12.2.

### 12.3 Results and Discussion

The experimentation and study of the observed findings entirely relies upon the appropriate subject understanding and the association with the obtained results published

**Table 12.2** Physical properties of pilot fuels

Fuels	Viscosity (cSt, 40 °C)	Cetane number	CV (MJ kg <sup>-1</sup> )
Diesel	1.902	45–55	42.21
KOME	4.5	56.61	36.12
B10	2.181	–	41.5
B20	2.418	–	40.1

in literature. To identify the irreversibility taking place during combustion of the selected alternative fuel following parameters were considered for discussion.

### 12.3.1 Cylinder Pressure

Figure 12.2 represents the graphical trend of CP with crank angle (CA) at 100% engine load for all the tested fuel combinations. The CP graph reveals that, a late start of ignition was seen in case of dual fuel runs with all the selected pilot fuels, where the CA50 was observed at 10° for Diesel + PG and B20 + PG, while for B10 + PG it appeared at 13° after top dead centre (aTDC) respectively. For standard diesel operation, the CA50 was observed at 7° aTDC. This finding can be associated to the comparatively low adiabatic flame temperature of PG and its poor burning tendency that influences the combustion process. CA50 value shifted to right from top dead centre in case of PG operation, indicating a drop in specific power yield. DF operation with PG have shown marginally higher peak value of CP. A sharp ascent in the CP graph was observed at the top dead centre, whereas the highest reading of CP for standard diesel operation was recorded to be 6.11 MPa at 9° aTDC and 6.45 MPa for Diesel + PG run at 15° aTDC. Similarly, the peak value of CP during B10 alone operation was noticed to be 5.9 MPa at 15° aTDC and for that of B10 + PG the highest CP was observed to be 6.4 MPa which further shifted by 5° away i.e. 20° aTDC. Similarly, in case of B20 + PG the highest CP was noticed to be 6.25 MPa which is located at 20° aTDC. B10 and B20 as pilot fuels have showed slightly higher ignition lag as compared to diesel. This may be described as the comparatively higher density and specific gravity of B10 and B20 that requires comparatively higher time for atomization and vapourization leading to ignition lag.

### 12.3.2 Net Heat Release Rate

Figure 12.3 represents the deviation in NHRR trend with CA at 100% engine load. At the initial stage of the cycle, a negative value of NHRR was seen for all the tested fuel combinations. The latent heat of vapourization taken by the pilot fuel reflects as the negative value of NHRR. A quick ascent in NHRR was observed nearly 5° before

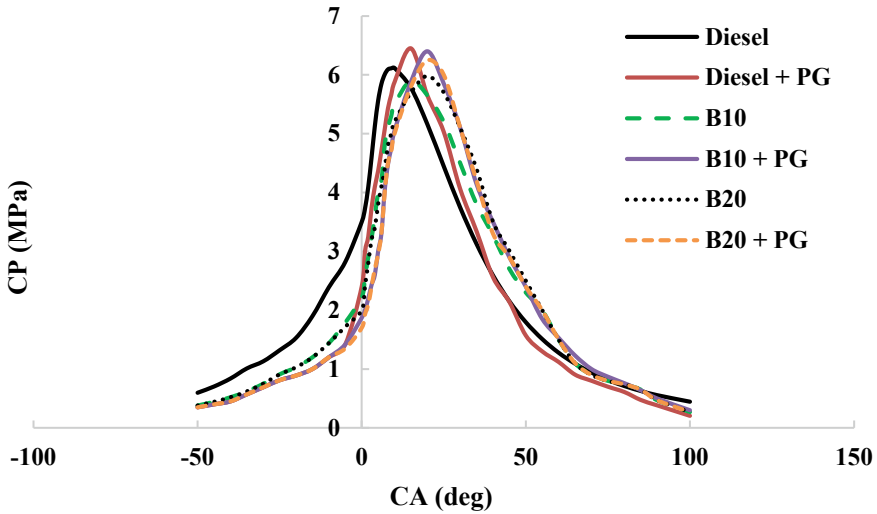


Fig. 12.2 Variation of CP with respect to CA

top dead centre, where the peak reading of NHRR for standard diesel operation was found to be  $53.23 \text{ J deg}^{-1}$  observed at  $1^\circ$  aTDC and that for Diesel + PG the highest value of NHRR found to be  $50.27 \text{ J deg}^{-1}$  observed at  $8^\circ$  aTDC. While the peak value of NHRR for B10 was found to be  $44.32 \text{ J deg}^{-1}$  located at  $1^\circ$  aTDC and in similar trend for B10 + PG the maximum value of NHRR was found to be  $48.03 \text{ J deg}^{-1}$  at  $8^\circ$  aTDC. Similarly, the peak value of NHRR for B20 was found to be  $40.65 \text{ J deg}^{-1}$  located at  $2^\circ$  aTDC and in similar trend for B20 + PG the maximum value of NHRR was found to be  $48.26 \text{ J deg}^{-1}$  observed at  $10^\circ$  aTDC. Presence of B10 and B20 as pilot fuel has showed a prominent second peak of NHRR observed in case of dual fuel operation that indicates the delayed combustion tendency of PG.

This demonstrates that, heat released was comparatively lower in rapid combustion phase and progressed towards the after burning stage of the cycle for PG operation as compared to engine operation with standard diesel run. The combustion trend of PG result to higher value of second peak of NHRR as noticed for dual-fuel activity. The inhomogeneity in air–fuel mixture formation due to PG induction causes an inefficient conversion of fuel energy into brake power (Yaliwal and Banapurmath 2021).

### 12.3.3 Mean Combustion Temperature

The change in MCT in line with CA was presented in Fig. 12.4. At the point during end of compression stroke a rapid climb in MCT graph is observed  $5^\circ$  before top dead centre. When the CIE was operated without PG induction, a sharp rise in MCT

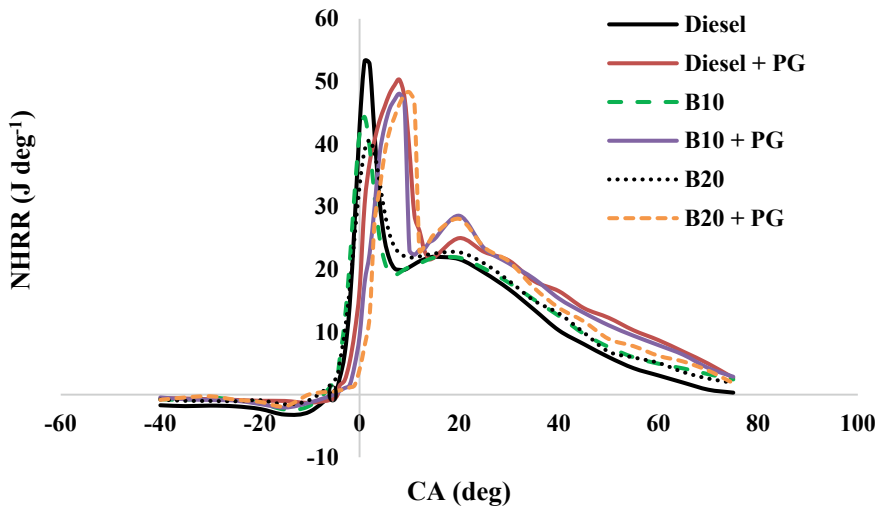


Fig. 12.3 Variation of NHRR with respect to CA

curve was observed where B20 alone operation reached highest MCT. Whereas, with PG induction the slope of MCT curve slightly falls. This could be referred to the lower flame velocity of PG that affects the spread of flame in the combustion chamber leading to comparatively slow combustion process. The maximum value of MCT was observed with standard diesel operation was recorded to be  $1426.5^{\circ}\text{C}$  at  $30^{\circ}$  aTDC and for B10 the same was found to be  $1417.2^{\circ}\text{C}$  at  $35^{\circ}$  after TDC. Similarly, during diesel + PG and B10 + PG operation the maximum MCT value was recorded to be  $1406^{\circ}\text{C}$  noted at  $40^{\circ}$  after TDC and  $1410.4^{\circ}\text{C}$  at  $45^{\circ}$  after TDC respectively. Similarly in case of B20 the maximum reading of MCT was recorded to be  $1456.1^{\circ}\text{C}$  at  $35^{\circ}$  aTDC, and for that of B20 + PG it was noticed at  $45^{\circ}$  after TDC with a lower value ( $1422.4^{\circ}\text{C}$ ). This shows a slow climb in MCT for engine run with PG and relatively reduced value of MCT was noticed while using biodiesel blends as pilot fuel.

The incomplete combustion caused by blends of KOME-PG affected rate of heat release in premixed combustion phase results in further drop in slope of MCT curve.

#### 12.3.4 BTE

Figure 12.5 represents the BTE of the DF engine with change in brake mean effective pressure (BMEP). The BTE of an engine represents the effective compression of heat energy into useful brake power. BTE increases with rise in BMEP, showing the enhanced rate of conversion of fuel energy into useful brake power. Diesel alone operation have showed highest BTE 27.65% followed by B10 (26.6%), B20 (25.95%),

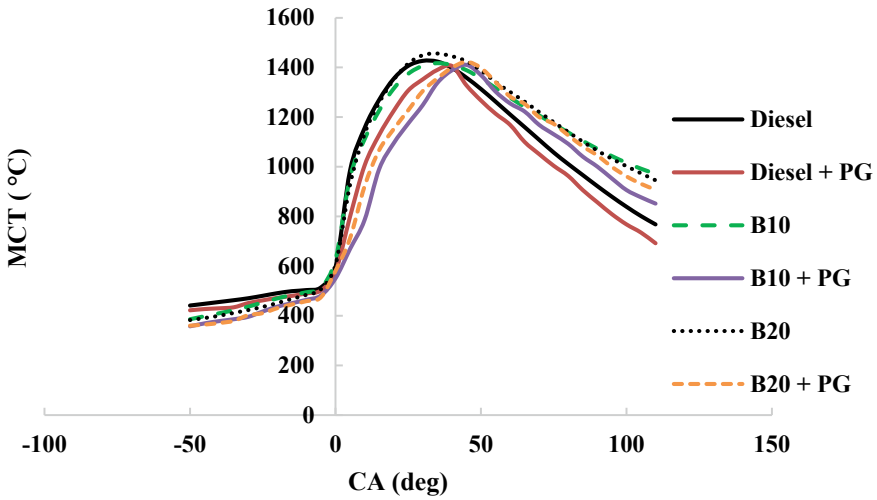


Fig. 12.4 Variation of MCT with respect to CA

Diesel + PG (24.2), B10 + PG (23.75%) and lowest BTE was observed for B20 + PG (23.26%) as observed at 80% engine loading. It is obvious that, diesel alone operation has showed best BTE than all the combinations of PG operation. It can be referred to the difference in fuel properties and the poor combustion characteristics of PG that again comparatively become poorer when B10 and B20 was considered as pilot fuel in place of diesel (Yaliwal and Banapurmath 2021). The lower CV of PG requires higher fuel supply rate to compensate for same rate of power output. Similar trends of result were also reported by Nayak and Mishra (2016) experimented with PG in DF mode.

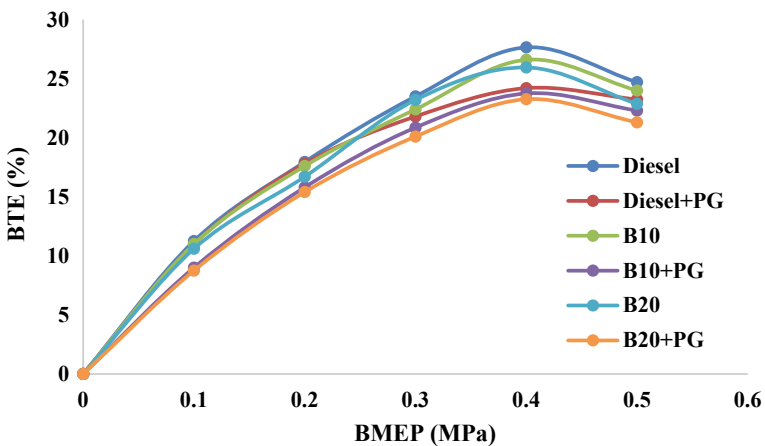


Fig. 12.5 Change in BTE with respect to BMEP

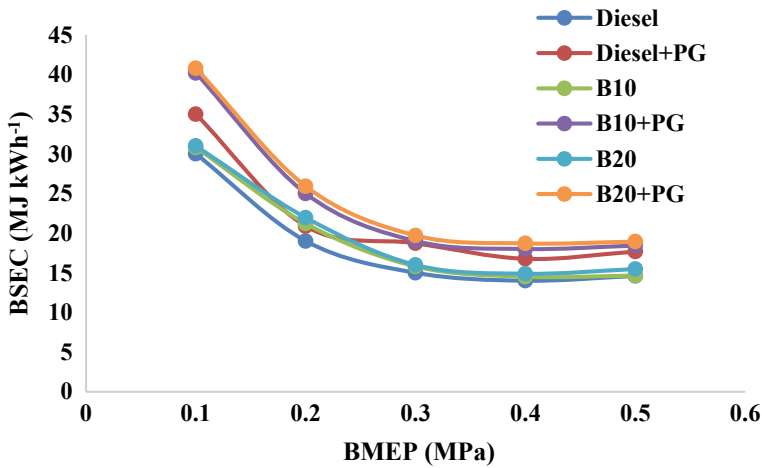


Fig. 12.6 Variation in BSEC with respect to BMEP

### 12.3.5 Brake Specific Energy Consumption (BSEC)

The BSEC represents the measurement of effective utilization of supplied fuel energy per unit power output (Raman and Kumar 2020). Figure 12.6 illustrates the change in BSEC trend with variation in BMEP. The observations indicate decreasing trend of BSEC with increase in BMEP for all the tested fuel combinations. May be owing to the increase of in-cylinder temperature and pressure at higher engine load resulting enhanced heat release rate. The induction of PG in dual fuel operation have showed higher BSEC. The reason behind this could be the lower CV of PG, its combustion characteristics low flame speed, low cetane index, and presence of CO also inhibits the combustion process (Yaliwal and Banapurmath 2021). Again, higher viscosity and low volatility of biodiesel blends also affects the vapourization process leading to retarded combustion process as compared to base result. At full engine load Diesel + PG, B10 + PG and B20 + PG required 17.67, 18.43 and 18.93 kJ kWh<sup>-1</sup> BSEC respectively to give the same power output as that of diesel alone operation (14.6 kJ kWh<sup>-1</sup>). At the same engine loading B10 has shown 14.65 kJ kWh<sup>-1</sup> and B20 has shown 15.47 kJ kWh<sup>-1</sup> BSEC.

## 12.4 Conclusions

The experimentation was purposeful to assess the engine combustion and performance attributes of a DF engine. The subsequent findings were strained from the analysis:



- The peak value of NHRR and CP curve moved away from the TDC during DF operation for all the tested pilot fuels. This indicates an increase in ignition lag in case of PG induction.
- The MCT curve reveals that, diesel, B10 and B20 mode operation without PG induction showed comparatively sharp rise in combustion temperature while the slope of MCT curve slightly falls for all the pilot fuels in DF mode operation.
- The BSEC increased by 21, 26.2 and 29.6% for Diesel + PG, B10 + PG, and B20 + PG respectively as compared to base result (standard diesel), while the BTE decreased by 12.4, 14, 15.8% for Diesel + PG, B10 + PG, and B20 + PG respectively as compared to base result.

Hence, PG as inducted fuel can be considered to run small scale gensets for power generation in rural areas. While B10 and B20 blend of KOME can be used as a partial substitution of diesel. The combustion characteristics of dual-fuel run indicates that combustion improving techniques like use of a suitable cetane enhancer as fuel additive, preheating of intake air can be considered as an option to suppress the negative combustion characteristics of PG.

## References

- Akkoli KM, Banapurmath NR, Shivashimpi MM, Soudagar MEM, Badruddin IA, Alazwari MA, Yaliwal VS, Mujtaba MA, Akram N, Goodarzi M, Safaei MR, Venu H (2021) Effect of injection parameters and producer gas derived from redgram stalk on the performance and emission characteristics of a diesel engine. *Alexandria Eng J* 60(3):3133–3142
- Bates R, Dolle K (2018) Dual fueling a diesel engine with producer gas produced from woodchips. *Adv Res* 14(1):1–9
- Caliguiri C, Renzi M (2017) Combustion modelling of a dual fuel diesel—producer gas compression ignition engine. *Energy Procedia* 142:1395–1400
- Chunakaw P, Sriudom Y, Jainoy W, Sisa J, Chuenprueng K, Chanpeng W (2016) Modified compression ratio effect on brake power of single piston gasoline engine utilizing producer gas. *Energy Procedia* 89:85–92
- Dewangan A, Mallick A, Yadav AK, Kumar R (2020) Combustion-generated pollutions and strategy for its control in CI engines: a review. *Mater Today Proceed* 21. <https://doi.org/10.1016/j.matpr.2019.12.155>
- Jena SP, Acharya SK (2019) Investigation on influence of thermal barrier coating on diesel engine performance and emissions in dual-fuel mode using upgraded biogas. *Sustaina Environm Resear* 29:24. <https://doi.org/10.1186/s42834-019-0025-4>
- Nayak SK, Mishra PC (2019) Achieving high performance and low emission in a dual fuel operated engine with varied injection parameters and combustion chamber shapes. *Energy Convers Manage* 180:1–24
- Nayak CK, Acharya SK, Swain RK (2016) Performance of a twin cylinder dual-fuel diesel engine using blends of neat Karanja oil and producer gas. *Int J Ambient Energy* 37(1):36–45
- Raman R, Kumar N (2020) Performance and emission characteristics of twin cylinder diesel engine fueled with mahua biodiesel and DEE. *Transp Eng* 2. <https://doi.org/10.1016/j.treng.2020.100024>
- Sahoo A, Mishra A, Mishra S, Jena SP (2021) Optimization of operating parameters of a diesel engine with diethyl ether as a fuel add-on. *J Inst Eng (India) Ser C* <https://doi.org/10.1007/s4032-021-00763-y>

- Suryawanshi S, Yarasu R. Mixing performance analysis of producer gas carburetors for a dual fuel CI engine. *J Inst Eng (India) Ser C* 102(5):1251–1259
- Yaliwal VS, Banapurmath NR (2021) Combustion and emission characteristics of a compression ignition engine operated on dual fuel mode using renewable and sustainable fuel combinations. *SN Appl Sci*. <https://doi.org/10.1007/s42452-020-03987-2>

# Chapter 13

## Influence of Biogas Up-Gradation on Exhaust Emissions of a Dual-Fuel Engine with Thermal Barrier Coating



Sanjaya Kumar Mishra, Pradipta Kumar Dash, Shakti Prakash Jena, and Premananda Pradhan

### Nomenclature

Ca(OH) <sub>2</sub>	Calcium hydroxide
CaZrO <sub>3</sub>	Calcium zirconium oxide
CE	Coated engine
CH <sub>4</sub>	Methane
CIE	Compression ignition engine
CO	Carbon monoxide
CO <sub>2</sub>	Carbon dioxide
DAS	Data acquiring system
HC	Hydrocarbon
H <sub>2</sub> S	Hydrogen sulphide
MEA	Mono ethanol amine
MgZrO <sub>3</sub>	Magnesium zirconium oxide
NaOH	Sodium hydroxide
NO	Nitric oxide
RBG	Raw biogas
TBC	Thermal barrier coating
UBG	Upgraded biogas
YSZ	Ytria stabilized zirconia

---

S. K. Mishra · P. K. Dash · S. P. Jena (✉) · P. Pradhan  
Department of Mechanical Engineering, SOA Deemed to be University, Bhubaneswar 751030,  
India  
e-mail: [shaktiprakash.mech@gmail.com](mailto:shaktiprakash.mech@gmail.com)

### 13.1 Introduction

Diesel engines are being used as the key lifeline of the human race for transportation, agriculture, construction, and small-scale power production. In general, the majority of the CIE operates on standard diesel, which is getting exhausted more rapidly, which insists the researchers all over the globe to discover a suitable and renewable source of energy to fit in as a substitute (Jena et al. 2015; Jena and Acharya 2020). The use of renewable gaseous fuel in dual-fuel engines can be an innovative way, as they reduce the dependency on the conventional fuels. Different researchers experimented with hydrogen, compressed natural gas, producer gas, biogas as a source of renewable gaseous fuel. Biogas is produced from organic wastes through anaerobic digestion could be considered as a source of green energy. Researchers experimented on different biomass to optimize the production rate of biogas. Crocarno et al. (2015) produced biogas from *Vestiveria Zizanoides*, a type of rapidly growing grass by anaerobic digestion in a cost-effective way. Liu et al. (2015) studied the impact of urea dosage up to 2% weight of the grass feedstock. They observed 18% higher methane enriched biogas during the ensilage process in the presence of urea. Jena et al. (Crocarno et al. 2015) carried out experimentation to generate biogas using semi-dried banana leaves and reported 65.28% methane enriched biogas. Jena et al. (2020) performed an experimentation on the impact of additives on biogas production from banana leaves. They noticed that presence of ferrous additives has reduced the lag-phase of methane production drastically in the anaerobic digestion process. Different researchers observed the emission and performance trends of diesel engines in dual-fuel run operating on biogas. For example, (Ambarita 2017) performed experimentation on a diesel engine taking biogas and noticed that biogas with 70% methane ( $\text{CH}_4$ ) percentage can replace up to 87.51% of diesel consumption. Verma et al. (2017) experimented to observe the influence of  $\text{CH}_4$  concentration in biogas on dual-fuel performance. They concluded that by increasing  $\text{CH}_4$  concentration in supplied biogas the dual-fuel mode performance parameters improved with suppression in HC and CO emissions. Barik and Murugan (2014) performed an experiment to produce biogas on large scale and achieved 73% methane content in the produced biogas and used it as inducted fuel in a CIE. Their findings reveal that dual-fuel run exhibited higher HC and CO emissions in the exhaust with a decrease in NO and soot formation.

To improve the performance of dual-fuel engines using biogas few researchers have also worked on the purification of biogas by removing  $\text{CO}_2$  and hydrogen sulfide ( $\text{H}_2\text{S}$ ) present in the raw biogas. As  $\text{H}_2\text{S}$  is corrosive, it can cause corrosion to biogas storing tanks as well as the engine components. Tippayawong and Thanompongchart (2010) performed the purification of biogas by using 0.1 mol concentration of three different chemical solutions mono ethanol amine (MEA), NaOH, and calcium hydroxide ( $\text{Ca}(\text{OH})_2$ ). The saturation point of absorption was determined when the pH level reached in between 7 and 8. They found that  $\text{Ca}(\text{OH})_2$  reached saturation after around 50 min as compared to 100 min observed for NaOH and MEA. Maile et al. (2007) studied the absorption rate of  $\text{CO}_2$  from the biogas using different molar

concentration of NaOH solution. They observed that increasing NaOH concentration in the solution increases the CO<sub>2</sub> removal efficiency. Barik et al. (2017) performed purification of raw biogas using NaOH solution and achieved upgraded biogas with 90.6% methane content.

Besides purification of biogas further advanced combustion techniques need to be adopted to minimize the exhaust emission parameters of the diesel engines running with biogas. Thermal barrier coating (TBC) on components of the combustion chamber was employed by different researchers to suppress the heat loss within the combustion chamber. As a result, this will lead to an increase in mean combustion temperature that would improve the performance and emission characteristics. Taymaz (2020) used a mixture of CaZrO<sub>3</sub> and MgZrO<sub>3</sub> as topcoat and NiCrAl as bond coat for thermal barrier coating. The results indicated a reduction in fuel consumption as well as engine emissions for coated engine (CE) operation. While the oxides of nitrogen emissions were increased because of a leap in mean combustion temperature due to coating. Karthikeyan (2018) performed experimentation on the CIE with TBC to run upon different blends of neem biodiesel. He noticed a decreasing trend in HC emission for the coated engine as referred to base results. Mohapatra et al. (2018) experimented on YSZ coated CIE accompanied with an injection of steam to reduce NO emissions from the CE. Elumalai et al. (2021) used partially stabilized zirconia as coating on piston top to improve the emission characteristics. The HC emission decreased by 22.42% and CO emission reduced by 31.98%. Fei et al. (2021) applied YSZ coating on piston of marine diesel engine to improve the performance at part load operation. They achieved 5% increase in brake thermal efficiency during part load run.

In this experiment, we have selected semi-dried banana leaves as the feedstock for biogas production using sewage water as the reacting medium in the digester. To improve the combustion quality of the produced biogas by CO<sub>2</sub> removal, a scrubbing unit was used to purify the biogas produced from the digester. A diesel engine with YSZ coating was selected to run in dual-fuel mode at different substitution rates of biogas to investigate the influence of coating over exhaust emissions.

## 13.2 Experimental Methodology

### 13.2.1 Biogas Production and Purification

Anaerobic digestion is an appropriate process to generate biogas from biomass. Semi-dried banana leaves were collected from local farms and chopped into the required size (10–20 mm). Sewage water after pre-treatment was brought from the local sewage water recycling plant. A floating dome biogas plant was used for large scale biogas production, which is divided into 2 parts: dome and digester. The specifications of the biogas digester are represented in Table 13.1. Based on the dry weight of banana leaves, 2% of urea was mixed with sewage water and stirred properly. In each batch,

**Table 13.1** Specifications of the biogas plant

Specifications	Details
Digester diameter, (m)	1.2
Digester height, (m)	1.96
Dome diameter, (m)	1.03
Dome height, (m)	1.22
Digester volume, (m <sup>3</sup> )	2.22
Dome volume, (m <sup>3</sup> )	1.02

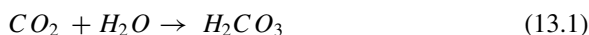
**Table 13.2** Specification of the scrubber

Specifications	Values
Material	Polyvinyl chloride
Types	Vertical
Height, (mm)	1370
Diameter, (mm)	160
Packing material	Iron chips
Biogas induction pressure, (MPa)	0.14–0.18
Biogas flow rates, (kg h <sup>-1</sup> )	1
Scrubber solution	NaOH + water
Solution flow rates, (kg h <sup>-1</sup> )	900

10 kg of semi-dried banana leaves mixed with sewage water solution before feeding to the digester. A 1.2 cm hose pipe was connecting the dome with the inlet of the cylindrical column packed bed scrubber along with accessories like flow control valve, gas flow meter and pressure gauge to control and measure the biogas flow rate during experimentation.

Table 13.2 presents the complete specification of the scrubber fabricated for the experimentation. Prior to the purification process, 15 L of 1 N NaOH solution was prepared and stored in a container.

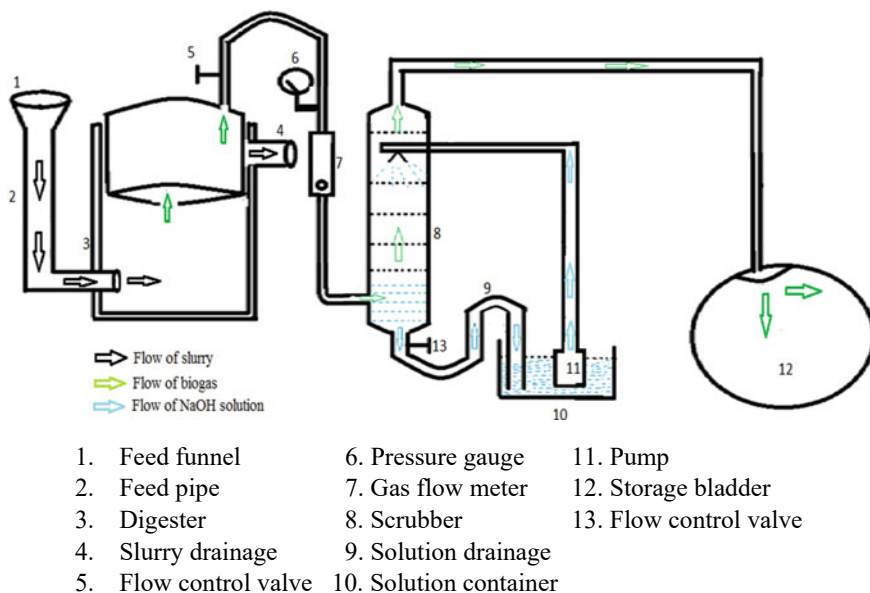
The outlet of the scrubber was connected to a bladder with storing limit of 1 m<sup>3</sup> (Material: Synthetic rubber) for biogas collection. The schematic diagram of the biogas plant with the scrubbing unit is shown in Fig. 13.1. Raw biogas from the digester was steadily supplied at 1 kg h<sup>-1</sup> to the scrubber at a pressure range of 0.14–0.18 MPa. The 1 N NaOH solution was sprayed from the top of the scrubber at 900 kg h<sup>-1</sup> using a circulation pump. Four layers of iron chips were used in the scrubber to improve the contact of biogas with the solution. A trace amount of H<sub>2</sub>S gas present in the raw biogas (RBG) will react with the iron chip to form ferrous sulfide; as a result, the H<sub>2</sub>S will be eliminated from the upgraded biogas (UBG). The chemical reaction of purification can be expressed as:





A layer of jute material is provided above the sprinkler to remove moisture from the purified biogas. The composition of RBG and UBG was verified by a Gas Chromatograph (model GC2010 Chromatography and Instrument Co, India).

The compositions and calorific values of RBG and UBG were shown in Table 13.3.



**Fig. 13.1** Schematic diagram of a biogas plant with the scrubbing unit

**Table 13.3** Concentration and higher heating value of RBG and UBG

Gas compositions	RBG, (%vol)	UBG, (%Vol)
CH <sub>4</sub>	68.08	87.02
CO <sub>2</sub>	28.82	04.85
H	0.0642	1.122
CO	0.8338	0.075
H <sub>2</sub> S	0.21	0.0
Calorific value, (MJ kg <sup>-1</sup> )	24.62	31.46

**Table 13.4** Specifications of the engine setup

Manufacturer	Kirloskar
Engine details	4- stroke, water-cooled diesel engine
Engine speed	1500 rpm
Rated power	3.5 kW
Compression ratio	18:1
Bore	87.5 mm
Stroke	110 mm

### 13.2.2 Experimental Setup

A single cylinder water-cooled 4-stroke CIE was modified to run in dual-fuel mode. The detailed specifications of the selected diesel engine are shown in Table 13.4. A biogas injector was drilled in the inlet piping 3 m away from the inlet valve to facilitate proper mixing of inducted biogas with the intake air. The engine emissions were recorded through an online AVL DIGAS (model 444N, India) exhaust gas analyzer, used to check the composition such as CO<sub>2</sub>, CO, HC, and NO in the engine exhaust. The smoke opacity was recorded by an AVL (model 437C, India) smoke meter. A data acquiring system (DAS) was employed for recording the purpose of the experimental observations.

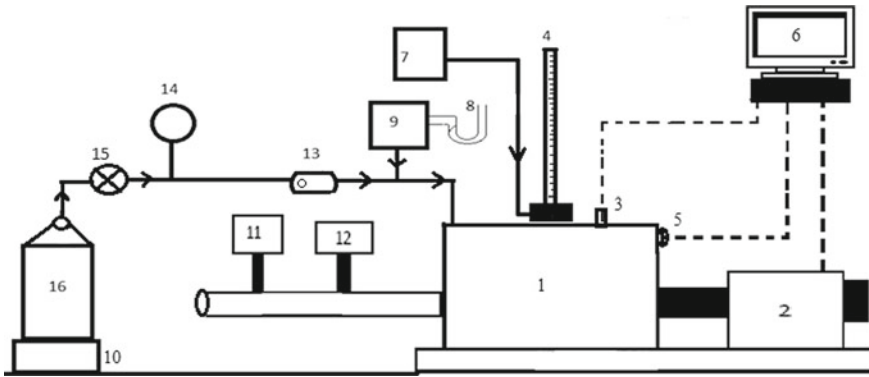
### 13.2.3 Experimental Procedure

The schematic layout of the diesel engine was given in Fig. 13.2. The detail of coating synthesis by plasma spray method was documented by the authors in earlier articles (Elumalai et al. 2021; Jena and Acharya 2019). The engine was first run with diesel and after reaching the steady exhaust temperature during each engine loading; observations were recorded to generate base results. Then the YSZ coated piston and valves were assembled in place of the base piston and valves to record the emissions of the CE with standard diesel. During the dual-fuel run, RBG was supplied at 3 variations in substitution rate (0.6, 0.8 and 1 kg h<sup>-1</sup>) to record observations of the engine emissions. Again, the same procedure was repeated by inducting UBG to investigate the consequence of purification over engine emissions. The snapshot of the uncoated and coated piston and valves are shown in Fig. 13.3.

## 13.3 Results and Discussion

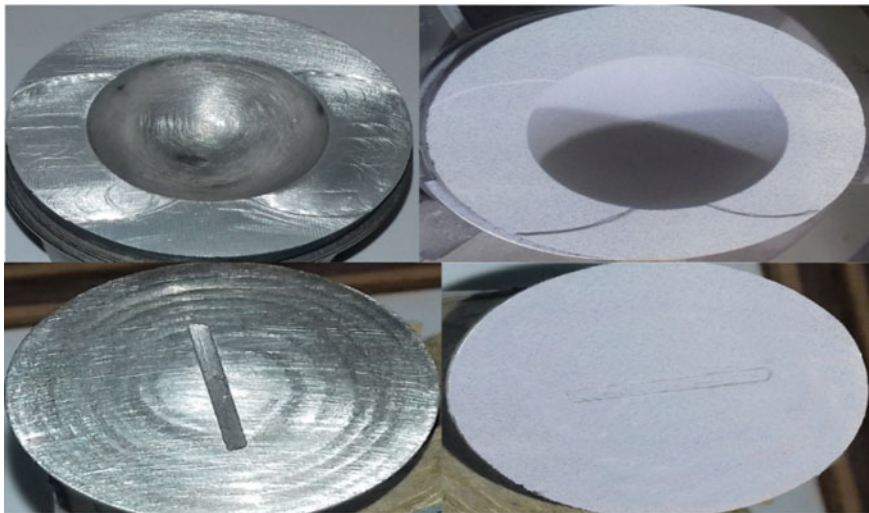
Experimentation was carried out to inspect the influence of the coating on exhaust emissions of a dual-fuel test setup operating with RBG and UBG.





- |                   |                        |                        |
|-------------------|------------------------|------------------------|
| 1. Engine         | 7. Fuel tank           | 13. Gas flow meter     |
| 2. Loading unit   | 8. Manometer           | 14. Pressure gauge     |
| 3. Pizeo sensor   | 9. Air box             | 15. Flow control valve |
| 4. Burette        | 10. Weighing machine   | 16. Biogas cylinder    |
| 5. Rotary encoder | 11. Smoke meter        |                        |
| 6. DAS            | 12. Multi gas analyzer |                        |

**Fig. 13.2** Block diagram of engine setup



**Fig. 13.3** Snapshot of valves and piston before coating (left) and after coating (right) (Jena et al. 2017b)

### 13.3.1 CO Emission

Figure 13.4 represents the trend of CO emission with change in engine load. As observed with augment in engine loading the CO emissions decrease, maybe because of an increase in diesel injection at higher engine loads increased the heat release rate that leading to improved oxidation of the supplied gaseous fuel.

The hike in biogas substitution has shown augmented CO emissions than the base result. The reduced combustion chamber temperature because of the high molar heat capacity of biogas charge and decrease in volumetric oxygen intake leads to incomplete oxidation of the intake fuel results a rise in CO emissions. UBG operated dual-fuel operations have shown lower CO emissions as compared to RBG. This can be referred to as the decrease in CO<sub>2</sub> content in UBG may have lowered the combustion suppressing the influence of CO<sub>2</sub>, reflecting improved combustion with lower CO emission. Barik and Murugan (2014) also reported similar trend of CO emission in their dual-fuel operation with biogas.

From Fig. 13.4 it was noticed that CO emission at 100% engine loading raised by 43, 48.2 and 51% for RBG substitution 0.6, 0.8 and 1 kg h<sup>-1</sup>, respectively, than

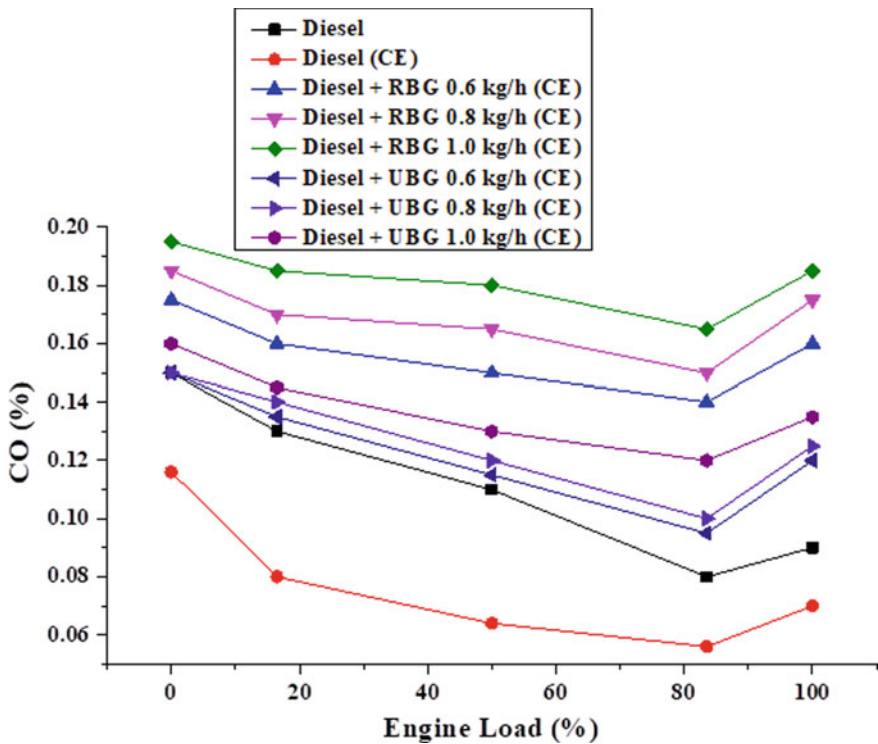


Fig. 13.4 Change in CO emission with respect to engine loading

that of diesel, whereas for UBG run the percentage of augment in CO emission is reduced to 25.2, 28.1 and 33.2% for the said induction rates, respectively.

### 13.3.2 CO<sub>2</sub> Emissions

Figure 13.5 depicts that with the hike in engine loading the CO<sub>2</sub> emissions raises may be caused by the boost in temperature of combustion that helped in improved combustion of supplied fuel.

Coated engine running with standard diesel gives slightly increased CO<sub>2</sub> emissions as referred to base results. The elevated mean temperature of combustion caused by adiabatic insulation of coating amplifies the oxidation reaction resulting in enhanced CO<sub>2</sub> emission. A reducing trend of CO<sub>2</sub> emissions was noticed with the increase in biogas induction. The reason could be because of higher ignition delay due to the presence of biogas, deficiency of fresh air and slow-burning rate of biogas leading to poor combustion, as a result, decreases the CO<sub>2</sub> emissions. CO<sub>2</sub> emission for RBG was higher than dual-fuel operation with UBG as well as from diesel

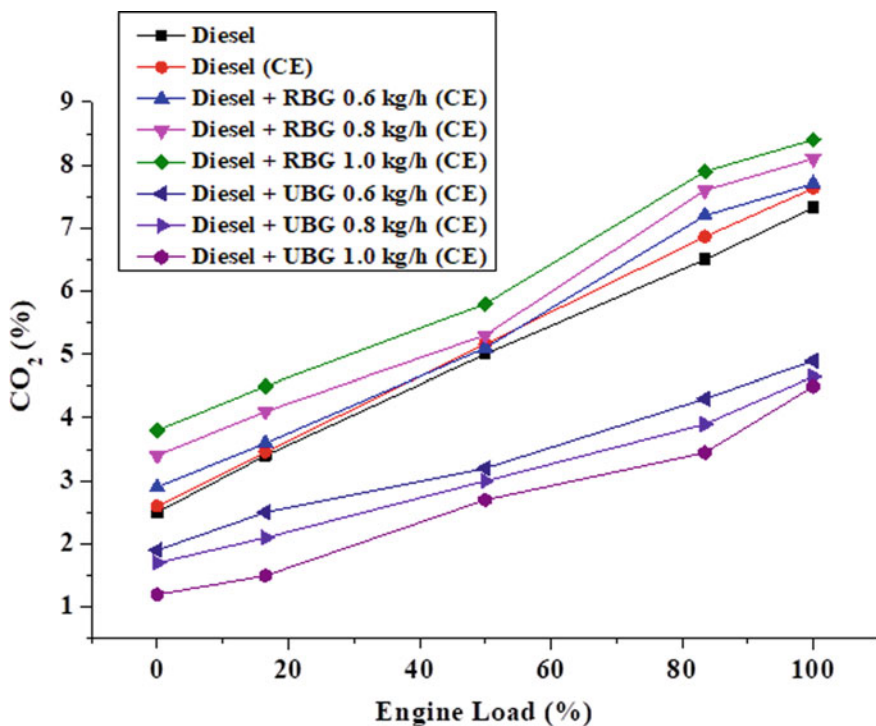


Fig. 13.5 Change in CO<sub>2</sub> emission with respect to engine loading

alone operation, maybe due to presence of higher CO<sub>2</sub> content in RBG increases the corresponding CO<sub>2</sub> emission.

The CO<sub>2</sub> emission increased by 5, 9, and 12% for RBG substitutions 0.6, 0.8, and 1 kg h<sup>-1</sup>, respectively, than that of standard diesel run, whereas in the case of UBG substitution CO<sub>2</sub> emission reduced by 33, 36, and 38% from the base result for the said substitution rate, respectively, at 100% engine loading operation.

### 13.3.3 HC Emission

Figure 13.6 presents the change in HC emission at different biogas substitution. It was found that HC emissions drops with the rise in engine loading possibly caused by the increase in ignition centers in the combustion zone at higher loads that result in better combustion characteristics. Engine with coating shows lower HC emission for diesel alone operation, possibly as a result of the rise in mean combustion temperature leading to inefficient utilization of the supplied fuel. However, the trend of HC emission raises proportionally with biogas flow rate maybe because of the decreased volumetric fresh air supply that leads to partial oxidation of the intake charge. RBG operation has shown higher HC emission than UBG dual-fuel run.

The HC emission raised by 42, 51, and 55% for RBG flow rates of 0.6, 0.8, and 1 kg h<sup>-1</sup>, respectively, as referred with standard diesel at 100% engine load, while in the case of UBG substitution the increase in HC emission reduced to 27, 31, and 35% for the said flow rates, respectively.

### 13.3.4 NO Emission

Figure 13.7 depicts the observations of NO emission trends with respect to engine loading under the variation in biogas substitution. A reduced NO emission was observed with hike in biogas flowrate. The reason may be stated as the hike in specific heat absorption because of the supplied biogas that reduces the combustion chamber temperature.

Again, the increase in substitution of biogas that minimizes the volumetric oxygen intake to the engine cylinder and enlarges the ignition delay resulting in a drop in mean temperature of combustion and hence reduced the NO emission (Barik and Murugan 2014).

At 100% engine load run, the NO emission reduced by 48, 49, and 51% for RBG substitutions 0.6, 0.8, and 1 kg h<sup>-1</sup>, respectively, in reference to the standard diesel run, whereas it decreased by 26, 35, and 41% for the said substitutions of UBG, respectively.

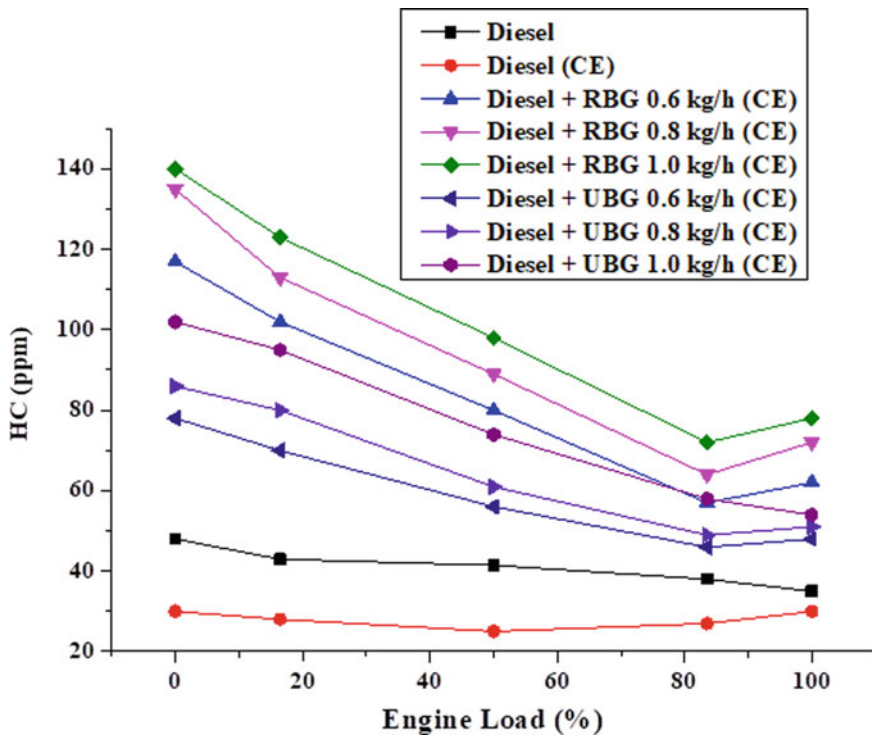


Fig. 13.6 Change in HC emission with respect to engine loading

### 13.3.5 Smoke Opacity

Figure 13.8 represents the observations of variation in smoke opacity trends with the change in engine loading and variation in biogas substitutions. It is noticed from the graph that smoke opacity is proportional to engine loading, while in dual-fuel run a considerable deviation of smoke opacity curve was observed. This is perhaps endorsed to decrease in diesel supply with the hike in biogas substitution that minimizes the presence of aromatic structure molecules in the fuel charge and CH<sub>4</sub> present with the inducted biogas has an affinity to release lower smoke (Jena and Acharya 2019). Thermal barrier coating has an activist influence on smoke opacity, as the mean temperature of combustion constantly rises on account of the adiabatic impact of coating, resulting in fast attainment of activation energy of the injected diesel. As a result, this suppresses the buildup of pilot fuel injected in the combustion zone by increasing evaporation rate and reduces the presence of fuel-rich regions that could cause smoke formation Hence, it accelerated the oxidation of soot precursors leading to lower smoke emission. Yilmaz and Gumus also found similar results of smoke emission during their dual-fuel experiment with coated engine using biogas (Yilmaz and Gumus 2017).

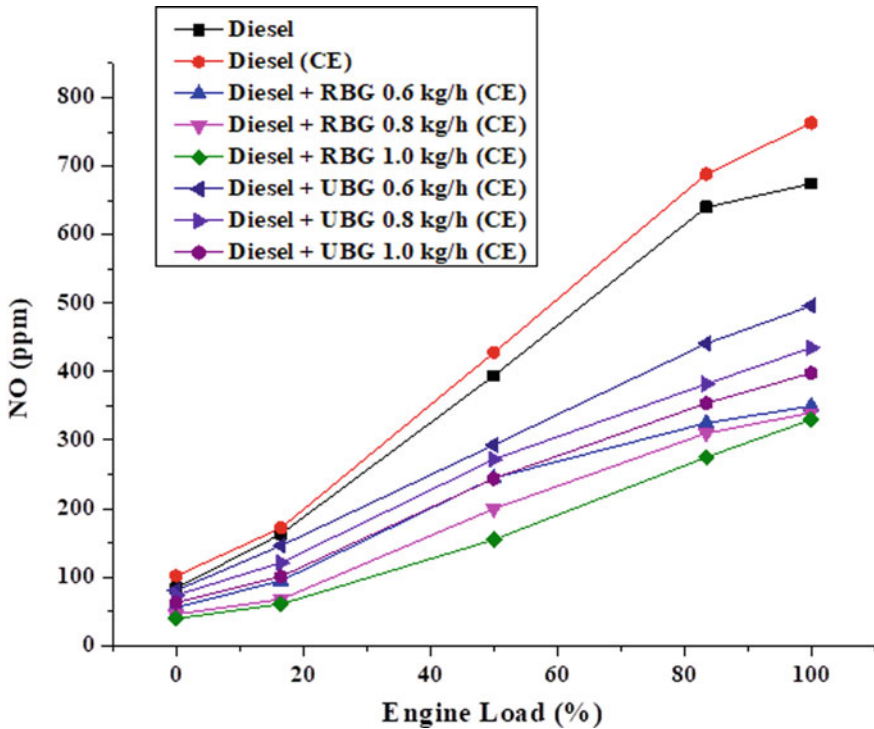


Fig. 13.7 Change in NO emission with respect to engine loading

The smoke opacity was reduced by 42, 50, and 55% with RBG substitutions 0.6, 0.8, and 1 kg h<sup>-1</sup>, respectively, compared to standard diesel at 100% engine loading whereas; smoke opacity was reduced by 53, 56, and 58% for the selected UBG substitutions, respectively.

### 13.4 Conclusions

The experimentation was purposeful to assess the engine emissions characteristics of a dual-fuel engine with thermal barrier coating under variation in biogas substitutions. The following insertions were drained:

- The scrubbing unit used in the experiment effectively improved the quality of the produced biogas by absorbing CO<sub>2</sub> where the methane content increased from 68.08 to 87.02%.
- The calorific value of the biogas was increased from 24.68 to 31.46 MJ kg<sup>-1</sup> due to scrubbing with NaOH solution.

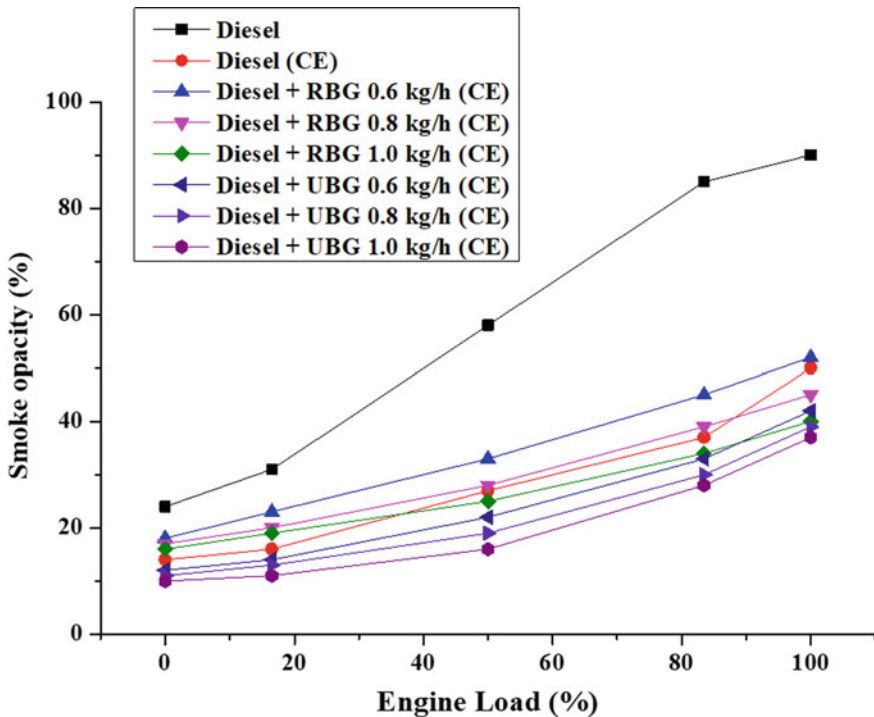


Fig. 13.8 Change in smoke opacity with respect to engine loading

- Considering the dual-fuel mode run, UBG induction with  $0.6 \text{ kg h}^{-1}$  substitution gives the best findings in terms of HC and CO emissions.
- HC and CO emissions were increased with biogas substitution. The induction rate of UBG at  $0.6 \text{ kg h}^{-1}$  have shown 27% increase in HC emission and 25.2% increase in CO emission. Whereas engine operation with RBG at  $0.6 \text{ kg h}^{-1}$  showed 42% increase in HC emission and 43% increase in CO emission.
- Engine emissions such as smoke opacity and NO emissions were reduced with biogas substitution. The induction rate of UBG at  $0.6 \text{ kg h}^{-1}$  have shown 26% decrease in NO emission and 53% decrease in smoke opacity. Whereas engine operation with RBG at  $0.6 \text{ kg h}^{-1}$  showed 48% reduction in NO emission and 42% reduction in smoke opacity.

Based on the observed findings, it was confined that a diesel engine with YSZ thermal barrier coating defines encouraging results regarding minimization of the various exhaust emissions in dual-fuel operation using biogas. Further improvements can be achieved by the adaptation of a supercharger at the inlet manifold to enhance the oxygen density in the intake air or with the addition of a cetane enhancer in the pilot fuel to improve the emission characteristics.



## References

- Ambarita H (2017) Performance and emission characteristics of a small diesel engine run in dual-fuel (diesel-biogas) mode. *Case Stud Therma Eng* 10:179–191
- Barik D, Murugan S (2014) Investigation on combustion performance and emission characteristics of a DI (direct injection) diesel engine fueled with biogas-diesel in dual fuel mode. *Energy* 72:760–771
- Barik D, Murugan S, Samal S, Sivaram NM (2017) Combined effect of compression ratio and diethyl ether (DEE) port injection on performance and emission characteristics of a DI diesel engine fueled with upgraded biogas (UBG)-biodiesel dual fuel. *Fuel* 209:339–349
- Crocamo A, Bernardino SD, Giovanni RD, Fabbicino M, Dias SM (2015) An integrated approach to energy production and nutrient recovery through anaerobic digestion of *Vetiveria Zizanioides*. *Biomass Bioenergy* 81:288–293
- Elumalai PV, Sivakandhan C, Parthasarathy M, Iqbal SM, Arunkumar M (2021) Investigation on the mitigation of environmental harmful emissions by incorporating nanoparticles to biofuel water nano emulsion in low heat rejection engine. *Heat Mass Transf.* <https://doi.org/10.1007/s00231-021-03028-7>
- Fei CG, Qian ZQ, Ren J, Zhou XJ, Zhu SW (2021) Numerical and experimental research on thermal insulation performance of marine diesel engine piston based on YSZ thermal barrier coating. *Coatings.* <https://doi.org/10.3390/coatings11070765>
- Jena SP, Acharya SK, Deheri C (2015) Thermodynamic analysis of a twin cylinder diesel engine in dual fuel mode with producer gas. *Biofuels* 7:1759–1769
- Jena SP, Mohanty UK, Mahapatra S (2020) Anaerobic digestion of semi-dried banana leaves in sewage water under the influence of certain additives. *Materi Today Proc.* <https://doi.org/10.1016/j.matpr.2020.02.830>
- Jena SP, Acharya SK (2019) Investigation on influence of thermal barrier coating on diesel engine performance and emissions in dual-fuel mode using upgraded biogas. *Sustain Environ Res* 29:24. <https://doi.org/10.1186/s42834-019-0025-4>
- Jena SP, Acharya SK (2020) Thermodynamic analysis of a thermal barrier-coated CI engine in a dual-fuel mode using biogas. *Int J Ambi Energ*:1–9. <https://doi.org/10.1080/01430750.2020.1722223>
- Jena SP, Acharya SK, Das, Patnaik PP, Bajpai S (2017b) Investigation of the effect of  $\text{FeCl}_3$  on combustion and emission of diesel engine with thermal barrier coating. *Sustain Environ Res*:1–7
- Karthikeyan V (2018) Experimental analysis on thermally coated diesel engine with neem oil methyl ester and its blends. *Heat Mass Transf.* <https://doi.org/10.1007/s00231-018-2286-6>
- Liu S, Ge X, Liew N, Liu Z, Li Y (2015) Effect of urea addition on giant reed ensilage and subsequent methane production by anaerobic digestion. *Bioresour Technol* 192:682–688
- Maile OI, Muzenda E, Tesfagiorgis H (2007) Chemical absorption of carbon dioxide in biogas purification. *Procedia Manuf* 7:639–646
- Mohapatra D, Swain RK, Jena SP, Acharya SK, Patnaik PP (2018) Effect of steam injection and  $\text{FeCl}_3$  as fuel additive on performance of thermal barrier coated diesel engine. *Sustain Environ Res.* <https://doi.org/10.1016/j.serj.2018.03.004>
- Taymaz I (2002) The effect of thermal barrier coatings on diesel engine performance. *Surf Coat Technol.* <https://doi.org/10.1016/j.surfcoat.2006.07.123>
- Tippayawong N, Thanompongchart P (2010) Biogas quality upgrade by simultaneous removal of  $\text{CO}_2$  and  $\text{H}_2\text{S}$  in a packed column reactor. *Energy* 35:4531–4535
- Verma S, Das LM, Kaushik SC (2017) Effects of varying composition of biogas on performance and emission characteristics of compression ignition engine using exergy analysis. *Energy Convers Manage* 138:346–359
- Yilmaz IT, Gumus M (2017) Investigation of the effect of biogas on combustion and emission of TBC diesel engine. *Fuel* 188:69–78



# Chapter 14

## Predicting the Performance Enhancement of Proton Exchange Membrane Fuel Cell at Various Operating Conditions by Artificial Neural Network



Tino Joe Tenson and Rajesh Baby

### 14.1 Introduction

Due to the increasing oil prices, nowadays, world is in search for new and renewable energy sources. There are many energy alternatives like solar, wind, geothermal and so on, still these technologies have not replaced the conventional non-renewable energy sources. Due to the fast depletion of these conventional energy sources, many alternatives are catching up and trying to fill the gap created by the shortage of fossil fuels. Fuel cells are very promising as a source of energy with its distinct features such as high reliability, flexibility in installation and operation, reduction in carbon footprint as a result of less greenhouse gas emissions. Furthermore, it facilitates improved environmental quality with no harmful pollutant emissions. Fuel cells are having the potential to effectively utilize the co-generation opportunities and is capable for attaining energy efficiency over 80%, silent and smooth operation, at present they are more compact and lighter.

Though, fuel cells are having all these merits, more research and development opportunities are available in order to reduce the high cost of the platinum catalyst and ways to produce the fuel (hydrogen) at low cost. Making of an effective supply chain for the distribution of hydrogen and the need to improve the infrastructure of this supply chain are the challenges ahead to implement this technology. At present, many vehicle manufacturers are extensively researching on the adoption of fuel cell technology in the automobile sector. Presently many European countries, USA and

---

T. J. Tenson

Department of Mechanical Engineering, Providence College of Engineering, Chengannur, Kerala, India

R. Baby (✉)

Department of Mechanical Engineering, St. Joseph's College of Engineering and Technology, Palai, Kerala, India

e-mail: [rajeshbaby@sjcetpalai.ac.in](mailto:rajeshbaby@sjcetpalai.ac.in)

Japan have made some head way in the manufacturing and operation of fuel cell-based cars and buses. Toyota Mirai fuel cell car is very popular in Japan. Hyundai's Nexo and Honda Clarity are fuel cell cars (Karanfil 2019; Wang et al. 2020a).

Battery packs in the laptops and cell phones will be replaced in the near future with portable fuel cells. These fuel cells can be refuelled quickly, thereby eliminating the waiting time associated with the for charging at present. Also, fuel cell battery packs are good alternatives to power electronic gadgets in remote locations and emergency situations as they do not require an electric grid. Fuel cell can also be used to power data centres. Polymer electrolyte membrane (Proton Exchange Membrane), direct methanol, alkaline, phosphoric acid, molten carbonate and solid oxide and regenerative or reversible fuel cells are the various fuel cells in practice. These fuel cells are used depending on various applications.

## 14.2 Working of a PEMFC

Operation of all varieties of fuel cells are same and the fuel is some form of hydrogen. Oxidation at anode and reduction at cathode occurs in all the cases. Fuel cells supply electricity as long as fuel and oxidizer are supplied. It consists of anode (negative electrode) and cathode (positive electrode) and an electrolyte. The electrode used here is a proton –conducting membrane, named polymer electrolyte membrane (PEM) or proton exchange membrane. Hydrogen at high purity levels is used as the fuel. PEMFCs operate at relatively low temperature (50–80 °C) and is capable of adjusting their output to meet changing power demands. At the anode the hydrogen is converted as  $2\text{H}^+ + 2\text{e}^-$  and the anode absorbs these electrons and water is formed. The fuel, hydrogen and the oxidizer, oxygen is fed to the anode and cathode through a flow field usually made with the graphite plate and the electrons flow through the external circuit through current collector (Ramezanizadeh et al. 2019).

## 14.3 Literature Review

Literature highlighting various optimization techniques used for the performance enhancement of PEMFC is detailed in this section. Zhang et al. (2020) developed a porous media flow field and performed its optimization using genetic algorithm. The data driven surrogate model is selected as the fitness evaluation function in this study. Porous media flow field gives reasonable improvement in cell performance in various regimes of its operation. Lee et al. (2004) developed an empirical model of PEMFC performance using artificial neural networks. Nafion 115 and nafion 1135 are the electrolytes they used in their studies. Saengrung et al. (2007) studied about the neural network model for a commercial PEMFC system. Back-propagation (BP) and radial basis function (RBF) networks are used in the ANN model. Their main aim was the prediction of the performance of the PEMFC. Bicer et al. (2016) uses artificial

neural network approach for smart grid applications to maximizing the performance of fuel cells and found that this model is suitable for predicting the outlet parameters.

Cao et al. (2019) presented an improved seagull optimization algorithm. This algorithm is useful for solving non-linear modelling problem associated with fuel cells. Parameters to be optimized for PEM fuel cell stacks with good performance can be achieved with this technique. The dynamics behaviour of PEMFC output current/voltage relation is properly captured by the simulation. From the results, authors suggested that improved seagull optimization technique is highly promising for identification of various operating parameter of the PEMFC. Yuan et al. (2020a) proposed a new methodology for the optimum selection of parameters in PEMFC models. An improved version of the Sunflower optimization technique is employed in this study. They found that this algorithm is capable of minimizing the sum of squared error. Again Yuan et al. (2020b) presented a new approach for optimal parameter estimation for a PEMFC model.

El-Fergany et al. (2019), using whale optimization algorithm developed a semi-empirical PEM fuel cells model. They applied this algorithm to obtain unidentified parameters of the PEMFC model. Whale optimization technique is directly applied to minimize the objective function under pre-defined constraints. Model results were compared with the experimental results of typical PEMFCs commercially available and found that the developed whale optimization algorithm contributes to the development of a precise PEMFC model. Guo et al. (2019) proposed a hybrid algorithm that combined the teaching-learning based optimization and differential evolution algorithm in order to estimate the PEMFC model parameters. It is found that the proposed model is capable of accurately predicting the stack voltage in various operational situations. Wang et al. (2020b) used a novel artificial intelligence framework combining a data driven surrogate model and an optimization algorithm based on stochastic principles to improve the maximum power density of PEMFCs. Chowdhury et al. (2018) optimized the channel to land width ratio of PEMFC based on the numerical investigations and concluded that channel to land width of 1.0 mm/1.0 mm would be best suitable for PEMFC channel geometry. They performed optimization studies keeping constant voltage of 0.4 V and constant channel depth of 1.0 mm. Furthermore, it is found that pressure drop is more dependent on channel width in comparison with land width.

On the basis of literature survey, it was found that flow of reactant gases and other operating parameters and its analysis has a crucial role on the transfer of proton and the conductivity of the cell, thereby the fuel cell performance can be improved. In the present work, numerical investigations are carried out to find the power density at various conditions. With limited number of results of the numerical investigations, an artificial neural network is created and predictions are made for the performance of fuel cells at various operating conditions (mass flow rate of the fuel and the oxidizer, cell voltage, temperature) of the serpentine flow channel PEMFC.

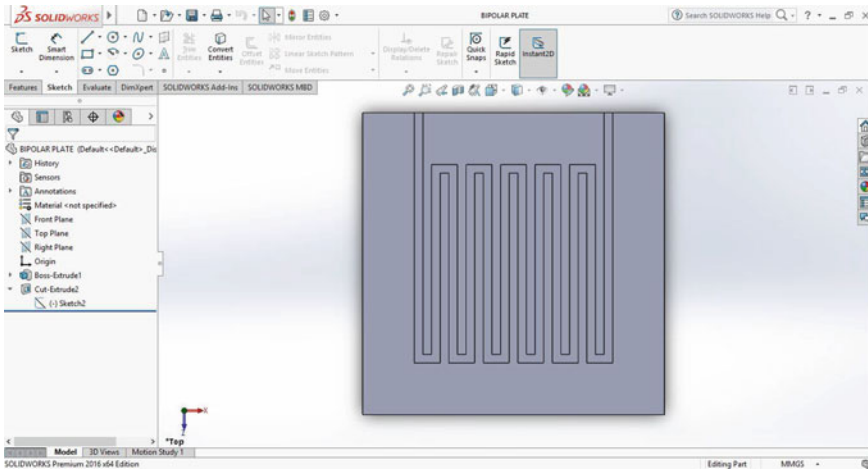


Fig. 14.1 CAD model of the flow field with 50 cm<sup>2</sup> active area

## 14.4 Numerical Investigations

The numerical model used in the present study is three-dimensional, laminar, steady state, single phase and non-isothermal and details of the numerical investigations including grid independence study and validation are detailed in (Tenson and Baby 2018) by the same authors and not included in this chapter. A screenshot of the numerical model is given in Fig. 14.1.

## 14.5 Artificial Neural Network and Results

An artificial neural network (ANN) is a computational methodology designed to simulate the way the human brain processes and analyzes information. The development of artificial intelligence is based on the principles of artificial neural networks and solves problems difficult by human or statistical standards. Neural network is a series of algorithms capable of recognizing the underlying relationships in a set of data through a process very similar to the data capturing and analysis happening in human brain. ANN is a non-linear signal processing system. Usually ANNs are having input, hidden and output layers. Details of neural network and its capabilities are detailed in Tenson and Baby (2017) by the same authors.

In the present study, ANN is used to fit a function between current density ( $I_{ANN}$ ) and the input variables. The flow rate of hydrogen and oxygen is expressed in terms of standard cubic centimetres per minute (SCCM). A total of 192 data points is available from the numerical simulations and 80% of the data points, in the present case it is one fifty-four data points, are used for training the network. Thirty-eight data

points remaining are utilized to test the performance and accuracy of the network. Since four inputs (mass flow rate of hydrogen, oxygen, cell voltage and operating temperature) are given and one output ( $I_{ANN}$ ) is obtained, the number of neurons considered in input and output layers are four and one, respectively. Similar to the grid independence study for numerical computations, neuron independence study is required to fix the no. of neuron in the hidden layer. The results of the neuron independence study are shown in Table 14.1. In Table 14.1, MSE represents the mean square error, MRE, mean relative error and  $R^2$  is absolute fraction of variance. In order to find the best performing neural network, MSE, MRE and  $R^2$  are determined, by varying the number of neurons in the hidden layer. The set with number of neurons in the hidden layer having high MRE and MSE values and low value  $R^2$  is selected as the optimum network (Srivasta et al. 2016). According to Table 14.1, in the present case, 7 neurons in the hidden layer which satisfies the conditions mentioned above is selected to carry out further simulations. The proposed ANN model with four inputs and power density as output is depicted in Fig. 14.2.

$I_{ANN}$  and  $I_{Target}$  are the current densities obtained from ANN and numerical study respectively. By adopting the neural network with 7 neurons in the hidden layer (highlighted with bold values in Table 14.1) the values of MSE and MRE are 0.0012 and 0.1241 respectively. Corresponding  $R^2 = 0.981$ . Power density obtained through the numerical model and the power density predicted by the ANN are used in the abscissa and ordinate respectively, in Fig. 14.3. From the parity plot, it can be seen that the major part of the test data lies within 10% of the parity line. From the parity plot, one can understand the goodness of fit.

**Table 14.1** Results of neuron independence study

Sl. No.	No. of neurons in the hidden layer	MRE	MSE	$R^2$
1	1	0.7896	0.0512	0.972
2	2	0.6214	0.0214	0.981
3	3	0.5287	0.0201	0.961
4	4	0.3342	0.078	0.979
5	5	0.2897	0.0142	0.984
6	6	0.1826	0.0121	0.998
<b>7</b>	<b>7</b>	<b>0.1241</b>	<b>0.0012</b>	<b>0.981</b>
8	8	0.1648	0.0125	0.979
9	9	0.2147	0.0015	0.965
10	10	0.1989	0.0215	0.978
11	11	0.2749	0.0421	0.987
12	12	0.3452	0.0524	0.974
13	13	0.4458	0.0478	0.982
14	14	0.5142	0.0541	0.995
15	15	0.6581	0.0072	0.997

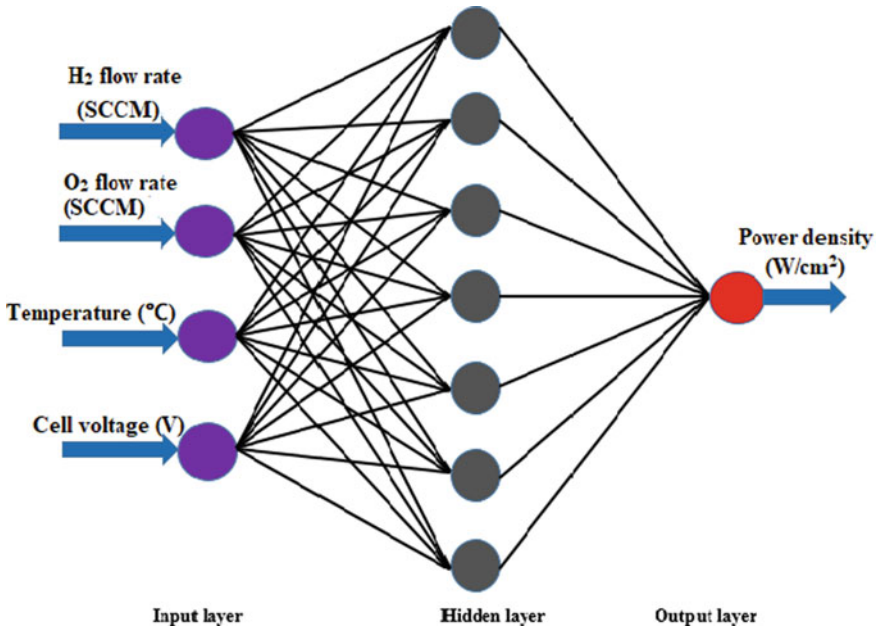


Fig. 14.2 Proposed ANN model

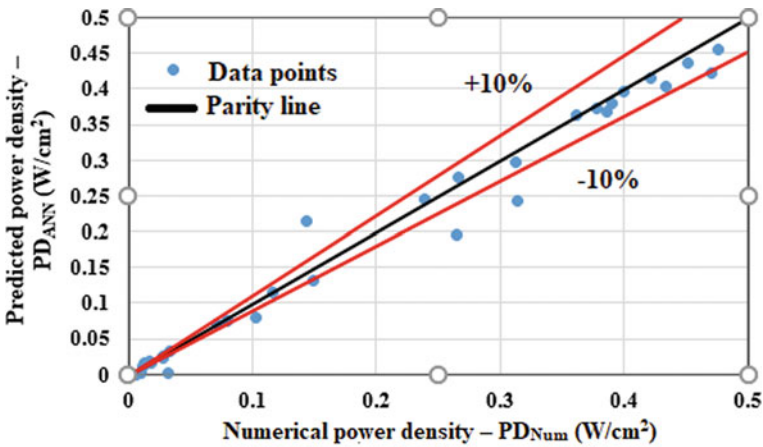


Fig. 14.3 Parity plot

Results of the numerical investigations and the prediction of various parameters by ANN used in the present work is shown in Table 14.2. Results predicted by ANN is indicated by giving a bold values in the concerned rows. Results in the row (Sl. No. 16) showed the best performance and is indicated with bold and italic figures. The

maximum relative error reported is 7.69. In Table 14.2, relative error is not calculated for the cases that are not having the numerical results.

**Table 14.2** Results of prediction by the optimum neural network

Sl. No.	Hydrogen flow rate (SCCM)	Oxygen flow rate (SCCM)	Temperature (°C)	Cell voltage (V)	$I_{\text{Target}}$ (I/cm <sup>2</sup> )	$I_{\text{ANN}}$ (I/cm <sup>2</sup> )	Relative error (%)
1	450	300	60	0.4	0.9242	0.9149	1
2	450	300	60	0.42	0.9124	0.9183	0.64
<b>3</b>	<b>450</b>	<b>300</b>	<b>60</b>	<b>0.49</b>		<b>0.8214</b>	
4	450	300	60	0.55	0.6628	0.6785	2.36
<b>5</b>	<b>470</b>	<b>350</b>	<b>65</b>	<b>0.57</b>		<b>0.4729</b>	
<b>6</b>	<b>500</b>	<b>400</b>	<b>70</b>	<b>0.712</b>		<b>0.1278</b>	
7	450	300	60	0.65	0.2056	0.2214	7.68
<b>8</b>	<b>450</b>	<b>300</b>	<b>62.5</b>	<b>0.589</b>		<b>0.3254</b>	
9	450	300	50	0.48	0.9042	0.9172	1.43
<b>10</b>	<b>450</b>	<b>400</b>	<b>55</b>	<b>0.5124</b>		<b>0.8745</b>	
11	450	300	50	0.65	0.0602	0.0573	4.81
<b>12</b>	<b>500</b>	<b>475</b>	<b>55</b>	<b>0.8</b>		<b>0.0078</b>	
13	450	300	70	0.63	0.1864	0.1953	4.77
<b>14</b>	<b>450</b>	<b>300</b>	<b>67.5</b>	<b>0.525</b>		<b>0.8947</b>	
15	600	1200	50	0.45	0.9602	0.9729	1.32
<b>16</b>	<b>600</b>	<b>1200</b>	<b>66.5</b>	<b>0.46</b>		<b>0.9924</b>	
17	600	1200	50	0.57	0.2994	0.3068	2.47
<b>18</b>	<b>650</b>	<b>1250</b>	<b>69.5</b>	<b>0.62</b>		<b>0.6748</b>	
19	600	1200	50	0.88	0.0046	0.0043	6.52
<b>20</b>	<b>600</b>	<b>1200</b>	<b>56</b>	<b>0.902</b>		<b>0.0004</b>	
21	600	1200	60	0.52	0.8802	0.8709	1.05
<b>22</b>	<b>600</b>	<b>1000</b>	<b>62.5</b>	<b>0.46</b>		<b>0.8978</b>	
23	600	1200	65	0.4	0.9484	0.9724	2.53
24	600	1200	65	0.68	0.165	0.177	7.27
<b>25</b>	<b>600</b>	<b>1157</b>	<b>54.5</b>	<b>0.5</b>		<b>0.9214</b>	
26	600	1200	70	0.4	0.8956	0.8861	1.06
<b>27</b>	<b>550</b>	<b>950</b>	<b>55</b>	<b>0.45</b>		<b>0.9147</b>	
28	600	1200	70	0.5	0.7974	0.7761	2.67
<b>29</b>	<b>600</b>	<b>1200</b>	<b>58</b>	<b>0.61</b>		<b>0.1245</b>	
30	600	1200	70	0.72	0.0792	0.0812	2.52
31	600	1200	70	0.85	0.0156	0.0168	7.69

## 14.6 Conclusions

With the help of various parameters such as flow rates of reactant gases, voltage of the cell and the temperature, the influence of various flow channel designs on PEMFC with serpentine flow field has been carried out. The conclusions made from this study are as follows:

1. Various operating conditions such as hydrogen and oxygen flow rates, cell voltage, temperature was selected for study. Of all the flow rates, it is found that hydrogen and oxygen with 600 and 1200 SCCM respectively gives maximum current density.
2. Numerical analysis shows that with the increase in temperature there is an improvement in the performance of the PEMFC, but further increase in temperature ( $>70\text{ }^{\circ}\text{C}$ ) there is a reduction in cell performance because as the temperature increases, there is a significant increase in the rate of reaction, which will result in the water accumulation in the cell area. So effective water management system is required for high temperature condition otherwise there is a drastic reduction in the performance.
3. From the different results obtained using the artificial neural networks, PEMFC of hydrogen and oxygen flow rates of 600 and 1200 SCCM respectively with a cell voltage 0.46 V and temperature of  $66.5\text{ }^{\circ}\text{C}$  gives  $0.9924\text{ A/cm}^2$  current density, which is the best result predicted by ANN. Non-traditional optimization techniques like genetic algorithm can be used with ANN to further predict the global optimum.

## References

- Bicer Y, Dincer I, Aydin M (2016) Maximizing performance of fuel cell using artificial neural network approach for smart grid applications. *Energy* 116:1205–1217
- Cao Y, Li Y, Zhang G, Jermsittiparsert K, Razmjoo N (2019) Experimental modeling of PEM fuel cells using a new improved seagull optimization algorithm. *Energy Rep* 5:1616–1625
- Chowdhury MZ, Genc O, Toros S (2018) Numerical optimization of channel to land width ratio for PEM fuel cell. *Int J Hydrogen Energy*:1–12
- El-Fergany AA, Hasanien HM, Agwa AM (2019) Semi-empirical PEM fuel cells model using whale optimization algorithm. *Energy Convers Manage* 201:112197
- Guo C, Lu J, Tian Z, Guo W, Darvishan A (2019) Optimization of critical parameters of PEM fuel cell using TLBO-DE based on Elman neural network. *Energy Conver Manage* 183:149–158
- Karanfil G (2019) Importance and applications of DOE/optimization methods in PEM fuel cells : a review. *Int J Energy Res (Wiely)*:1–22
- Lee W-Y, Park G-G, Yang T-H, Young-GiYoon C-S (2004) Empirical modeling of polymer electrolyte membrane fuel cell performance using artificial neural networks. *Int J Hydrogen Energy* 29:961–966
- Ramezanizadeh M, Zazari MA, Ahmadi MH, Chen L (2019) A review on the approaches applied for cooling fuel cells. *Int J Heat Mass Transf* 139:517–525
- Saengrunga A, Abtahi A, Zilouchian A (2007) Neural network model for a commercial PEM fuel cell system. *J Power Sources* 172:749–759



- Srivasta P, Baby R, Balaji C (2016) Geometric optimization of a PCM-based heat sink-A coupled ANN and GA approach. *Heat Transf Eng* 37(10):875–888
- Tenson TJ, Baby R (2017) Performance evaluation and optimization of proton exchange membrane fuel cells. In: Proceedings of the 24th national and 2nd international ISHMT-ASTFE heat and mass transfer conference. BITS Pilani, Hyderabad, India
- Tenson TJ, Baby R (2018) Numerical investigations on a proton exchange membrane fuel cell of active area 50 cm<sup>2</sup>. *IOP Conf Ser Mater Sci Eng* 396:012056
- Wang Y, Diaz DFR, Chen KS, Wang Z, Adroher XC (2020a) Materials, technological status and fundamentals of PEM fuel cells—a review. *Mater Today* 32:178–203
- Wang B, Xie B, Xuan J, Jiao K (2020b) AI-based optimization of PEM fuel cell catalyst layers for maximum power density via data-driven surrogate modeling. *Energy Convers Manage* 205:112460
- Yuan Z, Wang W, Wang H, Razmjoooy N (2020a) A new technique for optimal estimation of the circuit-based PEMFCs using developed sunflower optimization algorithm. *Energy Rep* 6:662–671
- Yuan Z, Wang W, Wang H, Yildizbasi A (2020b) Developed coyote optimization algorithm and its application to optimal parameters estimation of PEMFC model. *Energy Rep* 6:1106–1117
- Zhang G, Wu L, Jiao K, Tian P, Wang B, Wang Y, Liu Z (2020) Optimization of porous media flow field for proton exchange membrane fuel cell using a data-driven surrogate model. *Energy Convers Manage* 226:113513

# Chapter 15

## Role of Phase Change Material Thermal Conductivity on Predicting Battery Thermal Effectiveness for Electric Vehicle Application



Virendra Talele, Pranav Thorat, Yashodhan Pramod Gokhale,  
Archana Chandak, and V. K. Mathew

### Abbreviations

Amp	Ampere
BTMS	Battery thermal management system
C-rate	Charge rate of battery
EV	Electric vehicle
Li-ion	Lithium-ion battery
N-ECS	N-Eicosane
PCM	Phase change material
Volt	Voltage

### 15.1 Introduction

Annual worldwide greenhouse gas (GHG) emissions from traditional internal combustion engine automobiles account for about 13% of total global GHG emissions. Electric vehicles, including hybrid electric vehicles and all-electric vehicles (HEVs/EVs), provide an environmentally friendly alternative to traditional automobiles and are increasingly being utilized in place of conventional automobiles

---

V. Talele (✉) · P. Thorat · A. Chandak · V. K. Mathew  
Department of Mechanical Engineering, MIT School of Engineering, MIT ADT University, Pune,  
Maharashtra 412201, India  
e-mail: [virendratalele1@gmail.com](mailto:virendratalele1@gmail.com)

Y. P. Gokhale  
Institute for Mechanical Process Engineering, Otto-Von-Guericke University Magdeburg,  
Universitätsplatz 2, 39106 Magdeburg, Germany

in an attempt to reduce greenhouse gas emissions. In hybrid and electric vehicles, lithium-ion batteries are widely used because of their high potential energy and volumetric energy density, which surpasses alternative battery chemistries such as lead–acid and nickel–metal hydride in terms of performance (Lan et al. 2016; Jaguemont et al. 2016). However, as lithium-ion batteries have grown in popularity, heat problems have emerged. Due to the rising demand for electric cars (EVs), lithium batteries are being utilized at a high pace, which generates a lot of heat from the battery. Batteries are very sensitive to temperature fluctuations, and this has a negative impact on battery life. As a result, it is critical to developing efficient battery thermal management systems in order to increase heat dissipation. In order to satisfy the demands for high power, quick charging rates, and better driving performance, numerous researchers have created different battery thermal management systems (BTMSs) throughout the years (Weng et al. 2019; Opitz et al. 2017). These frequent battery thermal systems have to be properly monitored and controlled in order to prevent safety and thermal-related problems. From the available literature, it has been determined that the BTMS may be generally classified into two categories: active cooling and passive cooling. The forced circulation of air- and water-cooling systems is referred to as the active cooling system, and the system just like extended surface-Fins-PCM is referred as passive cooling; the main significant difference between both is that in the case of active cooling strategy we are required to source input energy for working of thermal management system, whereas in case of passive cooling arrangement, we don't require external input to source cooling system (Feng et al. 2014; Park and Jung 2013; Yang et al. 2016; Ye et al. 2019; Alsatian et al. 2010). In the modern automotive industry where the need for a high energy density pack battery is demanded proportionate to the cost of saving for the mileage of vehicle, the need for research in passive thermal management systems is engrossed.

The primary goal of a battery temperature management system (BTMS) is to keep battery modules at a consistent temperature throughout operating operations under a variety of environmental circumstances, as well as to enhance safety performance and cycle lifetime. A large number of recent research have focused on forced air-based cooling techniques, using experimental and modeling approaches in various arrangement structures, which have the potential to directly reduce temperature increase in the battery. However, if the temperature goes beyond 60 °C, it would be impossible to cool the batteries to temperatures below 50 °C using air cooling. Air-cooling strategies are insufficient under stressful and abusive conditions, particularly at high discharge rates and at high operating or ambient temperatures above 40 °C, and non-uniform distribution of temperature on the battery's surface becomes inevitable as a result of the battery's limited heat exchange capability. Liquid-based cooling methods have also been widely studied, and because of their greater thermal conductivity, they are unquestionably one of the best options for electric vehicles (EVs) operating in high-temperature settings exposed to fast charge/discharge cycles. However, the components of BTMS, such as pipes and pumps, are extremely complex, heavy, and power-hungry, and they have the potential to deplete the limited amount of energy stored in the batteries (Wang et al. 2017). When compared to the conventional thermal management techniques listed above, the phase change materials (PCM) cooling

system is the best alternative. Due to the fact that this PCM cooling system does not need the use of a pump or blower, it is both cost-efficient and easy to design and install. The passive thermal management system is the name given to this technique of cooling PCMs. It is possible for PCMs located near to the battery module of an electric car to absorb the excess heat produced by the battery of the vehicle. Upon reaching the melting point of the PCM, heat will be stored in the form of latent heat, and the temperature rise will be kept to an absolute minimum. PCMs experience the phase change phenomena as a result of absorbing or releasing the large amount of heat generated by the battery. This passive PCM cooling technique helps to keep the operating temperature of batteries within a reasonably narrow temperature range, while they are being used. Since a result, PCMs are the most effective option for an efficient thermal management system of an electric car battery, as they maintain a consistent temperature distribution regardless of the weather conditions (Mathew and Hotta 2018, 2019, 2020a, b, 2021; Karvinkoppa and Hotta 2017; Mathew and Patil 2020; Kurhade et al. 2021a, b; Mathew et al. 2021). Zaho et al. (2019) reviewed the various thermal management system techniques available, finding that PCMs are a highly effective technology for battery thermal management systems when compared to other methods. Using composite PCMs, Karimi et al. (2016) conducted an experimental study on a cylindrical lithium-ion battery thermal management system and discovered that metal matrix-PCM composites may reduce the maximum temperature difference between the battery surface and the composite PCM by as much as 70%. Azizi and Sadrameli (2016) proposed a thermal management system for a LiFePO<sub>4</sub> battery pack that included composite PCM and aluminum wire mesh plates, and they discovered that the maximum temperature of the battery surface had been reduced by 19%, 21%, and 26% at 1-C, 2-C, and 3-C discharge rates, respectively, when the system was implemented. 1-C indicates that the battery will fully discharge in one hour; similarly, 2-C indicates that the battery will totally drain in two hours; and vice versa. They are widely used due to their numerous advantageous properties, which include high latent heat, a wide melting point range, effective thermal conductivity, adaptable molding during phase change, low corrosion and flammability, and low cost. Organic PCMs are nontoxic and inflammable and have a high melting point range. A poor heat conductivity, on the other hand, prevents the adoption of PCM-based thermal management systems in some applications (Talluri et al. 2020).

The use of phase change materials in the thermal management of Li-ion battery packs is a popular method for thermal management of Li-ion battery packs (PCM). The latent heat stored in PCM due to its phase shifts over a narrow temperature range enables the temperature increase within the battery to be reduced. By modifying the chemical composition of PCM, the melting point and temperature range across which it acts as a heat absorber may be tuned. It is critical to remember that most PCMs have a relatively low thermal conductivity,  $K$ , typically between 0.17 and 0.35  $\text{WmK}^{-1}$  at room temperature (RT) (Zhang et al. 2017). For reference, silicon and copper have thermal conductivities of 145  $\text{WmK}^{-1}$  and 381  $\text{WmK}^{-1}$ , respectively. PCMs absorb heat from the batteries rather than dissipate it. PCM is also used in battery cells to protect the Li-ion cell from severe temperature changes. This is a different technique from that utilized in computer chip thermal management.

Expanded materials with high thermal conductivities and melting points were chosen from prior literature studies because they demonstrate improved heat transmission in the thermal management system of lithium batteries in electric vehicles. The critical criteria for selecting a suitable PCM for passive BTMS are not only thermal conductivity but also the melting point of the PCM. At the same hand, high melting points throughout the working range are not desired since PCM serves as an insulating material beyond the melting point, which is inefficient. Present study is focused on monitoring behavior of high voltage lithium-ion batteries submerged with two different cases of PCM with different melting point and incrementing thermal conductivity which range is cases from 0.24, 1, 3, and 6 w/mk.

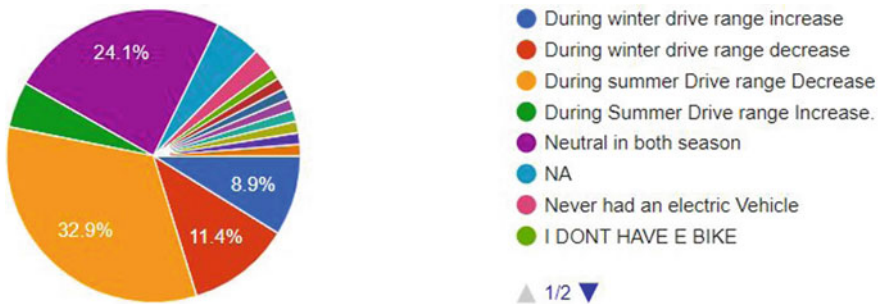
## 15.2 Methodology

### 15.2.1 Geological Investigation

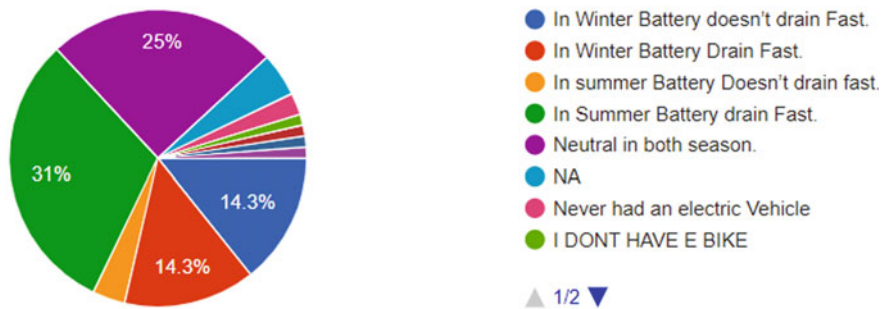
In view of the practical implementation of any research study, it is important to verify the problem statement and validate the results in an optimum manner. In the present study, the verification and preparation of problem statement are fascinating from a geological investigation which is dually performed through online mode, in which standard creation of questionnaire survey is floated into the public media to get the ground report and finding of effectiveness on working of electrical vehicle for different geological location around the world. For the quality monitoring of findings from the survey, a standard proposed literature study is also performed to engross scientific findings to the study. There are various effects of ambient temperature on the range and equivalent fuel economy of battery electric vehicles (BEVs). In isolation, hot and cold ambient temperatures resulted in modest reductions in driving range and equivalent fuel economy. Driving range and equivalent fuel economy reductions slightly differ due to the temperature dependency of both the recharge allocation factor (RAF) and battery discharge capacity. On average, an ambient temperature of 110 °F resulted in a 22% decrease in the combined driving range and an 8% decrease in combined equivalent fuel economy. On average, an ambient temperature of 85 °F resulted in a 4% decrease of combined driving range and a 5% decrease of combined equivalent fuel. From the scientific evidences, it has been found out that change in ambient temperature greatly influences the driving range of EVs; in summer seasons, the driving range significantly reduces by 25%. Based on these findings, it is important to produce the best alternative cooling system which can increase the shelf life of battery packs and increase the range of EVs.

To verify and validate our scientific facts on ground-level requirements on performance lost and drive range decrease of lithium-ion batteries of EV in the summer season, a standard set of questionnaires was created and floated in-between public media to know the actual user's perspective. Figure 15.1 shows the summary of three questions (a) Performance change in using EV in summer season versus winter

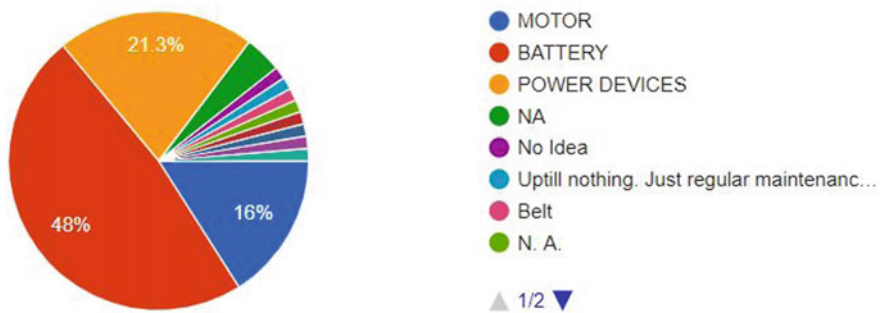
season (b) Battery state of health in summer versus winter (c) Which part of vehicle comes under frequent maintenance.



(a) Performance change in winter vs summer



(b) Battery state of health in seasons



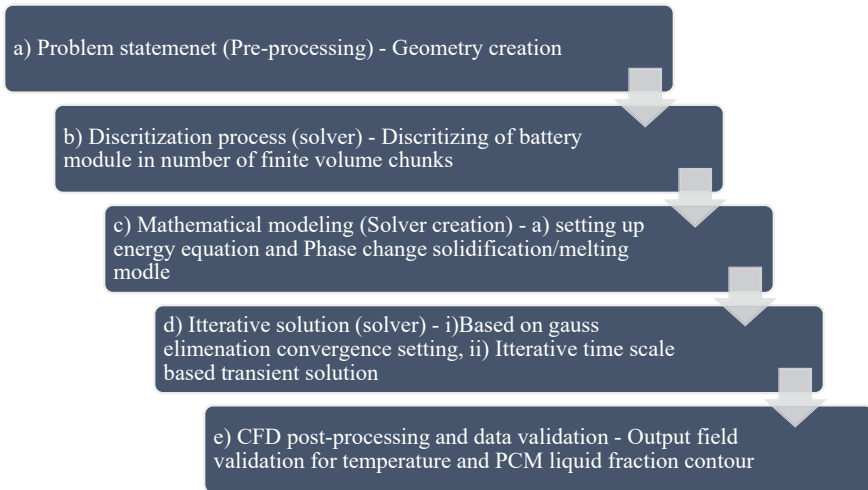
(c) EV part under frequent maintenance.

**Fig. 15.1** Statistical post-processing of questionnaire based on EV performance and working conditions under different atmospheric conditions

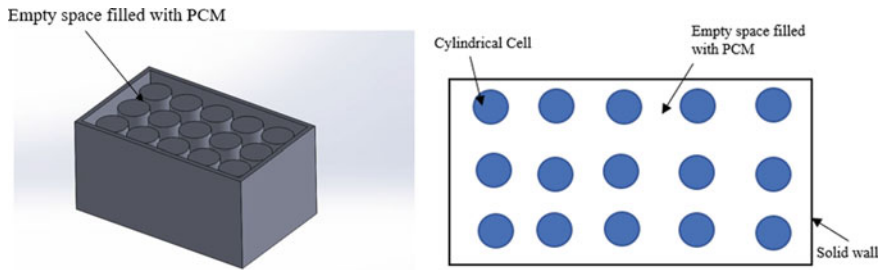
Based on scientific findings through standard literature and conducting a ground-level survey within the public media, we can verify and validate the problem statement—(a) The performance of an electric vehicle is greatly influenced by its geological location and surrounding temperature; from Fig. 15.1a, the performance of electric vehicle decreases in hot regions where the atmospheric temperature is high; similarly, from Fig. 15.1b, it has been observed that in summer battery drain fast which comes as a significant reason of reduction in overall mileage of EV because the fuel in a cell of battery backs is highly volatile, whereas in summer season due to high surrounding temperature, energy loss occurs in battery packs, due its volatile behavior it has been observed that from Fig. 15.1c, LIBs are frequently maintained in EV. To increase the total drive range of electric vehicles, it is necessary to build the most optimum thermal management system in electric vehicles which can monitor and optimize temperature within SAE standard manufacture stated range of below 50 °C.

### 15.2.2 CFD Methodology

In the present study, a numerical setup is developed using commercial coded Ansys software with Fluent Workbench 2020 R1 version. Figure 15.2 detailed flow included in the numerical scheme.



**Fig. 15.2** Detailed flowchart of CFD investigation



**Fig. 15.3** Geometry creation

### 15.2.2.1 Geometry Creation (Preprocessing)

A 19.4 V lithium-ion battery pack for use in an unmanned ground vehicle (UGV) has been developed and investigated. The battery pack is constructed from 15 cells made up of 5S3P high-capacity cylindrical lithium-ion batteries having (18 mm in diameter and 65 mm in height), as shown in Fig. 15.3. Since the batteries produce a large amount of heat during discharge and the insulated enclosure isolates them from outside air, there is an uncertainty that the operating temperatures inside the battery pack will increase significantly. The batteries are designed to work at a 50 °C limit. Present a detailed analysis that includes numerical simulations on a new battery system with a distinct geometry structure. To understand the various heat transfer mechanisms that contribute to the battery and vehicle output, a novel CFD-coupled three-dimensional computational model of a lithium-ion battery pack is developed. The layout integrates a special, close-packed square geometry in which batteries are submerged in a layer of PCM. Previous research studies have only examined computational simulations of phase change material-dependent (PCM) thermal management systems but do not evaluate the thermal efficiency of systems with and without the phase change material in integrated timescale based on different thermal conductivity.

### 15.2.2.2 Discretization of Geometry (Meshing)

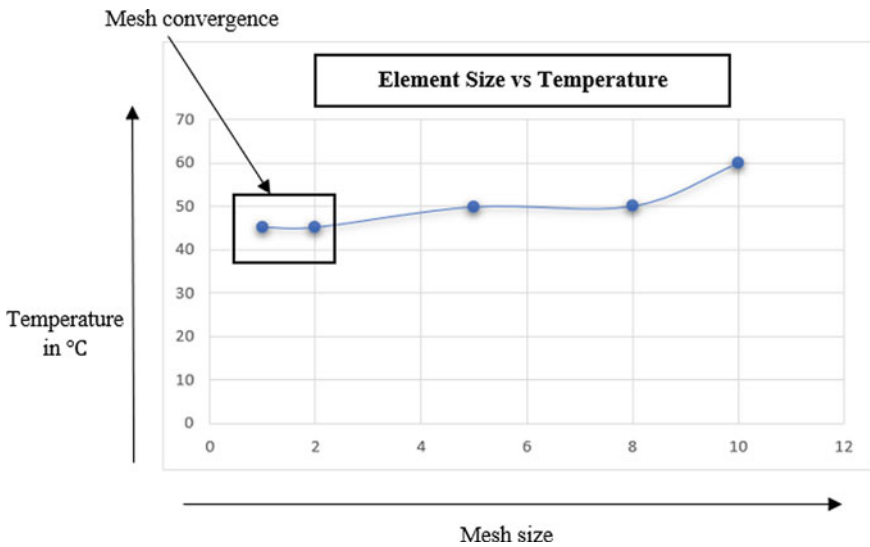
Discretization is the process of dividing whole geometry into a number of finite volume chunks. The output field result is totally dependent on the quality of the mesh. In the present study, we performed a detailed mesh independency study based on skewness factor to find optimum mesh creation on element size. Table 15.1 shows the variation in the input field on a fixed time scale which is set based on the threshold limit working of the battery to reach a temperature of 45–46 °C which is achieved for the case of without PCM at the selected mesh of 2 mm at 500 S. Table 15.1 shows representation on mesh selection.

In present study, mesh is selected for 2 mm because it results in best-fit output temperature without causing any further divergence in results (Fig. 15.4). The time



**Table 15.1** Mesh independent study

S. No.	Element size (mm)	Skewness factor	Temperature	Fixed time (s)	Time is taken by the solver (s)
1	10	1	Divergence (Floating point error)	500	–
2	5	0.97245	49.87 °C	500	300
3	2	0.847632	45.136 °C	500	1200
4	1	0.846571	45.136 °C	500	2500

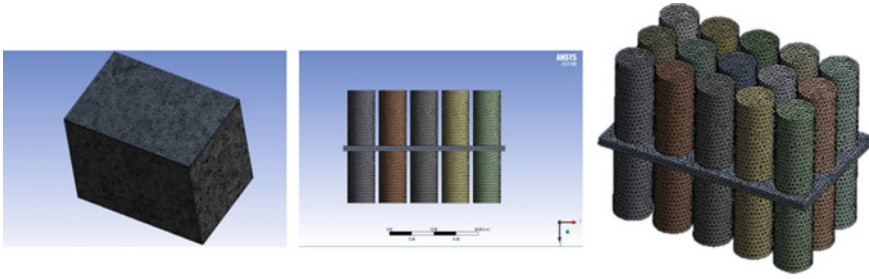


**Fig. 15.4** Mesh convergence achieved at 2 mm

achieved by solver scheme to converge solution is less as compared to 1 mm mesh size, in quality check skewness is monitored for different mesh size where lower bound limit is set to be lower than 0.98 in which for the selected mesh size 2 mm skewness factor is achieved 0.84 which confirms quality check of numerical scheme. Figure 15.5 shows the selected tetrahedral mesh for the geometry in which total nodes are 83,290 with total elements is 356,209 at selected 2 mm mesh size.

**15.2.2.3 Mathematical Modeling (Solver Creation)**

To model PCM, Voller and Prakash (1987), Talele et al. (2021) proposed the enthalpy porosity approach, which was implemented in this study. When using the Fluent solver, this technique makes use of the solidification and melting model, with the



**Fig. 15.5** Conformal tetrahedral mesh creation

mushy zone constant set to  $C = 10^5$ . During this mushy period, the liquid fraction ( $\alpha$ ) of PCM ranges from 0 to 1. When liquid fraction rate is 0, it is called as solid; when liquid fraction rate is 1, it is called liquid.

### Continuity Equation

The general version of the three-dimensional continuity equation is provided by Eq. (15.1). When dealing with an incompressible flow, the density ( $\rho$ ) may be assumed to be constant.

$$\frac{\partial \rho}{\partial t} + \frac{\partial u}{\partial x} + \frac{\partial v}{\partial y} + \frac{\partial w}{\partial z} = 0 \quad (15.1)$$

### Energy Equation

The total enthalpy ( $H$ ) of the material is computed as the sum of the sensible heat  $S_h$ , and the latent heat  $L_h$ , and is given in Eq. (15.2).

$$H = S_h + L_h \quad (15.2)$$

The liquid fraction ( $\alpha$ ) is defined as  $\alpha = 0$ , if  $T < T_{\text{solidus}}$ ;  $\alpha = 1$ , if  $T > T_{\text{liquidus}}$  and  $\alpha = \frac{T - T_{\text{solidus}}}{T_{\text{liquidus}} - T_{\text{solidus}}}$  if  $T_{\text{solidus}} < T < T_{\text{liquidus}}$ .

For the solidification and melting model, the energy equation in vectorial form is given under Eq. (15.3).

$$\frac{\partial(\rho H)}{\partial t} + \nabla \cdot (\rho v H) = \nabla \cdot (k \nabla T) + S_h \quad (15.3)$$

**15.2.2.4 Boundary Condition**

In present study, simulation is carried over fixed time scale for different C rates of battery pack which is given over as a volumetric heat generation rate. The correlation to calculate for assigning C-rates is on based of discharge current of battery pack in which total for 4 cases of C-rates results are monitored such as 0.5-C, 1-C, 1.5-C, and 2-C rate. In present study, we considered battery pack as 2-C rate gives output current of 18.6 A; 1.5-C rate gives 13.95 A; 1-C rate gives 9.30 A, and 0.5-C rate gives 4.65 A. The total internal resistance for lithium battery is 0.1 Ω; hence, the formula to calculate power is shown below as “4” which is divided by the volume of battery as calculated for cylindrical lithium-ion cell. Table 15.2 shows heat generation rate distribution for single cells with respect to the C-rates.

$$\text{Battery Watt} = I^2r \tag{15.4}$$

*I* = current.

*r* = Internal resistance.

In present investigation, we used pressure-based solver scheme having active energy and solidification/melting module active. To solve the problem of phase change transformation, there is need to determine appropriate solidification and melting property of PCM material which is shown in Table 15.3.

The liquefaction of PCM can be monitored using liquid fraction rate as shown in Eq. 15.2. In comparison of thermophysical property of paraffin wax versus N-Eicosane, it is monitored that both share same thermal conductivity but the melting range if N-Eicosane is lower than paraffin wax. N-Eicosane melts around the range of 36.5, whereas paraffin wax melts at the range of 43 °C to 49.5 °C. To calibrate exact influence of thermophysical property of PCM on cooling of battery pack, we determine empirical equation for finding exact effectiveness of battery on working temperature limits. The empirical formula to determine battery effectiveness is shown below with Eq. 15.5. As we seen from literature to enhance cooling strategy of passive thermal management system, it is necessary to use high thermal conductive material; hence, in present investigation, we determine objective analysis of PCM on different thermal conductivity rates which range in cases for paraffin wax and N-Eicosane as such—Case (1) 0.24 w/mK, Case (2) 1 w/mK, Case (3) 3 W/mK, and Case (4) 6 W/mK. In total, we investigated 12 cases in 3 configurations such as—Configuration

**Table 15.2** Power source calculation

S. No.	C-Rate	Current (ampere)	Heat generation rate (w/m <sup>3</sup> )
1	2	18.6	4706
2	1.5	13.95	2651
3	1	9.30	1176
4	0.5	4.65	294.11

**Table 15.3** Property of PCM material

S. No.	Property	Paraffin wax (P116)	N-Eicosane
1	Density (kg/m <sup>3</sup> )	760	785
2	Thermal conductivity (W/mK)	0.24	0.23
3	Dynamic viscosity	1.9	0.00355
4	Specific heat (J/Kg k)	2950	2460
5	Latent heat of fusion (KJ/Kg k)	266	241
6	Melting point °C	43–49.5 (melting range)	36.5

(1) Without PCM at 2-C, 1.5-C, 1-C, and 0.5-C rate, Configuration (2) submerged cells in layer of paraffin wax PCM—for 0.24 W/mK Case (1) 2-C, 1.5-C, 1-C, and 0.5-C rate. For 1 W/mK paraffin wax PCM Case (2) at 2-C, 1.5-C, 1-C, and 0.5-C rate. For 3 W/mK paraffin wax PCM Case (3) at 2-C, 1.5-C, 1-C, and 0.5-C rate and for 6 W/mK paraffin wax PCM Case (4) at 2-C, 1.5-C, 1-C, and 0.5-C rate. The same cases are repeated for incrementing thermal conductivity value of PCM on the cases of N-Eicosane phase change material. The thermophysical property of solid body battery pack is shown below Table 15.4.

The present study is solved using transient-based iterative solver in which time is kept as a fixed quantity to determine cooling rate of PCM influence battery pack.

**Table 15.4** Thermophysical property of assigned material

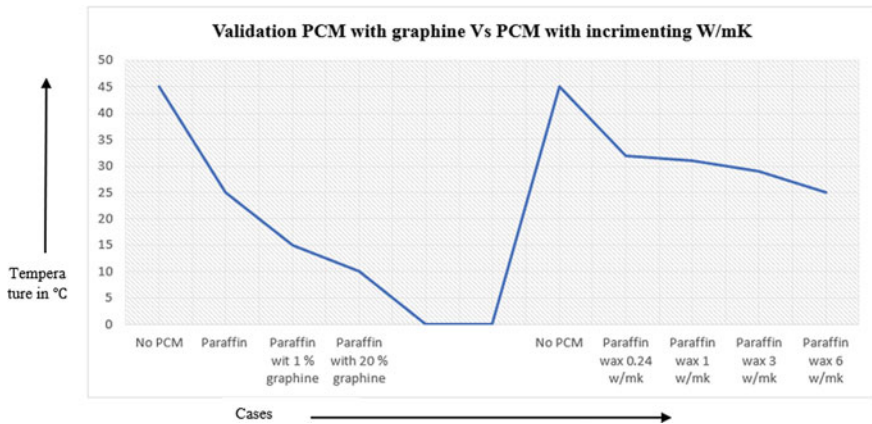
S. No.	Property	Bakelite	Aluminum
1	Density Kg/m <sup>3</sup>	1390	2710
2	Specific heat (Cp)	920	887
3	Thermal conductivity	0.24	239
<i>Assignment of material</i>			
S. No.	Parts	Name of material	Type of cell zone condition
1	Cell	Aluminum	Solid
2	Holder	Bakelite	Solid
3	Lower lid and upper lid	Aluminum	Solid
4	Phase change material	Paraffin wax/N-Eicosane	Fluid

The fixed time taken as 500 S which is derived based on highest working threshold limit of battery pack. For 2-C rate on achieving temperature of 45 °C, time taken by battery pack is 500 S; therefore, in solving methodology based on charging rate of battery pack, 500 S is taken as fixed quantity.

$$\begin{aligned} &\text{To determine battery effectiveness} \\ &= \frac{\text{Temperature without PCM}}{\text{Temperature with PCM at varyin thermal conductivity}} \end{aligned} \tag{15.5}$$

**15.2.2.5 Post-Process Validation**

The present study is validated by Goli et al. (2014) in which they performed thermal investigation of battery pack filled with submerged layer of paraffin wax PCM which further modified with layer of graphene to increase thermal conductivity of PCM. From validation, it is monitored that by increase thermal conductivity rate of PCM significant amount of temperature drop is observed around the battery pack. Achieved results from CFD investigation are post-processed to see graphical contour of temperature plot around the battery pack and PCM (Fig. 15.6).



**Fig. 15.6** Validation graph

### 15.3 Results

#### 15.3.1 Battery Pack Scientific Evidence and Discussion

The present study was focused to determine thermal behavior of battery pack for different thermophysical configuration phase change material for paraffin wax and N-Eicosane on fixed time scale of 500 S on with and without PCM. The results are shown below on different cases which is majorly classified for 3 set of configurations.

#### Configuration (1) Battery Pack Without PCM at Fixed Time Scale of 500 S

Case (1) 2-C rate at 18.6 A.

Maximum temperature achieved at working of 18.6 A for 2-C rate is 44.136 °C (Fig. 15.7).

Case (2) 1.5-C rate at 13.95 A.

Maximum temperature achieved at working of 13.95 A for 1.5-C rate is 39.819 °C (Fig. 15.8).

Case (3) 1-C rate at 9.30 A.

Maximum temperature achieved at working of 9.30 A for 1-C rate is 35.496 °C (Fig. 15.9).

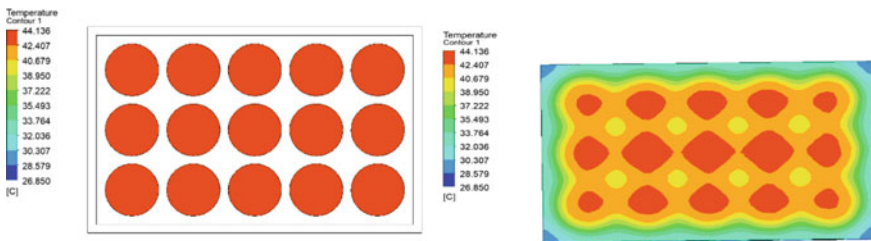


Fig. 15.7 Without PCM at 2-C rate for 500 S

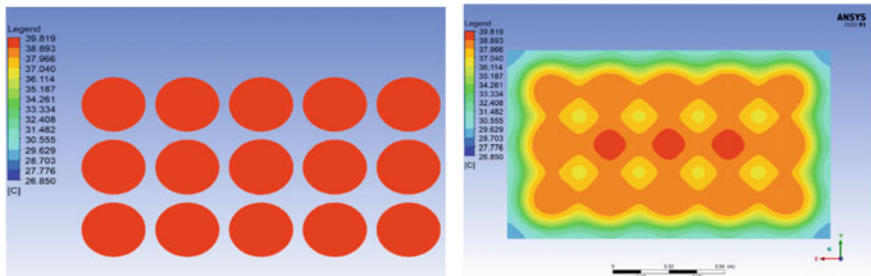


Fig. 15.8 Without PCM at 1.5-C rate for 500 S

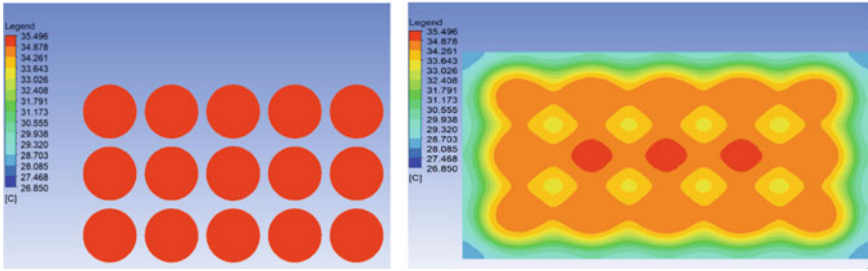


Fig. 15.9 Without PCM at 1-C rate for 500 S

Case (4) 0.5 C rate at 4.65 A.

Maximum temperature achieved at working of 4.65 A for 1-C rate is 31.173 °C (Fig. 15.10).

In the primary stage of investigation, battery pack is subjected to volumetric heat generation based on distribution of C-rate and given input current. The maximum temperature achieved is for 2-C rate which is 44.136 °C at fixed time of 500 S. The minimum temperature is achieved at 0.5-C rate which is about 31.173 °C. Based on achieved temperature limit in further cases, a layer of PCM is submerged around the periphery of cell to monitor battery cooling effectiveness (Fig. 15.11).

**Configuration (2) Battery Pack With Submerged Paraffin Wax PCM at 0.24 W/mK**

In present configuration, we investigated case of battery pack submerged with layer of paraffin wax PCM having thermal conductivity of 0.24 W/mK. To determine exact proportionate of cooling effect in respective case, following imperial equation is used.

$$T_{total} = T_{without PCM} - T_{with PCM} \tag{15.6}$$

Case (1) 2-C rate at 18.6 A (Fig. 15.12).

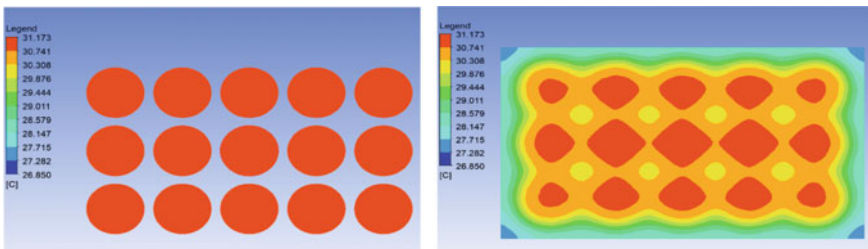


Fig. 15.10 Without PCM at 0.5-C rate for 500 S

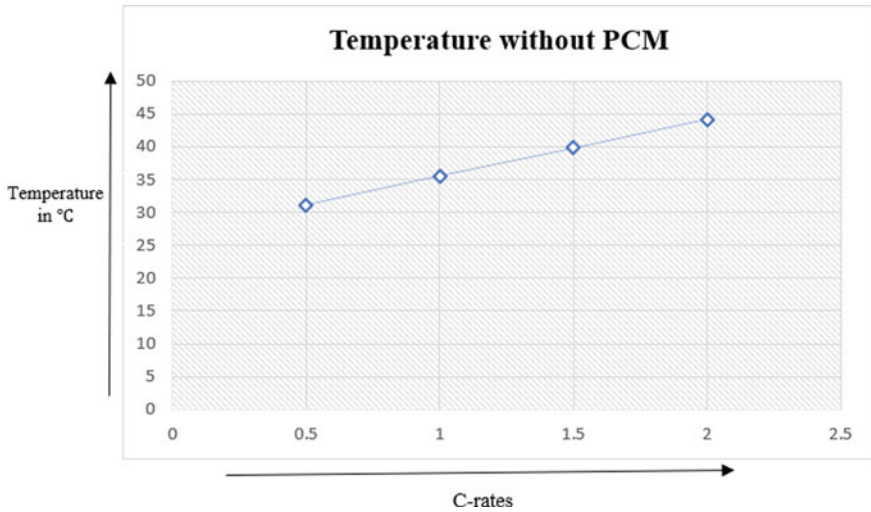


Fig. 15.11 Temperature distribution along the C-rates

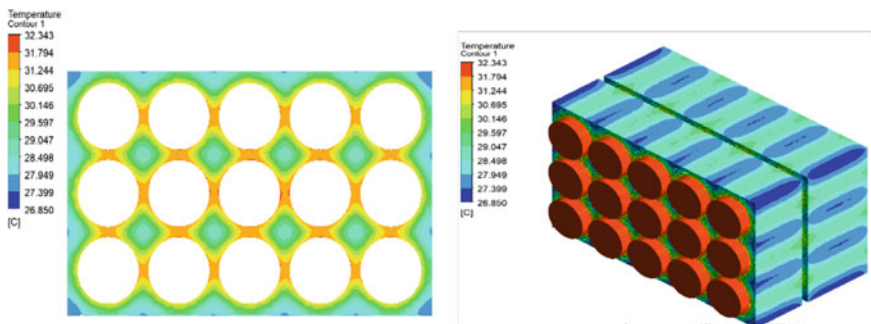


Fig. 15.12 Submerged PCM temperature distribution for 2-C rate

Maximum temperature achieved around battery pack filled with paraffin wax PCM of 0.24 W/mK for 2 C rate at 18.6 A is around 32.434 °C. The total temperature difference with respect to the cooling rate is around 11.793 °C which is tabulated based on given Eq. (15.6).

Case (2) 1.5-C rate at 13.95 A (Fig. 15.13).

Maximum temperature achieved around battery pack filled with paraffin wax PCM of 0.24 W/mK for 1.5-C rate at 13.95 A is around 30.979 °C. The total temperature difference with respect to the cooling rate is around 8.84 °C which is tabulated based on given Eq. (15.6).

Case (3) 1-C rate at 9.30 A (Fig. 15.14).



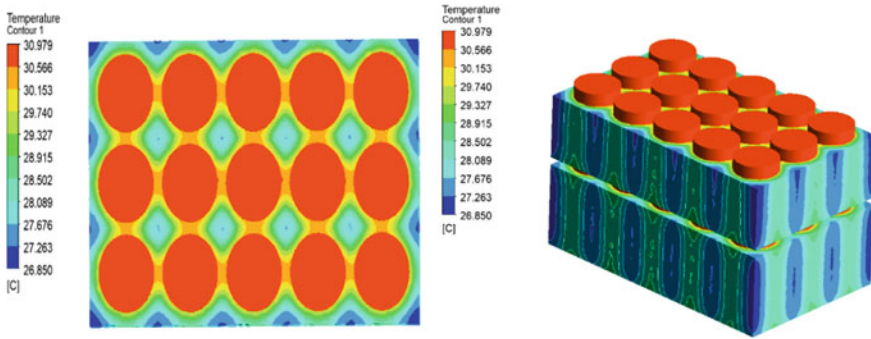


Fig. 15.13 Submerged PCM temperature distribution for 1.5-C rate

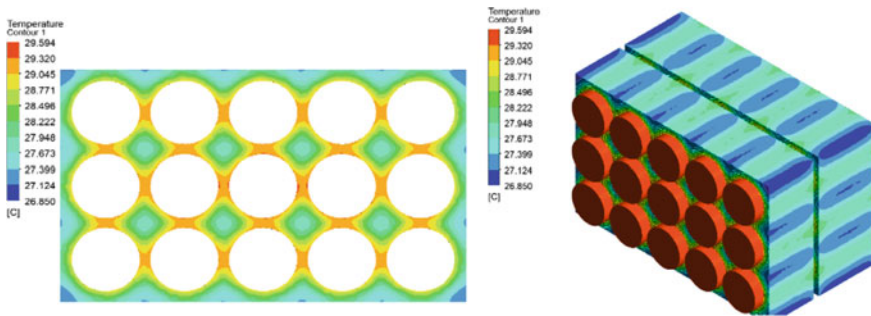


Fig. 15.14 Submerged PCM temperature distribution for 1-C rate

Maximum temperature achieved around battery pack filled with paraffin wax PCM of 0.24 W/mK for 1-C rate at 9.30 A is around 29.549 °C. The total temperature difference with respect to the cooling rate is around 6.002 °C which is tabulated based on given Eq. (15.6).

Case (4) 0.5-C rate at 4.65 A (Fig. 15.15).

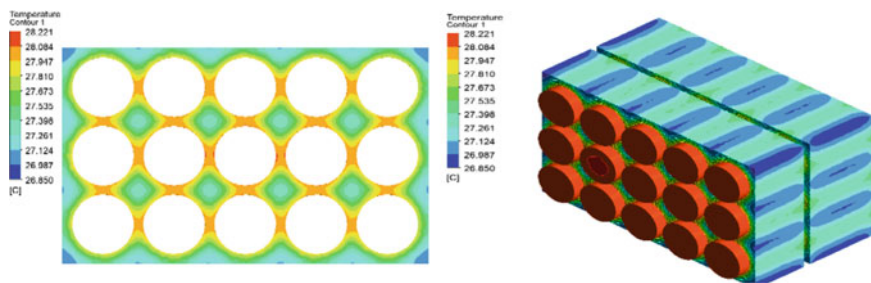


Fig. 15.15 Submerged PCM temperature distribution for 1-C rate

Maximum temperature achieved around battery pack filled with paraffin wax PCM of 0.24 W/mK for 0.5-C rate at 4.65 A is around 28.22 °C. The total temperature difference with respect to the cooling rate is around 2.952 °C which is tabulated based on given Eq. (15.6).

### Configuration (3) Battery Pack With Submerged Paraffin Wax of 1 W/mK Thermal Conductivity

In the present configuration, we investigated battery pack filled with submerged layer of PCM having thermal conductivity of 1 W/mK to identify its respective cooling effect against C-rates.

Case (1) 2-C rate at 18.6 A (Fig. 15.16).

Maximum temperature achieved around battery pack filled with paraffin wax PCM of 1 W/mK for 2-C rate at 18.6 A is around 31.083 °C. The total temperature difference with respect to the cooling rate is around 13.083 °C which is tabulated based on given Eq. (15.6), and comparative temperature difference with previous case of paraffin wax filled with 0.24 W/mK is around 1.26 °C.

Case (2) 1.5-C rate at 13.95 A (Fig. 15.17).

Maximum temperature achieved around battery pack filled with paraffin wax PCM of 1 W/mK for 1.5-C rate at 13.95 A is around 30.026 °C. The total temperature difference with respect to the cooling rate is around 9.793 °C which is tabulated based on given Eq. (15.6), and comparative temperature difference with previous case of paraffin wax filled with 0.24 W/mK is around 0.953 °C.

Case (3) 1-C rate at 9.30 A (Fig. 15.18).

Maximum temperature achieved around battery pack filled with paraffin wax PCM of 1 W/mK for 1-C rate at 9.30 A is around 28.966 °C. The total temperature difference with respect to the cooling rate is around 6.53 °C which is tabulated based on given Eq. (15.6), and comparative temperature difference with previous case of paraffin wax filled with 0.24 W/mK is around 0.628 °C.

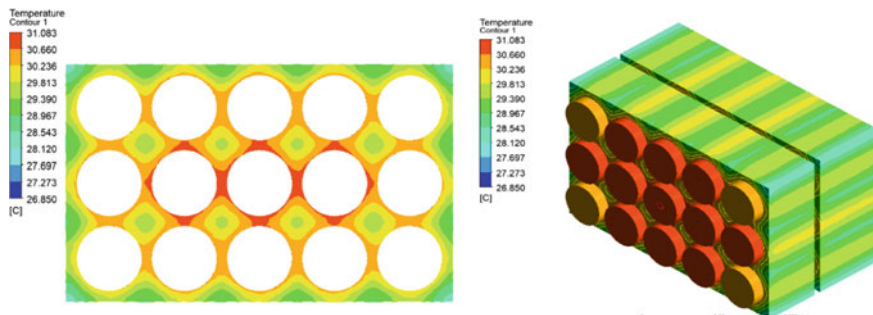


Fig. 15.16 Submerged PCM temperature distribution for 1-C rate

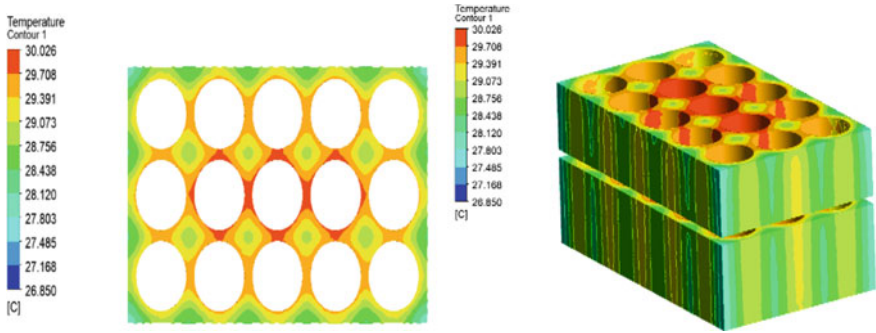


Fig. 15.17 Submerged PCM temperature distribution for 1.5-C rate

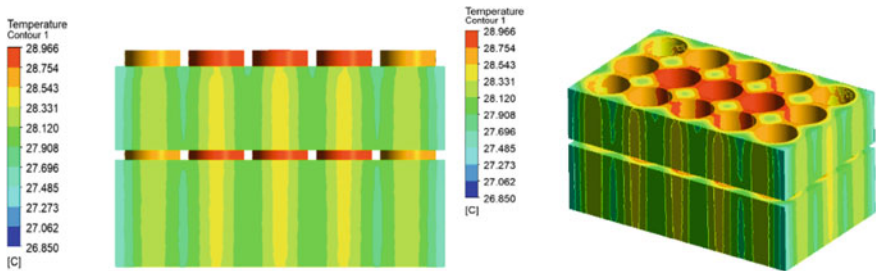


Fig. 15.18 Submerged PCM temperature distribution for 1-C rate

Case (4) 0.5-C rate at 4.65 A (Fig. 15.19).

Maximum temperature achieved around battery pack filled with paraffin wax PCM of 1 W/mK for 0.5-C rate at 4.65 A is around 27.907 °C. The total temperature difference with respect to the cooling rate is around 3.266 °C which is tabulated based on given Eq. (15.6), and comparative temperature difference with previous case of paraffin wax filled with 0.24 W/mK is around 0.314 °C.

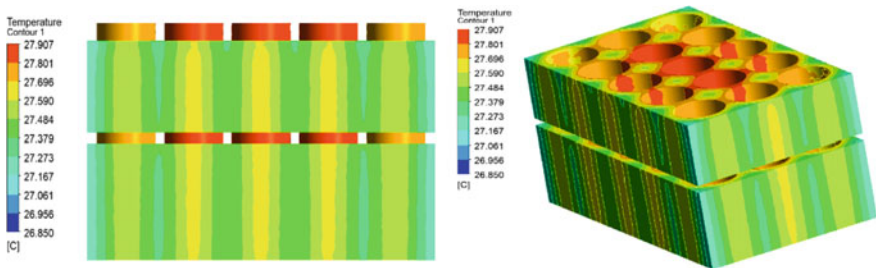


Fig. 15.19 Submerged PCM temperature distribution for 1-C rate

### Configuration (4) Battery Pack With Submerged Paraffin Wax of 3 W/mK Thermal Conductivity

In the present configuration, we investigated battery pack filled with submerged layer of PCM having thermal conductivity of 3 W/mK to identify its respective cooling effect against C-rates.

Case (1) 2-C rate at 18.6 A (Fig. 15.20).

Maximum temperature achieved around battery pack filled with paraffin wax PCM of 3 W/mK for 2-C rate at 18.6 A is around 30.583 °C. The total temperature difference with respect to the cooling rate is around 13.636 °C which is tabulated based on given Eq. (15.6), and comparative temperature difference with previous case of paraffin wax filled with 0.24 W/mK is around 1.76 °C and compared to 1 W/mK difference is about 0.5 °C.

Case (2) 1.5-C rate at 13.95 A (Fig. 15.21).

Maximum temperature achieved around battery pack filled with paraffin wax PCM of 3 W/mK for 1.5-C rate at 13.95 A is around 29.648 °C. The total temperature difference with respect to the cooling rate is around 10.171 °C which is tabulated based on given Eq. (15.6), and comparative temperature difference with previous case of paraffin wax filled with 0.24 W/mK is around 1.331 °C, and compared to 1 W/mK, difference is about 0.378 °C.

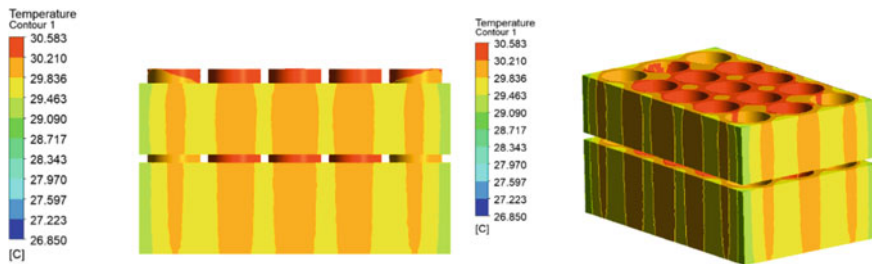


Fig. 15.20 Submerged PCM temperature distribution for 2-C rate

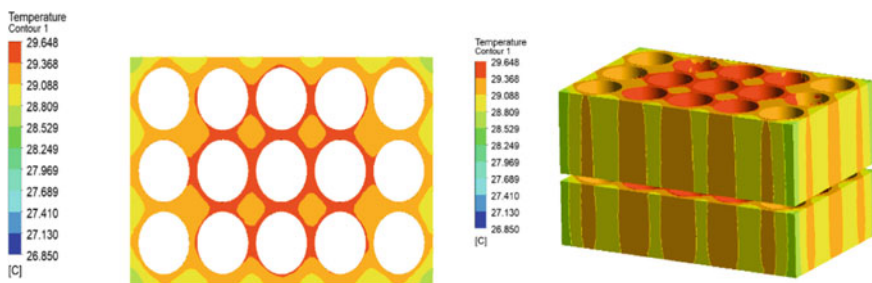


Fig. 15.21 Submerged PCM temperature distribution for 1.5-C rate

Case (3) 1-C rate at 9.30 A (Fig. 15.22).

Maximum temperature achieved around battery pack filled with paraffin wax PCM of 3 W/mK for 1-C rate at 9.830 A is around 28.714 °C. The total temperature difference with respect to the cooling rate is around 6.782 °C which is tabulated based on given Eq. (15.6), and comparative temperature difference with previous case of paraffin wax filled with 0.24 W/mK is around 0.88 °C, and compared to 1 W/mK difference is about 0.252 °C.

Case (4) 0.5-C rate at 4.65 A (Fig. 15.23).

Maximum temperature achieved around battery pack filled with paraffin wax PCM of 3 W/mK for 0.5-C rate at 4.65 A is around 27.781 °C. The total temperature difference with respect to the cooling rate is around 3.392 °C which is tabulated based on given Eq. (15.6), and comparative temperature difference with previous case of paraffin wax filled with 0.24 W/mK is around 0.44 °C and compared to 1 W/mK difference is about 0.126 °C.

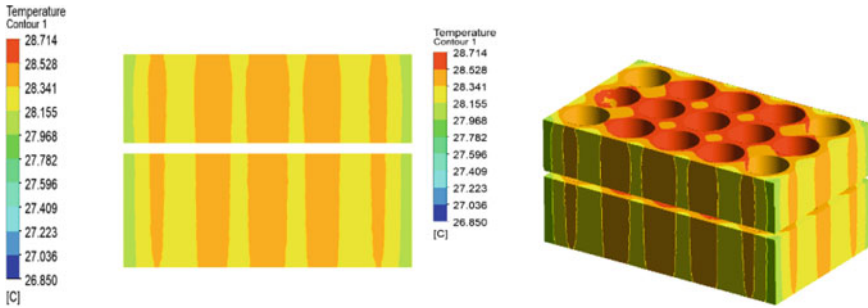


Fig. 15.22 Submerged PCM temperature distribution for 1-C rate

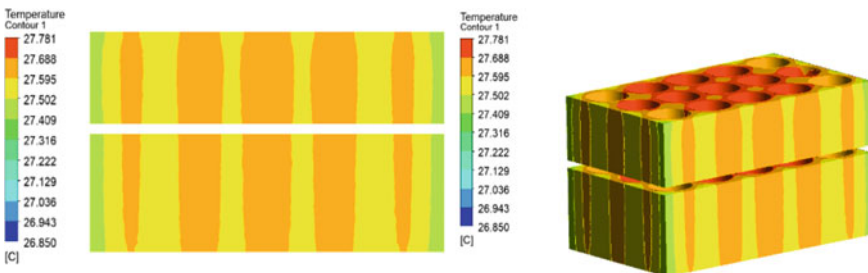


Fig. 15.23 Submerged PCM temperature distribution for 0.5-C rate

**Configuration (5) Battery Pack With Submerged Paraffin Wax of 6 W/mK Thermal Conductivity**

In the present configuration, we investigated battery pack filled with submerged layer of PCM having thermal conductivity of 6 W/mK to identify its respective cooling effect against C-rates.

Case (1) 2-C rate at 18.6 A (Fig. 15.24).

Maximum temperature achieved around battery pack filled with paraffin wax PCM of 6 W/mK for 2-C rate at 18.6 A is around 30.398 °C. The total temperature difference with respect to the cooling rate is around 13.378 °C which is tabulated based on given Eq. (15.6), and comparative temperature difference with previous case of paraffin wax filled with 0.24 W/mK is around 1.945 °C, compared to 1 W/mK difference is about 0.685 °C, and compared to 3 W/mK difference is about 0.185 °C.

Case (2) 1.5-C rate at 13.95 A (Fig. 15.25).

Maximum temperature achieved around battery pack filled with paraffin wax PCM of 6 W/mK for 1.5-C rate at 13.95 A is around 29.509 °C. The total temperature difference with respect to the cooling rate is around 10.31 °C which is tabulated based on given Eq. (15.6), and comparative temperature difference with previous

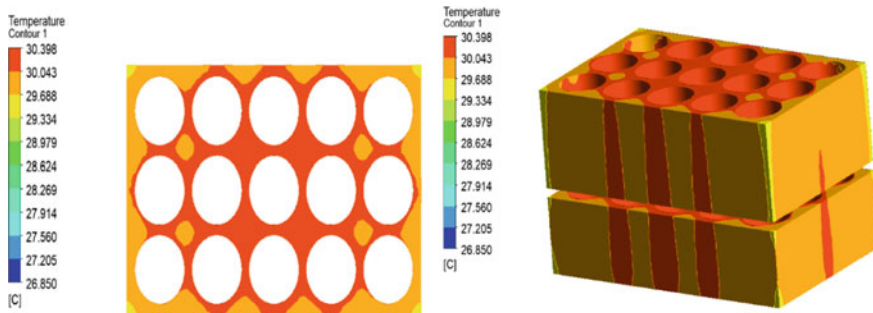


Fig. 15.24 Submerged PCM temperature distribution for 2-C rate

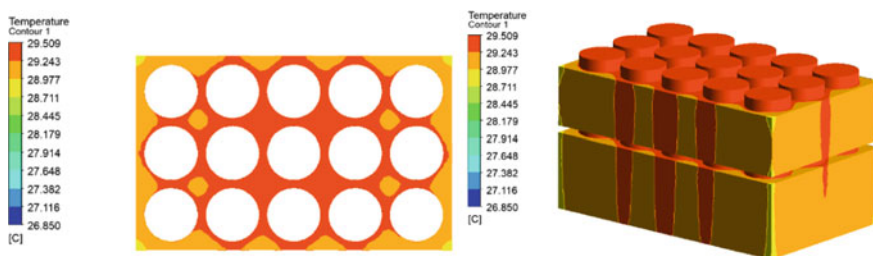


Fig. 15.25 Submerged PCM temperature distribution for 1.5-C rate



case of paraffin wax filled with 0.24 W/mK is around 1.47 °C, compared to 1 W/mK difference is about 0.517 °C, and compared to 3 W/mK difference is about 0.139 °C.

Case (3) 1-C rate at 9.30 A (Fig. 15.26).

Maximum temperature achieved around battery pack filled with paraffin wax PCM of 6 W/mK for 1-C rate at 9.30 A is around 28.621 °C. The total temperature difference with respect to the cooling rate is around 6.875 °C which is tabulated based on given Eq. (15.6), and comparative temperature difference with previous case of paraffin wax filled with 0.24 W/mK is around 0.973 °C, compared to 1 W/mK difference is about 0.345 °C, and compared to 3 W/mK difference is about 0.093 °C.

Case (4) 0.5-C rate at 4.65 A (Fig. 15.27).

Maximum temperature achieved around battery pack filled with paraffin wax PCM of 6 W/mK for 0.5-C rate at 9.30 A is around 27.735 °C. The total temperature difference with respect to the cooling rate is around 3.438 °C which is tabulated based on given Eq. (15.6), and comparative temperature difference with previous case of paraffin wax filled with 0.24 W/mK is around 0.486 °C, compared to 1 W/mK difference is about 0.172 °C, and compared to 3 W/mK difference is about 0.046 °C (Fig. 15.28).

The working of phase change material is typically based on its natural effusivity rate. In case of paraffin wax, it converts its phase from solid to liquid with the increment of time by providing appropriate delay effect to the system and absorbing induced latent heat. With increasing thermal conductivity of PCM, more amount of

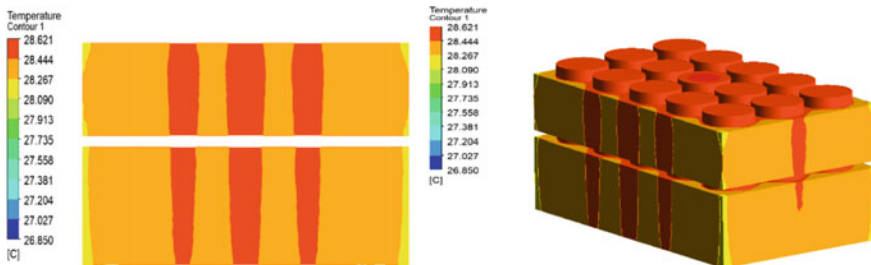


Fig. 15.26 Submerged PCM temperature distribution for 1-C rate

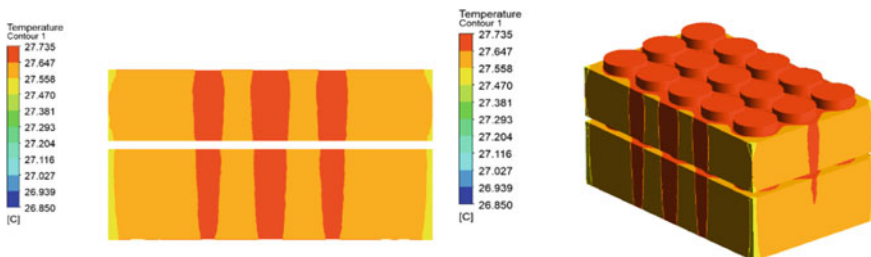
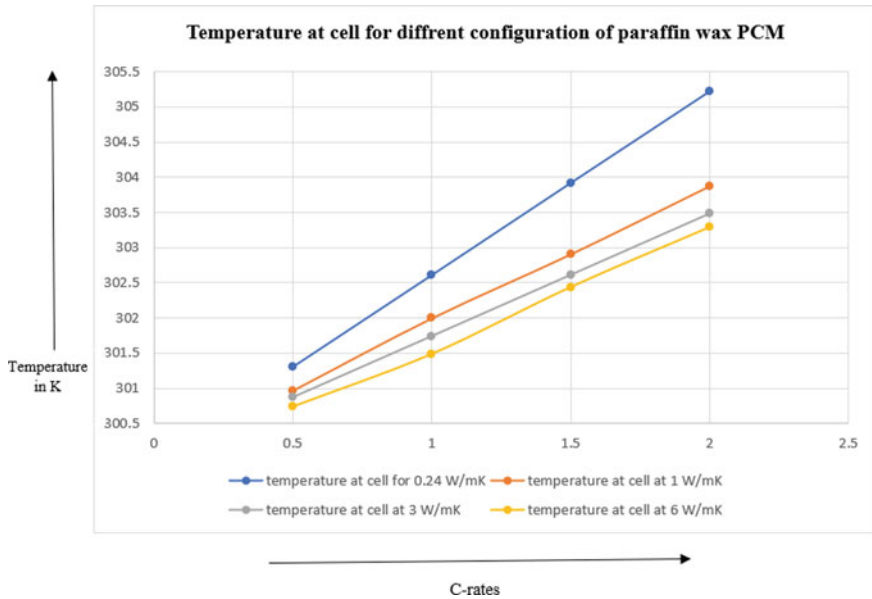
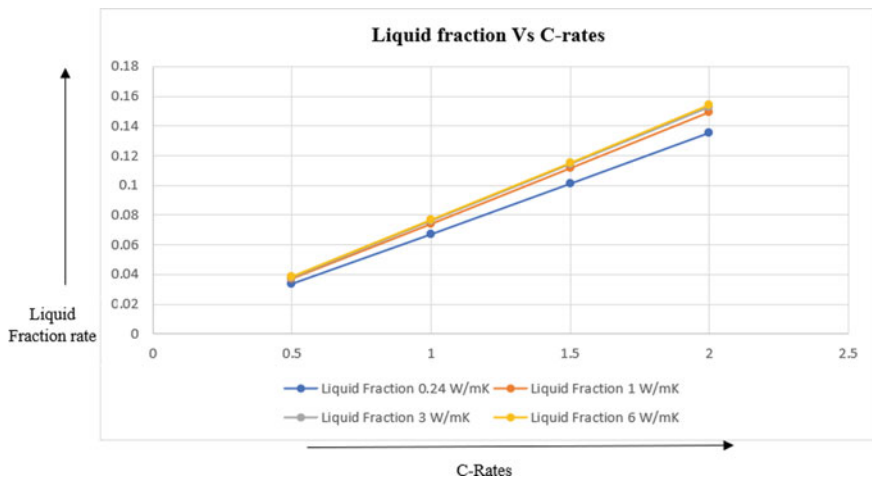


Fig. 15.27 Submerged PCM temperature distribution for 0.5-C rate



**Fig. 15.28** Temperature distribution over submerged cell for different configurations of paraffin wax-infused thermal conductivity

cooling is achieved because increasing thermal conductivity helps PCM to change its phase earlier. Figure 15.29 indicates liquid fraction rate of PCM relatively increase by increasing thermal conductivity.



**Fig. 15.29** Liquid fraction rate for different W/mK versus C-rate



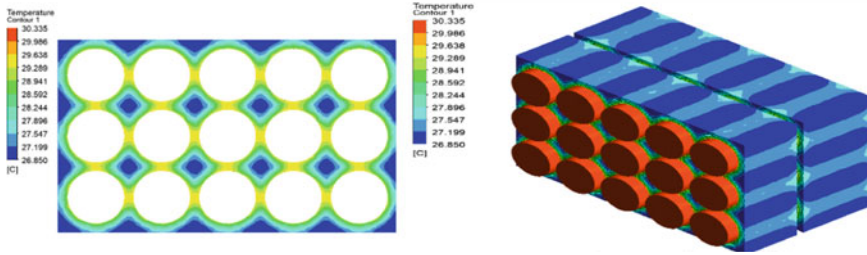


Fig. 15.30 Submerged PCM temperature distribution for 2-C rate

**Configuration (6) Battery Pack With Submerged N-Eicosane PCM of 0.23 W/mK Thermal Conductivity**

From the suggested configuration 6, battery pack is investigated for submerged layer of N-Eicosane. The main key-highlight difference between paraffin wax and N-Eicosane is about melting temperature of PCM which we can see from Table 15.4. The N-Eicosane is investigated for given C-rates as per increasing thermal conductivity in cases. The difference associated in cooling rates is tabulated from given Eq. (15.6).

Case (1) 2-C rate at 18.6 A (Fig. 15.30).

Maximum temperature achieved around battery pack submerged with N-Eicosane PCM of 0.23 W/mK for 2-C rate at 18.6 A is around 30.335 °C. The total temperature difference with respect to the cooling rate is around 13.081 °C which is tabulated based on given Eq. (15.6) and temperature difference found to be lower than paraffin wax considering same case of 0.24 W/mK.

Case (2) 1.5-C rate at 13.95 A (Fig. 15.31).

Maximum temperature achieved around battery pack submerged with N-Eicosane PCM of 0.23 W/mK for 1.5-C rate at 13.95 A is around 29.474 °C. The total temperature difference with respect to the cooling rate is around 10.345 °C which is tabulated based on given Eq. (15.6).

Case (3) 1.0-C rate at 9.30 A (Fig. 15.32).

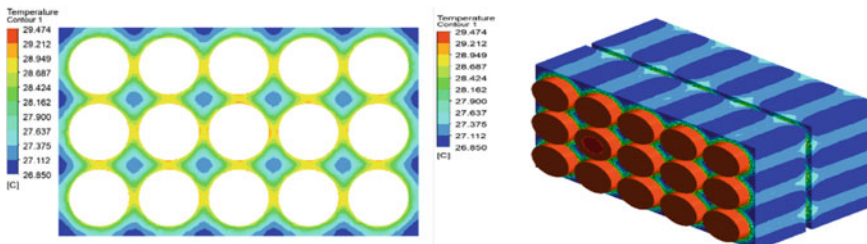


Fig. 15.31 Submerged PCM temperature distribution for 1.5-C rate

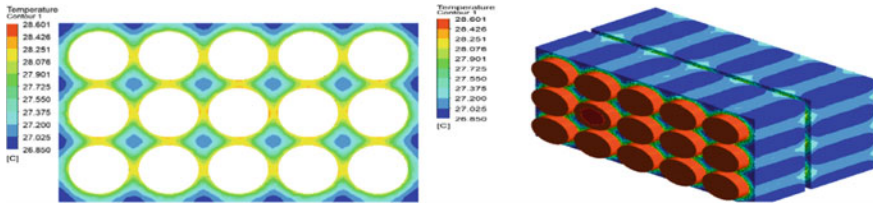


Fig. 15.32 Submerged PCM temperature distribution for 1-C rate

Maximum temperature achieved around battery pack submerged with N-Eicosane PCM of 0.23 W/mK for 1-C rate at 9.30 A is around 28.601 °C. The total temperature difference with respect to the cooling rate is around 6.859 °C which is tabulated based on given Eq. (15.6).

Case (4) 0.5-C rate at 4.65 A (Fig. 15.33).

Maximum temperature achieved around battery pack submerged with N-Eicosane PCM of 0.23 W/mK for 0.5-C rate at 4.65 A is around 27.726 °C. The total temperature difference with respect to the cooling rate is around 3.447 °C which is tabulated based on given Eq. (15.6).

**Configuration (7) Battery Pack With Submerged N-Eicosane PCM of 1 W/mK Thermal Conductivity**

Case (1) 2-C rate at 18.6 A (Fig. 15.34).

Maximum temperature achieved around battery pack submerged with N-Eicosane PCM of 1 W/mK for 2-C rate at 18.6 A is around 29.155 °C. The total temperature difference with respect to the cooling rate is around 14.951 °C which is tabulated based on given Eq. (15.6), and compared to the previous case, N-Eicosane with 0.23 W/mK difference is 1.15 °C.

Case (2) 1.5-C rate at 13.95 A (Fig. 15.35).

Maximum temperature achieved around battery pack submerged with N-Eicosane PCM of 1 W/mK for 1.5-C rate at 13.95 A is around 28.601 °C. The total temperature difference with respect to the cooling rate is around 11.218 °C which is tabulated

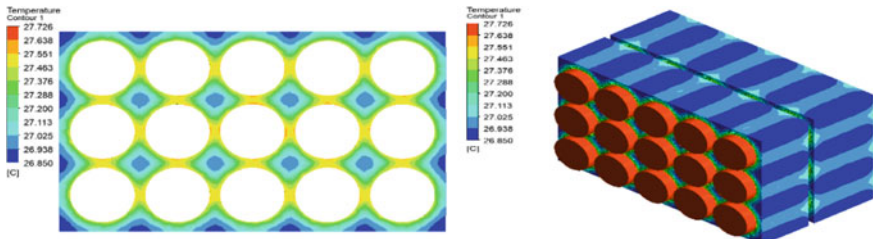


Fig. 15.33 Submerged PCM temperature distribution for 0.5-C rate

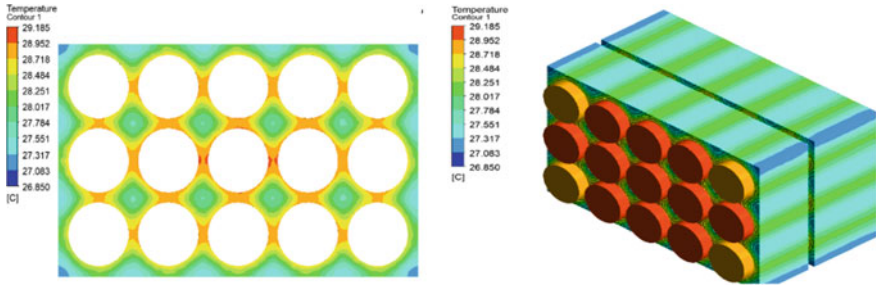


Fig. 15.34 Submerged PCM temperature distribution for 2-C rate

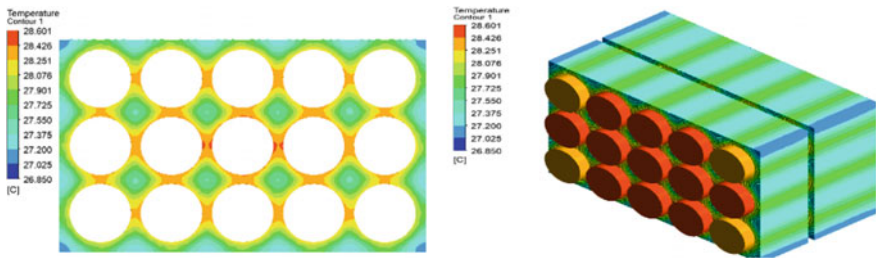


Fig. 15.35 Submerged PCM temperature distribution for 1.5-C rate

based on given Eq. (15.6), and compared to the previous case, N-Eicosane with 0.23 W/mK difference is 0.873 °C.

Case (3) 1.0-C rate at 9.30 A (Fig. 15.36).

Maximum temperature achieved around battery pack submerged with N-Eicosane PCM of 1 W/mK for 1-C rate at 9.30 A is around 28.017 °C. The total temperature difference with respect to the cooling rate is around 7.479 °C which is tabulated based on given Eq. (15.6), and compared to the previous case, N-Eicosane with 0.23 W/mK difference is 0.53 °C.

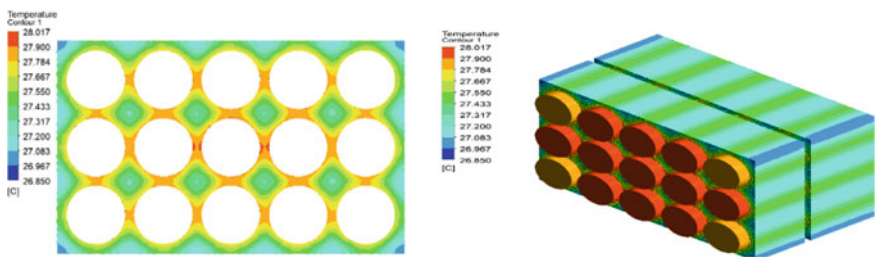
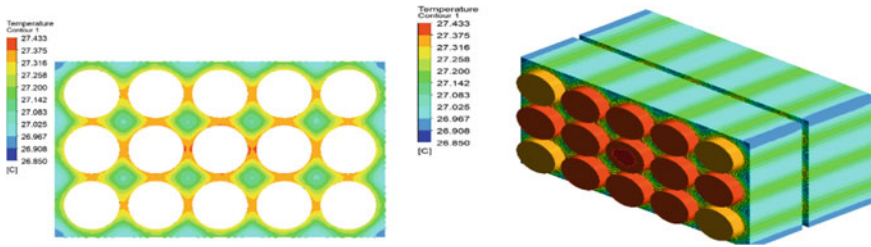


Fig. 15.36 Submerged PCM temperature distribution for 1-C rate



**Fig. 15.37** Submerged PCM temperature distribution for 0.5-C rate

Case (4) 0.5-C rate at 4.65 A (Fig. 15.37).

Maximum temperature achieved around battery pack submerged with N-Eicosane PCM of 1 W/mK for 0.5-C rate at 4.65 A is around 27.433 °C. The total temperature difference with respect to the cooling rate is around 3.74 °C which is tabulated based on given Eq. (15.6), and compared to the previous case, N-Eicosane with 0.23 W/mK difference is 0.293 °C.

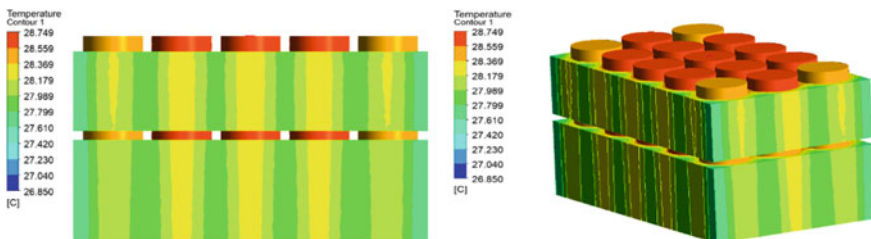
**Configuration (8) Battery Pack With Submerged N-Eicosane PCM of 3 W/mK Thermal Conductivity**

Case (1) 2-C rate at 18.6 A (Fig. 15.38).

Maximum temperature achieved around battery pack submerged with N-Eicosane PCM of 3 W/mK for 2-C rate at 18.6 A is around 28.749 °C. The total temperature difference with respect to the cooling rate is around 15.387 °C which is tabulated based on given Eq. (15.6), and compared to the previous case, N-Eicosane with 0.23 W/mK difference is 1.586 °C, and compared with previous configuration of 1 W/mK is about 0.436.

Case (2) 1.5-C rate at 13.95 A (Fig. 15.39).

Maximum temperature achieved around battery pack submerged with N-Eicosane PCM of 3 W/mK for 1.5-C rate at 13.95 A is around 28.274 °C. The total temperature difference with respect to the cooling rate is around 11.572 °C which is tabulated based on given Eq. (15.6), and compared to the previous case, N-Eicosane



**Fig. 15.38** Submerged PCM temperature distribution for 2-C rate

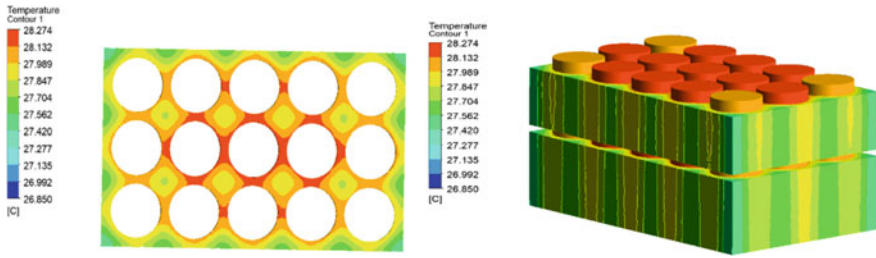


Fig. 15.39 Submerged PCM temperature distribution for 1.5-C rate

with 0.23 W/mK difference is 1.2 °C, and compared with previous configuration of 1 W/mK is about 0.327.

Case (3) 1.0-C rate at 9.30 A (Fig. 15.40).

Maximum temperature achieved around battery pack submerged with N-Eicosane PCM of 3 W/mK for 1-C rate at 9.30 A is around 27.799 °C. The total temperature difference with respect to the cooling rate is around 7.697 °C which is tabulated based on given Eq. (15.6), and compared to the previous case, N-Eicosane with 0.23 W/mK difference is 0.802 °C, and compared with previous configuration of 1 W/mK is about 0.272.

Case (4) 0.5-C rate at 4.65 A (Fig. 15.41).

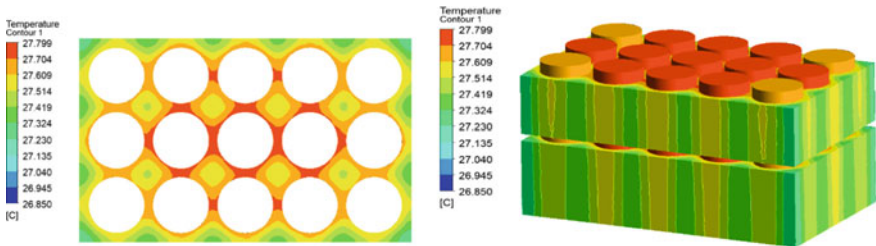


Fig. 15.40 Submerged PCM temperature distribution for 1-C rate

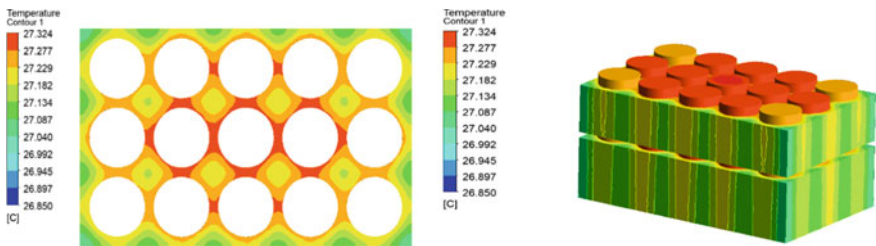
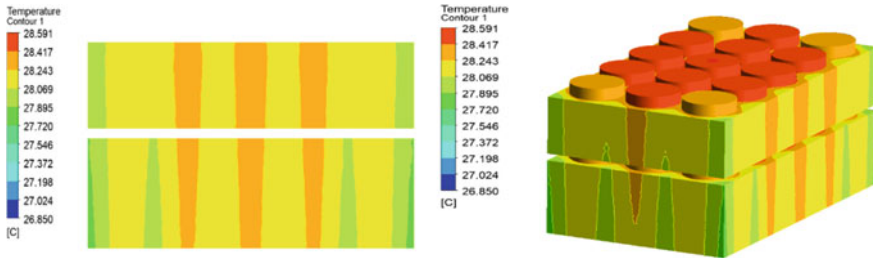


Fig. 15.41 Submerged PCM temperature distribution for 0.5-C rate





**Fig. 15.42** Submerged PCM temperature distribution for 2-C rate

Maximum temperature achieved around battery pack submerged with N-Eicosane PCM of 3 W/mK for 0.5-C rate at 4.65 A is around 27.324 °C. The total temperature difference with respect to the cooling rate is around 3.84 °C which is tabulated based on given Eq. (15.6), and compared to the previous case, N-Eicosane with 0.23 W/mK difference is 0.402 °C, and compared with previous configuration of 1 W/mK is about 0.109.

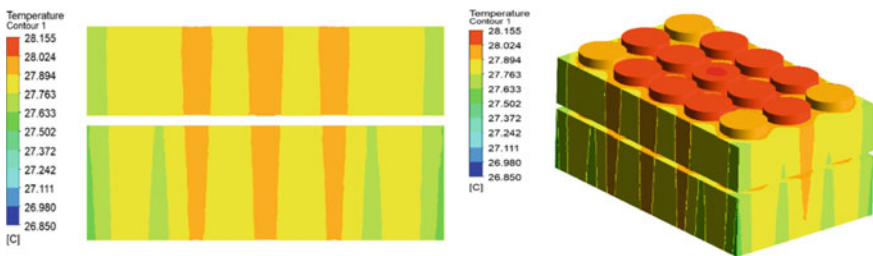
**Configuration (9) Battery Pack With Submerged N-Eicosane PCM of 6 W/mK Thermal Conductivity**

Case (1) 2-C rate at 18.6 A (Fig. 15.42).

Maximum temperature achieved around battery pack submerged with N-Eicosane PCM of 6 W/mK for 2-C rate at 18.6 A is around 28.591 °C. The total temperature difference with respect to the cooling rate is around 15.545 °C which is tabulated based on given Eq. (15.6), and compared to the previous case, N-Eicosane with 0.23 W/mK difference is 1.744 °C, compared with previous configuration of 1 W/mK is about 0.594 °C, and compared with 3 W/mK, temperature difference is about 0.158 °C.

Case (2) 1.5-C rate at 13.95 A (Fig. 15.43).

Maximum temperature achieved around battery pack submerged with N-Eicosane PCM of 6 W/mK for 1.5-C rate at 13.95 A is around 28.155 °C. The total temperature difference with respect to the cooling rate is around 11.664 °C which is tabulated



**Fig. 15.43** Submerged PCM temperature distribution for 1.5-C rate

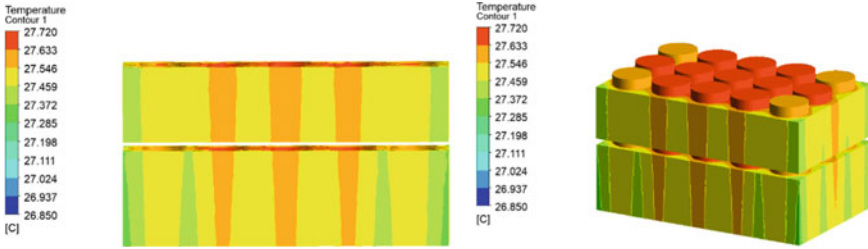


Fig. 15.44 Submerged PCM temperature distribution for 1-C rate

based on given Eq. (15.6), and compared to the previous case, N-Eicosane with 0.23 W/mK difference is 1.315 °C, compared with previous configuration of 1 W/mK is about 0.442 °C, and compared with 3 W/mK, temperature difference is about 0.115 °C.

Case (3) 1.0-C rate at 9.30 A (Fig. 15.44).

Maximum temperature achieved around battery pack submerged with N-Eicosane PCM of 6 W/mK for 1-C rate at 9.30 A is around 27.720 °C. The total temperature difference with respect to the cooling rate is around 7.776 °C which is tabulated based on given Eq. (15.6), and compared to the previous case, N-Eicosane with 0.23 W/mK difference is 0.881 °C, compared with previous configuration of 1 W/mK is about 0.351 °C, and compared with 3 W/mK, temperature difference is about 0.079 °C.

Case (4) 0.5-C rate at 4.65 A (Fig. 15.45).

Maximum temperature achieved around battery pack submerged with N-Eicosane PCM of 6 W/mK for 0.5-C rate at 4.65 A is around 27.285 °C. The total temperature difference with respect to the cooling rate is around 3.888 °C which is tabulated based on given Eq. (15.6) and compared to the previous case N-Eicosane with 0.23 W/mK difference is 0.441 °C, compared with previous configuration of 1 W/mK is about 0.148 °C, and compared with 3 W/mK temperature difference is about 0.039 °C (Fig. 15.46).

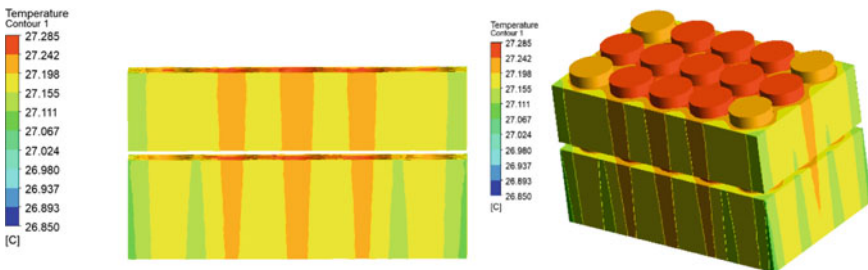
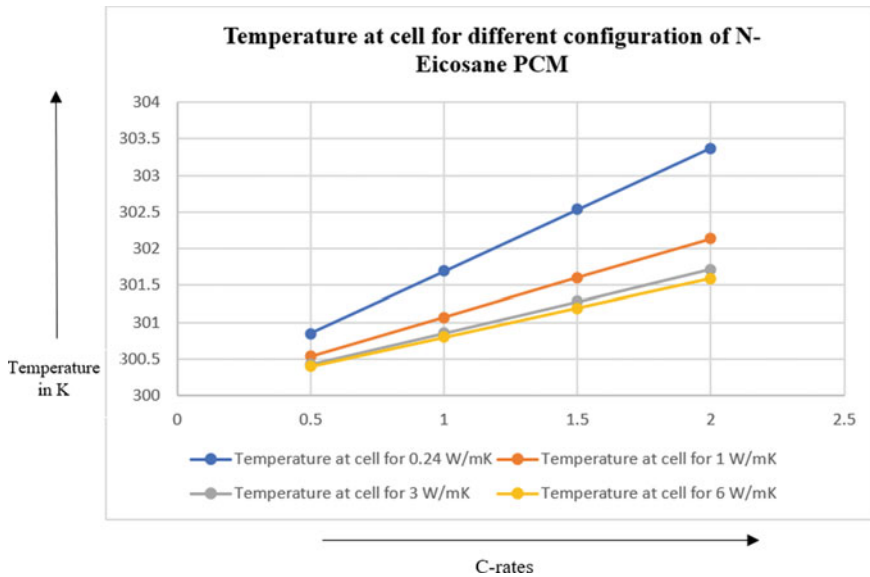


Fig. 15.45 Submerged PCM temperature distribution for 1-C rate



**Fig. 15.46** Temperature distribution over submerged cell for different configurations of N-Eicosane-infused thermal conductivity

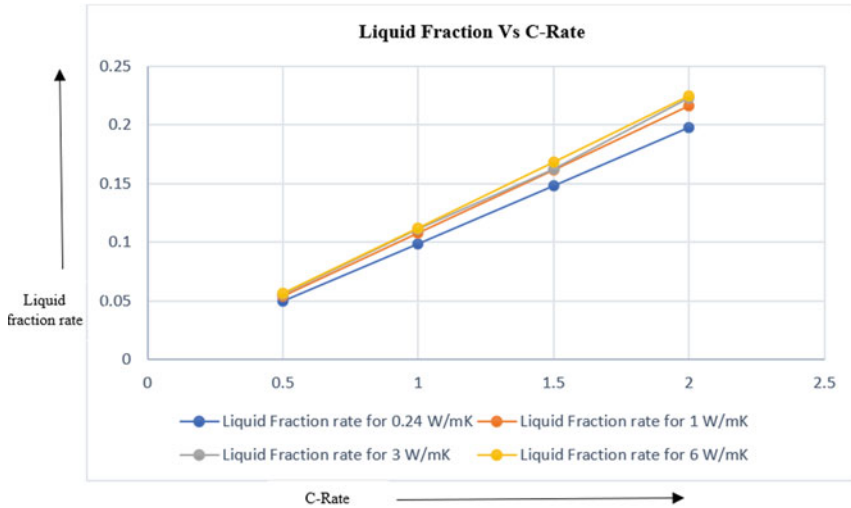
In the case of cell submerged with N-Eicosane PCM, there is more significant drop of temperature is observed with respect to the increasing thermal conductivity. In the configuration of 0.24 W/mK, temperature for 2-C rate is seen about 303.5 K, but by increasing thermal conductivity, effusivity rate of PCM gets increase due to which temperature drops from 303.5 K to 301.5 K which can be seen for the case of 6 W/mK at 2-C rate. The increasing thermal conductivity causes PCM to melt faster by changing its phase from solid to liquid which can be seen in Fig. 15.47 of liquid fraction rate.

In case of N-Eicosane PCM submerged cell, it is observed that liquid fraction for 6 W/mK and liquid fraction for 3 W/mK did not have much difference with respect to its liquid state; at highest threshold limit of 2-C rate, this phenomenon is observed because of natural tendency of N-Eicosane PCM to give up its latent heat and change its phase from solid to liquid more early due to its lower melting temperature as compared to paraffin wax.

### 15.3.2 Battery Effectiveness for Comparative Configurations

In present study, we calculated battery effectiveness for the case of paraffin wax and N-Eicosane for 2-C rate and cases for increasing thermal conductivity of PCM. The empirical correlation of battery effectiveness is developed using Eq. (15.5).





**Fig. 15.47** Liquid fraction versus C-rates for N-Eicosane PCM

Battery effectiveness is presented as non-dimensional quantity which is proportionately calculated between battery without PCM and battery filled with PCM. Below Sect. 15.3.2.1 presents calculate battery effectiveness for paraffin wax at 2-C rate, and Sect. 15.3.2.2 presents battery effectiveness calculated for N-Eicosane at 2-C rate.

### 15.3.2.1 Battery Effectiveness for Paraffin Wax

#### Battery Effectiveness for 2-C Rate

(1) Paraffin wax (2-C) 0.24 W/mK

$$\frac{\text{Temperature without PCM}}{\text{Temperature with PCM at } 0.24\text{W/mK}} = 1.3646$$

(2) Paraffin wax (2-C) 1 W/mK

$$\frac{\text{Temperature without PCM}}{\text{Temperature with PCM at } 1\text{W/mK}} = 1.4199$$

(3) Paraffin wax (2-C) 3 W/mK

$$\frac{\text{Temperature without PCM}}{\text{Temperature with PCM at } 3\text{W/mK}} = 1.4431$$

(4) Paraffin wax (2-C) 6 W/mK

$$\frac{\text{Temperature without PCM}}{\text{Temperature with PCM at 6W/mK}} = 1.4519$$

### Battery Effectiveness for 1.5-C Rate

- (1) Paraffin wax (1.5-C) 0.24 W/mK

$$\frac{\text{Temperature without PCM}}{\text{Temperature with PCM at 0.24W/mK}} = 1.2853$$

- (2) Paraffin wax (1.5-C) 1 W/mK

$$\frac{\text{Temperature without PCM}}{\text{Temperature with PCM at 1W/mK}} = 1.32615$$

- (3) Paraffin wax (1.5-C) 3 W/mK

$$\frac{\text{Temperature without PCM}}{\text{Temperature with PCM at 3W/mK}} = 1.343059$$

- (4) Paraffin wax (1.5-C) 6 W/mK

$$\frac{\text{Temperature without PCM}}{\text{Temperature with PCM at 6W/mK}} = 1.35001$$

### Battery Effectiveness for 1-C Rate

- (1) Paraffin wax (1-C) 0.24 W/mK

$$\frac{\text{Temperature without PCM}}{\text{Temperature with PCM at 0.24W/mK}} = 1.1994$$

- (2) Paraffin wax (1-C) 1 W/mK

$$\frac{\text{Temperature without PCM}}{\text{Temperature with PCM at 1W/mK}} = 1.2254$$

- (3) Paraffin wax (1-C) 3 W/mK

$$\frac{\text{Temperature without PCM}}{\text{Temperature with PCM at 3W/mK}} = 1.23503$$

- (4) Paraffin wax (1-C) 6 W/mK

$$\frac{\text{Temperature without PCM}}{\text{Temperature with PCM at 6W/mK}} = 1.2402$$

### Battery Effectiveness for 0.5-C Rate

- (1) Paraffin wax (0.5-C) 0.24 W/mK

$$\frac{\text{Temperature without PCM}}{\text{Temperature with PCM at 0.24W/mK}} = 1.1046$$

- (2) Paraffin wax (0.5-C) 1 W/mK

$$\frac{\text{Temperature without PCM}}{\text{Temperature with PCM at 1W/mK}} = 1.1170$$

- (3) Paraffin wax (0.5-C) 3 W/mK

$$\frac{\text{Temperature without PCM}}{\text{Temperature with PCM at 3W/mK}} = 1.12209$$

- (4) Paraffin wax (0.5-C) 6 W/mK

$$\frac{\text{Temperature without PCM}}{\text{Temperature with PCM at 6W/mK}} = 1.12359$$

In present investigation, battery effectiveness is calculated for submerged layer of paraffin wax PCM for four different cases of thermal conductivity along with the given input of C-rates. In respective to the contribution for each C-rates, battery effectiveness is monitored to be increased with increasing thermal conductivity. The more thermal conductivity of material helps PCM to absorb maximum amount of heat from source by changing its phase from solid to liquid. The effectiveness is tending to be decrease with decreasing given C-rate because higher temperature from heat source helps PCM to change its phase faster as compared to lower heat source (Fig. 15.48).

### 15.3.2.2 Battery Effectiveness for Paraffin Wax

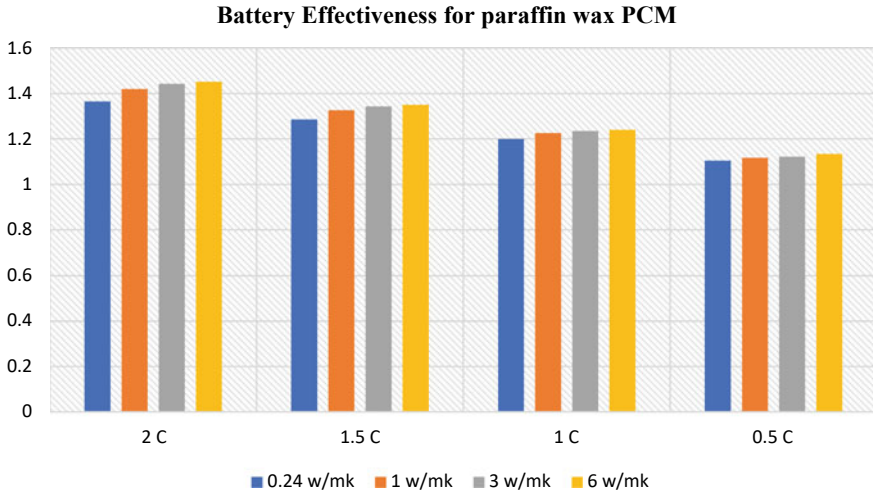
#### Battery Effectiveness for 2-C Rate

- (1) N-Eicosane PCM (2-C) 0.24 W/mK

$$\frac{\text{Temperature without PCM}}{\text{Temperature with PCM at 0.24W/mK}} = 1.454$$

- (2) N-Eicosane PCM (2-C) 1 W/mK

$$\frac{\text{Temperature without PCM}}{\text{Temperature with PCM at 1W/mK}} = 1.5122$$



**Fig. 15.48** Battery effectiveness for different C-rates for paraffin wax PCM

(3) N-Eicosane PCM (2-C) 3 W/mK

$$\frac{\text{Temperature without PCM}}{\text{Temperature with PCM at 3W/mK}} = 1.535$$

(4) N-Eicosane PCM (2-C) 6 W/mK

$$\frac{\text{Temperature without PCM}}{\text{Temperature with PCM at 6W/mK}} = 1.5456$$

**Battery Effectiveness for 1.5-C Rate**

(1) N-Eicosane PCM (1.5-C) 0.24 W/mK

$$\frac{\text{Temperature without PCM}}{\text{Temperature with PCM at 0.24W/mK}} = 1.3509$$

(2) N-Eicosane PCM (1.5-C) 1 W/mK

$$\frac{\text{Temperature without PCM}}{\text{Temperature with PCM at 1W/mK}} = 1.3992$$

(3) N-Eicosane PCM (1.5-C) 3 W/mK

$$\frac{\text{Temperature without PCM}}{\text{Temperature with PCM at 3W/mK}} = 1.4083$$

- (4) N-Eicosane PCM (1.5-C) 6 W/mK

$$\frac{\text{Temperature without PCM}}{\text{Temperature with PCM at 6W/mK}} = 1.4142$$

### **Battery Effectiveness for 1-C Rate**

- (1) N-Eicosane PCM (1-C) 0.24 W/mK

$$\frac{\text{Temperature without PCM}}{\text{Temperature with PCM at 0.24W/mK}} = 1.24107$$

- (2) N-Eicosane PCM (1-C) 1 W/mK

$$\frac{\text{Temperature without PCM}}{\text{Temperature with PCM at 1W/mK}} = 1.2669$$

- (3) N-Eicosane PCM (1-C) 3 W/mK

$$\frac{\text{Temperature without PCM}}{\text{Temperature with PCM at 3W/mK}} = 1.27688$$

- (4) N-Eicosane PCM (1-C) 6 W/mK

$$\frac{\text{Temperature without PCM}}{\text{Temperature with PCM at 6W/mK}} = 1.2805$$

### **Battery Effectiveness for 0.5-C Rate**

- (1) N-Eicosane PCM (0.5-C) 0.24 W/mK

$$\frac{\text{Temperature without PCM}}{\text{Temperature with PCM at 0.24 W/mK}} = 1.1243$$

- (2) N-Eicosane PCM (0.5-C) 1 W/mK

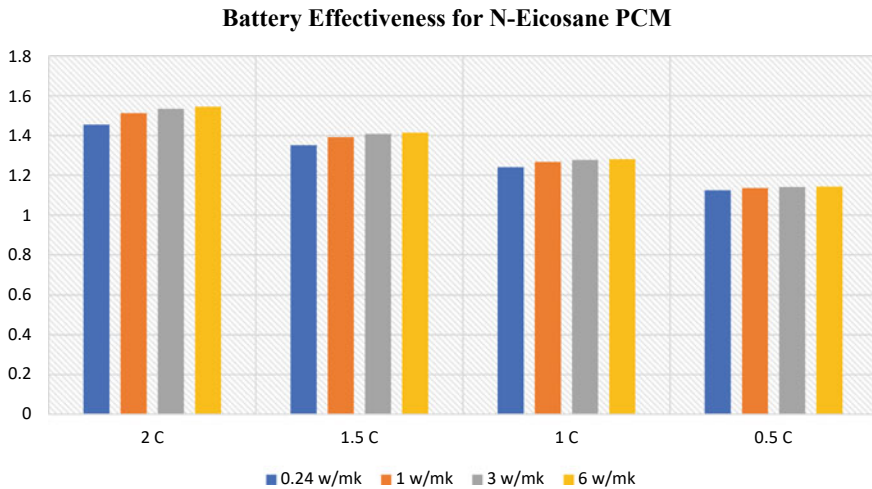
$$\frac{\text{Temperature without PCM}}{\text{Temperature with PCM at 1 W/mK}} = 1.1359$$

- (3) N-Eicosane PCM (0.5-C) 3 W/mK

$$\frac{\text{Temperature without PCM}}{\text{Temperature with PCM at 3 W/mK}} = 1.1408$$

- (4) N-Eicosane PCM (0.5-C) 6 W/mK

$$\frac{\text{Temperature without PCM}}{\text{Temperature with PCM at 6W/mK}} = 1.1424$$



**Fig. 15.49** Battery effectiveness on different C-rates for N-Eicosane PCM

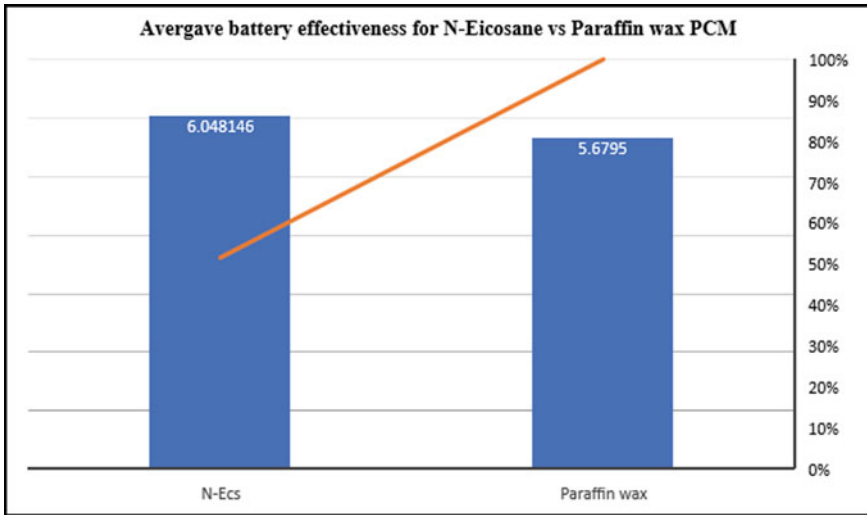
In case of N-eicosane, same trend of effectiveness is monitored as the highest contribution is working effectiveness of N-Eicosane is for 2-C rate with highest thermal conductivity case. With lowering the C-rate of battery pack, contributing effectiveness for PCM is less because the effusivity rate of PCM works more precisely in the range of melting point of PCM (Fig. 15.49).

Comparative effectiveness of PCM for N-Eicosane vs paraffin wax suggested with Petro averaging method as shown in Fig. 15.50. In case of N-Eicosane, average battery effectiveness is about 6.048146 and in case of paraffin wax is about 5.6795. The battery effectiveness is much higher in case of N-Eicosane as compared to paraffin wax because N-Eicosane having lower thermal melting point and higher effusivity rate as compared to paraffin wax. The average battery effectiveness difference between both cases makes around 0.36864 with error percentage of 6.0951%.

## 15.4 Conclusion

In present study, thermal conductivity influences phase change material for passive thermal management system is developed for 18.6 A 5S3P battery pack submerged with layer with 90% layer of paraffin wax and N-Eicosane PCM. The following points are drawn from the investigation:

- (1) By conducting ground-level survey on various electric vehicle customers, it is found that in summer season end users of EV are facing major problem with battery heating cause loss of mileage in vehicle; also, end requirement suggests battery pack is the highest contributing to the servicing of vehicle. Based on following requirement, we developed passive thermal management



**Fig. 15.50** Comparative battery effectiveness for N-Eicosane versus paraffin wax PCM

strategy to enhance shell life of battery pack by causing delay effect to high rise of temperature which proportionately increase mileage of vehicle.

- (2) Investigation of phase change material is proposed based on fixed time scale method which is tabulated based on time required battery pack to reach at 45 °C for 2-C rate. The fixed time is taken as 500 S for which different C-rates are investigated.
- (3) Phase change material changes its phase from solid to liquid which is monitored using liquid fraction rate; it is monitored that by increasing thermal conductivity of material it helps PCM to increase its thermal effusivity rate causing to absorb more amount of heat from high-power density cell working at different C-rates. Increase thermal conductivity also causes to increase liquid fraction rate which ranges from 0 to 1.
- (4) In comparative analysis between N-Eicosane vs paraffin wax, it is concluded that N-Eicosane cools down high heat source battery faster than paraffin wax which can be seen for 2-C rate working without PCM temperature achieved is about 44.136 °C; in case of paraffin wax, temperature achieved is about 32.343 °C, and in case of N-Eicosane, temperature is about 30.335 °C.
- (5) In comparative analysis of increasing thermal conductivity of PCM suggest, by influence of increased thermal conductivity, helps PCM to increase its liquid fraction rate with proportionate cooling of battery cell. Comparative performance of N-Eicosane is better than paraffin wax because N-Eicosane has tendency to melt down at lower temperature causing increasing its thermal effusivity rate; it is similarly concluded with numerical validation of battery effectiveness in which N-Eicosane is having average effectiveness value as 6.0481

and paraffin wax having average effectiveness value of 5.6795 making error difference of around 6.0951%.

**Author Contribution** **Virendra Talele**—Conceptualization, Designing, Methodology, Idealization, Modeling, Resources and Data validation, Review Edit, Drafting. **Pranav Thorat**—Conceptualization, Designing, Methodology, Idealization, Modelling, Resources and Data validation, **Yashodhan Pramod Gokhale**—Conceptualization, Designing, Methodology, Idealization, Modeling, Resources and Data validation, **Archana Chandak**—Conceptualization, Methodology, Review and Edit, **Mathew V K**—Conceptualization, Designing, Methodology, Idealization, Modeling, Resources and Data validation.

**Funding** The study has no sponsored.

## References

- Alsatian A, Mayas AT, Al-Hallaj S (2010) Thermo-mechanical behaviours of the expanded graphite-phase change material matrix used for thermal management of Li-ion battery packs. *J Mater Process Technol* 210:174–179
- Azizi Y, Sadrameli S (2016) Thermal management of a LiFePO<sub>4</sub> battery pack at high temperature environment using a composite of phase change materials and aluminium wire mesh plates. *Energy Convers Manage* 128:294–302
- Feng X, Fang M, He X, Ouyang M, Lu L, Wang H, Zhang M (2014) Thermal runaway features of large format prismatic lithium-ion battery using extended volume accelerating rate calorimetry. *J Power Sources* 266:294–301
- Goli P, Legedza S, Dhar A, Salgado R, Renteria J, Balandin AA (2014) Graphene-enhanced hybrid phase change materials for thermal management of Li-ion batteries. *J Power Sources* 248:37–43
- Jagemont J, Boulon L, Dubé Y (2016) A comprehensive review of lithium-ion batteries used in hybrid and electric vehicles at cold temperatures. *Appl Energy* 164:99–114
- Karimi G, Azizi M, Babapoor A (2016) Experimental study of a cylindrical lithium ion battery thermal management using phase change material composites. *J Energy Storage* 8:168–174
- Karvinkoppa MV, Hotta TK (2017) Numerical investigation of natural and mixed convection heat transfer on optimal distribution of discrete heat sources mounted on a substrate. *IOP Conf Ser: Mater Sci Eng* 263(6):062066
- Kurhade AS, Rao TV, Mathew VK, Patil NG (2021a) Effect of thermal conductivity of substrate board for temperature control of electronic components: A Numerical study. *Int J Mod Phys C* 26:2150132
- Kurhade A, Talele V, Rao TV, Chandak A, Mathew VK (2021b) Computational study of PCM cooling for electronic circuit of smart-phone. *Mater Today Proc*
- Lan C, Xu J, Qiao Y, Ma Y (2016) Thermal management for high power lithium-ion battery by minichannel aluminum tubes. *Appl Therm Eng* 101:284–292
- Mathew K, Patil N (2020) Convective heat transfer on the optimum spacing of high heat dissipating heat sources—a numerical approach. In: *Emerging trends in mechanical engineering*. Springer, Singapore, pp 73–84
- Mathew VK, Patil NG, Hotta TK (2021) Role of constrained optimization technique in the hybrid cooling of high heat generating IC chips using PCM-based mini-channels. In: *Constraint handling in metaheuristics and applications*, pp 231–249
- Mathew VK, Hotta TK (2018) Numerical investigation on optimal arrangement of IC chips mounted on a SMPS board cooled under mixed convection. *Therm Sci Eng Prog* 7:221–229



- Mathew VK, Hotta TK (2019) Role of PCM based mini-channels for the cooling of multiple protruding IC chips on the SMPS board-a numerical study. *J Energy Storage* 26:100917
- Mathew VK, Hotta TK (2020a) Experiment and numerical investigation on optimal distribution of discrete ICs for different orientation of substrate board. *Int J Ambient Energy* 15:1–8
- Mathew VK, Hotta TK (2020b) Experimental investigation of substrate board orientation effect on the optimal distribution of IC chips under forced convection. *Exp Heat Transf* 30:1–22
- Mathew VK, Hotta TK (2021) Performance enhancement of high heat generating IC chips using paraffin wax based mini-channels-a combined experimental and numerical approach. *Int J Therm Sci* 164:106865
- Opitz A, Badami P, Shen L, Vignarooban K, Kannan AM (2017) Can Li-Ion batteries be the panacea for automotive applications? *Renew Sustain Energy Rev* 68:685–692
- Park S, Jung D (2013) Battery cell arrangement and heat transfer fluid effects on the parasitic power consumption and the cell temperature distribution in a hybrid electric vehicle. *J Power Sources* 227:191–198
- Talele V, Thorat P, Gokhale YP, Mathew VK (2021) Phase change material based passive battery thermal management system to predict delay effect. *J Energy Storage* 44(Part B):103482. ISSN 2352-152X. <https://doi.org/10.1016/j.est.2021.103482>
- Talluri T, Kim TH, Shin KJ (2020) Analysis of a battery pack with a phase change material for the extreme temperature conditions of an electrical vehicle. *Energies* 13(3):507
- Voller VR, Prakash C (1987) A fixed grid numerical modelling methodology for convection-diffusion mushy region phase-change problems. *Int J Heat Mass Transf* 30(8):1709–1719
- Wang Z, Li X, Zhang G, Lv Y, Wang C, He F, Yang C, Yang C (2017) Thermal management investigation for lithium-ion battery module with different phase change materials. *RSC Adv* 7(68):42909–42918
- Weng J, Ouyang D, Yang X, Chen M, Zhang G, Wang J (2019) Alleviation of thermal runaway propagation in thermal management modules using aerogel felt coupled with flame-retarded phase change material. *Energy Convers Manag* 200:112071
- Yang X-H, Tan S-C, Liu J (2016) Thermal management of Li-ion battery with liquid metal. *Energy Convers Manage* 117:677–686
- Ye B, Rubel MR, Li H (2019) Design and optimization of cooling plate for battery module of an electric vehicle. *Appl Sci* 9(4):754
- Zhang J, Li X, He F, He J, Zhong Z, Zhang G (2017) Experimental investigation on thermal management of electric vehicle battery module with Paraffin/expanded graphite composite phase change material. *Int J Photo Energy* 2929473
- Zhao Y, Zou B, Li C, Ding Y (2019) Active cooling based battery thermal management using composite phase change materials. *Energy Procedia* 168:4933–4940

# Chapter 16

## Thermal Design and Numerical Investigation of Cold Plate for Active Water Cooling for High-Energy Density Lithium-Ion Battery Module



Virendra Talele, Rushikesh Kore, Hemalatha Desai, Archana Chandak, Hemant Sangwan, Gaurav Bhale, Amit Bhirud, Saurabh Pathrikar, Anurag Nema, and Naveen G. Patil

### 16.1 Introduction

In the designing process of high-powered Lithium-ion battery packaging, thermal management is an important aspect to keep the core working temperature of the cell below 60 °C. Nowadays, there are many techniques developed to increase the efficiency of various components. Whilst developing new techniques, we have to look for the thermal cooling of the components. This can be done with various processes such as plate heat exchanger, heat sinks, and air cooling. These are some techniques of cooling, but they have some drawbacks. To overcome such drawbacks, researchers had developed the cold plate technique. Cold plates are made up of metals. Cold plate cooling involves a simple working principle in which plates absorb electric waste heat and they dissipate it through the flow paths using liquid cooling. This type of cooling system is far better than the air cooling system. Heat sinks and fans type space-consuming cooling systems can be replaced by cold plates. These types of cold plates were used in NASA'S Apollo programmes. Liu et al. (2017) performed an experimental study using a simplified liquid cooling system along with the pump. The thermal performance of the system was carried out using various heat fluxes. They found that 18.9 kW/m<sup>2</sup> heat was dissipated in the form of a convective heat

---

V. Talele (✉) · R. Kore · A. Chandak · H. Sangwan · G. Bhale · A. Bhirud · S. Pathrikar · A. Nema  
Department of Mechanical Engineering, MIT School of Engineering, MIT ADT University, Pune,  
Maharashtra, India  
e-mail: [virendratalele1@gmail.com](mailto:virendratalele1@gmail.com)

H. Desai  
Mechanical and Aerospace Engineering Department, University of California, Los Angeles,  
CA 90095, USA

N. G. Patil  
School of Engineering, Ajeenkya DY Patil University, Lohegaon, Pune, India

coefficient. Wu et al. (2012) studied system properties of multifunctional electronic equipment along with its structure and heat design in which they studied effects of various fins arrangement with implemented active cooling strategy. The use of multi-chip module at the centre of the multifunctional equipment will result from a decrease in temperature. CFD investigation was performed by Madani et al. (2020) on a cold plate along with the various arrangement. They studied the effect of conduit circulation in the lithium-ion battery pack. As a result, they concluded that with the use of an appropriate mass flow rate, the thermal characteristics of the battery can be reduced. Apart from this, cooling path can also help to reduce the temperature by appropriately distributing heat. The investigation was carried on working fluid which is used in PHP's by Taft et al. (2012). They carried out analysis using R-134a and HFO-1234yf and stated that the above two fluids are best suitable for PHP'S, and their result shows that because of use of the above fluids. Subcooling is increased with rise in PHP pressure at small vapour pressure, and the effect of dynamic angle along with surface tension was studied by them. Cai et al. (2007) exhibited the application of PHP used in aircraft electronics for cooling because it is cost-effective, ability to transfer heat at elevated rate, has passive operation, etc. Burbhan et al. (2013) performed numerical simulation on PHP'S used for cooling various equipment. Various coolants were tested at varying airspeed, temperature, and input current. Pulse heat pipe worked efficiently along with various coolants but out of that water coolant showed most effective results. In a V-type inlet/outlet microchannel heat sink arrangement, the property of nanofluids under steady-stream conditions was studied by Abdollahi et al. (2017). They used four different types of nanofluids. They employed three different volumes and three different nanoparticle diameters 30,40, and 60 nm. Their results state that  $\text{SiO}_2$  has a good heat transfer rate in comparison with other verified nanofluids. Along with this, they also proposed that reducing thickness with a rise in volume portion of nanoparticles will result in Nusselt number value. Dede and Liu (2013) conducted a study on a microchannel heat sink with multi-pass branches on it. They carried out an experimental investigation on a multi-pass microchannel heat sink. Ethylene glycol was used as a water coolant in a single-phase. They had compared the test results with the measured data, analytical estimates, and numerical results. Their results confirm that multi-pass branching heat sink has good cooling performance with low-thermal resistance of  $0.34 \text{ cm}^2 \text{ K/W}$  and pressure drop. Pandey et al. (2021) carried out comparative investigation on cold plate heat sink with pin fin and parallel channel. They used Ansys CFD processing method to carry out performance analysis. They performed the analysis at different Reynold's number and concluded that pin fin had the best results as compared to the parallel channel. A numerical study was conducted by Deng et al. (2019) on battery cooling with help of cold plate cooling technique. They used cold plate on the lithium-ion battery. Cold plates were mounted along with battery pack, and CFD simulation was carried out on the model using STAR-CCM+. After simulation, they concluded that  $1 \text{ g}\cdot\text{s}^{-1}$  of flow rate can achieve maximum heat dissipation by maintaining good temperature range. Along with that they studied variation in heat dissipation with respect to cold plate numbers. A comparative investigation was carried out by Osman et al. (2021) on cold plate which is being used to cool various

electronic equipment. Three different channels along with different configurations were used to carry out the study. They used water-based cold plate with various flow arrangements. Large pressure variation was observed in wavy channel. Their study states that the wavy channel has the best performance as compared with other two channels as per their assessment standard. Cold plate investigation was carried out using FEM method by Amrut et al. (2021). This investigation was conducted to study the temperature variation in battery packs. They had used six noded part for their study. Various performance parameters were investigated such as fluid flow rate of coolant at elevated temperatures and variation of temperature in the overall all battery in presence and absence of radiation. The main motto of FEM code was to carry out thermal analysis of cold plates developed with various channels, and their test results were verified with help of CFD. Thermal characteristics of the liquid cold plate along with oblique fin configuration were studied by Om et al. (2018). They used three unique oblique fin configurations to study the thermal characteristics and their effect on flow. Ethylene glycol was used as cooling fluid, and test result of different configuration was obtained. Their outcome concludes that there is an increment in the Nusselt number value with louved oblique fin configuration. Wiriyasart and Naphon (2019) performed numerical analysis on liquid impingement on cold plate. In this experiment, cold plate behaviour under various parameters such as temperature and fluid flow rate was studied. Diverse fin shapes were used to experiment along with different working fluid. They used 3D and 2D turbulent model to analyze the temperature and flow patterns in the cold plate. Their experimental outcome states that as the Reynolds number is increasing, there will be a decrease in the thermal characteristics. Their test results were validated using CFD. Garimella and Sobhan (2003) examined various cooling processes which are extremely useful for cooling mini and microchannels. The work of various researchers along with their test results was studied by them. They also studied various numerical schemes given by the researchers. The most appropriate test result along with a numerical scheme that has good thermal characteristics was discussed. Jiang et al. (2019) performed a numerical study on cold plates. They studied the arrangements of cold plates in aircraft after that they proposed a process in which they obtained the readings for fluid flow amount and heat load along with the use of Kalman filter. Obtained readings were used to analysis the thermal distribution across the operating board. Thermal distribution was done online. Ho and Leong (2017) analyzed a cold plate with water as a working fluid was used to evaluate the temperature variation and hydraulic characteristics. They improved the performance of the cold plate with help of cylinder-shaped holes. The test results were compared with the help of graphs between the fluid velocity inside the plate and distance. Apart from this, Reynolds and Nusselt numbers were also obtained and used for comparison. In recent years, there are several studies are performed to understand the creation of temperature and its distribution for electronic and battery thermal management in which cooling type is broadly classified as active cooling strategy and passive cooling strategy out of which in the present manuscript active cooling strategy (Kurahde et al. 2021; Mathew and Hotta 2018, 2019, 2020, 2021a, b; Patil and Hotta 2018, 2020a; Patil et al. 2020; Talele et al. 2021). Cooling strategies are classified based on it is working schematic in which if the external aid

of power is used to cool down the system, it is classified as an active cooling strategy. In the passive cooling strategy, there is no aid of external power to cool down the system.

Numerous publications on thermal modelling of batteries are available, using various methods such as finite element modelling (FEM) or lumped parameter modelling (LPM), linear parameter varying (LPV) modelling, or partial differential equation modelling (PDE). In most of the models discussed above, a thermal model is used in conjunction with an electrochemical model to simulate the battery temperature profile under a variety of operating circumstances, cooling rates, and geometries. In the present study, cold plate-based active cooling strategy is used for the battery module subjected to the constant current profile of 1C, 2C, and 3C charge rate. A comparative study is developed between batteries without a thermal management system and batteries with an active cooling strategy to reflect the difference and effectiveness of the active cooling strategy. A strong correlation is established between input flow rate (Reynolds number) to the increasing Nusselt number which reduces the surface temperature of a battery module. The correlation is plotted using a linear regression model for multi-objective analysis in for which  $R^2$  value is monitored. The correlation suggests the best tradeline for configuration 3 has an input flow rate of 1 m/s.

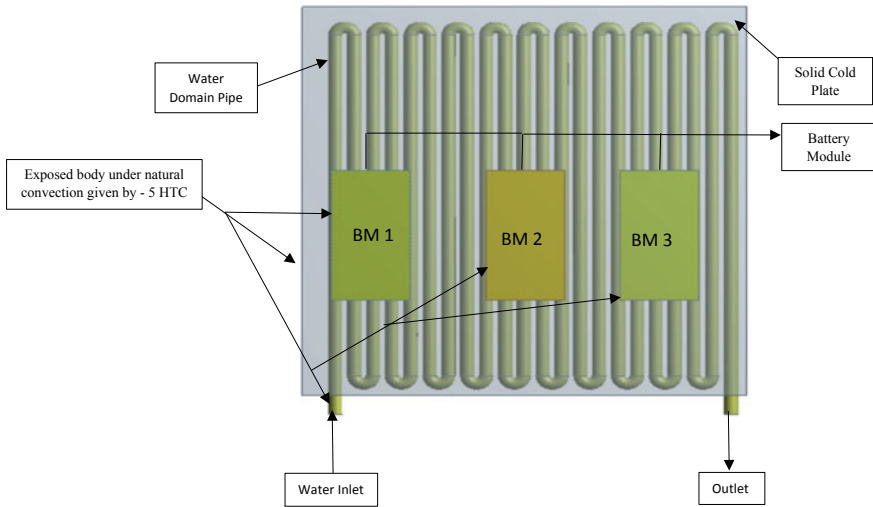
## 16.2 Numerical Methodology

### 16.2.1 Domain Creation

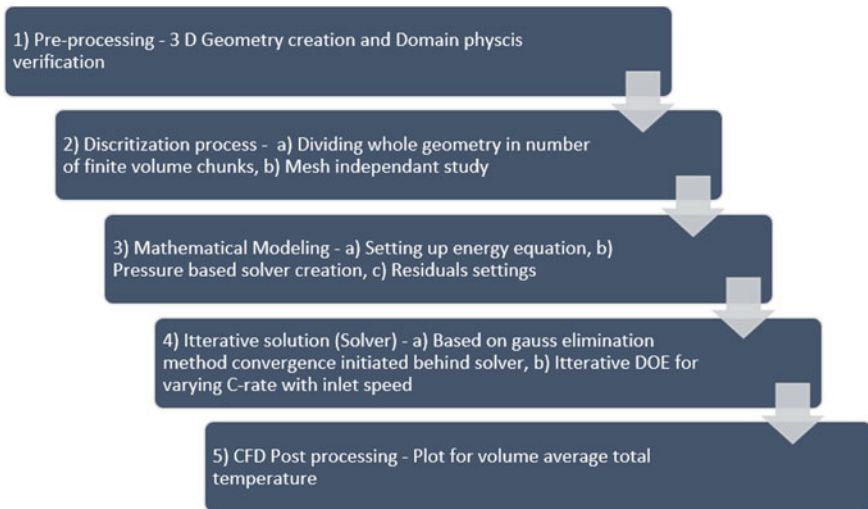
In the present study, the heat source is applied to a three-battery module which is kept on top of a cold plate, and the battery is to be connected in a series arrangement which is in constant charge current of 3C, 2C, and 1C rate. Figure 16.1 shows the detailed 3D model.

### 16.2.2 Methodology

The primary stage of numerical analysis is creating a domain justifying cell condition as such solid or fluid. The geometry of the cold plate is developed using Ansys cad design modeller and then transferred to volume meshing using Ansys ICEM CFD Mesher (Fig. 16.2). The deviation in output results is dependent on the quality of mesh which is calibrated based on skewness factor or aspect ratio. In the present study, conformal mesh is created over the geometry where a selection of mesh size is calibrated using mesh independent study for case 1 water inlet 0.5 M/s for 1C rate. Table 16.1 indicates mesh independent study.



**Fig. 16.1** 3-dimensional domain creation

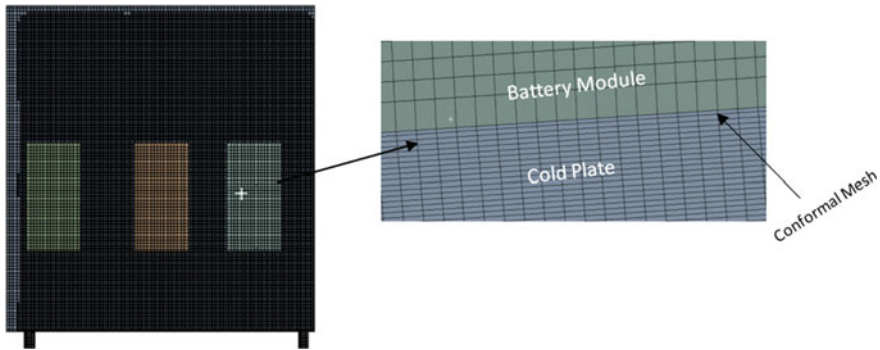


**Fig. 16.2** CFD investigation process flow

The selected mesh size for the present study is 2 mm because it is a convergence solution with lesser deviation and low-computational time. The achieved skewness for 2 mm is 0.94926 with a cell count of 3.2 million for conformal mesh creation. Figure 16.3 shows the creation of conformal mesh.

**Table 16.1** Mesh independent study

S. No.	Mesh size (mm)	Skewness	Total temperature °C	Time for convergence (S)
1	10	1	Divergence	Divergence
2	6	0.98658	32.65	350
3	4	0.97492	29.01	721
4	3	0.95972	28.99	1900
<b>5 (Selected)</b>	<b>2</b>	<b>0.94962</b>	<b>28.749</b>	<b>2765</b>
6	1	0.94832	28.761	5874

**Fig. 16.3** Conformal mesh creation

### 16.2.3 Boundary Condition

In the present study, assignment of material is given as aluminium for the cold plate and battery module. The solid domain is set for cold plate, battery module, and fluid domain are set for fluid channel. Water as fluid is used in a present investigation which is assigned for the pipe. Table 16.2 shows the properties of aluminium and water used in the present investigation. Table 16.3 shows the configuration taken for investigation.

### 16.2.4 Numerical Formulation

In the present study, commercial coded Ansys software is used to develop a model based on lumped system conjugate heat transfer mode. Pressure-based flow equation Navier Stokes equation is used in a study in which mass, momentum, and energy equation are solved. The C-rate in terms of current is given as input in the battery model feature, and inlet velocity is kept as laminar flow. Below Eq. 16.1 shows the 3D

**Table 16.2** Property of assigned material domain

Aluminium (isotropic solid)—cold plate, BM		
S. No.	Property	Value
1	Density ( $\rho$ )	2712 kg/m <sup>3</sup>
2	Specific heat (Cp)	897 J/Kg K
3	Thermal conductivity	237 W/mK
Water (fluid)—pipe		
1	Density	1 g/cm <sup>3</sup>
2	Thermal conductivity	0.598 W/mK
3	Dynamic viscosity	8.90 × 10 <sup>-4</sup>

**Table 16.3** Configuration with sub-cases under investigation

Configuration 1			
Cold plate at 0.5 m/s water inlet			
Cases	Water inlet velocity (m/s)	C-rate	Current (Ampere)
a	0.5	3	15.6
b	0.5	2	10.4
c	0.5	1	05.2
Configuration 2			
Cold plate at 1 m/s water inlet			
a	1	3	15.6
b	1	2	10.4
c	1	1	05.2
Configuration 3			
Cold plate at 3 m/s water inlet			
a	3	3	15.6
b	3	2	10.4
c	3	1	05.2

fluid flow equation based on the law of conversation of mass given for incompressible fluid flow (Patil and Hotta 2018).

Governing continuity equation:

$$\frac{\partial u}{\partial x} + \frac{\partial v}{\partial y} + \frac{\partial w}{\partial z} \tag{16.1}$$

Governing momentum equation is given by Eqs. 16.2–16.4 in steady state for 3-dimensional model.

$$u \frac{\partial u}{\partial x} + v \frac{\partial u}{\partial y} + w \frac{\partial u}{\partial z} = -\frac{1}{\rho} \frac{\partial P}{\partial x} + v \left( \frac{\partial^2 u}{\partial x^2} + \frac{\partial^2 u}{\partial y^2} + \frac{\partial^2 u}{\partial z^2} \right) + f_x \tag{16.2}$$



$$u \frac{\partial v}{\partial x} + v \frac{\partial v}{\partial y} + w \frac{\partial v}{\partial z} = -\frac{1}{\rho} \frac{\partial P}{\partial y} + v \left( \frac{\partial^2 u}{\partial x^2} + \frac{\partial^2 u}{\partial y^2} + \frac{\partial^2 u}{\partial z^2} \right) + f_y \quad (16.3)$$

$$u \frac{\partial u}{\partial x} + v \frac{\partial u}{\partial y} + w \frac{\partial u}{\partial z} = -\frac{1}{\rho} \frac{\partial P}{\partial z} + v \left( \frac{\partial^2 u}{\partial x^2} + \frac{\partial^2 u}{\partial y^2} + \frac{\partial^2 u}{\partial z^2} \right) + f_z \quad (16.4)$$

In the 3D steady state, numerical formulation  $f_x, f_y, f_z$  represents an occurrence of the body force component along the directional axis of  $x, y,$  and  $z,$  respectively.

The 3D form of energy equation derived under steady-state 3D formulation is given by Eq. (16.5).

$$u \frac{\partial T}{\partial x} + v \frac{\partial T}{\partial y} + w \frac{\partial T}{\partial z} = \frac{k}{\rho C} \left( \frac{\partial^2 T}{\partial x^2} + \frac{\partial^2 T}{\partial y^2} + \frac{\partial^2 T}{\partial z^2} \right) + q_s + \emptyset \quad (16.5)$$

### 16.2.5 Results Validation

In the present study, achieved numerical results are validated with Patil and Hotta (2021), where they performed conjugate heat transfer analysis over a cold plate for identical IC chips. From the validation of work, it concludes that thermal cooling effectiveness with conjugate heat transfer increases as the input flow rate of fluid channel increases in steady-state solver for non-identical IC chip. In the present study, recreation of literature is given for identical battery modules spaced equally over the cold plate to investigate temperature distribution with different flow rates and increasing C-rate.

## 16.3 Results and Discussion

In present study, results are tabulated for suggested configuration from Table 16.3. The contour plots for total temperature with volume average are monitored over the entire domain which includes cold plate and battery module. A comparative result between battery modules without cooling strategy vs battery module under cooling strategy suggests increased working conjugate heat transfer effectiveness of active cooling strategy which is calculated with below Eq. 16.6.

$$\text{To determine battery effectiveness} = \frac{\text{Temperature without active cooling}}{\text{Temperature with active cooling}} \quad (16.6)$$

### 16.3.1 Temperature Distribution for Without Active Cooling Strategy

- (a) 1C rate (pure conduction mode with natural convection as 5HTC at boundary layer) (Fig. 16.4).
- (2) 2C rate (pure conduction mode with natural convection as 5 HTC at boundary layer) (Fig. 16.5).
- (c) 3C rate (pure conduction mode with natural convection as 5 HTC at boundary layer) (Fig. 16.6).

This section represents achieved temperature with respect to the given heat input of constant current phase which is distributed in C-rate. The maximum temperature is 44.891 °C which is achieved for 3C-rate, and the minimum temperature of 35.870 °C is achieved for 1C rate. The present numerical scheme is developed based on lumped model conjugate heat transfer mode in which temperature is a function of input load and indirect area in contact. To model convective heat transfer mode across the exposed body, an HTC of 5 is given to the exposed bodies as shown in Fig. 16.7.

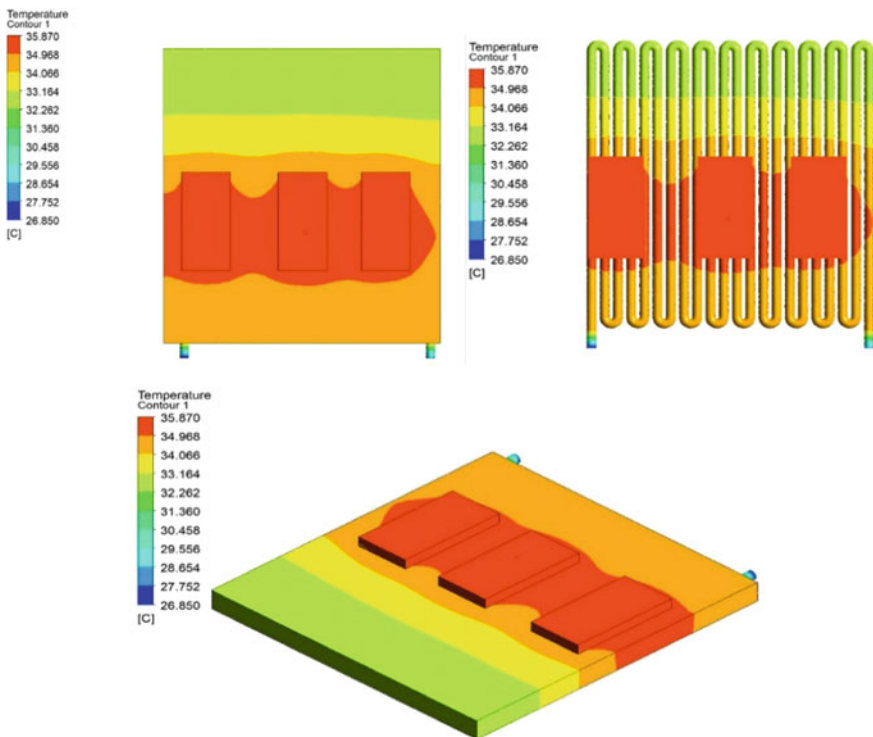


Fig. 16.4 1C rate without active cooling

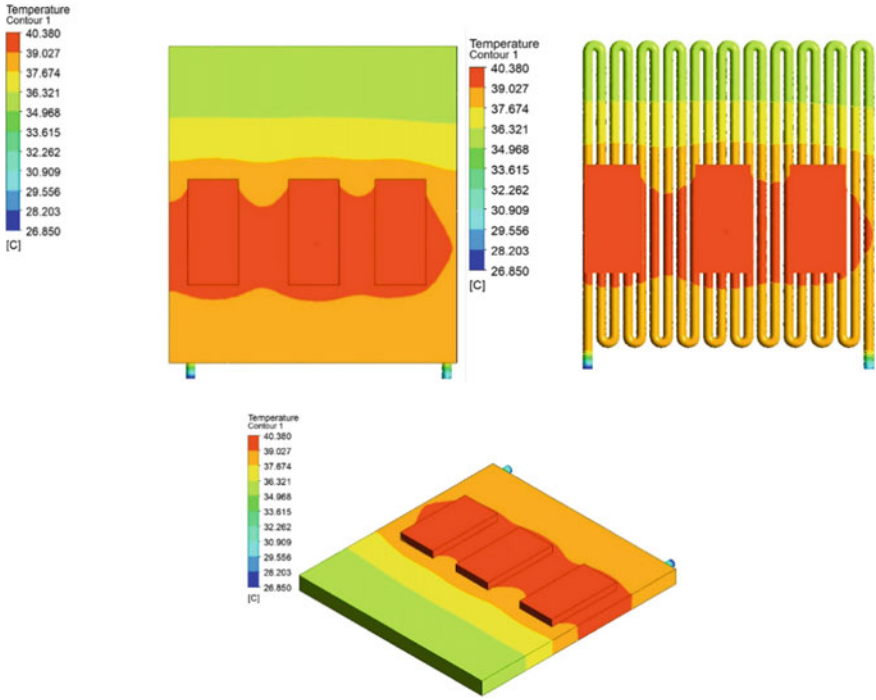


Fig. 16.5 2C rate without active cooling

### 16.3.2 Active Cooling Strategy Based on Conjugate Heat Transfer Model

#### Configuration (1)

- Case (a) Water inlet at 0.5 m/s for 1C rate (Fig. 16.8).
- Case (b) Water inlet at 0.5 m/s for 2C rate (Fig. 16.9).
- Case (c) Water inlet at 0.5 m/s for 3C rate (Fig. 16.10).

In the present configuration, the inlet velocity of a fluid is set to be 0.5 m/s over varying c-rate for cases. The maximum achieved temperature is 30.64 °C for 3C rate, 29.700 °C for 2C rate, and 28.749 °C for 1C-rate. The monitored results highlighted in Fig. 16.8 show high-heat source region is near the outlet port.

#### Configuration (2)

- Case (a) Water inlet at 1 m/s for 1C rate (Fig. 16.11).
- Case (b) Water inlet at 1 m/s for 2C rate (Fig. 16.12).
- Case (c) Water inlet at 1 m/s for 3C rate (Fig. 16.13).

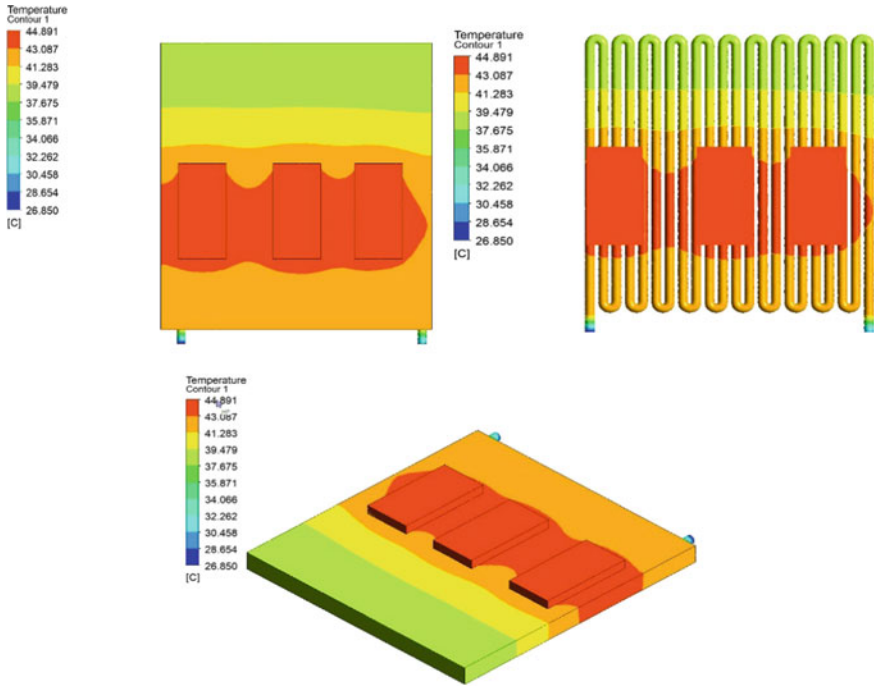


Fig. 16.6 3C rate without active cooling

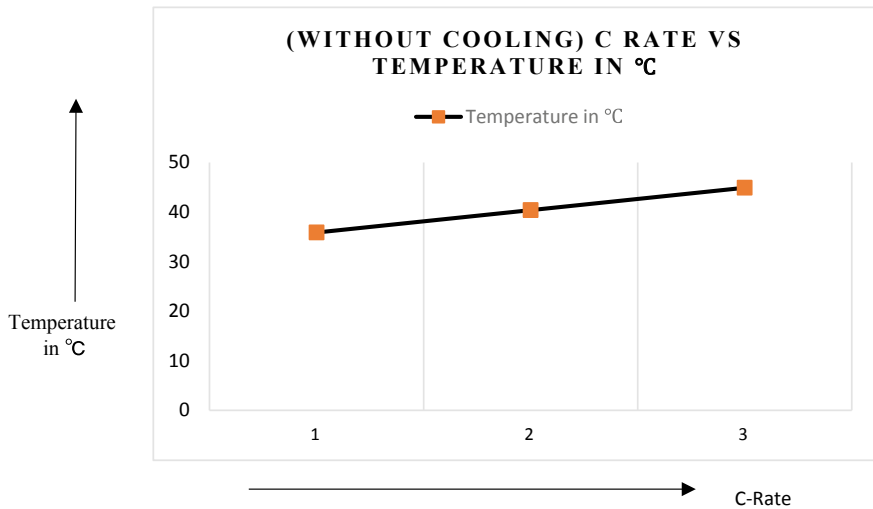
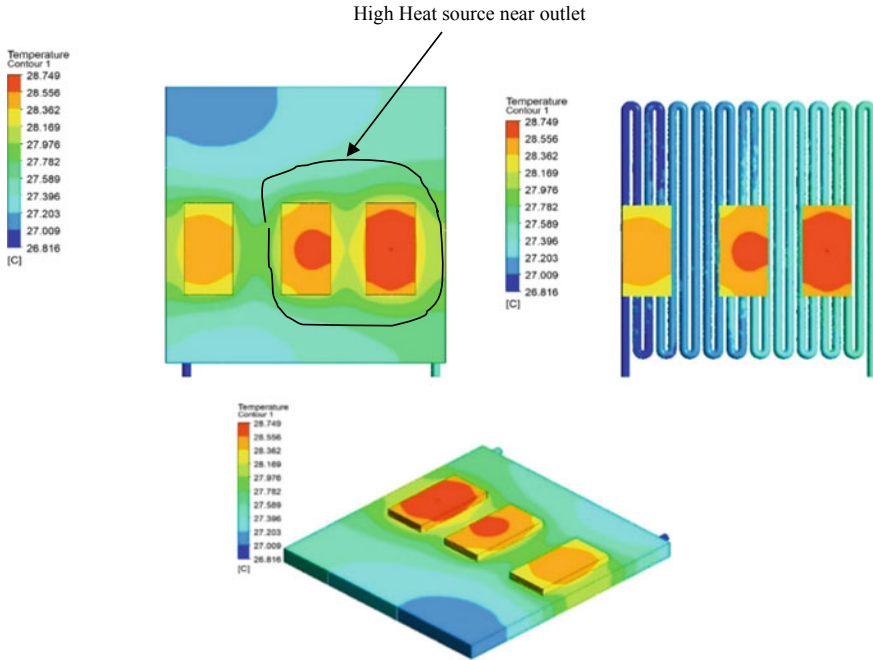


Fig. 16.7 Without cooling C rate versus temperature



**Fig. 16.8** 1C rate without active cooling

In the present configuration, inlet velocity of a fluid is set to be 1 m/s over varying c-rate for cases. The maximum achieved temperature is 30.146 °C for 3C rate, 29.322 °C for 2C rate, and 28.498 °C for 1C rate.

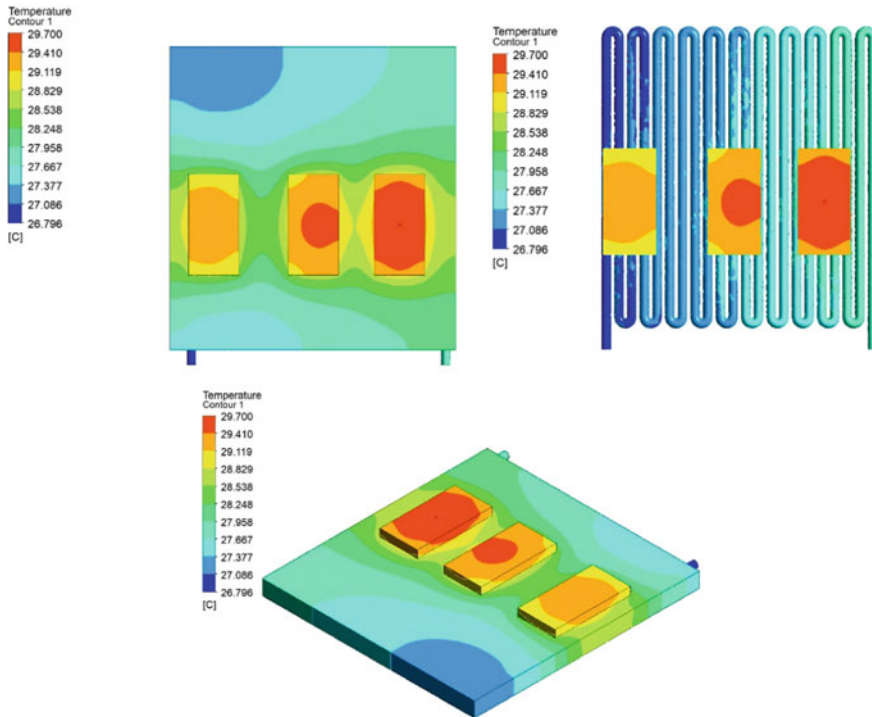
**Configuration (3)**

- Case (a) Water inlet at 3 m/s for 1C rate (Fig. 16.14).
- Case (b) Water inlet at 3 m/s for 2C rate (Fig. 16.15).
- Case (c) Water inlet at 3 m/s for 3C rate (Fig. 16.16).

In the present configuration, inlet velocity of a fluid is set to be 3 m/s over varying c-rate for cases. The maximum achieved temperature is 29.966 °C for 3C rate, 29.187 °C for 2C rate, and 28.408 °C for 1C rate.

**16.3.3 Cooling Effectiveness**

The cooling effectiveness is calculated for the function of the inlet velocity of the water. Effectiveness is taken as the ratio of achieved temperature without active cooling to the achieved temperature with active cooling. The achieved effectiveness denotes inlet velocity is a strong function of cooling high-heat source battery



**Fig. 16.9** 2C rate without active cooling

modules. Furthermore, a correlative multi-objective analysis is performed for the function of inlet velocity to the achieved temperature for varying C-rate. A linear regression model is generated based on multi-objective analysis which suggests a strong correlation between increased inlet velocity to the working effectiveness of cold plate.

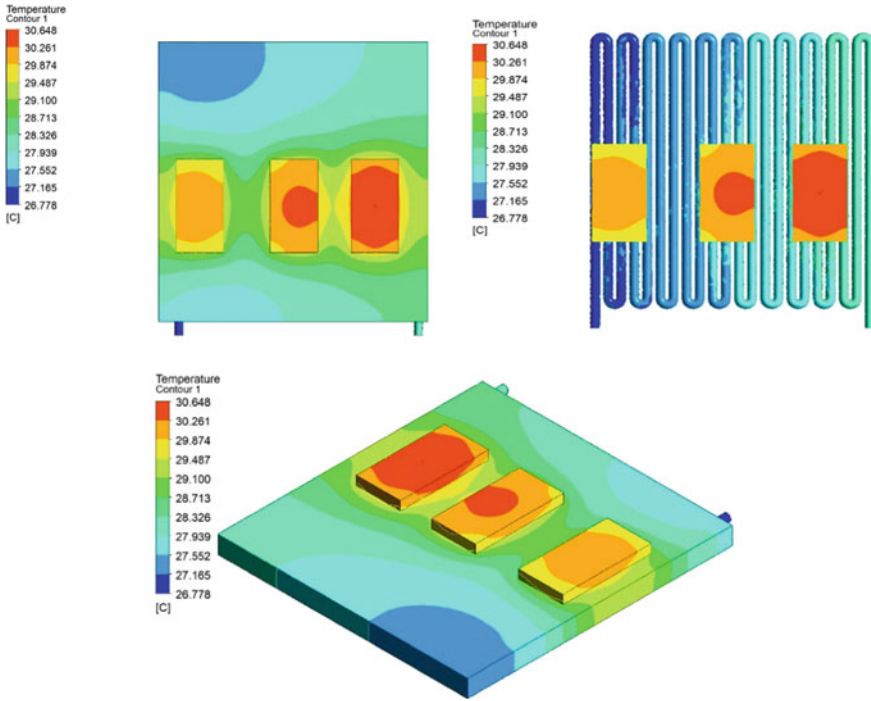
Configuration (1) Water inlet at 0.5 m/s.

Case (a) 1C rate

$$\begin{aligned}
 \text{To determine battery effectiveness} &= \frac{\text{Temperature without active cooling}}{\text{Temperature with active cooling}} \\
 &= \frac{35.87}{28.749} = 1.247
 \end{aligned}$$

Case (b) 2C rate

$$\begin{aligned}
 \text{To determine battery effectiveness} &= \frac{\text{Temperature without active cooling}}{\text{Temperature with active cooling}} \\
 &= \frac{40.38}{29.700} = 1.359
 \end{aligned}$$



**Fig. 16.10** 3C rate without active cooling

Case (c) 3C rate

$$\begin{aligned}
 \text{To determine battery effectiveness} &= \frac{\text{Temperature without active cooling}}{\text{Temperature with active cooling}} \\
 &= \frac{44.891}{30.648} = 1.464
 \end{aligned}$$

Configuration (2) Water inlet at 1 m/s.

Case (a) 1C rate

$$\begin{aligned}
 \text{To determine battery effectiveness} &= \frac{\text{Temperature without active cooling}}{\text{Temperature with active cooling}} \\
 &= \frac{35.87}{28.498} = 1.258
 \end{aligned}$$

Case (b) 2C rate

$$\text{To determine battery effectiveness} = \frac{\text{Temperature without active cooling}}{\text{Temperature with active cooling}}$$

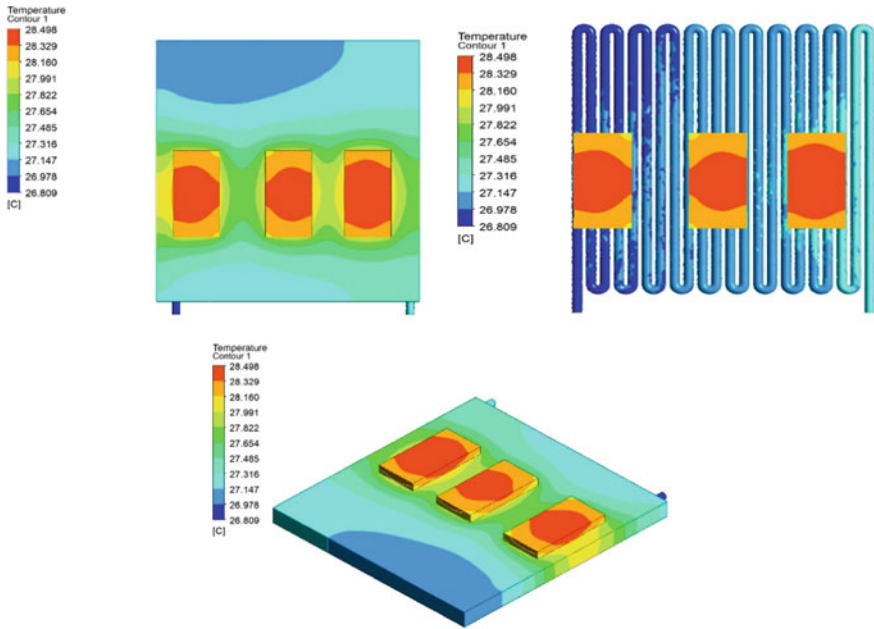


Fig. 16.11 1C rate without active cooling

$$= \frac{40.38}{29.322} = 1.377$$

Case (c) 3C rate

$$\begin{aligned} \text{To determine battery effectiveness} &= \frac{\text{Temperature without active cooling}}{\text{Temperature with active cooling}} \\ &= \frac{44.891}{30.146} = 1.489 \end{aligned}$$

Configuration (3) Water inlet at 3 m/s.

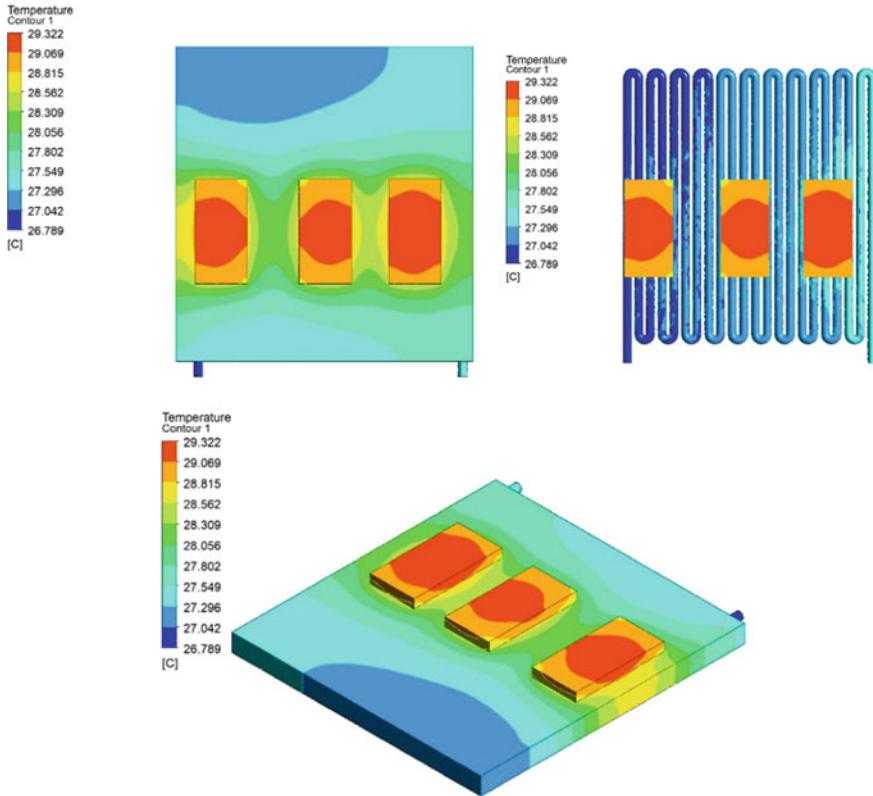
Case (a) 1C rate

$$\begin{aligned} \text{To determine battery effectiveness} &= \frac{\text{Temperature without active cooling}}{\text{Temperature with active cooling}} \\ &= \frac{35.87}{28.408} = 1.262 \end{aligned}$$

Case (b) 2C rate

$$\text{To determine battery effectiveness} = \frac{\text{Temperature without active cooling}}{\text{Temperature with active cooling}}$$





**Fig. 16.12** 2C rate without active cooling

$$= \frac{40.38}{29.187} = 1.388$$

Case (c) 3C rate

$$\begin{aligned} \text{To determine battery effectiveness} &= \frac{\text{Temperature without active cooling}}{\text{Temperature with active cooling}} \\ &= \frac{44.891}{29.996} = 1.499 \end{aligned}$$

The multi-objective analysis is performed for the function of input velocity which is varied in 3 configurations as such 0.5, 1, and 3 m/s with the achieved effectiveness for cases on varying C-rate (Fig. 16.17). Output result from linear regression plot over multi-objective strategic analysis suggests increasing inlet velocity is a strong function of increasing cooling effectiveness. In the present study, numerical data are synced with calculated battery effectiveness over fixed variable of inlet velocity. R<sup>2</sup> value is a regressive coefficient that indicates a strong correlation with input and target

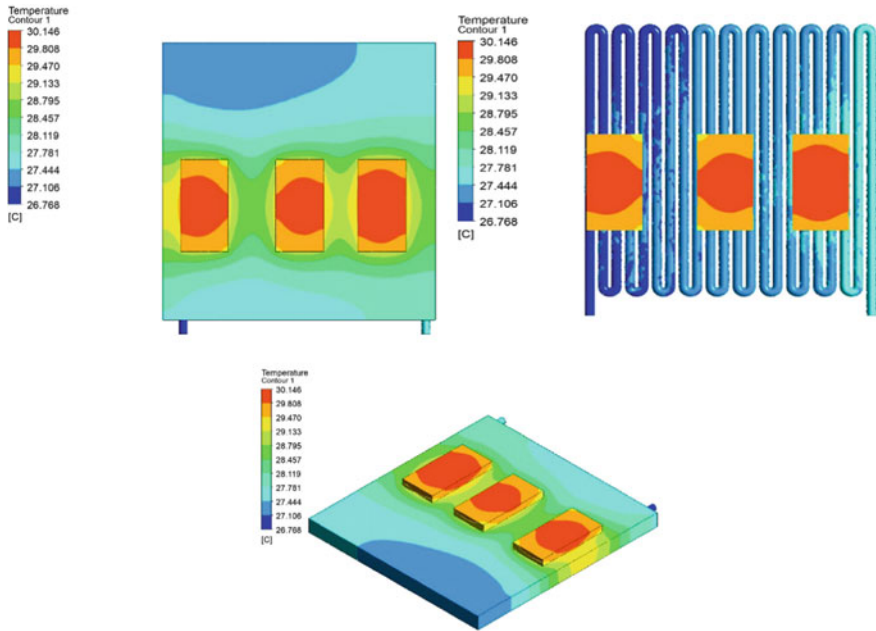


Fig. 16.13 3C rate without active cooling

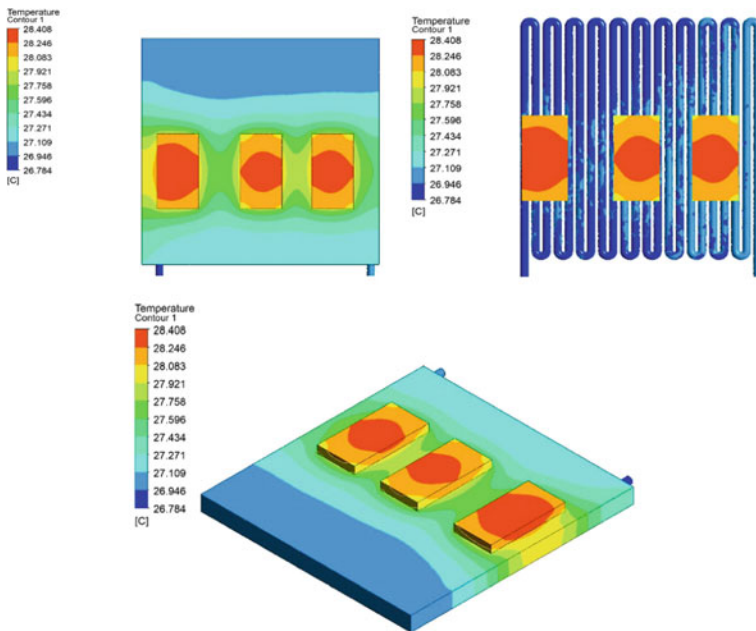


Fig. 16.14 1C rate without active cooling

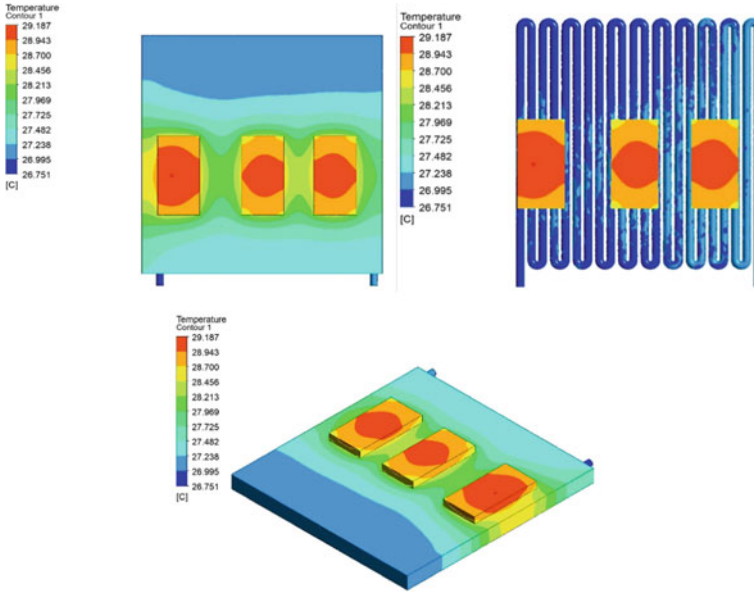


Fig. 16.15 2C rate without active cooling

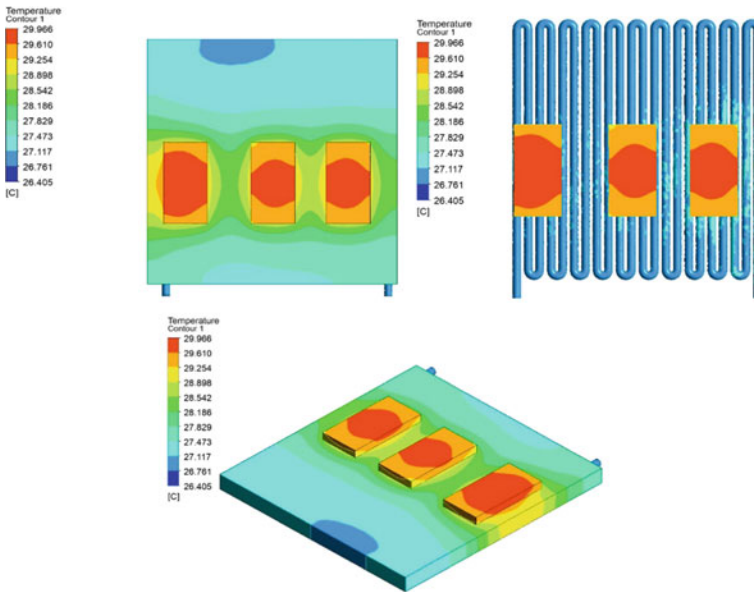


Fig. 16.16 3C rate without active cooling

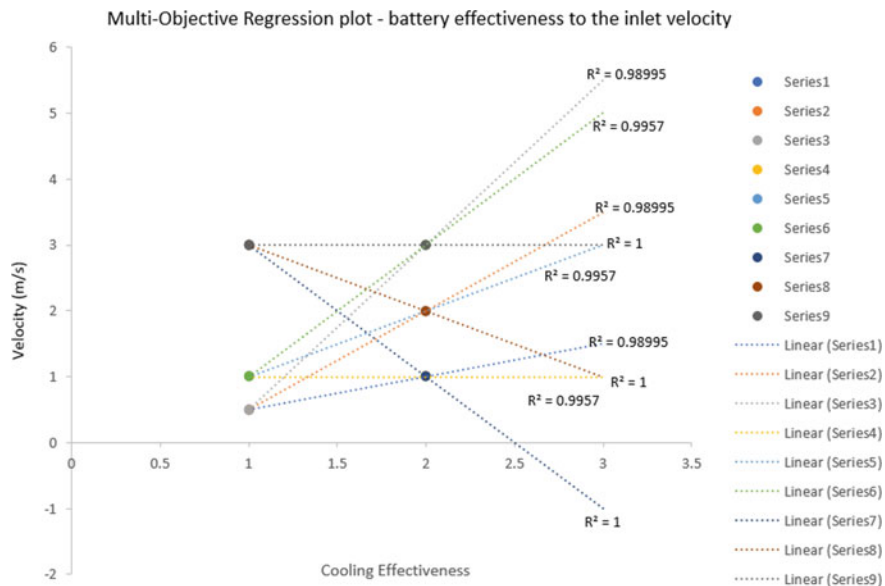
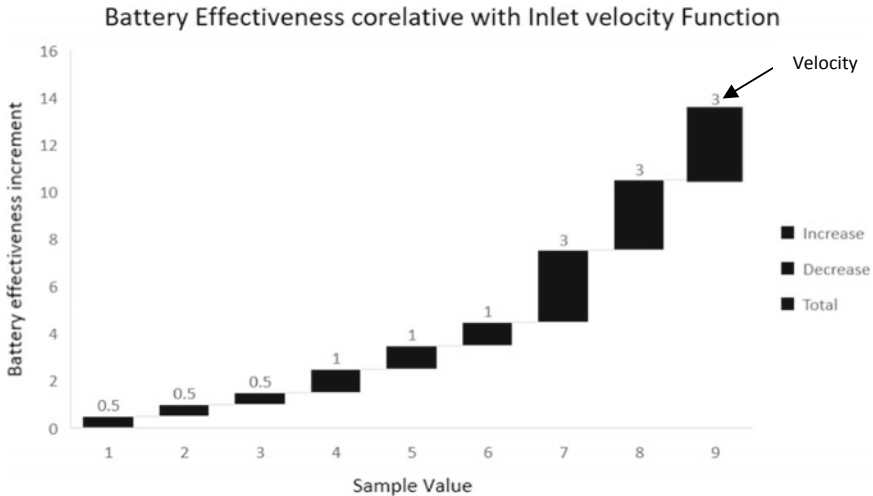


Fig. 16.17 Multi-objective correlation plot

data. A regression coefficient is established between the cases, for configuration 3 having an inlet velocity of 3 m/s, the achieved  $R^2$  value is 1. Figure 16.18 represents the exact value difference between battery effectiveness for given inlet velocity. When a cold plate is subjected to lower inlet velocity, the high-heat source temperature is monitored at the battery module placed near outlet port. This happened because fluid is subjected to conjugate heat transfer since it absorbs maximum amount of temperature near inlet through means of pure conduction, when the fluid reaches to outlet port, fluid loose up its latent heat by absorbing heat in a fluid channel which is indirect contact with battery module through the cold plate.

### 16.4 Conclusion

In the present study numerical investigation for steady state, a mode is carried over the cold plate to study conjugate heat transfer characteristics for cold plate subjected with high-heat source battery module working for three different C rates. The battery module subjected to the constant current condition is cooled by means of supplied fluid flow rate in cold plate. It is monitored by increasing the input flow rate of water, there is an increase in convective heat transfer coefficient of battery modules by reducing its surface temperature. The following are the points which are concluded through the present study:



**Fig. 16.18** Battery effectiveness increment plot in correlation with inlet temperature

- (1) Developed numerical scheme for presented configuration with respect to its cases, battery effectiveness is calculated with a suitable correlation as increment in flow rate using multi-objective optimization strategy which suggests increasing flow rate (velocity inlet m/s) is a strong function of increasing heat transfer coefficient of battery module (Nusselt number) due to which battery module subjected to heat source temperature cools faster.
- (2) Furthermore, recommendations are aligned with the thermal design view which suggests for an active cooling strategy using the cold plate, at the location near to outlet port, there is more amount of hotspot creation takes place because water subjected to absorb the maximum amount of latent heat at the inlet port hence when it moves along outlet port, it had already given up its capacity of cooling effectiveness. The thermal design optimization of a cooling channel having multiple inlet and outlet ports can solve this problem which is recommended from a future research perspective.

## References

- Abdollahi A, Mohammed HA, Vanaki SM, Osia A, Golbahar Haghighi MR (2017) Fluid flow and heat transfer of nanofluids in microchannel heat sink with V-type inlet/outlet arrangement. *Alex Eng J* 56(1):161–170
- Amrut SR, Sachin Bhardwaj M, Babu Rao P, Seetharamu KN (2021) Steady-state thermal investigations on cold plate using FEM. *Therm Sci Eng Prog* 23:100905
- Burban G, Ayel V, Alexandre A, Lagonotte P, Bertin Y, Romestant C (2013) Experimental investigation of a pulsating heat pipe for hybrid vehicle applications. *Appl Therm Eng* 50(1):94–103

- Cai Q, Chen C-L, Asfia J (2007) Experimental investigations of an avionics cooling system for aerospace vehicle. *J Spacecr Rocket* 44(2):439–444
- Dede EM, Liu Y (2013) Experimental and numerical investigation of a multi-pass branching microchannel heat sink. *Appl Therm Eng* 55(1–2):51–60
- Deng T, Zhang G, Ran Y, Liu P (2019) Thermal performance of lithium-ion battery pack by using cold plate. *Appl Therm Eng* 160:114088
- Garimella SV, Sobhan CB (2003) Transport in microchannels—a critical review. *Annu Rev Heat Transf* 13(13):1–50
- Ho JY, Leong KC (2017) Cylindrical porous inserts for enhancing the thermal and hydraulic performance of water-cooled cold plates. *Appl Therm Eng* 121:863–878
- Jiang H, Dong S, Li A, Meng F (2019) Online parameter estimation of cold plate based on extended Kalman filter. *Energy Procedia* 158:1850–1855
- Kurhade A, Talele V, Rao TV, Chandak A, Mathew VK (2021) Computational study of PCM cooling for electronic circuit of smart-phone. *Mater Today Proc* 47:3171–3176
- Liu F, Duan B, Yu X, Wu R, Luo X (2017) A study on a simplified liquid cooling system with a pump serving as cold plate. 2017 18th International conference on electronic packaging technology (ICEPT)
- Madani SS, Schaltz E, Knudsen Kær S (2020) Thermal analysis of cold plate with different configurations for thermal management of a Lithium-ion battery. In: *Thermal and safety properties of materials, cells and batteries 2019–2020*
- Mathew VK, Hotta TK (2018) Numerical investigation on optimal arrangement of IC chips mounted on a SMPS board cooled under mixed convection. *Therm Sci Eng Prog* 7:221–229
- Mathew VK, Hotta TK (2019) Role of PCM based mini-channels for the cooling of multiple protruding IC chips on the SMPS board—a numerical study. *J Energy Storage* 26:100917
- Mathew VK, Hotta TK (2020) Experiment and numerical investigation on optimal distribution of discrete ICs for different orientation of substrate board. *Int J Ambient Energy* 15:1–8
- Mathew VK, Hotta TK (2021a) Experimental investigation of substrate board orientation effect on the optimal distribution of IC chips under forced convection. *Exp Heat Transf* 34(6):564–585
- Mathew VK, Hotta TK (2021b) Performance enhancement of high heat generating IC chips using paraffin wax based mini-channels—a combined experimental and numerical approach. *Int J Therm Sci* 164:106865
- Om NI, Zulkifli R, Gunnasegaran P (2018) Influence of the oblique fin arrangement on the fluid flow and thermal performance of liquid cold plate. *Case Stud Therm Eng* 12:717–727
- Osman OS, El-Zoheiry RM, Elsharnoby M, Nada SA (2021) Performance enhancement and comprehensive experimental comparative study of cold plate cooling of electronic servers using different configurations of mini-channels flow. *Alex Eng J* 60(5):4451–4459
- Pandey J, Husain A, Zahid Ansari M, Al-Azri N (2021) Performance analysis of cold plate heat sink with parallel channel and pin-fin. *Mater Today Proc*
- Patil NG, Hotta TK (2018) Role of working fluids on the cooling of discrete heated modules: a numerical approach. *Sādhanā* 43(11):1–9
- Patil NG, Hotta TK (2020a) A combined numerical simulation and optimization model for the cooling of IC chips under forced convection. *Int J Mod Phys C* 31(06):2050081
- Patil NG, Hotta TK (2021) Heat transfer characteristics of high heat generating integrated circuit chips cooled using liquid cold plate—a combined numerical and experimental study. *J Therm Sci Eng Appl* 13(1):011019
- Patil NG, Mujawar MA, Biradar SA, Adimurthy M, Katti VV (2020) Influence of spent air confinement on pressure distribution over a flat plate impinged by an array of jets. *Int J Ambient Energy* 8:1–8
- Taft BS, Williams AD, Drolen BL (2012) Review of pulsating heat pipe working fluid selection. *J Thermophys Heat Transf* 26(4):651–656
- Talele V, Thorat P, Gokhale YP, Mathew VK (2021) Phase change material based passive battery thermal management system to predict delay effect. *J Energy Storage* 44(Part B):103482. ISSN 2352-152X

- Wiriyasart S, Naphon P (2019) Liquid impingement cooling of cold plate heat sink with different fin configurations: high heat flux applications. *Int J Heat Mass Transf* 140:281–292
- Wu JH, Zhou Q, Zhou Q, Chen J, Si HP, Lin KY, Zhang CB (2012) Heat design of multi-functional structure of electronic equipment with material properties in control system. *Adv Mater Res* 625:159–166

# Chapter 17

## An Effective Reduction of Exhaust Emissions from Combustive Gases by Providing a Magnetic Field Through the Fuel Supply Line: SI Engine, CI Engine, and LPG Gas Stove



Rakesh Kumar Sidheshware, S. Ganesan, and Virendra Bhojwani

### 17.1 Introduction

Transport is the second-largest sector to produce CO<sub>2</sub> emission worldwide with a range of 33 Gigatonnes, and transport is the main reason for urban air pollution causing a serious public health problem in the majority of developing nations with limited use of emission control technologies. In developing countries, air pollution contributes for tens of thousands of fatalities and trillions of dollars in medical expenditures and annually reduces productivity. The Global Ambient Air Quality Database of the World Health Organization (2018) estimated that around 7 million people die annually from polluted air fine particles which have severe effect on health like leading to stroke, heart disease, lung cancer, chronic obstructive pulmonary diseases, respiratory infection, and also including pneumonia. Similar effect can be noticed for the LPG emission, i.e. household emission. LPG emissions can include large volume and build fast to reach harmful level with the possibility of a large amount of carbon monoxide (CO) and can lead to headache, dizziness, lethargy, and death. LPG emissions of hydrocarbons have a considerably lesser environmental impact (ozone reactivity which contributes to smog) than gasoline. Nitrogen oxide is very reactive gas and highly hazardous to living beings. The accumulation of NO<sub>x</sub> may also be

---

R. K. Sidheshware (✉)

Sathyabama Institute of Science and Technology, Chennai, Tamil Nadu, India  
e-mail: [rakesh1987thermal@gmail.com](mailto:rakesh1987thermal@gmail.com)

S. Ganesan

Mechanical Engineering Department, Sathyabama Institute of Science and Technology, Chennai, Tamil Nadu, India

V. Bhojwani

Department of Mechanical Engineering, MIT School of Engineering, MIT-ADT University, Pune, Maharashtra, India



harmful to the stored products in the warehouse environment. For instance, only a few ppm of  $\text{NO}_x$  in ambient may alter the colour of the stock from white to yellowish. Due to its ozone reactivity and smog, production cause severe environmental problem.

According to The Economics Times, nearly 280 million of India's populations are domestic LPG gas stove users. Currently, India stands second in terms of LPG consumption in worldwide. With this usage, many peoples inhale toxic emissions from the combustion of gases. Many methods are adopted to reduce the emissions like MPFI, EGR, PCV, and catalytic converter. Current research emphasizes on applying a magnetic field on the fuel line which ionizes the fuel.

Hydrogen molecules, carbon molecules, and other organic composites are part of the natural resources of fuels. Saturated and unsaturated hydrocarbons may be categorized as fuels. Each type has its molecular structure and setup. This structure describes the properties of gasoline like hydrogen atoms and carbon atoms that formed the molecules of hydrocarbons. The molecules of these hydrocarbons have single or multiple bonds between the atoms of hydrogen and carbon. Magnetic flow decreases the intermolecular forces between these molecules. The reduction in fuel viscosity results in more significant air–fuel mixing and homogeneity. The standardized combination of air–fuel mixture contributes to enhancement in fuel combustion and ultimately increases in combustion efficiency. To lower the fuel consumption and emissions of internal combustion engines, this unique approach can be introduced. The experiments carried out showed that a magnetic field reduces exhaust emissions.

According to the WHO, air pollution kills about 7 million people worldwide every year (Rohit et al. 2020). The data indicate that approximately 90% of the population breathes air containing high-pollution levels, resulting in about 7 million deaths per year from such exposure. In India, January 2019, the air quality index of the state-run Central Pollution Control Board shows that the concentration of toxic particulate matter which is also known as PM 2.5 was 440 and approximately 12 times higher than the recommended level of US Government, i.e. 35. It is therefore imperative that everyone grasps and examines the causes of air pollution in surroundings profoundly. Vehicles are one of the primary sources of emissions of pollutants, especially in urban areas. Hydrocarbons (HC), particulate matter (PM), and carbon monoxides are the primary contaminants associated with automotive pollution. Hydrocarbons (HC) are known to be fuel molecule particles that are not entirely burned. They react when sunlight and nitrogen oxides are present, and the reaction results in the formation of ground-based ozone. Ozone so created primarily leads to smog and irritates the eyes, nose and affects the lungs. Some HC exhausts are too toxic to cause the cancer. CO emission results in incomplete combustion of hydrocarbon-based fuels. Govindasamy et al. (2007) investigated the effect of 9000 gauss power magnets on the 2-stroke spark-ignited engine with zirconia catalyst activated. The pre-flame reaction in the combustion chamber is initiated due to magnetic flux. Table 17.1 shows the emission test with copper coated and the zirconia coated engine, and it is compared with the base engine under the effect of the magnetic field.

Okoronkwo et al. (2010) conducted tests on exhaust emission using HGA 200 computerized exhaust gas analyzer on a one-cylinder four-stroke engine resulted in a 50% reduction in hydrocarbon emission and 35% reduction of CO emission.

**Table 17.1** The percentage of HC and CO emission for copper and zirconia coated engine (Govindasamy and Dhandapani 2007)

Exhaust emission	Base engine (%)	Copper coated engine (%)	Zirconia coated engine (%)
Reduction in CO	13.3	23.5	29.5
Reduction in HC	22.1	37.3	44.2

**Table 17.2** Shows the reduction in emission of exhaust gases (Salih and Ahmed 2016)

Parameter	Remark	%
Carbon monoxide	Reduction	38.04
HC	Reduction	21.89
Carbon dioxide	Increase	3.43
Exhaust temperature	Increase	4.34

The test concludes that the introduction of electromagnets to the engine’s fuel line significantly reduces the emission.

Salih et al. (2016) investigated the effect of magnetic field on boiler fuelled with diesel. Magnetic lines are penetrated through the 2000 gauss strength fuel line and substantially controls the emission during combustion. Table 17.2 shows the reduction in emission of exhaust gases.

Patel et al. (2014) measure the exhaust gas emissions such as CO, CO<sub>2</sub>, HC, and NO<sub>x</sub> under the influence of permanent magnets of 2000 gauss on the fuel line single-cylinder four-stroke diesel engines, results in a drastic reduction in emission due to fuel magnetization. The percentage of reduction in HC and NO<sub>x</sub> are 30% and 27.7%, respectively. For CO, emission reduces to a higher percentage under higher loading conditioning. CO<sub>2</sub> reduced by 9.72% on average of all loads.

El Fatih et al. (2010) conducted tests on exhaust emission on the spark-ignition engine using a magnetic field for different idling engine speeds. The effective result revealed that improvement in exhaust gases, viz. CO, NO, and CH<sub>4</sub>. The following Table 17.3 shows a reduction in emission under the effect of the magnetic field at different idling speed.

Faris et al. (2012) applied the magnetic force of permanent magnets on the two-stroke gasoline engine to reduce the rate of exhaust emission. The permanent magnet used 2000, 4000, 6000, and 9000 gauss strength in a two-stroke engine’s fuel line. The trail shows significant result in overall performance as well as reduction in emission of gases, around 14% reduction in gasoline fuel consumption when used 9000 and

**Table 17.3** Shows the reduction in emission of exhaust gases under magnetic field at different idling speed (Fatih and Saber 2010)

Exhaust emission	Carbon monoxide	Nitrogen oxide	Methane
Reduction (%)	7	30	40

**Table 17.4** Shows the reduction in emission of exhaust gases under magnetic field (Garg and Agarwal 2013)

Make model	% decrease in HC	% decrease in CO
Maruti, India (vehicle)	40	30
Hyundai 4 cylinder	21	99
Suzuki 4 cylinder	41	91
Jeep	81	68

6000 gauss power, whereas, in case of emissions of CO, HC, and CO<sub>2</sub> are 30%, 40%, and 10%, respectively.

Karande et al. (2015) investigated the emission on 3 cylinders, four strokes gasoline engine of 800 cc under the effect of the electromagnetic effect of specifications: 1 kHz to 38 kHz frequency, 12 V voltage, 350 mA, and 4.2-W power. Effective reduction of HC emission of 7% was observed for 4 kg load.

Garg et al. (2013) performed the test on Indian vehicles to carry out the emission test. Test investigated the exhaust gases for four-wheelers under the magnetization process's effect, i.e. fuel is magnetized. The author tested on HC and CO emission with the help of the opacimeter emissions test. Table 17.4 shows the emission tested by using magnetizer fuel energizer.

Fuel energizer conserves the fuel by increasing the combustion efficiency, and thereby less CO is being emitted.

Shweta Jain et al. (2012) experimentally investigated the magnetic fuel conditioner in IC engine. They have reported improvement in the fuel properties like viscosity reduction in ferrite magnets ranging from 1000–1800 gauss. The test result displayed a reduction in smoke percentage under the influence of the magnetic field. Table 17.5 shows smoke percentage reduction for different loading conditions of IC engines.

Abdul Mujeebu et al. (2011) investigated the combustion and emission characteristics are compared to those of the traditional burner and two compact pre-mixed LPG burners based on submerged and porous surface combustion (short as MSB and SSB, respectively). The MSB pre-heating and reaction zones are composed of porcelain and alumina spheres of 30 mm, respectively, and alumina (Al<sub>2</sub>O<sub>3</sub>) pore

**Table 17.5** Shows smoke % reduction for different loading conditions of IC engines (Abdul Mujeebu et al. 2011)

Load on engine (Kg)	% of smoke without magnetic fuel conditioner	% of smoke with magnetic fuel conditioner
0	2.5	1.03
2	2.43	0.94
4	2.41	0.92
6	2.04	0.99
8	2.24	0.79
10	2.24	0.79

density foams of 26 and 8 ppm are produced in SSB zones. Application of MSB and SSB reduces  $\text{SO}_2$  and  $\text{NO}_x$  emissions to 76% and 75%, respectively. The thermal efficiencies of CB, MSB, and SSB are 47%, 59%, and 71%, respectively, with a thermal load of 0.62 kw.

Research carried on five commercially available household LPG stoves under various operating conditions, 89 laboratory tests were carried out by Guofeng Shen et al. (2017). The mean thermal efficiency was  $51 \pm 6\%$ , meeting the guidelines under the International Organization for Standardization. Emission factors of  $\text{CO}_2$ , CO, THC,  $\text{CH}_4$ , and  $\text{NO}_x$  based on useful energy delivered (MJd) were  $142 \pm 17$ ,  $0.77 \pm 0.55$ ,  $130 \pm 196$ ,  $5.6 \pm 8.2$ , and  $46 \pm 9$  mg/MJd, respectively.

Rekha Sahoo and Animesh Jain (2019) used CuO of 0.5% mass fraction nanoparticles blended with diesel fuel by means of a mechanical homogenizer and an ultrasonicator. Physicochemical properties of CuO nano-fuel have been calculated and compared to renewable diesel fuel. Their stability characteristics have been examined under static conditions. The CuO nanoparticles in the fuel affect engine efficiency and emissions characteristics under the magnetic field strength of 3000 gauss. Mounting permanent magnets in the fuel line improved fuel properties such as aligned and directed hydrocarbon molecules for better atomization of fuel resulting in better engine emissions. The experimental analysis showed that use of CuO nano-fuel results in improved efficiency and emission characteristics. The engine test results with magnetic fuel conditioning showed that the CuO nano-fuel has a better mechanical efficiency of 7% and BSFC reduction by 6%.

Agarwal et al. (2015) examined the Traditional LPG Cooking Stove's efficiency. For a series of tests, a traditional LPG burner is used. Burner's thermal efficiency depends on parameters like loading height, pot diameter, and weight. The conventional burner could achieve a maximum thermal efficiency of 61.66%. Emission levels are calculated at various power levels of following emissions, namely CO,  $\text{CO}_2$ , and  $\text{NO}_x$ . The overall emission of  $\text{NO}_x$  is up to 49 ppm. The experimental performed under IS 4246 (2002) water boiling test and a separate parameter to test emission.

## 17.2 Fuel Conditioning Technique Used to Control Emissions

Many techniques are employed to reduce the exhaust emission of internal combustion engines, viz. catalytic converter, thermal management strategies, evaporative, and crankcase emission controls. Some modifications are required to incorporate these technologies, i.e. changing the existing model. Present work focuses on conditioning the fuel leading to complete combustion, resulting in a percentage decrease in emissions. Applying permanent magnets on the fuel line changes the fuel's properties, especially viscosity and also affects the intermolecular structure. Magnets do not require any power or any special modifications to existing models of the engine.

Hydrocarbon fuels consist primarily of hydrogen and carbon molecules, all atoms consist of nucleus and electrons, where electrons revolve around the nucleus and also spin in its own axis. The magnetic moment already exists in molecules; electrical charges are positive and negative. Due to the covalent bond arrangement between hydrogen and carbon atom, subsequently, the fuel is thus not deliberately bonded with oxygen during fuel–air mixing process. The particle of hydrogen in fuel exists in two distinct states, i.e. para and ortho states. Ortho state of hydrogen atom favours complete combustion and that can be achieved by applying magnetic field on the fuel line. Magnetized fuel weakens the intermolecular forces between hydrogen and carbon atom leading to maximum oxygen acquisition towards hydrogen and carbon atoms. This leads to more significant energy saving and a decline in HC, carbon monoxide, and nitrogen oxides. The ionizing fuel also leads to the dissolution of carbon accumulation in the carburetor, jets, injector, and combustion chamber, thus preserving a specified engine state. The use of magnetic fields contributes to ionization and realignment.

### 17.3 Experimental Setup

The following major instruments are used in testing the performance of the internal combustion engine and LPG cooking gas stove.

#### 17.3.1 AVL 437 Smoke-Metre

- (a) Accuracy and reproducibility:  $\pm 1\%$  full scale reading.
- (b) Measuring range: 0–100% capacity in % and 0– $\infty$  absorption m<sup>-1</sup> detector: selenium photocell dia. 45 mm
- (c) Maximum smoke: 2100 C temperature at entrance (Fig. 17.1).

#### 17.3.2 Specifications and Operating Conditions of Research Engine Test Rig

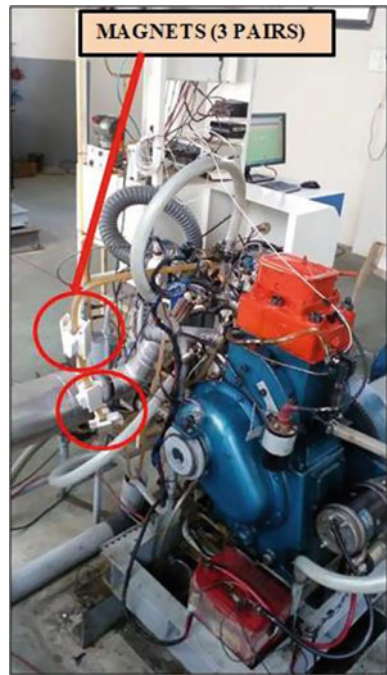
Research engine used to conduct the emission testing, in this both type of fuels, i.e. diesel and petrol can be used by changing the cylinder head (Fig. 17.2).

- (a) Product: research engine test rig of 1 cylinder, 4 stroke, multifuel, VCR, code 240.
- (b) Engine: make Kirloskar, single cylinder, 4 strokes, water cooled, stroke 110 mm, bore 87.5 mm, 661 cc. Diesel mode: 3.5 KW@ 1500 rpm, CR range 12–18. Injection variation: 0–250 BTDC, petrol mode: 4.5 KW@ 1500 rpm, speed range 1200–1800 rpm, CR range 6–10.



**Fig. 17.1** AVL 437 smoke-metre

**Fig. 17.2** Actual image of research engine test rig showing magnet positioning on fuel line



(c) Dynamometer: type eddy current, water cooled.

Operating conditions of the engine:

- (I) No engine modification is required; conditioning of fuel is achieved by just implanting the pair of magnets on the fuel line.
- (II) Measure quantity of fuel are taken into the fuel tank.
- (III) Maintain the cooling water circulation to regulate the operating temperature of engine. The rotameters reading should be kept as per the specified level.
- (IV) Initially, engine subjected to no load condition.
- (V) Increase the load on the engine gradually in steps by rotating dynamometer.
- (VI) Keep the track of load and respective fuel flow rate.
- (VII) Conduct the trail for both, i.e. base operation and magnetization operation and 3000 gauss power applied to external fuel line.
- (VIII) Above arrangements are kept same for both mode of operation, diesel and petrol engine.
- (IX) For petrol engine, compression ratio kept 10 with ranging speeds between 1300 and 1800 rpm, keeping load of 15 kg constant.
- (X) For diesel engine, compression ratio of 17.5:1 with varying loads from 0 to 8 kg, thereby keeping engine speed at constant level.
- (XI) Change the compression ratio of engine by changing angle of cylinder head.

### ***17.3.3 Specifications of LPG Gas Stove***

- (a) Weight: 5 kg
- (b) Material: carbon steel
- (c) Working pressure: 539.3–21,657.3 kPa
- (d) Pressure: 0 to 24.8 bar
- (e) Stove: single CI burner (stainless steel body)
- (f) Pressure gauge
- (g) Flow metre.

Operating conditions of the LPG (Sidheshware et al. 2019):

- (i) Domestic LPG of 5 kg used for investigating the thermal efficiency using water testing under IS 4246 (2002).
- (ii) The setup is in accordance to IS standards. Emission test carried out by collecting the flue gases with the help of collecting hood (see Fig. 17.3).
- (iii) Different sized vessel used to investigate the thermal efficiency of the stove and consequently emission test conducted as per IS standards.
- (iv) The pressure is monitored with a pressure gauge, and the flow rate is measured with help of flow metre gauge.
- (v) The collecting hood is so designed that maximum flue gases pass through it, and PUC probe is inserted inside the hood to measure this flue gases (Fig. 17.4).

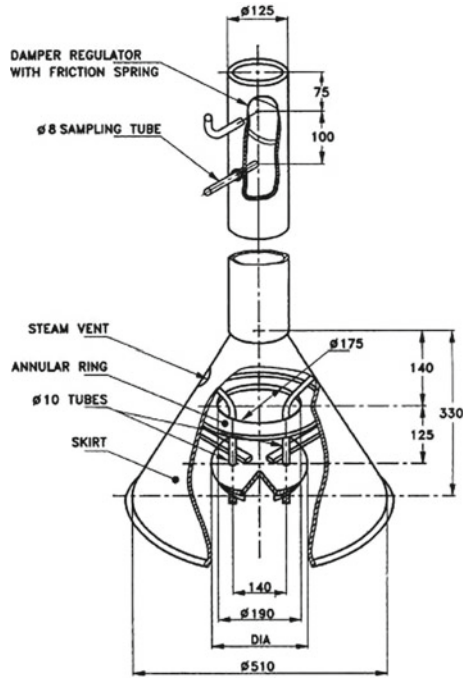


Fig. 17.3 LPG gas stove hood for gas analyzer (IS 4246 2002)

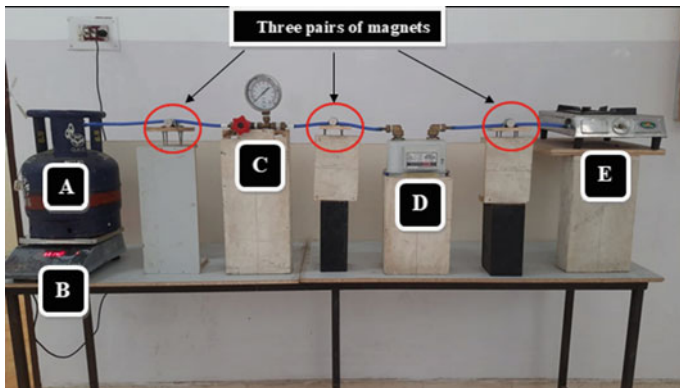


Fig. 17.4 Actual setup of domestic LPG gas stove with 3 pairs of magnets of 5000 gauss power. a LPG gas cylinder, b measuring weight, c pressure gauge, d flow rate gauge, e gas stove



### 17.3.4 Specifications of Permanent Magnet

- (a) Type: neodymium magnet
- (b) Magnetic strength: 3000 gauss
- (c) No. of pair: 3
- (d) Dimensions: 2 m (diameter) and 4 cm (length) (Fig. 17.5).

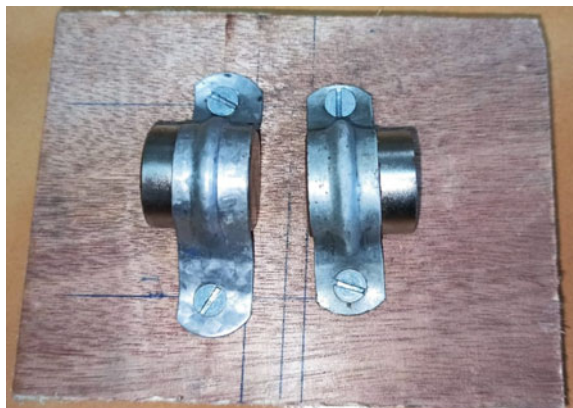
## 17.4 Analyzes of Exhaust Emission of Hydrocarbon Fuel Under Magnetization Process

Engine operating under base operation (non-magnetization process), it was found that the engine consumes more fuel. Fuel is de-clustered in the current analysis using the magnetic field. Moreover, oxygen can reach de-clustered fuel molecules, and in doing so, combustion enhancement takes place. Improved combustion increases engine thermal efficiency, making it easier to use the fuel better and improve fuel economy. Exhaust CO and HC emission decrease due to better combustion (Faris et al. 2012). Thus, the fuel line's impact on the number of constituent pollutants presents in the exhaust after the combustion.

Incomplete combustion comprises HC and CO emissions, and the CO<sub>2</sub> emissions are a part of total combustion. Complete fuel combustion is possible with the magnet field. As a result, HC and CO emissions decrease, whilst CO<sub>2</sub> increases at the same time. The by-products of partial fuel combustion are CO and HC emissions.

In SI engine, load on engine is kept constant throughout the operation with varying engine speed, and accordingly, fuel flow rate changes as per the engine requirement. Trail is conducted with compression ratio of 10, for both under non-magnetic field and with magnetic field (3000 gauss power). Whereas in CI engine, engine speed is kept constant with varying engine load, and same accordingly, fuel flow rate changes as per the engine requirement. Trail is conducted with compression ratio of 17.5, for

**Fig. 17.5** Permanent magnets of 3000 gauss (1 pair) applied to fuel line



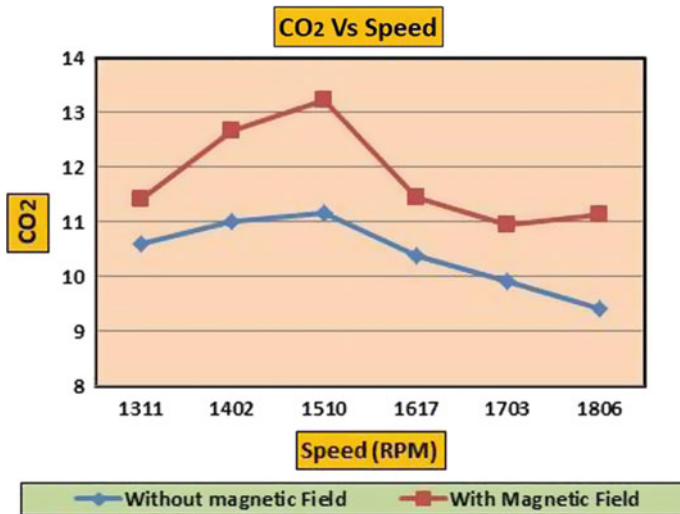


Fig. 17.6 Variation of CO<sub>2</sub> versus speed for SI engine

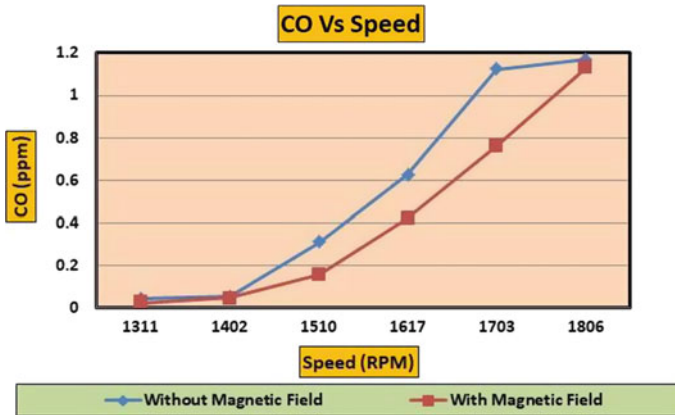
both non-magnetic field and magnetic field (3000 gauss power). In LPG cooking gas stove, a constant gas flow rate and magnetic field of 3000 gauss are maintained with varying loading condition.

#### 17.4.1 Increase in CO<sub>2</sub> Emission—SI Engine

Figure 17.6 illustrates the CO<sub>2</sub> emissions under magnetic effect. The readings were obtained for both magnetic field and non-magnetic effect for a range of speeds, i.e. 1300 rpm to 1800 rpm. 3000 gauss power magnet intensity mounted to the line of fuel. The experimental findings suggest that a magnetic field increases CO<sub>2</sub> compared to a non-magnetic effect of up to 13%. The rise comes mostly by conversion of CO to CO<sub>2</sub>; it is mainly because of complete mixing of oxygen atom with both hydrogen and carbon atoms. With the aid of a gas analyzer, the CO<sub>2</sub> percentage for various engine speeds has been registered.

#### 17.4.2 Reduction in CO Emission—SI Engine

Figure 17.7 shows an overall decrease of 28% in CO emissions with 3000 gauss magnet power. Magnetic force weakens the hydrocarbon chain intermolecular bonds within the molecules and changes the fuel's thermo-physical properties. The CO and HC emissions decrease in percentage due to loss of intermolecular strength. In



**Fig. 17.7** Variation of CO versus speed for SI engine

the combustion chamber, HC molecules are present as a group, which is subdivided and transformed into smaller units after using a magnetic field. The de-clustering processes weakened or break the intermolecular bond between the molecules and de-cluttered to oxygen, causing complete air and fuel mixing. This contributes to more potent fuel combustion.

### 17.4.3 Reduction in HC Emission—SI Engine

Figure 17.8 indicates the exhaust gas emissions of HC. Trail conducted for magnetic fields and without magnetic fields to record the HC emissions. 3000 gauss magnet power mounted on the line of fuel. Test findings confirm that HC emissions were decreased up to 7.5% under the magnetic field effect compared to a non-magnetic field. The HC emissions are recorded for different engine speeds. A decrease in HC emissions means a reduction in (unburned HC) UBHC in the exhaust gases due to complete combustion of the HC fuel.

### 17.4.4 Increase in NO Emission—SI Engine

General forms of nitrogen oxides are  $\text{NO}_2$  and  $\text{NO}$ . Nitrogen oxides emissions are dangerous to the atmosphere and are produced during the combustion reaction at high temperature. The temperature of the engine and the chemical reaction must be optimized to preserve the nitrogen emission cap. 3000 gauss magnet power added to the line of fuel. Figure 17.9 shows up to 43% of increment in nitrogen oxides under the magnetic field effect and compared with non-magnetic field testing. The

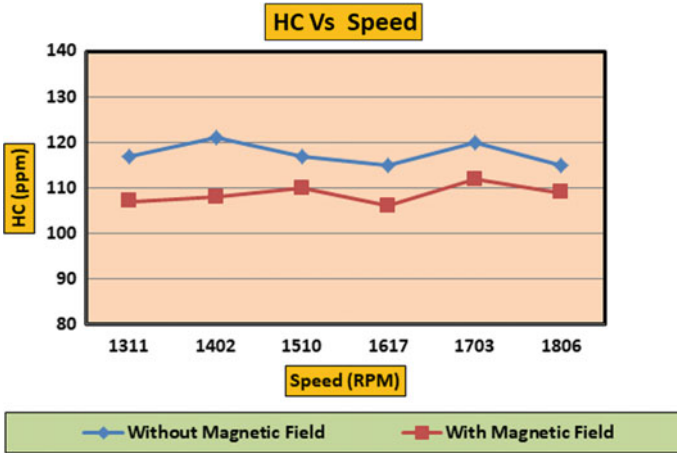


Fig. 17.8 Variation of HC versus speed for SI engine

combustion temperature raises due to complete combustion achieved when fuel gets magnetized and ultimately results in the formation of nitrogen oxides, in case of magnetic field testing.

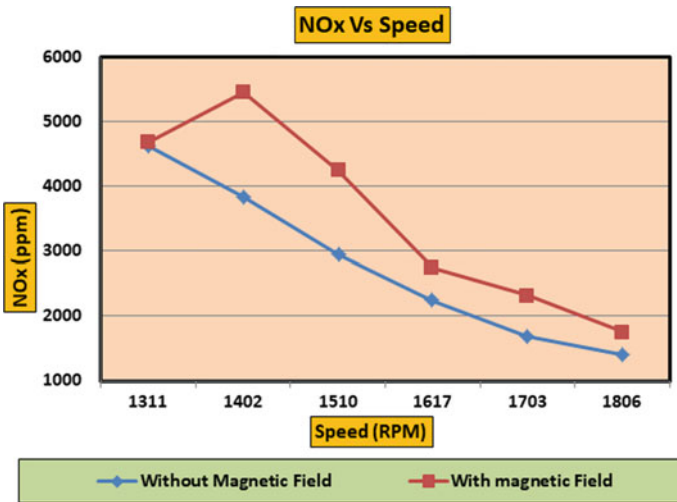


Fig. 17.9 Variation of NO<sub>x</sub> versus speed for SI engine for SI engine

### 17.4.5 Increases in CO<sub>2</sub> Emission—CI Engine

On application of magnet on the fuel line shows impact on performance and reduction in emission. Hydrogen atom present in the working fluid of respective system has greater influence towards magnetic field. The intermolecular force between hydrogen and carbon atom gets weakened, thereby letting the oxygen atom to combine with hydrogen and carbon atom during fuel–air mixing process. This leads to complete combustion, consequently reducing the carbon dioxide, carbon mono-oxide, and HC, but due to complete combustion resulting in higher operating temperature and which could lead to formation of oxides of nitrogen. The effect of magnetic field on the type of fuel is also having greater impact. Like petrol fuel has greater affinity towards magnetic field as compared to diesel fuel, now this is mainly depends on physical property of the fuel, i.e. viscosity. For petrol, viscosity reduction observed to be 23%, whereas for diesel fuel is 9% (Sidheshware et al. 2019). Therefore, the system performance significantly depends on the property of the fuel. So therefore, the emission results for the engine operating for diesel fuel (CI engine) are observed to be less as compared to petrol fuel (SI engine).

Figure 17.10 confirms the increment in percentage of CO<sub>2</sub> in the CI engine's exhaust gas emission. The experimental carried out for both with and without magnetic field effect, under different loading conditions. 3000 gauss magnet strength introduced to the fuel line. Up to a 4.3% rise in CO<sub>2</sub> emissions has been observed primarily because of CO emissions have been converted into CO<sub>2</sub> emissions in magnetic fields.

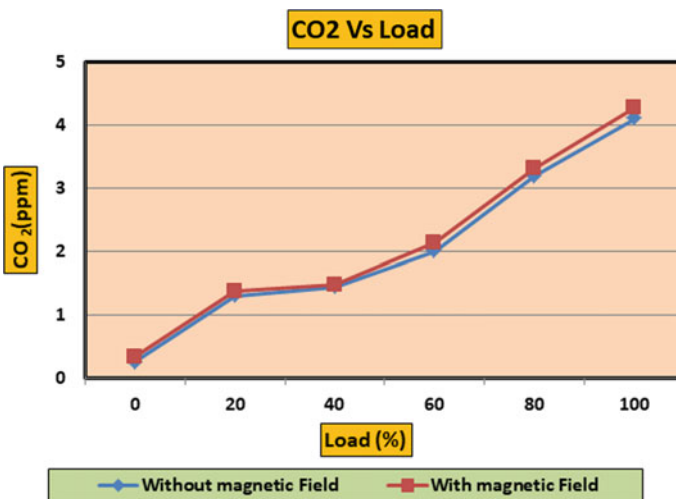


Fig. 17.10 Variation of CO<sub>2</sub> versus load for CI engine

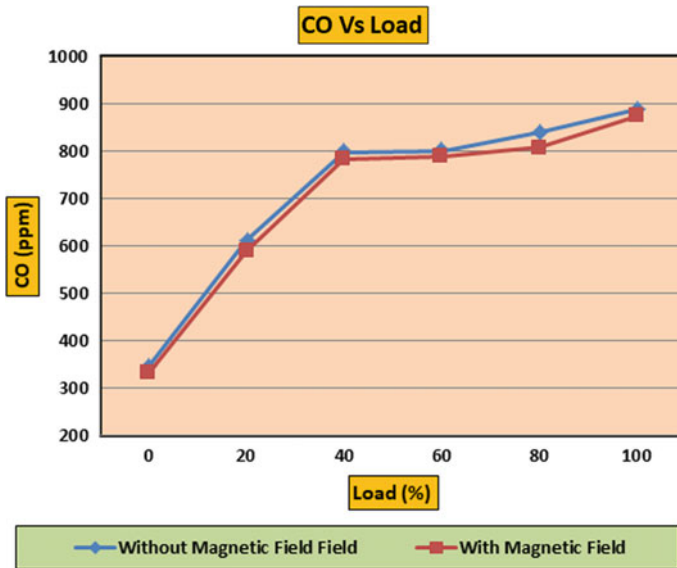


Fig. 17.11 Variation of CO versus load for CI engine

#### 17.4.6 Reduction in CO Emission—CI Engine

With a gas analyzer at different loads, the CO percentage was reported. CO emission with no magnetic field was a datum for the present study. Magnetic strength 3000 gauss applied to the fuel line. Figure 17.11 shows a 3% reduction in CO emission under the magnetic field effect compared to the test carried out under non-magnetic fields. CO emission occurs due to incomplete combustion, due to lack of oxygen atoms binding with hydrocarbon molecules. A complete combustion process occurs when hydrogen and oxygen molecules combine, leading to effective mixing of air-fuel mixture.

#### 17.4.7 Reduction in HC Emission—CI Engine

Figure 17.12 shows that the magnetic field influences HC emissions. Experimental readings for various loading conditions were considered. A gas analyzer was used to record HC emissions for various loads from 0 to 8 kg. The decrease in HC emission has been observed for various loads under magnetic fields. 3000 gauss magnetic strength applied to the line of fuel. The experiments' outcome suggests that the magnetic field effect is overall up to 5% greater than that of non-magnetic fields. The reduction in HC emissions is due to the fuel being completely combusted in the chamber. A higher load on the fuel line with a magnetic field is not as useful as low

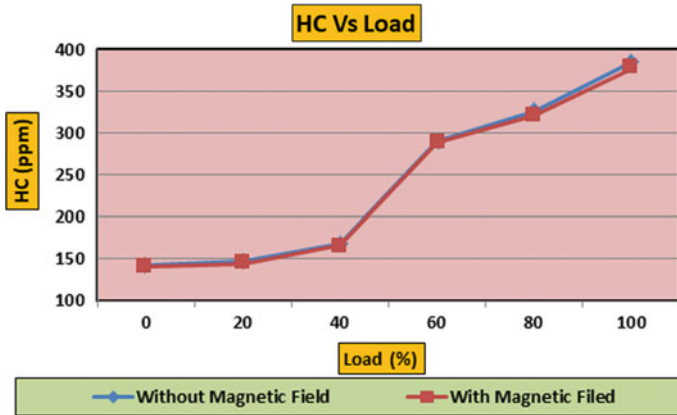


Fig. 17.12 Variation of HC versus load

loads. The explanation is that when the load on the engine increases, the mixture flow rate and speed also increase; this results decrease in interaction between fuel and magnetic field at various loads on the engine. Consequently, a decrease in CO and HC emissions at higher loads was not expected. It is a well-known fact that the presence of HC and CO in the exhaust gas is a sign of incomplete combustion.

#### 17.4.8 Increment in NO Emission—CI Engine

The oxides of nitrogen are  $\text{NO}_2$  and  $\text{NO}$ . Generally, the reason for the formation of oxides is high-operating temperature, i.e. during combustion process, high-temperature gases are released. Figure 17.13 shows an overall up to 5% increase under magnetic field effect as compared to a non-magnetic field. Due to the conditioning of fuel, proper mixing of the air–fuel mixture occurs, resulting in complete combustion and increasing the cylinder temperature. At peak temperature,  $\text{NO}$  forms and is exhausted to the atmosphere. Other oxides like  $\text{N}_2\text{O}_4$ ,  $\text{N}_2\text{O}$ , and  $\text{N}_2\text{O}_5$  are decomposed spontaneously at the ambient condition of  $\text{NO}_2$ .

#### 17.4.9 Reduction in CO and $\text{CO}_2$ Emissions—LPG Gas Stove

The system was designed according to IS 4246 (2002) guidelines (Sidheshware et al. 2019). Initially, water testing was carried out for different loading conditions, i.e., 1 L, 6 L, and 9 L. Furthermore, the hood was designed so that normal combustion of the burner did not interfere. The emission testing performed with the help of a

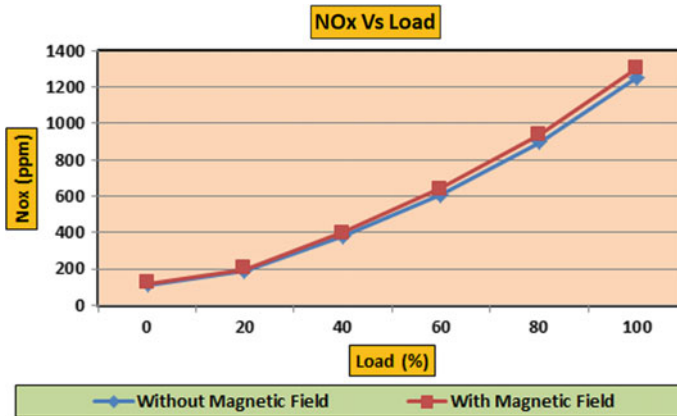


Fig. 17.13 Variation of NO<sub>x</sub> versus load

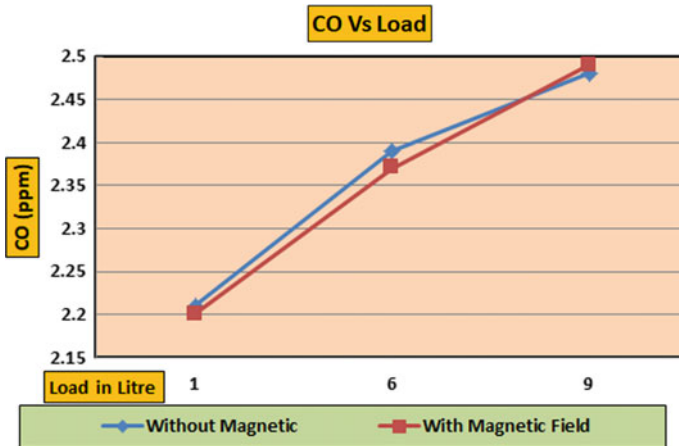
gas analyzer instrument make ACE 9000. Emission testing carried for CO, CO<sub>2</sub>, and NO<sub>x</sub>.

To analyze the emission from the LPG, the regular hood has been used to fix all the exhaust gases to the analyzer to mitigate dilution. The pan was filled with 1 kg of water and covered by a hood for separate extraction of the exhaust gas from the produced steam, which is ventilated by the integrated vertical channels. The exhausts then sampled a test connected to an emission analyzer at the hood exits. Combustion was inspected for CO and CO<sub>2</sub> concentrations were measured within few minutes of ignition. The control valve opening area mounted in the hood exit can be changed. Magnetic strength 3000 gauss applied to the fuel line. Figure 17.14a and b shows up to 0.3% improvement in CO<sub>2</sub> emission and for CO emission up to 0.8% maximum for 6 L loading condition under the effect of magnetic field arrangement.

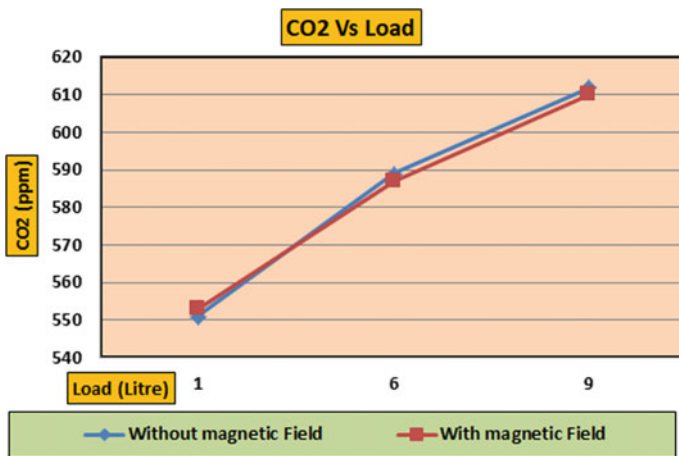
#### 17.4.10 Reduction in NO Emission—LPG Gas Stove

A further test with stack monitoring (combustion) was performed for the calculation of NO<sub>x</sub>. The experiment was performed for different loading conditions, i.e. 1 L, 6 L, and 9 L of water boiling test. Fuel consumed to boil was also recorded. Magnetic strength of 3000 gauss applied to the fuel line. Tests were compared between magnetic and non-magnetic field. From Fig. 17.15, it is observed that for the 1 L water boiling test, NO<sub>x</sub> emission decrease up to 1.78% compared to the magnetic and non-magnetic field, and for the 6 L and 9 L water boiling test, NO<sub>x</sub> reduces to 3.27% and 2.85%, respectively. This was evident that magnetic field effect on a gaseous state with fringe.





(a)

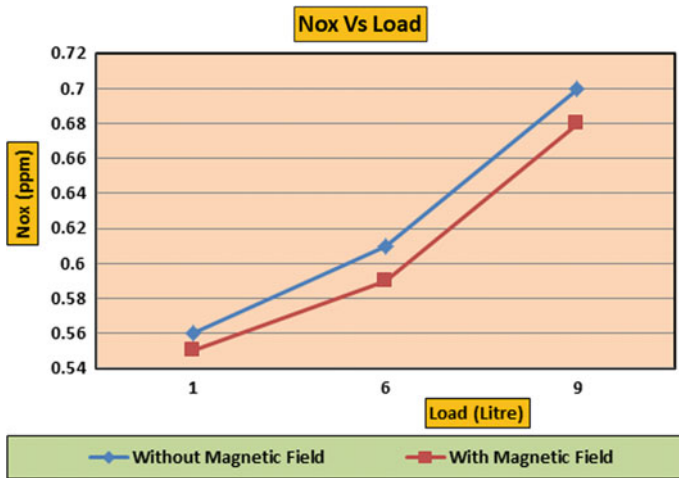


(b)

Fig. 17.14 a Variation of CO versus load; b variation of CO<sub>2</sub> versus load

### 17.5 Conclusion

An internal combustion engine is experimentally tested for SI and CI engine's emission with 3000 gauss power magnets on the fuel line, and the results are compared to non-magnetic fields. The present work deals with reducing emissions from the engine when fuel is conditioned with magnet. A response from hydrocarbon fuel to the magnetic field decreases emissions up to 17 and 4% decrease in emissions when introducing the magnetic field on fuel lines for both SI and CI engines. The general decrease in HC and CO has been observed, whilst the CO<sub>2</sub> percentage increased, clearly showing the assurance that fuel is fully combusted. The magnetic effect has



**Fig. 17.15** Variation of  $\text{NO}_x$  versus load

shown a lesser effect on the gaseous state, as molecules are apart. In the case of emission, the LPG gas stove results in a 2.8% drop in CO emission, 1.1% descents in  $\text{CO}_2$ , and 2.8% drop observed for NO emission.

## References

- Abdul Mujeebu M, Abdullah MZ, Mohamad AA (2011) Development of energy efficient porous medium burners on surface and submerged combustion modes. *Energy* 36:5132–5139. <https://doi.org/10.1016/j.energy.2011.06.014>
- Agarwal P, Anand A, Gupta R (2015) Performance analysis of conventional LPG cooking stove. *Int J Appl Bioeng* 9(1)
- Farisa AS, Al-Naserib SK, Jamal N, Isse R, Abed M, Fouad Z, Kazim A, Reheem N, Chalooob A, Mohammad H, Jasim H, Sadeq J, Salim A, Abas A (2012) Effects of magnetic field on fuel consumption and exhaust emissions in two-stroke engine. *Energy Procedia* 18:327–338
- El Fatih FA, Saber GM (2010) Effect of fuel magnetism on engine performance and emissions. *Aust J Basic Appl Sci* 4(12):6354–6358. ISSN: 1991-8178
- Garg R, Agarwal AK (2013) Fuel energizer: the magnetizer. *Int J Innov Res Dev* 2(4):617–627. ISSN: 2278-0211
- Govindasamy P, Dhandapani S (2007) Performance and emission achievements by magnetic energizer with a single cylinder two stroke catalyst coated spark ignition engine. *J Sci Ind Res* 66:457–463
- <https://www.nettinc.com/information/emissions-faq/what-are-lpg-emissions>
- IS 4246 (2002) Indian Standard domestic gas stoves for use with liquefied petroleum gases—specification (Fifth Revision)
- Jain S, Deshmukh S (2012) Experimental investigation of magnetic fuel conditioner (M.F.C) in I.C. engine. *IOSR J Eng (IOSRJEN)* 2(7):27–31. ISSN: 2250-3021

- Karande N, Kore SK, Momin A, Akkiwate R, Sharada PK, Kumbhar SK (2015) Research publish journals experimental study the effect of electromagnetic field on performance & emission of IC engine. *Int J Mech Ind Technol* 3(1):27–34. ISSN: 2348-7593
- Okoronkwo CA, Nwachukwu CC, Ngozi-Olehi LC, Igbokwe JO (2010). The effect of electromagnetic flux density on the ionization and the combustion of fuel (an economy design project). *Am J Sci Ind Res* 1(3):527–531. ISSN: 2153-649X. <https://doi.org/10.5251/ajsir.2010.1.3.527.53>
- Patel PM, Rathod GP, Patel TM (2014) Effect of magnetic field on performance and emission of single cylinder four stroke diesel engine. *IOSR J Eng (IOSRJEN)* 4(5):28–34. ISSN (e): 2250-3021, ISSN (p): 2278-8719
- Sahoo RR, Jain A (2019) Experimental analysis of nanofuel additives with magnetic fuel conditioning for diesel engine performance and emissions, *Fuel* 236, pp 365–372. <https://doi.org/doi.org/10.1016/j.fuel.2018.09.027>
- Sidheshware R, Ganesan S, Bhojwani VK (2020) Enhancement of internal combustion engine. Efficiency by magnetizing fuel in flow line for better charge combustion. *Heat Transf Res* 51(5):419–431. 1064-2285/20
- Rohit S et al (2020) A systematic study on the analysis of the emission of CO, CO<sub>2</sub> and HC for four-wheelers and its impact on the sustainable ecosystem. *Sustainability* 12:6707. <https://doi.org/10.3390/su12176707>
- Salih AM, Mutez Ahmed A-R (2016) The effect of magnetic field on the boiler performance fueled with diesel. *Int J Sci Eng Res* 7(2). ISSN 2229-5518
- Shen G, Hays MD, Smith KR, Williams C, Faircloth JW, Jetter JJ (2017) Evaluating the performance of household liquefied petroleum gas cook stoves. *Environ Sci Technol*. <https://doi.org/10.1021/acs.est.7b05155>
- Sidheshware R, Ganesan S, Bhojwani VK (2019) Experimental investigation on the viscosity and specific volume of gasoline fuel under the magnetization process. *Int J Ambient Energy*. 0143-0750. <https://doi.org/10.1080/01430750.2019.1653987>

# Chapter 18

## Thermo-Hydraulic Performance of High Heat Flux Electronic Chip Cooling Through Microchannel Heat Sinks with Fins on Base Plate



Vasujeet Singh, Pruthiviraj Nemalipuri, Harish Chandra Das, Vivek Vitankar, Malay Kumar Pradhan, Asita Kumar Rath, and Swaroop Jena

### *Abbreviations*

MCHS	Micro channel heat sink
HTC	Heat transfer coefficient
TR	Thermal resistance
SOUS	Second order upwind scheme
BPT	Base plate temperature
PD	Pressure drop

---

V. Singh · P. Nemalipuri (✉) · H. C. Das  
Department of Mechanical Engineering, NIT Meghalaya, Shillong, India  
e-mail: [pruthiviraj@nitm.ac.in](mailto:pruthiviraj@nitm.ac.in)

V. Vitankar  
NIT Meghalaya, Shillong, India

FluiDimensions, Pune, India

M. K. Pradhan  
Government of Odisha, OSDMA, Bhubaneswar, India

A. K. Rath  
Department of Mechanical Engineering, Raajdhani Engineering College, Bhubaneswar, Odisha, India

S. Jena  
Directorate of Factories and Boilers, Government of Odisha, Bhubaneswar, India

## *Nomenclature*

$W$	Base plate width
$\rho_f$	Density of fluid
$L$	Base plate length
$\rho$	Density of solid heat sink material
$L_{ch}$	Length of channel
$\nu$	Kinematic viscosity
$W_{ch}$	Width of channel
$D_c$	Diameter of circular fin
$H_{ch}$	Height of channel
$L_r + L_c$	Length of pyramidal fin
$S_l$	Dimension of square fin
$W_r$	Width of pyramidal fin
$H_f$	Height of fin
$q''$	Heat flux
$u_{in}$	Inlet velocity
$T_w$	Area weighted average of base plate temperature
$P_{out}$	Outlet pressure
$T_f$	Mass weighted average of coolant temperature
$Re$	Reynolds number
$k$	Thermal conductivity
$D_h$	Hydraulic diameter
$R_{th}$	Conduction resistance
$h$	Heat transfer coefficient
$R_c$	Convection resistance
$q$	Heat transfer rate
$P$	Pressure difference
$C_d$	Drag coefficient
$Nu$	Nusselt number
$f$	Friction factor
$\nu$	Kinematic viscosity

## **18.1 Introduction**

For the safe and reliable operation of electronic devices, the generated heat should be transferred to the surrounding through the cooling device effectively. The temperature generated from the heated surface while the processor operating at base load condition is 40 °C and this temperature reach up to 60 °C to 70 °C (Mathew and Hotta 2018) during the processor operating at full load condition if a microprocessor is continuously working at this high temperature without any cooling system, then

the processor will damage because of high heat generated by the processor. Therefore, the researchers have done comprehensive research regarding heat transfer and pressure drop using MCHS. Air cooling system is the simplest commercial and widely used cooling technique nowadays in most commercial and non-commercial electronic devices. The only disadvantage with this cooling system is that it is only effective for low heat flux generating devices such as TV, radio, tape recorder, etc. (Kanargi et al. 2018; Yu et al. 2013; Khattak and Ali 2019; Popovici et al. 2016). Because of the low thermal conductivity of air compared to other refrigerants, an updated version of this cooling system uses a small fan inside to blow the air over the heated surface so that both natural and forced convection cooling can be accomplished for low heat flux generating devices. For high heat flux generating devices, water or any other efficient coolant through the MCHS is the best option to cool those devices. In the mini rectangular pin fin heat sink, Naphon et al. (2009) have numerically contemplated the heat exchange and flow analysis of de-ionized water as a working liquid. They have used the FVM approach to solve the governing equations with standard  $k-\varepsilon$  turbulence model and considered the impact of heat sink channel width, coolant mass flow rate, and distinctive working states of the CPU temperature. The results demonstrate the variation between the base plate temperature and coolant speed which is inverse to each other. The numerical examination of heat exchange and liquid flow in MCHS has been carried out by Chai et al. (2019), utilizing the triangular ribs inside the MCHS. Also, they have considered the dependence of thermophysical properties on temperature. To make the system more practical, they have considered the effects of viscous heating, channel geometry and ribs spacing. Effect of all these parameters is taken into account by making the non-dimensional parameters related to a converging-diverging ratio, width and height of the channel including the spacing between ribs. The thermophysical properties of the system is examined in the range of  $187 < Re < 715$ . In case of triangular ribs, Nusselt Number (Nu) is 1.01 to 2.01 times higher and friction factor ( $f$ ) is increased by 1.06 to 9.09 times, in case of offset triangular ribs, Nu is 1.01 to 2.16 times and  $f$  is 1.04 to 7.43 times larger than the straight channel. Xu et al. (2005) has proposed a microchannel in which channel has been cut in parallel and several microchannels cut in the transverse direction that divides flow domain into the number of non-mixing flow domains. In these number of independent flow domains, the system's overall heat transfer performance is increased due to the developing region of the thermal boundary layer, which also includes the decrease in the pressure drop compared to a heat sink with transverse microchannel. Cao and Xu (2015) modulated the fluid flow and temperature fields by making the pores inside the microchannel, pores section has been designed in the form of a conical mesh which was 10–100  $\mu\text{m}$  in size and inserted inside the microchannel. Simulation results illustrate that Nu is 1.4–4.1 times greater than microchannel without pores. Wang (2009) numerically investigated the fluid flow and heat transfer characteristics of square cross-section mini-channel by inserting the baffles at various angles on the lower and upper walls of the channels with the Reynolds number ranging from 100 to 1000. The thermal and hydraulic performance of the system has been investigated by changing the baffle height and fluid flow angle to baffle ranging from 45 to 90°. Authors examined that the numerical results at 45°

in line and staggered baffles has the same results and the maximum thermal performance of microchannel is at baffle height of 0.2 times the channel height and at  $45^\circ$  inclination angle. Wang et al. (2007) further experimentally investigated the effect of jet diameter and jet plate spacing on the thermal and hydraulic performance of heat sink using the  $\text{TiO}_2$  water nanofluid, heat sink is made by aluminum with a dimension of  $50 \text{ mm} \times 50 \text{ mm} \times 3 \text{ mm}$ . The non-dimensional parameters created by considering the ratio of jet plate spacing to jet diameter, and examined the performance of the system by varying the non-dimensional parameters from 0.4 to 0.8 and nanofluid concentration from 0.005 to 0.015% by volume and mass flow rate from 8 to 12 gm/s. Experimental results shows that non-dimensional parameter has significant effect on thermal and flow behaviour due to increase in turbulent intensity. Yousefi et al. (2013) have experimentally studied a hybrid cooling scheme for high heat flux and power devices. The proposed scheme is a combination of microchannel and jet impingement technology and aims to improve the temperature uniformity of cooled objects. The use of matrix thermocouples did the measurement of temperature distribution of heat sink. From the results, they have commented that the proposed scheme has the capacity for optimization of temperature uniformity of cooled object. From experiment, it was found that there has been a global decrease in the temperature of heat sink along the direction of flow. Non-conventional cooling technologies such as thermoelectric cooling system, heat pipes and vapour chambers are more efficient than simple natural convection and forced convection air cooling system (So and Pisano 2015; Jaworski 2012; Elnaggar 2014; Elnaggar et al. 2011). Still, these non-conventional cooling systems are expensive, not so easy to install, and have complex working principles compared to the conventional cooling system. Tan and Demirel (2015) have tentatively concentrated heat sink thermal performance with one and two implanted heat pipes. They have used experimental methodology for the estimation of heat conveyed by the inserted heat pipes. The outcomes reveal that the two heat pipes exchanged 36% of the dissipated heat and four installed heat pipes conveyed about 48% of total dissipated heat on the base plate. A test study was made by Rezania et al. (2012) to compute the TR of a heat sink with seven horizontally installed heat pipes. They have contemplated the TR in a heat sink and proposed a two-stage methodology to estimate the performance in their examination. Estimating the heat sink's thermal performance with and without heat pipes where the fins take 64% of the base plate heat and the heat pipe takes 30% heat of the base plate, the impact of inclination angle and nanofluids on the heat exchange performance of the CPU has been considered by Xu et al. (2008). They have observed that the inclination angle prominently affects cooling performance and directly impacts the boiling limit. From the outcomes, it was evitable that there was a drastic increment in the TR of heat pipes at a threshold angle for a given CPU temperature. As the CPU temperature increased, there was a decrease in the threshold angle, from  $60^\circ$  to  $30^\circ$ . Introducing nano-particles ( $\text{Al}_2\text{O}_3$ ) in the coolant decreases the thermal resistance of the cooling system. Liang and Hung (2010) have studied the thermal performance of a heat sink with U-shape finned heat pipes for CPU experimentally. Bessel's modified equation was implemented to obtain the convection heat transfer coefficient between the fins and ambient air. U-shaped heat pipes have two symmetrical parts, each part has a

condenser and a half of evaporator section. These symmetrical parts had similar temperature drop between evaporator and condenser section, which resulted in identical heat transport rate and thermal resistance. The optimum heat transport rate was 50 W for the heat pipes of lowest thermal resistance. A good number of research works have been carried out in the area of cooling of electronic device experimentally, analytically and numerically. From the literature survey it can be concluded that the performance evaluation of MCHS in extreme working conditions such as high heat flux flooding limit and dry out condition need to be addressed with utmost care. The current research work is concentrated on improving heat transfer and flow performance of MCHS by adopting various shapes of micro dimension fins on the base plate; by increasing the number of fins from 10 to 40 in a high heat flux working condition. The SOUS (second-order upwind scheme) was used to solve the diffusion convection of heat in the MCHS with the SIMPLE algorithm.

## 18.2 Geometry Creation

To increase the efficiency of the electronic chip cooling system, various techniques used by the researchers and MCHS is among them. Augmentation of heat transfer rate through a microchannel heat sink using various shaped fins on the base plate has attracted the researcher's attention in place of simple plain MCHS. In this research, a microchannel is modelled in Ansys design modeller; Silicon material is chosen for MCHS due to various difficulties in designing the micro dimension associated with other materials (So and Pisano 2015; Jaworski 2012; Elnaggar 2014). The total area of the base plate is  $W \times L$ , and the thickness of the plate is ( $t$ ), which is perpendicular to the plane of the paper. Each microchannel has the cross-sectional area  $W_{ch} \times H_{ch}$  as shown in Fig. 18.1b and the length of the channel is  $L$ , Fig. 18.1a and b depicts the top and front view of MCHS.

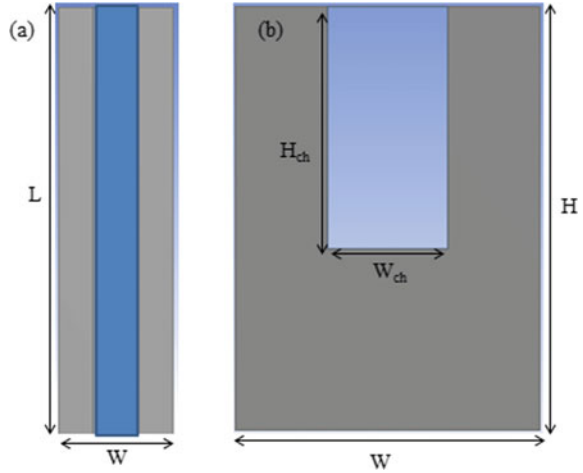
For up-gradation in the MCHS design, different shapes of fins such as cylindrical, pyramidal and square fins have been constructed on the base plate of microchannels as shown in Fig. 18.2b, c and d with height  $H_f$  of each fin. The various-shaped fins increased from 10 to 40 in each heat sink with an increment of 10 fins for three different configurations (cylindrical, square and pyramidal) on the base plate of the heat sink (Tables 18.1 and 18.2).

## 18.3 Discretization

The geometry from the design modeller was imported to Ansys Mesher for the discretization of the domain. Figure 18.3 depicts the generated mesh module for a single plain microchannel heat sink. For accurate prediction of temperature and velocity distribution, the attention is concentrated near the MCHS walls with finer mesh. The grid independence test was performed to obtain accurate results.



**Fig. 18.1** Top (a) and front (b) view of plain microchannel without fins



### 18.4 Computational Analysis

The computational analysis of heat transfer and fluid flow through the MCHS is performed by solving the continuity, Navier–Stokes and energy equations within the domain.

Continuity equation:

$$\frac{\partial u}{\partial x} + \frac{\partial v}{\partial y} + \frac{\partial w}{\partial z} = 0 \tag{18.1}$$

Momentum equation:

$$u \frac{\partial u}{\partial x} + v \frac{\partial u}{\partial y} + w \frac{\partial u}{\partial z} = -\frac{1}{\rho} \frac{\partial p}{\partial x} + \nu \left( \frac{\partial^2 u}{\partial x^2} + \frac{\partial^2 u}{\partial y^2} + \frac{\partial^2 u}{\partial z^2} \right) \tag{18.2}$$

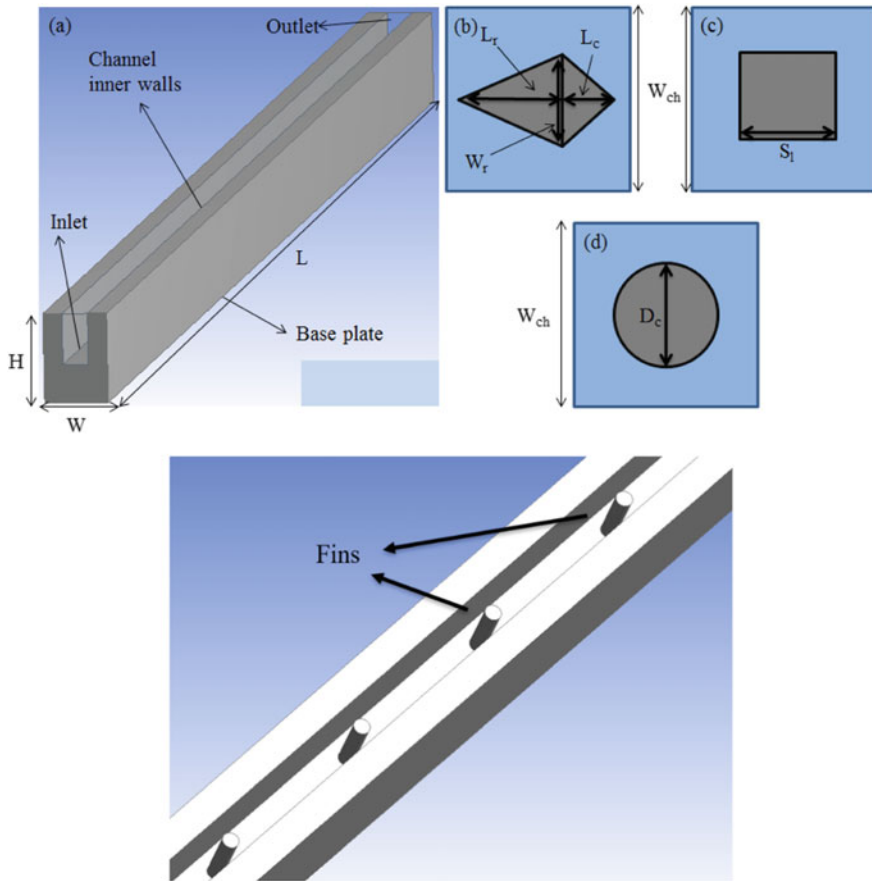
$$u \frac{\partial v}{\partial x} + v \frac{\partial v}{\partial y} + w \frac{\partial v}{\partial z} = -\frac{1}{\rho} \frac{\partial p}{\partial y} + \nu \left( \frac{\partial^2 v}{\partial x^2} + \frac{\partial^2 v}{\partial y^2} + \frac{\partial^2 v}{\partial z^2} \right) \tag{18.3}$$

$$u \frac{\partial w}{\partial x} + v \frac{\partial w}{\partial y} + w \frac{\partial w}{\partial z} = -\frac{1}{\rho} \frac{\partial p}{\partial z} + \nu \left( \frac{\partial^2 w}{\partial x^2} + \frac{\partial^2 w}{\partial y^2} + \frac{\partial^2 w}{\partial z^2} \right) \tag{18.4}$$

where  $p, \rho, \nu$  are pressure density and kinematic viscosity of the flowing fluid, and  $u, v$  and  $w$  are the velocities in three mutual perpendicular directions respectively.

Conversation of Energy equation for coolant:

$$u \frac{\partial T}{\partial x} + v \frac{\partial T}{\partial y} + w \frac{\partial T}{\partial z} = \frac{k_f}{\rho C_p} + \left( \frac{\partial^2 T}{\partial x^2} + \frac{\partial^2 T}{\partial y^2} + \frac{\partial^2 T}{\partial z^2} \right) \tag{18.5}$$



**Fig. 18.2** 3D microchannel with different shapes fins

**Table 18.1** All geometry with various up-gradations

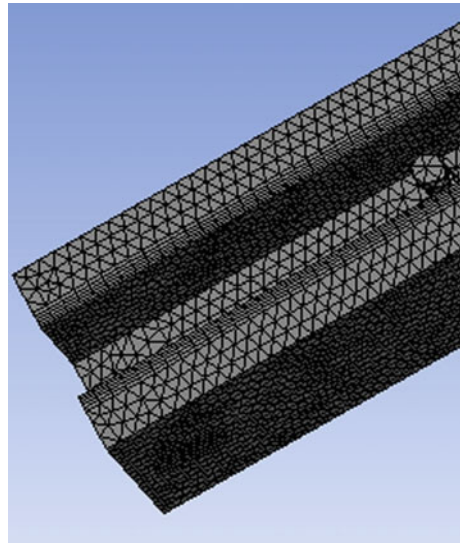
S. No.	Up-gradation	Shape of Up-gradation	Number of Up-gradation	Number of MCHS
1	Plain channel	–	–	1
2	Fins on base plate	Cylindrical	10, 20, 30, 40	4
3		Square	10, 20, 30, 40	4
4		Pyramidal	10, 20, 30, 40	4

where  $\rho$ ,  $T$ ,  $k_f$ , and  $C_p$  are the density, temperature, thermal conductivity, and specific heat respectively. Energy equation for fluid contains conduction, convection, and capacitance terms.

**Table 18.2** Dimensions of various parameters in MCHS

Parameters	Specifications (mm)
Thickness of base plate ( $H$ )	0.35
Width of base plate ( $W$ )	0.25
Length of base plate ( $L$ )	10
Height of channel ( $H_{ch}$ )	0.2
Width of channel ( $W_{ch}$ )	0.1
Length of pyramidal fin ( $L_c + L_r$ )	0.05
Width of pyramidal fin ( $W_r$ )	0.04
Length of square fin ( $S_f$ )	0.04
Diameter of cylindrical fin ( $D_{cyl}$ )	0.04
Height of each fin ( $H_f$ )	0.15

**Fig. 18.3** Meshing



Temperature distribution for MCHS:

$$k_s \left( \frac{\partial^2 T}{\partial x^2} + \frac{\partial^2 T}{\partial y^2} + \frac{\partial^2 T}{\partial z^2} \right) = 0 \tag{18.6}$$

Thermal conductivity of MCHS is  $k_s$ , energy equation for MCHS will only contain the conduction terms because there is no bulk motion of fluids particles so all individual term which contains velocity will vanish out from Eq. 18.5 and get the energy equation for solid.

**Table 18.3** Thermophysical properties of fluid and solid

Material	Density (kg/m <sup>3</sup> )	Thermal conductivity (W/m-K)	Dynamic viscosity kg/(m-s)	Specific heat (J/kg-K)	Inlet temperature (K)
Coolant (Water)	998.2	0.6	0.001003	4182	293
Microchannel (Silicon)	2328	148	-	700	-

## 18.5 Boundary Conditions

Boundary conditions act as the driving element for the computational analysis and the boundary conditions used in this simulation are given below: The inlet velocity is constant  $u_{in} = \text{constant}$  and the outlet is maintained at atmospheric condition. The inlet Re is varied from 100 to 1000 and the temperature of the fluid at the inlet is 293 K for all configurations. At the base plate the constant heat flux 1000 kW/m<sup>2</sup> is imposed and all outer walls of the microchannel (except the inner wall) are assigned as the adiabatic boundary condition (Table 18.3).

$$-k_s \frac{\partial T}{\partial y} = q \quad (18.7)$$

$$\frac{\partial T}{\partial x} = \frac{\partial T}{\partial z} = 0 \quad (18.8)$$

## 18.6 Calculation of Performance Parameters

Reynolds Number (Re)

$$\text{Re} = \frac{\rho_f u_{in} D_h}{\mu} \quad (18.9)$$

Heat transfer Coefficient and Nusselt Number (HTC & Nu)

$$h = \frac{q'' L W}{A(T_w - T_f)} \quad (18.10)$$

$$N_u = \frac{h D_h}{k} \quad (18.11)$$

$q''$  is heat transfer per unit area at the bottom of MCHS,  $A$  is channel inner wall area which is in contact with flowing fluid,  $h$  is Heat transfer coefficient,  $D_h$  is hydraulic

diameter,  $k$  is the thermal conductivity of flowing fluid,  $T_w$  is area-weighted average temperature distribution at inner walls of the microchannel,  $T_f$  is the mass-weighted average temperature of flowing fluid.

### 18.6.1 Thermal Resistance (TR)

Total Thermal Resistance is the sum of conduction thermal resistance and convection thermal resistance.

Conduction thermal resistance

$$R_{th} = \frac{(T_2 - T_w)}{q} \quad (18.12)$$

Convection thermal resistance

$$R_c = \frac{(T_w - T_f)}{q} \quad (18.13)$$

where  $q$  is the total amount of heat flow rate from the base plate of MCHS,  $T_2$  is the area-weighted average temperature at the base plate,  $T_w$  is the area-weighted average temperature at the inner wall of the microchannel,  $T_f$  is the mass-weighted average temperature of flowing fluid.

Fanning friction factor ( $f$ )

$$C_d = \frac{\Delta P \cdot D_h}{2\rho_f \cdot L \cdot u_{in}^2} \quad (18.14)$$

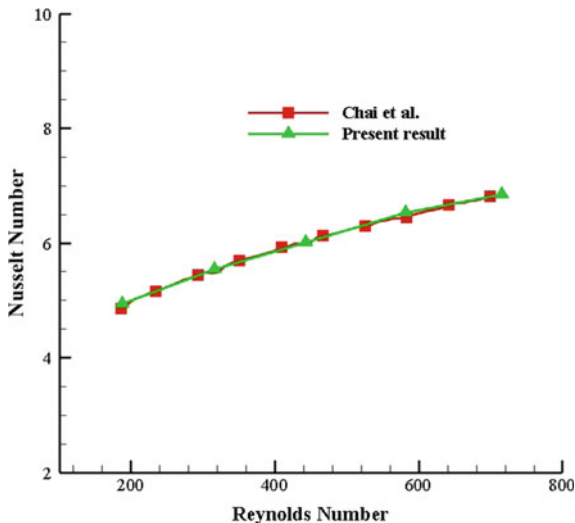
where ( $P$ ) is pressure drop which is calculated by taking the difference of mass-weighted average pressure distribution at inlet and outlet of microchannel,  $D_h$  is hydraulic diameter,  $\rho_f$  is the density of flowing fluid,  $L$  is the length of flow domain,  $u_{in}$  fluid flow velocity.

## 18.7 Results and Discussion

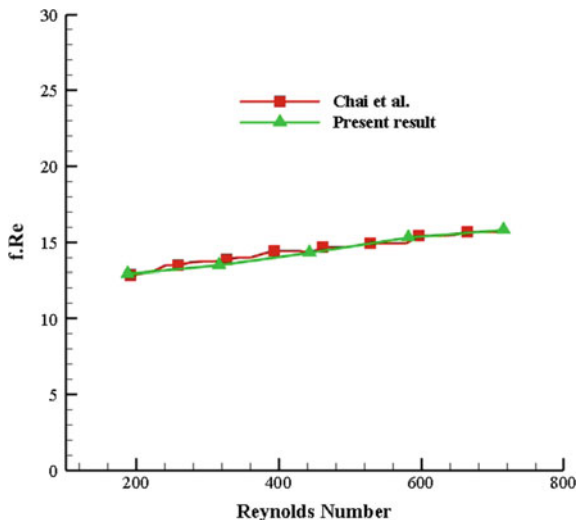
Validation of the computational method was carried out by comparing the simulated results with Chai et al. (Yu et al. 2013) and it is observed that the  $N_u$  and the channel friction factor are in good agreement (Figs. 18.4 and 18.5).

Grid independence test was carried out for the validation of the adopted CFD methodology for all the geometries. From this grid independence study it is observed that the variation in the output (base plate temperature) is negligible with the number

**Fig. 18.4** Validation of Nu



**Fig. 18.5** Validation of friction factor



of cells. All details of grid independency test for plain channel and 10 fins on the base plate for each geometry is depicted in Table 18.4.

The variation of base plate temperature with channel inlet Re is depicted in Figs. 18.6, 18.7 and 18.8 for all configurations of a microchannel along the plain channel. It is observed that the base plate temperature lies between 28 °C and 40 °C for all configurations at Re below 200. With the increase in Re, the base plate temperature is gradually decreasing for all configurations. A minimum base plate temperature of 28.063 °C is observed with 40 cylindrical fins on the base plate at the allowable Re

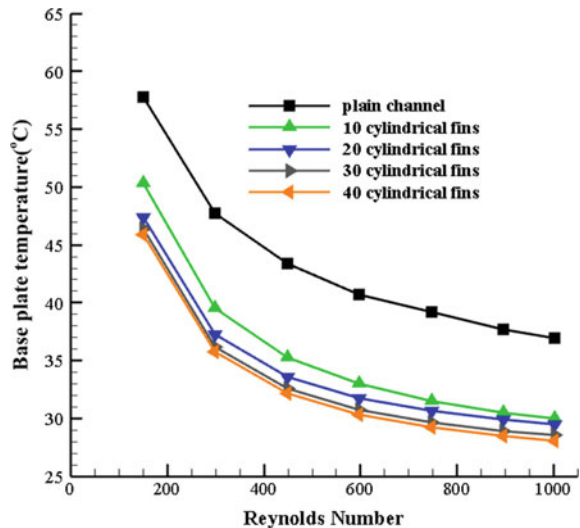
**Table 18.4** Grid independence study

S. No.	Geometry	Number of cells	Base plate temperature (°C)
1	Plain channel	801,259	32.8496
		101,578	33.2589
		1,211,512	36.9686
		1,536,445	36.9684
2	10 cylindrical fins on base plate	7,498,632	26.2846
		1,125,691	28.5917
		1,483,791	29.9532
3	10 square fins on base plate	1,863,570	29.9542
		718,349	26.4819
		1,121,344	27.9960
		1,529,736	29.6623
4	10 pyramidal fins on base plate	1,754,862	29.6521
		758,469	28.5941
		1,025,710	29.0154
		1,372,891	30.7231
		1,634,859	30.7214

of 1000. It is observed that base plate temperature with 40 pyramidal fins on a base plate is 30.356 °C which is 2 °C higher than cylindrical fin on the base plate at same Re (1000) since conduction heat transfer rate is directly related to the cross-sectional area through which heat is transferred and there is a decrement in cross-section area in case of pyramidal fin along its height. There will be more conduction resistance in pyramidal fins as compared to cylindrical fins. With same Re (1000), the square fin is showing 28.155 °C base plate temperature and a plain channel is showing a temperature of 37.986 °C. Variation of pressure drop in all configurations (cylindrical, square and pyramidal) of the MCHS is depicted in Figs. 18.9, 18.10 and 18.11. It is observed that pressure drop is increased with an increase in Re because of higher entry loss at a higher value of Re in the MCHS. A minimum pressure drop of 151.941 kPa is observed for a plain channel at an allowable Re of 1000; it is obvious because there is no obstacle inside the flow field. As the number of obstacles increases inside the flow field by constructing various-shaped fins, the pressure drop increases, 40 square fins resulting maximum value of pressure drop 978.008 kPa with Re (1000), because flow gets separated after passing each square fin inside the microchannel. A minimum pressure drop of 368.347 kPa is observed at Re (1000) in case of 40 pyramidal fins on a base plate among all shapes of fins (cylindrical, square and pyramidal). A significant pressure difference is observed between 40 square and 40 pyramidal fins at 1000 Re because the pyramidal shape is aerodynamic compared to a flat square bluff shape of the square fin. A pressure drop of 747.910 kPa is observed with 40 cylindrical fins on the base plate at the same

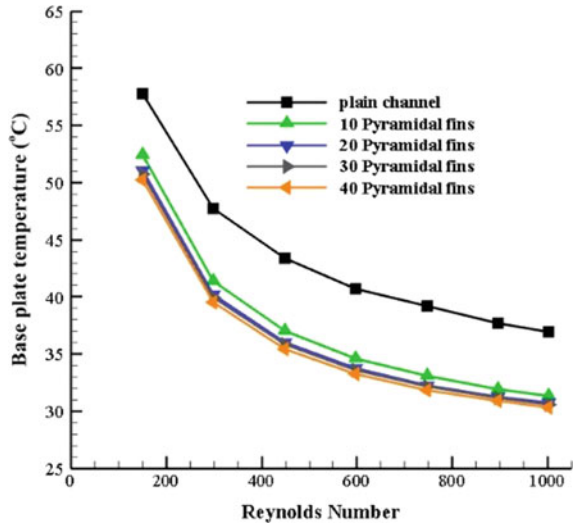
Re (1000) between the pyramidal fin and square fin. Variety of the  $C_d$  is portrayed in Figs. 18.12, 18.13 and 18.14 for every arrangement of the MCHS. For laminar fluid flow,  $C_d$  is inversely proportional to fluid velocity and fluid velocity is directly proportional to Re as shown by Eq. 18.14. As Re increases,  $C_d$  diminishes for all designs of the MCHS. HTC is increased with the rise in Re because the increased Re results in an increment of the fluid speed, so fluid will take more heat from MCHS as shown in Figs. 18.15, 18.16 and 18.17. A plain channel is showing a minimum HTC of 33.994 kW/m<sup>2</sup>K at Re (1000). As the number of fins increased on the base plate of the microchannel, the HTC increased drastically and a maximum value of HTC (74.757 kW/m<sup>2</sup>K) is attained with 40 cylindrical fins because more surface area is in contact with the fluid flow. A minimum value of HTC (57.736 kW/m<sup>2</sup>K) is observed for 40 pyramidal fins and 72.313 kW/m<sup>2</sup>K for 40 square fins on the base plate of an MCHS. The variation of  $N_u$  with Re were depicted in Figs. 18.18, 18.19 and 18.20. Variation of TR were shown from Figs. 18.21, 18.22 and 18.23 and it is observed that with an increase in Re, TR is decreasing for all configurations. A maximum value of TR is 6.787 K/w at Re (1000) for plain channel and a minimum value of TR (3.225 K/w) is observed for 40 cylindrical fins on the base plate at Re (1000). It is because the uniform cross-section area throughout the length in case of cylindrical fins. With the same Re (1000), 40 square fins are on a base plate having a value of 3.262 K/w thermal resistance.

**Fig. 18.6** Variation of BPT for cylindrical fins

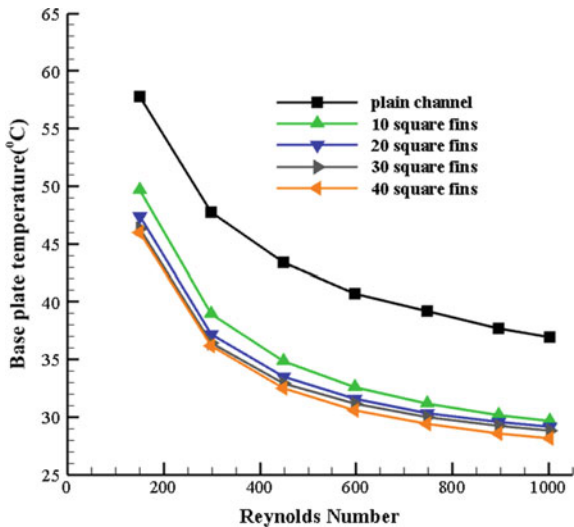




**Fig. 18.7** Variation of BPT for pyramidal fins



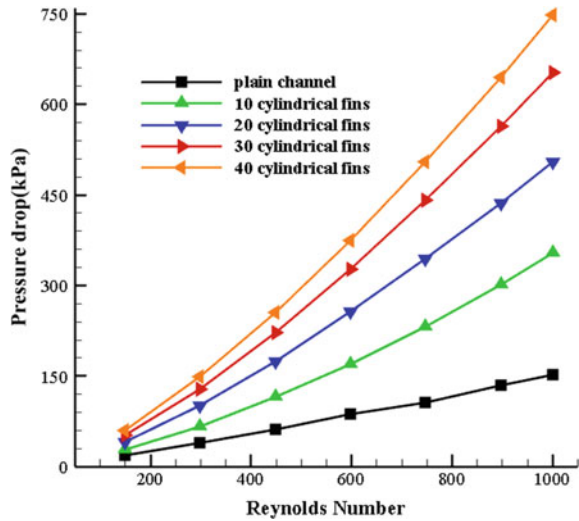
**Fig. 18.8** Variation of BPT for square fins



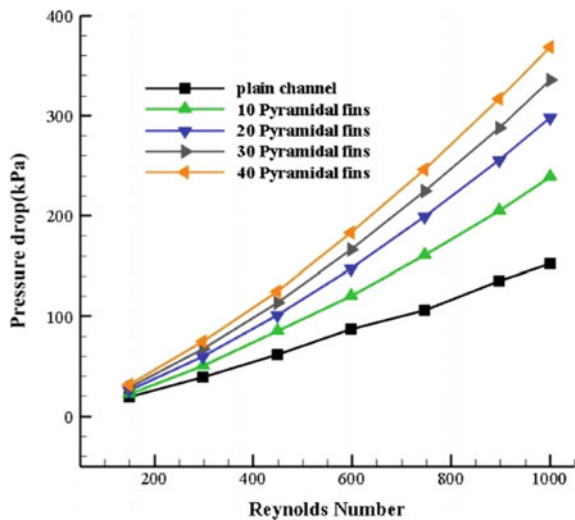
### 18.7.1 Variation of BPT, HTC, Nu, PD, $C_d$ and TR with Number of Fins

In Fig. 18.24, the variation of base plate temperature with the number of fins was depicted for all three configurations at Re (1000). It is observed that base plate temperature is decreasing for all configurations; a maximum decrement of 1.890 °C takes place for cylindrical fins from 29.95 °C to 28.06 °C when cylindrical fins increase from 10 to 40. The minimum decrement of 0.995 °C takes place for triangular

**Fig. 18.9** Variation of PD for cylindrical fins

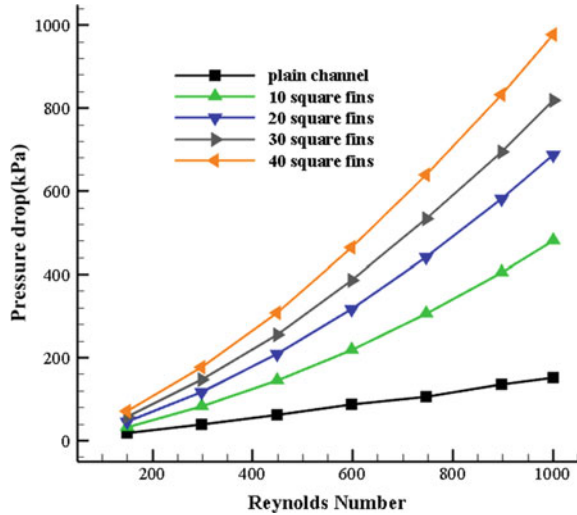


**Fig. 18.10** Variation of pressure drop for pyramidal fins

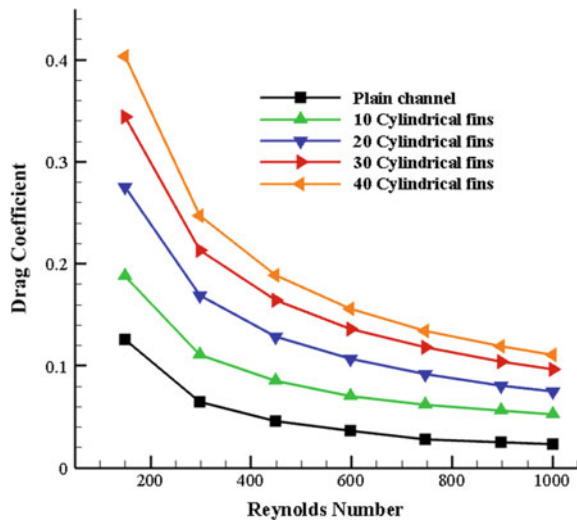


fins from 31.35 °C to 30.356 °C and a decrement of 1.506 °C takes place in case of square fins as it is increased from 10 to 40. Figure 18.25 shows the variation of HTC with an increase in the number of fins at 1000 Re. Variations of HTC are just inverse to the variations of base plate temperature with the number of fins. Maximum increment of HTC (12.085 kW/m<sup>2</sup>K) occurs for cylindrical fins from 62.76 kW/m<sup>2</sup>K to 74.75 kW/m<sup>2</sup>K when cylindrical fins increase from 10 to 40. A minimum increment of 3.615 kW/m<sup>2</sup>K in HTC takes place for pyramidal fins from 54.12 kW/m<sup>2</sup>K to 57.73 kW/m<sup>2</sup>K when pyramidal fins increase from 10 to 40. The behaviour of N<sub>u</sub> is similar to the variation of HTC depicted in Fig. 18.26. In Fig. 18.27, variations of

**Fig. 18.11** Variation of pressure drop for square fins

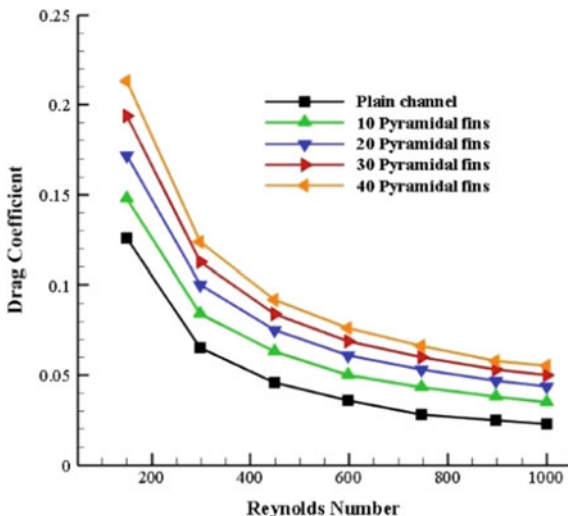


**Fig. 18.12** Variation of drag coefficient for cylindrical fins

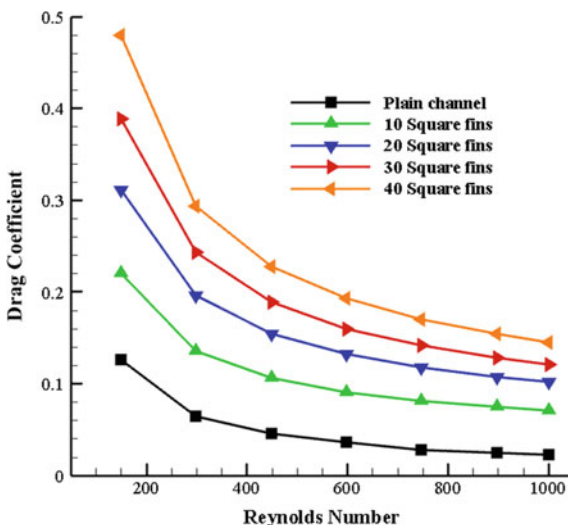


pressure drop with the number of fins were illustrated for all configurations at Re (1000). Pressure drop is increasing for all configurations with the number of fins. A maximum increment of 496.405 kPa in pressure occurs for square fins from 481.60 to 978.006 kPa when square fins increase from 10 to 40 on the base plate. A minimum increment of 130.043 kPa in pressure drop takes place for the pyramidal fin on the base plate from 238.30 to 368 kPa. The variation of Cd is similar to the pressure drop variation with the number of fins depicted in Fig. 18.28. In Fig. 18.29, the variation of TR with the number of up-gradations (fins) was depicted and observed that the TR is decreased for all three configurations with the increase in the number of fins.

**Fig. 18.13** Variation of drag coefficient for pyramidal fins

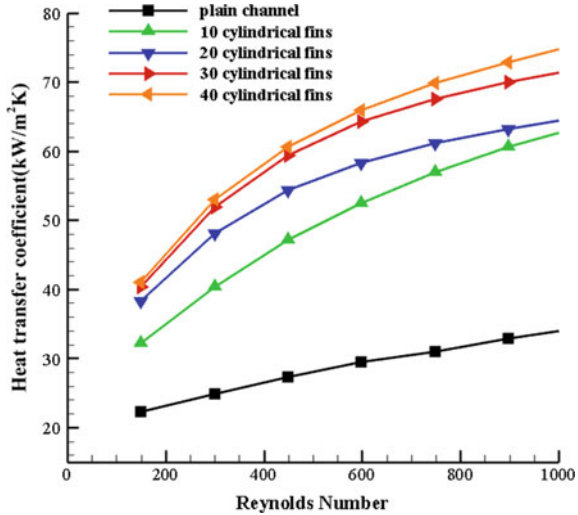


**Fig. 18.14** Variation of drag coefficient for square fins

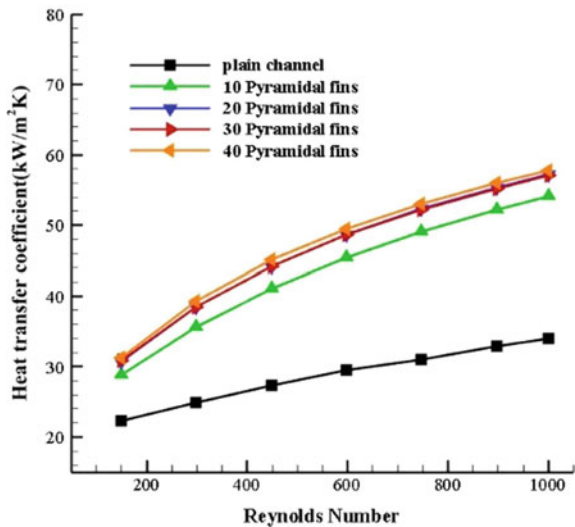


The maximum decrement of 0.775 K/w in TR occurs for cylindrical fins on a base plate from 3.981 K/w to 3.225 K/w when cylindrical fins increase from 10 to 40. The minimum decrement of 0.398 K/w in base plate temperature occurs for the pyramidal fin on a base plate of the microchannel from 4.54 to 4.14 K/w when pyramidal fin increases from 10 to 40 on the base plate of a MCHS.

**Fig. 18.15** Variation of HTC for cylindrical fins



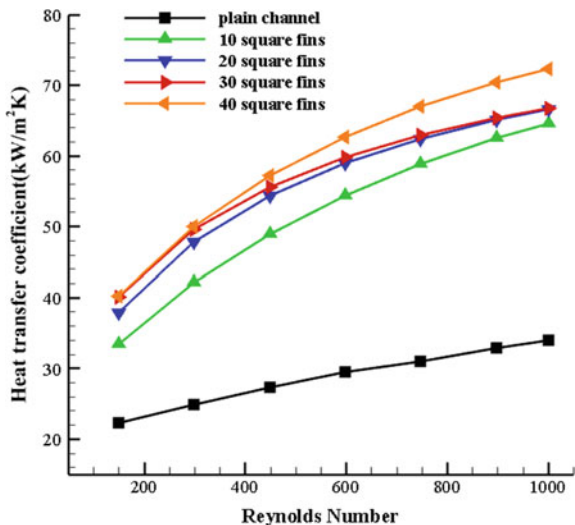
**Fig. 18.16** Variation of HTC for pyramidal fins



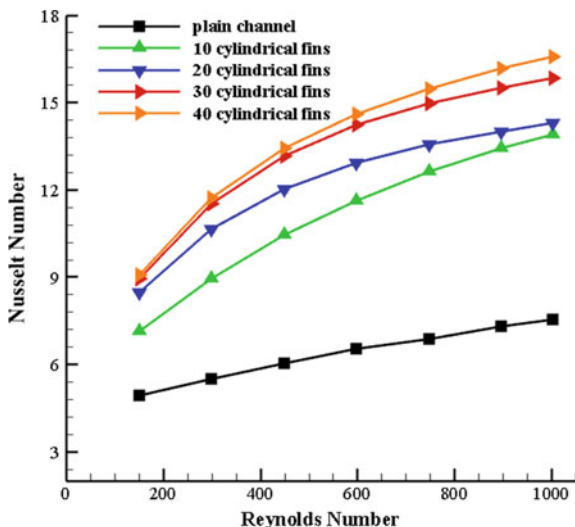
**18.7.2 Temperature Contours and Pressure Contours**

The temperature contours with Re (1000) for all configuration fins (cylindrical, pyramidal and square) of 40 numbers in the microchannel heat sink were illustrated from Figs. 18.30, 18.31, 18.32 and 18.33. The temperature distribution of a single microchannel heat sink was depicted in three parts; the top portion of Fig. 18.30 represents the first 3.33 mm. The second portion represents the middle 3.33 mm of a heat sink and the third portion represents the last 3.33 mm of the same microchannel.

**Fig. 18.17** Variation of HTC for square fins



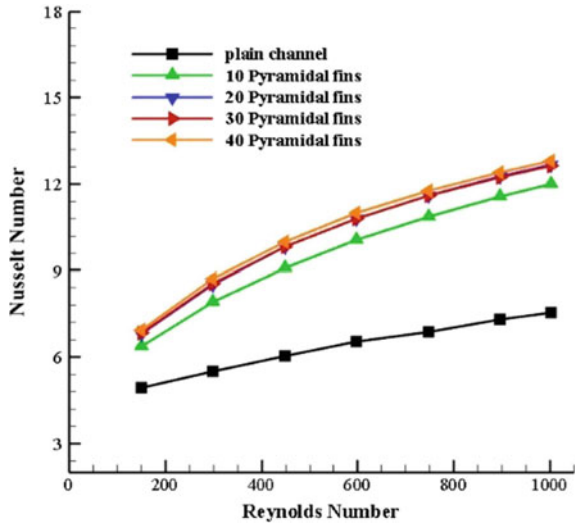
**Fig. 18.18** Variation of Nu for cylindrical fins



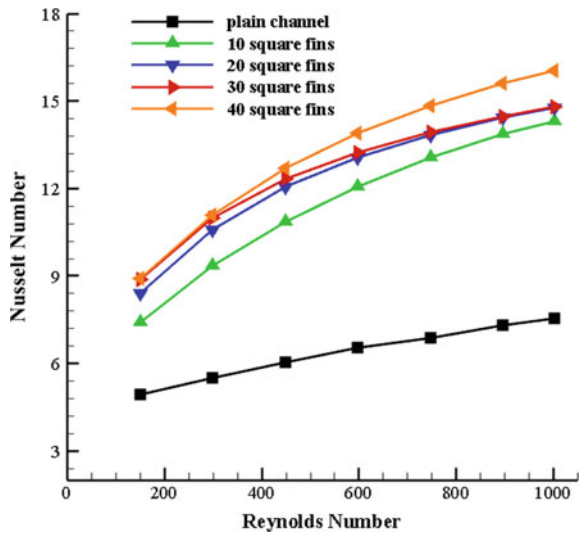
The blue region near the inlet indicates the minimum temperature of 293 K, as fluid inside the channel moves forward, fluid temperature increases and the blue region converts to green, yellow and then orange.

The contours of pressure distribution with Re (1000) for all configuration fins (cylindrical, pyramidal and square) in the microchannel heat sink were portrayed from Figs. 18.34, 18.35, 18.36 and 18.37. The orange region at the inlet section of the channel, indicating maximum fluid pressure, converts to orange, yellow, green and

**Fig. 18.19** Variation of Nu for pyramidal fins

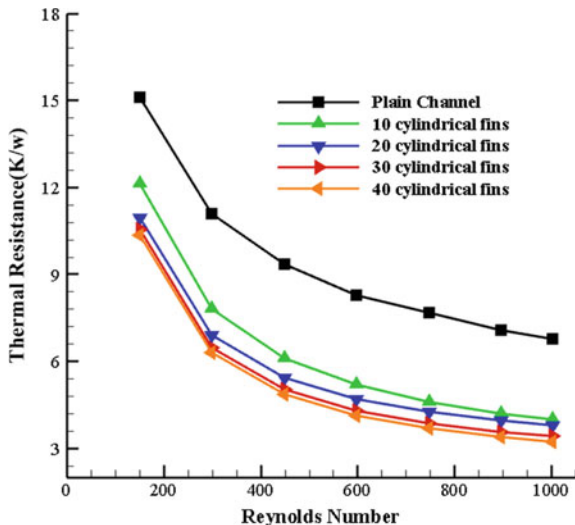


**Fig. 18.20** Variation of Nu for square fins

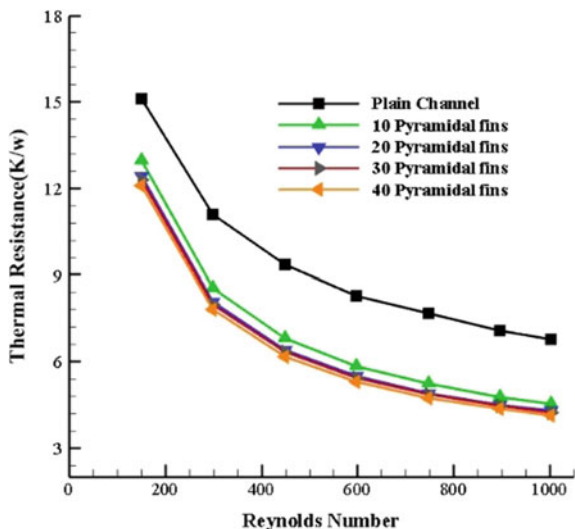


finally blue. As the fluid inside the channel moves forward, fluid pressure decreases due to friction losses inside the channel.

**Fig. 18.21** Variation of TR for cylindrical fins



**Fig. 18.22** Variation of TR for pyramidal fins

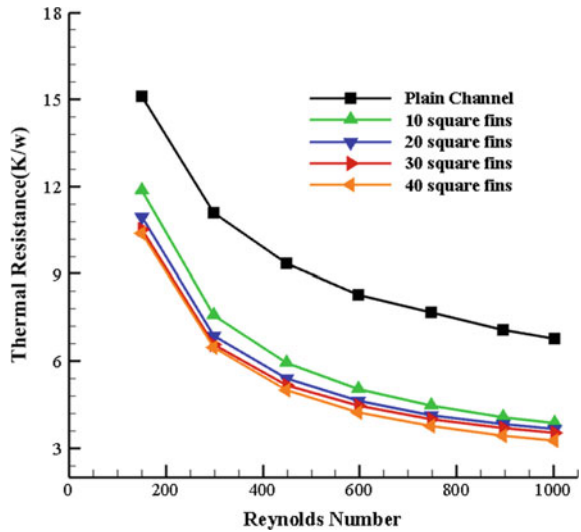


### 18.7.3 Velocity Streamline

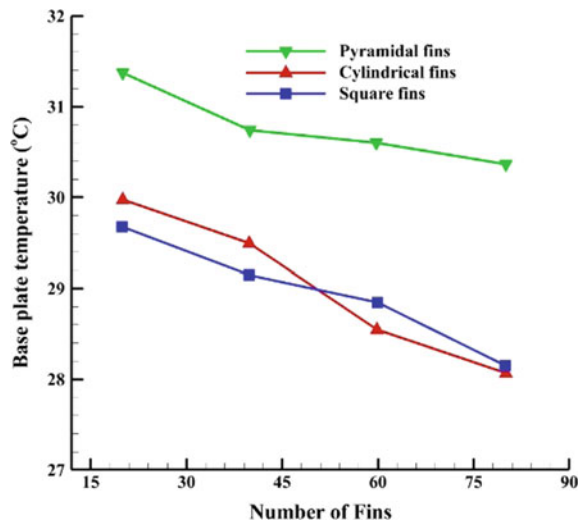
The velocity streamlines for 40 cylindrical, square and pyramidal fins on the base plate of MCHS was depicted in Fig. 18.38. A small section of 3 fins was shown for each microchannel for the clear representation of streamlines.



**Fig. 18.23** Variation of TR for square fins



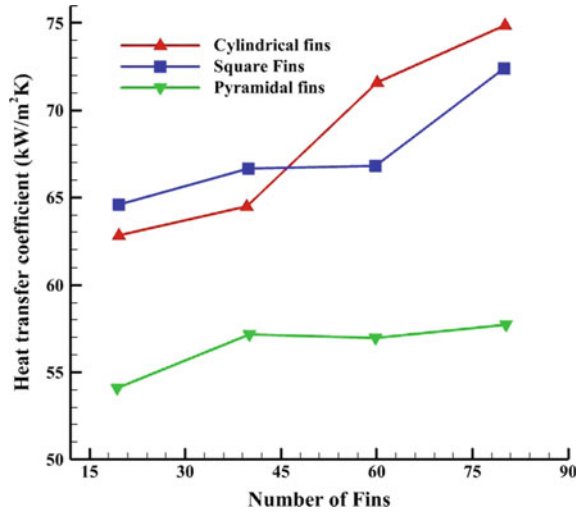
**Fig. 18.24** Variation of BPT with number of fins



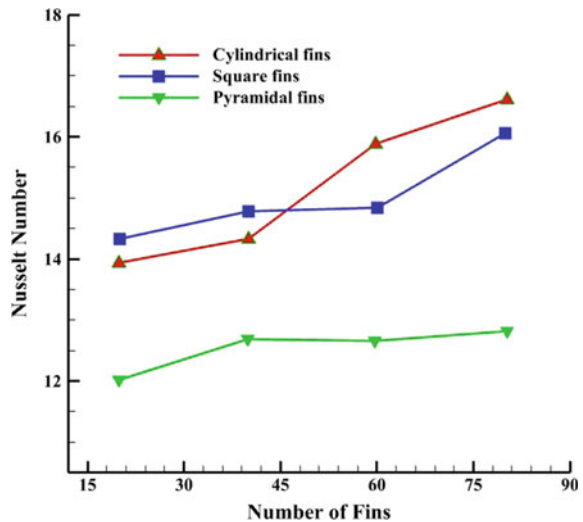
### 18.8 Conclusions

In the current research, the MCHS is modelled with different fin shapes (cylindrical, pyramidal and square fins) and configurations (10, 20, 30 and 40 fins). The variation of base plate temperature, HTC, Nu, TR,  $C_d$  and pressure drop in the MCHS with different fin shapes and configurations are studied. From the results and discussions, the following conclusions can be established:

**Fig. 18.25** Variation of HTC with number of fins

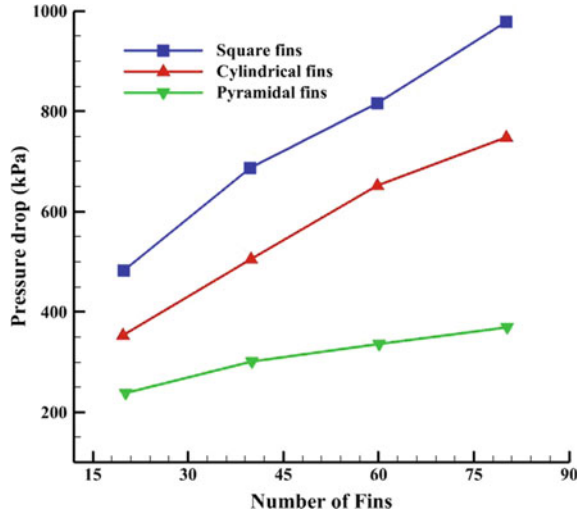


**Fig. 18.26** Variation of Nu with number of fins

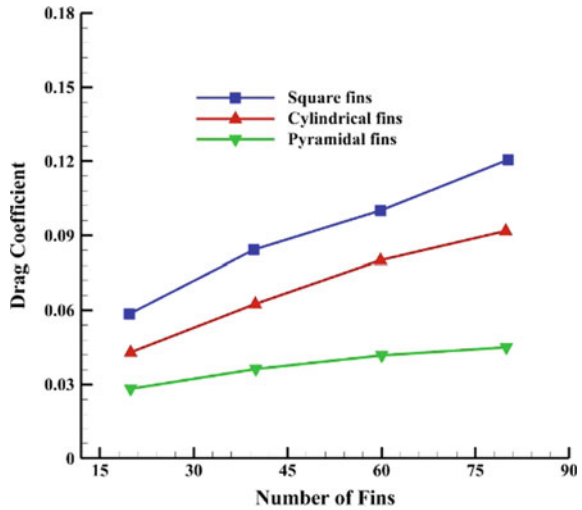


- The performance of the microchannels heat sink can be improved by constructing the fins on the base plate. Base plate temperature observed 36.96 °C in the case of a plain channel and this temperature is reduced to 28.063 °C by constructing the 40 cylindrical fins on the base plate of the microchannel heat sink.
- HTC and Nu are highest for 40 cylindrical fins on the base plate, so more heat is transferred from the base plate as the number of cylindrical fins increases from the plain channel to 40 cylindrical fins.

**Fig. 18.27** Variation of PD with number of fins



**Fig. 18.28** Variation of  $C_d$  with number of fins



- Pressure drop is minimum for pyramidal fins and maximum for square fins on the base plate; if electrical power consumption is a concern, it is better to use pyramidal fin on a microchannel base plate.
- The TR of a microchannel heat sink decreases with the construction of fins inside the microchannel heat sink. Plain MCHS shows 6.787 K/w TR with Re (1000). With same Re 40 cylindrical fins on the base plate have 3.225 K/w minimum value of thermal resistance.

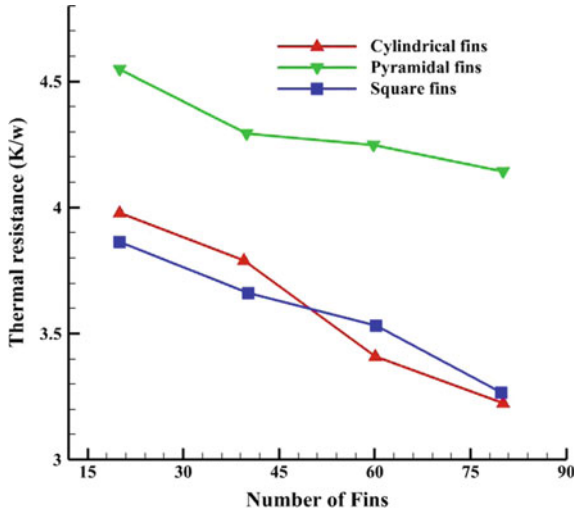


Fig. 18.29 Variation of TR with number of fins

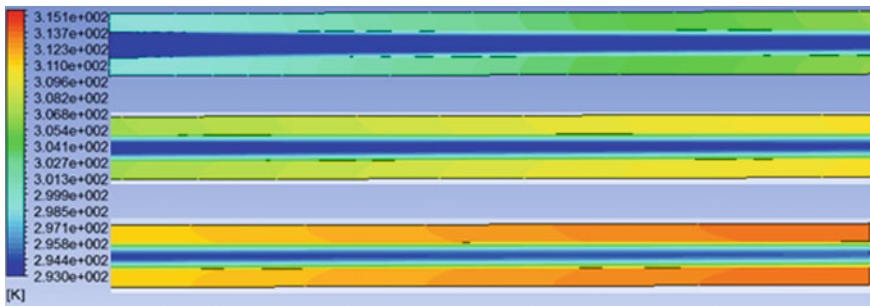


Fig. 18.30 Temperature contour for plain channel

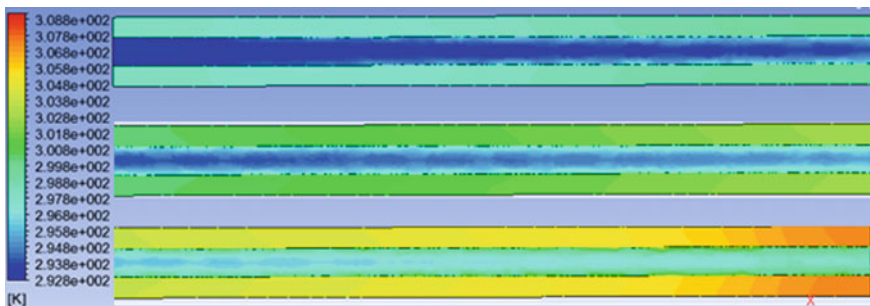


Fig. 18.31 Temperature contours of 40 cylindrical fins

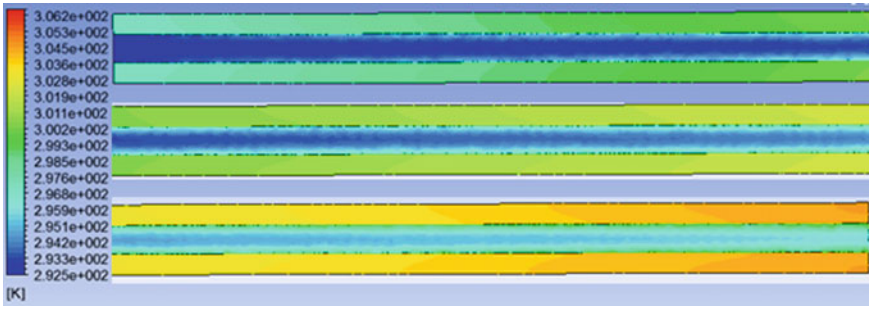


Fig. 18.32 Temperature contours of 40 pyramidal fins

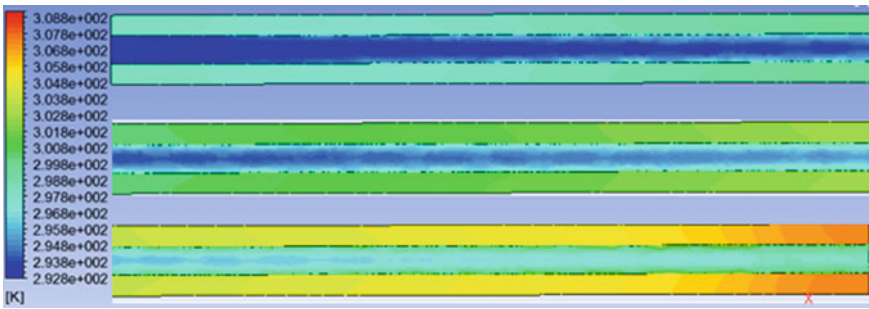


Fig. 18.33 Temperature contours of 40 square fins

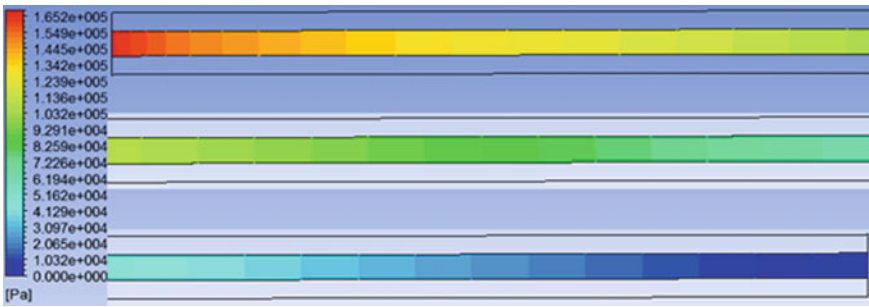


Fig. 18.34 Pressure contours of plain channel

- Suppose the number of fins has to increase, then cylindrical fin is the best option because maximum decrement of 1.890 °C in base plate temperature takes place for cylindrical and pressure drop increment is also in an acceptable limit.

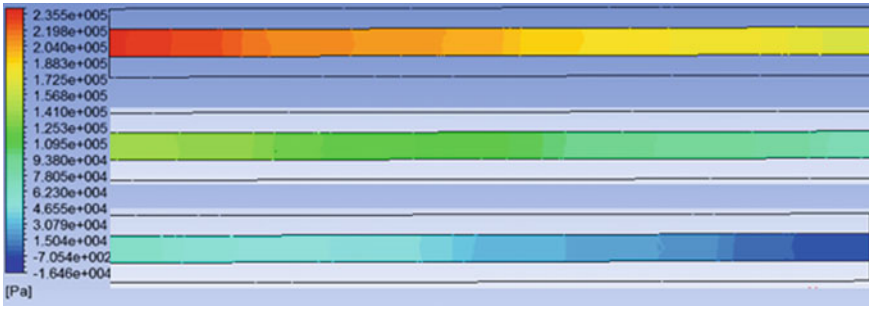


Fig. 18.35 Pressure contours of 10 cylindrical fins

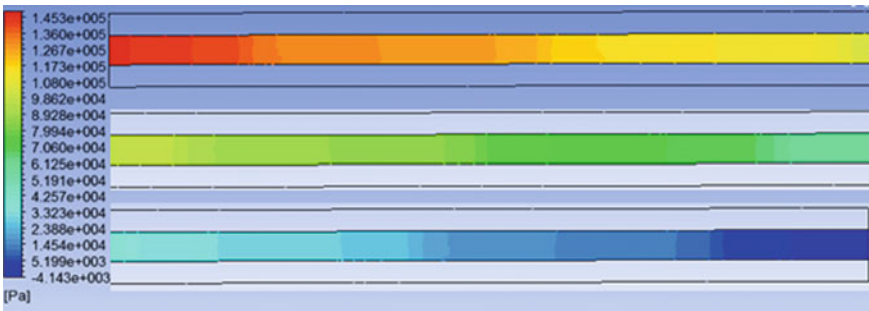


Fig. 18.36 Pressure contours of 10 square fins

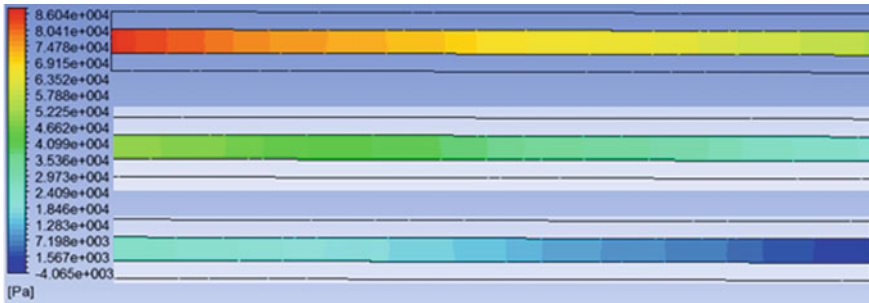
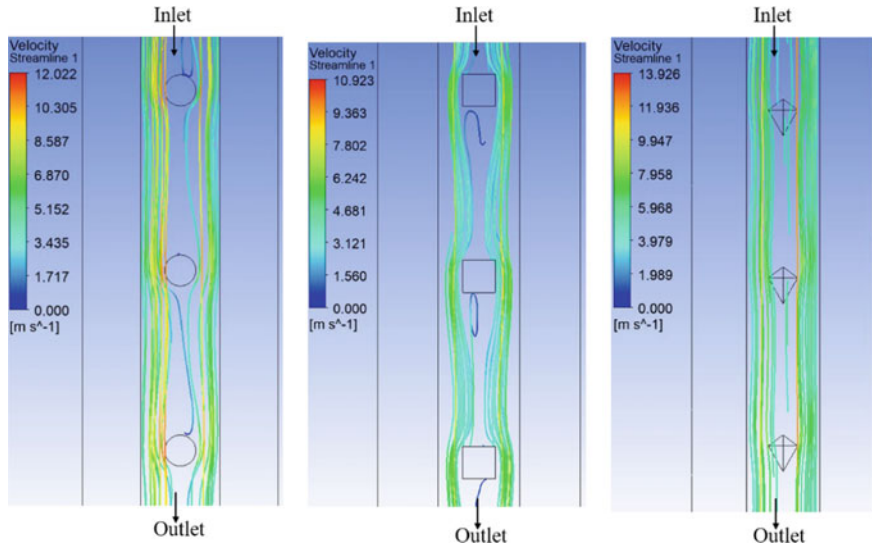


Fig. 18.37 Pressure contours of 10 pyramidal fins



**Fig. 18.38** Streamline contours for cylindrical, square and pyramidal fins

## References

- Cao Z, Xu J (2015) Modulated heat transfer tube with short conical-mesh inserts: a linking from microflow to macroflow. *Int J Heat Mass Transf* 89:291–307
- Chai L, Wang L, Bai X (2019) Thermohydraulic performance of microchannel heat sinks with triangular ribs on sidewalls—Part 2: average fluid flow and heat transfer characteristics. *Int J Heat Mass Transf* 128:634–648
- Elnaggar MH (2014) Numerical investigation of characteristics of wick structure and working fluid of U-shape heat pipe for CPU cooling. *Microelectron Reliab* 54:297–302
- Elnaggar MH, Abdullah MZ, Mujeebu MA (2011) Experimental analysis and FEM simulation of finned U-shape multi heat pipe for desktop PC cooling. *Energy Convers Manage* 52:2937–2944
- Jaworski M (2012) Thermal performance of heat spreader for electronics cooling with incorporated phase change material. *Appl Therm Eng* 35:212–219
- Kanargi B, Lee PS, Yap C (2018) A numerical and experimental investigation of heat transfer and fluid flow characteristics of an air-cooled oblique-finned heat sink. *Int J Heat Mass Transf* 116:393–416
- Khattak Z, Ali HM (2019) Air cooled heat sink geometries subjected to forced flow: a critical review. *Int J Heat Mass Transf* 130:141–161
- Liang TS, Hung YM (2010) Experimental investigation on the thermal performance and optimization of heat sink with U-shape heat pipes. *Energy Convers Manage* 51:2109–2116
- Mathew VK, Hotta TK (2018) Numerical investigation on optimal arrangement of IC chips mounted on a SMPS board cooled under mixed convection. *Therm Sci Eng Prog* 7:221–229
- Naphon P, Klangchart S, Wongwises S (2009) Numerical investigation on the heat transfer and flow in the mini-fin heat sink for CPU. *Int Commun Heat Mass Transf* 36:834–840
- Popovici CG, Hudîşteanu SV, Mateescu TD, Cherecheş N-C (2016) Efficiency improvement of photovoltaic panels by using air cooled heat sinks. *Energy Procedia* 85:425–432
- Rezania A, Rosendahl LA, Andreasen SJ (2012) Experimental investigation of thermoelectric power generation versus coolant pumping power in a microchannel heat sink. *Int Commun Heat Mass Transf* 39:1054–1058. <https://doi.org/10.1016/j.icheatmasstransfer.2012.07.010>

- So H, Pisano AP (2015) Micromachined passive phase-change cooler for thermal management of chip-level electronics. *Int J Heat Mass Transf* 58:1164–1171
- Tan SO, Demirel H (2015) Performance and cooling efficiency of thermoelectric modules on server central processing unit and Northbridge. *Comput Electr Eng* 46:46–55
- Wang J-C (2009) Superposition method to investigate the thermal performance of heat sink with embedded heat pipes. *Int Commun Heat Mass Transf* 36:686–692
- Wang J-C, Huang H-S, Chen S-L (2007) Experimental investigations of thermal resistance of a heat sink with horizontal embedded heat pipes. *Int Commun Heat Mass Transf* 34:958–970
- Xu JL, Gan YH, Zhang DC, Li XH (2005) Microscale heat transfer enhancement using thermal boundary layer redeveloping concept. *Int J Heat Mass Transf* 48:1662–1674
- Xu J, Song Y, Zhang W, Zhang H, Gan Y (2008) Numerical simulations of interrupted and conventional microchannel heat sinks. *Int J Heat Mass Transf* 51:5906–5917
- Yousefi T, Mousavi SA, Farahbakhsh B, Saghir MZ (2013) Experimental investigation on the performance of CPU coolers: effect of heat pipe inclination angle and the use of nanofluids. *Microelectron Reliab* 53:1954–1961
- Yu Y, Simon T, Cui T (2013) A parametric study of heat transfer in an air-cooled heat sink enhanced by actuated plates. *Int J Heat Mass Transf* 56:792–801



# Chapter 19

## Review on Characteristic Features of Jet Impingement that Favours Its Application in Solar Air Heaters



M. Harikrishnan, R. Ajith Kumar, and Rajesh Baby

### Nomenclature

$A$	Surface area of the absorber plate ( $\text{m}^2$ )
$d$	Hydraulic diameter of the jet (m)
$h$	Vertical distance between the plate and jet (m)
$h_c$	Convective heat transfer coefficient ( $\text{W}/\text{m}^2\text{K}$ )
$I$	Irradiation ( $\text{W}/\text{m}^2$ )
$m$	Mass flow rate (kg/s)
PP	Pumping power (W)
$Q_{\text{conv}}$	Rate of convection heat transfer (W)
QU	Useful heat gain (W)
$r$	Radial distance along the surface of plate (m)
$t_s$	Surface temperature of plate ( $^{\circ}\text{C}$ )
$t_a$	Temperature of fluid (air) ( $^{\circ}\text{C}$ )
$T_i$	Inlet temperature ( $^{\circ}\text{C}$ )
$T_o$	Outlet temperature ( $^{\circ}\text{C}$ )
$x$	Stream wise pitch between adjacent jet (m)
$y$	Span wise pitch between adjacent jet (m)
SAH	Solar air heater
Re	Reynolds number
Nu	Nusselt number
$\eta_t$	Thermal efficiency
AR	Aspect ratio

---

R. Baby (✉)

Department of Mechanical Engineering, St. Joseph's College of Engineering and Technology,  
Choondacherry P.O., Palai, Kottayam, Kerala 686579, India  
e-mail: [rajeshbaby@sjcetpalai.ac.in](mailto:rajeshbaby@sjcetpalai.ac.in)

M. Harikrishnan · R. Ajith Kumar

Department of Mechanical Engineering, Amrita Vishwa Vidyapeetham, Amritapuri, India

$\eta_{th}$	Thermohydraulic efficiency
TES	Thermal energy storage
SAHWJ	Solar air heat with jet impingement

## 19.1 Introduction

Over the last few years, there has been notable increase in our daily energy consumption due to the advances in the standard of living. Thermal engineers are always looking for better methods for meeting this unpredictable increase in energy consumption. As demand for energy continue to increase, the human mind must look into permanent type of energy sources (renewable energy sources). Amongst the renewable energy sources, the most important enduring and inexhaustible source of energy is the solar energy. Solar energy comes from the sun by a process called nuclear fusion. The energy of sun (solar energy) reaches the earth's surface by thermal radiation. Solar energy can be utilized by two common methods called direct method and indirect method. Some of the applications which comes under direct utilization of solar energy are solar cooker, solar heat collectors, solar photo-voltaic conversion, and so on.

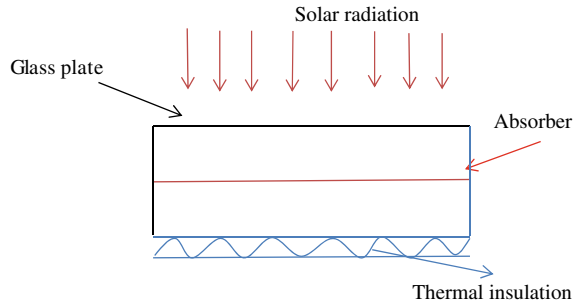
Amongst the solar heat collectors, solar air heaters hold a significant position, especially for low and medium temperature applications. Some of the applications of solar air heaters are comfort space heating, curing of plastics, regeneration of dehumidifying agents, dehydration of agricultural products, and so on. The unique feature of solar air heater is its simple design. In solar air heater, air is used as working fluid which reduces the number of units needed in the system. Moreover, the common problems encountered in mechanical systems like corrosion, leakage, etc., are also eliminated in solar air heaters.

## 19.2 Working of Solar Air Heaters

Solar air heater consists of metal frame, transparent glass cover, absorber plate (flat plate), a blower for supplying air and finally proper insulation for reducing thermal losses. The schematic representation of a simple solar air heater is shown in the Fig. 19.1.

In most of the practical situations, the air flows below the surface of the absorber plate. If the air flows over the upper surface, there will be considerable thermal losses due to convection from the cover plate. The main drawback of solar air heaters is its poor thermal performance due to lower value of convective heat transfer coefficient between the absorber plate and the flowing air. Since the main modes of heat transfer by which the air gets heated in solar air heater is by forced convection which is governed Newton's law of cooling. In consonance with Newton's law of cooling, the

**Fig. 19.1** Schematic representation of solar air heaters



rate of heat convected mainly depends upon the surface area, heat transfer coefficient, and the temperature difference.

$$Q_{\text{conv}} = h_c A (t_s - t_a) \quad (19.1)$$

One of the main reasons for lower value of heat transfer coefficient is the existence of laminar sublayer, which has to be ruptured for achieving maximum heat transfer. Since the rate of heat transfer in solar air heater mainly depends upon the surface area and value of heat transfer coefficient, several researchers have studied different methods for improving the above parameters. A better way of getting higher thermal performance in solar air heater is to generate more turbulence by introducing the jet impingement. If an extra turbulence into the flow field can be introduced, the rate of heat transfer increases because the turbulence will help to break the small viscous sublayer, and as a result, the convective heat transfer coefficient increases and this will lead to improvement in thermal performance.

The current study is thus focussed to examine the advancement in thermal performance of the solar air heater by introducing jet impingement. To attain the desired objective, the effect of various parameters that will influence the heat transfer characteristics of impinging jet has been elaborated. Secondly, the advancement of thermal performance in SAH with impinging jets has been reviewed.

### 19.3 Jet Impingement

Jet impingement cooling technology means cooling a heated surface with the help of an impinging jet. Impinging jet is a high-velocity jet which is ejected out through a hole or slot. The impinging jet hits the target to be heated or cooled, which brings out a rise in heat transfer rate between the target and the fluid. Higher heat transfer takes place due to striking of high-velocity fluid molecules on to the surface. Jet impingement is commonly used for cooling of gas turbine blades, drying of surface, paper materials, etc. Recently, a large number of analyzes are being made to examine

the feasibility of using jet impingement in electronics cooling. The characteristic features of jet impingement that attracts many industries are.

1. Intensive heat transfer rate between the surface and the fluid.
2. It provides an effective means for removing localized heat loads.

The heat transfer rate in jet impingement is a multiplex function of many variables like.

- Nozzle geometry
- Jet to target spacing
- Reynold's number
- Angle of impingement
- Type of confinement
- Type of working fluid.

If the application demands localized heating or cooling, the ideal choice is single jet impingement. When the entire surface needs to be heated or cooled, multiple slot jet impingement can be used. Several researchers have performed numerical and experimental studies on multi-jet impingement on the surface. They found that the flow through a multiple slot jet is rather complex and apart from the above mentioned design parameters, the heat transfer rate through a multi-slot jet impingement mainly depends upon.

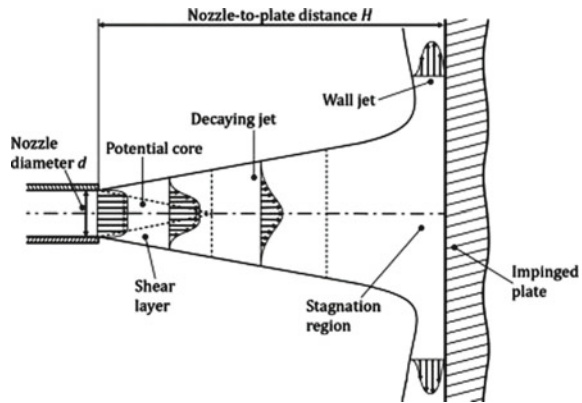
- Arrangement of jet slots
- Number of jets in span wise and stream wise directions
- Spacing between the jets.

### ***19.3.1 Various Flow Regions Associated with Impinging Jet***

The entire flow domain of the impinging jet is divided into three distinct regions (Carlomagno and Ianiro 2014), namely free jet region, stagnation region, and the wall jet region. Depending upon the shape of the nozzle and upstream Reynolds's number, the jet comes out from the nozzle with a particular temperature and velocity profile along with certain turbulent characteristics. The region very near to the outlet of the orifice is the free jet region. The main feature of this region is the existence of potential core. The existence of potential core implies that the velocity is exactly equal to the exit jet velocity from the nozzle. Due to momentum transfer between jet and the surrounding fluid, the thickness of the shear layer gradually increases with advancement in distance between jet and plate. It is evident from the figure that Fig. 19.2 in the free jet region, the interior part of the flow remains unaffected in the beginning even though the shear layer widens.

The region near to the plate is the stagnation region. In that region, the jet impinges normally on the surface. Once the jet impinges normally on the surface, there will be a reduction in the velocity components in axial direction. The reduction in axial velocity components gets converted into an increase in acceleration in horizontal

**Fig. 19.2** Various regions of impinging jets (Carlomagno and Ianiro 2014)



region. Finally, this increase in acceleration in horizontal direction forces the jet to flow radially along the plate. The jet flows parallel to the impinged surface, and that particular flow region is known as wall jet region. It may be noted that in the wall jet region, boundary layer begins to develop. One of the most important advantages of cooling a surface with impingement jet rather than the conventional parallel flow cooling is that the thickness of boundary layer formed in the wall jet region is relatively very thin. If the thickness of the velocity and thermal boundary is very small, it will bring out higher heat transfer rate. When the fluid flows radially over the surface, it entrains the surrounding fluid as a result, the thickness of the boundary layer grows as shown in Fig. 19.2. The transformation from laminar to turbulent boundary layer after certain distance when the flow attains the required velocity.

### **19.3.2 Impact of Design Variables on Heat Transfer Characteristics of Single Impinging Jet**

One of the main design parameters that has an important effect on the net heat transfer rate from the impinging plate to the air is the shape of the nozzle. Several researchers paid their attention for finding the optimum shape and dimensions of the nozzle for effective heat transfer for different applications that uses jet impingement. All the previous studies about single jet impingement concluded that in order to find optimum heat transfer, along with shape of the nozzle, the distance between the nozzle and the target also plays a significant role. Jet to target spacing is another important design parameter that has an important effect on impinging air heat transfer rate. If the distance between the target and jet is very low, we will not get optimum cooling in case of cooling applications. The main reason for this is that the jet after impingement absorbs heat from the surface due to collision between the molecules and the surface and becomes warmer. The warmer air is lighter, and it starts moving upwards due to buoyancy effects. At the same time, the incoming fresh air forces

this warmer air to flow over the target. So we will not get optimum cooling if the  $h/d$  ratio is low.

Similarly, if the distance between the jet and the target is very high, again, we will not get optimum cooling. If  $h/d$  ratio is very large, momentum exchange between the jet and the surrounding fluid increases, and complete degradation of potential core will result. We know that when we increase the Reynolds number, the value of both local and the average Nusselt number increases. From the previous studies, it was found that there is a secondary peak in Nusselt number distribution after a certain radial distance. The occurrence of secondary peaks is mainly due to the interference with the surrounding jets. It was found that secondary peaks occur at higher Reynolds number, and we cannot find a secondary peak at lower Reynolds number.

An experimental investigation to understand influence of the orifice geometry on local heat transfer distribution between flat plate and impinging air jet was studied by Gulati et al. (2009). Circular, rectangular, and square shaped nozzle of equivalent diameter 20 mm were examined. It was found that the rate of heat transfer at the stagnation point achieved for square and circular jets was almost same but it is higher in case of rectangular jet by almost 10%. The main reason for this increase in the value of heat transfer for rectangular jet is mainly due to higher turbulent intensities at the downstream side of the nozzle which is carried to the stagnation region. But the interesting thing we have to note is that the average Nusselt number for a particular upstream condition of the nozzle (Reynolds's number) and at a particular nozzle to target spacing has the same results for all the cross sections. They also found out that from Nusselt number distribution contours at low  $h/d$ , the contour retains the geometry of the nozzle, and at higher  $h/d$ , the contours tend to be axisymmetric.

Lee and Lee (2000) studied the heat transfer features of elliptic and circular jet and have found that stagnation Nusselt number value of impinging elliptic jet is higher than that of circular jet. Koseoglu and Baskaya (2010) investigated experimentally the importance of jet inlet geometry and aspect ratio for square, rectangular, circular, and elliptical. It was found that higher heat transfer rate at stagnation point is observed for elliptic jet and rectangular jet with higher aspect ratio than circular jet. The main reason for this behaviour is the strong mixing and large momentum exchange with the surrounding fluid of elliptic jet and rectangular jet compared to circular jet. It was concluded that jet with higher aspect ratio is an ideal choice for localized heating or cooling. The main corollary obtained from the investigation is that if the spacing between the jet and the plate is more, we get similar heat transfer characteristics along major and minor axis in all cases. From the local heat transfer distribution along the surface, it was found that there is a secondary peak in Nusselt number distribution after a certain radial distance. If the jet is circular, the secondary peaks are found at  $r/d = 1.9$  and for circular and rectangular nozzle, it occurs at 2.2.

Chaudhari et al. (2010) experimentally studied the influence of shape of the nozzle in synthetic jet impingement cooling. The main advantage of synthetic jet is the entrainment of surrounding fluid into the jet is more as compared to the conventional jet due to its pulsating nature. It was noticed that for space constrained application, rectangular shaped nozzle with large hydraulic diameter and smaller aspect ratio is the ideal choice when compared with circular and square shaped nozzle.

### 19.3.3 Impact of Design Variables on Heat Transfer Characteristics of Multi-impinging Jet

As mentioned earlier when the application demands localized heating or cooling, the ideal choice is single jet impingement. When the entire surface needs to be heated or cooled, multiple slot jet impingement is preferred. Culun et al. (2018) conducted a numerical study on multi-jet impingement and found a higher heat transfer rate for multi-square jet when compared with multi-circular jet. They also found out that if the jet-to-jet spacing ( $x/d$ ) is very small, the jet behaves like a single jet, and the average Nusselt number value is found to be highest for configuration one exit confined jet. The influence of arrangement style was also investigated numerically and found that the arrangement style does not have any influence in the value of average Nusselt number.

Caliskan et al. (2014) examined experimentally and numerically the influence of elliptic and rectangular multi-jet impingement. They found out that elliptic jets give higher heat transfer performance than rectangular jets when  $h/d = 2$  and Reynolds number 10,000. From their numerical results, the presence of an interesting flow feature called upwash flow was identified. Upwash flow is generated due to the collision of two adjacent wall jets. The jet issuing from the nozzle is entrained by this upwash flow. The vector velocity distributions for elliptic jet showing the entrainment effect of upwash flow are shown in Fig. 19.3.

So it is clear that in order to avoid severe interference with neighbouring jets in case of multi-jet applications, we need to find optimum jet-to-jet spacing. Severe jet interference would lead to complete degradation of potential core and stagnation effect completely diminishes.

Yong et al. (2015) studied the influence of jet-to-jet target spacing in both stream wise and span wise direction for two multi-jet arrangements (inline and zigzag). They have found an optimized value for both stream wise and span wise jet-to-jet target spacing not only on the basis of same jet Reynolds number but also in accordance with mass flow rate of coolant per unit area of the cooled surface. The investigation

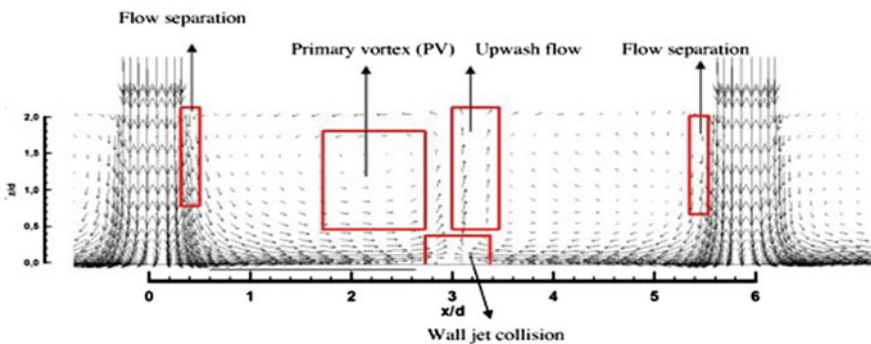


Fig. 19.3 Velocity vector distributions for elliptic jet with aspect ratio 0.5 (Caliskan et al. 2014)

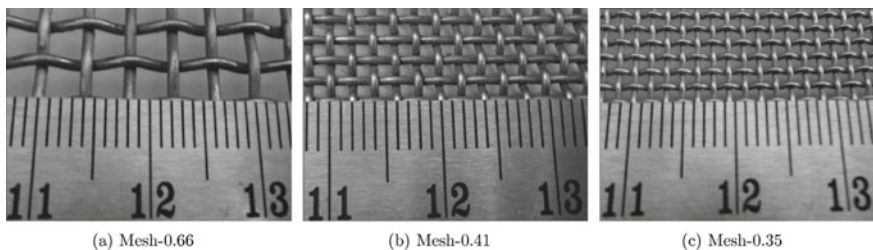
also showed that zigzag arrangement performance appears to be better than that of inline arrangement for this particular study. They also introduced a term called uniformity coefficient for finding the consistency of heat transfer of multiple jets.

Muvvala et al. (2016) numerically studied a comparison between single and multiple jet thermal behaviour over an electronic component. They observed a similar thermal behaviour beyond  $h/d = 15$  at all Reynolds number. At lower  $h/d$ , better thermal performance is observed for multi-jet. They have also made an investigation of jet arrangement on the basis of fixed mass flow rate and concluded that the thermal behaviour is inversely proportional to the number of jets.

Zhou and Lee (2004) conducted studies related to the advantages of generating turbulence with the installation of wire meshes. It was observed that at low- $h/d$  ratio, the value of average Nusselt number was increased to about 1.8% when compared with cases of jet without wire meshes. Hee Lee et al. (2001) introduced perforated plate between jet and target plate and studied the heat transfer characteristics experimentally. They have found that better thermal enhancement by the introduction perforated plate in the flow domain and also found out that the higher value of heat transfer rate is observed in case of square hole on perforated plate when compared with circular hole.

Muvvala et al. (2017a) experimentally studied the effect of perforation which means that in the same jet area, more number of square jets (4 and 9 jets) are introduced. They observed complete degradation of potential core and an increase in the value of turbulence intensities for all perforated nozzle. Investigation on the basis of fixed mass flow rate concluded that the thermal performance of perforated nozzles is better when compared with single nozzle but it requires more additional pumping power. Muvvala et al. (2017b) performed an experimental study to evaluate the performance of square orifice by introducing wire mesh at the nozzle outlet. The photographic view of three meshes investigated is shown in the Fig. 19.4.

They found out that by introducing wire meshes at the nozzle exit, the intensity of turbulence increases; at the same time, better heat transfer behaviour was observed at lower  $h/d$  value. Investigation on the basis of fixed mass flow rate concluded that the thermal performance of nozzles with wire meshes is better when compared with single nozzle but it requires more additional pumping power.



**Fig. 19.4** Photographs of three wire meshes used (Muvvala et al. 2017b)



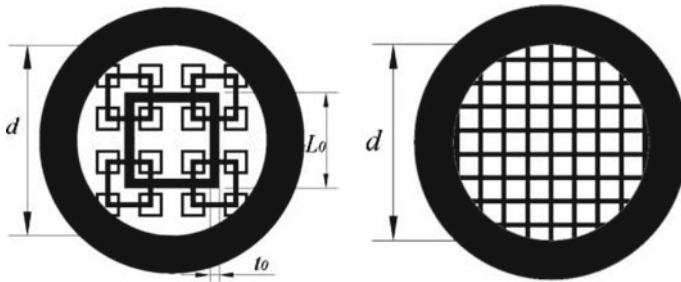


Fig. 19.5 Square fractal grid and regular grid (Cafiero et al. 2014)

Cafiero et al. (2014) studied the influence of using square fractal grids in increasing the upstream turbulence of impinging jets. The schematic representation of square fractal grid and regular grid investigated is shown in Fig. 19.5. The results showed an increase in stagnation Nusselt number, but at the same time, it decreases the uniformity of Nusselt number distribution.

Cafiero et al. (2017) studied experimentally using IR thermography the influence of shape of the grid on the thermal performance of impinging jets. The results obtained showed that the fractal square grid has better local heat transfer coefficient compared to square grid but when it comes to the uniformity of heat transfer rate square grid performs better. It also showed that at large  $h/d$  ratio, similar results are obtained for both square grid and circular fractal grid. It can be concluded that for application that requires localized heating or cooling with limitation of space like electronic cooling, square fractal grid is the better option comparing to square grid and circular fractal grid. The summary of literature review on jet impingement is detailed in Table 19.1 for quick reference.

## 19.4 Techniques Used to Improve the Low-Thermal Performance of Solar Air Heaters

Flat plate solar air heater is the cheapest and the easiest one which is very easy to operate amongst all the other types of solar collector. It was observed that lower value of convective heat transfer coefficient between the absorber plate and the air, low-thermal conductivity of air and high-thermal loss to the environment are the some of the disadvantages that limits the applications of solar air heaters. Some of the techniques that were suggested to conquer the demerits of solar air heater are

- Increase the surface area
- Creating more turbulence in the fluid flow
- Amplify the travelling duration of air
- Using high-thermal conductivity material
- Reducing the thermal losses by adding adequate insulation.

**Table 19.1** Summary of literature review on jet impingement

Authors	Type of work	Parameters	Findings
Gulati et al. (2009)	Experimental investigation	$d$ 20 mm Re 5000–15,000 $h/d$ 0.5–1.2 Shape of nozzle: square, circular, rectangular Type of jet: single jet	Rectangular jets show superior performance than other geometry in terms of local heat transfer rate
Lee and Lee (2000)	Experimental investigation	$d$ 25 mm Re 10,000 $h/d$ 2–4 Shape of nozzle elliptic AR 1, 1.5, 2, 3, 4 Type of jet: single jet	Elliptic jets with higher AR show superior performance than circular in terms of local heat transfer rate at low- $h/d$ value
Koseoglu and Baskaya (2010)	Experimental investigation	$m$ $1455.2 \times 10^{-6}$ kg/s $h/d$ 2,6,12 Type of jet: single jet	Increased heat transfer rate at stagnation point is observed for elliptic jet and rectangular jet with higher aspect ratio than circular jet
Chaudhari et al. (2010)	Experimental investigation	$d$ 3.8–8 mm Re 950–4000 $h/d$ 1–25 Type of jet: synthetic jet	For space constrained application, rectangular shaped nozzle is the ideal choice when compared to circular and square with respect to effective heat transfer
Culun et al. (2018)	Experimental investigation	$d$ 2 mm Re 15,000 $h/d$ 2, 3, 4 $x/d$ 2, 3, 4 $y/d$ 2, 3, 4 Shape of nozzle: square, circular Type of jet: multi-jet Arrangement: inline, staggered	Elliptic jet performs better than circular jet One exit confined jet shows efficient heat transfer Strong jet interference occurs when $x/d < 2$ Arrangement style does not have much effect in heat transfer
Yong et al. (2015)	Experimental investigation	Re 5000–25,000 $h/d$ 2–4 $x/d$ 2, 3, 4, 5 $y/d$ 2, 3, 4, 5 AR 0.5, 1, 2 Shape of nozzle: circular Type of jet: multi-jet Arrangement: inline, staggered	Evaluation on the basis of same jet Reynolds number optimum $x/d, y/d$ is 3 Evaluation on the basis of same mass flow rate optimum $x/d, y/d$ is 5 Staggered arrangement showed better performance than inline arrangement

(continued)

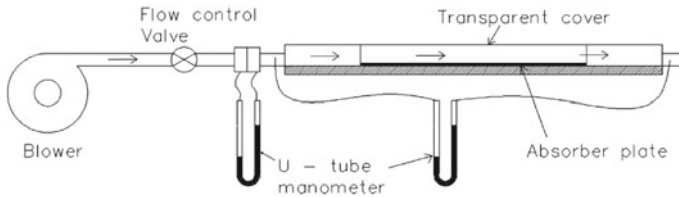
**Table 19.1** (continued)

Authors	Type of work	Parameters	Findings
Lee et al. (2001)	Experimental investigation	Re 23,000 $d$ 4–12 mm $h/d$ 1–3 Type of jet: multi-jet	Superior value of heat transfer rate is observed in case of square hole on perforated plate when compared with circular hole
Muvvala et al. (2017a)	Experimental investigation	$A = 4.6 \text{ mm} \times 4.6 \text{ mm}$ $h/d$ 2–9	Heat transfer rate of perforated nozzles is improved by 63% better when compared with single nozzle but it requires more additional pumping power
Muvvala et al. (2017b)	Experimental investigation	Porosity value 0.35, 0.41, 0.66 $h/d$ 2–9 $m = 2 \times 10^{-3} \text{ kg/s}$	The value of Nusselt number of nozzles with wire meshes is enhanced by 23% when compared with single nozzle but it requires more additional pumping power
Cafiero et al. (2014)	Experimental investigation	Re 16,000–30,100 $h/d$ 1–4	Use of fractal grid showed an increase in stagnation Nusselt number, but at the same time, it decreases the uniformity of Nusselt number distribution
Cafiero et al. (2017)	Experimental investigation	Re 15,000–18,800 $h/d$ 2–7	Square fractal grid is the better option comparing to square grid and circular fractal grid for space constrained application

It was observed that any modification in air flow channel would help in increasing the thermal performance of solar system, but at the same time, it would add additional running costs. Nowadays, it becomes a challenge for thermal engineers working in solar system to develop a system that should be thermally and economically efficient. Since solar air heater requires an external agent (blower) to enforce the air through the system and the power requirement depends upon the pressure drop as well as the frictional losses due to the motion of air over the surface. These parameters need to be examined for accessing the fulfilment of solar air heater for the required application. The thermal performance of solar air heater can be evaluated based on thermal efficiency and thermohydraulic efficiency (Hegazy 2000).

Thermal efficiency of solar air heater

$$\eta_t = \frac{QU}{IA} \tag{19.2}$$



**Fig. 19.6** Conventional solar air heater (Rajaseenivasan et al. 2015)

### Thermohydraulic efficiency of solar air heater

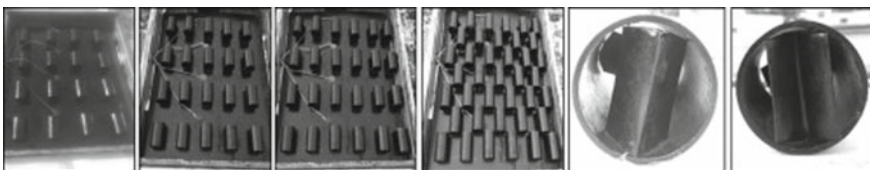
$$\eta_{th} = \frac{QU - PP}{IA} \quad (19.3)$$

The pumping power can be evaluated by finding the pressure drop across the length of the SAH with the help of suitable pressure measuring devices (Fig. 19.6).

Rajaseenivasan et al. (2015) compared experimentally the output of SAH having absorber plate fitted with circular and V-type turbulator with that of a conventional type solar air heater. The results illustrate that the addition of turbulator increases the pumping power of the system. Subsequently, the efficiency of the system decreases by 1–5% depending upon the arrangements of turbulators. The maximum outlet temperature of air that can be obtained by the addition of turbulator is 66 °C. The photographic view of circular and V-type turbulators used in the modified SAH is shown in Fig. 19.7.

Akpinar and Koçyiğit (2010) studied experimentally the performance of placing different obstacles in the absorber plate. Three obstacles were studied, namely triangular shaped obstacle, leaf shaped obstacle, and rectangular shaped obstacle. The result has shown that absorber plate with leaf type obstacle performs better when compared with other types. The advancement in thermal gain has totalled mainly from greater absorption of thermal radiation and heat transfer between air and absorber surface of leaf type obstacles. The addition of obstacles improves the air movement above the absorber, thereby creating turbulence in the flow field.

Akpinar and Koçyiğit (2010) also conducted energy and exergy analysis of the previous work, and obtained result also shows that the first and second law efficiencies of SAH with leaf type obstacles were higher when compared with other types. Al-Kayiem and Yassen (2015) studied a natural convection solar air heater at various



**Fig. 19.7** Circular and V-type turbulators (Rajaseenivasan et al. 2015)

angle of inclination  $30^\circ$ ,  $50^\circ$  and  $70^\circ$ , and the optimum performance obtained was at  $50^\circ$ . The result of work would help to solve the issue in predicting the free convection in thermal passages.

Lakshmi et al. (2016) examined the performance of trapezoidal corrugated solar air heater with sensible heat storage. Gravels were used as sensible storage material. They have found out both energy and exergy efficiency, and the result concluded that the value of exergy efficiency was very less when compared with energy efficiency. The reason for the lower value of exergy efficiency was due to the exergy losses from various parts of the collector. The exit air temperature of trapezoidal collector was higher when compared with flat plate collector. The value of thermal efficiency obtained in case of flat plate collector and trapezoidal plate collector was 15.8 and 21.5%.

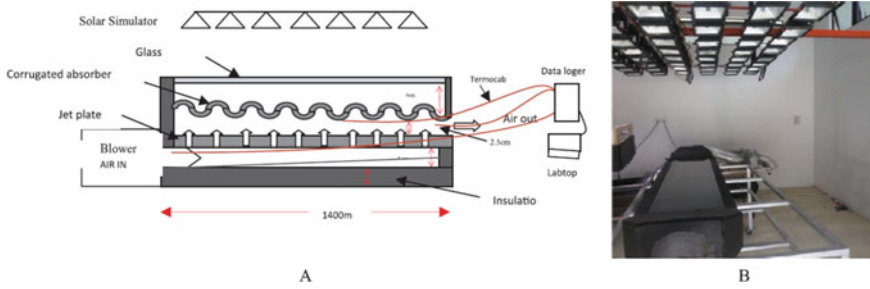
Bahrehand and Ameri (2015) conducted thermodynamic analysis of SAH with two glass cover plate and with two different type of fins (triangular and rectangular). It was found that by introducing two glass cover plate, we can reduce the heat losses and as a result considerable increase in thermal efficiency would result. They also found out that we can improve the thermal performance of SAH by using triangular fins rather than rectangular fins.

## 19.5 Solar Air Heat with Jet Impingement (SAHWJ)

Nowadays, jet impingement finds significant position in many engineering and industrial applications. The thinner boundary layer formation in jet impingement as compared to the conventional parallel flow, increased turbulence level, etc., is some of the unique features that attracts many industries like electronics, manufacturing, aerospace, etc. The application of jet impingement in solar air heater is not novel concept. Several researchers have studied the enhancement in thermal performance of SAH by implementing jet impingement. Breaking of laminar sublayer formed above the absorber plate by jet impingement and increased turbulence intensity associated with jet impingement attracts many researchers working in solar systems.

Rajaseenivasan et al. (2017) conducted an experimental study on impinging jet solar air heater. They have studied various parameters like angle of impingement, nozzle geometry, and mass flow rate. They have found that system showed better performance at  $30^\circ$  angle of attack, 5 mm diameter nozzle, and 0.016 kg/s mass flow rate. The superior thermal efficiency obtained was 55.8% at maximum mass flow rate. They have also found that absence of impingement was the reason for lower performance at  $90^\circ$  angle of attack.

Aboghrara et al. (2017) examined experimentally the outcome of a corrugated absorber plate SAH with jet impingement and compared the result with that of a flat plate. The performance was compared on the basis of thermal efficiency and found out an advancement in thermal efficiency of the corrugated absorber plate SAH with jet impingement. The schematic diagram and photographs of the experimental setup were shown in the Fig. 19.8. The advancement in mass flow rate by keeping the



**Fig. 19.8** Schematic representation of corrugated plate solar air B photographs of experimental setup (Aboghrara et al. 2017)

diameter constant increased the thermal efficiency. Comparison results concluded that the thermal efficiency of the system increases by 14%.

Soni and Singh (2017) studied experimentally SAHWJ by employing an inline jet plate. The schematic diagram of the experimental setup is shown in Fig. 19.9. They examined the performance mainly by collector efficiency and  $Nu$ . They have examined the influence of geometric parameters like jet diameter, hydraulic diameter of the channel and mass flow rate. They have found out that collector efficiency increases at all geometric configuration with an increase in mass flow rate. Yadav and Saini (2020) examined numerically the performance of SAHWJ employing inline jet plate. They investigated thermohydraulic behaviour of SAHWJ using RNG  $k-\epsilon$  turbulence model. They have found out that effect of jet diameter ratio and jet height ratio on the heat transfer performance numerically. Optimum jet height ratio needs to be investigated for reducing the interference between the jets. Vijayan et al. (2020) studied experimentally SAH with thermal storage. The rise in temperature during maximum sunshine hours is lower for the system with sensible thermal storage. It was observed that the system can extend the period of service up to 4 h with a maximum temperature difference of 8 °C. The exergy losses associated with SAH with thermal storage were more due to fluid friction. Singh et al. (2019) investigated experimentally the double pass finned wire mesh packed bed solar air heater. The schematic diagram of experimental setup is shown in Fig. 19.10. The performance was evaluated on the basis of thermal and thermohydraulic efficiency. The result has shown that by employing a double glass cover plate and fins at the lower part of the absorber would increase the thermal performance. Optimum angle of inclination of the fin was found to be 11°.

Singh et al. (2020) experimentally studied two designs of double pass solar air heaters. The schematic diagram of two designs is shown in Fig. 19.11. The second design had an additional wire meshes for storing thermal energy during peak sunshine hours. It was concluded that the design one can be utilized for instant high-thermal performance, whilst design 2 can be used for application that requires thermal backup. Moshery et al. (2020) studied the SAH with transverse ribs absorber plate. They compared the result with existing SAH. They studied the effect of solar intensity

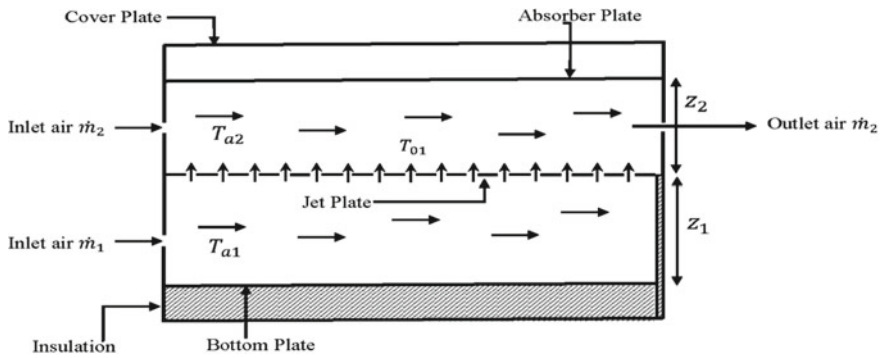


Fig. 19.9 Schematic diagram of SAHWJ employing inline jet plate (Soni and Singh 2017)

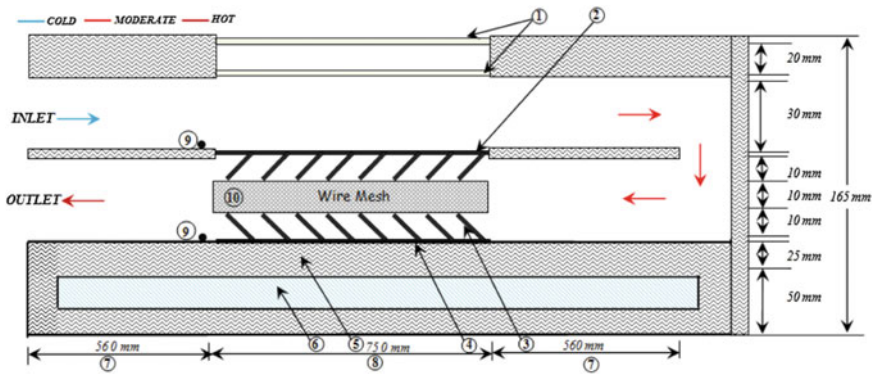


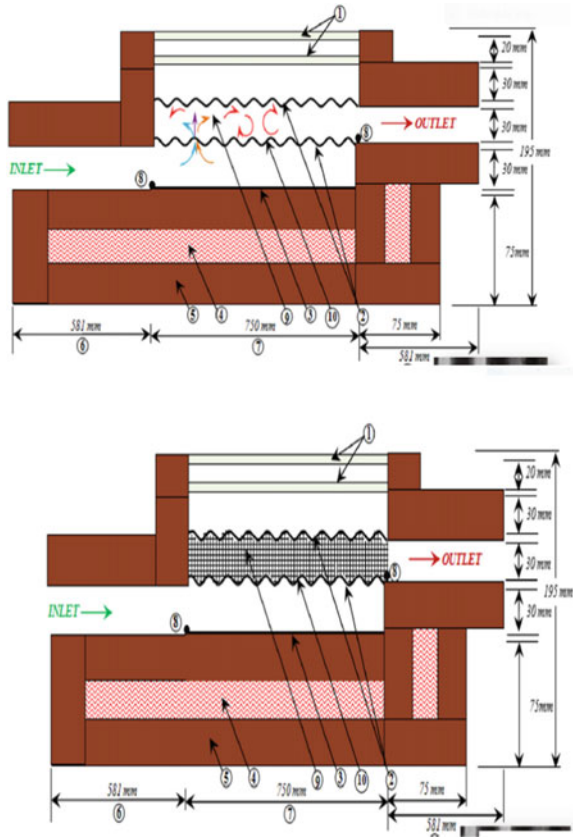
Fig. 19.10 Schematic diagram of double pass solar heater with fins and wire mesh (Singh et al. 2019)

levels and mass flow rate on the thermal efficiency of the system. The thermal efficiency achieved was 78% at mass flow rate was 0.039 kg/s. The summary of literature review on SAH with jet impingement and thermal backup is detailed in Table 19.2 for quick reference.

### 19.6 Concluding Remarks

Jet impingement finds significant position in many engineering and industrial applications. The thinner boundary layer formation in jet impingement in comparison with conventional parallel flow arrangement, increased turbulence level, able to achieve higher value of stagnation Nusselt number (localized heating or cooling), and so on is some of the essential characteristics that attracts many industries like electronics,

**Fig. 19.11** Schematic diagram of design 1 and design 2 (Singh et al. 2020)



manufacturing, aerospace, solar systems, etc. On the basis of review of single jet impingement, the following are the conclusions.

- When the Reynolds number is increased, the value of heat transfer rate for circular and other non-circular jets (square, elliptic, rectangular) also increases.
- The value of heat transfer rate of non-circular jets (square, elliptic, rectangular) was found to be higher in comparison with circular jets. It is also observed that the pressure losses and pumping power cost associated with rectangular jets are higher in comparison with other jets.
- It is reported that when the distance between plate and jet is low (space constrained applications), the value of convection heat transfer rate obtained with rectangular shaped nozzle is higher when compared with circular and square shaped nozzle.
- The different spreading rate along major and minor axis in rectangular jet and higher level of turbulence associated with it creates a difference in heat transfer rate (Nusselt number distribution) along its two axes.



**Table 19.2** Summary of literature review on SAH with jet impingement and SAH with thermal storage

Authors	Parameters studied	Findings
Rajaseenivasan et al. (2017)	Nozzle diameters: 3, 5, 7 mm Mass flow rate 0.012–0.016 kg/s Angle of attack 0°–90°	Optimum diameter identified as 5 mm Optimum angle of attack 0°–90° Mass flow rate 0.016 kg/s Collector efficiency = 55%
Aboghrara et al. (2017)	Nozzle diameter 3 mm Mass flow rate = 0.01–0.03 kg/s	Corrugated plate maximum $\eta_t$ = 68% Flat plate maximum $\eta_t$ = 53%
Soni and Singh (2017)	Jet diameter $D_j$ 6–8 mm, hydraulic diameter $D_h$ $D_j/D_h = 0.053$ –0.084 Mass flow rate 0.03–0.11 kg/s	Collector efficiency is maximum (48%) $D_j/D_h = 0.07$ Mass flow rate = 0.11 kg/s
Yadav and Saini (2020)	Re 3500–17,500 Jet diameter ratio 0.065–0.195 Jet height ratio 0–0.433	The best configuration for superior heat transfer with minimal pressure loss is obtained at Jet diameter ratio = 0.065 Jet height ratio 0.216
Vijayan et al. (2020)	Diameter of packed bed = 30 mm Thermal conductivity of packed bed = 0.72 W/m K Mass flow rate = 0.014–0.087 kg/s	Temperature range obtained with sensible storage solar air heater 45–60 °C
Singh et al. (2019)	Mass flow rate = 0.01–0.03 kg/s	The maximum temperature at the outlet of the solar air heater is 55 °C corresponding to mass flow rate of 0.01 kg/s
Singh et al. (2020)	Mass flow rate = 0.01–0.06 kg/s Number of holes = 40 Diameter of holes 7 mm	Thermal efficiency Design 1 = 94% Design 2 = 87.4%
Moshery et al. (2020)	Mass flow rate = 0.007–0.039 kg/s Height of rib 0.0017–0.0032 m Relative pitch 0.01–0.04 m Solar irradiance 500–1000 W/m <sup>2</sup>	Supreme thermal efficiency was found to be 78% at a mass flow rate of 0.039 kg/s and solar irradiance 1000 W/m <sup>2</sup>

On the basis of review on multi-jet impingement, the following conclusions were obtained.

- For application that uses multi-jet impingement, apart from the design parameters like nozzle geometry,  $h/d$ , Re, and so on, the jet-to-jet spacing places a critical

role in improving the performance. In order to avoid adjacent jet interference to minimum, optimum jet-to-jet spacing both in stream wise and span wise direction needs to be investigated for the particular application.

- The arrangement of nozzle in multi-jet impingement needs to be considered for evaluating the performance of the multi-jets. The studies have shown that wall jet collision of jet leads to an interesting flow feature called upwash flow. The generation of toroidal vortices and recirculation of the jet would significantly affect the entrainment as well as the turbulence level of the impinging jets.
- Introduction of wire meshes at the nozzle outlet or the fractal grids would result in an enhancement in the turbulence intensity level. Introduction of fractal grid especially square fractal grid would result in an increase in better heat transfer enhancement when compared with circular fractal grid and ordinary square grid.
- For space constrained application like electronic industry, square fractal grid is the better option comparing to square grid and circular fractal grid. The uniformity in Nu distribution and considerable rise in the rate of heat transfer favours the applications that have restriction in space.

Based on the review of SAH and SAHWJ, the following conclusions were obtained.

- Solar air heater thermal performance can be improved by many ways by placing different obstacles over the absorber plate, by employing double pass air flow, and by using corrugated plate absorber instead of flat plate absorber. In all the cases, the performance of SAH needs to be investigated on the basis of thermal efficiency and thermohydraulic efficiency.
- Use of two glass cover plates helps to decrease the thermal losses and by employing proper thermal storage system and can be extend the period of service during low-sunshine hours.
- By employing jet impingement in SAH, the thermal performance of the system enhances due to degradation of laminar boundary layer by the turbulence generated in the flow field. Studies revealed that the friction losses in the flow field due to jet impingement increase but are in acceptable limits.
- The literature has been found to be deficient on the study of variation in the nozzle geometry in solar air heater employing impingement of jets. Several studies related to the multi-jet impingement showed better advancement in heat transfer rate by employing elliptic jet, square jet, rectangular jet instead of circular jet. It is also observed that most of the recent works related to solar air heater concentrated on modifying the system with energy backup.
- Very few works are available regarding numerical and experimental examinations of solar system employing impingement of jets and thermal back up. Most of the studies focus experimental investigations on solar systems employing jet impingement.

## 19.7 Suggestion for Future Studies

On the basis of above remarks, it is highly recommended to examine the performance of SAHWJ and thermal backup numerically and experimentally for any desired application. Furthermore, for an energy efficient solar system, it is mandatory to examine the exergy analysis in order to analyze the quality of the energy. Very few studies have been reported regarding numerical, experimental, and thermodynamic analysis based on exergy on a SAHWJ and thermal backup, however, great scope for advancement still exists.

## References

- Aboghrara AM, Baharudin BTHT, Alghoul MA, Adam NM, Hairuddin AA, Hasan HA (2017) Performance analysis of solar air heater with jet impingement on corrugated absorber plate. *Case Stud Therm Eng* 10(May):111–120. <https://doi.org/10.1016/j.csite.2017.04.002>
- Akpınar EK, Koçyiğit F (2010) Energy and exergy analysis of a new flat-plate solar air heater having different obstacles on absorber plates. *Appl Energy* 87(11):3438–3450. <https://doi.org/10.1016/j.apenergy.2010.05.017>
- Akpınar EK, Koçyiğit F (2010) Experimental investigation of thermal performance of solar air heater having different obstacles on absorber plates. *Int Commun Heat Mass Transf* 37(4):416–421. <https://doi.org/10.1016/j.icheatmasstransfer.2009.11.007>
- Al-Kayiem HH, Yassen TA (2015) On the natural convection heat transfer in a rectangular passage solar air heater. *Sol Energy* 112:310–318. <https://doi.org/10.1016/j.solener.2014.11.031>
- Bahremand D, Ameri M (2015) Energy and exergy analysis of different solar air collector systems with natural convection. *Renew Energy* 74:357–368. <https://doi.org/10.1016/j.renene.2014.08.028>
- Cafiero G, Discetti S, Astarita T (2014) Heat transfer enhancement of impinging jets with fractal-generated turbulence. *Int J Heat Mass Transf* 75:173–183. <https://doi.org/10.1016/j.ijheatmasstransfer.2014.03.049>
- Cafiero G, Castrillo G, Greco CS, Astarita T (2017) Effect of the grid geometry on the convective heat transfer of impinging jets. *Int J Heat Mass Transf* 104:39–50. <https://doi.org/10.1016/j.ijheatmasstransfer.2016.08.003>
- Caliskan S, Baskaya S, Calisir T (2014) Experimental and numerical investigation of geometry effects on multiple impinging air jets. *Int J Heat Mass Transf* 75:685–703. <https://doi.org/10.1016/j.ijheatmasstransfer.2014.04.005>
- Carlomagno GM, Ianiro A (2014) Thermo-fluid-dynamics of submerged jets impinging at short nozzle-to-plate distance: a review. *Exp Therm Fluid Sci* 58:15–35. <https://doi.org/10.1016/j.expthermflusci.2014.06.010>
- Chaudhari M, Puranik B, Agrawal A (2010) Effect of orifice shape in synthetic jet based impingement cooling. *Exp Therm Fluid Sci* 34(2):246–256. <https://doi.org/10.1016/j.expthermflusci.2009.11.001>
- Culun P, Celik N, Pihitili K (2018) Effects of design parameters on a multi jet impinging heat transfer. *Alexandria Eng J* 57(4):4255–4266. <https://doi.org/10.1016/j.aej.2018.01.022>
- Gulati P, Katti V, Prabhu SV (2009) Influence of the shape of the nozzle on local heat transfer distribution between smooth flat surface and impinging air jet. *Int J Therm Sci* 48(3):602–617. <https://doi.org/10.1016/j.ijthermalsci.2008.05.002>

- Hee Lee D, Min Lee Y, Taek Kim Y, Youl Won S, Suk Chung Y (2001) Heat transfer enhancement by the perforated plate installed between an impinging jet and the target plate. *Int J Heat Mass Transf* 45(1):213–217. [https://doi.org/10.1016/S0017-9310\(01\)00134-X](https://doi.org/10.1016/S0017-9310(01)00134-X)
- Hegazy AA (2000) Thermohydraulic performance of air heating solar collectors with variable width, flat absorber plates. *Energy Convers Manag* 41(13):1361–1378. [https://doi.org/10.1016/S0196-8904\(99\)00190-9](https://doi.org/10.1016/S0196-8904(99)00190-9)
- Koseoglu MF, Baskaya S (2010) The role of jet inlet geometry in impinging jet heat transfer, modeling and experiments. *Int J Therm Sci* 49(8):1417–1426. <https://doi.org/10.1016/j.ijthermalsci.2010.02.009>
- Lakshmi DVN, Layek A, Kumar PM (2017) Performance analysis of trapezoidal corrugated solar air heater with sensible heat storage material. *Energy Procedia*, 109(November 2016):463–470. <https://doi.org/10.1016/j.egypro.2017.03.069>
- Lee J, Lee SJ (2000) The effect of nozzle aspect ratio on stagnation region heat transfer characteristics of elliptic impinging jet. *Int J Heat Mass Transf* 43(4):555–575. [https://doi.org/10.1016/S0017-9310\(99\)00167-2](https://doi.org/10.1016/S0017-9310(99)00167-2)
- Moshery R, Chai TY, Sopian K, Fudholi A, Al-Waeli AHA (2021) Thermal performance of jet-impingement solar air heater with transverse ribs absorber plate. *Sol Energy* 214(December 2020):355–366. <https://doi.org/10.1016/j.solener.2020.11.059>
- Muvvala P, Balaji C, Venkateshan SP (2017a) Experimental investigation on heat transfer from square jets issuing from perforated nozzles. *Heat Mass Transf Und Stoffuebertragung* 53(7):2363–2375. <https://doi.org/10.1007/s00231-017-1979-6>
- Muvvala P, Balaji C, Venkateshan SP (2017b) Experimental investigation on the effect of wire mesh at the nozzle exit on heat transfer from impinging square jets. *Exp Therm Fluid Sci* 84:78–89. <https://doi.org/10.1016/j.expthermflusci.2017.01.015>
- Muvvala P, Venkateshan SP, Balaji C (2016) Numerical investigation of the local heat transfer behaviour to single and multiple jet impingement over an electronic component. August 2016. <https://doi.org/10.1615/tfesc1.hte.012687>
- Rajaseenivasan T, Srinivasan S, Srithar K (2015) Comprehensive study on solar air heater with circular and V-type turbulators attached on absorber plate. *Energy* 88:863–873. <https://doi.org/10.1016/j.energy.2015.07.020>
- Rajaseenivasan T, Ravi Prasanth S, Salamon Antony M Srithar K (2017) Experimental investigation on the performance of an impinging jet solar air heater. *Alexandria Eng J* 56(1):63–69. <https://doi.org/10.1016/j.aej.2016.09.004>
- Singh S, Dhruw L, Chander S (2019) Experimental investigation of a double pass converging finned wire mesh packed bed solar air heater. *J Energy Storage* 21(January):713–723. <https://doi.org/10.1016/j.est.2019.01.003>
- Singh S, Chaurasiya SK, Negi BS, Chander S, Nems M, Negi S (2020) Utilizing circular jet impingement to enhance thermal performance of solar air heater. *Renew Energy* 154:1327–1345. <https://doi.org/10.1016/j.renene.2020.03.095>
- Soni A, Singh SN (2017) Experimental analysis of geometrical parameters on the performance of an inline jet plate solar air heater. *Sol Energy* 148:149–156. <https://doi.org/10.1016/j.solener.2017.03.081>
- Vijayan S, Arjunan TV, Kumar A, Matheswaran MM (2020) Experimental and thermal performance investigations on sensible storage based solar air heater. *J Energy Storage* 31(April):101620. <https://doi.org/10.1016/j.est.2020.101620>
- Yadav S, Saini RP (2020) Numerical investigation on the performance of a solar air heater using jet impingement with absorber plate. *Sol Energy* 208(July):236–248. <https://doi.org/10.1016/j.solener.2020.07.088>
- Yong S, Zhang JZ, Xie GN (2015) Convective heat transfer for multiple rows of impinging air jets with small jet-to-jet spacing in a semi-confined channel. *Int J Heat Mass Transf* 86:832–842. <https://doi.org/10.1016/j.ijheatmasstransfer.2015.03.073>
- Zhou DW, Lee SJ (2004) Heat transfer enhancement of impinging jets using mesh screens. *Int J Heat Mass Transf* 47(10–11):2097–2108. <https://doi.org/10.1016/j.ijheatmasstransfer.2003.12.002>

# Chapter 20

## Thermal Management of Electronics Systems—Current Trends and Future Applications



Ganesan Dhanushkodi

### 20.1 Introduction

The reliability of electronics systems depends on many parameters such as temperature, humidity, electromagnetic interference, vibration. The factors affecting the reliability of electronics systems are classified into electromagnetic factors, environmental factors, and human factors. The most important environmental factor is the temperature of the semiconductor devices. When the electric current passes through the semiconductor devices, offers electrical resistance and produces heat due to Joule's heating effect. The heat produced at the junction of the electronics devices needs to be removed to limit the temperature rise of the junction. Electronics systems are being developed for various applications with a wide range of semiconductor devices. Electronics devices and printed circuit boards are made up of different types of materials ranging from plastics to gold. Due to the range of thermal conductivity and thermal expansion coefficient of materials, electronics systems face thermal stress (Steinberg 1991). To avoid thermal stress it is essential to maintain the component and PCB temperatures within their specification limit. The current trend shows that the heat generated per unit volume of the device continues to grow due to more functionality and higher clock speed (Moore and Shi 2014). Due to the increasing growth of consumer electronics, fast and reliable communication systems are the need of the hour. The aging of semiconductor devices depends on many factors such as hot carrier injection, bias temperature instability, dielectric breakdown, electromigration (Aragones et al. 2021). A thermal design ensures the reliability of electronics systems. The demand for effective thermal design techniques, meta-materials, and cost-effective cooling solutions are continues to grow (Kim et al. 2021). Thermal management cost is varying from 1 to 10% of the total cost of the system. The cost depends on the type of technique adopted to cool the electronics system. Many

---

G. Dhanushkodi (✉)  
Centre for Electromagnetics, SAMEER, Chennai, India  
e-mail: [dhanush.sameer@nic.in](mailto:dhanush.sameer@nic.in)

cooling techniques are available and the type of cooling technology will be decided by the type of electronics system, heat dissipated by the system, installation site, power backup, and cost budget, etc. This chapter presents the various technologies currently available for the effective thermal management of electronics systems. This chapter further discusses the future trends of various cooling technologies and their applications to various electronics systems.

## 20.2 Reliability of Electronics Systems

Thermal management of electronics systems plays a major role in determining the reliability of the electronics systems. Electronic device fails because of excess stress acting on it. Stress is developed due to electricity, heat, chemical reaction, electromagnetic radiation, etc. The common cause of failure is heat. Electronics device manufacturers specify the limiting temperature of each device. Thermal acceleration factor for electronics devices, time to failure concerning their case temperature is given by Arrhenius model (<https://www.jedec.org/standards-documents/dictionary/terms/arrhenius-equation-reliability>) as below:

$$A_T = \exp^{-\frac{E_{aa}}{k} \left\{ \frac{1}{T_1} - \frac{1}{T_2} \right\}} \quad (20.1)$$

where

- $A_T$  Acceleration factor due to changes in temperature
- $E_{aa}$  Apparent activation energy (eV)
- $k$  Boltzmann's constant ( $8.62 \times 10^{-5}$  eV/K)
- $T_1$  Absolute temperature of the ambient (K)
- $T_2$  Absolute temperature of the system (K).

The stress developed due to high temperature causes wire bond failure, die-attach failure, encapsulation failure, bulk silicon defect, oxide layer failure, etc. Failure due to thermal stress can be avoided by maintaining the temperature of the device within the temperature limit specified by the manufacturer. The challenge in the thermal design of the outdoor system is the variable environmental temperature and thermal cycling. The ambient temperature varies from  $-20$  to  $55$  °C. The temperature rise harms the efficiency of the system further affect the performance of the electronics systems. Boano et al. (2010) conducted the field testing of their sensors developed for an industrial application. The effect of temperature on the signal strength of the sensor network deployed in an oil refinery is studied. Experiment shows that the temperature directly affects the performance of the sensors and the signal strength reduces by 7 dBm when the average temperature of the enclosure increases from  $-10$  to  $50$  °C. The electric power consumed by the sensor system is also increased by 16% when the temperature increases to  $50$  °C.

## 20.3 Thermal Design Techniques

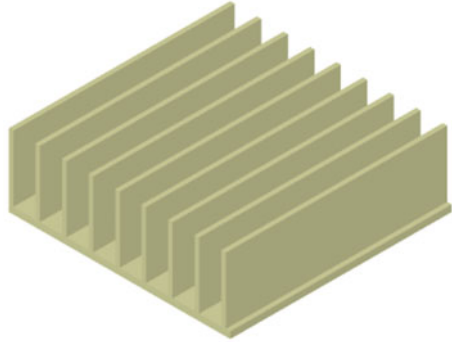
Cooling systems such as heatsink, heat exchanger, are to be designed to dissipate the heat generated by the electronics devices. The cooling solution ranges from natural convection heatsink to advanced cooling devices such as heat exchanger, are to be designed to cool chip level to shelter level (Breen et al. 2011). The cooling devices may be passive or semi-active or fully active. The cooling solutions are developed based on their application, heat flux, deployment condition, environmental conditions, etc. The following are the techniques currently used for the cooling of electronics systems.

### 20.3.1 Heatsink

Heatsink cooled by natural convection is the most preferred mode of cooling for low heat flux applications (Donovan and Rohrer 1971). Rectangular fins are formed on the surface of the hot spot device. Heat dissipation from the fins to ambient is governed by Newton's law of cooling. The natural convection heat transfer coefficient is less than  $5 \text{ W/m}^2 \text{ K}$ . Heatsink fin increases the surface area available for convection thus increases the heat transfer rate from the surface of the electronics systems and reduces the device temperature. Figure 20.1 shows the heatsink arrangement for the cooling of an FPGA device attached to a printed circuit board. The heatsink is dissipating the heat generated by the device to the proximate ambient through natural convection. The radiation component of heat transfer from the heatsink plays a significant role in the design of the heatsink. Many researchers (Rea and West 1976; Ellison 1979) investigated the radiation and convection heat transfer from an array of longitudinal rectangular extended surfaces. They developed a mathematical model of rectangular fin exchanges heat with the surrounding fluid. The Gray body view factor is a dominant factor that decides the heat dissipated to the ambient by radiation. They concluded that convection is the efficient mode of heat transfer from the fins. Fin effectiveness increases as the radiation heat transfer from the fin increases, thus the total heat transfer rate from the chip surfaces increases. For a conventionally used Aluminum heatsink cooled by natural convection, 15% of total heat transferred to the ambient is through radiation mode.

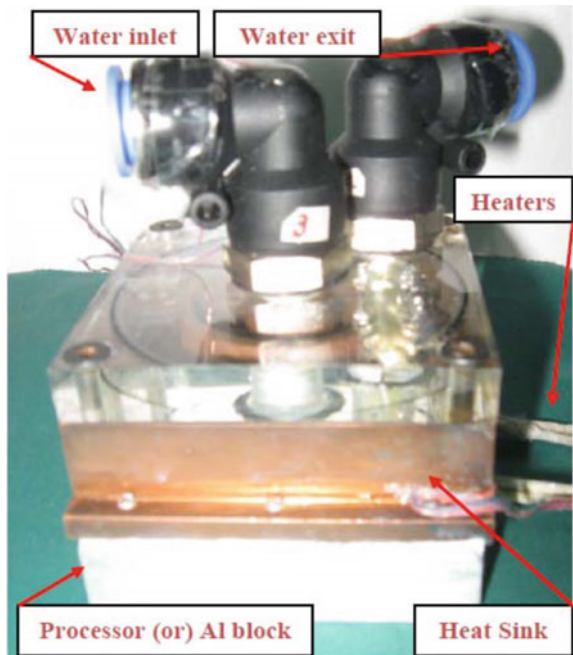
Electronics devices such as high power switches, IGBTs, multi-chip modules, flip-chip ball grid array, dissipate very high heat. Cooling of high power devices whose heat flux is more than  $100 \text{ W/cm}^2$  requires a large conduction area. In some applications providing a large surface to transfer heat by conduction and convection may not be possible. To meet the functional requirement of the system, liquid cooling is a feasible solution (Harikrishnan et al. 2011). Water, de-ionized water, glycol/water mixture, nano metal particle/water mixture, nanocarbon tube/water mixture, dielectric fluid such as fluorocarbons, are the commonly used fluids. Figure 20.2 shows the schematic of the liquid-cooled heatsink. A plenum is formed around the heatsink

**Fig. 20.1** Schematic of heatsink used for natural convection cooling



pins. The heat source is attached to the heatsink base and the water flows through the channel formed between the fins which removes the heat. The average water flows through the system is 17 mL/s and the thermal resistance of the heatsink is 0.32 °C/W. Water flows through the heatsink plenum is measured by using a water flow meter and the temperature of the processor is measured by using T-type thermocouples.

**Fig. 20.2** Experimental setup for water-cooled heatsink





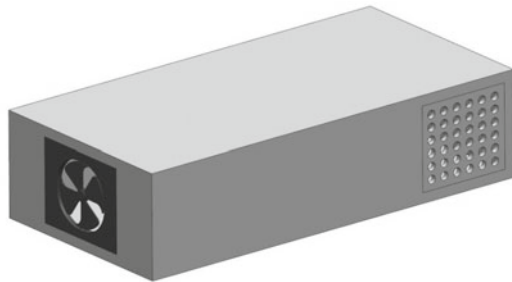
### 20.3.2 Vents and Louvers

One of the primary requirements of improving the thermal performance of the heatsink is to increase the airflow across the heatsink. Shrouds are designed on the external wall of an outdoor electronics system to augment the airflow inside the enclosure. Openings such as cut-outs, protrusions, louvers, slats, blinds (internally or externally), perforations, on the walls of the shrouds will increase the airflow across the heatsink. Shrouds with louvers provide a simple but effective solution for the thermal management of telecommunication systems deployed in outdoor conditions. These louvers allow the air to enter and also prevent the rainwater to pass through the openings. The schematic of the electronics enclosure with fan and perforation on the enclosure wall is shown in Fig. 20.3.

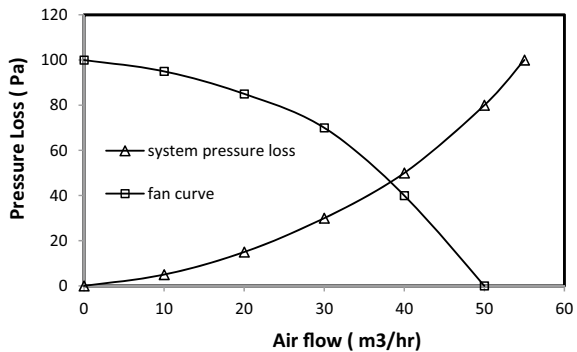
Airflow through the perforation or the louvers depends on the pressure drop exerted by the perforations (Ganesan 2010). Figure 20.4 shows the pressure drop characteristics of commonly used vents. Pressure loss across the vent depends on the flow through the vent, porosity, and diameter of the hole. The volumetric flow delivered by the fan is inversely proportional to the pressure drop across the electronics system. The delivery of the fan for various pressure losses is shown in the figure.

To increase the airflow into the enclosure, different types of vents were developed and their effect was studied. The author concluded that the vent which offers low

**Fig. 20.3** Schematic of an electronics enclosure with fan and vent holes



**Fig. 20.4** Pressure drop characteristics of electronics enclosure with fan and vents



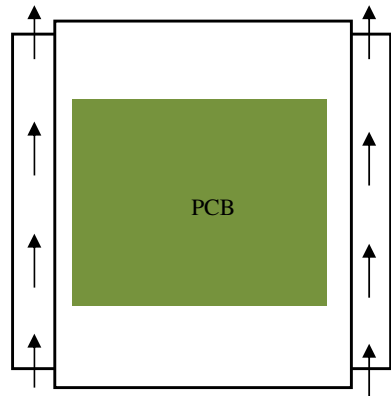
flow resistance allows more air circulation. Improved air circulation reduces the temperature of the electronics devices. Vents provided in the vicinity of the hot spots such as heatsink, further reduce the temperature.

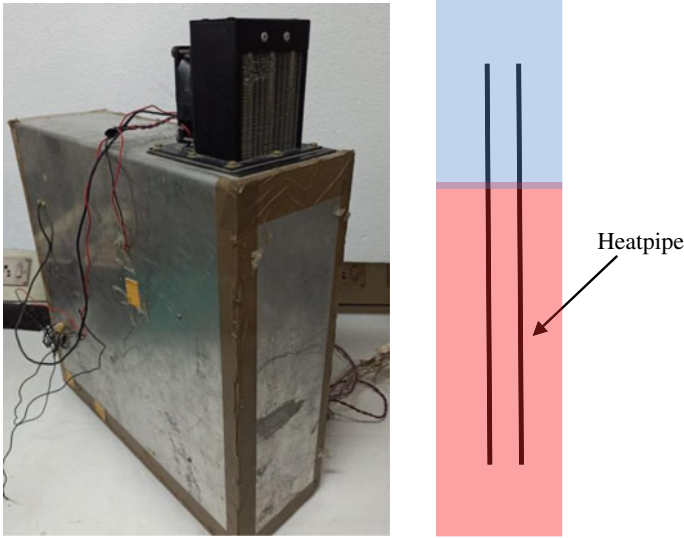
### 20.3.3 Heat Exchangers

Commercial and strategic communication systems are generally being deployed in outdoor conditions. The atmospheric air available to cool the system will have moisture, dust, etc. Heat exchangers are the best cooling option for moisture or dusty and hazardous environments Korte et al. (Korte et al. 2000). It avoids the direct contact of outside air into the electronics component. Rectangular channels are formed on the walls of the enclosure to enhance the heat transfer rate from the enclosure. The enclosure wall is made up of two parallel plates. The outer wall protects the electronics system from solar heat. Heat dissipated by the electronics devices is brought to the inner wall by air circulation inside the enclosure as shown Fig. 20.5. The space between the walls is used as a heat exchanger. The heat available at the inner wall is transferred to the ambient by circulating fluid. The heat transfer coefficient between the inner wall and the fluid can be increased by increasing the fluid flow through the channel. This double-shell enclosure prevents the failure of electronics due to dust, moisture, EMI, etc. because there is no direct contact of outer air with the electronics systems.

Enclosures with heat pipe arrangement as heat exchangers is an another way of dissipating the heat to the ambient (Wankhede et al. 2007). This system consists of two fluid streams, one for internal circulation and another for external circulation. Heat pipe connects the internal and external fluid stream. The heat generated by the electronics components is transferred to the internal air. The heat available in the internal air will be transferred to the heat pipe as shown in Fig. 20.6. The portion of the heat pipe present inside the enclosure works as an evaporator and the portion

**Fig. 20.5** Top view of the of double-shell enclosure as a heat exchanger for the cooling of electronics systems





**Fig. 20.6** Heatpipe-based heat exchanger for the cooling of electronics systems

protruded outside the enclosure is the condenser. Fins are attached to the condenser to transfer the heat to the ambient. Heat pipe-based heat exchanger enhances the heat transfer thus reduces the temperature of the electronics components.

### 20.3.4 Phase Change Materials

The heat dissipation from modern electronics such as wearable electronics systems, mobile systems, personal digital assistants, is variable with respect to usage. The heat generated by these systems is more during the ON time and less during the sleeping mode. Phase change material is a popular cooling mechanism to absorb the heat during the ON time and to dissipate the heat during OFF time (Kiziroglou 2015; Marongiu et al. 1997). The protection of electronics systems from environmental induced temperature spikes due to lightning, etc. is also a major concern. Phase Change Material (PCM)-based encapsulations can protect the electronics from environmental induced thermal spikes for a shorter duration. PCM-based enclosures are developed for the cooling of electronic sensors and networks installed in the harsh industrial environment often receives thermal spikes from other systems such as boilers, chemical reactors. PCM is a viable solution to control the temperature rise due to temperature/heat flux spike. The phase change material absorbs the heat available during the spike and releases the heat during normal operation time. In recent days the electronics systems are mounted outdoor to ensure efficient communication between the systems. These electronics enclosures are exposed to solar heating

thus the temperature of the enclosure increases due to solar heating. The PCM-filled enclosures absorb the solar heat during the daytime and maintain the temperature of the enclosure without further increase. The absorbed solar heat is dissipated to the ambient during the night.

## **20.4 Application of Thermal Management Technologies**

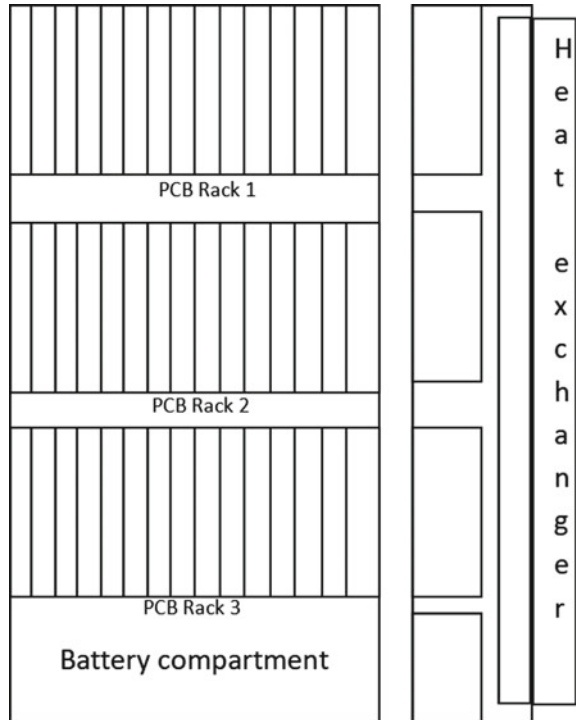
To improve the system requirements such as speed, compactness, data handling capacity, robustness, there is continuous development in the electronics packaging domain. As a result, the heat produced by the electronics per unit area/volume is increasing day by day. Various types of technologies ranges from natural convection fins to liquid-cooled heatsinks have been used for thermal management of electronics systems. Thermal engineering community is actively doing research in Innovative technologies such as thermoelectric modules, heat pipes, PCMs. Each technology is unique and having merits and demerits while using it for a specific application. Judicious selection of cooling technology for a particular application calls for a detailed study of cooling technologies and their applications. The following are application areas and commonly used cooling technologies.

### ***20.4.1 Thermal Design of Telecommunication Systems***

The reliability of telecommunication systems depends on the temperature of the electronics devices. The temperature of the electronics devices increases due to Joule heating effect. More than 78% of radio units are installed either in rooftops or in fields. Communication Systems supporting high-risk sites such as hospitals, health care centers, are installed at rooftops. One of the challenges in mobile broad band connectivity is to improve the power conversion efficiency which results in reduced thermal related issues. These requirements call for advanced thermal management techniques. Millimeter wave technology is under development for faster data transmission. Power amplifiers for millimeter wave technologies such as 5G transmitter systems are prone to thermal related failures.

Radio base stations are mainly installed for commercial communication purposes. To reduce the cable losses and to improve transmission efficiency the base stations are installed in outdoor environments. RF systems such as power amplifiers, couplers, switches, consume electrical power. The efficiency of the power amplifier is poor; more than 90% of the electrical energy is dissipated as heat. Cooling systems are used to transfer the heat from the power amplifier to the external ambient. In addition to RF systems, cooling systems such as fans, air conditioners, also consume electrical energy. Approximately 46% of total electrical energy is consumed by cooling devices. The energy consumption by the cooling devices such as fans, air conditioners, can be reduced up to 30% by proper selection and positioning of cooling devices. Due

**Fig. 20.7** Schematic of telecommunication rack with heat exchanger

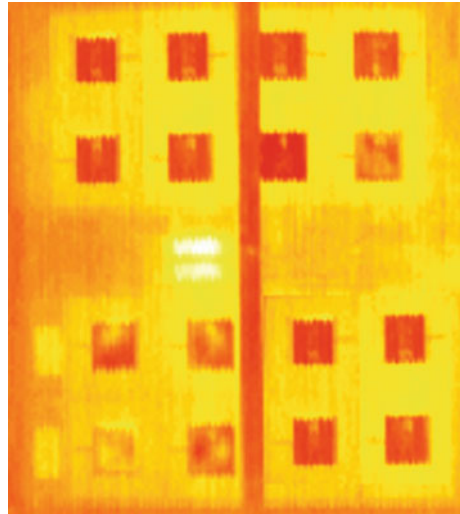


to practical reasons, the telecom racks are installed in harsh environments. Since the air available around the system contains dust, moisture, etc., external air is not preferred to enter into the communication system to carry away the heat produced by the electronics devices. Heat exchangers are employed to maintain the temperature of the devices. Figure 20.7 shows the schematic of the telecommunication rack with the heat exchanger. Additional battery backup may be recommended for the operation of fans installed in the heat exchanger. The trade-off between the cooling technology and the operational cost is also to be considered.

### 20.4.2 LED Cooling

The application of LED is increasing exponentially for the past few years for many applications such as digital displays, signboards, for advertising, public announcement, etc. The brightness level of outdoor display units is in the order of 1500 lumens whereas for indoor application is 300 to 600 lumens. Outdoor application of LEDs accounts for more than 35% of total production. JEDEC JESD 22-AI05D: Power and Temperature Cycling, January 2020 standard provides guidelines about the reliability aspects of LEDs and the list of tests to be conducted to ensure reliability. The heat

**Fig. 20.8** Infrared Thermal image of an array of LEDs used for lighting application



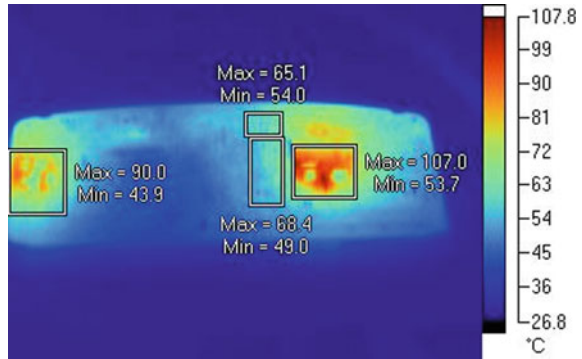
generated at the junction is a more concern to maintain the reliability of the LED. The light output from the LED also depends on the junction temperature. The luminosity of the LED diminishes over the period of operation. The luminosity decreases when the LED is operated at a high temperature (Narendran and Gu 2005; Singh and Tan 2016; Joshi and Brown 2019). Many authors have brought out the state of the art thermal control technology for thermal management of outdoor systems. The heat produced by the LEDs is conducted to the chassis through leads and interface materials.

The infrared thermal image of an array of LEDs packed on a metal-clad printed circuit board for industrial lighting application is shown in Fig. 20.8. Special reflecting films and filters are being used to reduce the heat gain by the outdoor display units. Natural convection with perforations on the sides of the panels is the preferred approach to cooling the LEDs. It needs improvement in thermal interface material, low thermal resistance conduction path to carry the heat over the large display area, etc.

### **20.4.3 Thermal Design of Automobile Electronics**

Thermal management of electric vehicles is a key to ensure vehicles reliability, economical operation, drivers comfort, etc., and to meet social concerns and statutory regulations. The vehicle is getting heated up due to internal loads such as charging or discharging of batteries, motors, IGBTs, control electronics. Advancement in material technology pushes the conversion efficiency of power electronics such as IGBTs to more than 98%, however, the reliability of power electronics is becoming more concerned (Broughton et al. 2018). The nominal output power is restricted by

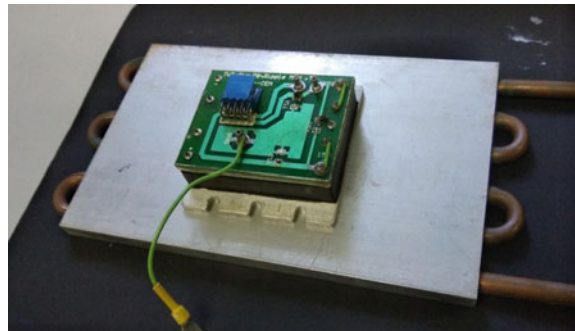
**Fig. 20.9** Thermal image of automobile control panel



the circuitry and the temperature of the power ICs. The heat flux of the power ICs such as IGBT, MOSFETs, are high and a large volume heatsink with the fan is required to cool the ICs. Today’s vehicle is driven by micro processor based control system. The thermal design of control system is also an important object of the research. Figure 20.9 shows the thermal image of automobile control system.

Cermak (Cermak et al. 2017) proposes a passive cooled heat pipe with heatsink arrangement. The authors conducted experiments to measure the output power capacity of 7.2 KW power systems. The power supplies were tested for various ambient conditions, the efficiency of the power supply decreases from 98.8 to 80.7% due to an increase in ambient from 26 to 46 °C. Thermal management of power supplies was done by using heat pipes and heatsink. The efficiency of the output power is increased from 80.7 to 85.7% at an ambient of 46 °C. Novel heat spreaders and heatsinks are designed to cool the IGBTs. Cold plates are used to cool the power electronics devices. The schematic of the cold plate is shown in Fig. 20.10. Channels are formed on the metallic cold plate and either water or automobile fuel is passed through the channel to dissipate the heat released by the power devices.

**Fig. 20.10** Cold plate arrangement for cooling of power electronics



### 20.4.4 Battery Cooling

Battery banks packed inside an enclosure is used to power-up broadband access network and base stations installed at remote places and e-vehicles, etc. Research and development are going on to minimize the cost and to maximize the lifetime of the batteries. Batteries get heated up during the charging process. The degradation of battery performance occurs mainly due to the corrosion of electrodes. Elevated battery temperature exponentially decreases the life of the battery. The charge storage capacity of a battery depends on the operating temperature and the number of charge and discharge cycles. When the operating temperature of the battery is increased from 25 to 55 °C, the maximum charge storage capacity will reduce by around 15%. It is proposed to use Peltier devices to control the temperature of the battery cabinet. The inside air temperature can be maintained at around 35 °C even for the external ambient of 45 °C. Compact Heat Exchangers and phase change materials also can be used for the Thermal Management of Battery Compartments. In addition to the thermal requirement, the battery cooling systems are designed to meet outgassing requirements.

## 20.5 Optimization of Cooling Systems

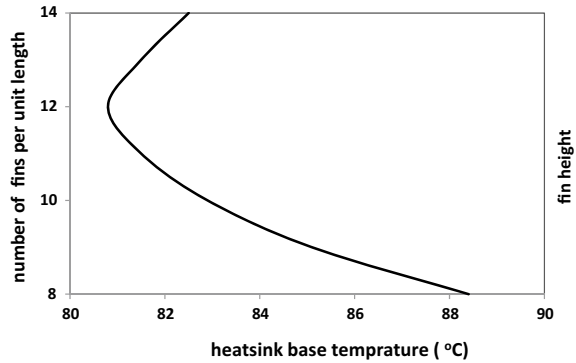
Heat transfer techniques such as the heatsink, fan, heat exchanger, heat pipe, thermoelectric coolers, phase change materials, are being used to cool the electronics systems. The heatsink is the most preferable cooling technique. Optimization of heatsink for minimum weight, fabrication cost, etc., and minimum power consumption in case of the heatsink with fans is essential to meet the cost budget. The optimization of the heatsink involves the optimization of the heatsink base area, fin height, and the spacing between the fins or the number of fins per unit length of the heatsink base.

Generally, the hot spot device or the high dissipating component is attached to the bottom of the heatsink base. The heat generated by the device is conducted to the heatsink base and is further conducted throughout the area of the base. By providing more base area the heat can be spread easily. The temperature gradient over the area of the heatsink base is defined as the spreading thermal resistance of the heatsink. The heatsink base area and the base thickness are optimized by using computational techniques such a way that the spreading resistance of the heatsink is less.

The height of the fin is playing a major role in the thermal performance of the heatsink. The base temperature of the heatsink can be reduced by increasing the heatsink fin height. Increasing fin height increases the area available for convection thus reduces the base temperature. Figure 20.11 shows the effect of fin height on heatsink base temperature. Beyond a certain height, the increase in fin height gives an adverse effect due to increased conduction resistance over the height of the fin. Similarly, the spacing between the fins is also optimized. This optimization improves



**Fig. 20.11** Optimization of heatsink



the thermal performance of the heatsink and also reduces the weight, material and fabrication cost, etc. of the heatsink.

For many applications like high power RF amplifiers, telecommunication racks, etc. the cooling devices such as fans, air conditioners, consume approximately 30% of the total power supply. Selection of appropriate fan or air conditioner in terms of the size, flow rate, COP, etc. can reduce the power consumption considerably.

## 20.6 Conclusion

Heat generation from the electronics systems is inevitable and reduces the reliability of the electronics systems. Thermal management of electronics systems is a major domain that applies suitable heat transfer technologies to cool the electronics systems. The current heat transfer techniques such as the heatsink, fan, heat exchanger, heat pipe, are discussed here and their application area is also presented in this chapter. The future applications such as high speed outdoor communication systems, LED, automotive electronics and batteries, etc. where the role of thermal designers is vital. This chapter throws light on future applications where thermal designers can pay more attention and develop new cooling technologies.

## References

- Aragones X, Barajas E, Crespo-Yepes A, Mateo D, Rodriguez R, Martin-Martinez J, Nafria M (2021) Aging in CMOS RF linear power amplifiers: an experimental study. *IEEE Trans Microw Theory Tech* 69(2):11
- Boano CA, Tsiftes N, Voigt T, Brown J, Roedig U (2010) The impact of temperature on outdoor industrial sensor net applications. *IEEE Trans Ind Inf* 6(3):451–459
- Breen TJ, Walsh EJ, Punch J, Shah AJ, Bash CE (2011) From chip to cooling tower data centre modelling: influence of server inlet temperature and temperature rise across cabinets. *ASME J Electron Pack* 133:011004-1-011004-8

- Broughton J, Smet V, Rao T, Joshi Y (2018) Review of thermal packaging technologies for automotive power electronics for traction purposes. *ASME J Electron Pack* 140:010801-1–11
- Cermak M, MajidBahrami M, Lau K (2017) Development of a passively cooled outdoor telecom power enclosure. In: 33rd IEEE SEMI-THERM symposium, pp 13–18
- Donovan RC, Rohrer WM (1971) Radiative and convective conducting fins on a plane wall, including mutual irradiation. *ASME J Heat Transfer* 93(1):41–46
- Ellison GN (1979) Generalized computations of the gray body shape factor for thermal radiation from a rectangular U-channel. *IEEE Trans Compon Hybrids Manuf Technol* 4:517–522
- Ganesan D (2010) Experimental study on pressure drop characteristics of Vent. *IEEE Trans Compon Pack Technol* 33:432–436
- Harikrishnan L, Palani N, Dhanushkodi G (2011) Design and performance study of liquid cooled heatsink for electronics components. In: National conference on refrigeration and air conditioning. IIT Madras, Chennai, India pp 115–122
- <https://www.jedec.org/standards-documents/dictionary/terms/arrhenius-equation-reliability>
- Joshi Y, Brown MJ (2019) Thermal management of outdoor digital displays—A review. In: 18th IThERM conference, pp 772–779
- Kim JC, Ren Z, Yuksel A, Dede EM, Bandaru PR, Oh D, Lee J (2021) Recent advances in thermal meta materials and their future application for electronics packaging. *ASME J Electron Pack* 143:010801-1–010801-15
- Kiziroglou Y (2015) Protection of electronics from environmental temperature spikes by phase change materials. *J Electron Mater* 44:4589–4594
- Korte DR, Quante AG, Wuppertal (2000) The benefit of a double shell construction for outdoor enclosures. In: Third international telecommunication energy special conference, Germany, pp 147–151
- Marongiu MJ, Clarksean RL, Kusha WA (1997) Passive thermal management of outdoor enclosures using PCM and enhanced natural convection. In: Proceedings of power and energy systems in converging markets, Australia, pp 504–511
- Moore AL, Shi L (2014) Emerging challenges and materials for thermal management of electronics. *Mater Today* 17(4):163–174
- Narendran N, Gu Y (2005) Life of LED based white light sources. *IEEE OSA J Display Technol* 1:167–171
- Rea SN, West SE (1976) Thermal radiation from finned heat sinks. *IEEE Trans Parts Hybrids Pack* 115–117
- Singh P, Tan CM (2016) Degradation Physics of high power LEDs in outdoor environment and the role of phosphor in the degradation process. *Sci Rep* 6:24052. <https://doi.org/10.1038/srep24052>
- Steinberg DS (1991) Cooling techniques for electronic equipment, 2nd edn. Wiley, pp 453–469
- Wankhede M, Khaire V, Goswami A, Mahajan SD (2007) Evaluation of cooling solutions for outdoor electronics. In: Thirteenth international workshop on thermal investigation of ICs and systems, pp 858–863

# Chapter 21

## Carbon Dioxide Storage and Its Energy Transformation Applications



Manoj S. Choudhari, Vinod Kumar Sharma, Mukesh Thakur,  
Sanjay Gupta, and Shajiullah Naveed Syed

### Abbreviations

$\text{CO}_2$	Carbon dioxide
$\text{H}_2$	Hydrogen
$\text{O}_2$	Oxygen
$Q_a$	Adsorption heat
$Q_c$	Heat rejected
$Q_{\text{ref}}$	Refrigeration effect
$Q_{\text{reg}}$	Desorption heat
$Q_s$	Waste heat
$T_a$	Ambient temperature
$T_{\text{ref}}$	Refrigeration output temperature
$T_{\text{reg}}$	Heat source temperature

---

M. S. Choudhari  
Department of Mechanical Engineering, RCET, Bhilai, Chhattisgarh 490024, India

V. K. Sharma (✉)  
Mechanical Engineering Department, National Institute of Technology Calicut, Kerala 673601,  
India  
e-mail: [vinsharma85@gmail.com](mailto:vinsharma85@gmail.com)

M. Thakur  
NMDC DAV Polytechnic Dantewada, Shri Atal Bihari Vajpayee Education City Jawanga,  
Dantewada, Chhattisgarh 494441, India  
e-mail: [shrimukeshthakur@gmail.com](mailto:shrimukeshthakur@gmail.com)

S. Gupta · S. N. Syed  
School of Mechanical Engineering, Vellore Institute of Technology, Vellore, Tamil Nadu 632014,  
India  
e-mail: [sunjay02@gmail.com](mailto:sunjay02@gmail.com)

S. N. Syed  
e-mail: [shajiullahnaveed18@gmail.com](mailto:shajiullahnaveed18@gmail.com)

## 21.1 Introduction

Global Energy demand increases drastically due to rapid growth in population, technological advancement, and people's living style. As per the studies of 2017, more than 80% of the energy demand is fulfilled by fossil fuels resulting in air pollution, global warming, energy crisis, and depletion of fossil fuels (Maggio 2012; Houghton 2005; Asif and Muneer 2007; Barbir et al. 1990). Earlier usage of wood, windmills, and animals (for transportation) as energy sources is shifted to fossil fuels in the eighteenth century with the steam engine's development as an industrial revolution. In the nineteenth century, it advanced for the internal combustion engine's progress, wherein petrol was introduced as fuel, resulting in a gradual shift from coal to oil. This new shift from coal to oil gained impulse in the twentieth century and resulted in oil is being the main source of energy Dell and Rand (2004). The primary energy sources are presented in Fig. 21.1.

The highest usage of fossil fuels is oil as every individual relies on it for transportation purposes; about 97% of fuel used for transportation comes from crude oil and burning of this fuel generates about 25% of global greenhouse emissions. As per the modern usage and growing demand, the forecasts show oil is going to deplete well before the end of the twenty-first century. Excessive usage of oil affects the environment by increasing air pollution and oil spills which is a serious concern that needs to be addressed. Use of fossil fuels outcomes in excessive emission of carbon dioxide, methane, greenhouse gases in the atmosphere results in global warming which has adverse effects like gradual heating of the earth's surface, oceans, and environmental changes worldwide (Bruce et al. 1996). The above reasons show us; there is a need to swap fossil fuels with clean and renewable energy. Hydrogen can play an essential role as an energy carrier and has the potential to replicate fossil fuels; it should be kept in mind that hydrogen is not readily available, but it needs to be produced, considering hydrogen as a fuel in the same sense of petrol will be misleading. The

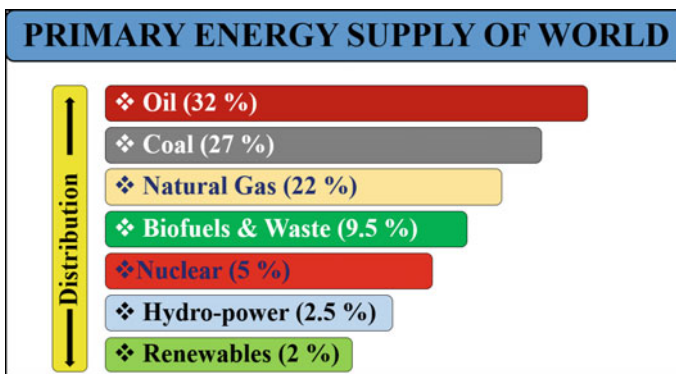


Fig. 21.1 Primary energy supply of world

three phases of hydrogen, i.e., production, transportation, and storage, are together called hydrogen economy.

Tremendous growth in the modern civilization results in rapid depletion of non-renewable energy resources. The excessive harnessing of fossil fuel has resulted in the emission of carbon dioxide (CO<sub>2</sub>) in a large quantity. Severe environmental issues like global warming and climate change are the result of emissions from fossil fuel consumption (Zanganeh and Shafeen 2007; Figueroa et al. 2008). CO<sub>2</sub> is released into the environment as a component in flue gases emitted by refineries, gas processing industries, power plants, iron and steel industries, chemical and petrochemical industries and cement industries. These industries are mainly responsible for anthropogenic CO<sub>2</sub> emissions (Figueroa et al. 2008). In fact, every year over 30 billion tonnes of CO<sub>2</sub> is released into the atmosphere (EPA 2009). Moreover, the problems like urban smog and acid rain may have CO<sub>2</sub> as one of the root causes (Chunshan 2006). Several methods have been suggested and implemented for reducing the concentration level of CO<sub>2</sub> in the environment: (1) improving the energy efficiency, (2) reducing the CO<sub>2</sub> emission by switching to non-fossil fuels like renewable energy, hydrogen and nuclear energy, (3) capturing the CO<sub>2</sub>. The most suitable approach among these is capturing CO<sub>2</sub> from industries (Stewart and Hessami 2005). CO<sub>2</sub> capture and sequestration/storage (CCS) has emerged as a solution offering a way of usage of fossil fuels while reducing CO<sub>2</sub> emissions by 85% or more. Albeit CCS cannot alone solve the problem of climate change, it will definitely prove to be one of the powerful tools to address the issue (Bernstein et al. 2006).

In addition to the hydrogen economy, the solid-state storage of carbon dioxide attracts the researchers' interest. In this chapter, the various methods and materials to safely store carbon dioxide are presented. In addition, the novel thermodynamic systems that can be developed using carbon dioxide adsorption phenomena are discussed and compared.

## 21.2 Carbon Dioxide Storage

Every single year almost 30 billion tons of carbon dioxide is free into the environment from multiple industries such as refineries, power plants, cement, gas processing, chemical, steel, causing severe issues which the world is facing today and every leader of the world is worried about these issues of global warming and climate change (Zanganeh and Shafeen 2007). In the last 150 years, the world has adopted the Industrial revolution, the Carbon dioxide level has enlarged from 280 to 403 ppm, and simultaneously the temperature has changed from 0.6 to 1 °C. In the future, the CO<sub>2</sub> level may increase drastically to 570 ppm and reach a temperature of 1.9 °C as per the study of the International Panel on Climate change till the time it reached 2100 years.

From the last three decades, intense research is being done to lessen the amount of CO<sub>2</sub> in the atmosphere, which can be done by either of the processes (Figueroa et al. 2008; Yang et al. 2008).

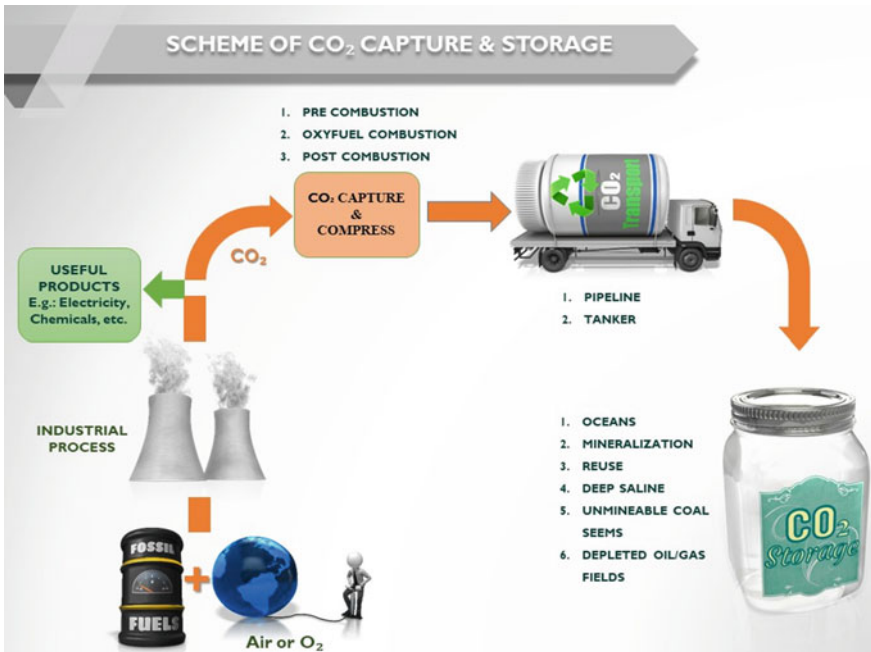


Fig. 21.2 Scheme of CO<sub>2</sub> capture and storage

1. Improving energy efficiency
2. Replicating fossil fuels with renewable energy sources
3. Storing CO<sub>2</sub>

Figure 21.2 shows the scheme of CO<sub>2</sub> capture and storage. The work process consists of capturing the CO<sub>2</sub> by using either of the methods mentioned, such as Pre, Post, or Oxyfuel combustion. Once the CO<sub>2</sub> is captured, it is transported to a site where it will be stored using various methods as explained above, such as in deep down oceans, so that it is completely secluded from the atmosphere.

## 21.3 Technologies for Capturing CO<sub>2</sub>

### 21.3.1 Post-combustion Capture

As shown in Fig. 21.3a (Figuroa et al. 2008), the CO<sub>2</sub> is removed from the combustion gases, in post-combustion capture. The scheme is generally applicable to fossil-fuel-burning power plants, where CO<sub>2</sub> is captured at low pressure (1 bar) from flue gases and low CO<sub>2</sub> concentration (3–20%) often at high temperatures (120–180 °C)

containing the impurities SO<sub>x</sub> and NO<sub>x</sub>. This is a well-developed technology that is also used in other industries apart from conventional power plants.

Various techniques are used for post-combustion capture. The most sales technique at present is to scrub the flue gas with an amine solution (Figueroa et al. 2008; Rubin et al. 2012; Rackley 2017). As amine scrubbing is a well-developed technology, it is believed that the first CO<sub>2</sub> capture large-scale plant will mainly be based on post-combustion CO<sub>2</sub> capture by amine absorption. The major part of the industrial sector is working toward the development of this technology; a few examples are ABB Lummus (USA), Fluor Daniel (USA), and Mitsubishi Heavy Industries (Japan) and Sargas (Norway). However, the low concentration of CO<sub>2</sub> in power plant flue gas (typically 4–14%) and need to handle the huge volume of gas demand large equipment sizes and high capital costs (Meisen and Shuai 1997). Further, regeneration of the solvents to release the CO<sub>2</sub> requires a large amount of energy.

Although several existing research and development (R&D) project impelled their interest to eliminate the limitations involved, the optimized methodology needs to be addressed to eliminate the discussed issues.

### ***21.3.2 Pre-combustion Capture***

In pre-combustion CO<sub>2</sub> capture, the fuel's carbon is separated, before the combustion process, as demonstrated in Fig. 21.3b. It is a two-step process. In the first step fossil fuel is converted into CO<sub>2</sub> and hydrogen gas (H<sub>2</sub>) (Steenefeldt et al. 2006). Then in a second step, the H<sub>2</sub> and the CO<sub>2</sub> are individually separated. A smaller installation can be used due to the higher partial pressure of the CO<sub>2</sub> as compared to the post-combustion process for CO<sub>2</sub> separation, although the separation procedure is the same. This technology demands a significant change in the existing power plants and may not be suitable. However, this technology is proven successful for new power plants.

### ***21.3.3 Oxyfuel Combustion Capture***

This process is similar to traditional post-combustion CO<sub>2</sub> capture where combustion is carried out in the presence of oxygen (O<sub>2</sub>), instead of air, as shown in Fig. 21.3c. The significant advantage of this technique is the exhaust gases contain only CO<sub>2</sub> and steam. Water is separated from the exhaust by cooling the gases to a temperature less than the condensation temperature of water vapor. Almost total CO<sub>2</sub> can be captured using this technique. At present oxygen is separated from the air at cryogenic temperatures, where the air is cooled to liquefying temperature and oxygen is separated from other gases. This process is costly and energy-intensive. However, recent developments in membrane technologies that separate oxygen from the air may

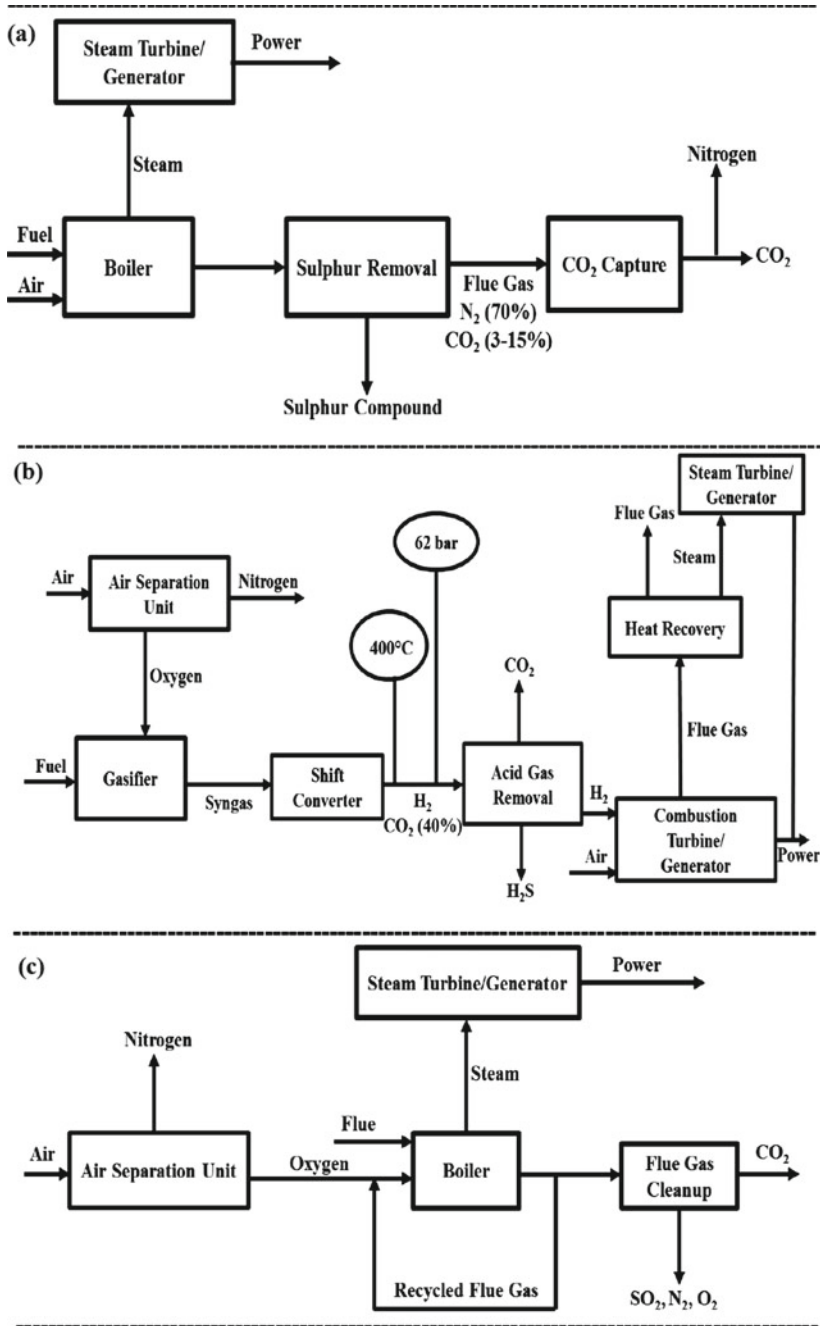


Fig. 21.3 Carbon dioxide capture in a post-, b pre-, and c oxy-combustion process (Figueroa et al. 2008)



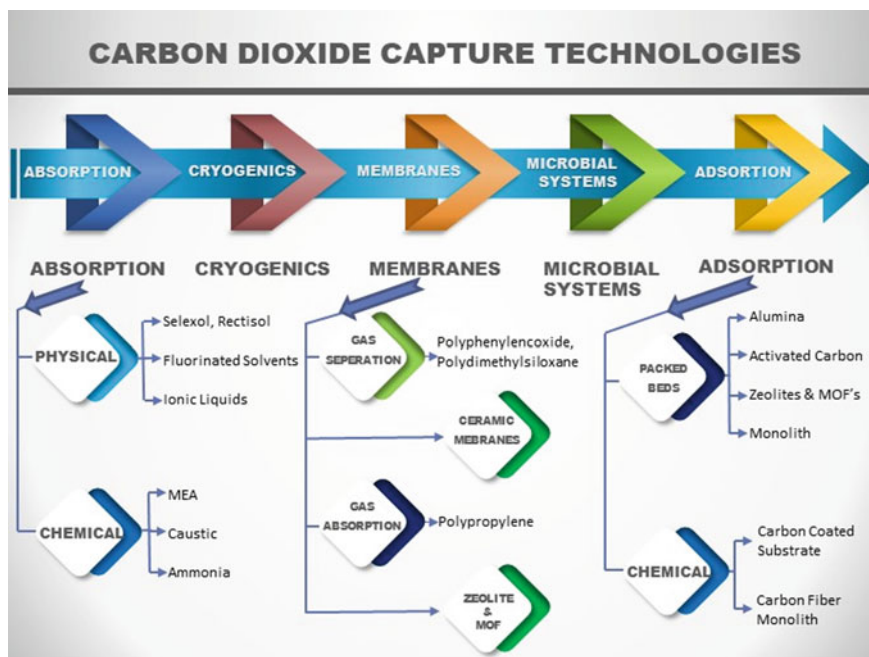


Fig. 21.4 Carbon dioxide capture technologies (Rubin et al. 2012)

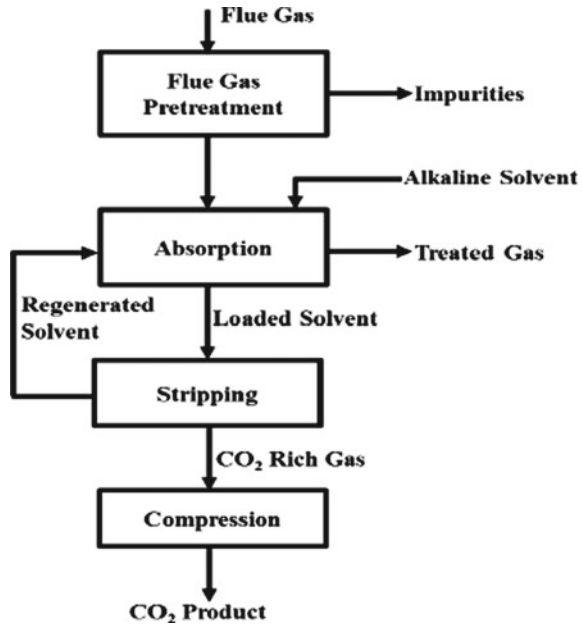
significantly lower the costs. The combustion of fossil fuels and pure oxygen generates high thermal stress; hence the development of new materials having prolonged thermal stability and durability is highly essential in this regard.

These separation techniques face challenges related to capturing technologies and materials required to sustain the high and low pressures of  $\text{CO}_2$  during the separation process. A wide range of solid materials are available for  $\text{CO}_2$  separation techniques, and nowadays some new materials are also emerging. Figure 21.4 shows the different carbon dioxide capture technologies and are discussed in subsequent sections.

### 21.3.4 Absorption Process

Both the chemical and physical adsorption processes are commonly used to separate  $\text{CO}_2$  in petroleum and chemical industries. Physical absorption on solvents depends on the operating pressure and temperature, generally occurs at high pressures and low temperature. Various physical solvents used for  $\text{CO}_2$  separation are *N*-methyl-2-pyrrolidone, methanol, propylene carbonate, polyethylene glycol dimethyl ether, and sulfolane. Chemical absorption which is based on chemical reactions between  $\text{CO}_2$  and one or more central absorbent such as aqueous solutions of mono-, di- or tri-ethanol amines, di isopropanol amine, potassium carbonate, sodium hydroxide and

**Fig. 21.5** Basic flow diagram for post-combustion capture of CO<sub>2</sub> using chemical absorption (Choi et al. 2009)



sodium carbonate, as shown in Fig. 21.5 (Choi et al. 2009). As CO<sub>2</sub> is acidic, the basic solvent acts as a recipe to absorb CO<sub>2</sub>. Some of the solvents such as amines (such as mono-, di- and triethanolamine), Selexol, Rectisol, ammonia solutions, and fluorinated solvents have been used commercially in absorption-based CO<sub>2</sub> separation. Amines are the most preferred absorbents for this purpose due to their high basicity and different reaction rates concerning the various acid gases. However, amines display high throughput CO<sub>2</sub> absorption but are associated with various disadvantages including (1) high regeneration energy, (2) poor regeneration of solvent, (3) low CO<sub>2</sub> loading capacity of the solvent, (4) equipment corrosion. In recent years, most researchers have been attracted to ionic liquids to mitigate the above shortcomings due to their great potential in the absorption of CO<sub>2</sub> and environment-friendly nature (Choi et al. 2009; Damen et al. 2006).

### 21.3.5 Cryogenic Process

The cryogenic process is filtering CO<sub>2</sub> from the air contaminated with a CO<sub>2</sub> percentage of typically more than 90%. The method of capturing CO<sub>2</sub> is by cooling the CO<sub>2</sub> and distilling it. Hence this process is also known as Cryogenic distillation at 31.1 and -56.6 °C, the critical and triple point temperatures. With this process's help, the output we get is liquefied CO<sub>2</sub> and can be transported easily, but needs the water to be pulled out before cooling (Tuiniera et al. 2010).

### 21.3.6 Membranes

Multiple kinds of membranes used for the separation of CO<sub>2</sub> such as Polymeric, Porous inorganic, and Palladium membranes, are economical and tailor finished. The membranes are porous assembly, and the essential factors depending on the selection are its Selectivity and Porousness. The Gas is fed into the system separated by the membrane, depending on the membrane's porosity; the CO<sub>2</sub> gets filtered and is sent to the other side of the membrane. Anyways much separation is not possible by using a single-stage. Therefore multi-stage processes are required, which lead to an increase in price and complication (Khoo and Tan 2006; Olajire 2010; Pires et al. 2011).

A fluid absorbent can also be used, like amine after passing through the gas membranes, through the liquid absorbent wherein, they get separated as CO<sub>2</sub> depleted and CO<sub>2</sub> rich stream (Spigarelli and Kawatra 2013). Different types of Adsorption membranes can also be used, such as activated alumina, activated carbons, zeolites, mesoporous silicates, silica gel, MOFs for the rich concentration of separated CO<sub>2</sub> (Li et al. 2011).

### 21.3.7 Microbial Systems

Photobioreactors for microalgal bio-fixation have recently gained lots of interest in CO<sub>2</sub> mitigation. Nowadays, several researchers have studied different biological methods using algae, bacteria, and plants for CO<sub>2</sub> separation among other available processes (Maeda et al. 1995; Kadam 2002). Due to lack of availability of information on microorganism growth and limited production of algae, removal of CO<sub>2</sub> by using algae is not capable of meeting the requirement set by the DOE/NETL (90% CO<sub>2</sub> capture at less than 35% increase in the cost of electricity) (Ebner and Ritter 2009). A few researchers successfully attempted the chemoautotrophic microorganism to produce inorganic chemicals instead of light energy for CO<sub>2</sub> removal (Kwak et al. 2006).

### 21.3.8 Adsorption

Adsorption is one of the alternative methods for capturing CO<sub>2</sub> with less pressure variation, faster reaction process, and a right amount of CO<sub>2</sub> storage than the other technologies discussed above, (Songolzadeh et al. 2012) says the price of Carbon dioxide capture is low with adsorption technology.

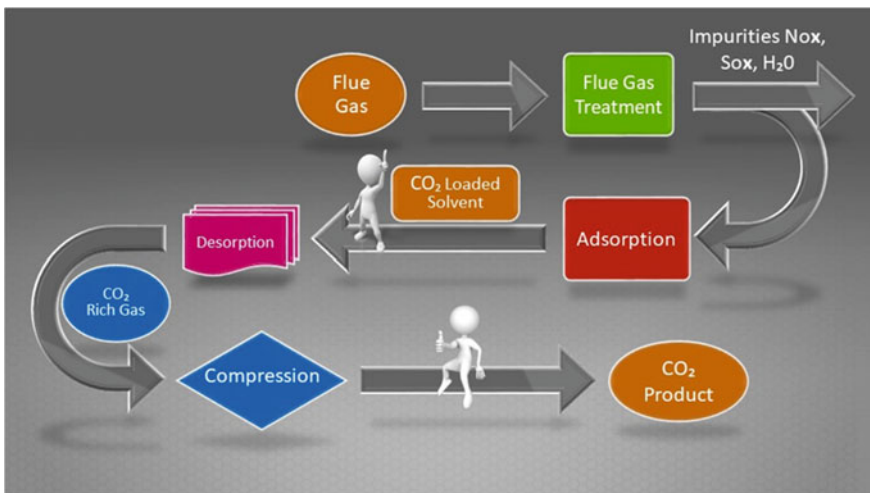
The adsorption process occurs between the Adsorbent, i.e., the solid material and the Adsorbate, i.e., gas. The Gas (adsorbate) is passed over the solid material, which is adsorbed by the solid (adsorbent). Adsorption process is either physical or chemical

adsorption. Physical adsorption is the process in which the gas (adsorbate) is passed over the solid surface (adsorbent), which adsorbs gas in the micro and mesopores of the adsorbent. Chemical adsorption takes place with chemical reactions among the adsorbent and adsorbate, which could not be wholly reversible but on the other hand, the physical adsorption method could be entirely reversed either by using heat or by pressure. The adsorption process's various parameters can be the surface area of the solid material, more the area—more the adsorption, temperature, pressure, and pore sizes (Ruthven 1984; Rouquerol et al. 1999; Ishida and Jin 1994).

The flowchart shown in Fig. 21.6, explains the working of the adsorption process. When gas is supplied to the bed that adsorbs  $\text{CO}_2$  and rejects other gases, when the bed reaches the stage of saturation, the same method is applied to all other beds. With the help of pressure and temperature variation, the  $\text{CO}_2$  can be regenerated from the bed (Spigarelli and Kawatra 2013).

Based on the microporous structure and morphology, the adsorbents are roughly classified into amorphous materials (e.g., silica gel, alumina, clays, other oxides, etc.), zeolites, and activated carbons as suggested by Ruthven (1984). Nowadays, most researchers are also focused on novel solid adsorbents like metal–organic frameworks for high  $\text{CO}_2$  adsorption capacity.

Activated carbons are inexpensive, insensitive to moisture, and exhibit a strong affinity for organic substances (Cook et al. 1999). They also exhibit high surface area, large micropore volume, broad pore size distribution, high  $\text{CO}_2$  adsorption capacity, and thermal stability (Choi et al. 2009; Lal 2008; Lozano-Castelló et al. 2002). Kim et al. (2003) reported that the chemically inert graphite surface area and large internal area of the activated carbons are the fundamental reasons for their strong adsorption capacity of non-polar molecules like  $\text{CO}_2$ . Moreover, activated



**Fig. 21.6** Flow chart representation for capturing  $\text{CO}_2$

carbon may be compacted efficiently into a packed bed with or without a binder and manufactured cheaply in vast quantities (Bagheri and Abedi 2011).

In the last few decades, numerous studies have been performed by many researchers on the preparation and characterization of the activated carbons focused on the CO<sub>2</sub> separation to reach an optimum adsorption capacity (Na et al. 2001; Wang et al. 2008; Siriwardane et al. 2001; Pevida et al. 2008; Przepiórski et al. 2004; Lu et al. 2008). These studies revealed that activated carbons could be synthesized with high microporosity and high surface area in the carbon matrix formed by an amorphous solid material of small pores, where the density of adsorbed phase CO<sub>2</sub> behaves like a liquid phase and thus provide a high storage density.

The activated carbons are usually developed and synthesized from various organic precursors rich in carbon content like petroleum coke, anthracite and lignite, bituminous coal, wood, and some types of polymers. Due to increasing usage, the activated carbons are manufactured cheaply from waste tires, biomass, wheat and sorghum and also from several agricultural waste materials, like walnut shells, oil palm stones, coconut shells, rice husk, cherry stones, corncobs, and date pits (Choi et al. 2009; Ruthven 1984). These agriculture waste products contain low ash and high carbon contents, and hence they yield good quality activated carbons producing large pore volumes and high surface area. The adsorbents are created in the micro and macroporous types of activated carbon by eliminating carbon atoms using different activation processes.

The synthesis of activated carbons from raw materials generally consists of two activation methods: physical and chemical (Lozano-Castelló et al. 2002). The physical activation process comprises carbonization and activation of the precursor material at high temperatures from 700 to 1000 °C under an inert atmosphere (Marsh and Rodriguez-Reinoso 2006). During the chemical activation, the carbonaceous material (precursor) is impregnated and heated under an inert atmosphere at higher temperatures of about 400–1000 °C with a chemical agent such as H<sub>3</sub>PO<sub>4</sub>, NaOH, KOH, and ZnCl<sub>2</sub>. The activation agents are crucial in the precursor materials' pyrolytic decomposition (Arash et al. 2011).

## 21.4 Features of a Promising Carbon Adsorbent for Gas Storage Systems

Numerous theoretical and experimental studies performed by many researchers have concluded that the CO<sub>2</sub> uptake mainly depends on the activated carbons' textural characteristics. Therefore, the activation processes and the preparation conditions which are essential for gas storage systems (Arash et al. 2011) need to be tuned to characterize a suitable carbon adsorbent that must have some desirable qualities such as:

1. High surface area (>1000 m<sup>2</sup>/g), which contributes a linear relationship with the CO<sub>2</sub> adsorption capacity (Sircar et al. 1996).

2. High microporosity to enhance small molecules' adsorption like CO<sub>2</sub> (Marsh and Rodriguez-Reinoso 2006).
3. A narrow pore size distribution centered around 8 Å, which optimizes the adsorbed phase (Matranga et al. 1992).
4. A relatively low mesoporosity facilitates the kinetics of the adsorption and desorption processes (Marsh and Rodriguez-Reinoso 2006).
5. High compactness increases the bulk density and consequently, the volumetric storage capacity (Prauchner and Rodríguez-Reinoso 2008).

These adsorbent characteristics are mostly obtained by measuring the N<sub>2</sub> and CO<sub>2</sub> adsorption isotherms, analyzed by different models or methods.

## 21.5 Applications of CO<sub>2</sub> Storage

Figure 21.7 shows the various usages of CO<sub>2</sub> in the fields of Refrigerants, plastics, Fire protection systems, chemical preparations, food products, environment, minerals, science, and safety (Pierantozzi 1993).

Since the Green House Gases contains 77% of CO<sub>2</sub>, the CO<sub>2</sub> has the worst effect on the environment (Rahman et al. 2017). Hence, the concept of sequestration and storage of CO<sub>2</sub> from the environment received great interest from researchers worldwide. From several studies, it is observed that CO<sub>2</sub> can be stored by adsorption in many materials like silica, zeolite, activated carbon, etc. These CO<sub>2</sub> storage technologies become a promising solution for the benefit of upcoming generations. Several

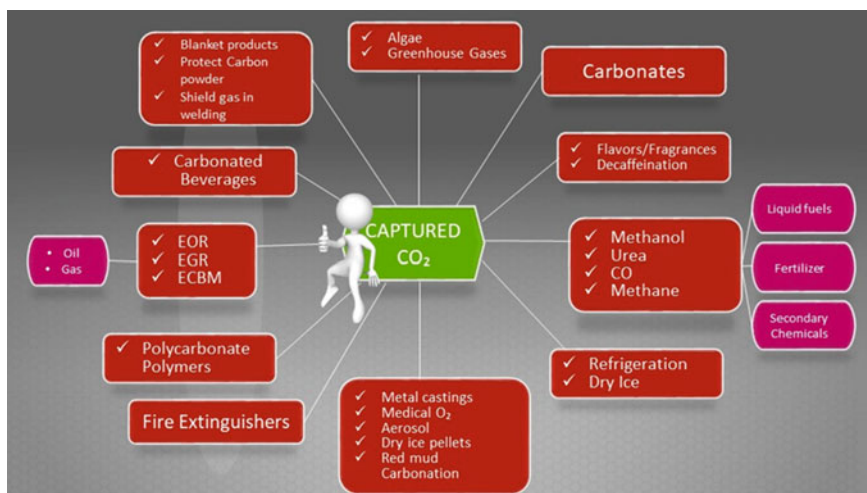


Fig. 21.7 Applications of captured CO<sub>2</sub> (Damiani et al. 2011)

studies are available in the literature on the characterization of adsorbent materials which helps to identify the CO<sub>2</sub> storage capacity. The adsorption/desorption characteristics, thermal stability of the used materials, and their reaction kinetics are the essential required parameters for the development of any sorption-based thermodynamic system.

Singh and Anil Kumar (2017a) theoretically and experimentally examined the adsorption and desorption characteristics of CO<sub>2</sub> for three different types of activated carbons namely Norit Darco (100 mesh size), Norit Darco (12–20 US mesh size), and Norit RB3 (steam activated rod). They observed that an increase in supply pressure increases the CO<sub>2</sub> adsorption capacity. Later, the simulation of experimentally measured isotherm is carried out using the D-A Model. Some researchers (Hill 1949, 1950; Everett 1965) theoretically studied the adsorption phenomena of CO<sub>2</sub> on the solid adsorbent. Young and Crowell (1952) investigated the thermodynamic properties of solid adsorbents and discovered the importance of spreading pressure and surface area on the physical adsorption process. For the enhancement of CO<sub>2</sub> adsorption capacity at lower partial pressures, the development of some amine-tethered mesoporous silica materials is presented by several researchers (Belmabkhout and Sayari 2009, 2010a; Hicks et al. 2008; Brunelli et al. 2012; Geoppert et al. 2012). In some studies (Belmabkhout and Sayari 2010b; Belmabkhout et al. 2011; Heydari-Gorgi and Yang 2011), for good support to amine tethering, the novel pore expanded mesoporous silica materials are proposed. It permits the exploitation of internal space, which cannot be possible with SBA-15, KIT-6, MSM-41, and zeolite, (Heydari-Gorji et al. 2011; Yang et al. 1999). On the other hand, the effect of CO<sub>2</sub> desorption and adsorption isotherms on PE-MSM-41 at different operating pressures (0–25 bar) and temperatures was investigated by Loganathan et al. (2015), and they found that the CO<sub>2</sub> desorption and adsorption is a reversible phenomenon as the isotherms coincide with each other.

Shen et al. (2010) carried out an experimental investigation on carbon dioxide reaction rates and storage of pitch-based activated carbon for the temperature range of 303 K–423 K and the pressure range of 0–1 bar pressure. Balsamo et al. (2013) observed that the operating temperatures are inversely proportional to the reaction kinetics, whereas the supply pressures are directly proportional to the reaction kinetics. An experimental investigation on CO<sub>2</sub> storage and reaction kinetics of zeolite 13X and activated carbon at operating temperatures of 298, 308, 318, and 328 K, and up to the pressure of 30 bar was carried out by Zhang et al. (2010) and they have concluded that, at low pressures, the zeolite 13X comparatively have more adsorption rates as compared to the activated carbon. Apart from this, they also observed that the activated carbon has higher adsorption capacities at higher pressures compared to zeolite 13X.

Many studies have been carried out for the investigation of CO<sub>2</sub> storage capacities of different adsorbent materials, but very little effort was given to the development of thermodynamic systems based on CO<sub>2</sub> adsorption. The thermodynamic systems like cooling and heating system based on CO<sub>2</sub> adsorption can be operated by utilizing waste heat as input, whereas the desired cooling output can be achieved by the heat



of desorption during the endothermic process. The several thermophysical and thermodynamic properties (like reaction kinetics, storage capacity, etc.) of adsorbent materials are required for the development of any solid–gas sorption thermodynamic system (Sharma and Anil Kumar 2014). The screening of suitable working pairs depends on the reaction kinetics, adsorption isotherms, adsorption and desorption heats, internal energy, specific heat capacity, etc. The activated carbon exhibits better thermal stability, high surface area, and better pore size distribution along with high adsorption capacity and fast kinetics. Hence, it is highly suitable for the adsorption of CO<sub>2</sub> compared to other solid adsorbents (Sircar et al. 1996; Damiani et al. 2011; Yates et al. 2000; Saxena et al. 2014; Knoblauch 1993). The economic suitability for large quantity and non-reactive to moisture makes activated carbon adopt it for many applications. Activated carbons are also analyzed for several applications like CO<sub>2</sub> purification and separation, thermodynamic devices and systems based on sorption, cryo-coolers, and energy storage systems (Liu et al. 2005; Jee et al. 2005; Saha et al. 2006; Baby and Prakash 2005; Schlappbach and Züttel 2001). Singh and Anil Kumar (2017b) recently conducted the thermodynamic analysis of activated carbon and CO<sub>2</sub>-based cooling system and found the maximum COP of 0.09 with CO<sub>2</sub>-Norit RB3 pair at an operating temperature of 80 °C and by maintaining the evaporator temperature at 15 °C. On the other hand, the heat pump working on a geothermal ground source for a low-temperature hydronic heating system was discussed by Banjac et al. (2007). Satpute and John Rajan (2018) have presented the recent development in cooling technologies based on solar PV system's.

### ***21.5.1 Adsorbent-Based Cooling System***

The refrigeration and air-conditioning systems are widely utilized in various applications like electronic industries, food preservation, chemical plants, petrochemical plants, automobiles, cold storage units etc. The refrigeration and air-conditioning industries have been phase-out from hydrochlorofluorocarbons (HCFCs) to hydrofluorocarbons (HFCs) refrigerant due to ozone layer depletion and global warming effect after the imposition of international restriction on the use of HCFCs and HFCs (Meunier 1993). However, the global warming problem is still being intensified owing to the utilization of HFC refrigerants. The energy utilized for running refrigeration and air-conditioning systems is around 15% across the world, as reported by the International Institute of Refrigeration (IIR) (Choudhury et al. 2010; El-Sharkawy et al. 2014).

During the hot climate season, particularly in India, refrigeration and air-conditioning units are intensively used, electricity demand is at its peak. Adsorption-based cooling system reduces the electricity demand, and these systems are driven by using low-grade thermal energy like solar energy or low-grade waste heat energy, minimizing the effects of global warming (Meunier 1993, 1998). The advantages of adsorption-based cooling systems include the more straightforward control, lesser operational cost, free of moving parts, less maintenance, non-toxic, and eco-friendly



compared to the mechanical vapor compression cooling system (Wang and Oliveira 2006; Wang and Wang 1997). The attractive features of the adsorption-based cooling systems are listed below (Ullah et al. 2013; Wang et al. 2009);

1. Adsorption-based heating/cooling systems can run up to 500 °C (high heat source temperature) without corrosion, while above 200 °C heat source temperature corrosion occurs in the case of absorption technology.
2. Adsorption-based cooling systems can be driven at heat source temperatures as low as 50 °C, but in the case of absorption technology, at least 70 °C of heat source temperature is required.
3. It is suitable for severe vibration applications than absorption systems.
4. The adsorption system's significant advantage is simple in design compared to the absorption system or vapor compressor system.

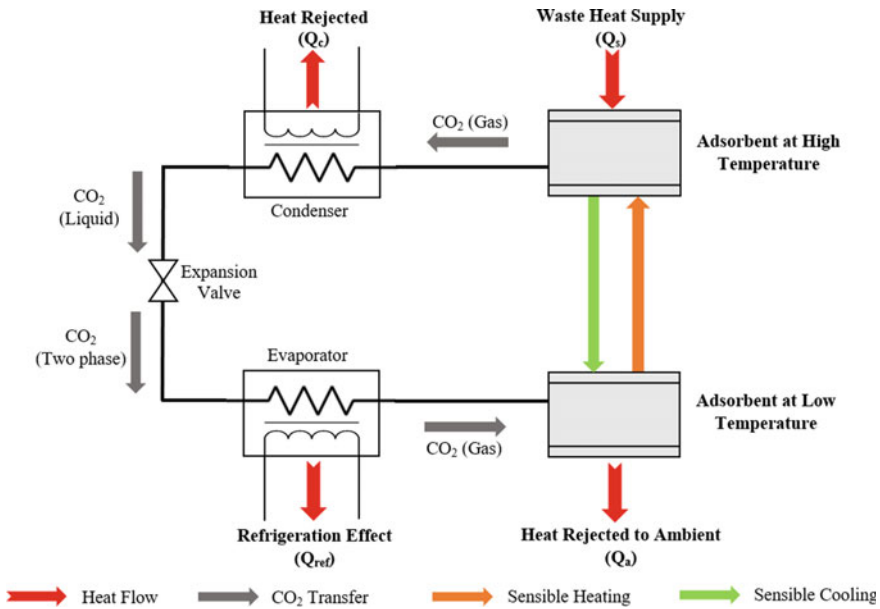
### 21.5.1.1 CO<sub>2</sub> Adsorbent-Based Vapor Adsorption Refrigeration System

The schematic of vapor adsorption refrigeration system based on CO<sub>2</sub> adsorbent is presented in Fig. 21.8. A set of a condenser, expansion valve, evaporator, and a sorption reactor constitutes the current system. Firstly, the refrigeration effect ( $Q_{ref}$ ) is produced by the evaporator by evaporating CO<sub>2</sub>. Then, the evaporated low-pressure CO<sub>2</sub> is supplied to the adsorber where it gets adsorbed as a low-temperature adsorbent. Since adsorption is the exothermic process, some amount of heat ( $Q_a$ ) gets generated which is rejected to ambient. After the adsorption process, the adsorber is detached from the evaporator and sensible heating is provided to reach the required condenser temperature and pressure. Once the adsorber reaches the equilibrium condition, the waste heat ( $Q_s$ ) is provided from the waste heat source to desorb CO<sub>2</sub> from the adsorbent. The desorbed CO<sub>2</sub> is allowed to condense in the condenser and  $Q_c$  amount of heat is rejected to the ambient. The expansion of CO<sub>2</sub> in between the condenser and evaporator through the expansion valve completes the operation.

### 21.5.1.2 CO<sub>2</sub> Adsorbent-Based Sorption Refrigeration System

The schematic of CSRS is presented in Fig. 21.9 at refrigeration output temperature ( $T_{ref}$ ) = 0 °C, ambient temperature ( $T_a$ ) = 25 °C, and heat source temperature ( $T_{reg}$ ) = 100 °C. A CSRS consists of two CO<sub>2</sub> transfer, two refrigeration, and two regeneration along with one sensible cooling and one sensible heating process. As compared to CO<sub>2</sub>-A VARS (Fig3.2), in CSRS there is no need for the expansion device, heat exchangers, etc. The CSRS needs a pair of two adsorbent materials for producing the desired refrigeration effect. In CSRS systems, the refrigeration effect is produced by utilizing the reaction heats which are involved in the adsorption/desorption of CO<sub>2</sub> on/from adsorbent materials.

Refer to Fig. 21.9: A<sub>1</sub>-A<sub>1</sub>' and A<sub>2</sub>-A<sub>2</sub>' are the adsorbents used in the high-pressure side and low-pressure side respectively. During the refrigeration process, adsorbent A<sub>1</sub> at point 1 desorbs CO<sub>2</sub> at refrigeration output temperature ( $T_{ref}$ ), which gets



**Fig. 21.8** Scheme of CO<sub>2</sub> adsorbent-based vapor adsorption refrigeration system (Naveed and Sharma 2021)

adsorbed by adsorbent A<sub>2</sub> at point 2 at ambient temperature ( $T_a$ ). The desorption heat (generated during the endothermic reaction) gets absorbed by adsorbent A<sub>1</sub> which is responsible for producing the refrigeration effect ( $Q_{ref}$ ) at refrigeration output temperature ( $T_{ref}$ ), and the adsorption heat ( $Q_a$ ) (generated during the exothermic reaction) gets released by adsorbent A<sub>2</sub> which is released to the ambient at  $T_a$ . Simultaneously, during the regeneration process, the adsorbent A<sub>2</sub>' desorbs CO<sub>2</sub> by absorbing the required heat of desorption ( $Q_{reg}$ ) from the waste heat source at  $T_{reg}$  and the same desorbed CO<sub>2</sub> gets adsorbed by adsorbent A<sub>1</sub>' results in the generation of adsorption heat ( $Q_a'$ ) which is rejected to ambient at  $T_a$ . After that, the sensible cooling is provided to adsorbent A<sub>1</sub>' to cool it from  $T_a$  to  $T_{ref}$  and to adsorbent A<sub>2</sub>' to cool it from  $T_{reg}$  to  $T_a$ , while sensible heating of adsorbent A<sub>1</sub> from  $T_{ref}$  to  $T_a$  and adsorbent A<sub>2</sub> from  $T_a$  to  $T_{reg}$ . Sensible cooling and heating are provided to the system to get it ready for the next cycle.

## 21.6 Conclusions

The study on carbon dioxide storage systems led to the following conclusions:

1. Solid-state CO<sub>2</sub> storage technique found promising for safe storage.

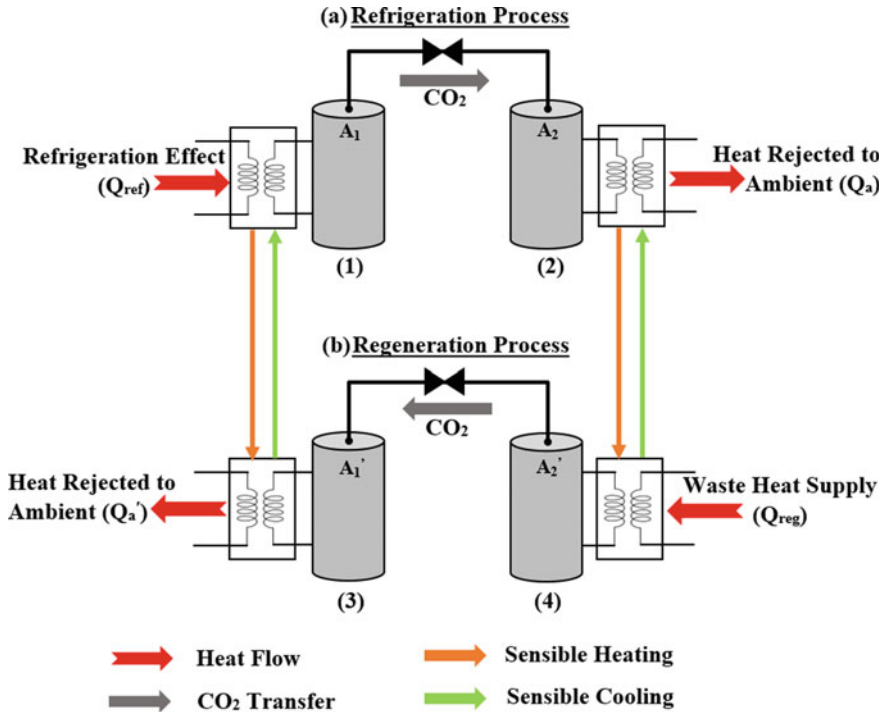


Fig. 21.9 Scheme of  $CO_2$  adsorbent-based sorption refrigeration system (Naveed and Sharma 2020)

2. The adsorption phenomena of  $CO_2$  on adsorbent materials is exothermic which can be utilized to develop thermodynamic systems.
3.  $CO_2$  sorption refrigeration system and vapor adsorption system can be the best alternative to the conventional refrigeration system.
4. The  $CO_2$  sorption refrigeration system possesses higher COP than the  $CO_2$  vapor adsorption system due to the utilization of heat of reactions.

## References

Arash A, Wan M, Mjalli F (2011) Comparative study of the textural characteristics of oil palm shell activated carbon produced by chemical and physical activation for methane adsorption. *Chem Eng Res Des* 89:567–664

Asif M, Muneer T (2007) Energy supply, its demand and security issues for developed and emerging economies. *Renew Sustain Energy Rev* 11:1388–1413

Baby R, Prakash M (2005) Improving the performance of an active carbon-nitrogen adsorption cryocooler by thermal regeneration. *Carbon* 43:2338–2343

- Bagheri N, Abedi J (2011) Adsorption of methane on corn cobs based activated carbon. *Chem Eng Res Des* 89:2038–2043
- Balsamo M, Budinova T, Erto A, Lancia A, Petrova B, Petrov N, Tsyntsarski B (2013) CO<sub>2</sub> adsorption onto synthetic activated carbon: kinetics thermodynamic and regeneration studies. *Sep Purif Technol* 116:214–221
- Banjac M, Bogosav V, Gojak M (2007) Low temperature hydronic heating system with radiators and geothermal ground source heat pump. *FME Transactions* 35:129–134
- Barbir F, Veziroğlu T, Plass H (1990) Environmental damage due to fossil fuels use. *Int J Hydrogen Energy* 15:739–749
- Belmabkhout Y, Sayari A (2009) Effect of pore expansion and amine functionalization of mesoporous silica on CO<sub>2</sub> adsorption over a wide range of conditions. *Adsorption* 15:318–328
- Belmabkhout Y, Sayari A (2010a) Stabilization of amine-containing CO<sub>2</sub> adsorbents: dramatic effect of water vapor. *J Am Chem Soc* 132:6312–6314
- Belmabkhout Y, Sayari A (2010b) Isothermal versus non-isothermal adsorption–desorption cycling of triamine-grafted pore-expanded MCM-41 mesoporous silica for CO<sub>2</sub> capture from flue gas. *Energy Fuels* 24:5273–5280
- Belmabkhout Y, Heymans N, Weireld G, Sayari A (2011) Simultaneous adsorption of H<sub>2</sub>S and CO<sub>2</sub> on triamine-grafted pore-expanded mesoporous MCM-41 silica. *Energy Fuels* 25:1310–1315
- Bernstein L, Lee A, Crookshank S (2006) Carbon dioxide capture and storage: a status report. *Climate Policy* 6:241–246
- Bruce J, Yi H, Haites E (1996) *Climate change 1995: economic and social dimensions of climate change: contribution of working group III to the second assessment report of the intergovernmental panel on climate change*. Cambridge University Press, Cambridge
- Brunelli N, Didas S, Venkatasubhai K, Jones C (2012) Tuning cooperativity by controlling the linker length of silica supported amines in catalysis and CO<sub>2</sub> capture. *J Am Chem Soc* 134:13950–13953
- Choi W, Seo J, Jang S, Jung J, Oh K (2009) Removal characteristics of CO<sub>2</sub> using aqueous MEA/AMP solutions in the absorption and regeneration process. *J Environ Sci* 21:907–913
- Choudhury B, Chatterjee P, Sarkar J (2010) Review paper on solarpowered air-conditioning through adsorption route. *Renew Sustain Energy Rev* 14:2189–2195
- Chunshan S (2006) Global challenges and strategies for control, conversion and utilization of CO<sub>2</sub> for sustainable development involving energy, catalysis, adsorption and chemical processing. *Catal Today* 115:2–32
- Cook T, Komodromos C, Quinn D, Ragan S (1999) *Carbon materials for advanced technologies*. Pergamon, New York, pp 269–302
- Damen K, Troost M, Faaji A, Turkenb W (2006) A comparison of electricity and hydrogen production systems with CO<sub>2</sub> capture and storage, part A: review and selection of promising conversion and capture technologies. *Prog Energy Combust Sci* 32:215–246
- Damiani D, Litynski J, McIlvried H, Vikara D, Srivastava R (2011) The US Department of Energy's R&D program to reduce greenhouse gas emissions through beneficial uses of carbon dioxide. *Greenhouse Gases Sci Technol*. <https://doi.org/10.1002/ghg.35>
- Dell R, Rand D (2004) *Clean energy, RSC clean technology monographs*. In: Clark JH (ed) *The royal society of chemistry*. Cambridge, UK
- Ebner A, Ritter J (2009) State-of-the-art adsorption and membrane separation processes for carbon dioxide production from carbon dioxide emitting industries. *Sep Sci Technol* 44:1273–1421
- El-Sharkawy I, Abdel Meguid H, Saha B (2014) Potential application of solar powered adsorption cooling systems in the Middle East. *Appl Therm Eng* 126:235–245
- EPA (2009) *Greenhouse gases threaten public health and the Environment/Science overwhelmingly shows greenhouse gas concentration at unprecedented levels due to human activity*. Environment/Protection Agency
- Everett D (1965) Interactions between adsorbed molecules. *Discuss Faraday Soc* 40:177–187

- Figueroa J, Fout T, Plasynski S, McIlvried H, Srivastava R (2008) Advance in CO<sub>2</sub> capture technology-the U.S. department of energy's carbon sequestration program. *Int J Greenhouse Gas Control* 2:9–20
- Geoppert A, Czaun M, May R, Surya Prakash G, Olah G, Narayanan S (2012) Carbon dioxide capture from the air using a polyamine based regenerable solid adsorbent. *J Am Chem Soc* 133:20164–20167
- Heydari-Gorgi A, Yang Y SA (2011) Effect of pore length on CO<sub>2</sub> adsorption over amine-modified mesoporous silicas. *Energy Fuels* 25:4206–4210
- Heydari-Gorji A, Belmabkhout Y, Sayari A (2011) Polyethylenimine-impregnated mesoporous silica: effect of amine loading and surface alkyl chains on CO<sub>2</sub> adsorption. *Langmuir* 27:12411–12416
- Hicks J, Drese J, Fauth D, Gray ML, Qi G, Jones CW (2008) Designing adsorbents for CO<sub>2</sub> capture from flue gas-hyperbranched aminosilicas capable of capturing CO<sub>2</sub> reversibly. *J Am Chem Soc* 130:2902–2903
- Hill T (1949) Statistical mechanics of adsorption V. thermodynamic and heat of adsorption. *J Chem Phys* 17:520–535
- Hill T (1950) Statistical mechanics of adsorption IX. Adsorption thermodynamics and solution thermodynamics. *J Chem Phys* 18:246–256
- Houghton J (2005) Global warming. *Rep Prog Phys* 68:1343–1403
- Ishida M, Jin H (1994) A new advanced power-generation system using chemical-looping combustion. *Energy* 19:415–422
- Lee J, Kim M, Lee C (2005) Pressure swing adsorption processes to purify oxygen using a carbon molecular sieve. *Chem Eng Sci* 60:869–882
- Kadam K (2002) Environmental implications of power generation via coal microalgae cofiring. *Energy* 27:905–922
- Khoo H, Tan R (2006) Life cycle investigation of CO<sub>2</sub> recovery and sequestration. *Environ Sci Technol* 40:4016–4024
- Kim B, Kum G, Seo Y (2003) Adsorption of methane and ethane into single walled carbon nanotubes and slit-shaped carbonaceous pores. *Korean J Chem Eng* 20:104–109
- Knoblauch K (1993) Activated carbon and carbon molecular sieves in gas separation and purification. *Gas Sep Purif* 7:195–196
- Kwak K, Jung S, Chung S, Kang C, Huh Y, Bae S (2006) Optimization of culture conditions for CO<sub>2</sub> fixation by a chemoautotrophic microorganism, strain YN-1 using factorial design. *Biochem Eng J* 31:1–7
- Lal R (2008) Sequestration of atmospheric CO<sub>2</sub> in global carbon pools. *Energy Environmental Science* 1:86–100
- Li J, Ma Y, McCarthy M, Sculley J, Yu J, Jeong H, Balbuena P, Zhou H (2011) Carbon dioxide capture-related gas adsorption and separation in metal-organic frameworks. *Coord Chem Rev* 255:1791–1823
- Liu X, Li J, Zhou L, Huang D, Zhou Y (2005) Adsorption of CO<sub>2</sub>, CH<sub>4</sub> and N<sub>2</sub> on ordered mesoporous silica molecular sieve. *Chem Phys Lett* 415:198–201
- Loganathan S, Tikmani M, Ghoshal AK (2015) Pore-expanded MCM-41 for CO<sub>2</sub> adsorption: experimental and isotherm modeling studies. *Chem Eng J* 280:9–17
- Lozano-Castelló D, Alcañiz-Monge J, De La Casa-Lillo M, Cazorla Amorós D, Linares-Solano A (2002) Advances in the study of methane storage in porous carbonaceous materials. *Fuel* 81:1777–1803
- Lu C, Bai H, Wu B, Su F, Fen-Hwang J (2008) Comparative study of CO<sub>2</sub> capture by carbon nanotubes, activated carbons and zeolites. *Energy Fuels* 22:3050–3056
- Maeda K, Owada M, Kimura N, Omata K, Karube I (1995) CO<sub>2</sub> fixation from the flue gas on coal-fired thermal power plant by microalgae. *Energy Convers Manage* 36:717–720
- Maggio GCG (2012) When will oil, natural gas, and coal peak? *Fuel* 98:111–123
- Marsh H, Rodriguez-Reinoso F (2006) Activated carbon. Elsevier, Amsterdam

- Matranga K, Myers A, Glandt E (1992) Storage of natural gas by adsorption on activated carbon. *Chem Eng Sci* 47:1569–1579
- Meisen A, Shuai X (1997) Research and development issues in CO<sub>2</sub> capture. *Energy Convers Manage* 38:37–42
- Meunier F (1993) Solid adsorption: an alternative to CFCs. *Heat Recovery Syst CHP* 13:289–295
- Meunier F (1998) Solid sorption heat powered cycles for cooling and heatpumping applications. *Appl Therm Eng* 18:715–729
- Na B, Koo K, Eum H, Lee H, Song H (2001) CO<sub>2</sub> recovery from flue gas by PSA process using activated carbon. *Korean J Chem Eng* 18:220–227
- Naveed SS, Sharma VK (2020) Thermodynamic simulation of CO<sub>2</sub>—Adsorbent based sorption refrigeration system. *FME Transactions* 48:187–194
- Naveed SS, Sharma VK (2021) Performance comparison between H<sub>2</sub>-metal hydrides and CO<sub>2</sub>-adsorbents based sorption refrigeration systems. *Int J Energy Res* 45:7851–7869
- Olajire A (2010) CO<sub>2</sub> capture and separation technologies for end-of-pipe applications—a review. *Energy* 35:2610–2628
- Pevida C, Plaza M, Arias B, Feroso H, Rubiera F, Pis J (2008) Surface modification of activated carbons for CO<sub>2</sub> capture. *Appl Surf Sci* 254:7165–7172
- Pierantozzi R (1993) Carbon dioxide, Kirk Othmer encyclopedia of chemical technology, 4th edn. Wiley, New York, pp 35–53
- Pires J, Martins F, Alvim-Ferraz M, Simoes M (2011) Recent developments on carbon capture and storage: an overview. *Chem Eng Res Des* 89:1446–1460
- Prauchner M, Rodríguez-Reinoso F (2008) Preparation of granular activated carbons for adsorption of natural gas. *Microporous Mesoporous Mater* 109:581–584
- Przepióński J, Skrodziewicz M, Morawski A (2004) High temperature ammonia treatment of activated carbon for enhancement of CO<sub>2</sub> adsorption. *Appl Surf Sci* 225:235–242
- Rackley S (2017) Carbon capture and storage. Butterworth-Heinemann, Elsevier, Burlington
- Rahman F, Aziz M, Saidur R, Bakar W, Hainin M, Putrajaya R, Hassan N (2017) Pollution to solution: capture and sequestration of carbon dioxide (CO<sub>2</sub>) and its utilization as a renewable energy source for a sustainable future. *Renew Sustain Energy Rev* 71:112–126
- Rouquerol F, Rouquerol J, Sing K (1999) Adsorption by powders and porous solids: principles, methodology and applications. Academic Press, United Kingdom
- Rubin E, Mantripragada H, Marks A, Versteeg P, Kitchin J (2012) The outlook for improved carbon capture technology. *Prog Energy Combust Sci* 38:630–671
- Ruthven D (1984) Principles of adsorption and adsorption processes. Wiley, London
- Saha B, Sharkawy I, Koyama S, Lee J, Kuwahara K (2006) Waste heat driven multi-bed adsorption chiller: heat exchangers overall thermal conductance on chiller performance. *Heat Transf Eng* 27:80–87
- Satpute J, John Rajan A (2018) Recent advancement in cooling technologies of solar photovoltaic (PV) system. *FME Transactions* 46:575–584
- Saxena R, Singh V, Anil Kumar E (2014) Carbon dioxide capture and sequestration by adsorption on activated carbon. *Energy Procedia* 54:320–329
- Schlapbach L, Züttel A (2001) Hydrogen-storage materials for mobile applications. *Nature* 414:353–358
- Sharma VK, Anil Kumar E (2014) Measurement and simulation of hydrogen storage and thermodynamic properties of LaNi<sub>4.7</sub>Al<sub>0.3</sub> hydride. *Int J Appl Eng Res* 9:985–994
- Shen C, Grande C, Rodrigues A (2010) Adsorption equilibrium and kinetics of CO<sub>2</sub> and N<sub>2</sub> on activated carbon beads. *Chem Eng J* 160:398–407
- Singh VK, Anil Kumar E (2017b) Measurement of CO<sub>2</sub> adsorption isotherms and kinetics of activated carbons suitable for the development of CO<sub>2</sub> based adsorption cooling systems. PhD Thesis, IIT Indore
- Singh V, Anil Kumar E (2017a) Measurement of CO<sub>2</sub> adsorption kinetics on activated carbon suitable for gas storage systems. *Greenhouse Gases Sci Technol* 7:182–201
- Sircar S, Golden T, Rao M (1996) Activated carbon for gas separation and storage. *Carbon* 34:1–12

- Siriwardane R, Shen M, Fisher E, Poston J (2001) Adsorption of CO<sub>2</sub> on molecular sieves and activated carbon. *Energy Fuels* 15:279–284
- Songolzadeh M, Ravanchi M, Soleimani M (2012) Carbon dioxide capture and storage: A general review on adsorbents. *World Acad Sci Eng Technol* 70:225–232
- Spigarelli B, Kawatra S (2013) Opportunities and challenges in carbon dioxide capture. *J CO<sub>2</sub> Utilization* 1:69–87
- Steeneveldt R, Berger B, Torp T (2006) CO<sub>2</sub> capture and storage closing the knowing-doing gap. *Chem Eng Res Des* 84:739–763
- Stewart C, Hessami M (2005) A study of methods of carbon dioxide capture and sequestration-The sustainability of a photosynthetic bioreactor approach. *Energy Convers Manage* 46:403–420
- Tuiniera M, Annalanda M, Kramer G, Kuipers J (2010) Cryogenic CO<sub>2</sub> capture using dynamically operated packed beds. *Chem Eng Sci* 65:114–119
- Ullah K, Saidur R, Ping H, Akikur R, Shuvo N (2013) A review of solar thermal refrigeration and cooling methods. *Renew Sustain Energy Rev* 24:499–513
- Wang R, Oliveira RRG (2006) Adsorption refrigeration-an efficient way to make good use of waste heat and solar energy. *Prog Energy Combust Sci* 32:424–458
- Wang L, Wang L (1997) Performance estimation of an adsorption cooling system for automobile waste heat recovery. *Appl Therm Eng* 12:1127–1139
- Wang Y, Zhou Y LC, Zhou L (2008) Comparative studies of CO<sub>2</sub> and CH<sub>4</sub> sorption on activated carbon in presence of water. *Colloids Surf a: Physicochemical Eng Aspects* 322:14–18
- Wang L, Wang R, Oliveira R (2009) A review on adsorption working pairs for refrigeration. *Renew Sustain Energy Rev* 13:518–534
- Yang Y, Kruk M, Jaroneic M, Sayari A (1999) Expanding the pore size of MCM-41 silicas: use of amines as expanders in direct synthesis and post synthesis procedures. *J Phys Chem* 103:3651–3658
- Yang H, Xu Z, Fan M, Gupta R, Slimane R, Bland A, Wright I (2008) Progress in carbon dioxide separation and capture: a review. *J Environ Sci* 20:14–27
- Yates M, Blanco J, Avila P, Martin M (2000) Honeycomb monoliths of activated carbons for effluent gas purification. *Microporous Mesoporous Mater* 37:201–208
- Young D, Crowell A (1952) *Physical adsorption of gases*. Butterworths, London
- Zanganeh K, Shafeen A (2007) A novel process integration, optimization and design approach for large-scale implementation of oxy-fired coal power plants with CO<sub>2</sub> capture. *Int J Greenhouse Gas Control* 1:47–54
- Zhang Z, Zhang W, Chen X, Xia Q, Li Z (2010) Adsorption of CO<sub>2</sub> on zeolite 13X and activated carbon with higher surface area. *Sep Sci Technol* 45:710–719